Istituto Nazionale di Fisica Nucleare

LNF–18/03
May 7, 2018

EuPRAXIA@SPARC_LAB

Conceptual Design Report

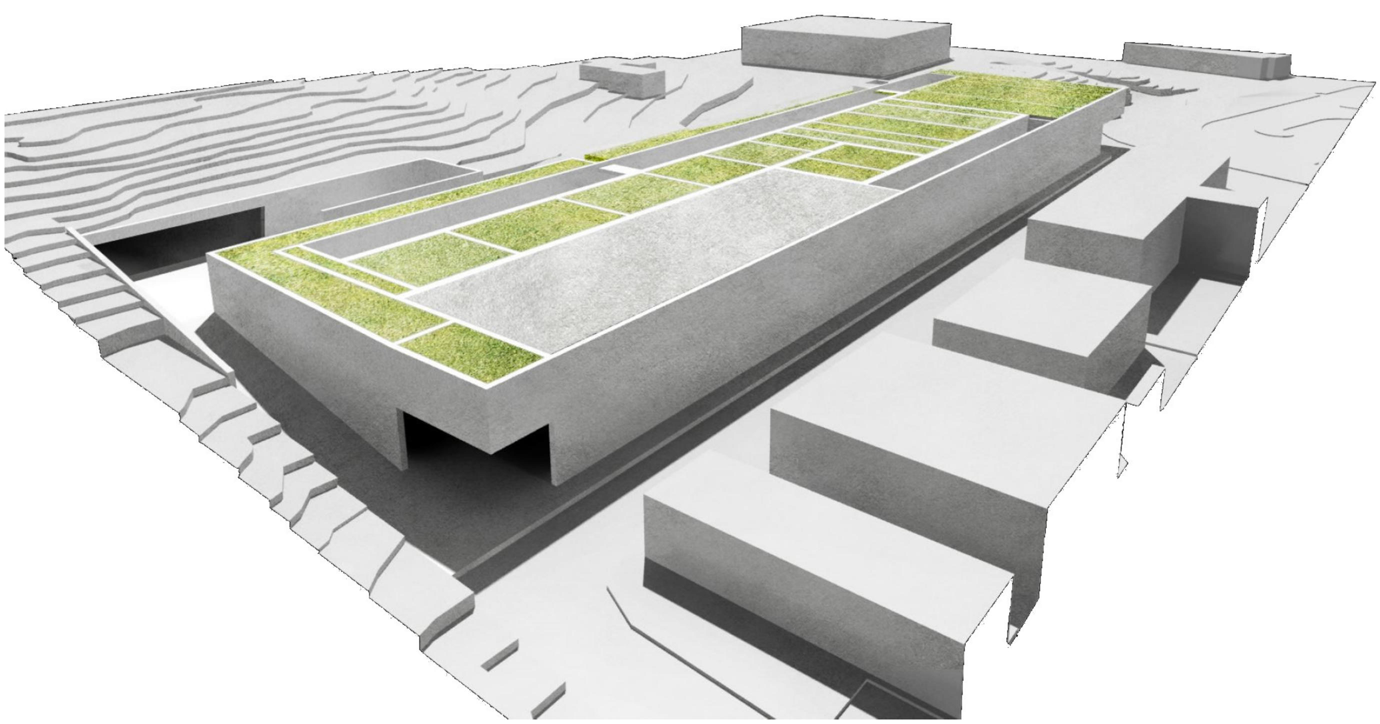

Authors

D. Alesini[a], M. P. Anania[a], M. Artioli[b], A. Bacci[c], S. Bartocci[d], R. Bedogni[a], M. Bellaveglia[a], A. Biagioni[a], F. Bisesto[a], F. Brandi[e], E. Brentegani[a], F. Broggi[c], B. Buonomo[a], P. Campana[a], G. Campogiani[a], C. Cannaos[d], S. Cantarella[a], F. Cardelli[a], M. Carpanese[f], M. Castellano[a], G. Castorina[g], N. Catalan Lasheras[h], E. Chiadroni[a], A. Cianchi[i], R. Cimino[a], F. Ciocci[f], D. Cirrincione[j], G. A. P. Cirrone[k], R. Clementi[a], M. Coreno[l], R. Corsini[h], M. Croia[a], A. Curcio[a], G. Costa[a], C. Curatolo[c], G. Cuttone[k], S. Dabagov[a], G. Dattoli[f], G. D'Auria[l], I. Debrot[c], M. Diomede[a,g], A. Drago[a], D. Di Giovenale[a], S. Di Mitri[l], G. Di Pirro[a], A. Esposito[a], M. Faiferri[d], M. Ferrario[a], L. Ficcadenti[g], F. Filippi[a], O. Frasciello[a], A. Gallo[a], A. Ghigo[a], L. Giannessi[f,l], A. Giribono[a], L. A. Gizzi[e], A. Grudiev[h], S. Guiducci[a], P. Koester[e], S. Incremona[a], F. Iungo[a], L. Labate[e], A. Latina[h], S. Licciardi[f], V. Lollo[a], S. Lupi[g], R. Manca[d], A. Marcelli[a,m,n], M. Marini[d], A. Marocchino[a], M. Marongiu[g], V. Martinelli[a], C. Masciovecchio[l], C. Mastino[d], A. Michelotti[a], C. Milardi[a], M. Migliorati[g], V. Minicozzi[i], F. Mira[g], S. Morante[i], A. Mostacci[g], F. Nguyen[f], S. Pagnutti[f], L. Palumbo[g], L. Pellegrino[a], A. Petralia[f], V. Petrillo[o], L. Piersanti[a], S. Pioli[a], D. Polese[d], R. Pompili[a], F. Pusceddu[d], A. Ricci[m], R. Ricci[a], R. Rochow[l], S. Romeo[a], J. B. Rosenzweig[p], M. Rossetti Conti[o], A. R. Rossi[c], U. Rotundo[a], L. Sabbatini[a], E. Sabia[f], O. Sans Plannell[a], D. Schulte[h], J. Scifo[a], V. Scuderi[k], L. Serafini[c], B. Spataro[a], A. Stecchi[a], A. Stella[a], V. Shpakov[a], F. Stellato[i], P. Tomassini[e], E. Turco[d], C. Vaccarezza[a], A. Vacchi[j], A. Vannozzi[a], G. Vantaggiato[e], A. Variola[a], S. Vescovi[a], F. Villa[a], W. Wuensch[h], A. Zigler[q], M. Zobov[a]

[a] *INFN - Laboratori Nazionali di Frascati, via E. Fermi 40, 00044 Frascati, Italy*
[b] *ENEA - Centro Ricerche Bologna, Via Martiri Monte Sole 4, 40129 Bologna, Italy*
[c] *INFN - Milano section, Via Celoria 16, 20133 Milan, Italy*
[d] *Universitá degli Studi di Sassari, Dip. di Architettura, Design e Urbanistica ad Alghero, Palazzo del Pou Salit - Piazza Duomo 6, 07041 Alghero, Italy*
[e] *Intense Laser Irradiation Laboratory (ILIL), Istituto Nazionale di Ottica (INO), Consiglio Nazionale delle Ricerche (CNR), Via G. Moruzzi 1, 56124 Pisa, Italy and INFN Pisa section, Pisa, Largo Pontecorvo 3, 56127 Pisa, Italy*
[f] *ENEA - Centro Ricerche Frascati, Via E. Fermi 45, 00044 Frascati, Italy*
[g] *Sapienza University of Roma and INFN, P.le Aldo Moro 2, 00185 Rome, Italy*
[h] *CERN, CH-1211 Geneva 23, Switzerland*
[i] *Universitá degli Studi di Roma Tor Vergata and INFN, Via della Ricerca Scientifica 1, 00133 Rome, Italy*
[j] *INFN - Trieste section, Via Valerio 2, 34127 Trieste, Italy*
[k] *INFN - Laboratori Nazionali del Sud, via S.Sofia 62, 95123 Catania, Italy*
[l] *Elettra-Sincrotrone Trieste, Area Science Park, 34149 Trieste, Italy*
[m] *RICMASS, Rome International Center for Materials Science Superstripes, 00185 Rome, Italy*
[n] *ISM-CNR, Basovizza Area Science Park, Elettra Lab, 34149 Trieste - Italy*
[o] *Universitá degli Studi di Milano and INFN, Via Celoria 16, 20133 Milan, Italy*
[p] *Department of Physics and Astronomy, University of California Los Angeles, Los Angeles, California 90095, USA*
[q] *Racah Institute of Physics, The Hebrew University of Jerusalem, 91904 Jerusalem, Israel*

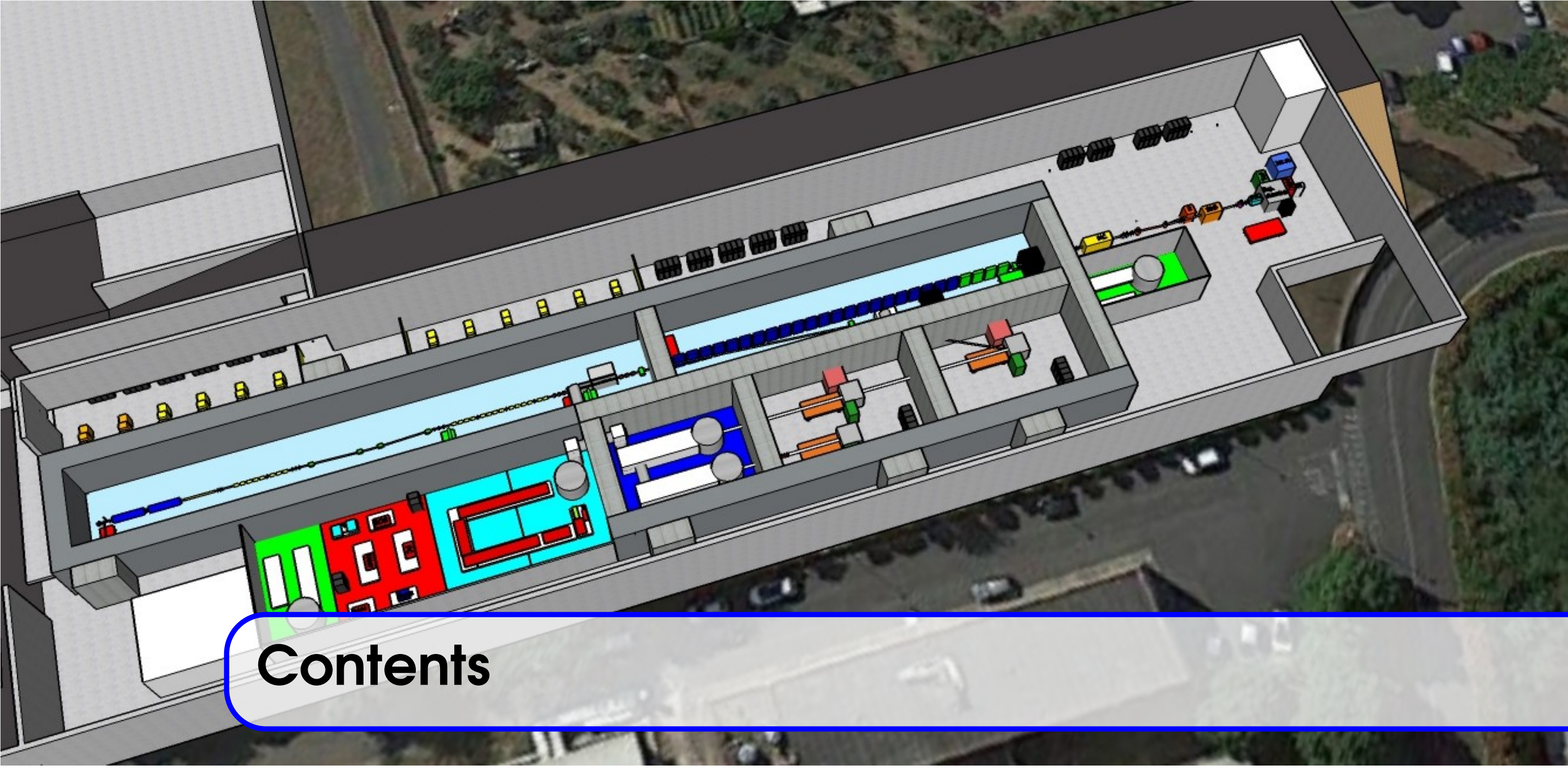

Contents

III Machine Technology

VI Appendixes

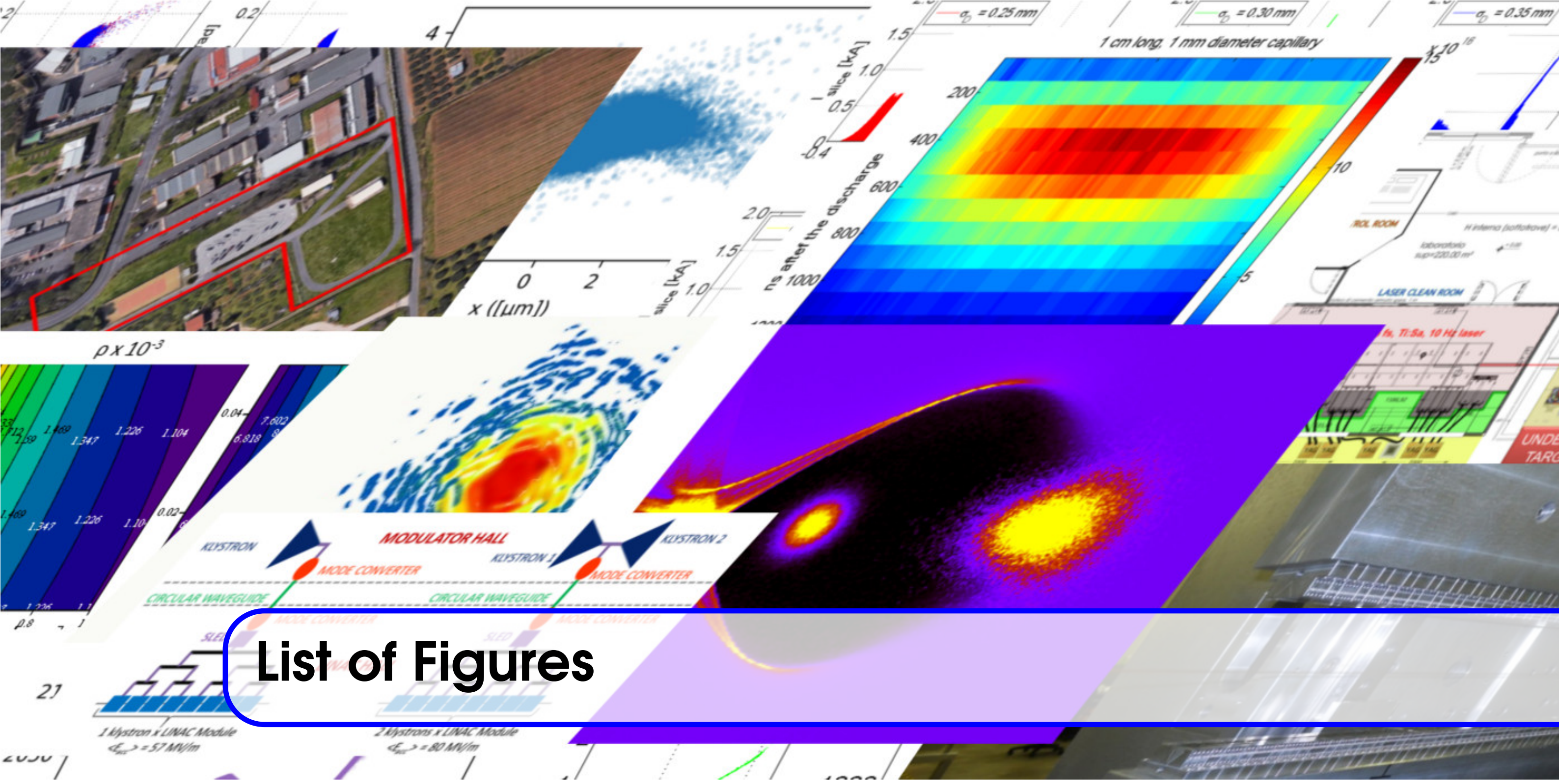

List of Figures

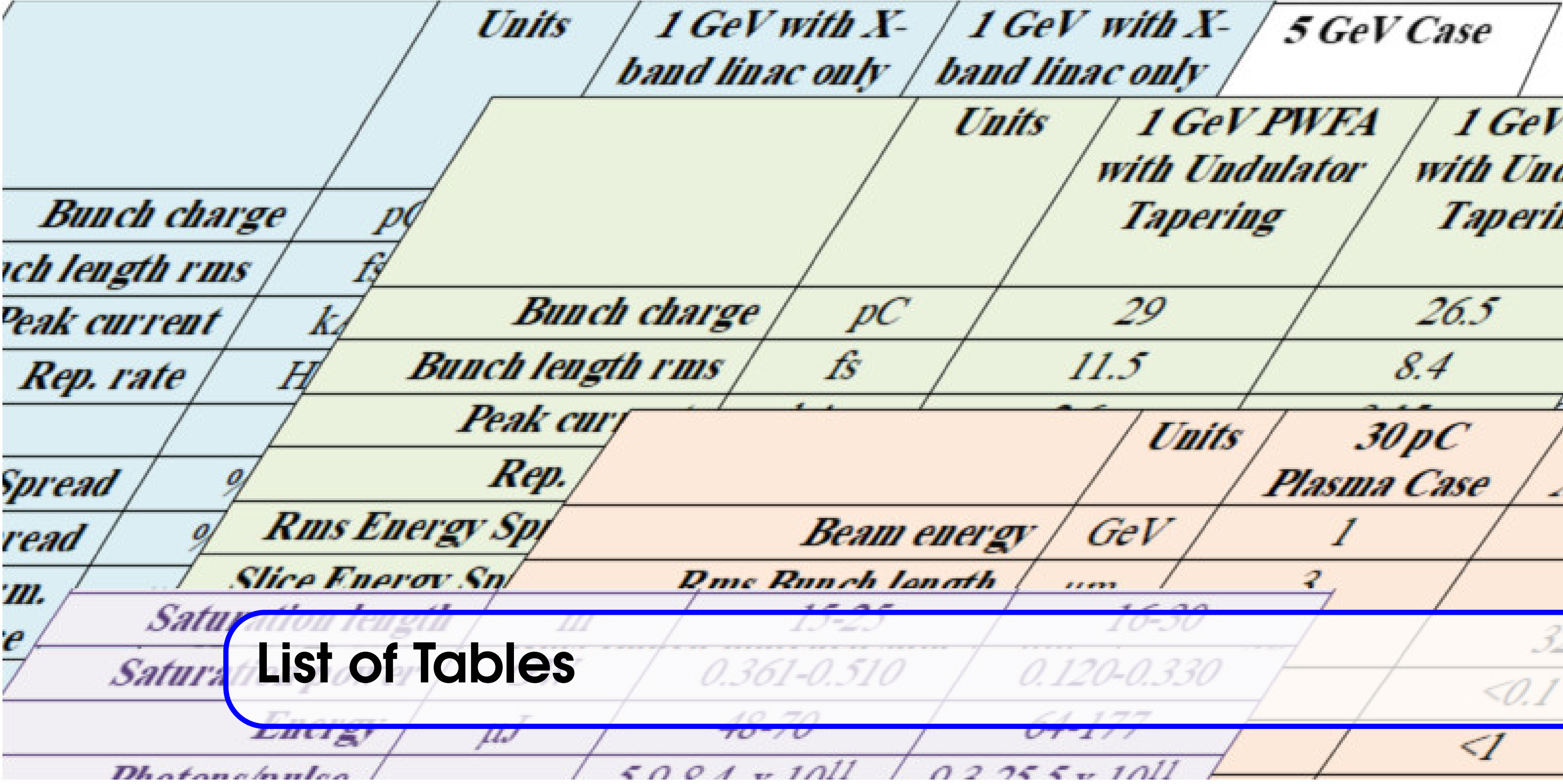

List of Tables

Executive Summary

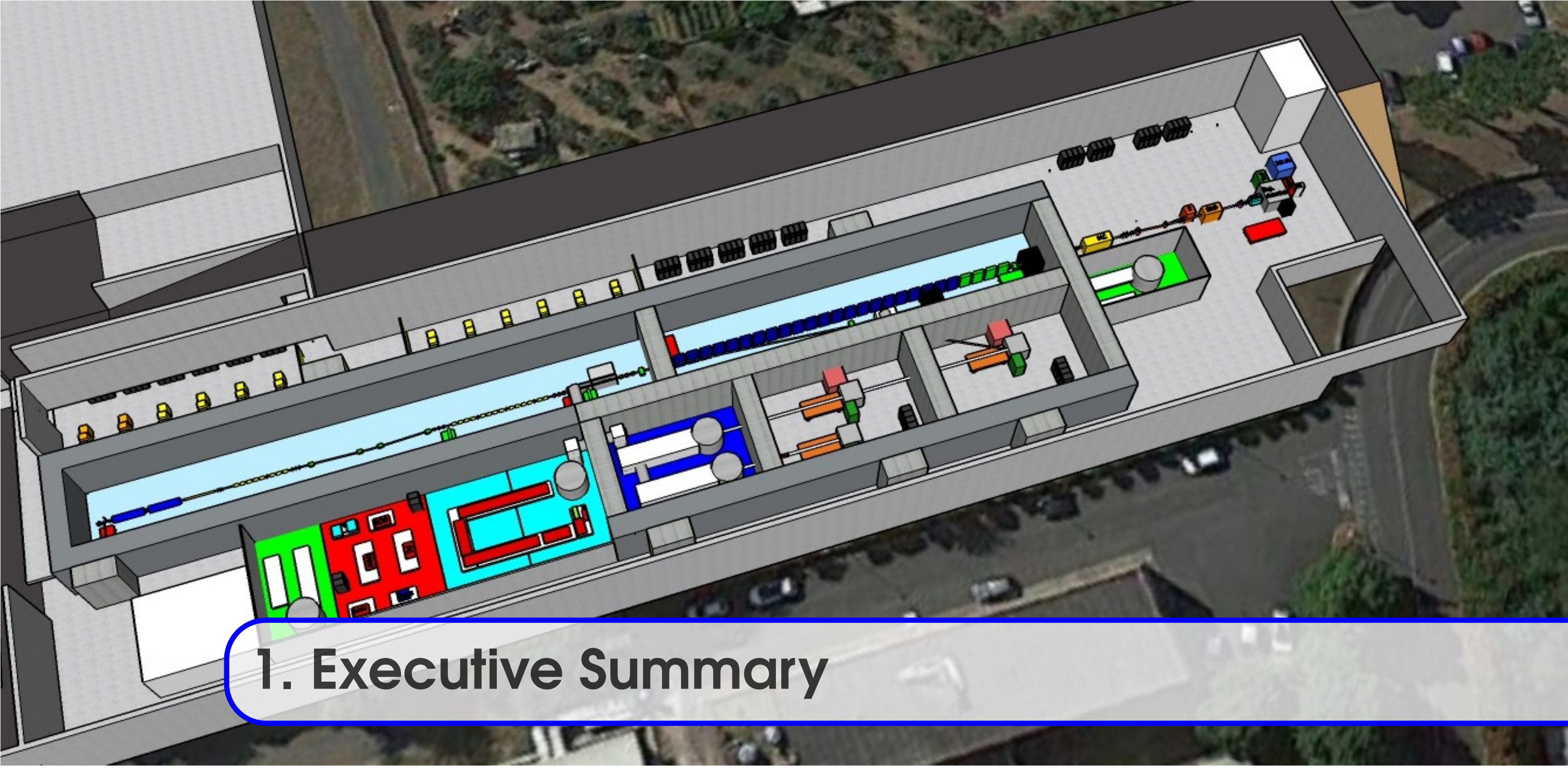

1. Executive Summary

Abstract

It is widely accepted by the international scientific community that a fundamental milestone towards the realization of a plasma driven future Linear Collider (LC) will be the integration of high gradient accelerating plasma modules in a short wavelength Free Electron Laser (FEL) user facility. To this end, in October 2019 the Horizon2020 Design Study EuPRAXIA (European Plasma Research Accelerator with eXcellence In Applications) will propose the first European Research Infrastructure that is dedicated to demonstrate usability of plasma accelerators delivering high brightness beams up to 1-5 GeV for users. In this report we discuss the EuPRAXIA@ SPARC_LAB project, intended to put forward LNF as host of the EuPRAXIA European Facility. The EuPRAXIA@SPARC_-LAB facility will equip LNF with a unique combination of a high brightness GeV-range electron beam generated in a state-of-the-art X-band RF linac, a 0.5 PW-class laser system and the first 5th generation light source driven by a plasma accelerator. These unique features will enable at LNF new promising synergies between fundamental physics oriented research and high social impact applications, especially in the domain of Key Enabling Technologies (KET) and Smart Specialisation Strategies (S3).

1.1 Introduction

Advancement in particle physics has historically been linked with the availability of particle beams of ever increasing energy or intensity. For more than three decades the collision energy in particle colliders has increased exponentially in time as it is described by the so-called Livingston curve. A recent version [1] of the Livingston curve is shown in Figure 1.1. It includes achievements with conventional and novel accelerators and indicates the present plans beyond 2014. It is seen that particle accelerators are a remarkable success story with beam energies having increased by 5 – 8 orders of magnitude since the first RF based accelerators in the 1920s. However, it is also evident that the exponential increase of beam energy with time has leveled off in conventional RF accelerators since the 1980s. Limits in conventional accelerators arise from technical limitations (e.g. breakdown effects at metallic walls of RF cavities, synchrotron power losses, maximum fields in super–conducting magnets) but also practical issues (size and cost). At the same time a new technology emerged, based on the revolutionary proposal of plasma accelerators by Tajima and Dawson in 1979 [2], and the invention of amplified chirped optical pulses (CPA) by Mourou and Strickland in mid 1980s [3]. Plasma-based concepts presently offer not only the high beam energies shown in Figure 1.1, but also the highest accelerating gradient compared to other novel acceleration techniques like high-frequency W-band metallic RF structures, dielectric wakefield structures or direct laser acceleration. Plasma-based accelerators in fact replace the metallic walls of conventional RF structures with an ionized gas, or plasma, see Figure 1.2 [4].

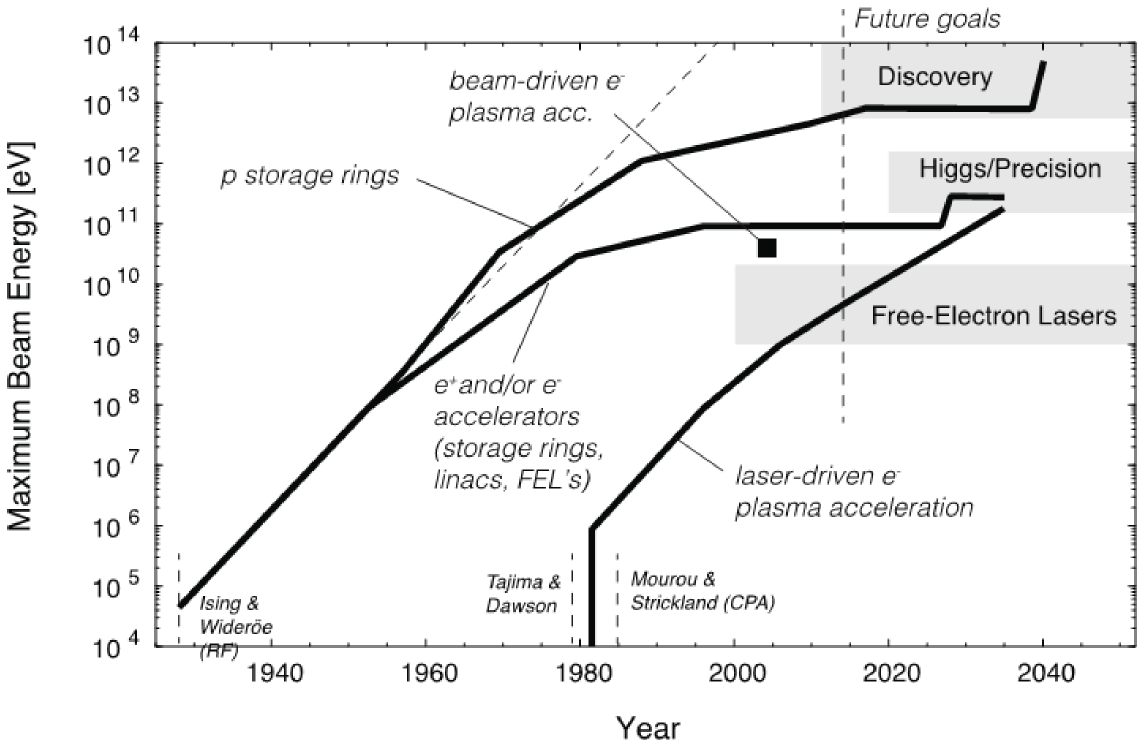

Figure 1.1: Livingston curve for accelerators [1], showing the maximum reach in beam energy versus time. Grey bands visualize accelerator applications. The left fork shows the progress in conventional accelerators from the first ideas in the 1920s. This main fork splits into two lines for electron/positron machines and for proton accelerators. A new fork of laser-driven plasma accelerators has emerged in 1980, reaching multi-GeV energies by now. Beam driven plasma acceleration results are indicated by the square point. Data beyond 2014 (vertical dashed line) indicate goals for the various technologies.

This revolutionary change permits one avoiding metallic or dielectric structure damage problems encountered in high-gradient operation. Laser beams (laser wakefield accelerator LWFA) or charged particle beams (particle wakefield accelerator, PWFA) may be adopted to excite space-charge oscillations in plasma. The resulting fields can be used for particle acceleration and focusing. Plasma accelerators have been built with active length ranging from the mm to the meter scale. Accelerating gradients up to 160 GV/m have been demonstrated in experiments [5] with improvements in accelerated beam quality that let us expect that advanced light sources (FEL, Compton, etc.) based on plasma-accelerators can be realized in the next decade [6]. To proceed towards high-energy physics (HEP) applications, however, one must demonstrate progress in beam quality and control [7].

It is widely accepted by the international scientific community that a fundamental milestone towards the realization of plasma driven future Linear Collider (LC) will be the integration of

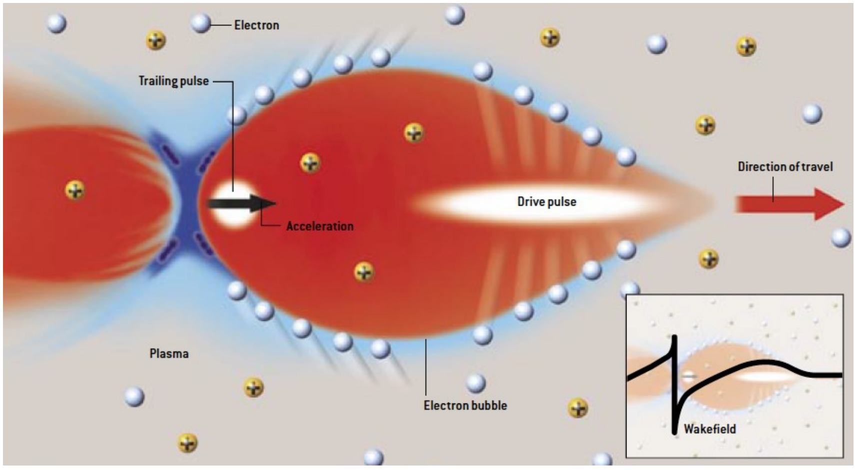

Figure 1.2: Wakefield accelerator relies on a charge disturbance known as a wakefield to provide the driving force. The drive pulse, which can be a short pulse of either a laser (LWFA) or an electron beam (PWFA), blows the electrons (blue) in an ionized gas, or plasma, outward, leaving behind a region of positive charge (red). Along the axis where the beam propagates, the electric field (plotted below) causes a trailing pulse of electrons injected near the rear of the bubble to feel a very strong forward acceleration. [4]

high gradient accelerating plasma modules in a short wavelength Free Electron Laser (FEL) user facility [1]. The capability of producing the required high quality beams and the operational reliability of the plasma accelerator modules will be certainly certified when such an advanced radiation source will be able to drive external user experiments. It is further expected that there will be unique photon–beam characteristics that give notable advantages to such a plasma based 5th generation light source. These characteristics include enabling ultra-short photon pulses based on high brightness electron beams that break the attosecond barrier and, when used in combination with next generation undulators, shorter wavelength photons at notably lower electron beam energy. The realization of such a 5th generation light source thus serves as a required stepping stone for HEP energy applications and is a promising new tool for photon science in its own right.

1.2 The EuPRAXIA Design Study

In October 2019, the Horizon2020 Design Study EuPRAXIA (European Plasma Research Accelerator with eXcellence In Applications) will propose the first European Research Infrastructure that is dedicated to demonstrate usability of plasma accelerators for users. EuPRAXIA is devoted to establish the scientific and technological basis required to build a compact and cost effective high energy (up to 5 GeV) machine based on plasma accelerator technology. As stated in the ongoing Horizon2020 European Design Study proposal [1]: "EuPRAXIA is supposed to bring together for the first time novel acceleration schemes, modern lasers, the latest correction/feedback technologies and large-scale user areas. It is of significant size, but significantly more compact than a conventional 5 GeV beam user facility. If the design study will be successful, EuPRAXIA could be constructed in the early 2020's. It would be the required intermediate step between proof-of-principle experiments and ultra-compact accelerators for science, industry, medicine or the energy frontier ("plasma linear collider"). Such a research infrastructure would achieve the required quantum leap in accelerator technology towards more compact and more cost-effective accelerators, opening new horizons for applications and research. The EuPRAXIA design study will cover three major aspects:

- The technical focus is on designing accelerator and laser systems for improving the quality of plasma-accelerated beams.

- The scientific focus is on developing beam parameters, two user areas and the user cases for a femtosecond FEL and High Energy Physics (HEP) detector science.
- The managerial focus is on developing an implementation model for a common European plasma accelerator. **This includes a comparative study of possible sites in Europe, a cost estimate and a model for distributed construction in Europe and installation at one central site.**"

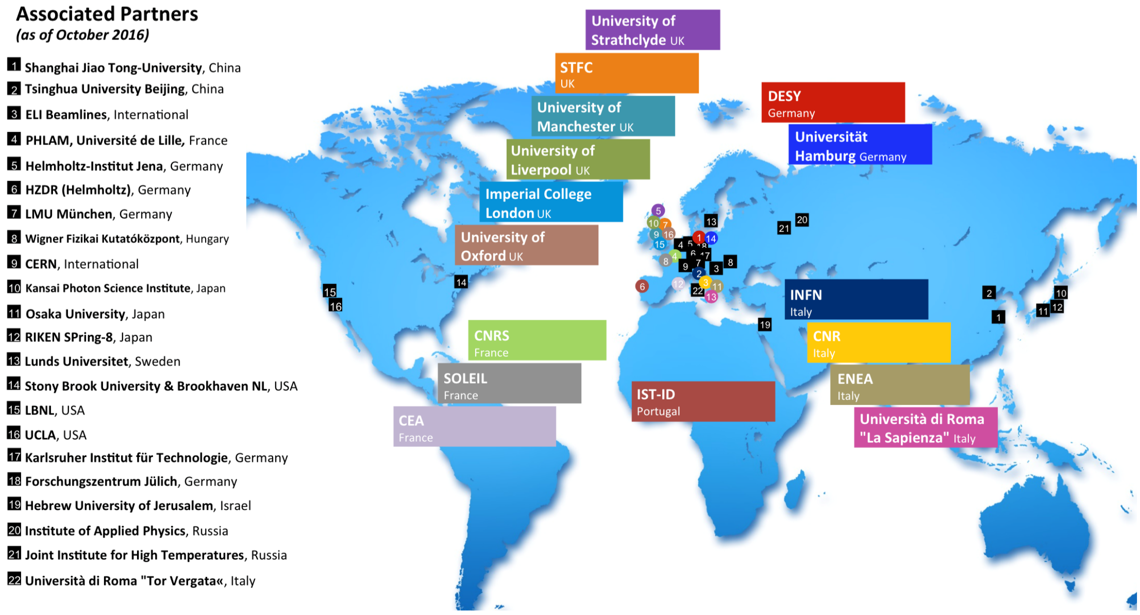

Figure 1.3: EuPRAXIA partners and associated partners.

The EuPRAXIA Design Study started its work in November 2015 with the aim of producing by the end of 2019 a Conceptual Design Report for a 5 GeV plasma-based accelerator with industrial beam quality and user applications. The study will design accelerator technology, laser systems and correction/feedback systems for improving the quality of plasma-accelerated beams. Several user areas will be developed for a novel Free Electron Laser, High Energy Physics detector science and other applications (e.g. health, industry). The EuPRAXIA collaboration, coordinated by R. Assmann (DESY), is the first plasma accelerator collaboration on this scale bringing together 16 European partner laboratories and additional 22 associated partners from the EU, Israel, China, Japan, Russia and the USA [1], see Figure 1.3. EuPRAXIA is structured into 14 working packages each headed by two work package leaders from different institutions. Eight work packages receive EU funding and their topics include: plasma and laser simulations (WP2), plasma accelerator structures (WP3), laser design (WP4), conventional beam physics (WP5), FEL radiation applications (WP6), and a table-top test beam for HEP and other applications (WP7). Two further EU work packages are concerned with the management of the collaboration (WP1) and the outreach to the public (WP8). In-kind work packages (WP9 – WP14) include additional approaches: beam driven plasma acceleration PWFA (WP9), hybrid acceleration schemes (WP14), alternative radiation generation (WP13) and laser sources such as fiber lasers (WP10). WP11 and WP12 connect to prototyping on plasma–based FEL's and facility access for experiments until 2019. Industry partners Amplitude Technologies, Thales and TRUMPF Scientific take part in the Scientific Advisory Board and contribute their experience towards a successful completion of the design report. The structure of the EuPRAXIA project, including management bodies, is shown in Figure 1.4. The Italian contribution cover a wide range of topics included mainly in WPs from

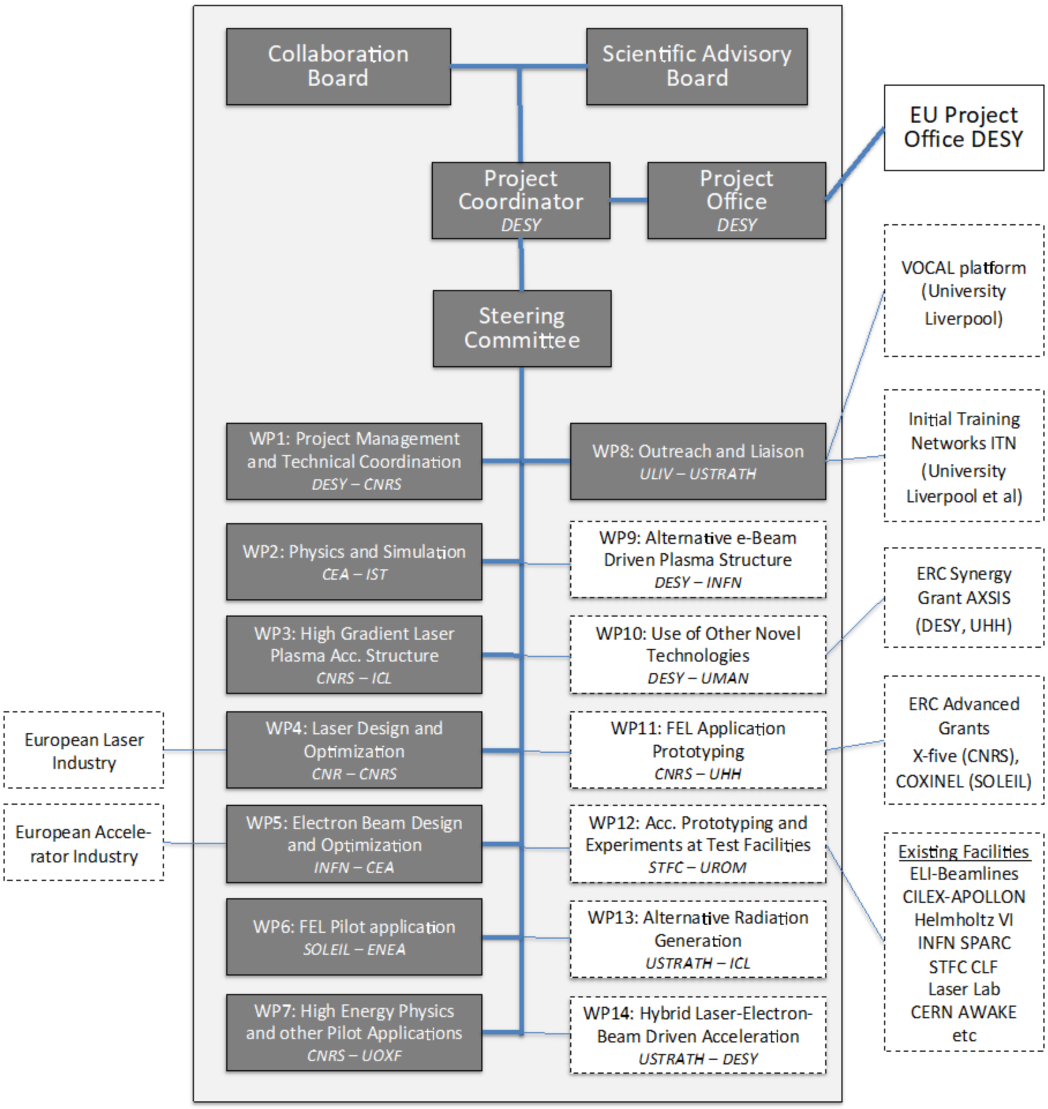

Figure 1.4: Structure of the EuPRAXIA project, including management bodies.

1 to 12, with significant responsibilities as co-leaders in WP4 (L. Gizzi, CNR-Pisa), in WP5 (E. Chiadroni, INFN–LNF), in WP6 (G. Dattoli ENEA–Frascati), in WP9 (M. Ferrario, INFN–LNF) and in WP12 (A. Mostacci Sapienza University, Rome). A. Cianchi from University of Roma "Tor Vergata" has been recently charged of the coordination of the sub-task of WP5 "Electron Beam Diagnostics". M. Ferrario has been also elected chairman of the EuPRAXIA Collaboration Board. The first iteration of the design parameter goals were defined in October 2016 [8] and approved by the EuPRAXIA Collaboration Board. The Self Amplification of Spontaneous Emission of radiation (SASE) FEL operational mode has been considered in detail. The parameters in the first study version for the electron beam at the entrance of the undulator are shown in Table 1.1 together with the expected photon beam characteristics.

The first parameter column targets at a SASE–FEL design at 1 GeV electron beam energy with

	Units	**1** GeV **case**	**5** GeV **case**
Bunch Charge	pC	30	30
Peak Current	kA	3	3
Rep. Rate	Hz	10	10
RMS norm. Emittance	µm	1	1
RMS Energy Spread	%	1	1
RMS Bunch Length	fs	10	10
Slice norm. Emittance	µm	<1	<1
Slice Energy Spread	%	0.1	0.1
Slice Length	µm	0.75	0.02
Undulator Period	cm	1.5	1.5
Undulator Strength K		0.872	0.872
Pierce parameter ρ	10^{-3}	>1	>1
Radiation Wavelength	nm	4	0.1

Table 1.1: Target Values for the 1 and 5 GeV electron beam parameters for a SASE FEL in the X-ray range.

comparable long wavelength in the soft x-ray range to allow a proof of principle demonstration. The 1 GeV operation aims at a very compact version of soft x-ray FEL's like FLASH [9] in Hamburg or FERMI [10] in Trieste. This would be a first breakthrough offering interesting light pulses for first pilot users. The second, more demanding parameter column, leads the way for a plasma-based SASE–FEL design at 5 GeV electron beam energy in the hard x-ray range. The practical realization of such an FEL however necessarily requires the experience from a previous iteration. One major figure of merit for electron beam quality is the beam energy spread. Especially for driving an FEL, this is an essential quantity, which directly defines the performance of the FEL design. These parameter goals and estimates are being evaluated and studied with the goal of establishing a second and more refined study version by the end of 2018. Developing a consistent set of beam parameters produced by a plasma accelerator able to drive a short wavelength FEL is one of the major commitments of the EuPRAXIA Design Study. The site selection for EuPRAXIA will be performed during the Preparatory Phase (expected in the years 2020–2022), following the delivery of the Conceptual Design Report by the Consortium (2019) and the inclusion of EuPRAXIA into the European Strategy Forum on Research Infrastructures (ESFRI) roadmap (expected in 2020).

1.3 The EuPRAXIA@SPARC_LAB concept

In this report we discuss the EuPRAXIA@SPARC_LAB project, intended to put forward LNF as host of the EuPRAXIA European Facility. In order to achieve this goal and to meet the EuPRAXIA requirements, some important preparatory actions must be taken at LNF:

- provide LNF with a new infrastructure, shown in Figure 1.5, with the size of about 130 m × 30 m, as the one required to host the EuPRAXIA facility;
- design and build the first-ever 1 GeV X-band RF linac and an upgraded FLAME laser up to the 0.5 PW range;
- design and build a compact FEL source, equipped with user beam line at 3 nm wavelength, driven by a high gradient plasma accelerator module.

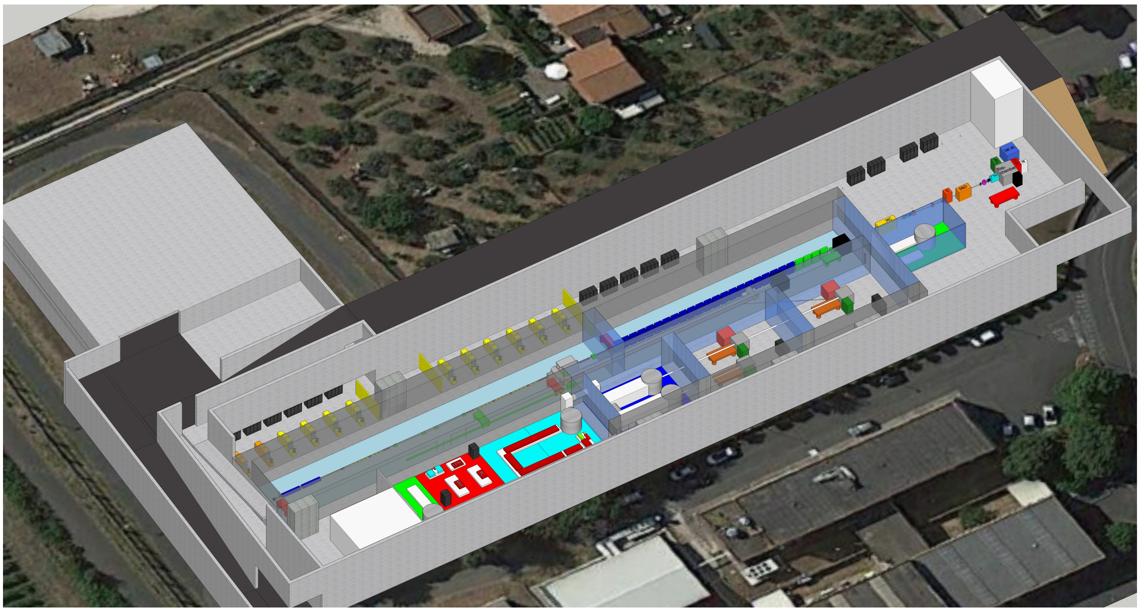

Figure 1.5: The layout of the EuPRAXIA@SPARC_LAB infrastructure at LNF.

We are convinced that the completion in the shortest possible time of the above mentioned program, will represent a formidable boost for the EuPRAXIA facility and will allow LNF to be in an excellent position for being chosen as the site hosting the European infrastructure. Synthetically, we call this project **EuPRAXIA@SPARC_LAB**. The collaboration is carried out with the support of groups from INFN (LNF, LNS, Milano, Rome and Rome Tor Vergata), Universities of Rome Sapienza, Rome Tor Vergata and Milano Statale, ENEA Frascati, CNR–INO Pisa, and CERN CLIC team. Associated partners are also University of California at Los Angeles (UCLA) and the Hebrew University of Jerusalem (HUJ). The new infrastructure will be able to accommodate any machine configuration resulting from the EuPRAXIA Design Study. At present, five different EuPRAXIA configurations are under investigation [11], based on a laser and/or a beam driven plasma acceleration approach that will find within the LNF infrastructure the necessary technological background.

The EuPRAXIA@SPARC_LAB facility ***by itself*** *will equip LNF with a unique combination of a high brightness GeV–range electron beam generated in a state-of-the-art linac, and a 0.5 PW–class laser system. Even in the unfortunate cases of LNF not being selected and/or of a failure of plasma acceleration technology, the infrastructure will be of top-class quality, user-oriented and at the forefront of new acceleration technologies. Indeed, this project will allow the establishment of a FEL user community, interested to exploit the proposed radiation source and the possible future extensions of the radiation spectrum, from the water window (4–2 nm), down to shorter wavelengths.*

These unique features will enable at LNF new promising synergies between fundamental physics oriented research and high social impact applications, especially in the domain of Key Enabling Technologies (KET) and Smart Specialisation Strategies (S3), as supported by EU research funding programs. EuPRAXIA@SPARC_LAB is in fact conceived by itself as an innovative and evolutionary tool for multi-disciplinary investigations in a wide field of scientific, technological and industrial applications. It could be *progressively* extended to be a high brightness "particle beams factory": it will be able to produce electrons, photons (from THz to γ-rays), neutrons, protons and positrons, that will be available for a wide national and international scientific community interested to take profit of advanced particle and radiation sources. We can foresee a large number of possible activities, among them:

- X-band RF technology implementation in the framework of the CLIC [12] and CompactLight [13] collaborations,
- Science with short wavelength Free Electron Laser (FEL),
- Physics with high power/intensity lasers and secondary particle generation,
- R&D on compact accelerators and radiation sources for medical applications,
- Detector development for x-ray FEL,
- Science with THz radiation sources,
- Nuclear photonics with γ-rays Compton sources,
- R&D on polarized positron sources,
- Quantum aspects of beam physics including the Quantum–FEL development,
- R&D in accelerator physics and industrial spin – off.

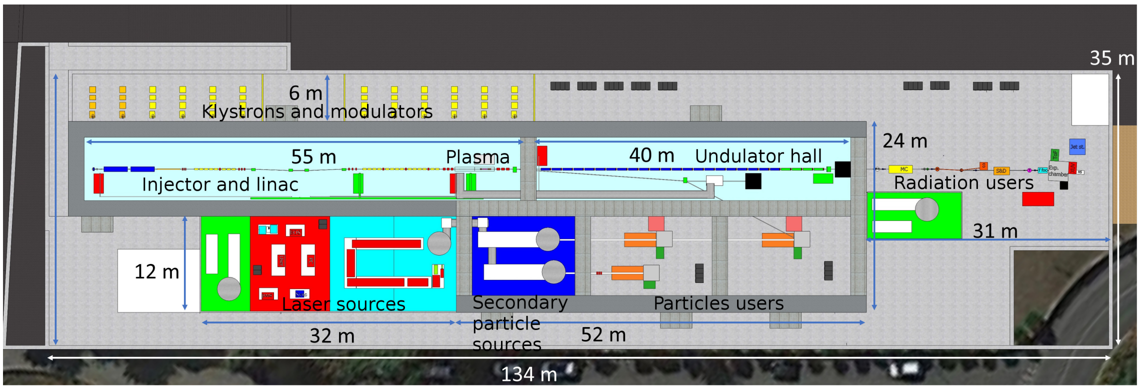

Figure 1.6: The layout of the EuPRAXIA@SPARC_LAB infrastructure.

In this summary, we will focus the attention to the core of the facility, i.e. linac, laser, plasma and undulator complexes, leaving to more detailed future studies the wide range of applications of the proposed facility. The layout of the EuPRAXIA@SPARC_LAB infrastructure is schematically shown in Figures 1.5 and 1.6. From left to right one can see a 55 m long tunnel hosting a high brightness 150 MeV S-band RF photoinjector equipped with a hybrid compressor scheme based on both velocity bunching and magnetic chicane. The energy boost from 150 MeV to 0.5–1 GeV will be provided by chain of high gradient X-band RF cavities. At the linac exit a 5 m long plasma accelerator section will be installed, which includes the plasma module ($\sim$1 m long) and the required matching and diagnostics sections. In the downstream tunnel a 40 m long undulator hall is shown, where the undulator chain will be installed. Further downstream after a 12 m long photon diagnostic section the users hall is shown. Additional radiation sources as THz and γ–ray Compton sources are foreseen in the other shown beam lines. The upper room is dedicated to Klystrons and Modulators. In the lower light-blue room will be installed the existing 300 TW FLAME laser (eventually upgraded up to 500 TW). The plasma accelerator module can be driven in this layout either by an electron bunch driver (PWFA scheme) or by the FLAME laser itself (LWFA scheme). A staged configuration of both PWFA and LWFA schemes will be also possible in order to boost the final beam energy beyond 5 GeV. In addition, FLAME is supposed to drive plasma targets in the dark–blue room in order to drive electron and secondary particle sources that will be available to users in the downstream 30 m long user area. The most innovative component of the project is the plasma accelerating module, shown in Figure 1.7 in one of its possible configurations. It consists in a 10 cm long, 0.5 mm diameter Sapphire capillary tube [14–16] in which the plasma is produced by a high voltage discharge in Hydrogen. As discussed later in this report plasma density ranging from 10^{16} – 10^{19} cm^{-3} has been already tested [17] producing accelerating gradients exceeding 100 GV/m in both LWFA and PWFA configurations.

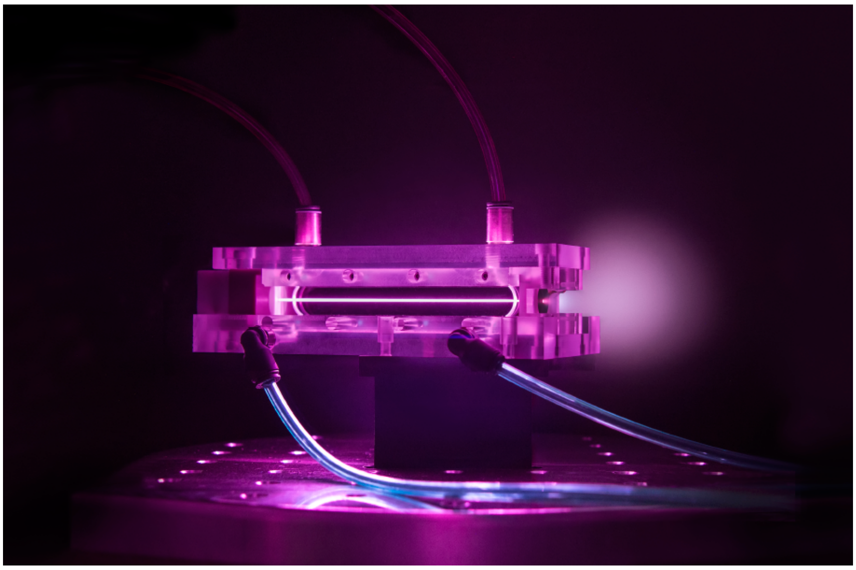

Figure 1.7: The plasma cell used at LBNL.

Another fundamental component included in the EuPRAXIA@SPARC_LAB proposal is the X-band accelerating technology adopted for the 1 GeV RF drive linac [18]. It is a very interesting option because it allows to reduce the overall drive linac length, taking profit of the high gradient (up to 80 MV/m) operation of the X-band accelerating structures. In addition it will allow implementing at LNF in the next 2 years the state of the art high gradient RF technology. This technology has already shown its usefulness for medical and industrial applications but it is also another possible technological option for compact radiation sources and for the future Linear Collider [19]. As stated in the support letter addressed to the LNF Director by the CLIC collaboration leaders:

"We wish to provide our very strong support for the EuPRAXIA@SPARC_LAB project being proposed by INFN Frascati. We sincerely believe that this is an excellent choice for the future of the laboratory. It is also very important for the CERN and the CLIC collaboration. We have discussed with INFN leaders and elaborated a mutually beneficial program of exchange of hardware and staff to advance both the LNF and CLIC projects. One of the key areas of the CLIC is the high-gradient, X-band radio frequency accelerator of the main linac. Significant resources have been invested to develop the necessary technology and considerable progress has been made and demonstrated by testing prototype systems in test stands at CERN. The LNF proposal is an opportunity to now implement this accelerator technology on a much larger scale than is possible in our test facilities. EuPRAXIA@SPARC_LAB will provide important benefits for high-gradient X-band technology including industrialization, larger-scale series production and long-term user operation. For these reasons, we have identified an initial set of collaboration activities. At the core is the loan to Frascati of a 50 MW *X-band klystron in order to jointly set up a local high gradient testing facility. INFN would complete the test stand including the modulator and supporting infrastructure and then carry out high–gradient testing. Preparation for the test stand in Frascati would involve training INFN staff at CERN on the existing test stands. The experts would return to Frascati to build and operate the test stand there, experience that is directly applicable to the EuPRAXIA@SPARC_LAB linac. Overall this would be part of the strategy to introduce this innovative accelerator technology that will become a core component of the LNF facility. EuPRAXIA@SPARC_LAB , with its high gradient accelerator and very low emittance beam, will in the longer term provide a unique and important opportunity for the CLIC study for beam testing. This includes experiments and tests in a number of areas including beam dynamics, RF system and beam instrumentation. Finally, the LNF based test stand and then the EuPRAXIA@SPARC_LAB facility will provide important*

continuity for a long standing and very productive collaboration which extends back to the early days of CTF3."

We expect to install and run at LNF the X-box test stand, shown in Figure 1.8, by the end of 2018. This facility will allow RF cavities test and personnel training well before the beginning of the linac operations.

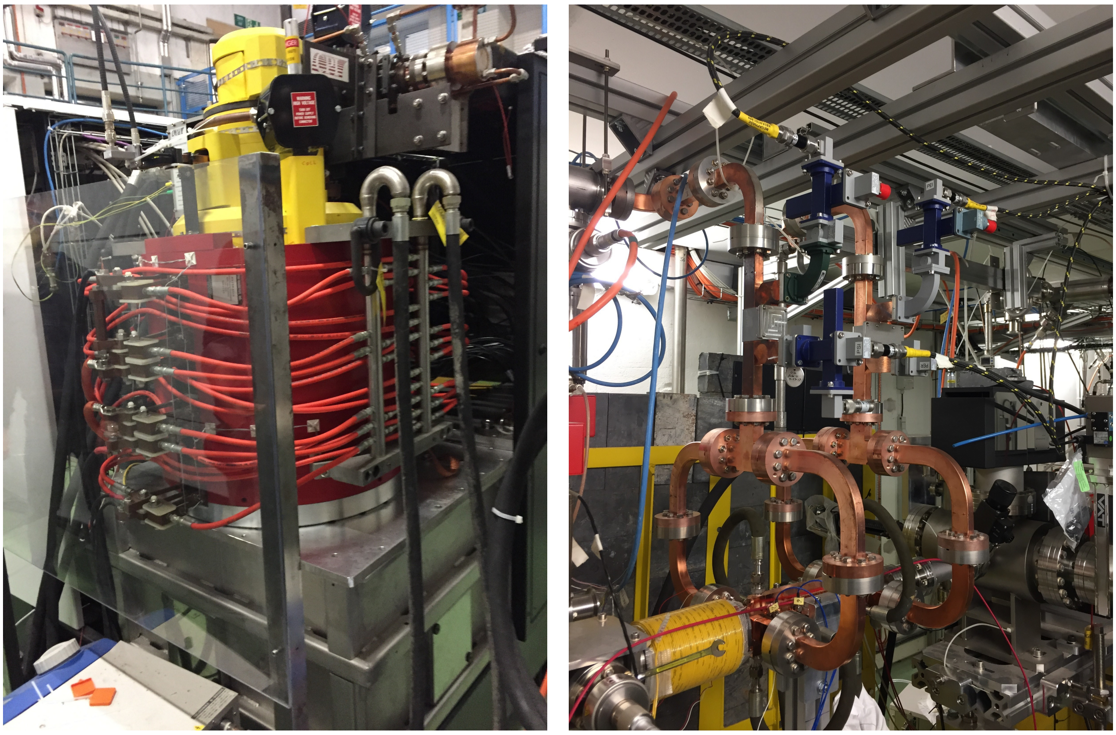

Figure 1.8: The klystrons of the CERN X-band facility.

Together with the driving motivation to candidate LNF to host the EuPRAXIA facility, the realization of the EuPRAXIA@SPARC_LAB infrastructure at the LNF by itself will allow INFN to consolidate a strong scientific, technological and industrial role in a competing international context. A national multi-purpose facility, along the scientific applications discussed in the following sections, not only paves the road for a strong role for the Italian contribution to the European EuPRAXIA one, but also to possible future large high energy physics (HEP) international projects. This project will represent a further step forward in the mainstream of a long lasting history of success in particle accelerators development in Frascati.

1.4 The EuPRAXIA@SPARC_LAB design goals

The EuPRAXIA@SPARC_LAB scientific program has foreseen three main directions:

- High gradient acceleration techniques for the next FEL and e^+e^- collider generations.
- Advanced radiation sources for photon science (FEL, Betatron, Compton, Channeling).
- Physics of high field interactions with matter.

The main required components enabling the accomplishment of the program are:

- The RF Linac upgrade up to 1 GeV
- The FLAME laser upgrade up to 0.5 PW

The experimental activity will be initially focused on the realization of a plasma driven short wavelength FEL with one user beam line, according to the beam parameter reported in the first column of Table 1.1, "1 GeV case". This goal is already quite challenging but it is affordable by the EuPRAXIA@SPARC_LAB collaboration and will provide an interesting FEL radiation spectrum in the so called "water window" whose applications are described in chapter 18. The first foreseen FEL operational mode is based on the Self Amplification of Spontaneous Emission (SASE) mechanism [20]. More advanced schemes like Seeded [21] and Higher Harmonic Generation [22] configurations will be also investigated. In the PWFA scenario driven by a single short electron bunch, the peak accelerating field is, in principle, limited to twice the value of the peak decelerating field within the bunch (transformer ratio R = 2). Therefore the maximum possible energy gain for a trailing bunch is less than twice the incoming driver energy. In this regime a driver bunch energy of 500 MeV is enough to accelerate the witness bunch up to 1 GeV . A method to increase the energy gain is the so called *ramped bunch train* [23] and consists of using a train of N_T equidistant bunches, see Figure 1.9, wherein the charge increases along the train producing an accelerating field resulting in a higher transformer ratio. For this application, it is essential to create trains of high-brightness tens of femtosecond long microbunches with stable and adjustable length, charge and spacing. A lot of efforts are now ongoing worldwide to produce the required bunch train configurations [24]. The method we will use to achieve the required bunch train quality is based on the *Laser Comb Technique* [25] that has been recently tested with the SPARC_LAB photoinjector [26]. Higher witness bunch energy will be accessible when the Comb technique will be implemented. With a transformer ratio of 6 the 5 GeV threshold will be also achievable with a 1 GeV driver bunch energy, thus exploiting the full energy provided by the X-band linac.

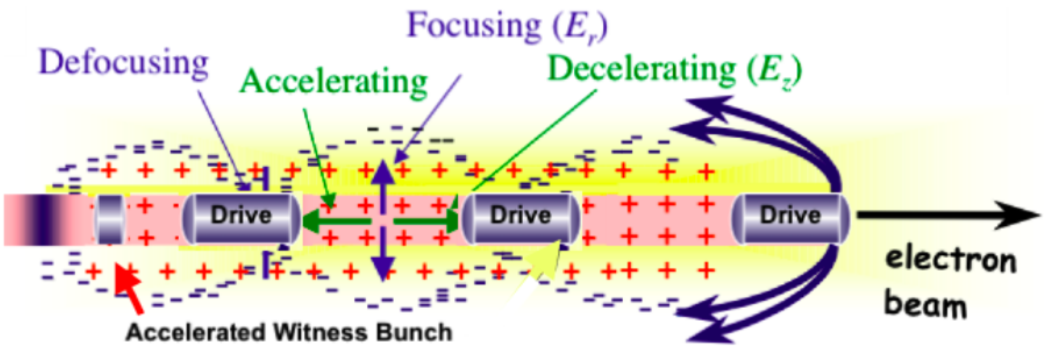

Figure 1.9: Multibunch excitation of a plasma wave.

In the LWFA scenario the 0.5 PW upgrade of the FLAME laser, temporarily in the existing dedicated building, is a necessary step to keep the FLAME laser in the group of leading installations and further establish expertise on advanced laser sciences. High energy staging in combination with high brightness beam external injection will be the main application of the upgraded FLAME system, leading to multi–GeV high brightness electron beam production as required by EuPRAXIA applications.

In addition, it will make it possible to implement a new scientific program based on lasers at the highest competitive level. Many laboratories worldwide have recognized the need for a major upgrade of their respective laser systems to the PW–scale power and, in several cases to the 10 PW power. These upgrades are driven by scientific motivations of paramount importance, which are emerging thanks to the parallel major effort in predictive numerical modeling of phenomena never approached so far in the Laboratory.

In this scenario, the upgrade of the FLAME laser system to 0.5 PW power and dual beam capability will enable new regimes of plasma-based particle accelerators and the access to the region of high electromagnetic fields of non-linear and quantum electrodynamics (QED) where new fundamental physics processes and promising new radiation emission mechanisms can be explored.

The science cases that will be developed with the FLAME 0.5 PW upgrade include:

- Electron acceleration beyond the GeV (including external injection and/or Trojan horse scheme, high energy staging, etc.);
- QED and generation of high energy radiation;
- Proton and ion acceleration beyond the TNSA regime.
- Coherent (betatron and Compton scattering) radiation sources

In fact, advances in laser–plasma acceleration are already being achieved with PW laser systems recently commissioned elsewhere and the 10 GeV barrier of electron energy gain is now within reach. At such a high energy, intense, hard X-ray emission from betatron radiation is expected [27] which is currently seen as an advanced source for a wide range of applications, including phase contrast imaging and 3D X-ray tomography [28].

Among the other phenomena, the most far reaching ones concern the possibility of entering the radiation-dominated regime of electron dynamics. Besides its impact on basic physics issues involving the fundamental nature of the electron charge distribution, this regime may lead to the realization of extremely powerful and controllable sources of high-energy radiation. These sources may revolutionize many areas of great social interest, from Health to Security, from Environment to Safety. In fact, a PW–scale laser system makes it possible to create conditions in which the electromagnetic field is so strong that electron motion no longer follows the laws of classical mechanics. In the classical view, an electron entering an intense laser field will be scattered away by the strong ponderomotive force and will not experience high fields. This regime is well explored in ultra-intense laser fields and is the basic mechanism that, for example, initiates the wakefield in a laser-driven acceleration scheme. When laser intensity is further increased, quantum processes govern the interaction of the electrons with the electromagnetic field and the force assumes a stochastic behavior. In this case, an electron approaching an intense laser field may be able to experience a strong acceleration that will make it radiate much more efficiently [29] than in the classical regime. Based on this principle, a powerful γ-ray source can be conceived in a compact, all-optical configuration. This is a key example of the physical processes, so far unexplored in the laboratory that can be addressed with a PW–scale laser.

We have investigated the possibility to fulfill the 1 GeV EuPRAXIA scenario by using both plasma acceleration options (LWFA and PWFA) and we have reported in chapter 4 the start-to-end simulations to support both designs. In Table 1.2 the achieved parameters are reported. We have investigated also the possibility to drive the FEL with higher charge/bunch i.e. 200 pC, in order to produce a larger number of photons as required by some application. This is possible in a conventional configuration, i. e. exploiting the full X-band RF linac energy (1 GeV) without using the plasma module and the results of start-to-end simulations are shown in Table 1.2.

The reported EuPRAXIA@SPARC_LAB FEL performances show that our FEL, driven by a plasma accelerator in SASE configuration, is expected to meet the challenging requests for the new generation synchrotron radiation sources. The peak brilliance will exceed of about 10 orders of magnitude that produced by the undulators of the 3rd generation sources. In addition the pulse duration could be very short (of the order of fs scale) with respect to what is currently attainable with storage ring based radiation source (ps scale). Possible applications of the EuPRAXIA@ SPARC_LAB FEL source at 3 nm are described in the next paragraph.

1.5 The FEL scientific program within EuPRAXIA@SPARC_LAB facility

The advent of Free Electron Lasers (FELs) opened up the way for an unprecedented, wide class of experiments exploiting the peculiar features of these radiation sources. Key elements are the high peak brilliance and the short pulse duration, which is of the order of tens of femtoseconds. FELs can therefore allow high time resolution measurements and may provide a high signal-to-noise ratio. By exploiting the high peak brilliance and the extremely short FEL pulses the so-called

	Units	Full RF case	LWFA case	PWFA case
Electron Energy	GeV	1	1	1
RMS Energy Spread	%	0.05	2.3	1.1
Peak Current	kA	1.79	2.26	2.0
Bunch Charge	pC	200	30	30
RMS Bunch Length	μm (fs)	16.7 (55.6)	2.14 (7.1)	3.82 (12.7)
RMS normalized Emittance	mm mrad	0.5	0.47	1.1
Slice Length	μm	1.66	0.5	1.2
Slice Charge	pC	6.67	18.7	8
Slice Energy Spread	%	0.02	0.03	0.034
Slice normalized Emittance (x/y)	mm mrad	0.35/0.24	0.45/0.465	0.57/0.615
Undulator Period	mm	15	15	15
Undulator Strength $K(a_w)$		0.978 (0.7)	1.13 (0.8)	1.13 (0.8)
Undulator Length	m	30	30	30
ρ **(1D/3D)**	$\times 10^{-3}$	1.55/1.38	2/1.68	2.5/1.8
Radiation Wavelength	nm (keV)	2.87 (0.43)	2.8 (0.44)	2.98 (0.42)
Photon Energy	μJ	177	40	6.5
Photon per pulse	$\times 10^{10}$	255	43	10
Photon Bandwidth	%	0.46	0.4	0.9
Photon RMS Transverse Size	μm	200	145	10
Photon Brilliance per shot	(s mm^2 mrad^2 bw(0.1%))$^{-1}$	1.4 $\times 10^{27}$	1.7 $\times 10^{27}$	0.8 $\times 10^{27}$

Table 1.2: Beam parameters from start-to-end simulations for full RF case and for plasma wakefield acceleration cases with electron (PWFA) or laser (LWFA) driver beam.

diffract-and-destroy regime can be explored, in which interpretable data are gathered before the sample is destroyed by the FEL pulse radiation [30] thus overcoming one of the main limitations of synchrotron radiation based experiments that is the sample radiation damage. This principle has been proven in several experiments on various samples, both biological [31–35] and non-biological [36, 37], at different wavelengths ranging from the UV to the hard X-rays region. Actually, this issue is particularly relevant since coherent diffraction imaging (CDI) of biological system using conventional methods is ultimately limited by radiation damage owing to the large amount of energy deposited in the sample by the photon beam [36].

The unique FEL features (energy range, time resolution and brilliance) can be exploited in several branches of physics, chemistry, material science and biology. The EX–TRIM (Eupraxia X-ray Time Resolved coherent IMaging) users endstation of EuPRAXIA@SPARC_LAB FEL will be designed and built to allow performing a wide class of experiments using the schematic apparatus displayed in Figure 1.10. Details about the main research lines, requirements for FEL beam parameters and the EX–TRIM experimental end-station are described in Chapter 18.

As specific example of EuPRAXIA@SPARC_LAB applications it is worth remarking that

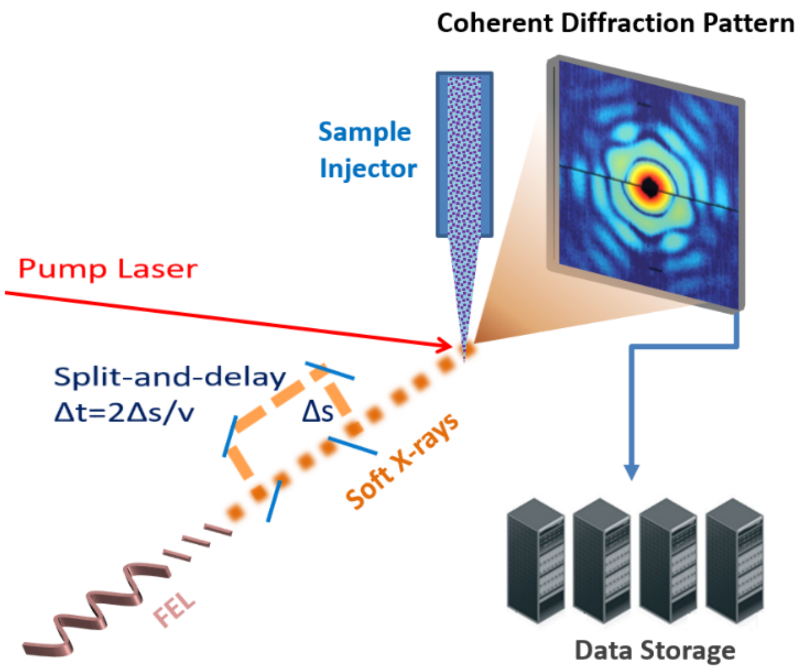

Figure 1.10: Simplified layout of an imaging experiment using the EuPRAXIA@SPARC_LAB FEL.

the FEL radiation in the soft X-ray spectrum open possibilities for novel imaging methodologies and time-resolved studies in material science, biology and medicine, along with non-linear optics applications, among them:

- ***Coherent Imaging of Biological samples in the water window.*** Exploiting the coherence of the EuPRAXIA@SPARC_LAB FEL radiation and its wavelength falling within the "water window", 2D and 3D images of biological samples in a wet environment can be obtained with high contrast with respect to the surrounding medium. This means that a wide class of biological objects, including protein clusters, viruses and cells can be profitably studied at the EuPRAXIA@SPARC_LAB facility.
- ***Clusters and nanoparticles.*** Considerable attention is continuously being addressed to the study of free clusters, since they are known to be a bridge between the gas and the condensed phases of matter. In particular, great interest arises in the correlations between the geometric structure and electronic properties of variable size clusters, underlying changes in optical, magnetic, chemical and thermodynamic properties. In the spectral range from 3 to 5 nm envisaged for the EuPRAXIA@SPARC_LAB FEL source, physical processes involving core levels are important. Clusters, as a form of matter intermediate among atoms and bulk solids, are ideal samples to study these processes.
- ***Laser ablation plasma.*** Laser ablation/desorption techniques are utilized extensively across a diverse range of disciplines, including production of new materials, and both extrinsic and in situ chemical analysis. Laser interactions may occur via direct absorption or through non-linear mechanisms such as multi-photon and avalanche excitation. In the case of ablation the use of ultra-fast laser pulses provides a powerful means of machining a wide variety of materials, including biological tissue. The absence of thermal relaxation of the energy allows unprecedented precision and essentially no associated damage, a fact that has stimulated

considerable interest also for industrial processes and applications. Electronically induced surface reactions in semiconductors, metal/adsorbate systems and multiphase composite materials could be investigated. Moreover, surface studies of the irradiated area with chemical sensitivity of CDI diagnostics of the ablated species may elucidate the mechanism of the electronic melting, desorption, and multi–photon ablation.

- ***Condensed Matter Science.*** A Free Electron Laser capable to deliver pulses in the 3 nm region is a great asset for Coherent Diffraction Imaging (CDI) experiments tackling many open questions in Condensed Matter physics. For instance, the quest for smaller and faster magnetic storage units is still a challenge of the magnetism. The possibility to study the evolution of magnetic domains with nanometer/femtosecond spatial/temporal resolution will shed light on the elementary magnetization dynamics such as spin-flip processes and their coupling to the electronic system. Moreover, the possibility to exploit different L–edges resonances would allow introducing the chemical selectivity necessary to account for the complex composition of technologically relevant magnetic media.
- ***Pump and probe experiments.*** The possibility of inducing changes in a sample via a pump pulse such as the stimulation of a chemical reaction or the generation of coherent excitations would tremendously benefit from intense and extremely short pulses in the soft X-ray region. As an example, resonant experiments with pulses tuned across electronic excitation will open up the way towards stimulated Raman or four wave mixing spectroscopies.

1.6 Experience with SPARC_LAB

The EuPRAXIA@SPARC_LAB facility will address new technological challenges at LNF. Nevertheless a wide experience in the development of Advanced Accelerator Concepts and Technology has grew up at LNF in the past decade thanks to the strong involvement of LNF scientist in the design, commissioning and operation (since 2005) of the SPARC_LAB test facility. SPARC_LAB (Sources for Plasma Accelerators and Radiation Compton with Lasers and Beams) [38] is in fact an interdisciplinary laboratory with unique features in the world. The SPARC_LAB layout is shown in Figure 1.11. It was born from the integration of a high brightness photo-injector (SPARC) [39–44], able to produce high quality electron beams up to 170 MeV energy with high peak current (> 1 kA) and low emittance (<2 mm mrad), and of a high power laser (> 200 TW) (FLAME) [45, 46], able to deliver ultra-short laser pulses (<30 fs).

The SPARC photo-injector is characterized by a copper photo-cathode, illuminated by a UV laser (266 nm) and embedded in a 1.6-cell standing wave RF gun (BNL/UCLA/SLAC type), operating at 2.856 GHz (S-band, normal conducting technology). The high peak field on the photo-cathode ($\geq$ 120 MV/m) allows the beam acceleration up to $\geq$ 5.6 MeV. The beam is then properly focused and matched into three constant gradient $2\pi/3$ traveling wave (TW) structures of the SLAC type, which boost the beam energy up to 180 MeV. The first accelerating section is also used as RF compressor (in the velocity bunching regime) by varying the beam injection phase [47]. Solenoid coils embedding the first two sections can be powered to provide additional magnetic focusing to better control the beam envelope and the emittance oscillations under RF compression. Several beam dynamics and FEL studies have been successfully demonstrated and novel radiation sources from THz to γ-rays have been developed with this machine layout. In particular, in the first phase of SPARC operation the low energy electron beam (5 MeV) was characterized out of the photo-injector and before the installation of the three accelerating sections, with the aim of studying the first few meters of beam propagation where space charge effects and plasma oscillations dominate the electron dynamics. In this regard, a new sophisticate diagnostic tool, called movable emittance-meter has been designed, installed and commissioned [41, 48]. Emittance oscillations driven by space charge in the drift downstream the RF gun have been observed, in agreement to what expected from our theoretical model and numerical simulations, and the first

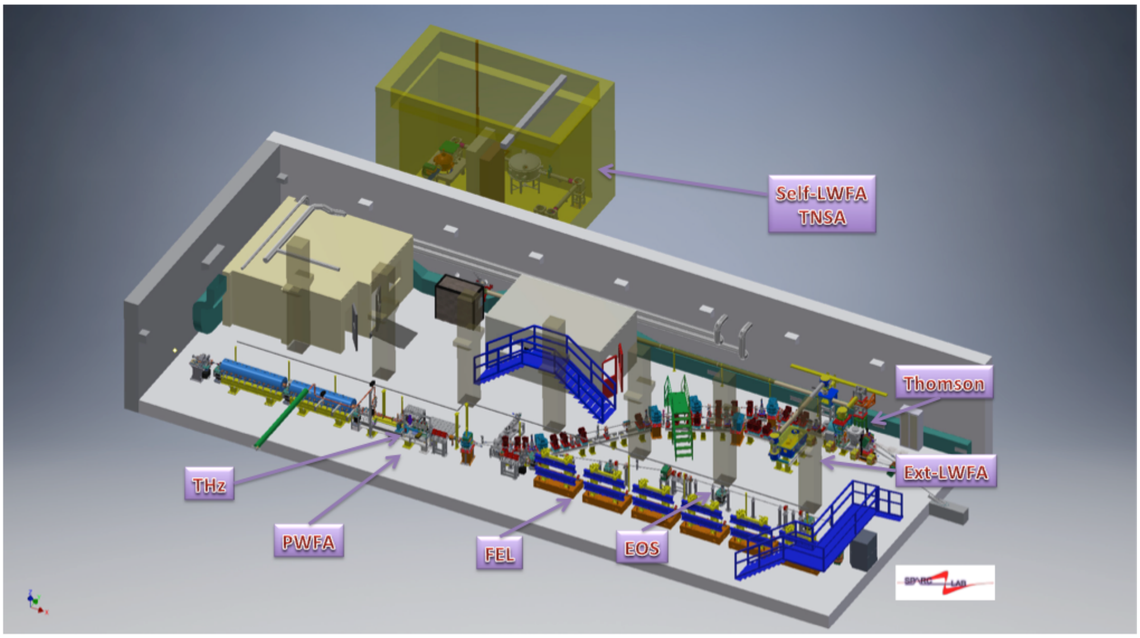

Figure 1.11: Layout of SPARC_LAB beam lines.

experimental observation of the double emittance minima effect, on which is based the optimized matching with the SPARC linac, has been achieved [40].

In addition, a new electron bunch compression scheme, named *Velocity Bunching* [47], has been successfully demonstrated [42] together with the possibility to generate a train of short electron pulses, the *COMB* scheme [49, 50], as the one required to drive PWFA experiments with high transformer ratio [51].

Taking profit of the short (∼100 fs) electron bunches as produced by the VB compression scheme, a source of both broad band and high energy (> 40 μJ) THz radiation has been developed and successfully commissioned [52], resulting in the first user experiment performed at SPARC_-LAB and documented in a recent Nature Communication paper [53]. THz radiation has been also generated and characterized taking advantage from the COMB like electron beam manipulation to provide a high intensity, narrow band (<30%) and tunable radiation source [54, 55].

A hybrid compression scheme (velocity bunching and dogleg) has been also tested demonstrating the reduction of relative arrival time jitter down to 19 fs RMS between the electron bunch and the external photo-cathode laser by control of the longitudinal beam dynamics [56]. This scheme can be also adopted in case of LWFA with external injection of high brightness electron bunches to reduce the time jitter, with benefits for the stability of the acceleration process.

Conventional and novel Free Electron Laser (FEL) emission schemes have been also tested and developed with this machine layout, producing coherent radiation tunable from 500 nm down to 37 nm (with harmonics); in addition new regimes of operation like Seeding, Single Spike, Harmonic Generation and Two-Color radiation have been observed [21, 22, 57–64].

The integration of the SPARC high brightness photo-injector and the high intensity FLAME laser has driven to the development and characterization of a γ-rays source from Thomson back-scattering [65]. Electron and photon beams have been synchronized at the scale of <50 fs [66, 67], an essential requirement for the recent successful operation of the X-rays (∼50 keV) Thomson back-scattering source [68–70] and for the future investigation of new ultra-compact acceleration techniques (> 1 GV/m) based on external injection of high quality electron beams in a plasma wave.

The operation of the FLAME laser alone has led to electrons acceleration up to 400 MeV in

2–4 mm long plasma wave [45] with less than 20% energy spread [71, 72]. Innovative electron beam transverse diagnostics based on betatron radiation have been conceived and tested [73–75]. Finally, preliminary experiments on ion acceleration by Target Normal Sheath Acceleration (TNSA) have been performed showing, for the first time, direct time-dependent measurements of energetic electrons ejected from solid targets by the interaction with a short-pulse high-intensity laser. Our snapshots have captured their evolution with an unprecedented temporal resolution, demonstrating a significant boost in charge and energy of escaping electrons when increasing the geometrical target curvature [76]. These results pave the way toward significant improvement in laser acceleration of ions using shaped targets allowing the future development of small scale laser-ion accelerators.

In Autumn 2015 a long shutdown was foreseen to prepare the facility to host plasma acceleration experiments. The last 3 m long low gradient ($\sim$15 MV/m) S-band TW accelerating section has been replaced by a 1.4 m long structure operating in the C–band at 5.712 GHz, with an average accelerating field of $\sim$ 35 MV/m [77], and a plasma chamber for PWFA experiments, hosting diagnostics, permanent magnet quadrupoles and the capillary, which represents the plasma accelerating structure [26]. The recent layout of SPARC is displayed in Figure 1.12.

The plasma interaction chamber, placed at the end of the linac, is fully equipped with diagnostics, both transverse and longitudinal, based on Electro–Optical sampling [26] and THz radiation [52, 54], with a H_2 plasma discharge capillary [78] and permanent quadrupole magnets for beam matching in and out from the plasma. At the end of the linac a diagnostics and matching section allows to characterize the 6D electron beam phase space and to match the beam to the beamlines.

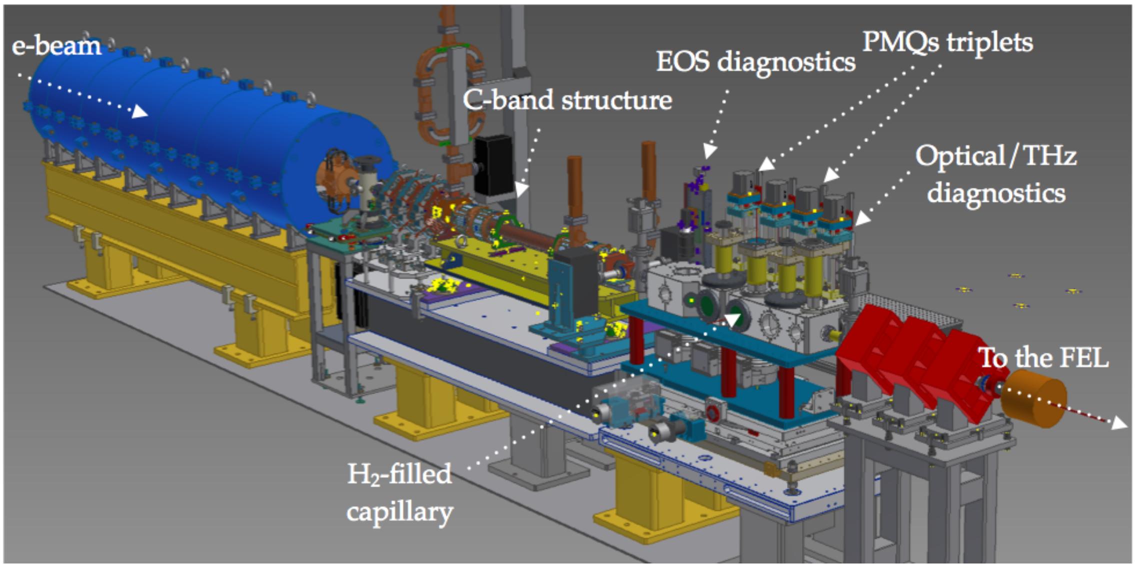

Figure 1.12: Update layout of the photo–injector. The third S-band structure has been replaced by a C–band structure and the plasma interaction chamber, fully equipped with beam and plasma diagnostics and permanent quadrupole magnets.

With the present layout, both active [79] and passive [80] plasma lens experiments have been successfully designed [81] and performed [82] to provide focusing gradients of the order of kT/m with radially symmetric focusing thus meet matching conditions requirements for the final focus of the incoming high brightness beam down to few microns size at the plasma accelerating module and the capture of the high divergent beam at the exit without loss of beam quality. Plasma-based lenses could result in a promising compact and affordable alternative to permanent magnets in the design of transport lines.

The external injection beam line for plasma acceleration is also under commissioning and preparatory experiments have been performed to set the electron beam dynamics and the laser transport parameters; in addition, laser–capillary interaction has been investigated [83] and further experiments to characterize the plasma source, study the electric discharge, measure the plasma density and the capillary geometry are underway.

The SPARC_LAB test facility will enable LNF in the next 5 years to establish a solid background in plasma accelerator physics and to train a young generation of scientists to meet all the challenges addressed by the EuPRAXIA@SPARC_LAB project.

1.7 The EuPRAXIA@SPARC_LAB infrastructure at LNF

The EuPRAXIA@SPARC_LAB project requires the construction of a new building to house the accelerator, the FEL, the Experimental room and the support laboratories.

The new facility will be built in the South–East part of LNF area. It will cover approximately an area of 9000 m^2 and it will be located at an elevation ranging from 205 to 218 m above sea level.

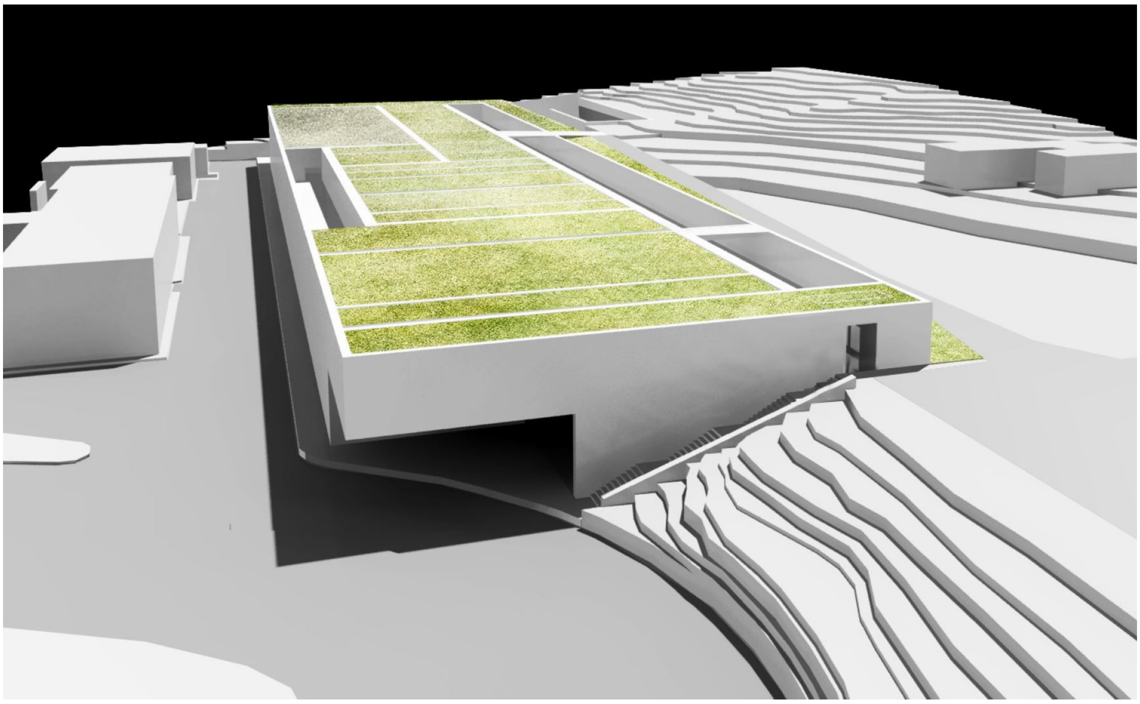

Figure 1.13: 3D view (West side) of the EuPRAXIA@SPARC_LAB building.

Figure 1.13 shows a 3D view of the new proposed building in its surroundings: the foreseen location takes advantage of the difference in height of the soil for a natural shielding from radiation.

The facility will have an L shape and presents a total length of 130 m and a width of 35 m (up to 86 m in a zone reserved for storage and auxiliary plants). It comprises a main building housing the accelerator machine and ancillary equipment, and another one under the natural ground level for plants and storage. Both will be built at the same depth, in cut and cover method.

The main building will be a parallelepiped 130 m long and 35 m wide that will be developed in East/South–West direction. It will have a roof garden for radioprotection reason and to minimize the visual impact on the environment.

The building for auxiliary plants will house a new electrical substation, primary refrigerating plants (dry cooler and pumps) and primary cooling circuit distribution systems. It will also house a parking area and a storage area.

The key of the architectural layout is mainly dictated by the requirements of the experiments. The building can be divided into three functional zones. The first includes:

- a Linac tunnel housing the injector, the main linear accelerator, plasma and matching. Its dimensions are approximately 58 x 8 m^2 with a height of 6 m. The tunnel will have the walls and a roof of concrete 2 m thick and two main accesses through shielding doors located on opposite sides;
- a modulator and klystron gallery will be adjacent and parallel to the linac tunnel. Being 9 m wide and 6 m high, it will allow, with proper penetrations, the access of the waveguides feeding the linac sections. In this area a 5 Tons crane will be installed to facilitate the movement of klystrons. The gallery will be extended to the overall length of the building to allow access to experimental rooms and to house the main electrical and cooling distribution;
- some laboratories (THz, Laser Sync, 2x500 TW rooms), with different dimensions, will be distributed along the linac tunnel. A large corridor allows access into them;
- a radiation users room will be located adjacent the linac, in the opposite side of services gallery. Walls and roof will have the same thickness of linac tunnel (2 m concrete). The entrance will be through a shielding door;
- the part above the ancillary laboratories will be dedicated to the control room, the racks room, a meeting room and offices. The access to the first floor is through a lift and a staircase. The control room will be located approximately midway along the accelerator.

The second functional zone of the building consists of a large hall including the Undulator/FEL hall and 2 HEP rooms

The Undulator/FEL hall is located downstream the linac tunnel and is at the same level. The dividing wall between the two areas will be a removable wall of 2 m concrete with adequate horizontal holes by means of which the electron beam vacuum chamber passes. The dimensions of this hall are approximately 35 x 10 m^2 with a height of 6 m. The roof will be 2 m concrete. The main access is in the services gallery by a shielding door. Adjacent to the undulator hall, two experimental rooms will be dedicated to HEP. A 1 m thick wall separates the Undulator/FEL hall from HEP rooms, but two chicanes allow the access from side to side.

The third functional zone of the building is the Experimental room. It is a big open space of about 34 x 33 m^2, 8.5 m height. 2 m removable shielding wall separates it from Undulator/FEL hall. The Experimental room will have a little gallery housing a meeting room and some offices for the external users. The first level will be reached by a staircase from ground floor and through an external stairway from *via W. Heisenberg*.

The roof level will be devoted to a garden that must contribute to ionizing radiation shield, and to minimize the impact on the environmental contest.

Another building, completely underground, will be built next to the main building and connected to it. It will be approximately 50 x 35 m^2 and will have two levels.

The first level will be at the same level of the Linac tunnel and will be a big storage area. The second one will be dedicated partly to conventional facilities for the experimental buildings and partly to a parking area. Here an electrical substation and cooling plants (dry coolers, chillers and pumping station) will be installed to feed and support the accelerator machine.

The building will have three main access for people and vehicles: one from *via W. Heisenberg* to the lower level, passes through the EuPRAXIA@SPARC_LAB building, near the linac tunnel; another one from *via W. Heisenberg* but through a sloping road accessing plants area and parking area. The third access will be from *piazzale G. Marconi* to the second level. In addition, an adequate number of emergency exits will be provided, in compliance with the safety rules.

1.8 Preliminary project cost estimate and timeline

The Project is organized in two phases. In the first one (Phase 1), all the elements which are mandatory to operate the infrastructure accordingly to EuPRAXIA requirements (the X-band 0.9 GeV linac, the plasma section, and the undulator) must be available at day one, soon after the completion of the Infrastructure. In the second one (Phase 2), the facility will be upgraded in energy (1.3 GeV), in the power of the laser, and equipped with the end user FEL station.

A preliminary evaluation of the costs of the project takes into account the following elements for Phase 1 (all costs are VAT excluded), see Table 1.3:

- **2,700 k€** for the EuPRAXIA@SPARC_LAB Infrastructure project, including the definitive and executive design, the management of the construction and the trials.
- **15,000 k€** for the EuPRAXIA@SPARC_LAB Infrastructure building, including the hub for services and storage. The cost has been evaluated through a metric estimate made by a civil engineer. The esteem is preliminary, but conservative, and will be optimized before launching the tenders.
- **6,500 k€** for the EuPRAXIA@SPARC_LAB technical services (ventilation, cooling, power, network, clean rooms, safety controls, shielding doors, etc...). The expected cost is for an assumption of a total installed power of 2 MW, and it is based on the experience of the recently approved bids for the construction of ELI–NP [84];
- **15,400 k€** for the injector and X-band 500 MeV linac. The evaluation is based on the experiences of the SPARC_LAB , STAR and ELI–NP projects, together with the specific expertise of the CERN CLIC team. The quote, for Phase 1, includes the option of using parts from SPARC_LAB laboratory;
- **1,000 k€** for the plasma beam line;
- **10,000 k€** for the FEL undulators and associated photon diagnostics. The evaluation is based on recent projects and on SPARC_LAB experience.

At a later stage (Phase 2), and as soon as resources will be available, the following components are necessary to implement the user facility:

- **2,000 k€** for an injector upgrade;
- **5,000 k€** for the FLAME laser upgrade up to 0.5 TW;
- **4,800 k€** for X-band klystron upgrade to bring energy up to 1.3 GeV;
- **1,000 k€** for further photon diagnostics;
- **5,000 k€** for the FEL user end station.

The total cost, VAT excluded, of EuPRAXIA@SPARC_LAB project is **50,600 k€** (Phase 1), and **17,800 k€** (Phase 2).

A very preliminary timeline of the project, see Figure 1.14, has been outlined setting the following milestones, for the construction of the infrastructure, and for the realization of the machine, respectively:

- by the end of 2018, the launch of the bid for the realization of the definitive and executive project, including the request for construction approvals;
- by the end of 2019, the completion of a Technical Design Report (**M1**);
- by the 1st quarter of 2020, the launch of the bid for the construction;
- by the 1st quarter of 2021, the start of the construction;
- by the 1st quarter of 2023, the building should be available and ready for installation (**M2**).
- by the end of 2020, the launch of bids for the material procurement of the X-band linac, the High Power Laser and the FEL undulator;
- by the end of 2023, the start of the installation of the machine (**M3, M4, M5, M6, M7**);
- by the 2nd quarter of 2024, the start of the commissioning of the facility, with the Phase 1 configuration which can satisfy EuPRAXIA requirements (**M8**).
- Plasma driven FEL demonstration at 3 nm by 1st quarter of 2025 (**M9**);

- User beamline ready by the 2nd quarter of 2025 (**M10**);
- Pilot user operations are expected to start by the end of 2025 (**M11**).

The separation in time between Phase 1 and Phase 2 will be dictated mainly by the availability of economical resources and not by technical difficulties.

Infrastructure	**Cost (k€)**	**Partial cost (k€)**	**Incremental cost (k€)**
Building Project	2,700		
Building Construction	15,000		
Building Technical Services	6,500	24,200	24,200
Components Phase 1			
Injector	600		
Compressor	300		
4 X-band Linac modules	11,000		
Beam diagnostics	1,500		
LLRF & Synch.	1,400		
Control System	600	15,400	39,600
Plasma module and diagnostics	500		
Plasma beam line	500	1,000	40,600
Undulators	9,000		
Photon Diagnostics	1,000	10,000	**50,600**
Components Phase 2			
Injector upgrade	2,000		
FLAME upgrade	5,000		
X-band Kly upgrade	4,800		
Photon Optics	1,000		
User end station	5,000	**17,800**	***68,400***

Table 1.3: Preliminary cost evaluation of the EuPRAXIA@SPARC_LAB facility.

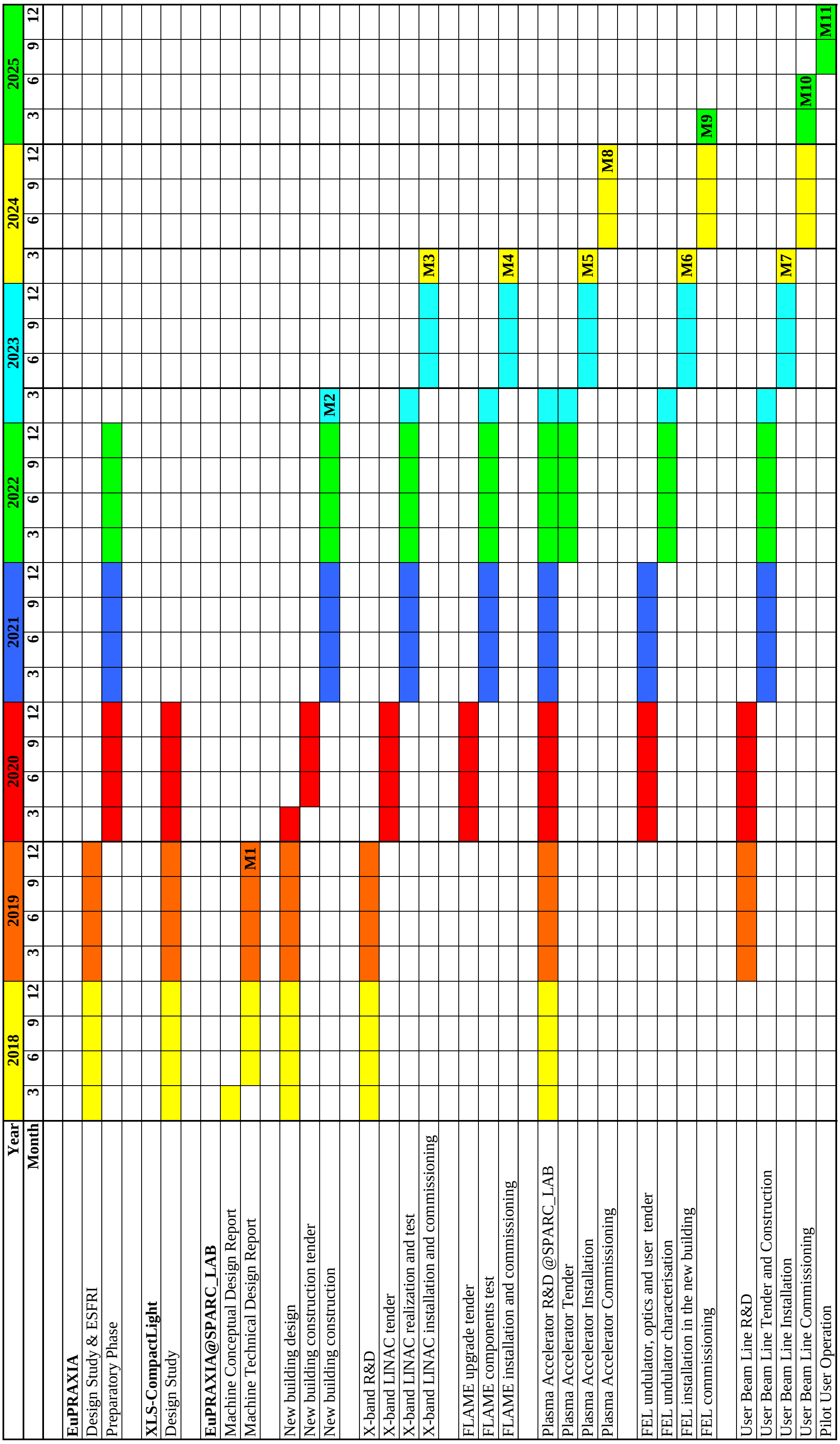

Figure 1.14: Timeline of the EuPRAXIA@SPARC_LAB project.

Bibliography

[1] Ralph Aßmann and Julia Grebenyuk. “Accelerator Physics Challenges towards a Plasma Accelerator with Usable Beam Quality”. In: *5th International Particle Accelerator Conference*. PUBDB-2015-00732. 2014.

[2] T Tajima and JM Dawson. “Laser electron accelerator”. In: *Physical Review Letters* 43.4 (1979), p. 267.

[3] Donna Strickland and Gerard Mourou. “Compression of amplified chirped optical pulses”. In: *Optics communications* 55.6 (1985), pp. 447–449.

[4] Chandrashekhar Joshi. “Plasma accelerators”. In: *Scientific American* 294.2 (2006), pp. 40–47.

[5] D Gordon et al. “Observation of electron energies beyond the linear dephasing limit from a laser-excited relativistic plasma wave”. In: *Physical review letters* 80.10 (1998), p. 2133.

[6] Victor Malka. “Laser plasma accelerators”. In: *Physics of Plasmas* 19.5 (2012), p. 055501.

[7] Massimo Ferrario. “Present and future accelerator options beyond the LHC”. In: *Annalen der Physik* 528.1-2 (2016), pp. 151–160.

[8] PA Walker et al. *EuPRAXIA Deliverable Report 1.2 Report defining preliminary study concept*. 2016.

[9] V Ayvazyan et al. “Generation of GW radiation pulses from a VUV free-electron laser operating in the femtosecond regime”. In: *Physical review letters* 88.10 (2002), p. 104802.

[10] Toru Hara. “Free-electron lasers: Fully coherent soft X-rays at FERMI”. In: *Nature Photonics* 7.11 (2013), p. 852.

[11] Paul Andreas Walker et al. “Horizon 2020 EuPRAXIA design study”. In: *Journal of Physics: Conference Series*. Vol. 874. 1. IOP Publishing. 2017, p. 012029.

[12] W. Wuensch. “Ultimate Field Gradient in Metallic Structures”. In: *Proc. of International Particle Accelerator Conference (IPAC’17), Copenhagen, Denmark, 14-19 May, 2017*. 8. 2017, pp. 24–29.

[13] URL: `https://compactlight.web.cern.ch`.

[14] A Zigler et al. “Elongated high-temperature, dense plasma produced by a high-power-laser heating of a capillary discharge”. In: *Physical Review A* 35.10 (1987), p. 4446.

[15] B Brill et al. “Density measurement of dense capillary discharge plasma using soft X-ray backlighting”. In: *Journal of Physics D: Applied Physics* 23.8 (1990), p. 1064.

[16] Y Ehrlich et al. “Generation of large, high density, homogeneous plasma by capillary discharge”. In: *Applied physics letters* 64.26 (1994), pp. 3542–3544.

[17] S Steinke et al. “Multistage coupling of independent laser-plasma accelerators”. In: *Nature* 530.7589 (2016), p. 190.

[18] Walter Wuensch. “Ultimate Field Gradient in Metallic Structures”. In: *8th Int. Particle Accelerator Conf.(IPAC’17), Copenhagen, Denmark, 14–19 May, 2017*. JACOW, Geneva, Switzerland. 2017, pp. 24–29.

[19] *See for example: Proc. of "International workshop on high-gradient acceleration", Valencia (Spain) , June 2017*. URL: `https://indico.cern.ch/event/589548/`.

[20] R Bonifacio. “R. Bonifacio, C. Pellegrini, and LM Narducci, Opt. Commun. 50, 373 (1984).” In: *Opt. Commun.* 50 (1984), p. 373.

[21] L Giannessi et al. “High-order-harmonic generation and superradiance in a seeded free-electron laser”. In: *Physical review letters* 108.16 (2012), p. 164801.

[22] M Labat et al. “High-gain harmonic-generation free-electron laser seeded by harmonics generated in gas”. In: *Physical review letters* 107.22 (2011), p. 224801.

[23] P Schutt, T Weiland, and VM Tsakanov. *Proceedings of the Second All-Union Conference on New Methods of Charged Particle Acceleration*. 1989.

[24] P Muggli et al. “Simple method for generating adjustable trains of picosecond electron bunches”. In: *Physical Review Special Topics-Accelerators and Beams* 13.5 (2010), p. 052803.

[25] M Boscolo et al. “A train of micro-bunches for PWFA experiments produced by RF photoinjectors”. In: *International Journal of Modern Physics B* 21 (2007), pp. 415–421.

[26] R Pompili et al. “First single-shot and non-intercepting longitudinal bunch diagnostics for comb-like beam by means of Electro-Optic Sampling”. In: *Nuclear Instruments and Methods in Physics Research Section A: Accelerators, Spectrometers, Detectors and Associated Equipment* 740 (2014), pp. 216–221.

[27] Silvia Cipiccia et al. “Gamma-rays from harmonically resonant betatron oscillations in a plasma wake”. In: *Nature Physics* 7.11 (2011), p. 867.

[28] Z Najmudin et al. “Compact laser accelerators for X-ray phase-contrast imaging”. In: *Phil. Trans. R. Soc. A* 372.2010 (2014), p. 20130032.

[29] TG Blackburn et al. “Quantum radiation reaction in laser–electron-beam collisions”. In: *Physical review letters* 112.1 (2014), p. 015001.

[30] Henry N Chapman et al. “Femtosecond diffractive imaging with a soft-X-ray free-electron laser”. In: *Nature Physics* 2.12 (2006), p. 839.

[31] Sébastien Boutet et al. “High-resolution protein structure determination by serial femtosecond crystallography”. In: *Science* (2012), p. 1217737.

[32] Henry N Chapman et al. “Femtosecond X-ray protein nanocrystallography”. In: *Nature* 470.7332 (2011), p. 73.

[33] M Marvin Seibert et al. “Single mimivirus particles intercepted and imaged with an X-ray laser”. In: *Nature* 470.7332 (2011), p. 78.

[34] Gijs Van Der Schot et al. “Imaging single cells in a beam of live cyanobacteria with an X-ray laser”. In: *Nature communications* 6 (2015), p. 5704.

[35] Max F Hantke et al. “High-throughput imaging of heterogeneous cell organelles with an X-ray laser”. In: *Nature Photonics* 8.12 (2014), p. 943.

[36] Richard Henderson. “The potential and limitations of neutrons, electrons and X-rays for atomic resolution microscopy of unstained biological molecules”. In: *Quarterly reviews of biophysics* 28.2 (1995), pp. 171–193.

[37] C Gutt et al. “Single-pulse resonant magnetic scattering using a soft x-ray free-electron laser”. In: *Physical Review B* 81.10 (2010), p. 100401.

[38] M Ferrario et al. “SPARC_LAB present and future”. In: *Nuclear Instruments and Methods in Physics Research Section B: Beam Interactions with Materials and Atoms* 309 (2013), pp. 183–188.

[39] D Alesini et al. “The SPARC project: a high-brightness electron beam source at LNF to drive a SASE-FEL experiment”. In: *Nuclear Instruments and Methods in Physics Research Section A: Accelerators, Spectrometers, Detectors and Associated Equipment* 507.1-2 (2003), pp. 345–349.

[40] M Ferrario et al. “Direct measurement of the double emittance minimum in the beam dynamics of the sparc high-brightness photoinjector”. In: *Physical review letters* 99.23 (2007), p. 234801.

[41] A Cianchi et al. “High brightness electron beam emittance evolution measurements in an rf photoinjector”. In: *Physical Review Special Topics-Accelerators and Beams* 11.3 (2008), p. 032801.

[42] M Ferrario et al. “Experimental demonstration of emittance compensation with velocity bunching”. In: *Physical review letters* 104.5 (2010), p. 054801.

[43] D Filippetto et al. “Phase space analysis of velocity bunched beams”. In: *Physical Review Special Topics-Accelerators and Beams* 14.9 (2011), p. 092804.

[44] M Ferrario et al. “Laser comb with velocity bunching: Preliminary results at SPARC”. In: *Nuclear Instruments and Methods in Physics Research Section A: Accelerators, Spectrometers, Detectors and Associated Equipment* 637.1 (2011), S43–S46.

[45] D Alesini et al. “The project PLASMONX for plasma acceleration experiments and a Thomson X-ray source at SPARC”. In: *Particle Accelerator Conference, 2005. PAC 2005. Proceedings of the*. IEEE. 2005, pp. 820–822.

[46] LA Gizzi et al. “Acceleration with self-injection for an all-optical radiation source at LNF”. In: *Nuclear Instruments and Methods in Physics Research Section B: Beam Interactions with Materials and Atoms* 309 (2013), pp. 202–209.

[47] L Serafini and M Ferrario. “Velocity bunching in photo-injectors”. In: *AIP conference proceedings*. Vol. 581. 1. AIP. 2001, pp. 87–106.

[48] A Mostacci et al. “Analysis methodology of movable emittance-meter measurements for low energy electron beams”. In: *Review of Scientific Instruments* 79.1 (2008), p. 013303.

[49] F Villa et al. “Laser pulse shaping for high gradient accelerators”. In: *Nuclear Instruments and Methods in Physics Research Section A: Accelerators, Spectrometers, Detectors and Associated Equipment* 829 (2016), pp. 446–451.

[50] A Mostacci et al. “Advanced beam manipulation techniques at SPARC”. In: *IPAC 2011-2nd International Particle Accelerator Conference*. 2011, pp. 2877–2881.

[51] E Chiadroni et al. “Beam manipulation for resonant plasma wakefield acceleration”. In: *Nuclear Instruments and Methods in Physics Research Section A: Accelerators, Spectrometers, Detectors and Associated Equipment* 865 (2017), pp. 139–143.

[52] E Chiadroni et al. “The SPARC linear accelerator based terahertz source”. In: *Applied Physics Letters* 102.9 (2013), p. 094101.

[53] Flavio Giorgianni et al. “Strong nonlinear terahertz response induced by dirac surface states in Bi 2 Se 3 topological insulator”. In: *Nature communications* 7 (2016), p. 11421.

[54] E Chiadroni et al. “Characterization of the THz radiation source at the Frascati linear accelerator”. In: *Review of Scientific Instruments* 84.2 (2013), p. 022703.

[55] Flavio Giorgianni et al. “Tailoring of highly intense THz radiation through high brightness electron beams longitudinal manipulation”. In: *Applied Sciences* 6.2 (2016), p. 56.

[56] Riccardo Pompili et al. “Femtosecond timing-jitter between photo-cathode laser and ultra-short electron bunches by means of hybrid compression”. In: *New Journal of Physics* 18.8 (2016), p. 083033.

[57] L Giannessi et al. “Self-amplified spontaneous emission free-electron laser with an energy-chirped electron beam and undulator tapering”. In: *Physical review letters* 106.14 (2011), p. 144801.

[58] L Giannessi et al. "Superradiant cascade in a seeded free-electron laser". In: *Physical review letters* 110.4 (2013), p. 044801.

[59] V Petrillo et al. "Observation of time-domain modulation of free-electron-laser pulses by multipeaked electron-energy spectrum". In: *Physical review letters* 111.11 (2013), p. 114802.

[60] F Ciocci et al. "Two color free-electron laser and frequency beating". In: *Physical review letters* 111.26 (2013), p. 264801.

[61] V Petrillo et al. "Dual color x rays from Thomson or Compton sources". In: *Physical Review Special Topics-Accelerators and Beams* 17.2 (2014), p. 020706.

[62] LL Lazzarino et al. "Self-amplified spontaneous emission free electron laser devices and nonideal electron beam transport". In: *Physical Review Special Topics-Accelerators and Beams* 17.11 (2014), p. 110706.

[63] C Ronsivalle et al. "Large-bandwidth two-color free-electron laser driven by a comb-like electron beam". In: *New Journal of Physics* 16.3 (2014), p. 033018.

[64] A Petralia et al. "Two-color radiation generated in a seeded free-electron laser with two electron beams". In: *Physical review letters* 115.1 (2015), p. 014801.

[65] C Vaccarezza et al. "The SPARC_LAB Thomson source". In: *Nuclear Instruments and Methods in Physics Research Section A: Accelerators, Spectrometers, Detectors and Associated Equipment* 829 (2016), pp. 237–242.

[66] *M. Bellaveglia et al., SPARC Internal Note*.

[67] M Bellaveglia et al. "The SPARC_LAB femtosecond synchronization for electron and photon pulsed beams". In: *Advances in X-ray Free-Electron Lasers Instrumentation III*. Vol. 9512. International Society for Optics and Photonics. 2015, p. 95120V.

[68] Piernicola Oliva et al. "Start-to-end simulation of a Thomson source for mammography". In: *Nuclear Instruments and Methods in Physics Research Section A: Accelerators, Spectrometers, Detectors and Associated Equipment* 615.1 (2010), pp. 93–99.

[69] Alberto Bacci et al. "Status of Thomson source at SPARC/PLASMONX". In: *Nuclear Instruments and Methods in Physics Research Section A: Accelerators, Spectrometers, Detectors and Associated Equipment* 608.1 (2009), S90–S93.

[70] U Bottigli et al. "Effect of different spectral distributions to image a contrast detail phantom in the mammography energy range". In: *IL NUOVO CIMENTO DELLA SOCIETÀ ITALIANA DI FISICA. C, GEOPHYSICS AND SPACE PHYSICS* 29.2 (2006), pp. 215–228.

[71] FG Bisesto et al. "The FLAME laser at SPARC_LAB". In: *Nuclear Instruments and Methods in Physics Research Section A: Accelerators, Spectrometers, Detectors and Associated Equipment* (2018).

[72] G. Costa et al. "Characterization of self-injected electron beams from LWFA experiments at SPARC_LAB". In: *Nuclear Instruments and Methods in Physics Research Section A: Accelerators, Spectrometers, Detectors and Associated Equipment* (2018). ISSN: 0168-9002. DOI: `https://doi.org/10.1016/j.nima.2018.02.008`. URL: `http://www.sciencedirect.com/science/article/pii/S016890021830158X`.

[73] V Shpakov et al. "Betatron radiation based diagnostics for plasma wakefield accelerated electron beams at the SPARC_LAB test facility". In: *Nuclear Instruments and Methods in Physics Research Section A: Accelerators, Spectrometers, Detectors and Associated Equipment* 829 (2016), pp. 330–333.

[74] A Curcio et al. “Trace-space reconstruction of low-emittance electron beams through betatron radiation in laser-plasma accelerators”. In: *Physical Review Accelerators and Beams* 20.1 (2017), p. 012801.

[75] A Curcio et al. “First measurements of betatron radiation at FLAME laser facility”. In: *Nuclear Instruments and Methods in Physics Research Section B: Beam Interactions with Materials and Atoms* 402 (2017), pp. 388–392.

[76] R Pompili et al. “Femtosecond dynamics of energetic electrons in high intensity laser-matter interactions”. In: *Scientific reports* 6 (2016), p. 35000.

[77] D Alesini et al. “The C-Band accelerating structures for SPARC photoinjector energy upgrade”. In: *Journal of Instrumentation* 8.05 (2013), P05004.

[78] MP Anania et al. “Plasma production for electron acceleration by resonant plasma wave”. In: *Nuclear Instruments and Methods in Physics Research Section A: Accelerators, Spectrometers, Detectors and Associated Equipment* 829 (2016), pp. 254–259.

[79] R Pompili et al. “Experimental characterization of active plasma lensing for electron beams”. In: *Applied Physics Letters* 110.10 (2017), p. 104101.

[80] A Marocchino et al. “Experimental characterization of the effects induced by passive plasma lens on high brightness electron bunches”. In: *Applied Physics Letters* 111.18 (2017), p. 184101.

[81] F Filippi et al. “Spectroscopic measurements of plasma emission light for plasma-based acceleration experiments”. In: *Journal of Instrumentation* 11.09 (2016), p. C09015.

[82] E Chiadroni et al. “Overview of Plasma Lens Experiments and Recent Results at SPARC_-LAB”. In: *arXiv preprint arXiv:1802.00279* (2018).

[83] FG Bisesto et al. “Laser–capillary interaction for the EXIN project”. In: *Nuclear Instruments and Methods in Physics Research Section A: Accelerators, Spectrometers, Detectors and Associated Equipment* 829 (2016), pp. 309–313.

[84] O Adriani et al. “Technical design report eurogammas proposal for the eli-np gamma beam system”. In: *arXiv preprint arXiv:1407.3669* (2014).

II Machine Physics

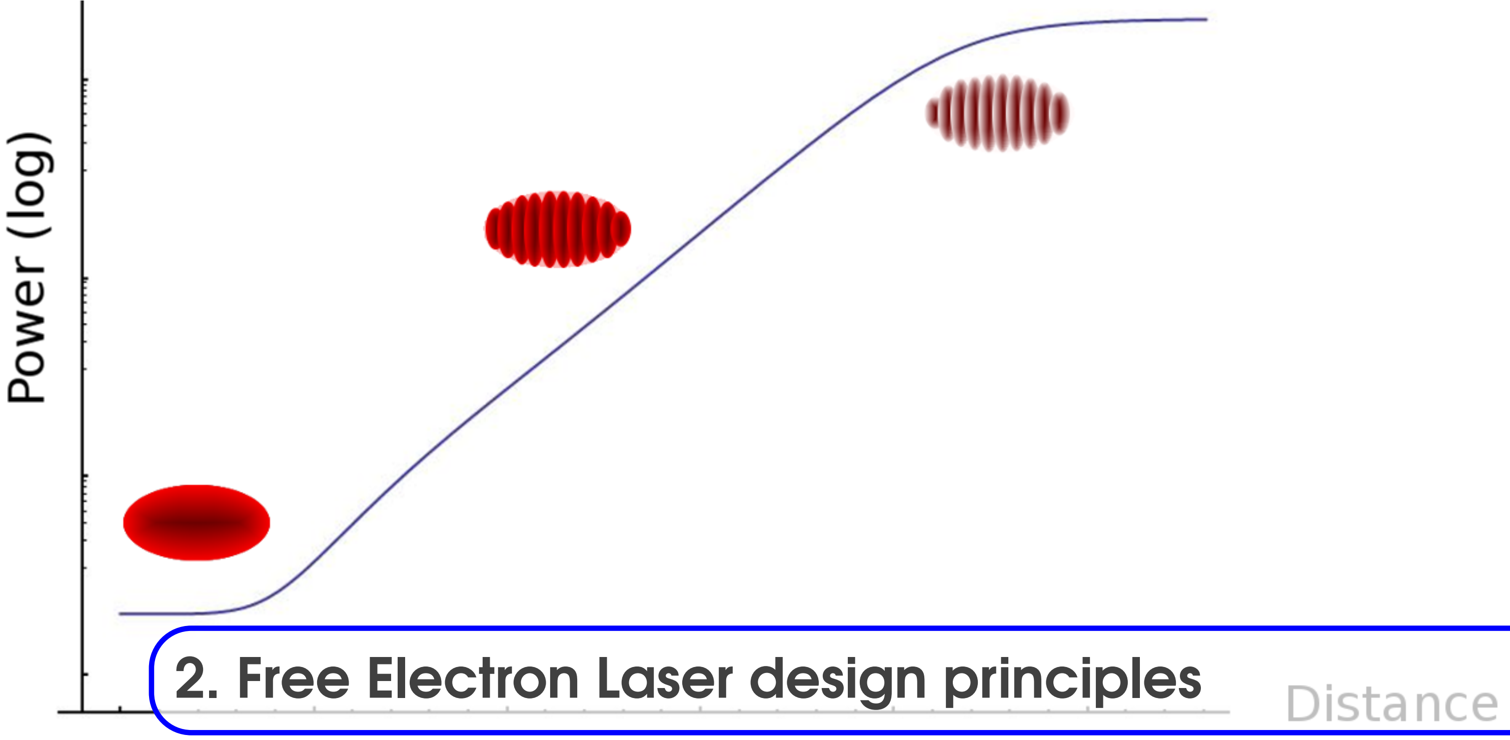

2. Free Electron Laser design principles

The choice of FEL configuration and radiation scheme for the EuPRAXIA@SPARC_LAB FEL is based on user-defined requirements of the properties of the output FEL pulses, i.e., radiation wavelength, peak power, polarization and required average repetition rate. The time structure of the pulse has to be matched to the characteristic timescales of physical processes under study. For X-ray imaging and other high intensity applications, the photons should be delivered in ultra-short, high intensity pulses. On the other hand, spectroscopic studies require limited peak intensity so as to avoid non-linear processes, but also a high repetition rate in order to collect sufficient data in acceptable experimental periods.

One interesting spectral region of operation is the water window between 2.5 nm and 4 nm . Users typically need about 10^{11} photons/pulse in a 0.1% bandwidth at tunable wavelength within the water window at the experimental end station. Such radiation allows to study materials and biological tissues below the threshold of absorption of carbon. The machine we are proposing aims to give radiation indeed in this range of wavelengths. Since no mirrors are available for confining radiation in a resonator at the wavelengths of interest, the SASE configuration is the most suitable for EuPRAXIA@SPARC_LAB .

Other requirements that drive the design are tunability, pulse duration, pulse-to-pulse stability, timing and synchronization and degree of polarization.

The layout of the EuPRAXIA@SPARC_LAB FEL is designed with the aim of covering as much as possible all the requests of the users. However, the constraints related to the available space in the building for allocating the undulator line have to be considered.

The performance of a Free Electron Laser (FEL) operating in the Self Amplifies Spontaneous Emission (SASE) regime depends on the quality of the electron beam, which is the active medium of the lasing process [1, 2]. Start to end (S2E) beam dynamics simulations from the injector up to the undulator exit are a fundamental tool to establish the optimal working point with realistic beam parameters. A number of reliable simulations tools (for example: ASTRA [3], GPT [4] and TSTEP [5] (injector), ELEGANT [6] (Linac), ARCHITECT [7] and QFLUID [8] (Plasma), PROMETEO [9], PERSEO [10] and GENESIS [11] (FEL)) have been developed in the last decade enabling the design of an effective FEL working point. Unfortunately the computing time needed to perform S2E simulations requires several CPU hours for each parameter set and the parameter space to investigate is very large. From the 3D FEL theory it has been possible to derive a number of effective analytical scaling laws [12–14] that allow a fast scan of the parameter space and the identification of an ideal FEL working point in a much shorter time. The results of the scaling laws analysis can be used as an excellent starting point for the unavoidable S2E optimization, thus reducing considerably the number of numerical iterations.

We report in this paragraph the scaling laws that have been used for our design study and the resulting target parameter table for two complementary cases, both enabling operation of a SASE FEL driven by a 1 GeV electron beam:

1. low charge (30 pC) plasma driven FEL and
2. high charge (200 pC) X-band RF linac driven FEL.

The Free-electron laser theory has been developed, starting from the eighties, in a set of historical works (see, for instance, refs. [1, 15, 16]), where from the Newton-Lorentz equations and the Maxwell system a set of differential equations for the electrons and for the radiation has been deduced. From these equations, scaling laws for the most important quantities of the process derive.

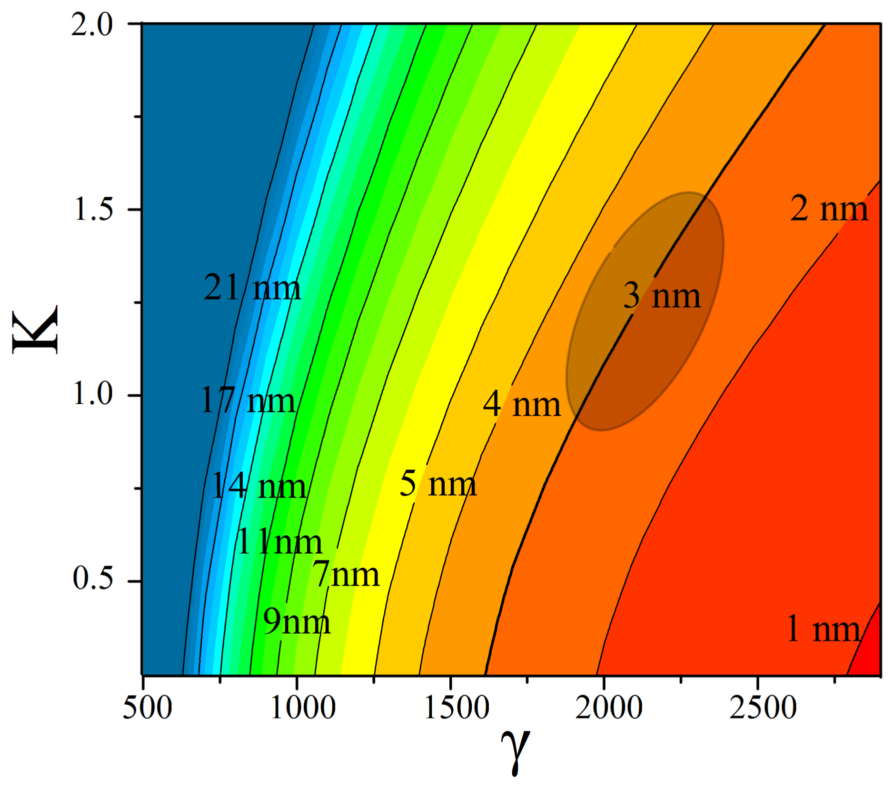

Figure 2.1: Radiation wavelength as function of electron Lorentz factor and undulator parameter K with an undulator period $\lambda_u = 1.5$ cm. A value of $\gamma = 2000$ corresponds to an electron beam energy $E = 1$ GeV. The marked area is to the possible operative parameter region.

In a Free Electron Laser an electron beam propagates in a periodic magnetic field, generated by a magnetic undulator. For a single electron of given energy E, the resonance condition for the wavelength of the on-axis emitted radiation, in a planar undulator, is

$$\lambda = \frac{\lambda_u}{2\gamma^2}\left(1 + \frac{K^2}{2}\right) \tag{2.1}$$

where λ_u is the period of longitudinal variation of the on-axis magnetic filed for a planar undulator, $\gamma = E/(mc^2)$ is the Lorentz factor depending on the electron beam energy and K is the undulator parameter defined as:

$$K = \frac{eB\lambda_u}{2\pi mc} = 0.934\,\lambda_u[cm]\,B[T] \tag{2.2}$$

B being the peak value of the on-axis magnetic field and e, m and c respectively the electron charge, the electron mass and the speed of light.

We have chosen as a target beam energy 1 GeV that allows FEL operation around 3 nm , within the so called "water window" (2-4 nm), that is an interesting wavelength for users aiming to applications in the biological domain. In addition the resulting machine layout is fully compatible with the available room in the LNF laboratory with the state of the art undulator technology [17]. Shorter wavelength will be also considered in the future depending on the undulator technology development. According to the literature in the field, short period undulator prototypes are now under development at 9 mm [18], 7 mm [19] and 4 mm [20]. The possibility of producing FEL radiation based on these prototypes is not yet demonstrated but we expect a fast growing interest in this technological development, see for example the recently approved H2020 Design Study: XLS (CompactLight) [21]. From eq. (2.1) one can see that changing the energy of the electrons and/or the undulator parameter controls the operational wavelength. The effective FEL tunability range is actually limited by technological constraints related to the undulator and linac design, as it will be clearer from the following discussion. In our design we expect a tunability range of 10–2 nm .

2.1 FEL Scaling Laws on the fundamental wavelength

The FEL process is a collective beam instability where billions of electrons cooperate to produce high peak power radiation within a narrow band around the resonant wavelength defined by eq. (2.1). During the beam propagation through the undulator chain the electron beam self-bunches on the scale of the resonant wavelength via the interaction with the emitted radiation (SASE instability) [22] and a fraction of the electron kinetic energy is exponentially transformed in to electromagnetic energy, see Figure 2.2.

The efficiency of energy transfer from electrons to the electric field and so the gain of the process are summarized by the FEL parameter ρ [1, 15, 16] referred to also as Pierce Parameter:

$$\rho = \frac{1}{4\pi\gamma}\left(2\pi\frac{J}{I_A}\left(\lambda_u K f_b(K)\right)^2\right)^{1/3}, \tag{2.3}$$

where $f_b(K) = J_0(\xi) - J_1(\xi)$ is the planar undulator Bessel correction factor, of argument $\xi = \frac{1}{4}\frac{K^2}{1+K^2}$, J the current density and I_A=17 kA the Alfven current.

In practical units, the above quantity writes

$$\rho \cong \frac{8.36\cdot 10^{-3}}{\gamma}\left[\left(\lambda_u[m]\,K f_b(K)\right)^2 J\left[\frac{A}{m^2}\right]\right]^{1/3} \tag{2.4}$$

The current can, in turn, be expressed in terms of the bunch RMS time duration σ_τ and of the bunch charge Q_b as

$$I = \frac{Q_b}{\sqrt{2\pi}\,\sigma_\tau}. \tag{2.5}$$

The current density J is therefore given by

$$J = \frac{I}{2\pi\sigma_x\sigma_y} = \frac{Q_b}{(2\pi)^{\frac{3}{2}}\sigma_x\sigma_y\sigma_\tau} \tag{2.6}$$

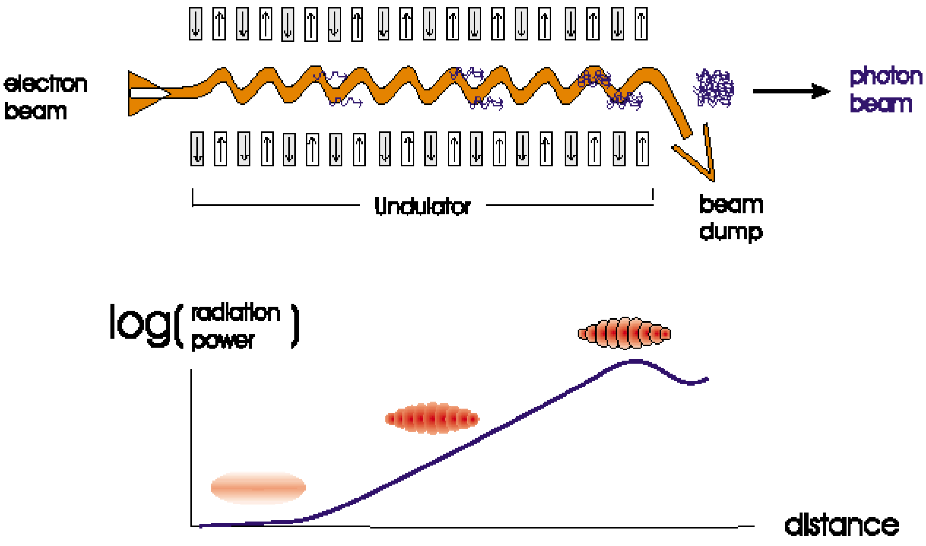

Figure 2.2: Schematic view of the basic SASE-FEL instability showing the exponential growth of radiation power along the undulator

where σ_x and σ_y are the RMS transverse dimensions of the electron beam. The gain length, determining the FEL-SASE growth rate, can be expressed in terms of ρ as follows

$$L_g = \frac{\lambda_u}{4\pi\sqrt{3}\rho}. \tag{2.7}$$

Following the model described in [13, 14], the power growth is fitted by the logistic equation:

$$\begin{aligned} P(z) &= P_0 \frac{A(z)}{1 + \frac{P_0}{P_S}\left[A(z) - 1\right]} \\ A(z) &= \frac{1}{9}\left[3 + 2\cosh\left(\frac{z}{L_g}\right) + 4\cos\left(\frac{\sqrt{3}}{2}\frac{z}{L_g}\right)\cosh\left(\frac{z}{2L_g}\right)\right] \end{aligned} \tag{2.8}$$

in which P_0 is the input seed, P_s the power reached at saturation and z the longitudinal propagation coordinate.

Accordingly, the saturation length, namely the length of the undulator necessary to reach the saturated power, is

$$L_S = 1.066\, L_g \ln\left(\frac{9P_S}{P_0}\right). \tag{2.9}$$

The Pierce parameter gives an estimate of the natural bandwidth of the FEL:

$$\frac{\Delta\omega}{\omega} \cong \rho \tag{2.10}$$

and rules also the power at saturation that writes :

$$P_S \cong \sqrt{2}\,\rho\, P_E \tag{2.11}$$

where P_E is the electron beam power, linked to the peak current and energy by the relation

$$P_E \cong m c^2 \gamma I. \tag{2.12}$$

The effect of inhomogeneous broadening, namely the gain deterioration due to non ideal electron beam qualities (non negligible energy spread and emittance), can be embedded in the previous formulae. The use of a $\tilde{\mu}$ parameters, expressed in terms of the beam emittances, relative energy spread and ρ allows to quantify these effects, which all contribute to increase the gain length.

We define the relative energy spread of the electron beam as

$$\begin{aligned} \sigma_\varepsilon &= \Delta E / E \\ \Delta E &= \sqrt{\langle E^2 \rangle - \langle E \rangle^2} \end{aligned} \tag{2.13}$$

with E the electron beam energy. The gain length can be redefined as

$$\begin{aligned} L_{g,3D}(\chi) &= \chi L_g \\ \chi &\cong 1 + \frac{0.185\sqrt{3}}{2} \tilde{\mu}_\varepsilon^2 \\ \tilde{\mu}_\varepsilon &= 2 \frac{\sigma_\varepsilon}{\rho} \end{aligned} \tag{2.14}$$

Furthermore, considering a transversally symmetric electron beam $\sigma_x = \sigma_y$, the factor:

$$\begin{aligned} \rho_D &= \mathrm{F}(\mu_D)\, \rho \\ \mathrm{F}(\mu_D) &= [1 + \mu_D]^{-1/3} \\ \mu_D &= \frac{\lambda_0 \lambda_u}{(4\pi \sigma_T)^2 \rho} \end{aligned} \tag{2.15}$$

represents the diffraction degradation for the Pierce parameter. A substantially similar analysis of the FEL three-dimensional and inhomogeneous effects, but with different notations and apparently slightly different expression is given in [12]. The electron beam quality influences the FEL gain length. In fact, the three dimensional and inhomogeneous broadenings, due to energy spread and to the normalized beam emittance $\varepsilon_{x,y}$, do not prevent the emission only if:

$$\begin{aligned} \frac{\Delta E}{E} &\ll \rho \\ \varepsilon_{x,y} &\approx \frac{\gamma \lambda}{4\pi} \end{aligned} \tag{2.16}$$

Furthermore, a condition of high current operation (I of the order of the kA), obtained by magnetic or RF compression of the electron beam, should be realized.

The SASE FEL radiation from a planar undulator is linearly polarized in the plane of the electron's wiggle motion.

The transverse coherence of the FEL radiation is quite good [23]. In fact, although many transverse modes are excited at the beginning of the undulator, by the end of the exponential growth only the highest growth rate mode (generally the fundamental mode TEM_{00}) dominates.

As regards the longitudinal coherence, the SASE radiation exhibits a sequence of M uncorrelated temporal spikes [22], whose mutual distance is about $2\pi L_c$, where the cooperation or coherence length L_c is defined as follows:

$$L_c = \frac{\lambda}{2\pi\sqrt{3}\rho} \tag{2.17}$$

	Units	Full RF case	Plasma case
Electron Energy	GeV	1	1
Bunch Charge	pC	200	30
Peak Current	kA	2	3
RMS Energy Spread	%	0.1	1
RMS Bunch Length	fs	40	4
RMS matched Bunch Spot	μm	34	34
RMS norm. Emittance	μm	1	1
Slice length	μm	0.5	0.45
Slice Energy Spread	%	0.01	0.1
Slice norm. Emittance	μm	0.5	0.5
Undulator Period	mm	15	15
Undulator Strength K		1.03	1.03
Undulator Length	m	12	14
Gain Length	m	0.46	0.5
Pierce Parameterρ	x 10^{-3}	1.5	1.4
Radiation Wavelength	nm	3	3
Undulator matching β_u	m	4.5	4.5
Saturation Active Length	m	10	11
Saturation Power	GW	4	5.89
Energy per pulse	μJ	83.8	11.7
Photons per pulse	x 10^{11}	11	1.5

Table 2.1: Beam parameters for the EuPRAXIA@SPARC_LAB FEL driven by X-band linac or Plasma acceleration

and $M \approx L_b/(2\pi L_c)$, where L_b is the electron bunch length. A very interesting radiation mode, the *single spike* regime, occurs when the length of the electron beam is shorter than $2\pi L_c$. Under this condition, the radiation presents a single spike structure [24, 25] both in the temporal and in the spectral domains. Therefore, a substantial coherence in each single radiation shot is achieved, with, however, low shot-to-shot stability. Due to the slippage, saturation is reached quite early. This can be compensated by chirping the electron beam and tapering the undulator. This regime permits the operation at low charge, with a control of emittance and energy spread at the maximum level. Finally, the number of photons per pulse can be estimated by:

$$n_{ph} = \frac{\lambda P_s}{hc}\sigma_{ph} \tag{2.18}$$

σ_{ph} being the time duration of the photon pulse.

A parametric study based on the previous scaling laws suggests to investigate the EuPRAXIA @SPARC_LAB FEL performances and the beam parameters around the values reported in Table 2.1.

With these parameters the power growth into the undulator can be obtained by scaling laws and plotted in Fig. 2.3. The degradation effect on the FEL performance is described in Figs. 2.4 and 2.5, where we show the dependence on energy spread and emittance.

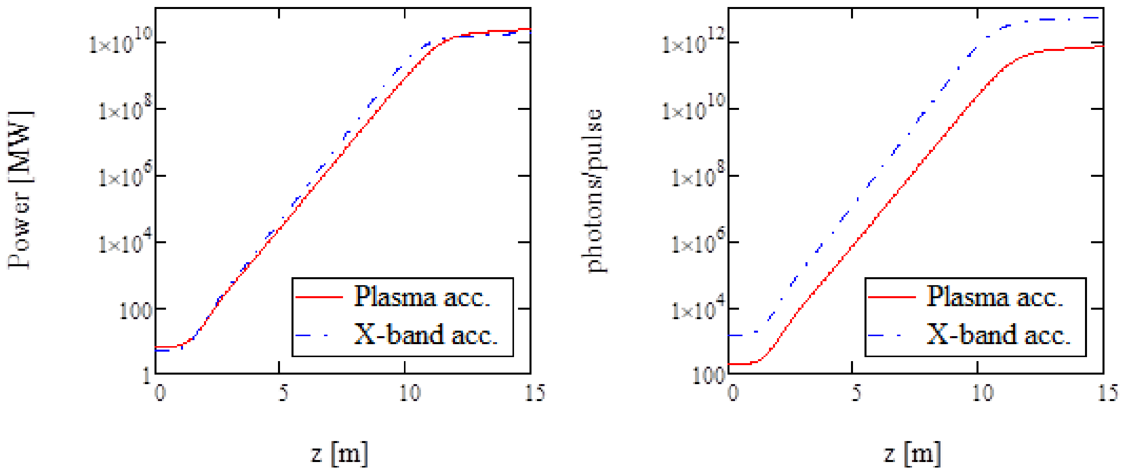

Figure 2.3: Power growth along the active undulator length (without focusing sections) for the reference parameters in the two configuration with Plasma acceleration and X-band Linac acceleration

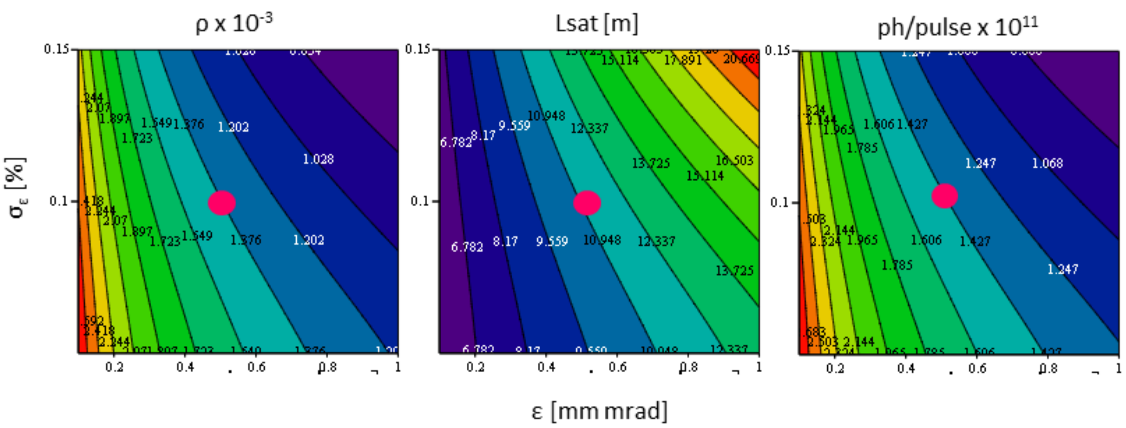

Figure 2.4: Dependence of the main FEL output parameters on relative energy spread σ_ε and normalized beam emittance ε. The ρ parameter, the saturation length L_{sat} and the number of photons per pulse at saturation are mapped for the Plasma case of Table 2.1. The circle refers to the value corresponding to the working point.

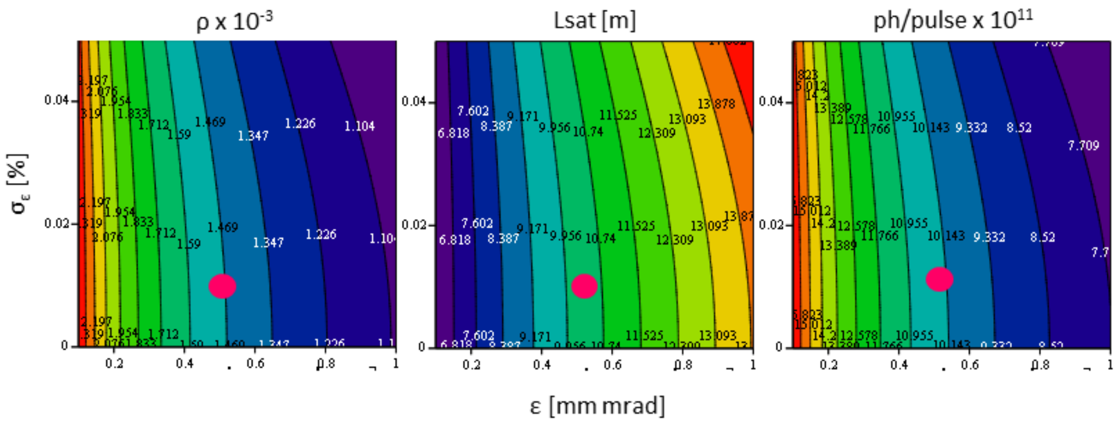

Figure 2.5: Dependence of the main FEL output parameters on relative energy spread σ_ε and normalized beam emittance ε. The ρ parameter, the saturation length L_{sat} and the number of photons per pulse at saturation are mapped for the Full X-band case of Table 2.1. The circle refers to the value corresponding to the working point.

2.2 Radiation on the harmonics

The FEL radiates also on the harmonics of the wavelength obtained by eq. (2.1). The Non-Linear Higher Harmonic Generation (NLHG) is a by-product of the FEL mechanism itself. It is a consequence of the higher order bunching occurring when the level of the fundamental harmonics is substantively large. It occurs either in oscillator and SASE devices. The NLHG mechanism provides the emission at [13, 14]

$$\lambda_n = \frac{\lambda_u}{2n\gamma^2}\left(1+\frac{K^2}{2}\right) \tag{2.19}$$

where for a linearly polarized undulator n is an odd integer and the relevant growth along the longitudinal coordinate is:

$$P_n(z) = \Lambda_n(z) + \Pi_n(z) \tag{2.20}$$

where the first term represents the linear part of the coherent harmonic lasing, namely

$$\Lambda_n(z) = P_{0,n} A_n(z) \tag{2.21}$$

$A_n(z)$ being the same as in the second term of eqs. (2.8). The Pierce parameter of the harmonics is:

$$\rho_n = \rho\left[\frac{f_{b,n}}{f_{b,1}}\right]^{\frac{2}{3}} \tag{2.22}$$

with: $f_{b,n} = J_{\frac{n-1}{2}}(n\xi) - J_{\frac{n+1}{2}}(n\xi)$, of argument $n\xi = \frac{n}{4}\frac{K^2}{1+K^2}$.
The gain length is:

$$L_{g,n} = \frac{\lambda_u}{4\pi\sqrt{3}\rho_n}. \tag{2.23}$$

The second term, namely the non-linear harmonics contribution, is provided by

$$\Pi_n(z) = \Pi_{0,n} \frac{\exp\left(\frac{nz}{L_g}\right)}{1 + \frac{\Pi_{0,n}}{P_{S,n}}\left[\exp\left(\frac{nz}{L_g}\right) - 1\right]}$$
$$\Pi_{0,n} = c_n \left(\frac{P_0}{9\rho_1 P_E}\right)^n P_{S,n}, \qquad c_3 = 8, \quad c_5 = 116 \tag{2.24}$$

The harmonic saturated power $P_{S,n}$ is:

$$P_{S,n} = \frac{1}{\sqrt{n}} \left(\frac{f_{b,n}}{n f_b}\right)^2 P_S \tag{2.25}$$

while the number of photons emitted at the n-th harmonics $\lambda = \lambda/n$ in a $\sigma_{ph,n}$ pulse length can be obtained from eq. (2.25) as

$$n_{ph,n} \cong \frac{\lambda P_{s,n}}{nhc} \sigma_{ph,n} \cong \chi_n n_{ph}$$
$$\chi_n = \frac{1}{n\sqrt{n}} \left(\frac{f_{b,n}}{n f_b}\right)^2 \frac{\sigma_{ph,n}}{\sigma_{ph}} \tag{2.26}$$

The parameter χ_n represents the harmonic conversion efficiency (which for the third harmonic is around 0.1%). Results of the FEL performance on the 3rd and 5th harmonics, given by the FEL scaling laws, are summarized in Figure 2.6 and Table 2.2.

	Units	**Plasma case**		**X-band case**	
		3rd h	5th h	3rd h	5th h
Radiation wavelength	nm	1	0.6	1	0.6
Pierce Parameter ρ	x 10^{-3}	0.67	0.33	0.58	0.28
Gain Length	m	0.72	1.23	0.83	1.42
Saturation power	GW	27.39	0.91	15.77	0.52
Energy	µJ	0.55	0.002	0.32	0.01
Photons/pulse	x 10^8	8.25	0.27	47.52	1.57

Table 2.2: Output main parameters on the 3rd and 5th harmonic for the EuPRAXIA@SPARC_LAB FEL driven by X-band linac or Plasma acceleration

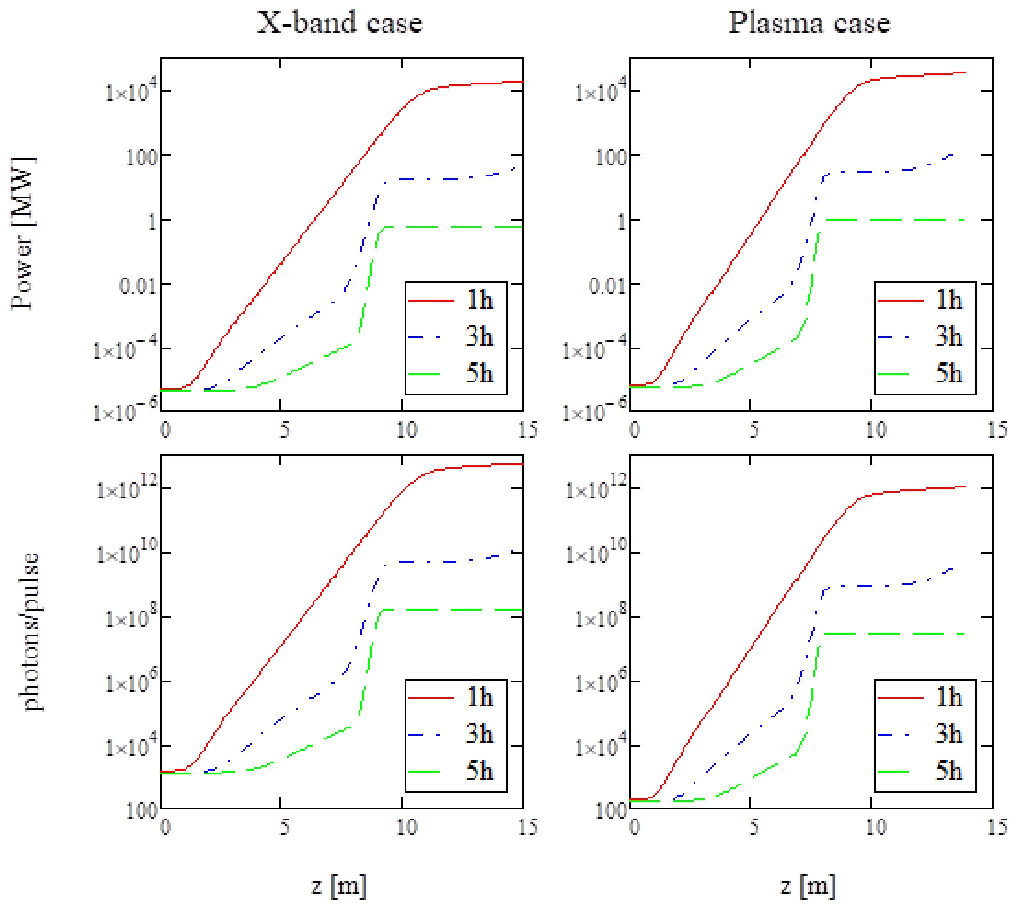

Figure 2.6: Power growth and Number of photons per pulse along the active undulator length (without focusing sections) for the reference parameters in the two configuration with Plasma acceleration and X-band Linac acceleration. The fundamental wavelength (continuous line), 3rd (dash-dot)) and 5th (dash) are plotted.

Bibliography

[1] R Bonifacio, C Pellegrini, and LM Narducci. "Collective instabilities and high-gain regime in a free electron laser". In: *Optics Communications* 50.6 (1984), pp. 373–378.

[2] C Pellegrini, A Marinelli, and S Reiche. "The physics of x-ray free-electron lasers". In: *Reviews of Modern Physics* 88.1 (2016), p. 015006.

[3] K Flöttmann. "ASTRA: A space charge tracking algorithm. user's manual available at http://www. desy. de/mpyflo". In: *Astra dokumentation* (2013).

[4] URL: `http://www.pulsar.nl/gpt`.

[5] Lloyd M Young. *TStep: An electron linac design code*. Tech. rep.

[6] Michael Borland. *Elegant: A flexible SDDS-compliant code for accelerator simulation*. Tech. rep. Argonne National Lab., IL (US), 2000.

[7] A Marocchino et al. "Efficient modeling of plasma wakefield acceleration in quasi-non-linear-regimes with the hybrid code Architect". In: *Nuclear Instruments and Methods in Physics Research Section A: Accelerators, Spectrometers, Detectors and Associated Equipment* 829 (2016), pp. 386–391.

[8] P Tomassini and A R Rossi. "Matching strategies for a plasma booster". In: *Plasma Physics and Controlled Fusion* 58.3 (2015), p. 034001.

[9] G Dattoli, PL Ottaviani, and S Pagnutti. "The PROMETEO Code: A flexible tool for Free Electron Laser study". In: *Nuovo Cimento. C* 32.2 (2009), pp. 283–287.

[10] L Giannessi. "Overview of Perseo, a system for simulating FEL dynamics in Mathcad". In: *Proceedings of the Free-Electron Laser Conference*. 2006. URL: `www.perseo.enea.it`.

[11] Sven Reiche. "GENESIS 1.3: a fully 3D time-dependent FEL simulation code". In: *Nuclear Instruments and Methods in Physics Research Section A: Accelerators, Spectrometers, Detectors and Associated Equipment* 429.1-3 (1999), pp. 243–248.

[12] Ming Xie. "Design optimization for an X-ray free electron laser driven by SLAC linac". In: *Particle Accelerator Conference, 1995., Proceedings of the 1995*. Vol. 1. IEEE. 1995, pp. 183–185.

[13] Giuseppe Dattoli, PL Ottaviani, and Simonetta Pagnutti. "Nonlinear harmonic generation in high-gain free-electron lasers". In: *Journal of applied physics* 97.11 (2005), p. 113102.

[14] G.Dattoli, P.L.Ottaviani, and S.Pagnutti. *Booklet for FEL Design*. Enea Edizioni Scientifiche, 2008. URL: `http://www.fel.enea.it/booklet-presentation.html`.

[15] H Haus. "Noise in free-electron laser amplifier". In: *IEEE Journal of Quantum Electronics* 17.8 (1981), pp. 1427–1435.

[16] GIUSEPPE Dattoli et al. "Progress in the Hamiltonian picture of the free-electron laser". In: *IEEE Journal of Quantum Electronics* 17.8 (1981), pp. 1371–1387.

[17] Franco Ciocci et al. "Segmented undulator operation at the SPARC-FEL test facility". In: *Advances in X-ray Free-Electron Lasers Instrumentation III*. Vol. 9512. International Society for Optics and Photonics. 2015, p. 951203.

[18] J Bahrdt and Y Ivanyushenkov. "Short period undulators for storage rings and free electron lasers". In: *Journal of Physics: Conference Series*. Vol. 425. 3. IOP Publishing. 2013, p. 032001.

[19] *J. Rosenzweig, private communication.*

[20] Shigeru Yamamoto. "Development of undulator magnets towards very short period lengths". In: *AIP Conference Proceedings*. Vol. 1741. 1. AIP Publishing. 2016, p. 020029.

[21] URL: `https://compactlight.web.cern.ch`.

[22] R Bonifacio et al. "Spectrum, temporal structure, and fluctuations in a high-gain free-electron laser starting from noise". In: *Physical review letters* 73.1 (1994), p. 70.

[23] Matteo D Alaimo et al. "Mapping the transverse coherence of the self amplified spontaneous emission of a free-electron laser with the heterodyne speckle method". In: *Optics Express* 22.24 (2014), pp. 30013–30023.

[24] JB Rosenzweig et al. "Generation of ultra-short, high brightness electron beams for single-spike SASE FEL operation". In: *Nuclear Instruments and Methods in Physics Research Section A: Accelerators, Spectrometers, Detectors and Associated Equipment* 593.1-2 (2008), pp. 39–44.

[25] F. Villa et al. "Generation and characterization of ultra-short electron beams for single spike infrared FEL radiation at SPARC_LAB". In: *Nuclear Instruments and Methods in Physics Research Section A: Accelerators, Spectrometers, Detectors and Associated Equipment* 865 (2017), pp. 0168–9002.

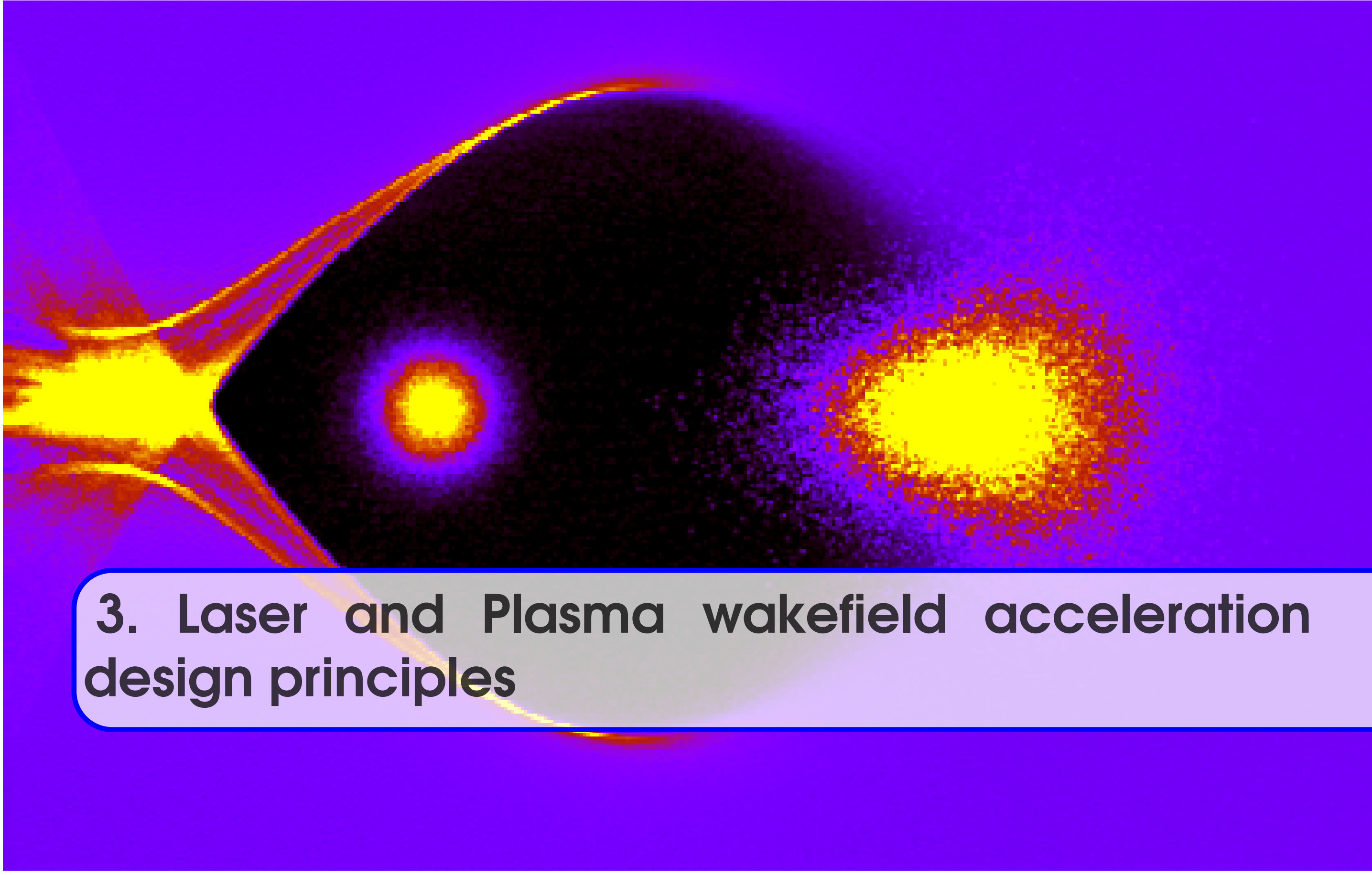

3. Laser and Plasma wakefield acceleration design principles

The concept of laser wakefield acceleration (LWFA) and plasma wakefield acceleration (PWFA) were first proposed in the late seventies by Tajima and Dawson [1], holding the promise of producing high energy particle beams in length scales much smaller than what was and is possible even today. Advancement in particle physics has historically been linked with the availability of particle beams of ever increasing energy or intensity.

Particle accelerators show a remarkable success story with beam energies having increased by 5 – 8 orders of magnitude since the first RF based accelerators in the 1920s. However, it is also evident that the exponential increase of beam energy with time has leveled off in conventional RF accelerators since the 1980s. Current RF limitations arise from technical and also from budget-cost limitations, limitations that can be overcome by the the revolutionary proposal of plasma accelerators by Tajima and Dawson in 1979 [1]. Plasma-based concepts presently offer not only high beam energies, but also the highest accelerating gradient compared to other novel acceleration techniques like high–frequency W–band metallic RF structures, dielectric wakefield structures or direct laser acceleration. Plasma-based accelerators in fact replace the metallic walls of conventional RF structures with plasma [2].

This revolutionary change permits one avoiding metallic or dielectric structure damage problems encountered in high-gradient operation. LWFA or PWFA may be adopted to excite space-charge oscillations in plasma (Fig. 3.1). The resulting fields can be used for particle acceleration and focusing. Plasma accelerators have been built with active length ranging from the mm to the meter scale. Accelerating gradients up to 160 GV/m have been demonstrated in experiments [3] with improvements in accelerated beam quality that let us expect that advanced light sources (FEL, Compton, etc.) based on plasma–accelerators can be realized in the next decade [4]. To proceed towards high–energy physics (HEP) applications, however, one must demonstrate progress in beam quality and control [5].

It is widely accepted by the international scientific community that a fundamental milestone towards the realization of a plasma driven future Linear Collider (LC) will be the integration of high gradient accelerating plasma modules in a short wavelength Free Electron Laser (FEL) user facility [6]. The capability of producing the required high quality beams and the operational reliability of

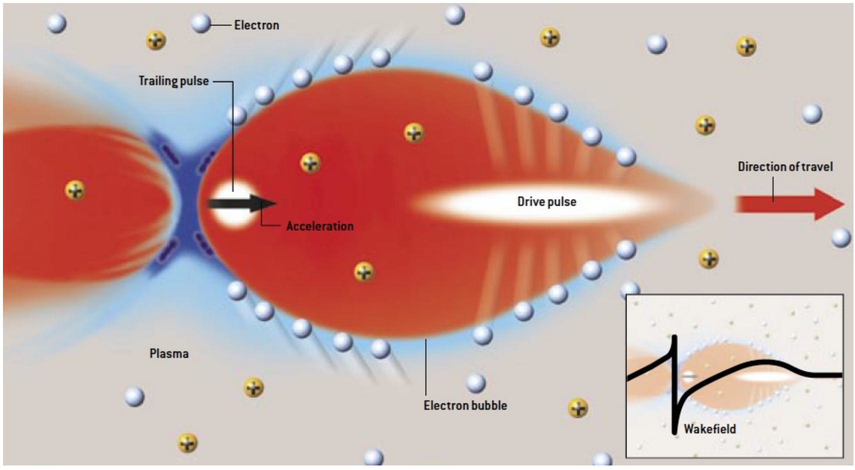

Figure 3.1: Wakefield accelerator relies on a charge disturbance known as a wakefield to provide the driving force. The drive pulse, which can be a short pulse of either a laser (LWFA) or an electron beam (PWFA), blows the electrons (blue) in an ionized gas, or plasma, outward, leaving behind a region of positive charge (red). Along the axis where the beam propagates, the electric field (plotted below) causes a trailing pulse of electrons injected near the rear of the bubble to feel a very strong forward acceleration. [2]

the plasma accelerator modules will be certainly certified when such an advanced radiation source will be able to drive external user experiments. It is further expected that there will be unique photon–beam characteristics that give notable advantages to such a plasma based 5th generation light source. These include enabling ultra-short photon pulses based on high brightness electron beams that break the attosecond barrier and, when used in combination with next generation undulators, shorter wavelength photons at notably lower electron beam energy. The realization of such a 5th generation light source thus serves as a required stepping stone for HEP energy applications and is a promising new tool for photon science in its own right.

In the following section, we report on some scaling laws that can be used as parameter guidelines [7–9]. The scaling laws are used to guide the choice of the main parameters (for the external injection case study) eventually tested and refined with numerical simulations. The envisioned case study consider a fully external injection scenario, meaning that bunches (both driver and witness for the PWFA case) are externally produced by a photo-injector and then delivered to the plasma accelerating section. Such a choice is based on the great reliability of photo-injectors to generate high quality bunches.

3.1 Laser Wakefield acceleration scaling laws

In the setting of LWFA, a high power laser acts as the generator (driver) of the plasma wave where an electron bunch (witness) is accelerated. In order to reach high energies, the natural diffraction of the laser pulse must be prevented. To this end, it is possible either to exploit non-linear effects in the laser propagation that realize a self-guiding (like in [10] and [11], for example), foresee a setting where a transverse plasma tapering acts like an optical waveguide (like in [12]) or employ a dielectric capillary as an hollow waveguide [13].

The relevant parameter for the laser pulse is its dimensionless strength parameter, whose value (for a bi-Gaussian pulse), in practical units, reads:

$$a_0^2 \approx 7.3 \times 10^{-19} \left[\lambda_l(\mu\text{m})\right]^2 I_0 \left[\text{W/cm}^2\right], \tag{3.1}$$

where λ_l is the laser wavelength and I_0 its intensity. LWFA usually requires a very high power laser pulse with a pulse length (duration) τ such that $c\tau k_p < 1$, with c speed of light and $k_p = \omega_p/c = 2\pi/\lambda_p = \sqrt{4\pi n_0 e^2/mc^2}$ the plasma wave vector modulus. The value of a_0 determines the regime of the plasma wave, namely a linear regime for $a_0^2 \ll 1$, a quasi-linear regime for $a_0^2 \sim 1$ and a non linear regime for $a_0^2 \gg 1$. Field gradients are usually measured in units of

$$E_0\,[\text{V/m}] = c\,m\,\omega_p/e \approx 96\sqrt{n_0\left[\text{cm}^{-3}\right]}, \tag{3.2}$$

where m is the electron rest-mass and e its charge modulus. In the three different regimes we will usually have $E_{\max} \ll E_0$, $E_{\max} \sim E_0$ and $E_{\max} > (>)E_0$. However, increasing the non linearity of the plasma wave may set in unwanted, in our setting, non-linear effects in laser propagation [14], like self focusing, that would prevent the full exploitation of stronger field gradients, particularly if the plasma density n_0 is close to 10^{18} cm^{-3} or larger. This is the reason behind the rough estimation of energy increase stating that $\Delta\gamma$ scales as n_0^{-1} , with γ the electrons Lorentz factor. Moreover, the plasma wavelength depends on the plasma wave regime: the reported value λ_p is valid for linear regime while, for non linear regime, $\lambda_{\text{nl}} > \lambda_p$.

Another important aspect to take into account is the laser propagation velocity. It is possible to show that, if the condition $k_l\,\sigma_l \gg 1$ (σ_l being the laser transverse size) is met, the laser group velocity v_g, which is equal to the plasma wave phase velocity, is

$$v_g = c\sqrt{1-\frac{\omega_p^2}{\omega_l^2}}, \tag{3.3}$$

with ω_p (ω_l) the plasma (laser) pulsation, whereas if $k_l\sigma_l \leq 1$ its value is

$$v_g = c\sqrt{1-\frac{\omega_p^2}{\omega_l^2}-\frac{2c^2}{\omega_l\,\sigma_l}} \tag{3.4}$$

Results (3.3) and (3.4) are valid in the linear regime; non linear effects would further reduce the laser group velocity. Since v_g is usually smaller than the velocity of a relativistic electron beam, the injected bunch will slowly overtake the plasma wave, slipping from the injection phase to smaller and smaller accelerating fields; eventually, the bunch reaches regions where the gradient is decelerating, starting to lose energy. This phenomenon is known as dephasing and sets a limit for the maximum accelerating length at a given plasma density, laser wavelength and laser spot size It is common practice to report, instead of v_g, the laser resonant Lorentz factor defined as

$$\gamma_g = \left(1-\frac{v_g^2}{c^2}\right)^{-1/2}. \tag{3.5}$$

The efficiency of energy transfer from laser to plasma depends mainly on the driver pulse length. It turns out to be optimal if $c\tau \sim \lambda_p$ in linear regime and $c\tau \sim \lambda_{\text{nl}}/2$ for nonlinear regime.

Another limit for the accelerating length is set by the finite energy content of the laser pulse, which would eventually deplete. If $k_l\,\sigma_l \gg 1$, dephasing and depletion lengths scale as

$$L_d = \frac{\lambda_p^3}{2\lambda_l^2}\times\begin{cases}1 & \text{if } a_0^2 \ll 1\\ (\sqrt{2}/\pi)\,a_0^2/N_p & \text{if } a_0^2 \gg 1\end{cases} \tag{3.6}$$

$$L_{pd} = \frac{\lambda_p^3}{\lambda_l^2}\times\begin{cases}2/a_0^2 & \text{if } a_0^2 \ll 1\\ (\sqrt{2}/\pi)\,a_0^2 & \text{if } a_0^2 \gg 1\end{cases}, \tag{3.7}$$

where N_p is the number of plasma periods behind the laser. Generally speaking, in the nonlinear regime $L_d \sim L_{pd}$, while in the linear regime $L_d > L_{pd}$; this limit can be overcome by a longitudinal tapering of the plasma density in order to keep the witness bunch at the correct phase value.

Finally, given the aforementioned physical limits, it is possible to estimate the maximum energy gain by

$$\Delta W_d\,[\mathrm{MeV}\,] \approx \frac{630\, I_0\left[\mathrm{W/cm^2}\right]}{n_0\left[\mathrm{cm^{-3}}\,\right]} \times \begin{cases} 1 & \text{if } a_0^2 \ll 1 \\ (2/\pi)/N_p & \text{if } a_0^2 \gg 1 \end{cases} \tag{3.8}$$

when the limit is given by dephasing and

$$\Delta W_{pd} \approx \begin{cases} 3.4\times 10^{21}/\lambda_l^2\,[\mu\mathrm{m}\,]\, n_0\left[\mathrm{cm^{-3}}\,\right] & \text{if } a_0^2 \ll 1 \\ 400\, I_0\left[\mathrm{W/cm^2}\right]/n_0\left[\mathrm{cm^{-3}}\,\right] & \text{if } a_0^2 \gg 1 \end{cases} \tag{3.9}$$

for pump depletion limited acceleration.

3.2 Plasma Wakefield acceleration scaling laws

The PWFA requirements can mostly leverage on the results and consideration drawn for LWFA, where the driver instead of being a laser is a charged driver bunch, i.e. an electron bunch.

We recall that PWFA is based on the following underlying process: a charged bunch is injected into the plasma, the break of neutrality produced by the bunch induces a following wake, where we can place a second bunch that gets accelerated [1, 15]. The bunch that enters the plasma, because of Coulomb repulsion, pushes away the background electrons. These ejection electrons leave behind a depleted region of ions. The Gauss's theorem suggests that the ion bubble left behind has a transverse linear focusing field, and a longitudinal linear accelerating field [16, 17]. This scenario resembles the structure of a RF accelerating cavity. The advantage of this new setup consists of the maximum electric field that can be produced. Since the plasma can sustain the self-generated field, the maximum producible fields are order of magnitude higher than a RF. The maximum field sustained by the plasma, also known as the cold-wavebreaking-limit [18], reported for the LWFA as Eq. (3.2).

It is clear that for a modest density, $n_0 \sim 10^{16}\ \mathrm{cm^{-3}}$, the wavebreaking limit is approximately 9.6 GV/m. The acceleration of a bunch is achieved by wisely placing a second bunch into the wake, at the right distance from the driver. The witness is placed in the electronic depleted region (bubble) formed by the driver. The bubble has a finite length that is approximated by the plasma wavelength $\lambda_p = \frac{2\pi c}{\omega_p}$. Consequently, we observe that the background density is a very important aspect for PWFA. The background density regulates the accelerating field, and for this reason, it has to be finely tuned and controlled. A possible way to control the background gas is to use a capillary gas tube with a plasma discharge to pre-ionize the gas.

The driver is generally characterised by the physical parameters (charge, current, dimension, emittance and energy spread) and by two dimensional parameters that identify if the plasma response is in the linear or nonlinear regime. The α parameter, the ratio between peak bunch density in respect to the background density,

$$\alpha = \frac{n_{\mathrm{bunch}}}{n_0}. \tag{3.10}$$

suggests that when larger than unity a nonlinear response is expected. However, while in the case of a well known distribution, e.g. a bi-Gaussian distribution, the α parameter carries several information in just a single number the same parameter need to be accompanied by a dimensionless parameter identifying the charge distribution. The reduced charge factor [19–21],

$$Q_{\mathrm{rc}} = Q_{\mathrm{bunch}}\frac{k_p^3}{n_0\, e} \tag{3.11}$$

with Q_{bunch} the bunch charge, $k_p = 2\pi/\lambda_p$ the plasma wavenumber and e the electron charge; indicates the amount of charge a bunch is carrying compared to the maximum charge that can be accommodated in a plasma skin-depth volume. If the parameter is less than one, the response if linear, values around one denote a weakly nonlinear regime while values much larger than one denotes a fully blowout regime.

The driver optimised RMS length [16] is,

$$k_p \sigma_z = \sqrt{2} \tag{3.12}$$

while the optimised transverse RMS dimension is given by the matching condition,

$$\sigma_{x,y} = \sqrt[4]{\frac{2}{\gamma}} \sqrt{\frac{\varepsilon_{x,y}}{k_p}}, \tag{3.13}$$

with γ the relativistic factor and $\varepsilon_{x,y}$ the RMS normalised transverse emittance. The formed bubble has a radius that can be estimated [16] with,

$$R_{\text{bubble}} = 2.5\, \sigma_r \sqrt{\alpha}. \tag{3.14}$$

These set of rules offer a guideline to determine the bunch parameters for the experiment we are foreseeing To tailor the witness we can partially leverage on the aforementioned rules and scaling laws, and partially we need to identify specific requirements. The foreseen experiment is planned in the so-called *weakly-non-linear regime*, where the electric field induced by the driver bunch has neither a full sinusoidal behavior nor a full sawtooth shape. For such a reason we need to leverage on both linear regime scaling laws together with nonlinear scaling laws. For the transverse dimensions we can use the matching condition reported as Eq. (3.13).

To estimate the witness parameters we assume a driver bunch produces a linear wake of the form $E_{\text{acc}} = G\cos[k_p\xi]$ while the witness, instead, produces a decelerating self-wake of the form $E_{\text{dec}} = -g\sin[k_p(\xi_0 + \sigma_z - \xi)]$,with G and g the accelerating and decelerating fields respectively, and ξ the longitudinal co-moving coordinate. By requiring that the electric field felt by a particle located at the witness front $\xi = \xi_0 + \sigma_z$ experiences the same accelerating field of a particle at the bunch center $\xi = \xi_0$ we can estimate both the injection phase and the bunch length. Assuming beam loading compensation we observe that the energy spread growth is of the form $\sigma_E = \sqrt{3}/4(k_p\sigma_z)^2$, and requiring for modest growths (less than 5×10^{-3}) we retrieved $\sigma_z = 6\ \mu\text{m}$. Recalling that the bunch length is related to the injection phase, in a linear regime this relation is expressed as $k_p\sigma_z \sim \tan\varphi_0$, that in our case corresponds to an injection phase close to half plasma wavelength with respect to the maximum decelerating driver field. The injection phase is, in turn, related to the charge ratio ($\varphi_0 = Q_{\text{witness}}/Q_{\text{driver}}$), we retrieve that the witness charge has to be around 25–30 pC.

For the case of interest the witness charge and peak current is fixed by FEL applications, nonetheless for nonlinear regimes it is possible to analytically calculate the maximum charge that can be accommodated into the bubble [9],

$$Q_{\text{witness}} = \frac{\pi}{16} \frac{(k_p R_{\text{bubble}})^4}{E_t * E_0^{-1}} \tag{3.15}$$

with E_t the value of the electric field underneath the witness bunch, and in the assumption of a trapezoidal shaped witness bunch.

3.3 Choice of plasma module parameters for Laser Wakefield

In this section we will briefly recall principles leading to plasma module parameters choice for LWFA. Further details can be found in [22].

3.3.1 Plasma density and plasma wave regime

It is generally accepted that the best plasma wave regime choice for a plasma booster is the quasi linear regime, $a_0^2 \sim 1$ with a plasma density $n_0 \lesssim 10^{17}$ cm^{-3} . In fact, it allows to take advantage both of stronger accelerating fields then linear regime and greater stability with respect to non-linear regime. The main drawback for this choice is the absence of scaling laws; scalings for the linear regime usually perform decently for the laser behavior, while results for the non-linear regime give rough estimates for beam dynamics related aspects. Another problem comes from the dependence of transverse fields from the longitudinal coordinate, as in the linear regime: this complicates matching and may lead to charge loss in transport.

Due to the relatively low plasma density and a_0 value, laser propagation will not endure detrimental non-linear effects or be subject to instabilities [7], allowing for a smooth and predictable evolution. Moreover, increasing plasma density above the 10^{17} cm^{-3} value, would require a witness bunch length shorter than 1 mm, which are well beyond the current accelerator technology for charges in the few tens of pC range.

The expected accelerating gradients have an upper limit of 30 GV/m ; however, 3D effects and deviation from the ideal setting, lead to a safer evaluation around 10 GV/m . With such values, the target electron energy of 1 GeV should be achieved in an acceleration length around 5 cm , which is short enough to avoid significant dephasing and pump depletion effects. In fact, using the linear regime estimates, both L_d and L_{pd} result to be in the order of 1 m. Energy spread growth may still constitute a problem for two reasons. The first one is the presence of a relatively long tail in the trailing area of beams compressed by velocity bunching; the second resides in the negligible effect of beam loading. The combination of these properties with a correct injection in the plasma wave (i.e. the current peak resting on the longitudinal field peak) results in the tail being subject both to defocussing force or a large accelerating gradient variation, leading also to charge loss or halo formation, while the peak current would get the curvature of longitudinal plasma electric field imprinted on its longitudinal phase space. Since the tail comprises around 10 % of total charge and has low slice current, its loss during acceleration or subsequent transport should not constitute a serious problem in view of driving a free electron laser, while the curvature induced energy spread can not be easily predicted and must be checked by simulations.

Another non ideal feature whose effect cannot be predicted by scalings is the unavoidable presence of plasma ramps at the capillary tips, due to gas leakage. It has been shown how these features can be fruitfully exploited to ease matching into/from plasma [23]; however, this would require a lengthy optimization both of transport and of capillary engineering so, in this CDR, we will start by setting the maximum acceptable ramp length for avoiding an excessive beam degradation.

3.3.2 Laser guiding and parameters

As stated before, there are two suitable options for guiding the driving laser pulse beyond its natural Rayleigh length in a plasma booster, namely plasma transverse tapering (plasma channel) and hollow waveguides. Both methods mimic the operation mode of optical fibers, in that a plasma channel realizes a transverse tapering of refraction index like a graded index fiber, whereas a hollow waveguide copies the core/cladding structure of step index fibers, with the core being represented by vacuum (plasma) and the cladding by glass.

Both methods allow monomode guiding, fundamental for plasma acceleration, that requires to inject the laser with a correct matched size and zero envelope slope. Even at perfect matching, a small amount of pulse energy still excites higher order modes that will eventually decay.

The two methods differ in that, even at perfect matching, hollow waveguides are lossy (through the capillary walls) while plasma channels are not. Moreover, the matched spot size value for the former does not depend from the capillary geometry, being a function of the refraction index

Laser parameters				
E [J]	τ [fs]	σ_{tr} [μm]	Z_r [mm]	a_0
6	110	35	4.8	1

Plasma parameters		
n_0 [cm^{-3}]	L [cm]	R_{in} [μm]
10^{17}	6	$\gtrsim 350$

Table 3.1: Laser and plasma reference parameters.

tapering, whereas for the latter is a fixed fraction of the capillary internal radius. As a consequence, for a hollow waveguide, a fixed fraction of laser energy impinges on the capillary itself, with the risk of damages, that may however be prevented by an adequate shielding. Other than that, both have similar performances, as long as the conditions $k_l\,\sigma_l \ll 1$ and $k_p\,\sigma_l \ll 1$ are met; since failing to satisfy the former determines a sharp and problematic decrease of laser group velocity in plasma, we will always require it to be verified. The latter condition results to be rather neutral (provided it does not fall under $O(1)$) [24] for the plasma channel for which, at most, causes a deformation of the plasma wave outer shape due to varying plasma density; on the other hand, it is crucial for the hollow waveguide since, if it not respected, causes a strong interaction between the plasma electrons and the capillary inner boundaries. This may result in a deep modification of the plasma wave, depending on electrons kinematics properties; in practice, no results are found in plasma accelerator literature of what would happen, since those effects fall into the field of plasma-surfaces interaction. On the other hand, a hollow waveguide does not require a pre-ionized and tapered plasma, like the plasma waveguide; indeed, ionization and tapering can be quite easily attained either by the flow of an electric current (discharge capillary) or by an ad hoc ionizing laser pulse. That being said, a final choice depends on the $k_p\sigma_l$ parameter value which, in turn, is set by laser energy, pulse length ($\approx$ plasma wavelength) and the $a_0 \sim 1$ constraint. We assume a worst case scenario, where we have an energy of 6 J on target. Setting $c\tau \sim \lambda_p$ requires $\sigma_l \approx 20$ μm and the laser resonant Lorentz factor is $\gamma_g = 68$. For avoiding excessive slippage and ease of operation we increase laser size to 35 μm , so that $\gamma_g = 87$. This choice sets $\tau \approx 100$–110 fs . In both situations $k_p\,\sigma_l$ is of $O(1)$, so a plasma channel must be considered.

In Table 3.1 we summarize the choices made for the LWFA module.

3.4 Plasma Wakefield parameters choice

Considering a COMB technique to create driver and witness at once, the natural choice for the density is 10^{16} cm^{-3} that allows for a plasma wavelength of $\lambda_p = 334$ μm a suitable and controllable distance for such a technique. Moreover, considering bunches with an energy of 500 MeV we calculate $\sigma_{z,D} = 75$ μm $\sigma_{x,D} = 4$ μm and $\sigma_{x,W} = 1.55$ μm for a longitudinal shape shorter than $\sigma_{z,W} = 25$ μm . We have assumed a driver with a normalised emittance of 3 mm mrad and a witness with a normalised emittance of 1 mm mrad . Choosing a weakly nonlinear regime with a reduced charged factor around 0.8, the driver would be characterised by a charge around 200 pC . The witness charge for beam loading is estimated around 30 pC .

Bunch parameters				
bunch	Q [pC]	σ_x [μm]	σ_z [μm]	ε_x [mm mrad]
Driver	200	4	75	3
Witness	25–30	1.5	6	1

Plasma parameters		
n_0 [cm^{-3}]	λ_p [μm]	k_p [μm $^{-1}$]
10^{16}	334	0.02

Table 3.2: Plasma Wakefield acceleration reference parameters.

Bibliography

[1] T Tajima and J M Dawson. “Laser electron accelerator”. In: *Physical Review Letters* 43.4 (1979), p. 267.

[2] Chandrashekhar Joshi. “Plasma accelerators”. In: *Scientific American* 294.2 (2006), pp. 40–47.

[3] D Gordon et al. “Observation of electron energies beyond the linear dephasing limit from a laser-excited relativistic plasma wave”. In: *Physical review letters* 80.10 (1998), p. 2133.

[4] Victor Malka. “Laser plasma accelerators”. In: *Physics of Plasmas* 19.5 (2012), p. 055501.

[5] Massimo Ferrario. “Present and future accelerator options beyond the LHC”. In: *Annalen der Physik* 528.1-2 (2016), pp. 151–160.

[6] Ralph Aßmann and Julia Grebenyuk. “Accelerator Physics Challenges towards a Plasma Accelerator with Usable Beam Quality”. In: *5th International Particle Accelerator Conference*. PUBDB-2015-00732. 2014.

[7] E Esarey, C B Schroeder, and W P Leemans. “Physics of laser-driven plasma-based electron accelerators”. In: *Reviews of Modern Physics* 81.3 (2009), p. 1229.

[8] Thomas C Katsouleas et al. “Beam Loading in Plasma Accelerators”. In: *Part.Accel.* 22 (1987), pp. 81–99.

[9] M Tzoufras et al. “Beam loading by electrons in nonlinear plasma wakes”. In: *Physics of Plasmas (1994-present)* 16.5 (May 2009).

[10] S Kneip et al. “Near-GeV acceleration of electrons by a nonlinear plasma wave driven by a self-guided laser pulse”. In: *Physical review letters* 103.3 (2009), p. 035002.

[11] C E Clayton et al. “Self-guided laser wakefield acceleration beyond 1 GeV using ionization-induced injection”. In: *Physical review letters* 105.10 (2010), p. 105003.

[12] W P Leemans et al. “Multi-GeV electron beams from capillary-discharge-guided subpetawatt laser pulses in the self-trapping regime”. In: *Physical review letters* 113.24 (2014), p. 245002.

[13] B Cros et al. “Eigenmodes for capillary tubes with dielectric walls and ultraintense laser pulse guiding”. In: *Physical Review E* 65.2 (2002), p. 026405.

[14] Bradley Allan Shadwick, Carl B Schroeder, and Eric Esarey. “Nonlinear laser energy depletion in laser-plasma accelerators”. In: *Physics of Plasmas* 16.5 (2009), p. 056704.

[15] James Rosenzweig. “Nonlinear plasma dynamics in the plasma wakefield accelerator”. In: *IEEE transactions on plasma science* 15.2 (1987), pp. 186–191.

[16] Wei Lu et al. "Nonlinear theory for relativistic plasma wakefields in the blowout regime". In: *Physical review letters* 96.16 (2006), p. 165002.

[17] W Lu et al. "A nonlinear theory for multidimensional relativistic plasma wave wakefields". In: *Physics of Plasmas* 13.5 (2006), p. 056709.

[18] M Litos et al. "High-efficiency acceleration of an electron beam in a plasma wakefield accelerator". In: *Nature* 515.7525 (2014), p. 92.

[19] JB Rosenzweig et al. "Energy loss of a high charge bunched electron beam in plasma: Simulations, scaling, and accelerating wakefields". In: *Physical Review Special Topics-Accelerators and Beams* 7.6 (2004), p. 061302.

[20] P Londrillo, C Gatti, and M Ferrario. "Numerical investigation of beam-driven PWFA in quasi-nonlinear regime". In: *Nuclear Instruments and Methods in Physics Research Section A: Accelerators, Spectrometers, Detectors and Associated Equipment* 740 (2014), pp. 236–241.

[21] A Marocchino et al. "Efficient modeling of plasma wakefield acceleration in quasi-non-linear-regimes with the hybrid code Architect". In: *Nuclear Instruments and Methods in Physics Research Section A: Accelerators, Spectrometers, Detectors and Associated Equipment* 829 (2016), pp. 386–391.

[22] Andrea R Rossi et al. "The External-Injection experiment at the SPARC_LAB facility". In: *Nuclear Instruments and Methods in Physics Research Section A: Accelerators, Spectrometers, Detectors and Associated Equipment* 740 (2014), pp. 60–66.

[23] P Tomassini and A R Rossi. "Matching strategies for a plasma booster". In: *Plasma Physics and Controlled Fusion* 58.3 (2015), p. 034001.

[24] N E Andreev et al. "On laser wakefield acceleration in plasma channels". In: *Nuclear Instruments and Methods in Physics Research Section A: Accelerators, Spectrometers, Detectors and Associated Equipment* 410.3 (1998), pp. 469–476.

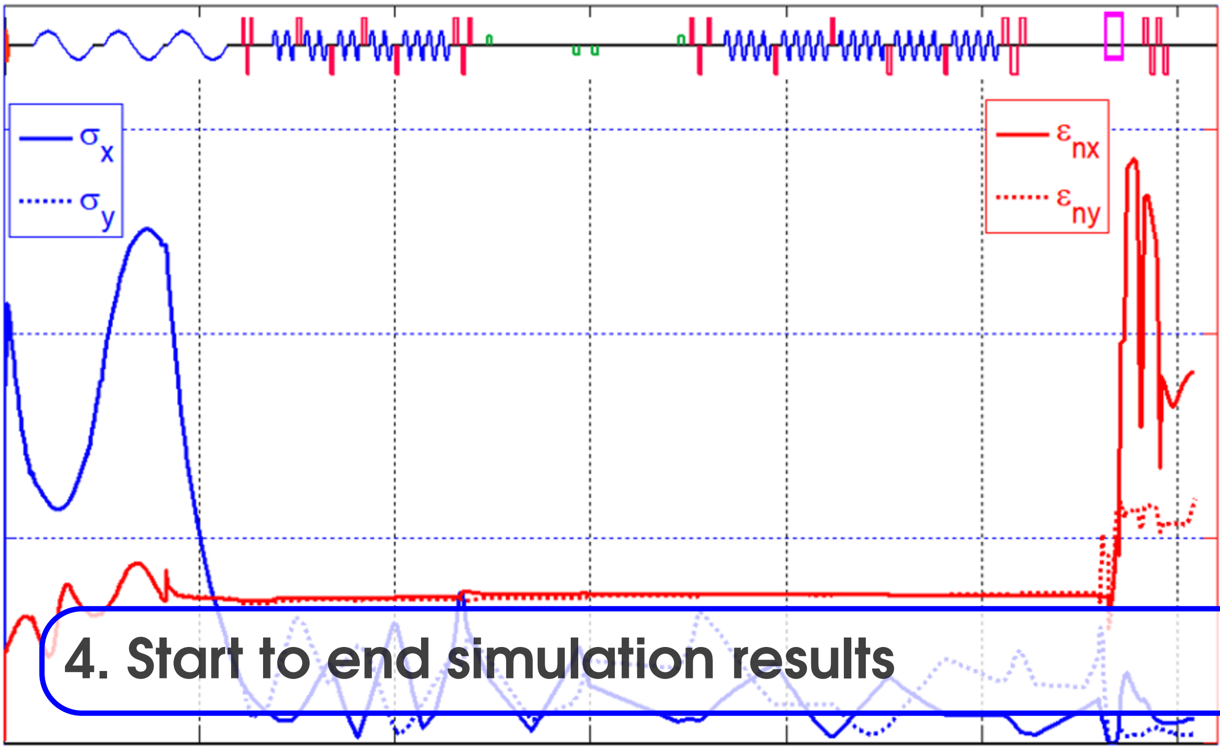

4. Start to end simulation results

As introduced in the previous chapters three main cases have been considered, full RF case, LWFA and PWFA cases. The envisioned plasma cases consider a fully external injection scenario, meaning that electron bunches (both for the PWFA and LWFA cases) are externally produced by a photo-injector and then delivered to the plasma accelerating section. Studies for the accelerator and start-to-end simulations of the electron beam dynamics have been performed by means of numerical codes and they are described in detail in chapters 5, 6, 7. The obtained results are here briefly summarized showing for each case the main beam parameters evolution along the entire accelerator line. The beam parameters for whole cases are reported in table 4.1 at the end of the chapter.

4.1 Full X-band case

In this case the 1 GeV energy for the electron beam is achieved by means of the 32 X-band RF accelerating sections as described in chapter 5, in the figures below the energy, energy spread and bunch length evolution along the Linac is shown together with the normalised transverse emittance and beam RMS sizes. The slice analysis of the beam current, energy spread and transverse emittance is shown in Fig. 4.1 and Fig. 4.2 as obtained at the undulator entrance.

4.2 LWFA case

The laser wakefield acceleration case is based on the external injection scheme [1] (a.k.a. plasma booster), where a high quality electron beam, generated by a conventional accelerator, is properly injected in a laser driven plasma wave for further acceleration. Advantages of external injection over internal injection schemes, where background plasma electrons are eventually captured in the plasma accelerating bucket, resides in the possibility, given by conventional accelerators, of fine tuning the incoming beam to match it into plasma wave, resulting in a much increased control that allows to preserve beam quality [2, 3] and increase stability [3, 4].

The incoming beam energy has been set to 500 MeV considering the need to reach a matched transverse dimension of few microns with the requirement of few kA peak current for driving an FEL. This requirement, together with the necessity of injecting a sufficiently short bunch to avoid

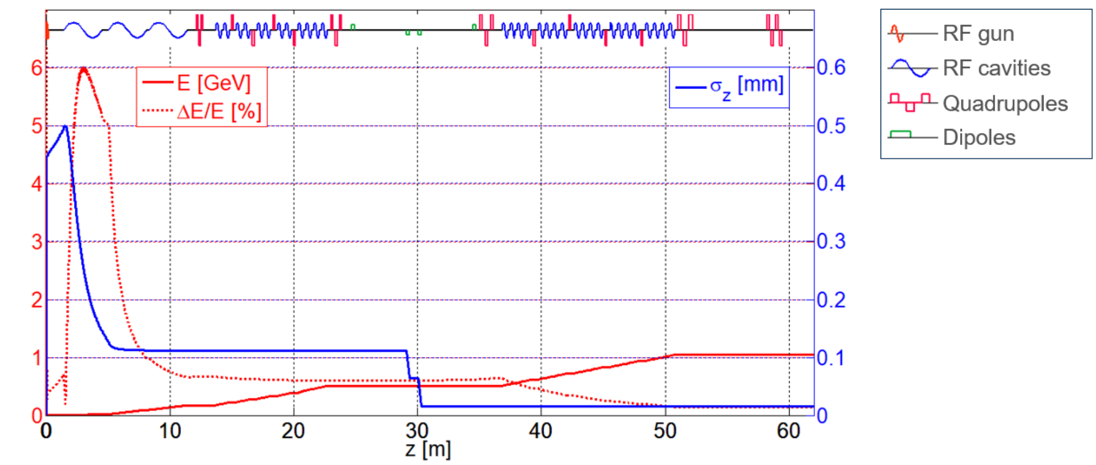

Figure 4.1: Start to end simulation results for the 200 pC bunch for the X-band case: evolution along the injector of the energy (E red line) and energy spread ($\Delta E/E$ red dotted-line) and longitudinal bunch length (σ_z blue line).

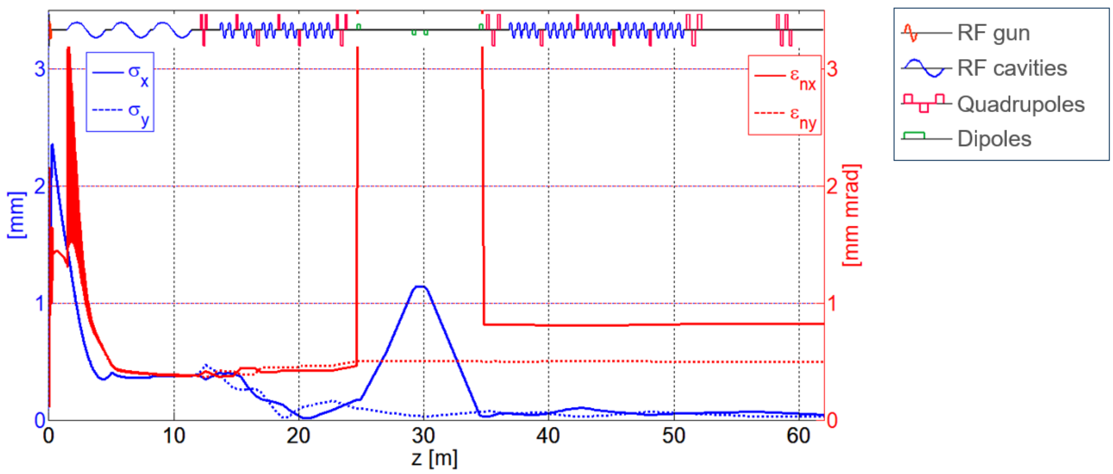

Figure 4.2: Start to end simulation results for the 200 pC bunch for the X-band case: evolution along the injector of the electron beam transverse normalised emittance (ε_{n_x} red line, ε_{n_y} red dotted-line) and spot sizes (σ_x blue line, σ_y blue dotted-line).

excessive energy spread increase in the plasma module, set also the beam charge to 30 pC. The plasma stage doubles initial energy in a 6 cm long capillary, exploiting an average accelerating field close to 10 GV/m. Given the driving laser energy content, final beam energy could be extended up to 4–5 GeV, preserving quality, by just increasing the capillary length.

Details of the simulation tools, simulation settings and simulated experimental setup are reported in Chapter 6. In Figure 4.3 the bunch longitudinal properties from photo-cathode to undulator injection, whereas in Figure 4.4 transverse size and emittance are depicted. Notice that those values are retrieved by using the data analysis procedure reported in Section 6.3.2, so that reported final parameter values must be intended as 90% of total charge.

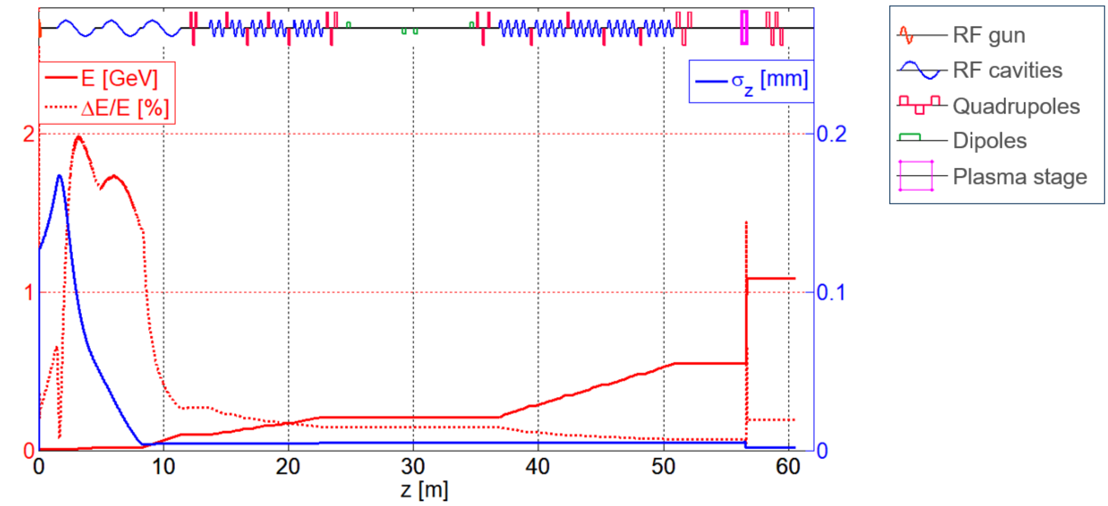

Figure 4.3: Start to end simulation results for the trailing bunch for the LWFA case: evolution along the injector of the energy (E red line) and energy spread ($\Delta E/E$ red dotted-line) and longitudinal bunch length (σ_z blue line).

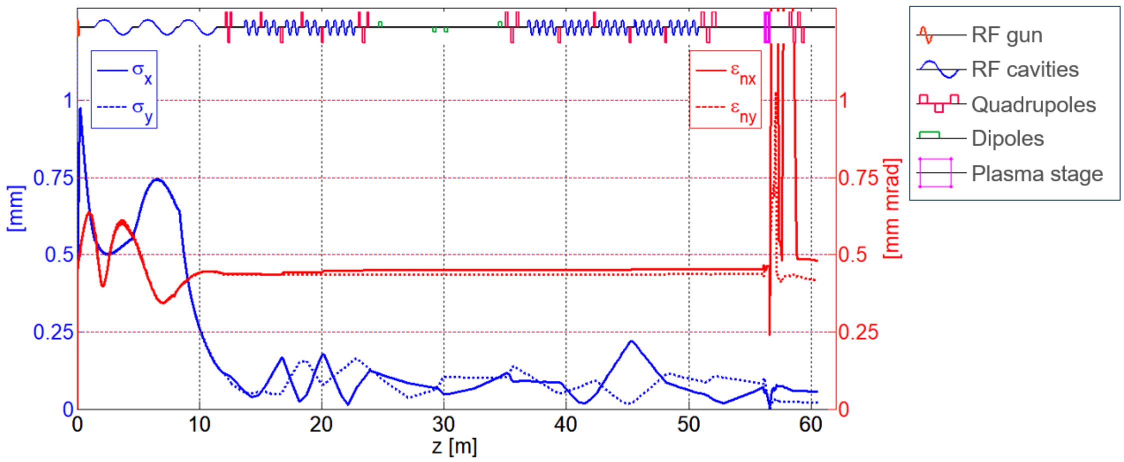

Figure 4.4: Start to end simulation results for the trailing bunch for the LWFA case: evolution along the injector of the electron beam transverse normalised emittance (ε_{n_x} red line, ε_{n_y} red dotted-line) and spot sizes (σ_x blue line, σ_y blue dotted-line).

4.3 PWFA case

The PWFA scheme is of the kind *external injection* [1], both a high quality electron driver and (especially) a high quality electron witness are extracted by a photo-cathode and pre-accelerated by a RF cavity so to be injected inside the plasma. The RF line allows for some fine tuning so to inject the beam into the plasma at a much increased control so to maintain beam quality over distance [5, 6]. The incoming beam energy has been set to 500 MeV considering the need to reach a matched transverse dimension of few microns with the requirement of few kA peak current for driving an FEL. The operational background density is set to 10^{16} cm^{-3} density, and so a plasma wavelength $\lambda_p \sim 334$ μm, that naturally place the trailing bunch in the accelerating phase of the wake generated by the driver. The driver charge, approximately 200 pC with a peak density about 10 times larger

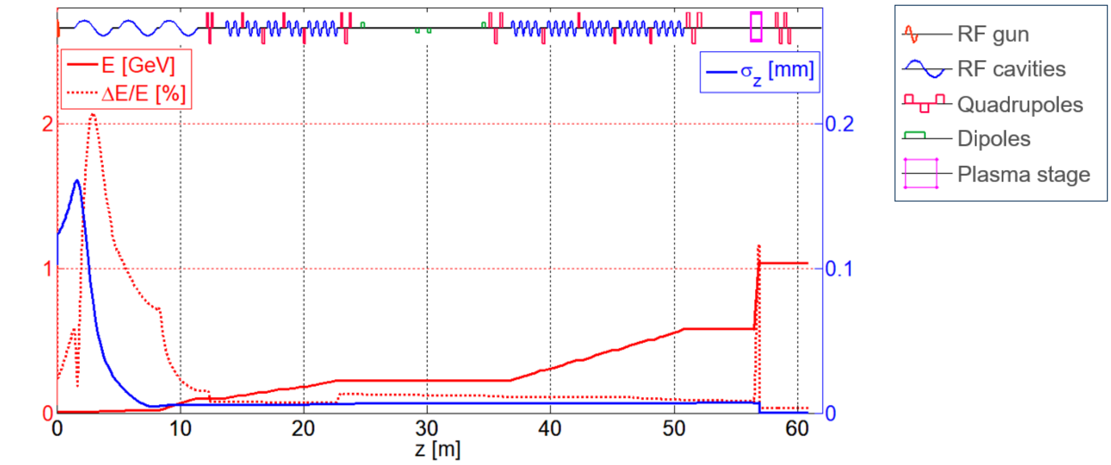

Figure 4.5: Start to end simulation results for the trailing bunch for the PWFA case: evolution along the injector of the energy (E red line) and energy spread ($\Delta E/E$ red dotted-line) and longitudinal bunch length (σ_z blue line).

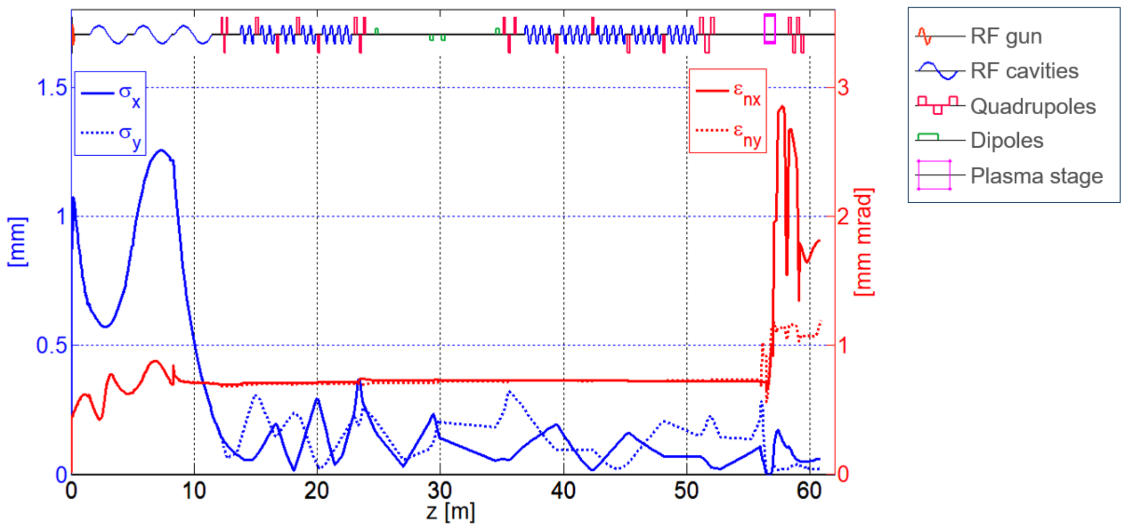

Figure 4.6: Start to end simulation results for the trailing bunch for the PWFA case: evolution along the injector of the electron beam transverse normalised emittance (ε_{n_x} red line, ε_{n_y} red dotted-line) and spot sizes (σ_x blue line, σ_y blue dotted-line).

than the background number density, place the working point in the so-called weakly nonlinear regime. The witness experiences an accelerating gradient of 1.1 GV/m exploiting energy doubling in approximately 40 cm.

The *comb-like* configuration for the electron beam, consisting of a 200 pC driver followed by a 30 pC witness bunch, has been achieved by means of the so-called *laser-comb technique*. Then the driver and witness bunches have been compressed respectively down to $\simeq$ 50 fs and 10 fs (FWHM) in the photo-injector and accelerated in the X-band booster linac up to the desired 500 MeV energy. Computational studies have been dedicated to provide at the plasma injection the driver arriving $\Delta t \simeq 0.58$ ps earlier then witness, corresponding the chosen Δt to $\simeq \lambda_p/2$ so to place the trailing bunch in the desired phase of the accelerating wake as mentioned before. In Fig. 4.5 and 4.6 the

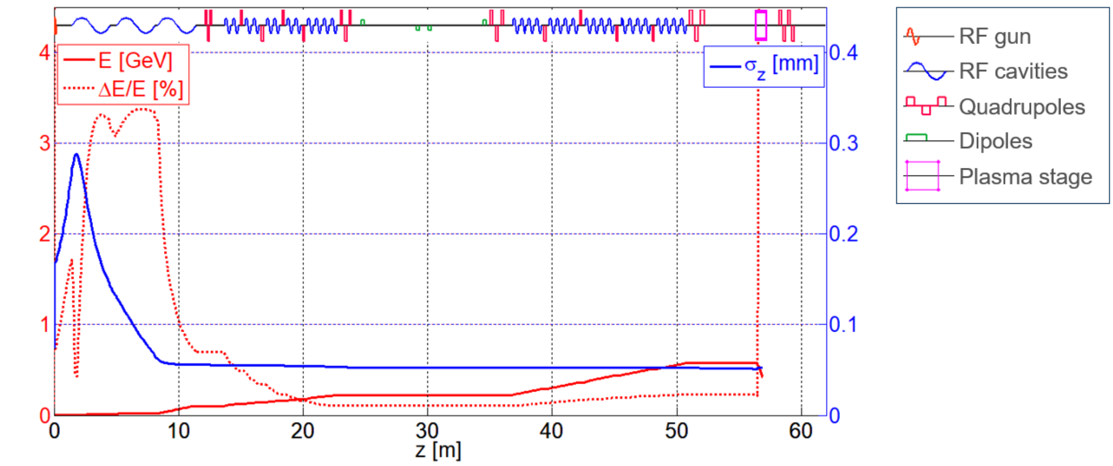

Figure 4.7: Start to end simulation results for the driver bunch for the PWFA case: evolution along the injector of the energy (E red line) and energy spread ($\Delta E/E$ red dotted-line) and longitudinal bunch length (σ_z blue line).

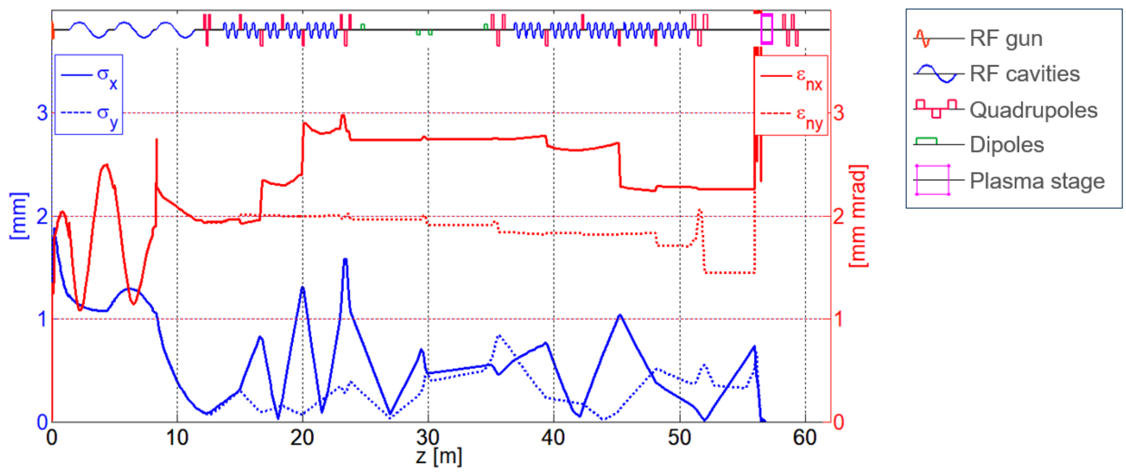

Figure 4.8: Start to end simulation results for the driver bunch for the PWFA case: evolution along the injector of the electron beam transverse normalised emittance (ε_{n_x} red line, ε_{n_y} red dotted-line) and spot sizes (σ_x blue line, σ_y blue dotted-line).

evolution along the linac of the trailing bunch longitudinal and transverse properties is reported, whereas in Fig. 4.7 and 4.8 the evolution along the linac of the driver bunch longitudinal and transverse properties is depicted. Notice that those values are retrieved by using the data analysis procedure reported in Section 6.3.2, so that reported final parameter values must be intended as 90% of total charge.

Details of the simulation tools, simulation settings and simulated experimental setup are reported in Chapter 7.

	Units	Full RF case	LWFA case	PWFA case
Electron Energy	GeV	1	1	1
RMS Energy Spread	%	0.05	2.3	1.1
Peak Current	kA	1.79	2.26	2.0
Bunch Charge	pC	200	30	30
RMS Bunch Length	μm (fs)	16.7 (55.6)	2.14 (7.1)	3.82 (12.7)
RMS normalized Emittance	mm mrad	0.5	0.47	1.1
Slice Length	μm	1.66	0.5	1.2
Slice Charge	pC	6.67	18.7	8
Slice Energy Spread	%	0.02	0.03	0.034
Slice normalized Emittance (x/y)	mm mrad	0.35/0.24	0.45/0.465	0.57/0.615
Undulator Period	mm	15	15	15
Undulator Strength $K(a_w)$		0.978 (0.7)	1.13 (0.8)	1.13 (0.8)
Undulator Length	m	30	30	30
Pierce parameter ρ **(1D/3D)**	$\times 10^{-3}$	1.55/1.38	2/1.68	2.5/1.8
Radiation Wavelength	nm (keV)	2.87 (0.43)	2.8 (0.44)	2.98 (0.42)
Photon Energy	μJ	177	40	6.5
Photon per pulse	$\times 10^{10}$	255	43	10
Photon Bandwidth	%	0.46	0.4	0.9
Photon RMS Transverse Size	μm	200	145	10
Photon Brilliance per shot	(s mm^2 mrad^2 bw(0.1%))$^{-1}$	1.4 $\times 10^{27}$	1.7 $\times 10^{27}$	0.8 $\times 10^{27}$

Table 4.1: Beam parameters from start-to-end simulations for full RF and for plasma wakefield acceleration cases with electron (PWFA) or laser (LWFA) driver beam

Bibliography

[1] CE Clayton and Luca Serafini. “Generation and transport of ultrashort phase-locked electron bunches to a plasma beatwave accelerator”. In: *IEEE Transactions on Plasma Science* 24.2 (1996), pp. 400–408.

[2] P Tomassini and A R Rossi. “Matching strategies for a plasma booster”. In: *Plasma Physics and Controlled Fusion* 58.3 (2015), p. 034001.

[3] Irene Dornmair, K Floettmann, and A R Maier. “Emittance conservation by tailored focusing profiles in a plasma accelerator”. In: *Physical Review Special Topics-Accelerators and Beams* 18.4 (2015), p. 041302.

[4] AR Rossi et al. “Stability study for matching in laser driven plasma acceleration”. In: *Nuclear Instruments and Methods in Physics Research Section A: Accelerators, Spectrometers, Detectors and Associated Equipment* 829 (2016), pp. 67–72.

[5] M Litos et al. “High-efficiency acceleration of an electron beam in a plasma wakefield accelerator”. In: *Nature* 515.7525 (2014), p. 92.

[6] M Tzoufras et al. “Beam loading by electrons in nonlinear plasma wakes”. In: *Physics of Plasmas (1994-present)* 16.5 (May 2009).

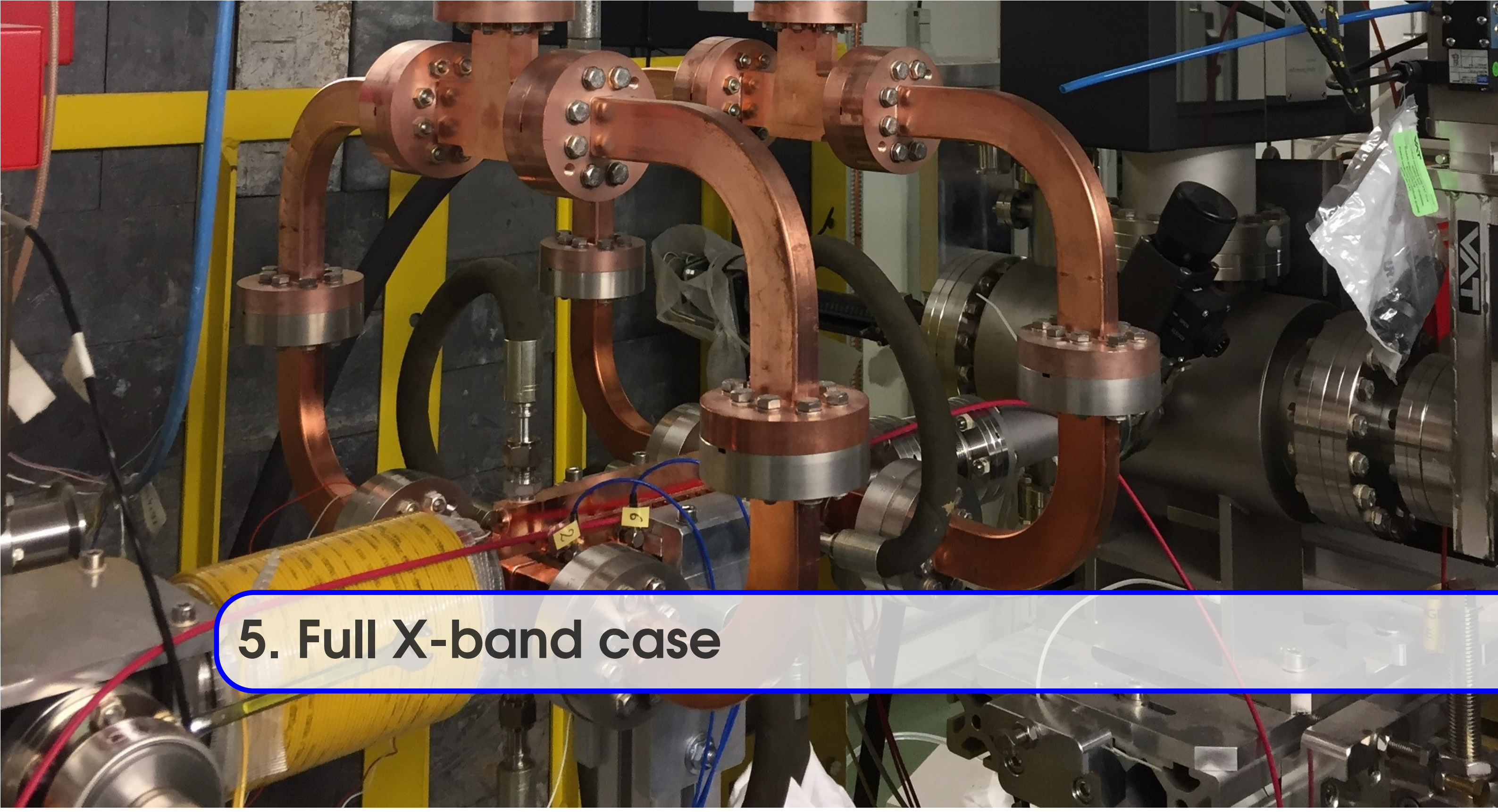

5. Full X-band case

5.1 Injector

After the last decades of R&D activity and machine test and development, the crucial role of high brightness photo-injectors in the fields of radiation generation and advanced acceleration schemes has been largely established, making them effective candidates to drive a plasma-based accelerator as pilot for user facilities. Indeed, these conventional photo-injectors are fundamental for the successful development of plasma-based accelerators whereas external injection schemes are considered, i.e. particle beam driven and laser driven plasma wakefield accelerators (PWFA and LWFA, respectively), since the ultimate beam brightness and its stability and reproducibility are strongly influenced by the RF-generated electron beam.

At the EuPRAXIA@SPARC_LAB facility, the main challenge for the RF photo-injector comes from the request of producing ultra-short, high quality electron beams.

High quality electron beams can be achieved in RF photo-injectors by means of RF guns, equipped with laser driven photo-cathodes, followed by booster sections. An emittance compensation scheme [1] based on a focusing solenoid at the exit of the RF gun can be used in photo-injectors to control emittance growth due to space charge effects. In addition from the invariant envelope theory [2], a proper matching of the transverse phase space of the electron beam, injected in the downstream accelerating sections (booster), can help to control the transverse emittance oscillations during the acceleration. Under the conditions of invariant envelope and proper phasing of space charge oscillations [3], the final emittance is almost compensated down to the thermal emittance value given by cathode emission with an expected emittance scaling like $\varepsilon_n \sim \sigma_{cath} \sim \sqrt{Q}$, where σ_{cath} is the hitting laser spot size on the photo-cathode, and Q the extracted electron charge. A compression stage can occur to shorten the beam length so to achieve the required high peak current. The so-called velocity bunching method [4] has opened up a new possibility of compressing the beam inside an RF structure and if integrated in the emittance compensation process [5] can provide the desired bunch current values with the advantage of compactness of the machine and absence of Coherent Synchrotron Radiation (CSR) effects present in a magnetic compressor [6]. It is interesting to notice that a shortened beam length also permits to contain the energy spread dilution due to RF curvature degradation; indeed the energy spread depends on the bunch length, σ_z, and the accelerating frequency, f_{RF}, as $\Delta\gamma/\gamma \approx 2(\pi f_{RF}\,\sigma_z/c)^2$, where an on crest operation, in full relativistic conditions, has been considered. To avoid the energy spread dilution due to RF curvature degradation effects, a $\sigma_z \leq 130$ µm must be injected in the X-band linac, ensuring a $\Delta\gamma/\gamma \leq 0.1\%$.

The EuPRAXIA@SPARC_LAB photo-injector is based on the experience at the SPARC_-LAB test facility [7] in operation at INFN laboratories at Frascati, and devoted to plasma-based experiments [8–10], both to accelerate and focus charge particles beams, and generation of advanced radiation, e.g. multi-color FEL [11–14], γ-rays through Thomson backscattering [15, 16] and both broad and narrow band high peak power THz radiation [17, 18]. The layout of the S-band photo-injector [19], operating at 2.856 GHz, is shown in Fig. 5.1: it consists of a 1.6 cell UCLA/BNL/SLAC type Standing Wave (SW) RF gun, including a copper photo-cathode with an emittance compensating solenoid followed by 3-meters long SLAC-type traveling wave (TW) sections operating at 2.856 GHz [20]. The first two accelerating sections are embedded by a solenoid; each solenoid is composed of 13 coils with the first coil and the other twelve coils in groups of three independently supplied. The beam line matching foresees a proper set of the emittance compensation solenoids and of the S-band cavity gradients in the velocity bunching scheme [4], according to the invariant envelope criteria [2]. In this configuration the first and second TW sections can operate far from the crest in the velocity bunching regime enabling the RF compression of the beam length, while the third section operates almost on crest in order to let the electron bunch gain the energy and freeze its phase space quality.

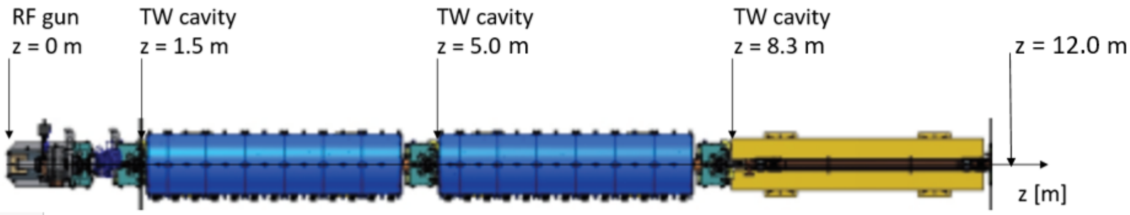

Figure 5.1: Layout of the SPARC-like high brightness S-band photo-injector consisting 1.6 cell UCLA/BNL type SW RF gun, equipped with a copper photo cathode and an emittance compensation solenoid, followed by three TW SLAC type sections; other two compensation solenoids surround the first and the second S-band cavities for the operation in the velocity bunching scheme.

A 200 pC electron beam has been studied up to the X-band linac entrance to provide a high density, high brightness electron beam suitable for driving radiation sources such as FELs or Compton backscattering. The beam dynamics has been explored by means of simulations to demonstrate the generation of high brightness ultra-short, femtosecond scale, bunches with up to 3 kA peak current to provide the proper peak current for SASE FEL operation at 3 nm.

Simulations have been performed with the multi-particles code TStep [21], which takes into account the space charge effects, relevant at very low energies. In our calculations the cylindrical symmetry of the beam has been assumed to allow us adopting a 2D model, which requires a reasonable number of particles and mesh points, and so computational time, with respect to a 3D one. In this specific case, 30k macro-particles have been considered as a good compromise between reliability and computational time.

An extensive simulation campaign led to consider a photo-cathode laser pulse with a Gaussian longitudinal profile of 0.9 ps RMS duration and a transverse uniform distribution of radius r = 350 µm . Figure 5.2 shows the shaped charge distribution at the cathode surface produced by such laser pulse as obtained with 2D TStep simulations.

The main operating parameters of the EuPRAXIA@SPARC_LAB photo-injector are summarized in Table 5.1.

The velocity bunching scheme in the first S-band cavity is adopted to longitudinally compress

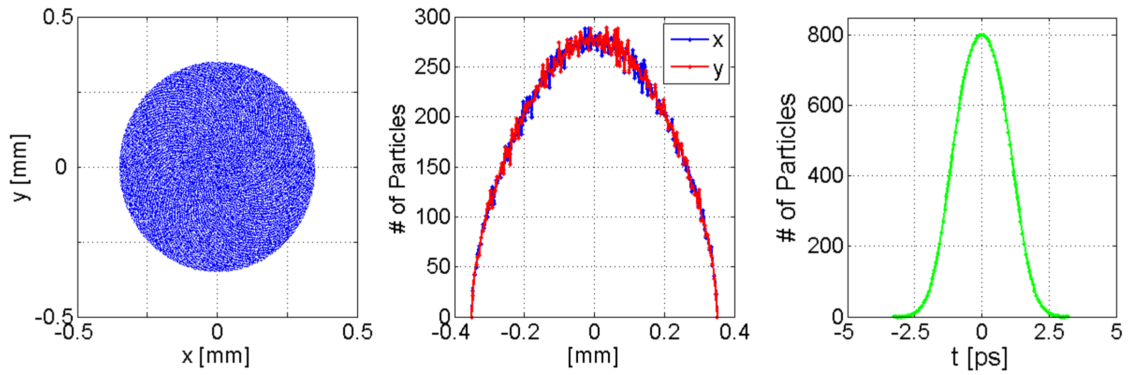

Figure 5.2: Charge distribution at cathode surface produced by the photo-cathode laser pulse as obtained with 2D TStep simulations.

Parameter	Unit	Value
Gun electric field amplitude	MV/m	120
Gun electric field operation phase	deg	30
Output gun beam energy	MeV	5.6
Amplitude of electric field in the three TW sections	MV/m	22.0/25.0/28.0
Magnetic field in the emittance compensating solenoid	kGauss	3
Magnetic field in the linac solenoid	kGauss	0.33
Total photo-injector length	m	12

Table 5.1: Main photo-injector parameters.

Beam Parameter	Unit	Value
Charge	pC	200
Energy	MeV	171.4
Energy spread	%	0.67
RMS bunch length	µm	112
RMS normalized emittance	mm mrad	0.37
Peak current	A	220
RMS size, σ_t	µm	390

Table 5.2: Output beam parameters: Moderate RF compression.

the beam of a factor 2.41, from 270 µm on crest to 112 µm , dephasing of few degrees with respect to the phase of zero crossing. Finally, the emittance minimization is obtained setting the gun solenoid at 3 kG and the one surrounding the first accelerating section at 0.33 kG. A slightly off-crest operation of the last two S-band cavities enables a further compensation of the energy spread at the X-band booster entrance. In this configuration the parameters of the electron beam exiting the photo-injector are listed in Table 5.2.

The simulation results are shown in Fig. 5.3 and Fig. 5.4 for the optimized beam. Figure 5.3 (left plot) shows the evolution of the transverse normalized emittance (red line), transverse spot size (blue line) and bunch length (green line), while the right plot illustrates the energy (blue line) and energy spread (green line) from the cathode down to the photo-injector exit as obtained with

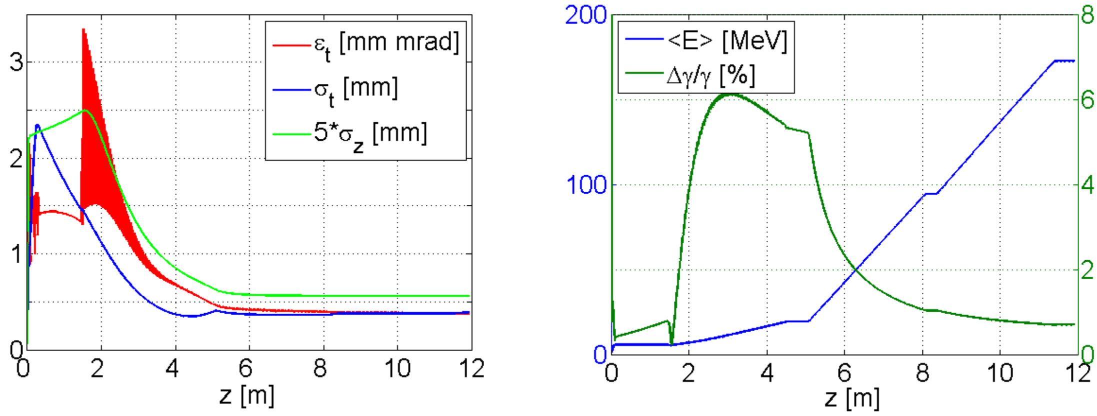

Figure 5.3: Evolution along the injector of the electron beam transverse normalized emittance (ε_t, red line), envelope (σ_t, blue line) and longitudinal bunch length (σ_z, green line) as obtained with the TStep code in case of hybrid compression.

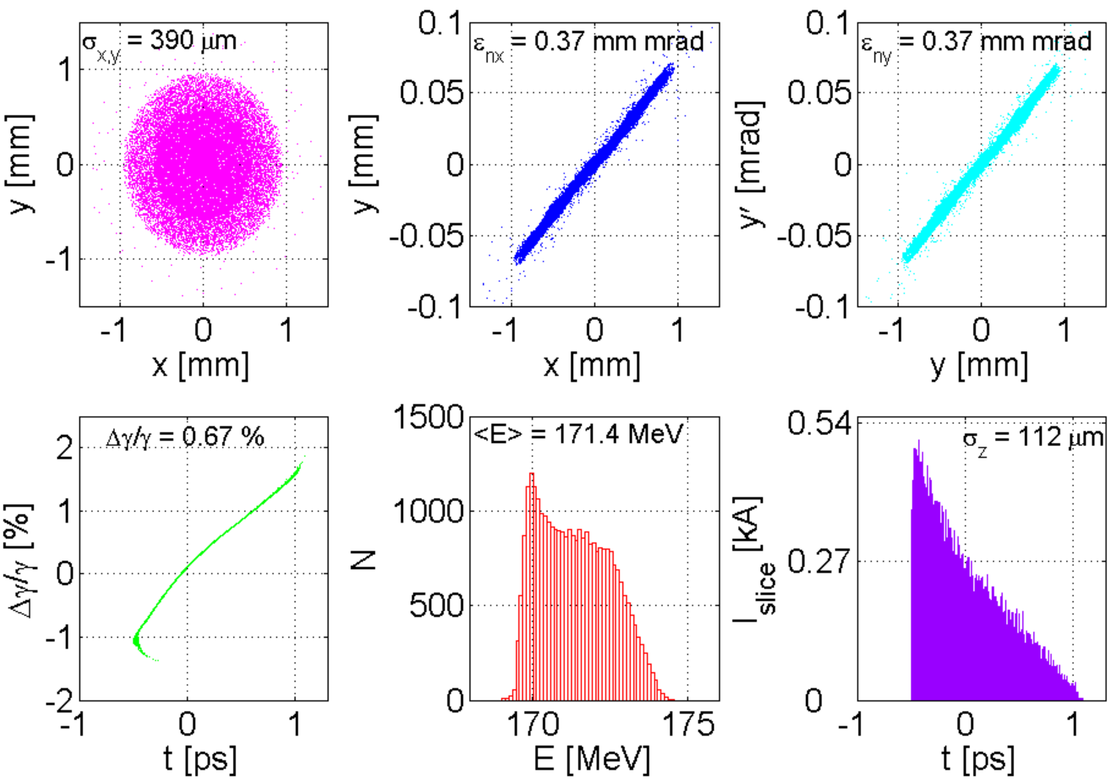

Figure 5.4: Upper plots: transverse (x and y) distribution and phase spaces. Lower plots: longitudinal phase space, energy and current profile. The results are output from TStep code at the photo-injector

the TStep code. Both longitudinal and transverse phase spaces are reported at the photo-injector exit as obtained with TStep in Fig. 5.4.

5.2 Linac

The Full X-band linac configuration is meant to provide a 200 pC electron beam able to drive SASE-FEL radiation and/or Compton interaction with the laser pulse. The high charge electron beam coming from the photo-injector is accelerated with the RF linac and the final longitudinal compression for the SASE-FEL operation occurs in the magnetic chicane, located between L1 and L2 Linac sections, according to a hybrid scheme of longitudinal compression: velocity bunching in the photo-injector plus magnetic compression in the linac.

The X-band linac mainly consists of two sections L1 and L2 located before and after the magnetic chicane respectively. Twelve X-band accelerating sections, 50 cm long, are foreseen for L1 and twenty for L2. According to the RF power system design (see X-band RF linac chapter 9) the maximum accelerating gradient applied is $E_{acc} \approx 60$ MV/m through all L1 and L2, to reach the required energy and energy spread for the electron beam in the conventional RF operation scheme. An increased power configuration can be also implemented progressively in a machine upgrade plan to provide overhead and flexibility to the operation, and ultimately to reach higher beam energies with the accelerating gradient raised up to ≈ 80 MV/m . Between L1 and L2 a 10 m long magnetic chicane is foreseen for phase space manipulation and/or longitudinal compression of the bunch; at the same time when the chicane dipoles are switched off, the straight beamline can accommodate the middle energy diagnostic station for beam parameters measurement. The two Linac sections L1 and L2 have been optimized to provide the required beam acceptance, from photo-injector and after the magnetic chicane, for the considered working points described in this and following chapters: the best focusing strength for the lattice has been found with a betatron phase advance per cell of about 20° and 30° for L1 and L2 respectively. In Table 5.3 the L1 and L2 main parameter list is reported.

Beam Parameter	Unit	L1			L2		
		PWFA	LWFA	Full X-band	PWFA	LWFA	Full X-band
Initial energy	GeV	0.102	0.098	0.171	0.222	0.212	0.502
Final energy	GeV	0.222	0.212	0.502	0.582	0.550	1.052
Active Linac length	m		6.0			10.0	
Acc. Gradient	MV/m	20.0	20.0	57.0	36.0	36.0	57.0
RF phase (0 crest)	deg	0	-20.0	-15.0	0	-19.5	+15.0
Initial energy spread	%	0.15	0.27	0.67	0.11	0.15	0.59
Final energy spread	%	0.11	0.15	0.59	0.07	0.07	0.14
Final Bunch length	mm	0.006	0.005	0.112	0.007	0.005	0.016

Table 5.3: L1 and L2 Linacs parameter list.

The TStep output from the photo-injector has been tracked trough the linac using the Elegant code [22], where the considered asymptotic values of the longitudinal and transverse wake functions have been calculated according to [23]:

$$W_{0\parallel} \approx \frac{Z_0\, c}{\pi\, a^2} \exp\left(-\sqrt{\frac{s}{s_1}}\right) (V/Cm) \tag{5.1}$$

$$W_{0\perp} \approx \frac{4 Z_0\, c\, s_2}{\pi\, a^4} \left[1 - \left(1 + \sqrt{\frac{s}{s_2}}\right) \exp\left(-\sqrt{\frac{s}{s_2}}\right)\right] (V/Cm^2) \tag{5.2}$$

$$s_1 = 0.41 \frac{a^{1.8}\, g^{1.6}}{L^{2.4}},\ s_2 = 0.17 \frac{a^{1.79}\, g^{.38}}{L^{1.17}} \tag{5.3}$$

where Z_0 is the free space impedance, c is the light velocity, a = 3.2 mm is the considered average iris radius, L = 8.332 mm is the cell length and g = 6.495 mm is the cavity length for the pill box model representing our X-band structure [24]; in Fig. 5.5 the calculated longitudinal and transverse wakefield for the considered X-band cell are shown.

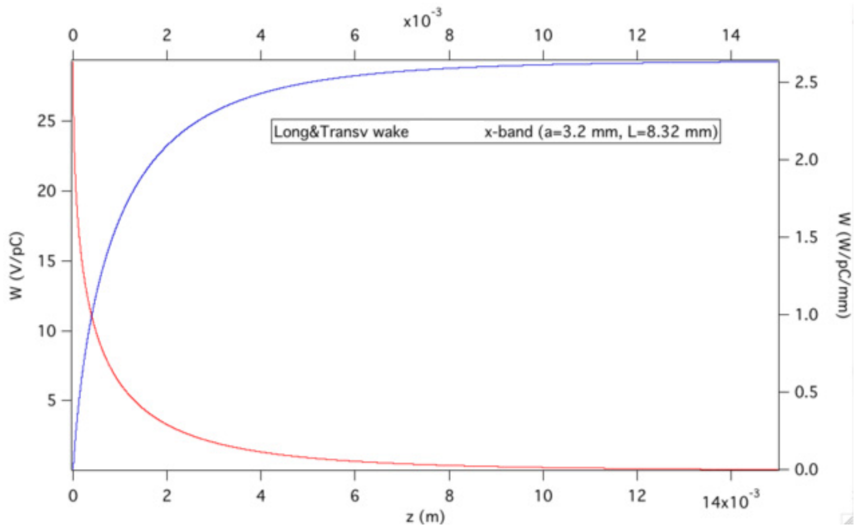

Figure 5.5: Longitudinal and transverse wakefield calculated for an iris radius of 3.2 mm and a cell length of 8.332 mm.

For this full X-band case an average gradient of $E_{acc} \approx 60$ MV/m is applied to all the RF accelerating sections, as reported in the previous table, adjusting the L1 an L2 RF phase in order to control and recover the correlated energy spread needed for the compression in the magnetic chicane. No phase space linearization is applied at this time prior the bunch compression in the chicane since the residual curvature of the longitudinal phase space distribution of the electron beam present at the photo-injector exit appears negligible and is quite completely recovered at the linac L1 exit, i.e. at the magnetic compressor entrance. In Fig. 5.6 the energy spread and the longitudinal distribution of energy and current are shown at the L1 linac entrance (i.e. photo-injector exit), before and after the BC bunch compressor and at the L2 linac exit, as obtained from the simulations performed with the Elegant code. In Fig. 5.7 instead the Twiss parameters are reported through all the Linac and up to the undulator entrance (above), while the energy spread and the bunch length evolution are shown below.

5.2.1 Magnetic compression

For simplicity a C-shape chicane with rectangular dipoles (no quadrupoles) has ben considered up to now, and the parameters have been chosen in order to minimize the emittance dilution due to the Coherent Synchrotron Radiation (CSR) in the bends, that is rather severe for short beams [25–28]; at the same time the chicane length has been kept as short as possible, minimizing also the initial correlated energy spread to ease its recovery in the final Linac section L2. Optimization of the magnetic compression stage is nevertheless in progress taking into account different dipole lattices. The final bunch length is adjusted using the R_{56} of the magnetic chicane and the RF phase of the linac L1, the considered momentum compaction is:

$$R_{56} \equiv \frac{\partial z}{d\delta} \approx 2\theta_B^2(\Delta L + \frac{2}{3}L_B) = 16 \text{ mm}, \tag{5.4}$$

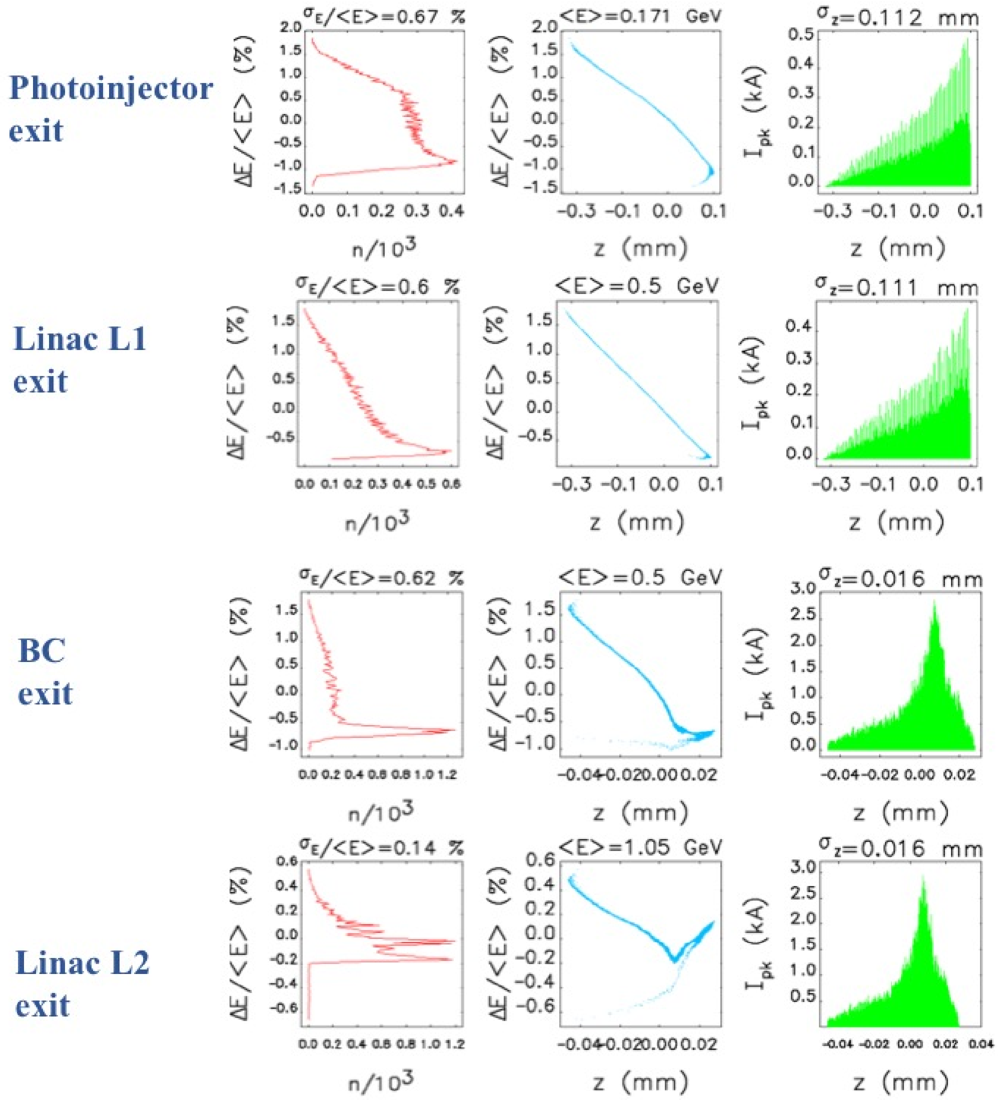

Figure 5.6: Longitudinal phase space of the full X-band accelerated electron beam; from above: photo-injector exit, L1 linac exit, BC compressor exit, L2 linac exit.

where θ_B is the bending angle, L_B the bend magnetic length and ΔL the drift length between the magnets, while for the second order momentum it holds (without quadrupoles):

$$T_{566} \approx -\frac{3}{2} R_{56} = 24 \text{ mm} ; \tag{5.5}$$

the main parameters of the magnetic bunch compressor are reported in Table 5.4.

In Fig. 5.8 the Twiss parameters and the dispersion function are shown through the BC chicane, while in Fig. 5.9 the transverse phase space emittance dilution is reported.

The full X-band case copes with the emittance dilution due to the CSR effect occurring in the magnetic chicane kept as short as possible due to room availability; neglecting up to now space charge effects and limiting the CSR effect study to the 1D approximation (as done with the Elegant code), it results in a final projected emittance dilution of about 60%, going from the initial $\varepsilon_{n,x,y}$= 0.5 mm mrad to the final $\varepsilon_{n,x,y}$= 0.8 mm mrad, nevertheless the beam quality results to be preserved in the slices corresponding to the highest current of the electron bunch, see sect. 5.4 (FEL performances) below.

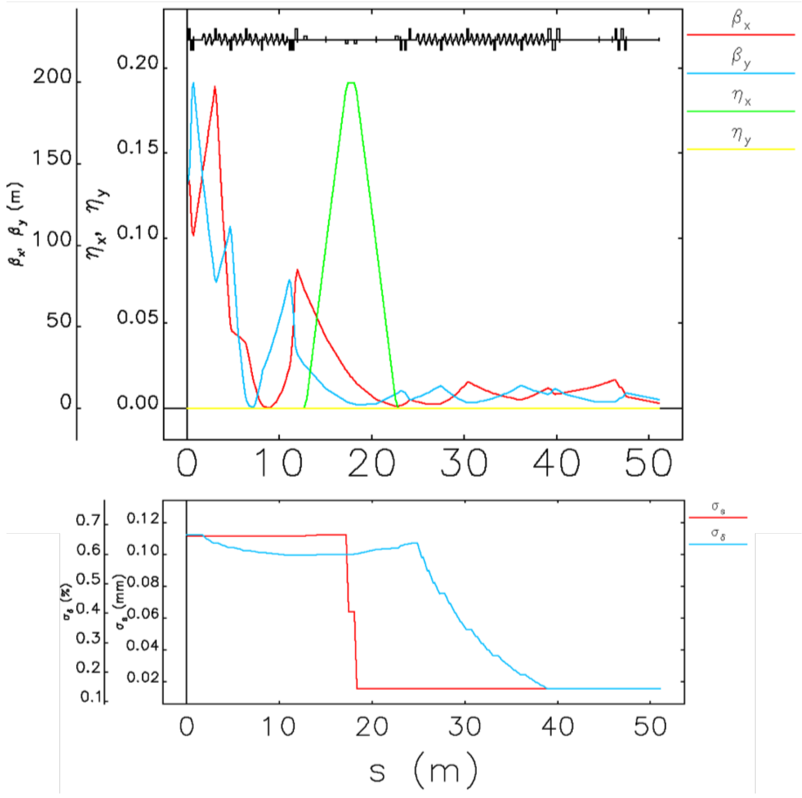

Figure 5.7: Upper plot: Twiss parameters and dispersion function through all the Linac, from photo-injector exit to the undulator entrance. Lower plot: Nominal RMS energy spread (blue) and RMS bunch length (red) along the entire Linac from photo-injector exit at 171 MeV to undulator entrance at 1 GeV.

Parameter	Symbol	Unit	Value
Beam Energy	E	GeV	0.500
Initial RMS bunch length	σ_{z_i}	μm	112.0
Final RMS bunch length	σ_{z_f}	μm	16.0
RMS total incoming relative energy spread	σ_δ	%	0.60
First order momentum compaction	R_{56}	mm	16.0
Second order momentum compaction	T_{566}	mm	24.0
Total chicane length	L_{total}	m	10.11
Dipole magnetic length	L_B	m	0.26
Dipole bend angle	$\|\theta_B\|$	deg	2.46
Maximum dispersion at chicane center	η_{max}	m	0.19
Projected CSR emittance dilution ($\gamma\varepsilon_0 = 0.5\ \mu$m)	$\Delta\varepsilon/\varepsilon_0$	%	60
CSR-induced relative energy spread (at 500 MeV)	$\sigma_{\delta CSR}$	%	0.03

Table 5.4: Parameters of the magnetic bunch compressor chicane BC.

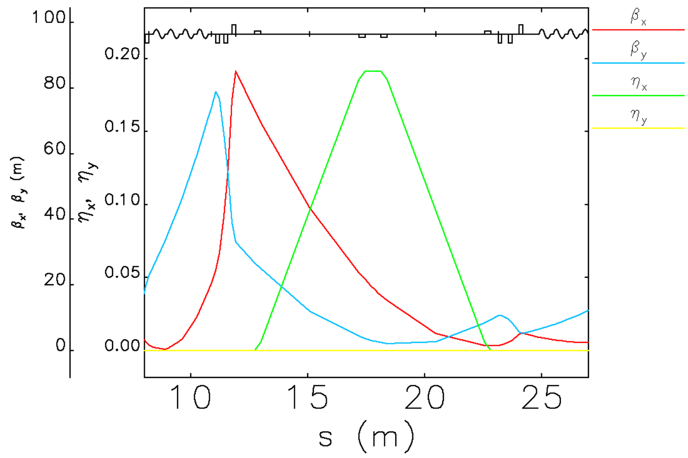

Figure 5.8: Dispersion and beta functions through the BC chicane for $R_{56} \approx 16$ mm.

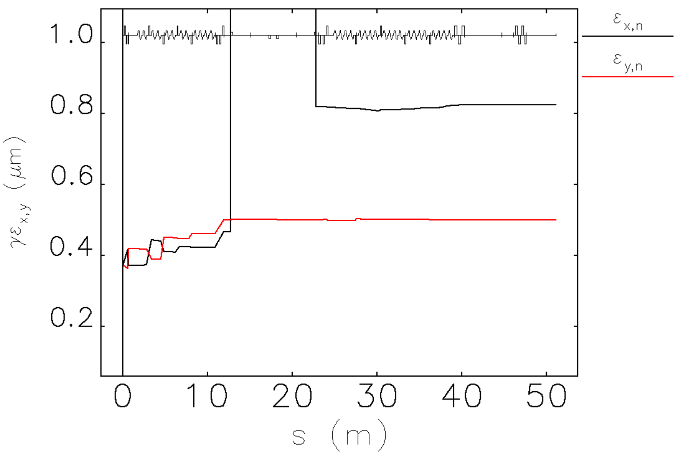

Figure 5.9: Transverse phase space emittance dilution along the Linac.

5.3 Transport of the Linac Beam inside the Undulator

The operation with beams accelerated by the X-band RF linac, without any auxiliary plasma acceleration stage, permits to achieve electron charges up to 400 pC and energies larger than 1 GeV . Two electron beam working points ((a) 100 pC and (b) at 200 pC) have been considered for the start to end simulations. Figure 5.10 shows the current I(A), the electron energy E(MeV), the normalized emittance ε_n and the energy spread $\Delta E/E$ along the electron beam coordinate s.

Electron beams with energy of about 1 GeV and slice emittance at about 0.4 mm mrad can be matched to an undulator with period $\lambda_w = 1.5$ cm and section length of the order of a meter using quadrupoles with total field of few T. The optimized choice done for this case has been to match to the undulator the best slices of the electron beam, using in the matching simulation phase the values of the slice energy and emittance. This led to values of the average β of about 3.4 m, corresponding to initial values of σ_x and σ_y of 33 µm and 23 µm, respectively [29]. In Fig. 5.11 the evolution of the RMS transverse dimensions, σ_x and σ_y, of the electron beam core along the undulator is presented for case (a).

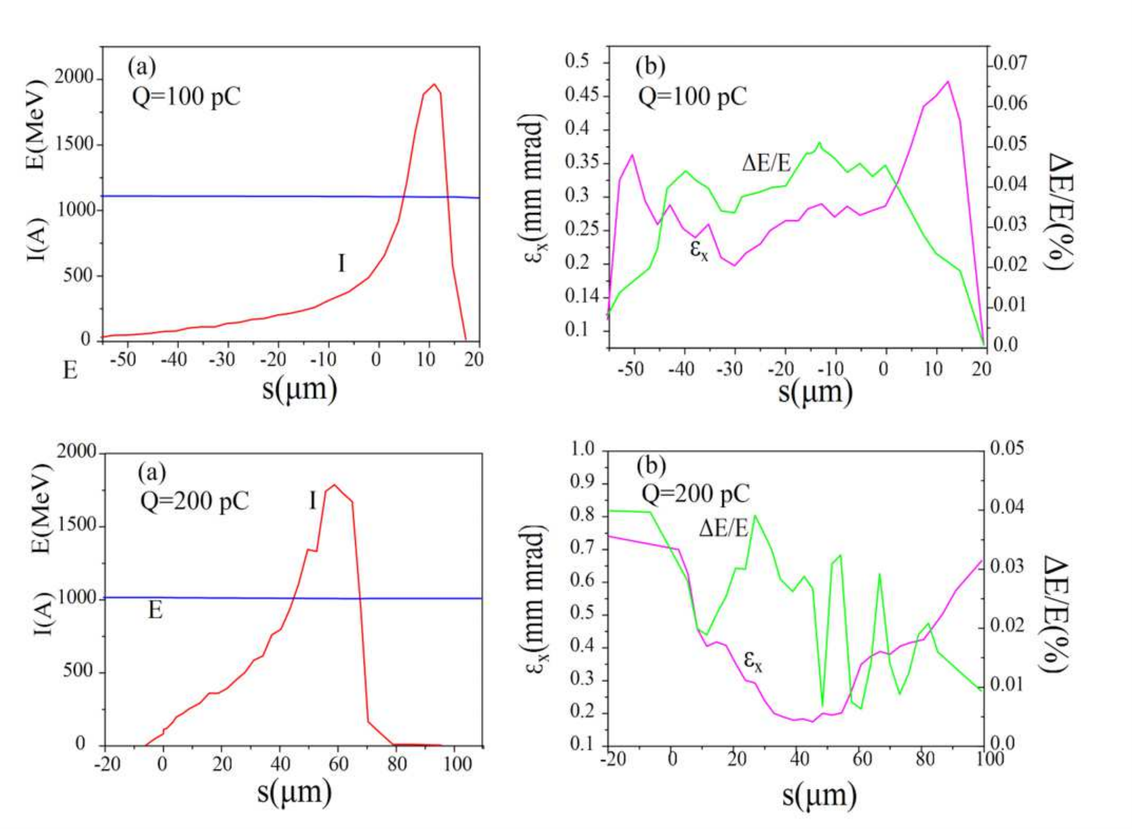

Figure 5.10: Upper windows $Q = 100\text{pC}$, lower windows $Q = 200$ pC . (a) in red I(A), in blue E(MeV), (b) emittance (mm mrad) and energy spread (%) vs the electron beam coordinate s (μm).

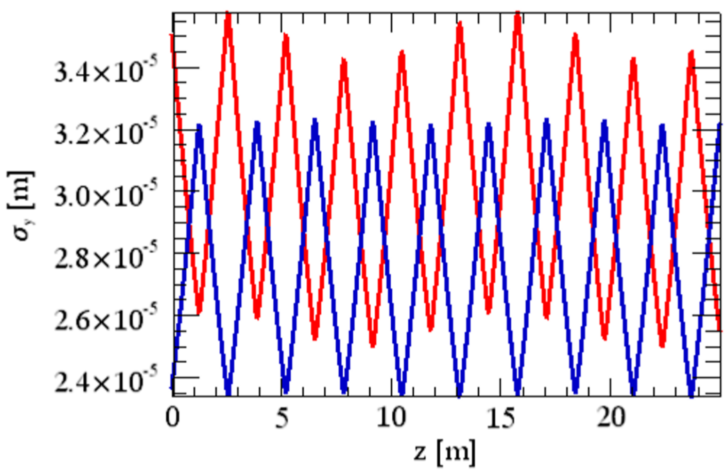

Figure 5.11: Transverse dimensions (RMS) σ_x (in red) and σ_y (in blue) of the electron beam along the undulator.

5.4 FEL performances

The characteristics of electrons, undulator and radiation of the two working points are listed in Table 5.5, third and fourth columns. The best slice has a peak current of about 2 kA , with emittance that in both cases are below 0.4 mm mrad and energy spread at or below 2×10^{-4}. Regarding

RF Linac	Units	(a) 100 pC	(b) 200 pC
Rep. rate	Hz	10	10
Exit linac energy	GeV	1.1	1
RMS Energy Spread	%	0.1	0.05
Peak Current	kA	2	1.79
Bunch Charge	pC	100	200
RMS bunch length	μm (fs)	12.7(38.2)	16.7 (55.6)
RMS norm. emittance	mm mrad	0.5	0.5
Slice Length	μm	1.25	1.66
Slice Charge	pC	10	6.67
Slice Energy Spread	%	0.018	0.02
Slice norm. emittance (x,y)	mm mrad	0.35-0.24	0.4-0.37
Undulator period	cm	1.5	1.5
Undulator strength K (a_w)		0.978 (0.7)	0.978 (0.7)
Pierce parameter ρ (1D/3D)	$\times 10^{-3}$	1.9/1.7	1.55/1.38
Radiation wavelength	nm (keV)	2.4 (0.52)	2.87(0.42)
Undulator length	m	15(30)	15(30)
Saturation power	MW	361(510)	120(330)
Radiation Energy	J	48(70)	164(177)
Photons per pulse	$\times 10^{11}$	5.9(8.4)	9.3(25.5)
Radiation Bandwidth	%	0.13(2.8)	0.24(0.46)
Radiation size	μm	65(75)	120(200)
Radiation divergence	μrad	17.5(16)	28(27)
Brilliance	(s mm^2 mrad^2 bw(0.1%)$^{-1}$ $\times 10^{28}$	3.8(2.2)	0.25(0.14)

Table 5.5: FEL performances of the linac driven electron beams.

case (a) at 100 pC , the energy of the best slice is about 1.1 GeV ($\gamma = 2158$). Assuming λ_u= 1.5 cm and $a_w = 0.7$, the radiation wavelength is $\lambda = 2.4$ nm. The transverse sizes σ_x and σ_y, after the matching, are about 33 μm and 23 μm, respectively. With these values, the 1D FEL parameter of the best slice is about 1.9×10^{-3}, while the 3D effects decrease it down to 1.7×10^{-3}, for a gain length $L_{g,3D} \approx 0.42$ m.

The FEL performances of the first electron beam (100 pC) obtained by GENESIS 1.3 [30] start-to-end simulations are presented in Fig.s 5.12. The radiation exponential growth (Fig. 5.12 (a)) follows the typical behavior of the short bunch regime [31, 32]: a first saturation at 15 m with 48 μJ marks the end of the exponential phase, where the radiation has completely slipped over the radiation. The saturation length turns out to be larger than the 3D analytical value [33, 34] evaluated for the best slice, because the different contributions of all the slices are naturally taken into account in the simulations. A further not exponential growth phase follows, leading the energy to about 70 μJ at 25 m. In this last phase, however, a deterioration of the temporal and spectral properties of the pulse takes place, with formation of secondary peaks, according to the FEL superradiance [35], as can be observed in Fig. 5.12 (b), where the contour curve of the radiated power is shown in the (s,z) plane.

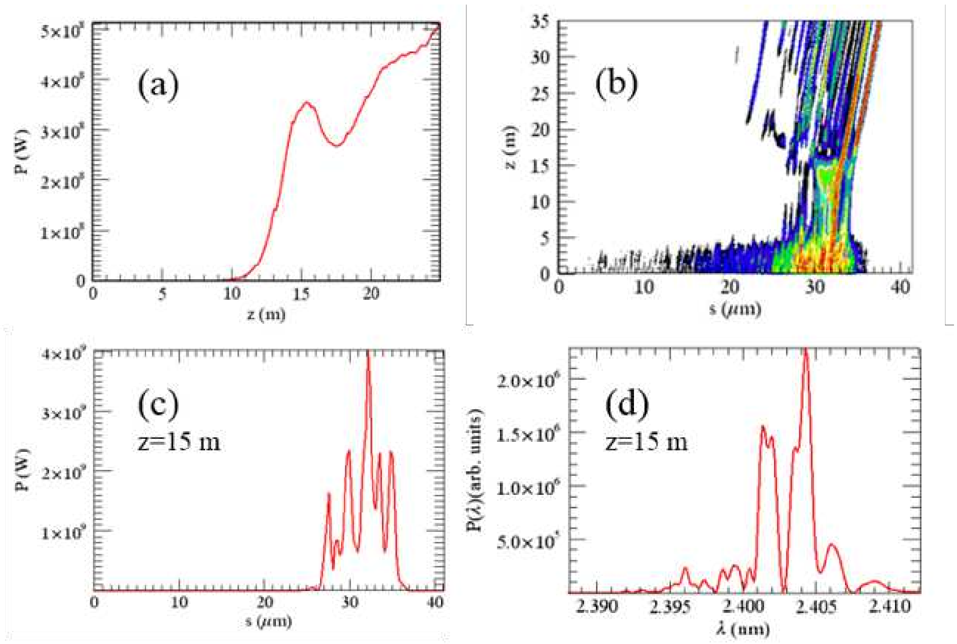

Figure 5.12: Case (a) at 100 pC : (a) power growth P(W) vs. the coordinate along the undulator z (m). (b) contour level of the radiated power in the (s,z) plane, with s (μm) coordinate along the electron beam. (c) Power and (d) spectral density at $z = 15$ m.

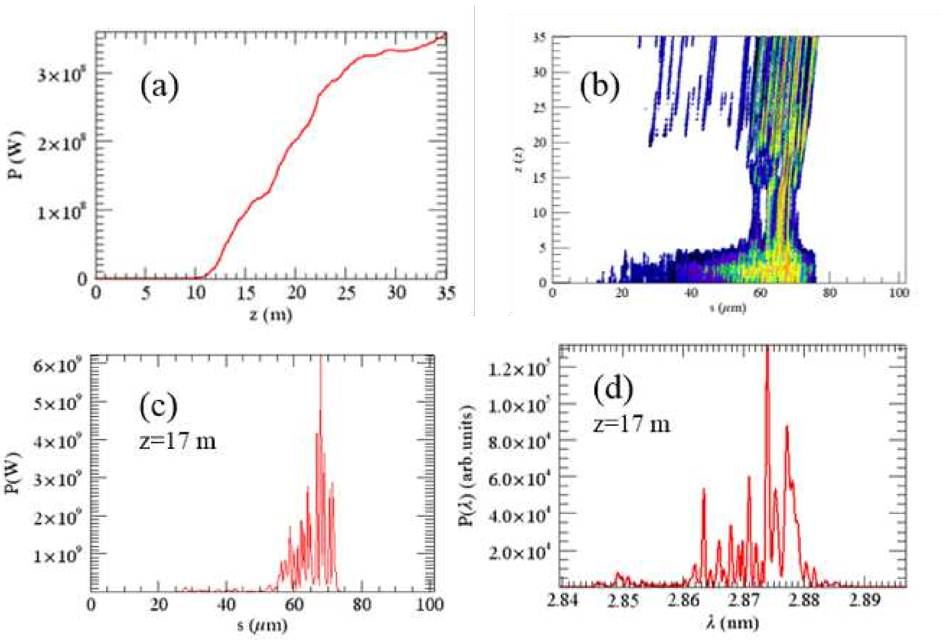

Figure 5.13: Case (b) at 200 pC : (a) power growth P(W) as function of the undulator coordinate z(m) for 200 pC . (b): contour plot of the radiated power in the (s,z) plane, with s (μm) coordinate along the electron beam, (c) power and (d) spectral density at $z = 17$ m.

The number of photons produced per shot is about 5.9×10^{11} at saturation and 8.4×10^{11} at the end of the undulator. Figure 5.12 (c) and (d) shows space and spectral power density close to the saturation, at $z = 15$ m. Since the cooperation length of the best slice is $L_c = 0.2$ μm , $2\pi L_c =$ 1.3 μm is shorter than electron beam length, 12 μm . The expected number of spikes [35] is about

10, as confirmed by the simulations. Cases with parameters degraded by percentages of 5% and 10% with respect to the nominal one have been analyzed. The results are reported in Table 2. $z1 =$ 15 m and $z2 = 30$ m are two position along the undulator. Decreases in emission respectively of 16% and 28% are evaluated.

The case with $Q = 200$ pC is described in Figs. 5.13. The beam and radiation properties are shown in Table 5.5, last column. The growth of the power is presented in Fig. 5.13 (a). A first saturation is reached in 15–17 m with an energy output of about 65 μJ. The radiation continues to increase with a slower rate, up to 178 μJ at 30–35 m. The contour plot of the power in the plans (s, z) is shown in Fig. 5.13 (b), while the power and spectral distribution at saturation are presented in (c) and (d). Since the beam is quite long, the radiation presents several SASE spikes. Even if the e-beam (b) is slightly worse than (a) in peak current, emittance and energy spread, while pulse and spectrum are less coherent, it produces more photons, due to its larger charge. In fact, the number of photons per shot n_p is 9×10^{11} at saturation and 2.5×10^{12} at the end of the undulator, for a brilliance respectively of 2.4–1.4×10^{27} (mm^2 mrad^2 s)$^{-1}$. A degradation of the beam parameters of 5% with respect to the values of case (b) does not compromise much the emission, with 12% of energy less than the nominal case. With 10% of degradation, instead, the emission produces 2×10^{12} photons per shot at 30 m, 21% less than case (b). Table 5.6 (columns 4-7) summarizes these results.

	(a)	(a)-5%	(a)-10%	(b)	(b)-5%	(b)-10%
Q(pC)	100	95	90	200	190	180
ε_x(mm mrad)	4.5	4.72	5	4.05	4.25	4.45
ε_y(mm mrad)	4.3	4.5	4.73	3.75	3.9	4.13
$\Delta E/E(e^{-4})$	1.85	1.94	2.03	1.8	1.97	2.02
I_{peak}(A)	1953.71	1856	1758	1788	1698	1600
z1(m)	15	15	15	15	15	15
E(z1)(μJ)	48	45	27	65	59	48
$N_{phot}(z1)(10^{11})$	5.95	5.4	3.2	9.3	8.5	6.97
z2(m)	30	30	30	30	30	30
E(z2)(μJ)	70	56	50.5	178	155	139
$N_{phot}(z2)(10^{11})$	8.4	6.74	6.09	25.5	22.4	20
Bandwidth(%)	0.1	0.1	0.1	0.16	0.16	0.16
Divergence(μrad)	15	15	15	27	27	28
Rad. Size (μm)	63	70	80	220	225	230

Table 5.6: Tolerance study: comparison between the nominal cases (a) at 100 pC and (b) at 200 pC and beams worsened by 5% and 10% in current, energy spread and emittance.

Bibliography

[1] Bruce E Carlsten. "New photoelectric injector design for the Los Alamos National Laboratory XUV FEL accelerator". In: *Nuclear Instruments and Methods in Physics Research Section A: Accelerators, Spectrometers, Detectors and Associated Equipment* 285.1-2 (1989), pp. 313–319.

[2] Luca Serafini and James B Rosenzweig. "Envelope analysis of intense relativistic quasilaminar beams in rf photoinjectors: mA theory of emittance compensation". In: *Physical Review E* 55.6 (1997), p. 7565.

[3] M Ferrario et al. "Direct measurement of the double emittance minimum in the beam dynamics of the sparc high-brightness photoinjector". In: *Physical review letters* 99.23 (2007), p. 234801.

[4] B Aune and Roger H Miller. *New Method for positron production at SLAC*. Tech. rep. 1979.

[5] L Serafini and M Ferrario. "Velocity bunching in photo-injectors". In: *AIP conference proceedings*. Vol. 581. 1. AIP. 2001, pp. 87–106.

[6] Paul Emma. *Accelerator physics challenges of X-ray FEL SASE sources*. Tech. rep. 2002.

[7] M Ferrario et al. "SPARC_LAB present and future". In: *Nuclear Instruments and Methods in Physics Research Section B: Beam Interactions with Materials and Atoms* 309 (2013), pp. 183–188.

[8] E Chiadroni et al. "Beam manipulation for resonant plasma wakefield acceleration". In: *Nuclear Instruments and Methods in Physics Research Section A: Accelerators, Spectrometers, Detectors and Associated Equipment* 865 (2017), pp. 139–143.

[9] Andrea R Rossi et al. "The External-Injection experiment at the SPARC_LAB facility". In: *Nuclear Instruments and Methods in Physics Research Section A: Accelerators, Spectrometers, Detectors and Associated Equipment* 740 (2014), pp. 60–66.

[10] R Pompili et al. "Experimental characterization of active plasma lensing for electron beams". In: *Applied Physics Letters* 110.10 (2017), p. 104101.

[11] L Giannessi et al. "Self-amplified spontaneous emission free-electron laser with an energy-chirped electron beam and undulator tapering". In: *Physical review letters* 106.14 (2011), p. 144801.

[12] L Giannessi et al. "Superradiant cascade in a seeded free-electron laser". In: *Physical review letters* 110.4 (2013), p. 044801.

[13] M Labat et al. "High-gain harmonic-generation free-electron laser seeded by harmonics generated in gas". In: *Physical review letters* 107.22 (2011), p. 224801.

[14] C Ronsivalle et al. "Large-bandwidth two-color free-electron laser driven by a comb-like electron beam". In: *New Journal of Physics* 16.3 (2014), p. 033018.

[15] Anna Giribono. "X-ray generation at SPARC_LAB Thomson backscattering source". In: *Nuovo Cimento C-Colloquia and Communications in Phisics*. Vol. 38. 2. Soc. Italiana di Fisica via Saragozza, 12, I-40123 Bologna, Italy. 2015.

[16] C Vaccarezza et al. "The SPARC_LAB Thomson source". In: *Nuclear Instruments and Methods in Physics Research Section A: Accelerators, Spectrometers, Detectors and Associated Equipment* 829 (2016), pp. 237–242.

[17] E Chiadroni et al. "The SPARC linear accelerator based terahertz source". In: *Applied Physics Letters* 102.9 (2013), p. 094101.

[18] E Chiadroni et al. "Characterization of the THz radiation source at the Frascati linear accelerator". In: *Review of Scientific Instruments* 84.2 (2013), p. 022703.

[19] D Alesini et al. "Status of the SPARC project". In: *Free Electron Lasers 2003*. Elsevier, 2004, pp. 586–590.

[20] Richard B Neal. "THE STANFORD 2-MILE LINEAR ACCELERATOR". In: *Phys. Today* 20.SLAC-PUB-0233 (1966), pp. 27–41.

[21] Lloyd M Young. *TStep: An electron linac design code*. Tech. rep.

[22] Michael Borland. *Elegant: A flexible SDDS-compliant code for accelerator simulation*. Tech. rep. Argonne National Lab., IL (US), 2000.

[23] Karl LF Bane. *Short range dipole wakefields in accelerating structures for the NLC*. Tech. rep. 2003.

[24] M Diomede et al. “Preliminary RF design of an X-band linac for the EuPRAXIA@ SPARC_-LAB project”. In: *arXiv preprint arXiv:1801.00707* (2018).

[25] Ya S Derbenev et al. *Microbunch radiative tail-head interaction*. Tech. rep. 1995.

[26] Evgenij L Saldin, Evgeny A Schneidmiller, and MV Yurkov. “On the coherent radiation of an electron bunch moving in an arc of a circle”. In: *Nuclear Instruments and Methods in Physics Research Section A: Accelerators, Spectrometers, Detectors and Associated Equipment* 398.2-3 (1997), pp. 373–394.

[27] Martin Dohlus, A Kabel, and T Limberg. “Wake fields of a bunch on a general trajectory due to coherent synchrotron radiation”. In: *Particle Accelerator Conference, 1997. Proceedings of the 1997*. Vol. 2. IEEE. 1997, pp. 2550–2552.

[28] R Li, CL Bohn, and JJ Bisognano. “Analysis on the steady-state coherent synchrotron radiation with strong shielding”. In: *Particle Accelerator Conference, 1997. Proceedings of the 1997*. Vol. 2. IEEE. 1997, pp. 1644–1646.

[29] M Quattromini et al. “Focusing properties of linear undulators”. In: *Physical Review Special Topics-Accelerators and Beams* 15.8 (2012), p. 080704.

[30] Sven Reiche. “GENESIS 1.3: a fully 3D time-dependent FEL simulation code”. In: *Nuclear Instruments and Methods in Physics Research Section A: Accelerators, Spectrometers, Detectors and Associated Equipment* 429.1-3 (1999), pp. 243–248.

[31] JB Rosenzweig et al. “Generation of ultra-short, high brightness electron beams for single-spike SASE FEL operation”. In: *Nuclear Instruments and Methods in Physics Research Section A: Accelerators, Spectrometers, Detectors and Associated Equipment* 593.1-2 (2008), pp. 39–44.

[32] F Villa et al. “Generation and characterization of ultra-short electron beams for single spike infrared FEL radiation at SPARC_LAB”. In: *Nuclear Instruments and Methods in Physics Research Section A: Accelerators, Spectrometers, Detectors and Associated Equipment* 865 (2017), pp. 43–46.

[33] Ming Xie. “Design optimization for an X-ray free electron laser driven by SLAC linac”. In: *Particle Accelerator Conference, 1995., Proceedings of the 1995*. Vol. 1. IEEE. 1995, pp. 183–185.

[34] G Dattoli, PL Ottaviani, and S Pagnutti. “Booklet for FEL design: a collection of practical formulae”. In: *Frascati: ENEA–Edizioni Scientifiche* (2007).

[35] R Bonifacio et al. “Spectrum, temporal structure, and fluctuations in a high-gain free-electron laser starting from noise”. In: *Physical review letters* 73.1 (1994), p. 70.

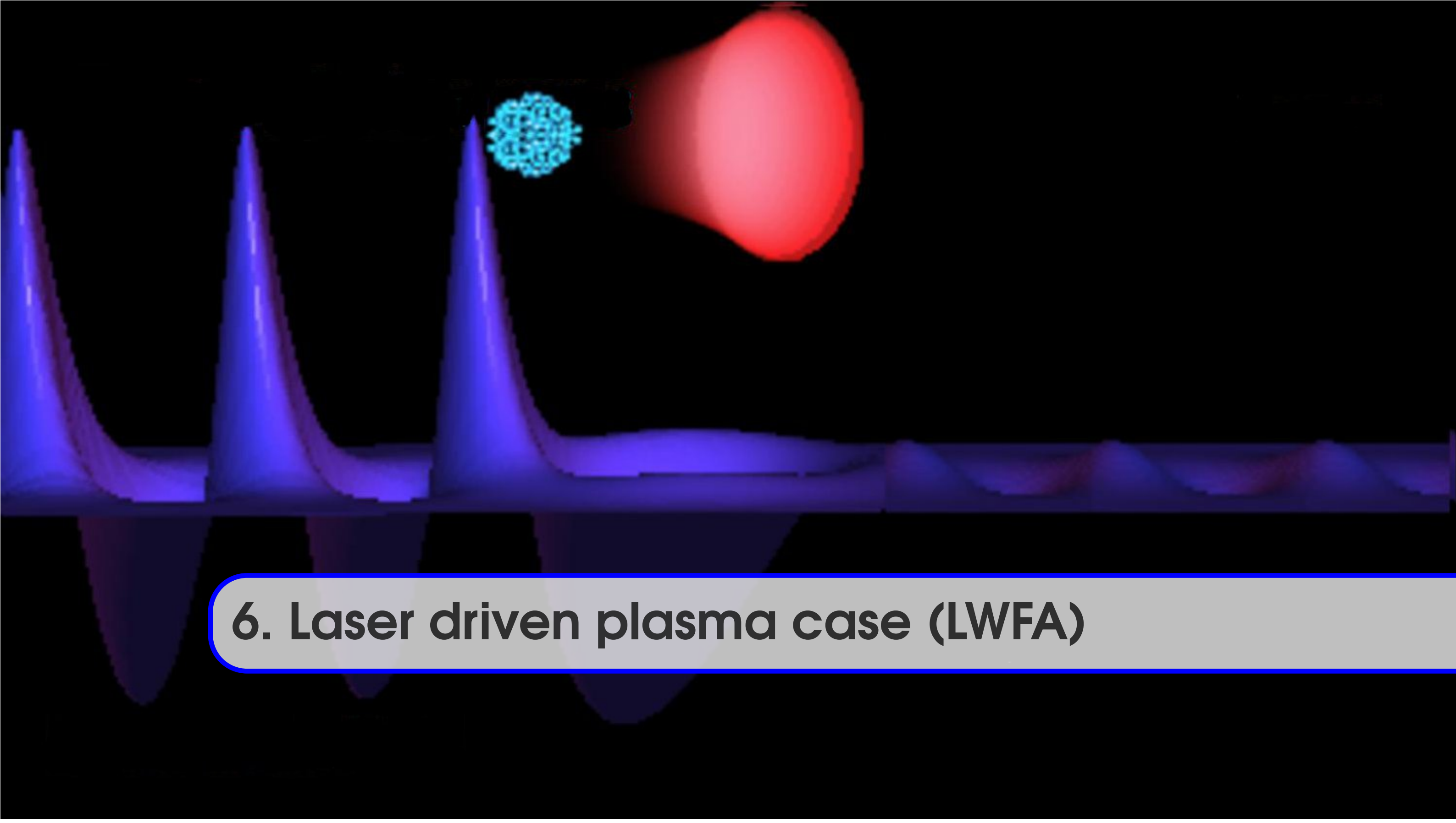

6. Laser driven plasma case (LWFA)

In this case the 1 GeV energy can be achieved by means of a single stage of plasma acceleration, few centimeters long, coupled with the RF Linac operating at about 500 MeV. The goal of the project is to operate plasma acceleration at approximately 10^{16} cm^{-3} , a plasma density that can be used to produce electric fields of 1–2 GV/m and characterized by a plasma wavelength of $\lambda_p \approx 300$ µm. This choice matches with the chosen beam input energy of ∼500 MeV, highly rigid bunch, that limits transverse bunch evolution and the consequent transverse emittance dilution within the plasma.

6.1 Injector

Detailed beam dynamics studies have been performed to provide a reliable working point for the EuPRAXIA@SPARC_LAB photo-injector aiming to drive a witness bunch suitable for external injection schemes, both in particle and laser driven plasma wakefield acceleration.

A case of interest foresees a 0.5 GeV witness beam energy at the plasma interface, with much less than 1 mm mrad slice emittance and 30 pC in 10 fs FWHM length, which turns into up to 3 kA peak current. Except for the final energy, these parameters are those requested to generate SASE FEL radiation at 3 nm with 1 GeV electron beam. A pure RF compression, applying the velocity bunching scheme, has been considered to produce in one stage a 3 kA beam at the end of the S-band TW sections at ∼100 MeV.

Beam dynamics simulations results from TStep code are presented below with 30k macro-particles.

A photo-cathode laser pulse with a Gaussian longitudinal profile of σ_z = 105 µm RMS length and a transverse uniform distribution with spot size σ_r = 175 µm has been chosen, as reported in Fig. 6.1.

The main operating parameters of the EuPRAXIA@SPARC_LAB photo-injector for the optimized witness beam in case of LWFA in external injection are summarized in Table 6.1.

The velocity bunching regime is applied to the first two S-band cavities to shorten the beam length from 102 µm (on crest) to ≈3 µm (RMS), both cavities working close to the zero crossing of the field. The emittance minimization is obtained setting the gun solenoid at ≈ 3 kG and those surrounding the first and second S-band cavities at 0.32 kG and 0.50 kG, respectively. A slightly off-crest operation of the third S-band cavity further reduces the energy spread at the injector exit. In this configuration the design electron beam parameters at the photo-injector exit are listed in Table 6.2.

The simulation results are shown in Fig. 6.2 for the optimized witness-like beam: the left plot shows the evolution of the transverse normalized emittance (red line), spot size (blue line) and longitudinal bunch length (green line), while the right plot illustrates the energy (blue line) and energy spread (green line) from the cathode down to the photo-injector exit as obtained with the TStep code. The longitudinal and transverse phase spaces at the photo-injector exit are reported in Fig. 6.3.

The longitudinal profile of the beam exiting the photo-injector is typical of the velocity bunching process showing a spike of current on the head of the bunch and a long tail, with a FWHM bunch length of 3 μm.

6.1.1 Photo-injector sensitivity studies

The introduction of jitters in the photo-injector affects the electron beam quality at the X-band linac entrance resulting in emittance and longitudinal length growth. Photo-injector sensitivity studies have been performed in terms of the exiting beam quality in order to test the robustness of the adopted working point, especially with regards to the compression phase stability, as needed to ensure a μm-scale bunch length. Taking advantage from the experience acquired at the SPARC_-LAB test facility, the maximum reasonable error values have been considered to face the most realistic situation (see Table 6.3), trying not to count only on the best performance of the machine systems.

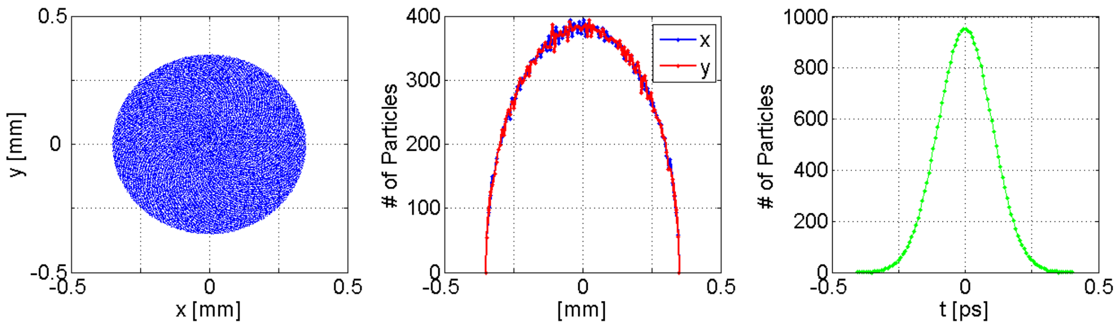

Figure 6.1: Charge distribution at the cathode surface produced by the photo-cathode laser pulse as obtained with 2D TStep simulations.

Parameter	Unit	Value
Gun electric field amplitude	MV/m	120
Gun electric field operation phase	deg	30
Output gun beam energy	MeV	5.6
Amplitude of electric field in the three TW sections	MV/m	20.0/20.0/28.0
Magnetic field in the emittance compensating solenoid	kGauss	3
Magnetic field in the linac solenoid	kGauss	0.32/0.50
Total photo-injector length	m	12

Table 6.1: Main photo-injector parameters.

Parameter	Unit	Value
Charge	pC	30
Energy	MeV	100
RMS energy spread	%	0.27
RMS bunch length	fs	10
Peak current (FWHM)	kA	4.0
RMS norm. emittance	mm mrad	0.44
Rep. rate	Hz	10

Table 6.2: Witness beam parameters at the end of photo-injector in case of pure RF compression.

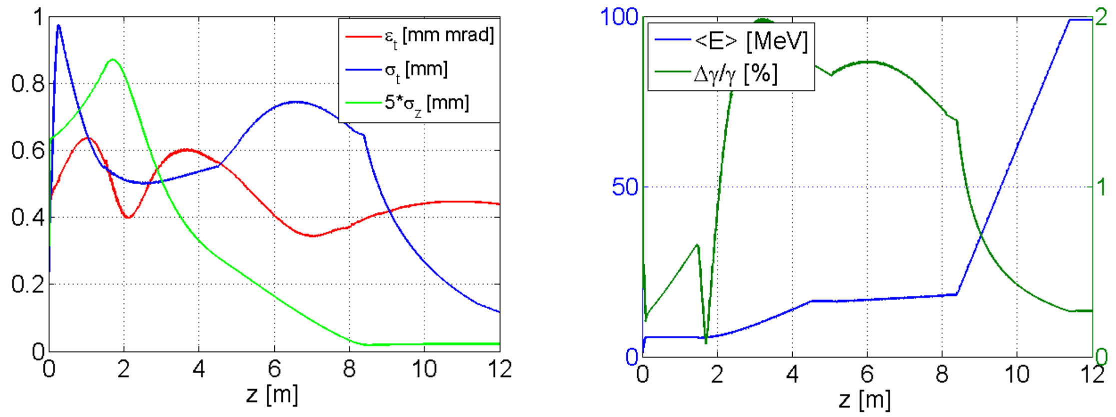

Figure 6.2: Evolution along the injector of the electron beam transverse normalized emittance (ε_n, red line), envelope (σ_t, blue line) and longitudinal bunch length (σ_z, green line) as obtained with the TStep code in case of pure RF compression.

Gun		
RF Voltage [ΔV_G]	%	$\pm$ 0.2
RF Phase [$\Delta\Phi_G$]	deg	$\pm$ 0.05, $\pm$ 0.1
S-band accelerating sections		
RF Voltage [ΔV_S]	%	$\pm$ 0.2
RF Phase [$\Delta\Phi_S$]	deg	$\pm$ 0.05, $\pm$ 0.1
Cathode laser system		
Charge fluctuation	%	$\pm$5

Table 6.3: Studied jitter for the RF gun, accelerating cavities and photo-cathode laser system.

Machine sensitivity studies have been performed on samples of 20 machine runs (due to computational limits). For each machine we have generated a tracking code input whose element errors are provided by means of the Matlab Latin Hypercube function that returns an n-by-p matrix. This matrix contains a latin hypercube sample of n machine run identifier on each of the p element errors: the n values are randomly distributed with one from each interval (0,1/n), (1/n,2/n), ..., (1-1/n,1), and they are randomly permuted. Furthermore a normal random distribution of minus and

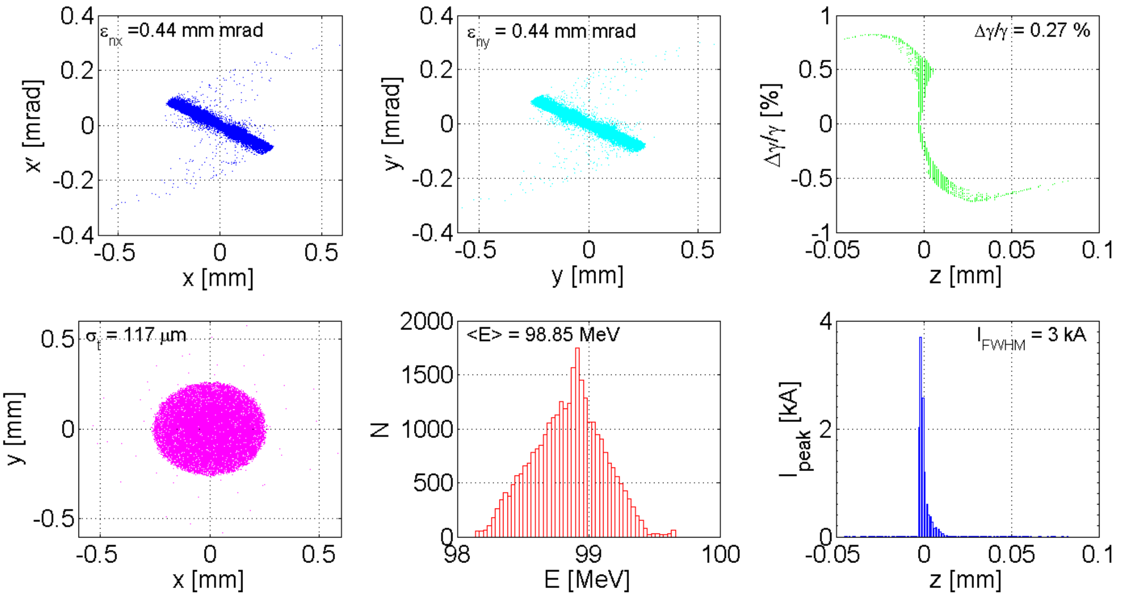

Figure 6.3: Upper plots: transverse (x and y) distribution and phase spaces. Lower plots: longitudinal phase space, energy and current profile. The results are output from TStep code at the photo-injector exit.

plus sign is also applied. In this way the error matrix randomly factorizes from -100% to +100% the considered error values listed in Table 6.3 for each element. Since the RF compression occurs in the accelerating cavities and it strongly depends on the RF phase stability, phase and voltage jitters on the accelerating cavities have been first introduced one by one with the aim to determine the most critical error contributions. Jitters on the RF gun power system and on the extracted beam charge have been introduced afterwards. Here we report the results of one of the cases studied.

Both the longitudinal and transverse phase space are reported in Figures from 6.4 to 6.8 for the following cases, respectively:

- $\Delta V_S = \pm 0.2\%$
- $\Delta \Phi_S = \pm 0.1$ degree
- $\Delta V_{S,G} = \pm 0.2\%$, $\Delta \Phi_{S,G} = \pm 0.1$ deg
- $\Delta V_{S,G} = \pm 0.2\%$, $\Delta \Phi_{S,G} = \pm 0.1$ deg, Q = $\pm 5\%$

The blue data show the ideal case where no jitters are foreseen. As highlighted in Fig. 6.5 the effect of the RF phase jitter on the beam length is dominant with respect to other jitter contributions, which do not cause significant lengthening and emittance degradation. Figure 6.8 underlines the importance of this contribution, reporting the beam parameters occurrence overall the 80 machine runs at the photo-injector exit in case of $\Delta V_{S,G} = \pm 0.2\%$, $\Delta \Phi_{S,G} = \pm 0.1$ deg and Q = ± 5 %.

The data analysis highlights the effect of the RF phase jitter on the beam length, while other jitter contributions do not cause significant degradation of the beam parameters. Less than 5% machine runs goes in peak currents lower than the required 3 kA and they correspond to absolute RF phase jitter higher than 0.05 deg. All the parameters are still compliant with the required ones and the analysis suggests that RF phase jitter lower than $\pm$ 0.05 deg can ensure the needed beam peak current. The results overall the 80 machine runs are summarized in Table 6.4.

6.2 Linac

For this working point the X-band RF linac is meant to provide an electron beam for injection in the plasma capillary, $Q = 30$ pC, $I = 3$kA (FWHM), with a 4 μm of transverse spot-size, the electron

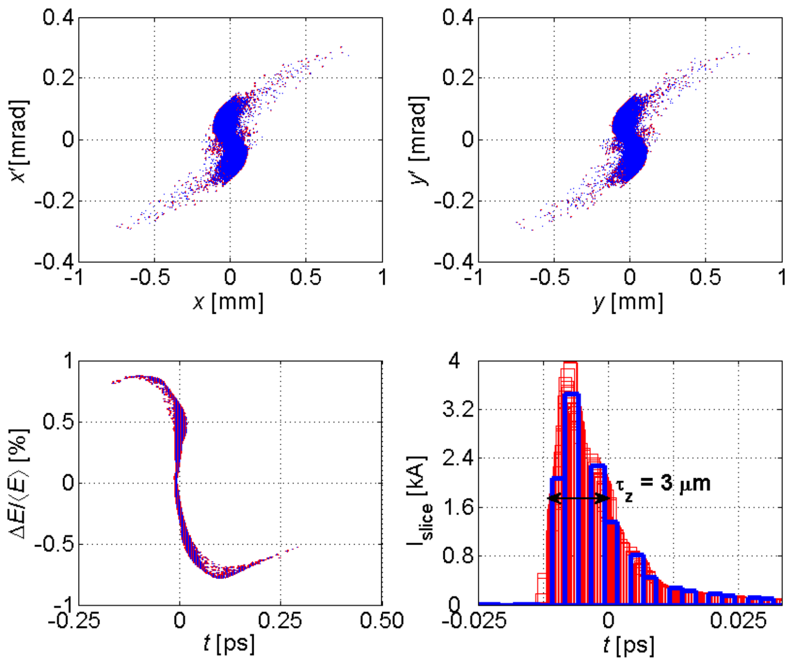

Figure 6.4: Transverse phase space (upper left (right): horizontal (vertical)) and longitudinal phase space (lower left) and current profile (lower right) in case only the amplitude jitter on the first accelerating section is included, i.e. $\Delta V_S = \pm 0.2\%$.

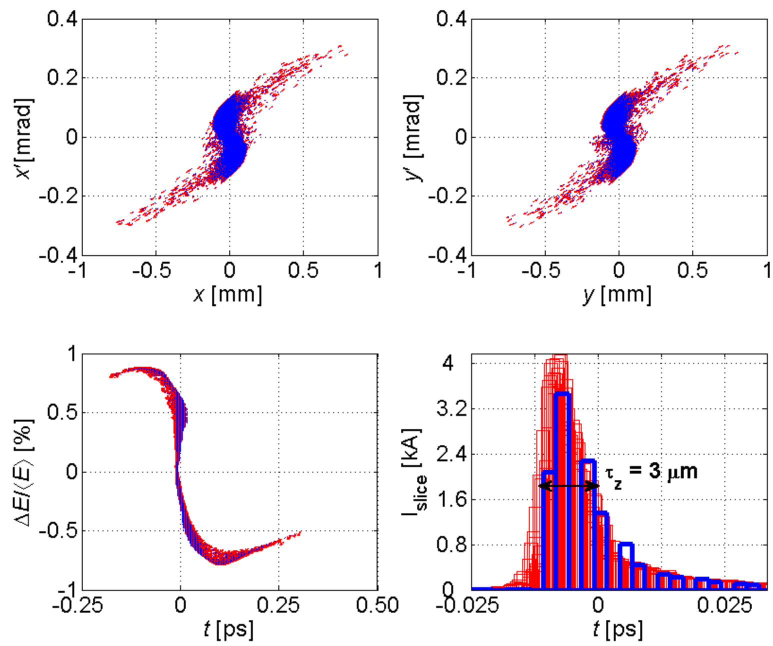

Figure 6.5: Transverse phase space (upper left (right): horizontal (vertical)) and longitudinal phase space (lower left) and current profile (lower right) in case only the phase jitter on the compression phase is included, i.e. $\Delta\Phi_S = \pm 0.1$ deg.

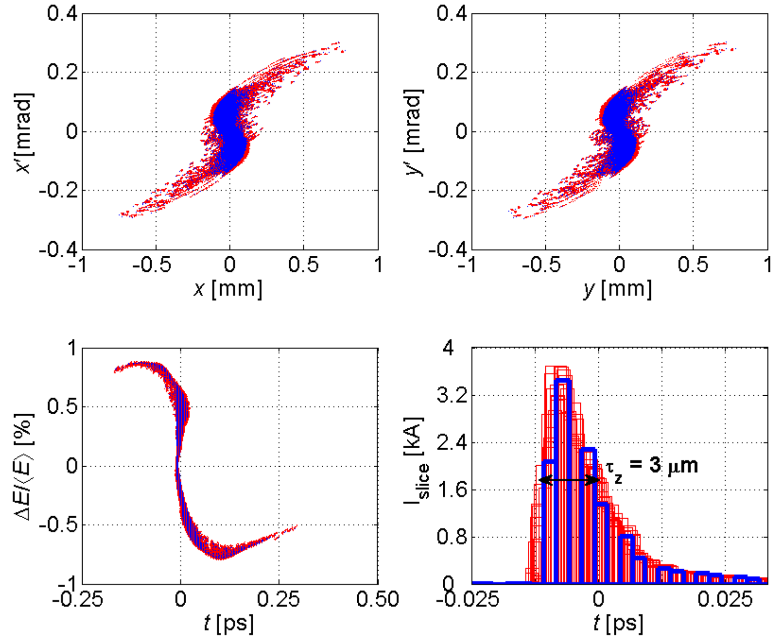

Figure 6.6: Transverse phase space (upper left (right): horizontal (vertical)) and longitudinal phase space (lower left) and current profile (lower right) in case amplitude and phase jitters, on both gun and first accelerating section, are included, i.e. $\Delta V_{S,G} = \pm 0.2\%$, $\Delta\Phi_{S,G} = \pm 0.1$ deg.

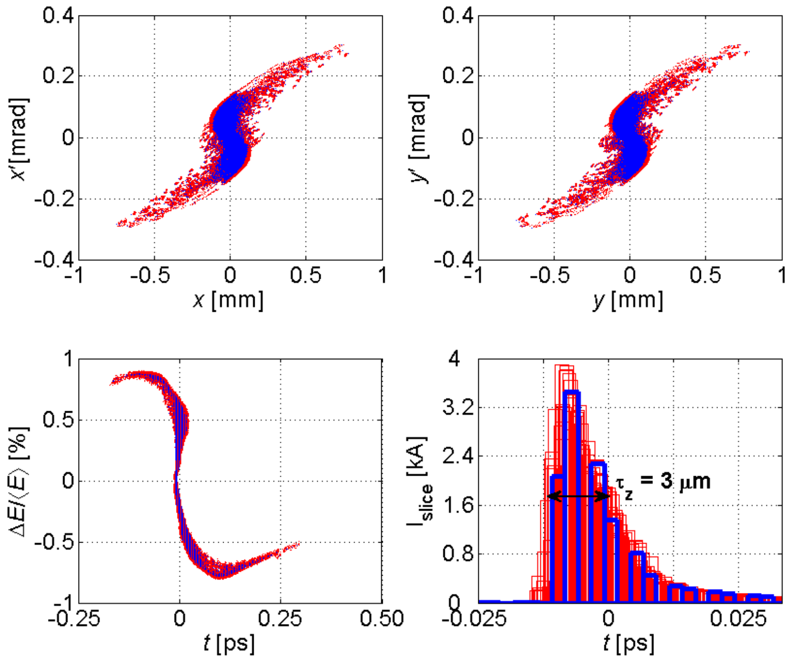

Figure 6.7: Transverse phase space (upper left (right): horizontal (vertical)) and longitudinal phase space (lower left) and current profile (lower right) in case all jitters are included, i.e. $\Delta V_{S,G} = \pm 0.2\%$, $\Delta\Phi_{S,G} = \pm 0.1$ deg, Q = $\pm 5\%$.

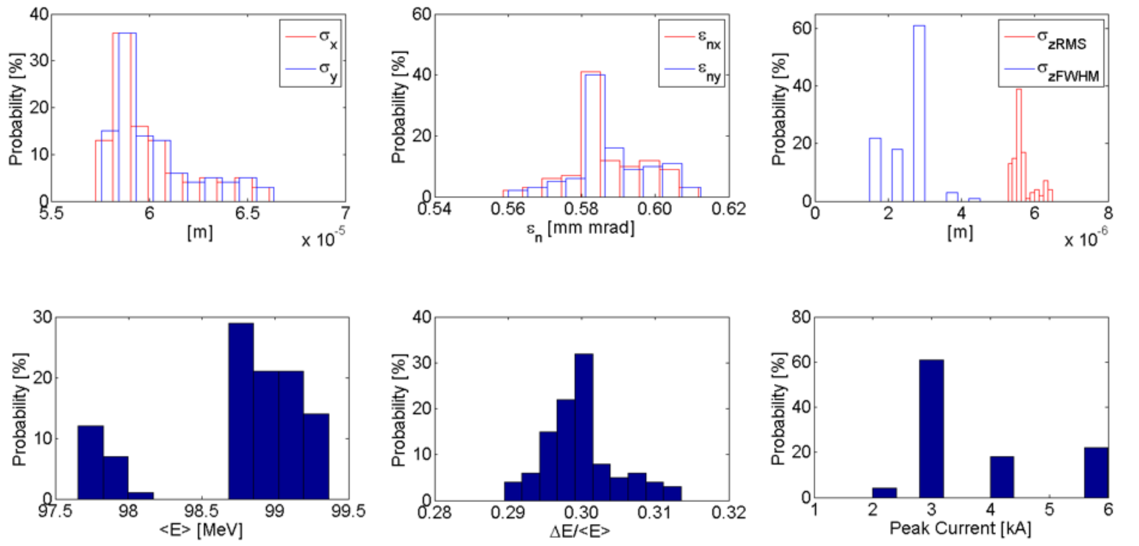

Figure 6.8: Beam parameters occurrence over 80 machine runs at the photo-injector exit in case of in case of $\Delta V_{S,G}$ = ±0.2%, $\Delta\Phi_{S,G}$ = ±0.1 deg, Q = ±5%.

At photo-injector exit	Without errors	With errors	
Energy	98.8	98.8 ± 0.5	MeV
Energy spread	0.30	0.30 ± 0.01	%
RMS norm. emittance	0.58	0.58 ± 0.02	mm mrad
FWHM bunch length	3	3 ± 0.2	μm
Peak current	3	3 ± 0.5	μm

Table 6.4: Simulated parameters for the 30 pC electron beam at the photo-injector exit without considering any jitter on the machine and in case of jitters as described in Table 6.3.

bunch is fully compressed in the photo-injector by means of the velocity bunching operation scheme. An accelerating gradient of E_{acc} ≈20–36 MV/m is applied in L1 and L2 linac section respectively (see Table 5.3), and the final electron beam energy is $E_{L2exit} \approx$ 550 MeV, with an energy spread less than 0.1%, see fig.6.9.

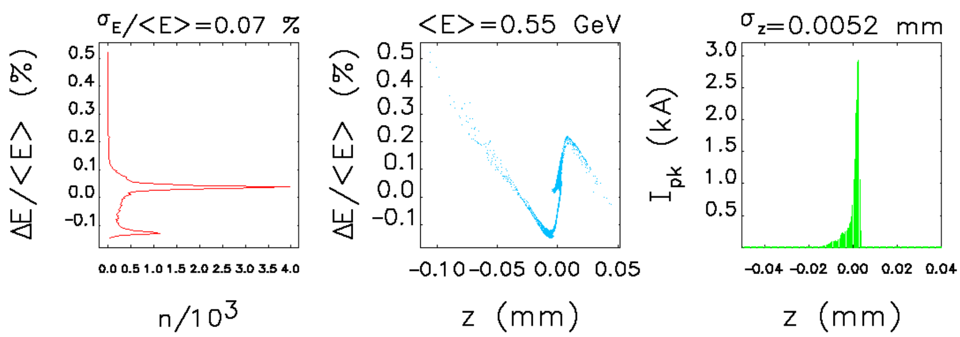

Figure 6.9: Longitudinal phase space of the LWFA accelerated electron beam at the L2 linac exit.

Before entering the plasma capillary a focusing triplet of permanent magnet quadrupoles (PMQ) is foreseen at a distance of few centimeters from the plasma entrance to obtain typical β-function $\beta_{x,y} \approx 1-5$ mm. The gradient of the first three PMQs is around $G \approx$300 T/m with a magnetic length of 5 – 10 cm, the emittance dilution due to chromatic effects in the quadrupoles is the main concern of the final focusing stage, see Fig. 6.10. A longitudinal position adjustment setup to tune the strength of the final focus array and latest generation of tunable permanent quadrupoles are under study to increase as much as possible the tunability of the magnet arrange and widen the energy acceptance of the transfer line.

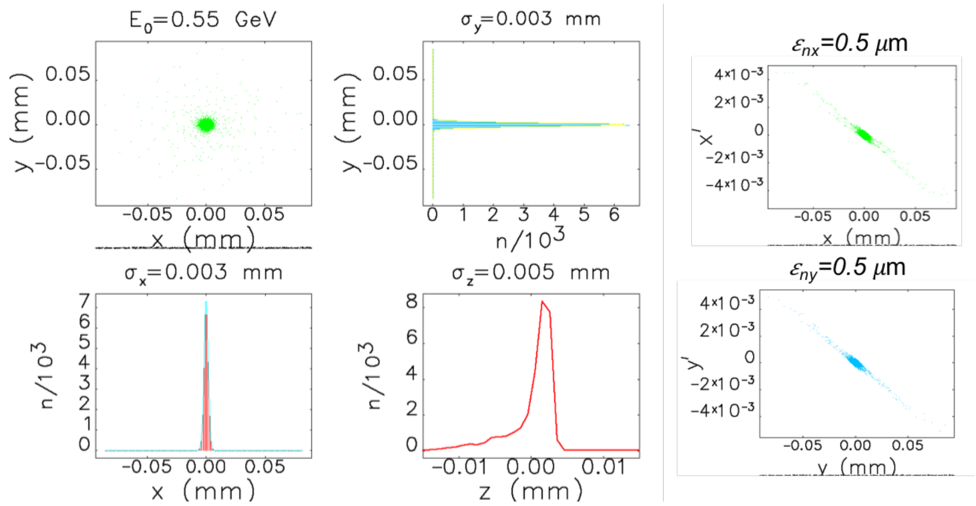

Figure 6.10: Left: Transverse and longitudinal distribution of the LWFA accelerated electron beam at the capillary entrance. Right: Transverse phase space of the beam at the capillary entrance.

6.3 Plasma

6.3.1 Simulation tool and settings

We performed simulations for the LWFA module by using the code QFluid [1]. QFluid is a hybrid code that models the plasma component as a fluid and uses a fully kinetic representation of the injected beam. Cylindrical symmetry is assumed for the plasma, whose effects are evaluated by solving for the pseudopotential ψ [2] a single partial differential equation. The beam is evolved with a fully 3D particle in cell technique. As for the laser pulse driver, it is evolved fully consistently employing the envelope equation in the paraxial approximation. The pulse is assumed to be Gaussian on the transverse plane and has a cosine squared profile of length τ (FWHM) on the longitudinal axis, for numerical reasons.

We simulated propagation and transport of the input bunch in a 6 cm long flat top plasma profile both with and without input and output ramps. For ramped settings, ramps are assumed to have exponential profiles with a varying characteristic length l_r, namely l_r = 0.5 λ_β, λ_β, $2\lambda_\beta$, where $\lambda_\beta \approx 5$ mm is the beam betatron wavelength in the flat top region. A plot of the different profiles is shown in Figure 6.11.

In all settings we used a simulation box of dimension $2\lambda_p \times 4\sigma_l$ and spatial sampling of $\lambda_p/200$ both in the longitudinal and transverse directions, while the time step is $dt = 1.5$ fs . The witness bunch is sampled with 2×10^5 macro-particles.

6.3.2 Data analysis

Since some particles move outside the accelerating and focusing region of the plasma bucket during transport, plots of the mean beam parameters may not represent the beam core evolution. In fact, even if particles are removed from simulations upon crossing simulation box boundaries, they still contribute to beam parameters as long as they remain within the box; some particles, mainly coming from unmatched, lower energy beam tail, never leave the box and contribute to a halo formation. For this reason, we perform a charge cut on the beam, before computing bunch global parameters, as follows.

Along the transverse dimensions, the Median Absolute Deviation (MAD) is calculated both for positions and momenta. A binning is then produced using a bin length around MAD/50 and the resulting distribution is fitted by a Gaussian model function. The resulting Gaussian RMS size, σ_G (one for each x, y, p_x and p_y), is finally used as basic unit for performing cuts: a particle is cut if it resides outside the hyper-ellipsoid whose semi-axes measure $n(\sigma_G^{(x)} \times \sigma_G^{(y)} \times \sigma_G^{(p_x)} \times \sigma_G^{(p_y)})$, with n an arbitrary 'cut' number; beam parameters are then calculated with remaining (surviving) particles.

The value of n has been chosen upon the following considerations: beam parameters σ_i, σ_{p_i}, σ_{i,p_i} and ε_i usually grow fast and almost linearly (together with surviving particle number) for $1 < n < 4$ and reach a quasi-saturated value for $n = 5$. For $5 < n <\sim 40$, they grow at a much slower pace, while surviving particle number remains almost stable; after $n \sim 40-50$ parameters start back to grow steadily up to the 100% charge value. For these reasons n is set equal to 5. Figure 6.12 shows how beam spot sizes and emittances vary with n.

Figure 6.13 reports the comparison between uncut beam transverse dimensions and a $5\sigma_G$ result, together with the amount of cut charge, which always remains at a more than acceptable level below 2%. Figure 6.14 shows the same comparison for emittances.

For longitudinal properties we proceed differently by only making use of robust statistics: bunch length and energy spread are both calculated as the MAD of the particle distribution, while relative energy spread is retrieved as MAD to median (med(.)) ratio. In order to retrieve an RMS equivalent value this ratio is multiplied by 1.4826 which is the σ/MAD ratio for a Gaussian.

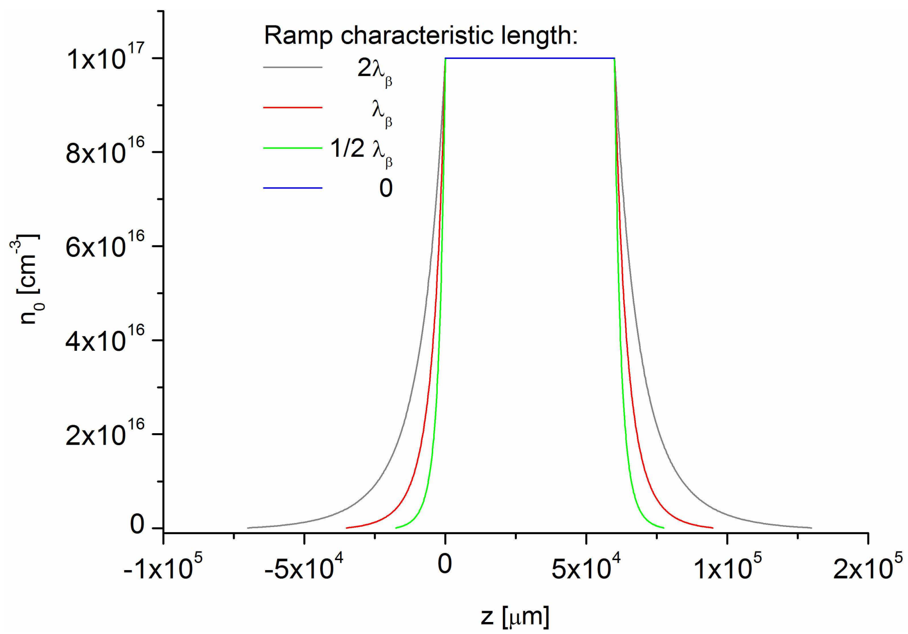

Figure 6.11: Plasma profiles.

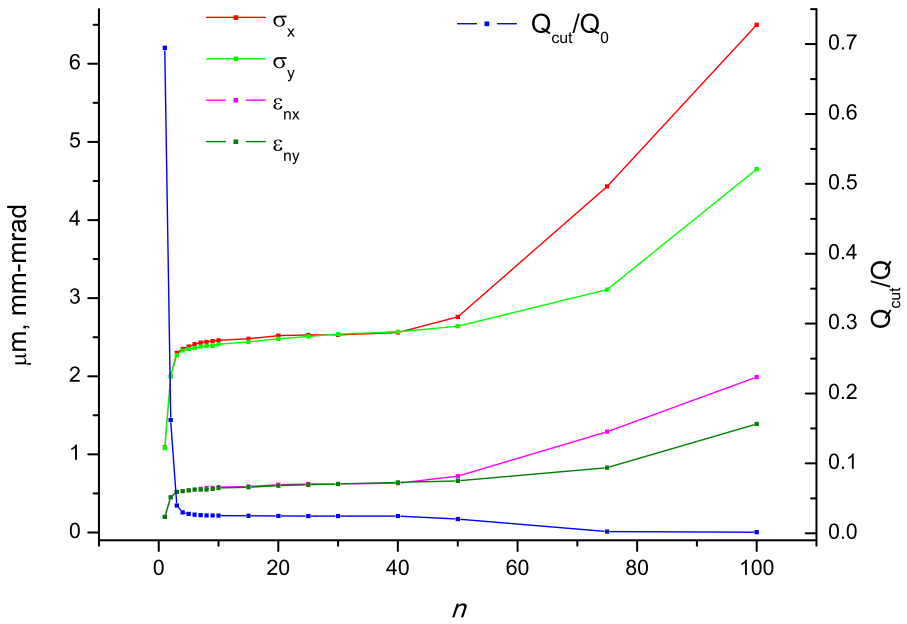

Figure 6.12: Beam transverse sizes (red, green), beam emittances (magenta, dark green) and charge cut (blue) as a function of n.

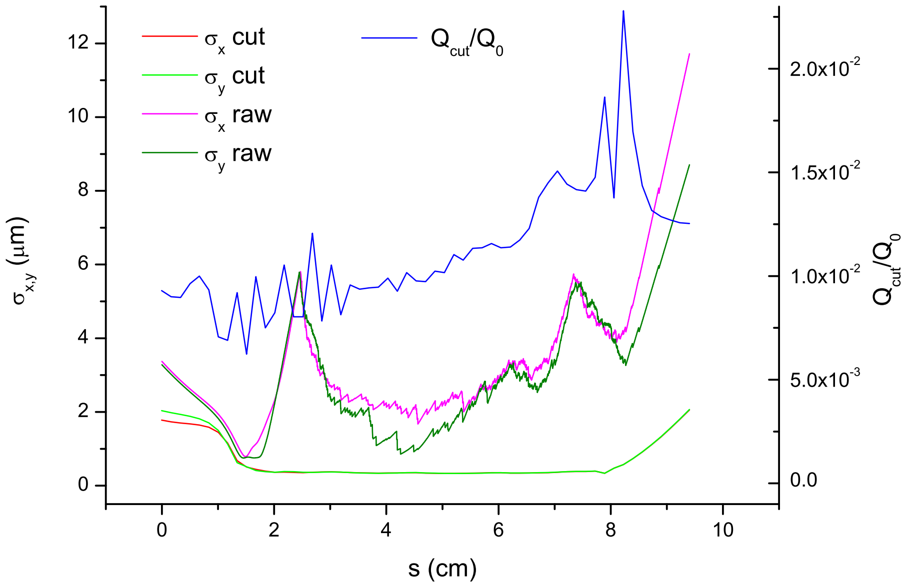

Figure 6.13: Cut (red, green) transverse beam sizes and raw transverse sizes (magenta, dark green). The blue line reports the amount of charge cut.

Fig. 6.15 compares standard σ_E/E versus $\mathrm{MAD}(E)/\mathrm{med}(E)$.

In order to get slice bunch properties, which are much more relevant for FELs than global properties, we employ a rolling window of length l_w that is moved along the beam longitudinal coordinate by steps dz_w. Calculated parameters are then assigned to the window midpoint position. The window length is usually set to a value between 0.5 μm and 1.0 μm while the number of sampling positions must be chosen such that two contiguous positions have their window spans partially overlapped. It is worth stressing that slice analysis is performed on uncut bunches.

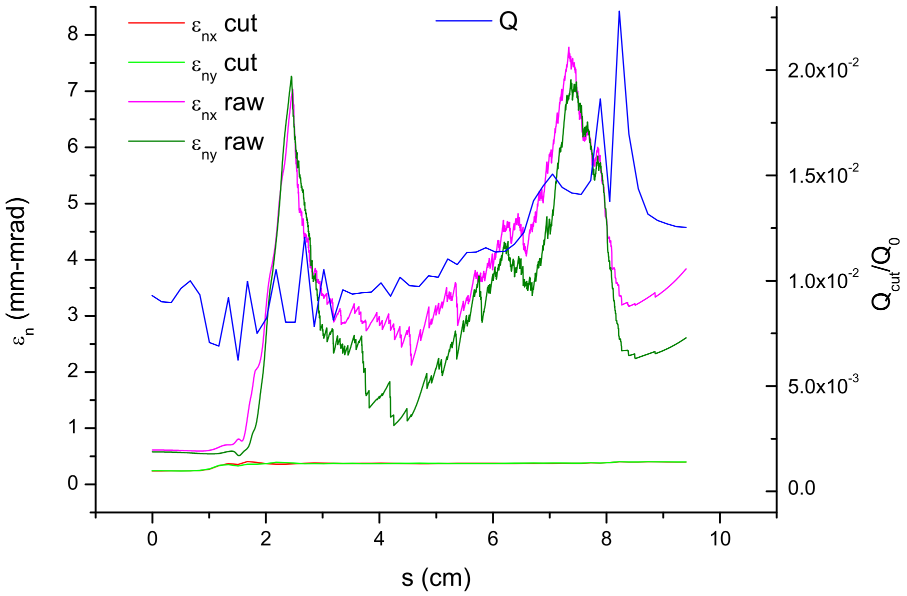

Figure 6.14: Cut (red, green) beam emittance and raw emittance (magenta, dark green). The blue line reports the amount of charge cut.

6.3.3 Simulation results: ideal plasma target

Optimization of the ideal setting requires to find both the correct matching size σ_m and injection phase $\phi_0 = k_p z_0$ with z_0 the distance between laser and beam barycenters. The laser driver is focused down to nominal matched size at the beginning of the plasma plateau at density n_0. Since the input beam is asymmetric in x and y directions, we start by symmetrizing its Twiss parameters (ideal case) keeping constant the two different emittances. Evaluating the matching condition for the equivalent fully symmetric beam (i.e. using an emittance given by the square mean root of the two values) returns a matched size of 0.5 μm; since this value is derived for the non-linear regime with negligible beam loading, we use it as a first estimation for the correct value. Starting from there, we change both β_m (matched Twiss beta function) and ϕ_0 to find the best performing configuration which result to be $\beta_T = 605$ μm and $\Delta t = \phi_0 / c k_p = 162.75$ fs. Complete (i.e. with no cuts) phase and configuration spaces for the best performing setup are reported in Figure 6.16. It is worth noting that best performances are selected based on slice properties, depicted in Figure 6.17.

The final beam energy demonstrates an average accelerating field in excess of 9 GV/m, perfectly in line with what expected.

6.3.4 Simulation results: plasma target with ramps

Simulations for the ramped setting have a different flow with respect to the ideal case. As before, the driving laser pulse is focused at matched size at the beginning of the plasma plateau, so that in the ramp it is still focusing. This means its starting spot size is larger than nominal value and the resulting driven plasma wave is mainly linear. Since QFluid can not operate at zero background density, we chose to start with an initial density of $n_i = 10^{14}$ cm^{-3}. Given the exponential ramp characteristic length l_r, the starting density value is found at a distance of $7 l_r$, requiring to extend the total simulation length. Moreover, in such low density plasmas, beam loading is usually dominating, so that no sound estimate for the matched beam spot size exists. Still, it has already been reported that ramps can help in funneling beams into plasma channels both with [1] and without [3] beam loading effects; they also help in reducing misalignment effects.

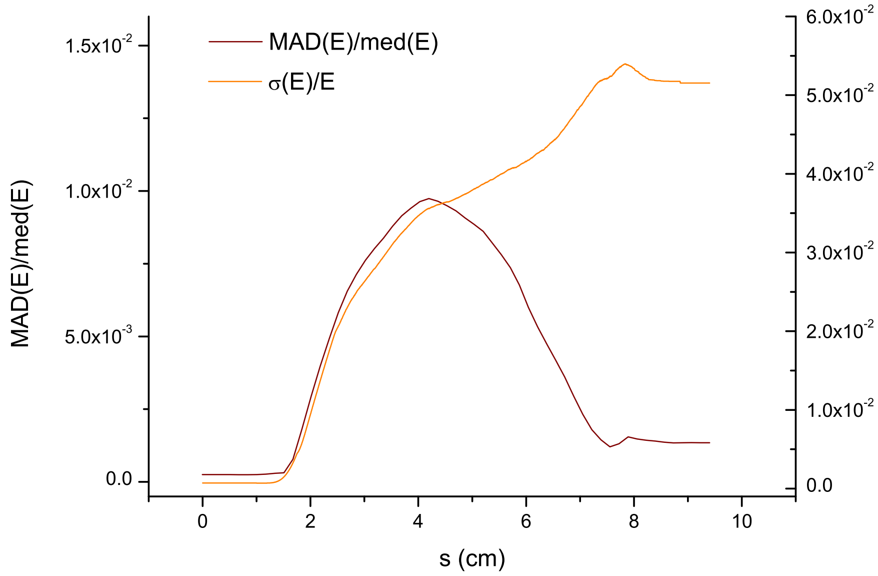

Figure 6.15: RMS relative energy spread (orange) and robust energy spread (dark red). See text for details.

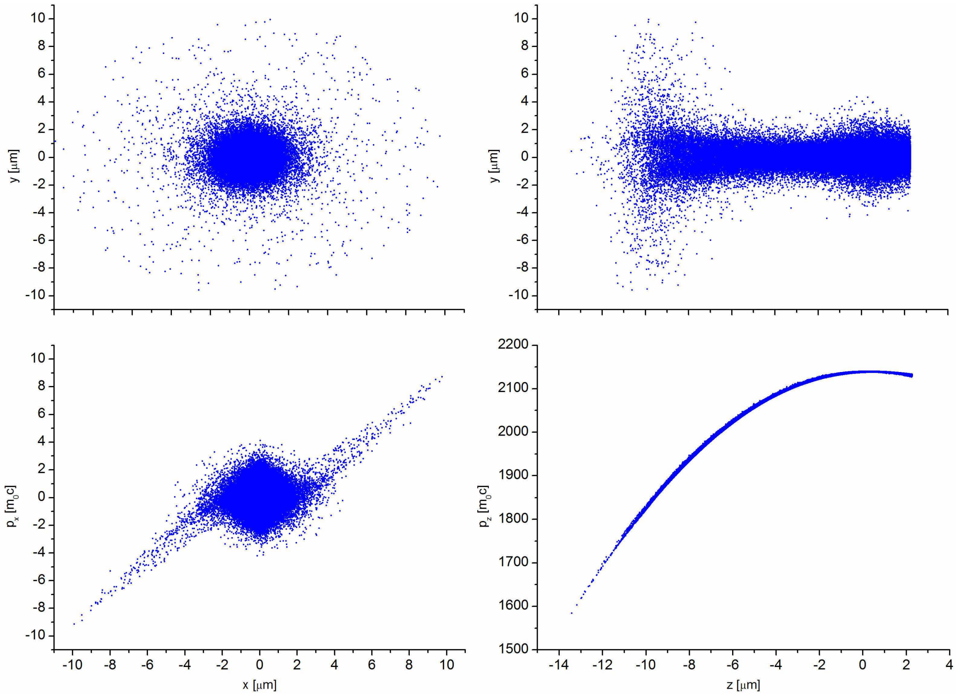

Figure 6.16: In clockwise direction starting from top left: transverse footprint, longitudinal footprint, longitudinal phase space and transverse phase space for the best case.

In the situation at hand, there are not sound estimates for matched beam size at the ramp beginning. In [1] and [3] it has been also shown that an initially converging beam can over perform a bunch in a waist. In order to estimate initial beam parameters β_T and α_T, we back-trace the beam from the matched condition at the beginning of the plasma plateau up to the ramp beginning, assuming a ballistic evolution subject to bubble regime equivalent plasma fields. We then vary those first estimates optimizing slice properties. In this way, we are able to produce a performing

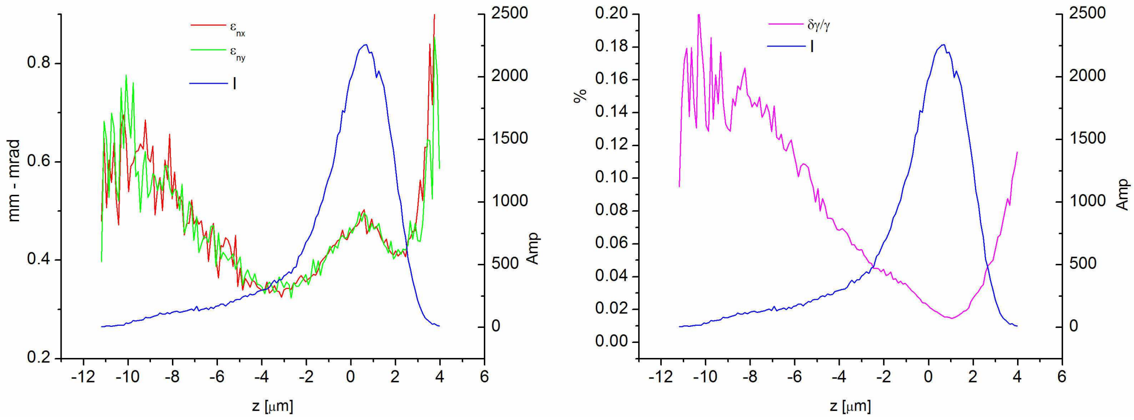

Figure 6.17: Slice analysis for the ideal beam setting. Slice emittance (left) and slice energy spread (right). The blue line represents the slice current in both plots.

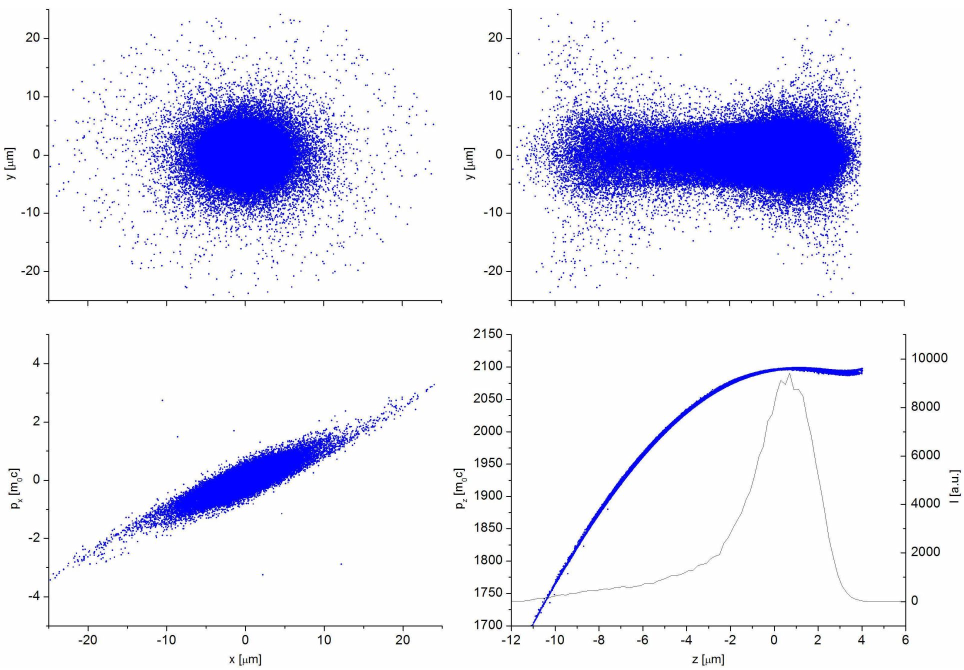

Figure 6.18: In clockwise direction starting from top left: transverse footprint, longitudinal footprint, longitudinal phase space and transverse phase space for the best performing case.

transport with the injection conditions $\beta_T = 2.1$ cm , $\alpha_T = 1$ and an injection delay $\Delta t = 142.25$ fs. The resulting slice beam parameters do not show significant differences with respect to the ideal setting, at least in the current peak area. We notice that, in presence of a ramp, the witness must be injected closer to the driver with respect to the ideal setting: this is due to the fact that in the ramp, due to low plasma density and larger driver spot size, the laser group velocity is larger than in the plateau.

The best performing beam, for the $l_r = 0.5\,\lambda_\beta$ setup, is displayed in Figure 6.18, while its slice analysis is depicted in Figure 6.19. It is worth noting how the presence of the ramp helped in defocussing the beam in an adiabatic way: in fact, its final spot size results to be much larger than the ideal scenario, while the emittance values remains almost unchanged.

Simulations for $l_r = \lambda_\beta$ long ramps succeeded to preserve beam quality at expense of a charge loss close to 10%, while it was not possible to optimize injection phase (i.e. final energy spread)

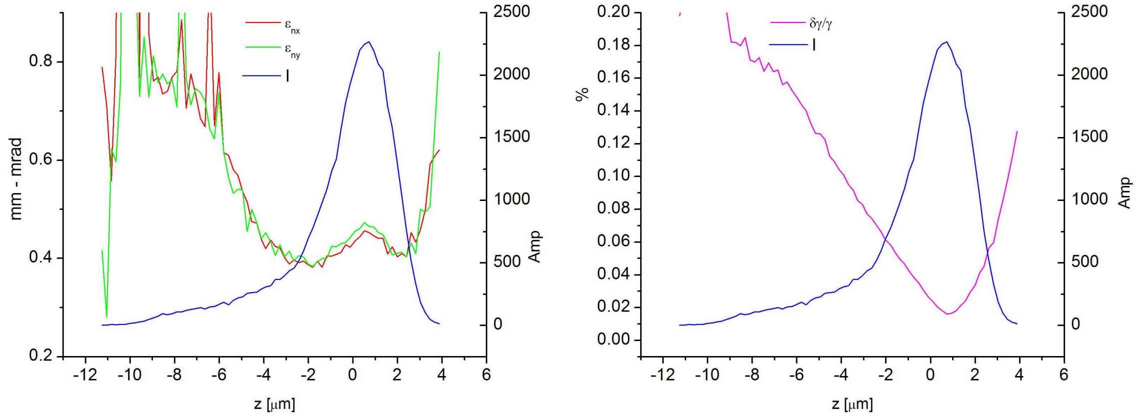

Figure 6.19: Slice analysis for the $l_r = 0.5\,\lambda_\beta$ long ramp beam setting. Slice emittance (left) and slice energy spread (right). The blue line represents the slice current in both plots.

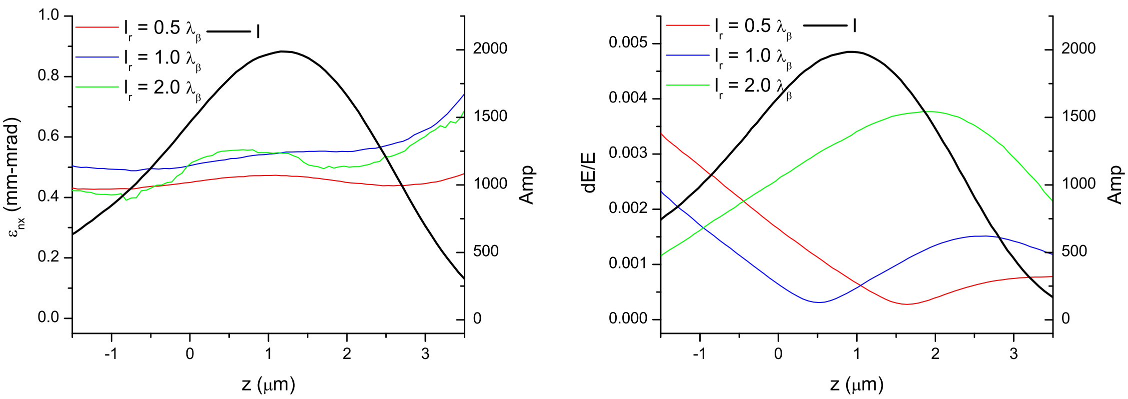

Figure 6.20: Slice performances comparison between ideal and $l_r = 0.5\lambda_\beta$ long ramp.

without a charge loss larger than 50%. Figure 6.20, shows a comparison of the slice analysis, in the current peak region, for ideal and ramped settings. No significant variations between the two $l_r = 0.5\,\lambda_\beta$ and $l_r = \lambda_\beta$ are present, while the $l_r = 2\,\lambda_\beta$, with a charge loss of 10%, is not optimized in energy spread. Since ramps characteristic length is typically close to capillary diameter, we do not expect l_r to exceed the $0.5\,\lambda_\beta \approx 2.5$ mm value.

6.3.5 Simulation results: S2E stability in plasma

The S2E simulations for LWFA up to plasma entrance targeted a beam with the required Twiss function values ($\beta_T = 2.1$ cm, $\alpha_T = 1$) for optimal injection. The results of plasma acceleration for that injection conditions are detailed in Section 4. We performed also a partial stability study around the chosen working point to assess its robustness, within the limit of QFluid capabilities: employing a cylindrical representation of the plasma component, jitters in pointing cannot be reliably simulated. For those, we stick to the positive results reported in [3].

Our stability analysis is restricted to small variations of α_T, β_T and ϕ_0 around the reference working points. As figure of merit we employ the beam slice emittance and energy spread around the current peak. A sample of results are reported in Figure 6.21. We notice, as expected, how a jitter in Twiss functions affects more emittance than energy spread, case d), while the converse is true for injection phase jitters, case c). Some setups may yield improved emittance at expenses of energy spread, case e) which is more critical for FEL performances.

Overall, considering all the setups simulated, the average slice emittance on peak current results

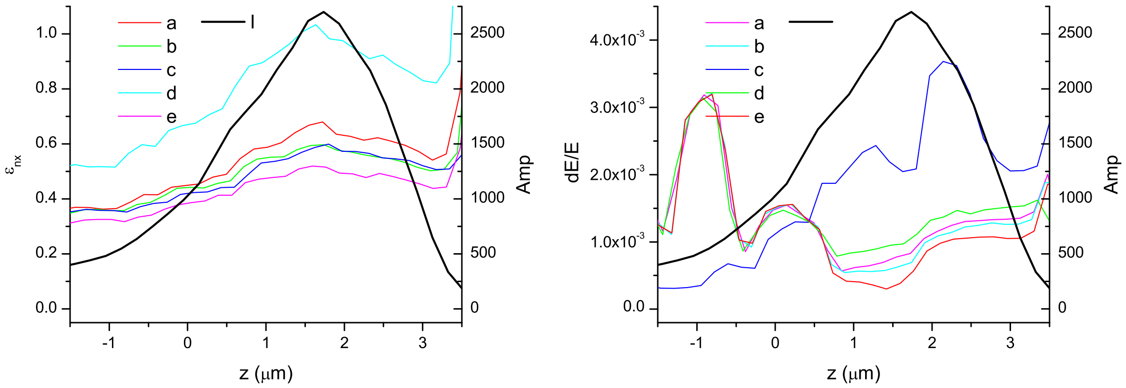

Figure 6.21: Slice performances stability. a) reference: $\alpha_T = 1.0$, $\beta_T = 2.1$ cm , $\Delta t = 145.25$ fs ; b) $\alpha_T = 1.0$, $\beta_T = 1.6$ cm , $\Delta t = 145.25$ fs ; c) $\alpha_T = 1.0$, $\beta_T = 1.8$ cm , $\Delta t = 136.50$ fs ; d) $\alpha_T = 0.5$, $\beta_T = 2.0$ cm , $\Delta t = 145.25$ fs ; e) $\alpha_T = 1.5$, $\beta_T = 2.2$ cm , $\Delta t = 145.25$ fs .

to be $\varepsilon_n = (0.62 \pm 0.11)$ mm mrad (with a sample minimum of 0.45 mm mrad and maximum of 0.87 mm mrad) while the average slice energy spread, in the same position, is $dE/E = 0.149 \pm 0.088$ (with a sample minimum of 0.063 and maximum of 0.359).

6.4 Transport

The beamline portion dedicated to match the beam at the entrance of the first undulator is called Transfer Line (TL) and the magnetic elements used in this portion are quadrupoles. At the entrance of the first undulator module it is needed to obtain values of the Twiss functions as close as possible to the ones that grant the periodicity of these functions in the modules.

The starting point of the TL will coincide with the output of the plasma channel. Here the bunch suddenly passes from a region characterized by an extremely strong field to a drift space. The beam inherits from plasma acceleration stage a relatively large energy spread and transverse momenta. Under these special conditions, at least second order effects should be kept in transfer matrices [4]. This makes analytical approaches more complex, with solutions that need to be carefully cross checked by particle simulations. We have then chosen a different approach which is based directly on the particle tracking, able to give a complete phenomenon description.

6.4.1 Transfer line design methodology

The code used for the TL parameters search is GIOTTO [5], an up-to-date Genetic Algorithm (GA) able to perform statistical analysis [5] and genetic optimizations of a beamline [6, 7]. This is possible because the software is able to drive and to communicate with a tracking code, ASTRA [8], through its input and output files.

Our approach to the design of the TL was to start from scratch, i.e. defining a chosen set of switched off quadrupoles with arbitrary positions, and change the strengths and the positions gradually, evaluating a Twiss parameters dependent fitness function for each solution. The final parameters that we needed to control in our optimization are the four values of the transverse Twiss functions $\alpha_x^{(T)}$, $\alpha_y^{(T)}$, $\beta_x^{(T)}$ and $\beta_y^{(T)}$ that must be equal to the values granting matching conditions in the undulator. In the meanwhile, values of transverse normalized beam emittances should remain constant as much as possible.

6.4.2 Procedure and results

The plasma accelerated beam employed to optimize the TL is the one described in Section 6.3.4. In order to avoid a misleading growth of the RMS beam transverse dimensions when transporting the full beam through the line we selected the beam region around the current peak (i.e. the part that would most likely produce radiation in the undulator), as shown in Figure 6.22. That slice(s) parameters are then used to assess matching inside undulator.

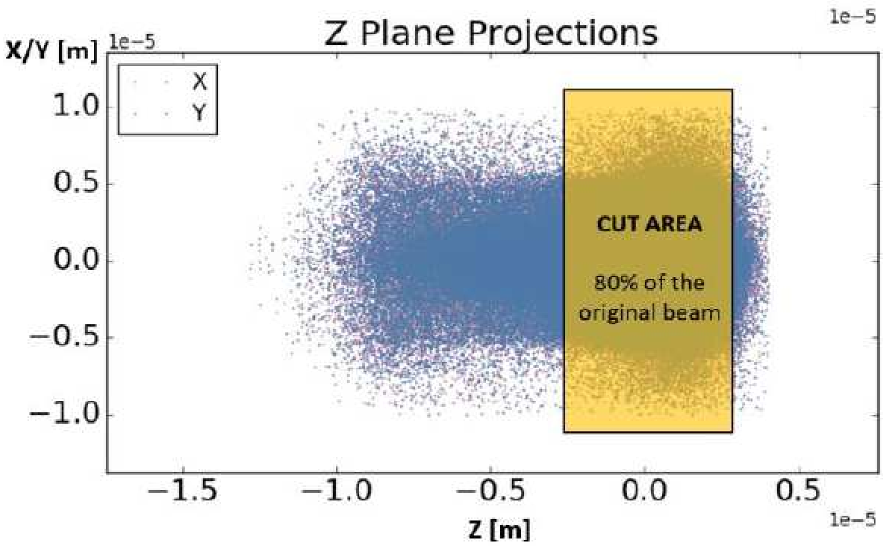

Figure 6.22: The beam that has been selected for matching, corresponding to peak current and lowest emittance; in this figure a large beam halo situated at the height of the tail is not shown to show better the selected (cut) area.

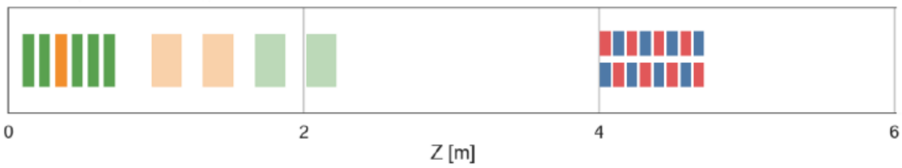

Figure 6.23: Schematic lattice of the matching transfer line. Orange and green elements are quadrupoles, with focusing and defocussing effect on the horizontal plane. Transparent colored elements are EMQ, colorful coloring means PMQ. In red and blue is shown (not in scale) the position of the first undulator module.

Following the design principles stated in Section 6.4.1, we investigated four different configurations in terms of line length and kind of focusing elements. Details has been reported in [9]. Among those configurations, we selected a 4 m long transfer line made out of six permanent magnet quadrupoles (PMQ) and four electromagnetic quadrupoles (EMQ) as depicted in Figure 6.23.

In Figure 6.24 we report beam transverse dimensions and emittances along transport in the transfer line after they have been analyzed as described in Section 6.3.2 and a 5 σ_G cut has been applied. Beam length does not change significantly along transport and final beam configuration allows for matching inside undulator.

Finally, we assessed TL flexibility with respect to incoming beam energy. To this end, we assumed to use tunable PMQ that are under development [10] and repeated the optimization for the same beam but changing its average energy to 500 MeV and 2 GeV. Gradients were moved inside a range compatible with the state of the art of PMQ/EMQ capabilities. The TL demonstrated to deal

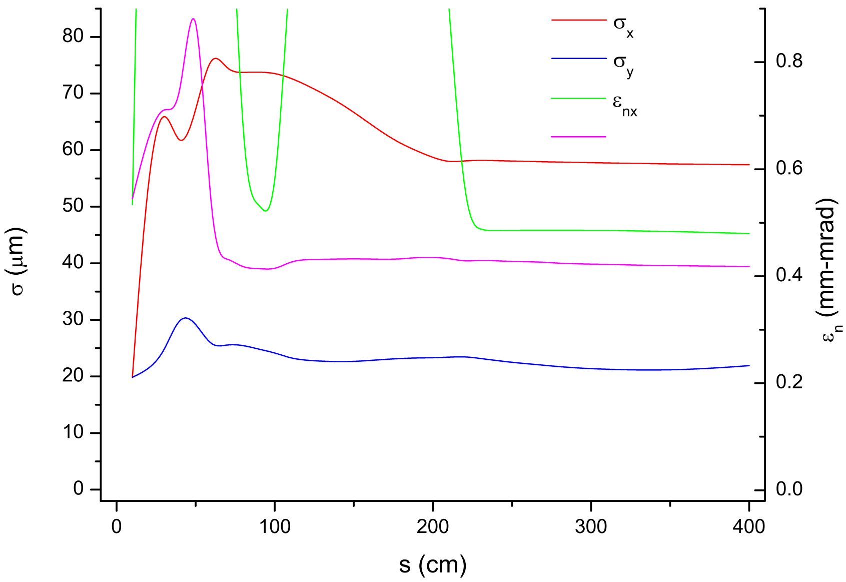

Figure 6.24: Bunch parameters along transport in the transfer line.

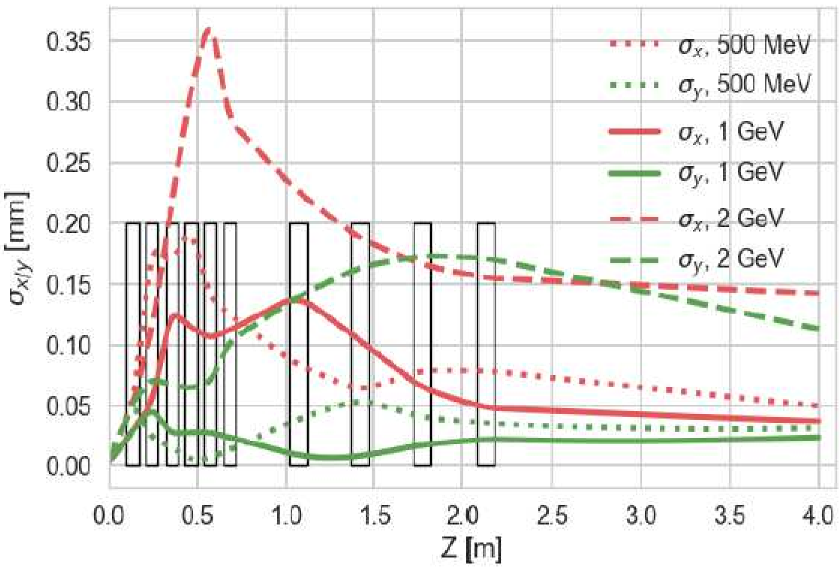

Figure 6.25: Comparison between beam envelopes for matched bunches of different energies.

very well with this strong changes in the beam parameters. In fact, design quadrupoles positions showed to be able to keep envelopes under control preventing beam losses. A visual comparison on the envelopes in the line all three investigate energies is reported in Figure 6.25.

6.5 Transport of the LWFA beam inside the undulator

The electron beams used in these calculations have been described in Section 6.3. The first case (beam A) has been obtained by assuming a plasma layer with sharp edges. Its total and slice characteristics are summarized in Table 6.5, third column and shown in Fig. 6.26, that gives in window (a) the current I(A) and the energy in MeV and in window (b) the energy spread in % and the emittance (in mm mrad) of the electron beam considered.

General critical issues for the optimization of the radiation output from plasma accelerated

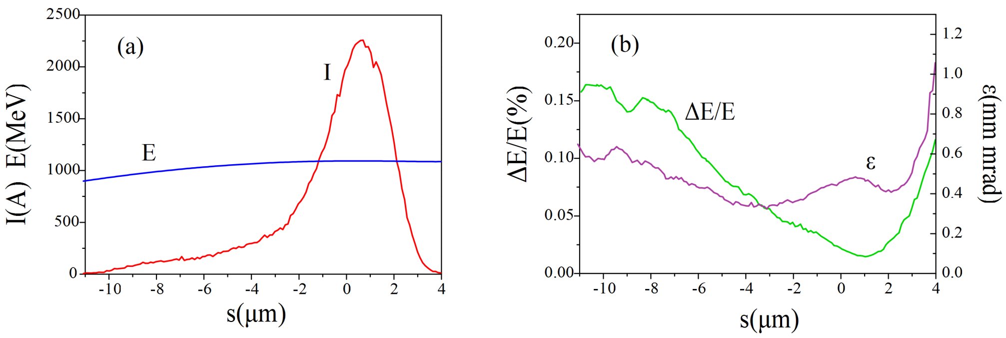

Figure 6.26: Cases (a1, a2): Window (a): Current (red line), energy (blue line) vs the electron beam coordinate s; window (b): energy spread (green line), emittance (violet line) vs s.

beams are the following: since the charge is quite low (in this case 30 pC), the beam should be strongly compressed for reaching a high values of peak current ($>$ 2 kA), preserving, at the same time, at least for the best slice, low emittance ($<$ 0.5 mm mrad) and low energy spread ($<$0.05%). In addition, the energy should be kept fairly constant in correspondence of the current peak, i.e. the correlated energy spread should not be larger than the uncorrelated one, otherwise the radiation does not start. The beam extraction from the plasma should maintain these conditions. Since the beam exits the plasma with a small transverse size of few microns, it has to be defocused to tens microns in the room between the end of the capillary and the beginning of the undulator. During the defocussing stage, the properties of the electron beam should not deteriorate. Electron, undulator and radiation characteristics are summarized in Table 6.5, third column. The best slice presents at the exit of the plasma transverse dimensions $\sigma_x = 0.49$ μm and $\sigma_y = 0.52$ μm , with emittance respectively of 0.45 mm mrad and 0.48 mm mrad. Using $a_w = 0.8$, the resonant wavelength turns out to be $\lambda = 2.7$ nm. The matching to the undulator has been done for the best slice (I = 2.3 kA) setting the quadrupoles at 23.5 T/m and led to values of the RMS x-y dimensions at the entrance of the undulator of about 33 μm and 22 μm. The transport of the beam core along the undulator is presented in Fig. 6.27.

6.6 FEL performances

The 1D FEL parameter calculated for the best slice [11, 12] is $\rho = 2 \times 10^{-3}$, while the 3D one is $\rho_{3D} = 1.75 \times 10^{-3}$, leading to a gain length of about 0.4 m. The cooperation length is about 0.5 μm and $2\pi L_c = 3.1$ μm . This corresponds to a situation of single spike operation ($L_b < 2\pi L_c$) [13]. This beam has been simulated with a flat magnetic field (A1) and with a tapered undulator field (case (A2)).

The growth of the power vs z(m) is shown in Fig. 6.28, window (a). In case (A1), with constant magnetic field, saturation is reached in about 12 m with emission of 12 μJ, then superradiance follows thus doubling the energy at 25–30 m. The contour curve of the power in the plane (s,z) is shown in Fig. 6.28, window (b). A slight tapering of -2%/m (case (A2)), optimized in slope and starting at 9 m, permits to increase the energy up to 63 μJ at 23 m. In these two cases, at 30 m, we have respectively a number of photons $n_{ph} = 3.4 \times 10^{11}$ (uniform magnetic field, case (A1)), and $n_{ph} = 8.5 \times 10^{11}$ (optimized tapering: case (A2)). Power density and spectrum are shown in windows (c) and (d). Case A1 without tapering is almost in single spike regime [14, 15], while in the tapered mode, power density and spectrum present few oscillations. Case (B) represents an electron beam accelerated in a more realistic plasma with a central plateau and ramps in the trailing and in the leading edges. The electron beam emits better than the previous one, because the

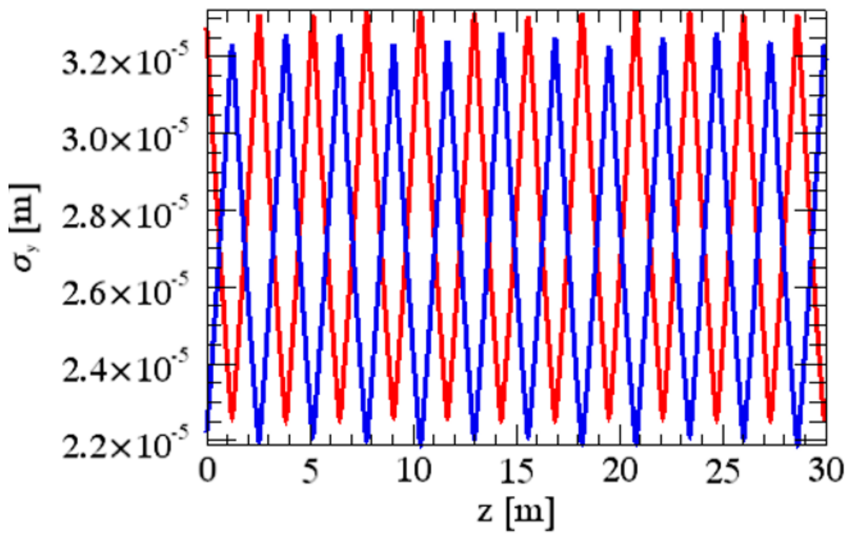

Figure 6.27: Transverse RMS dimensions σ_x (in red) and σ_y (in blue) of the electron beam along the undulator.

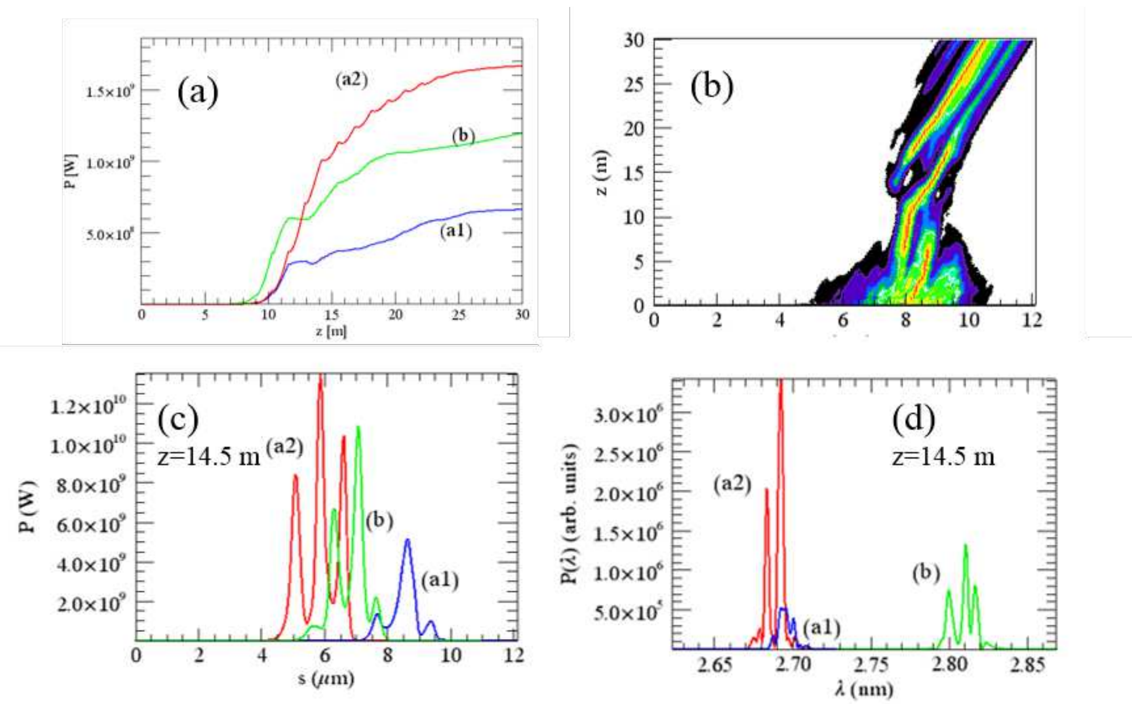

Figure 6.28: Laser plasma acceleration. (a): P(W) vs z(m). (b) contour curve of the power in the plane (s, z). Power density (c) and spectrum (d) of the radiation at 14.5 m. (a1, blue curve) flat undulator magnetic field, (a2,red curve) tapered undulator, (b, green curve) with ramp.

presence of the ramps gives further degrees of freedom for the beam shaping. Also in this case, a first saturation at 11 m gives 24 μJ, followed by a further growth to 43 μJ. Temporal and spectral density at 14 m are shown in green. The total number of photons arrives at 6×10^{11} per shot. The degradation of the beam parameters (case A1) is studied by worsening current, energy spread and

Laser driven	Units	No ramp (A1)	Ramp (B)	Tapering (A2)
RMS Energy Spread	%	0.022	0.025	0.022
Peak current	kA	2.26	2.26	2.26
Bunch charge	pC	30	30	30
Bunch length RMS	μm (fs)	2.14(7.1)	2.14(7.1)	2.14(7.1)
RMS norm. emittance	mm mrad	0.47	0.47	0.47
Slice Length	μm	1.34	0.5	1.34
Slice Charge	pC	18.7	18.7	18.7
Slice Energy Spread	%	0.015	0.015	0.015
Slice norm. emittance x,y	mm mrad	0.45-0.48	0.45-0.465	0.45-0.48
Undulator period	cm	1.5	1.5	1.5
K (a_w)		1.13(0.8)	1.13(0.8)	1.13(0.8)
$\rho(1D/3D)$	$\times 10^{-3}$	2-1.66	2-1.68	2-1.66
Radiation wavelength	nm (keV)	2.68 (0.46)	2.8 (0.45)	2.7 (0.46)
Saturation length	m	12-25	11-20	22
Energy at 15 and at 30 m	μJ	12-25	21-40	63 (at 30 m)
Photons/pulse at 15 and 30 m	$\times 10^{10}$	16-34	24-43	85(at 30 m)
Bandwidth (15 and 30 m)	%	0.15-0.23	0.25-0.4	0.3 (at 30 m)
Divergence(15 and 30 m)	μrad	50-51	49-49	53 (at 30 m)
Rad. size (15 and 30 m)	μm	123-144	125-145	155(at 30 m)
Brilliance per shot (15 and 30 m)	(sx mm^{2}mrad^{2}bw(0.1%))$^{-1}$	$1-2.1 \times 10^{27}$	2.06-1.7 $\times 10^{27}$	2.4 $\times 10^{27}$(at 30 m)

Table 6.5: Electron, undulator and radiation characteristics for laser plasma external injection beams.

emittance by 5% and 10%. The radiation emission diminishes by about respectively 18% and 40%. The results are summarized in Table 6.6, where results at the two position $z1 = 15$ m and $z2 = 30$ m are presented. In conclusion, electron beams at 30 pC, accelerated by laser plasma external injection, produces up to 8×10^{11} photons per shot with large temporal coherence and high monochromaticity (bandwidth <0.2%).

	(A)	(A)-5%	(A)-10%
Q(pC)	30	28.5	27
ε_x(mm mrad)	0.45	0.48	0.5
ε_y(mm mrad)	0.49	0.51	0.54
$\Delta E/E(\times 10^{-4})$	1.54	1.63	1.7
I_{peak}(A)	2258	2145	2032
z1 (m)	15	15	15
E(z1)(μJ)	16.1	11.5	9.4
$N_{phot}(z1)(\times 10^{11})$	2.18	1.55	1.3
z2(m)	30	30	30
E(z2)(μJ))	26	22	15.7
$N_{phot}(z2)(\times 10^{11})$	3.5	2.95	2.1
Bandwidth(%)	0.15	0.17	0.2
Divergence(μrad)	50	48	46
Rad. Size(μm)	155	180	190

Table 6.6: Tolerance study: comparison between the nominal case a1 and beams worsened by 5% and 10% in current, energy spread and emittance.

Bibliography

[1] P Tomassini and A R Rossi. “Matching strategies for a plasma booster”. In: *Plasma Physics and Controlled Fusion* 58.3 (2015), p. 034001.

[2] J Krall et al. “Propagation of radius-tailored laser pulses over extended distances in a uniform plasma”. In: *Physics of plasmas* 1.5 (1994), pp. 1738–1743.

[3] Irene Dornmair, K Floettmann, and A R Maier. “Emittance conservation by tailored focusing profiles in a plasma accelerator”. In: *Physical Review Special Topics-Accelerators and Beams* 18.4 (2015), p. 041302.

[4] Karl L Brown. *FIRST-AND SECOND-ORDER MATRIX THEORY FOR THE DESIGN OF BEAM TRANSPORT SYSTEMS AND CHARGED PARTICLE SPECTROMETERS.* Tech. rep. Stanford Linear Accelerator Center, Calif., 1971.

[5] Alberto Bacci, Marcello Rossetti Conti, and Vittoria Petrillo. “GIOTTO: A Genetic Code for Demanding Beam-dynamics Optimizations”. In: (2016).

[6] A Bacci et al. “Maximizing the brightness of an electron beam by means of a genetic algorithm”. In: *Nuclear Instruments and Methods in Physics Research Section B: Beam Interactions with Materials and Atoms* 263.2 (2007), pp. 488–496.

[7] A Bacci et al. “Electron Linac design to drive bright Compton back-scattering gamma-ray sources”. In: *Journal of Applied Physics* 113.19 (2013), p. 194508.

[8] K Flöttmann. “ASTRA: A space charge tracking algorithm. user’s manual available at http://www. desy. de/mpyflo”. In: *Astra dokumentation* (2013).

[9] M Rossetti Conti et al. “Electron beam transfer line design for plasma driven Free Electron Lasers”. In: *Nuclear Instruments and Methods in Physics Research Section A: Accelerators, Spectrometers, Detectors and Associated Equipment* (2018).

[10] A Ghaith et al. "Tunable High Gradient Quadrupoles For A Laser Plasma Acceleration Based FEL". In: *arXiv preprint arXiv:1712.03857* (2017).

[11] Giuseppe Dattoli, PL Ottaviani, and Simonetta Pagnutti. "Nonlinear harmonic generation in high-gain free-electron lasers". In: *Journal of applied physics* 97.11 (2005), p. 113102.

[12] Ming Xie. "Design optimization for an X-ray free electron laser driven by SLAC linac". In: *Particle Accelerator Conference, 1995., Proceedings of the 1995*. Vol. 1. IEEE. 1995, pp. 183–185.

[13] R Bonifacio et al. "Spectrum, temporal structure, and fluctuations in a high-gain free-electron laser starting from noise". In: *Physical review letters* 73.1 (1994), p. 70.

[14] JB Rosenzweig et al. "Generation of ultra-short, high brightness electron beams for single-spike SASE FEL operation". In: *Nuclear Instruments and Methods in Physics Research Section A: Accelerators, Spectrometers, Detectors and Associated Equipment* 593.1-2 (2008), pp. 39–44.

[15] F Villa et al. "Generation and characterization of ultra-short electron beams for single spike infrared FEL radiation at SPARC_LAB". In: *Nuclear Instruments and Methods in Physics Research Section A: Accelerators, Spectrometers, Detectors and Associated Equipment* 865 (2017), pp. 43–46.

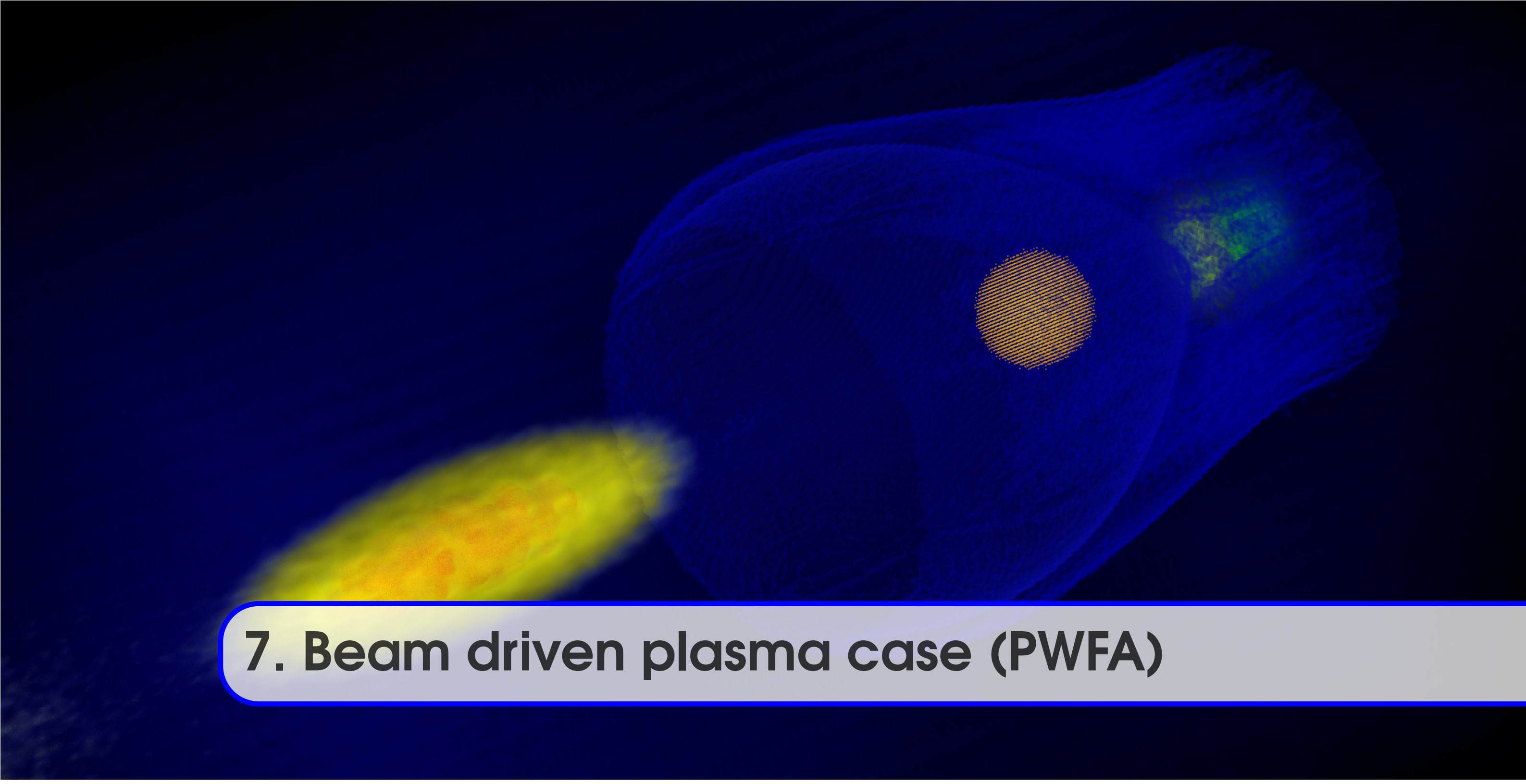

7. Beam driven plasma case (PWFA)

Like the LWFA case the 1 GeV energy can be achieved by means of a single stage of plasma acceleration, few centimeters long, coupled with the RF Linac operating at 500 MeV, to operate with plasma at approximately 10^{16} cm^{-3}, in order to produce electric fields of 1–2 GV/m, with a plasma wavelength of $\lambda_p \approx 330$ µm that allows for realistic bunch separation with the use of the laser comb technique [1, 2].

7.1 Injector

A comb-like configuration for the electron beam, consisting of a 200 pC driver followed by a 30 pC witness bunch, has been explored aiming to optimize the witness parameters and to set the longitudinal distance between the two bunches at the desired value. Such operating mode enables the possibility to pilot a PWFA stage where the passage of an ultra-relativistic bunch of charged particles (the driver) through a plasma drives a charge density wake useful to accelerate the trailing bunch.

The comb-like operation foresees the generation of two or more bunches within the same RF accelerating bucket through the so-called laser-comb technique [3, 4] consisting in a train of time-spaced laser pulses that illuminates the photo-cathode. The witness arrives earlier than the driver on the photo-cathode and then they are reversed in time at the end of the velocity bunching process, during which the longitudinal phase space is rotated. Experimental results have been obtained at SPARC_LAB where the laser-comb technique is routinely used in order to produce trains of multiple electron bunches [5] for narrow-band THz generation [6], two-color FEL experiments [7, 8] and resonant particle driven PWFA [1].

Computational studies have been dedicated to provide at the plasma two bunches, i.e. driver and witness, separated by at least 0.55 ps, which corresponds to $\lambda_p/2$, being the plasma wavelength λ_p = 330 µm for a plasma background density $n_p = 10^{16}$ cm^{-3}. Both driver and witness bunches must be compressed down to ∼50 fs and 10 fs (FWHM) respectively: the witness bunch length must be much less than the plasma wavelength in order to minimize the energy spread growth. In addition, one more request is on the minimization of the emittance growth, which unavoidably occurs because of the witness-driver overlapping during the velocity bunching regime.

The photo-cathode laser has been shaped in order to provide at the cathode a witness and a driver bunches separated by 4 ps. Gaussian longitudinal distribution with σ_z = 120 μm (RMS) and uniform transverse distribution of radius r = 0.35 mm have been assumed for the witness pulse at the cathode. Figure 7.1 depicts the transverse and longitudinal distributions of the photo-cathode laser at the cathode surface. The photo-cathode laser has been shaped, via the laser comb technique, also in intensity to provide at the cathode a 30 pC witness beam (red) separated by 4 ps from the 200 pC driver bunch (blue).

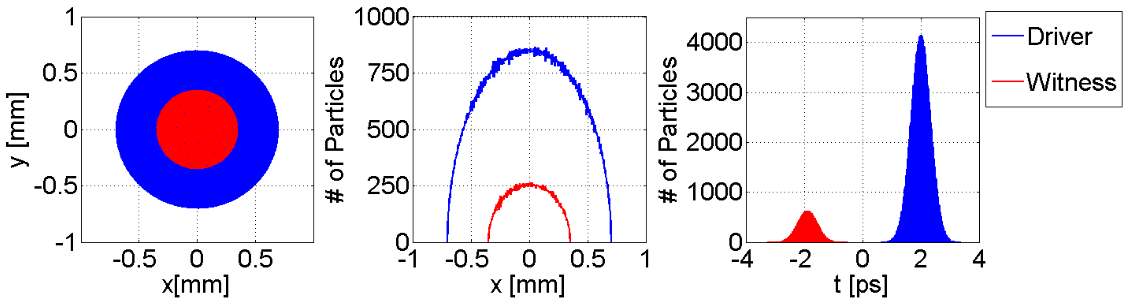

Figure 7.1: Transverse and longitudinal distributions of the photo-cathode laser at the cathode surface. The photo-cathode laser has been shaped, via the laser comb technique, also in intensity to provide at the cathode a 30 pC witness beam (red) separated by 4 ps from the 200 pC driver bunch (blue).

On the other hand, the driver spot size on the cathode has been chosen looking at the witness quality, being the witness emittance and longitudinal profile dependent on it. The behavior of the witness transverse normalized emittance as function of the driver spot size indicates σ_{rD} = 350 μm as the optimal value for the driver transverse dimension at the cathode surface, as shown in the plots in Fig. 7.2: once the accelerator set-up is chosen, it is possible to tune the phase space densities of the crossing beams to minimize the witness quality degradation.

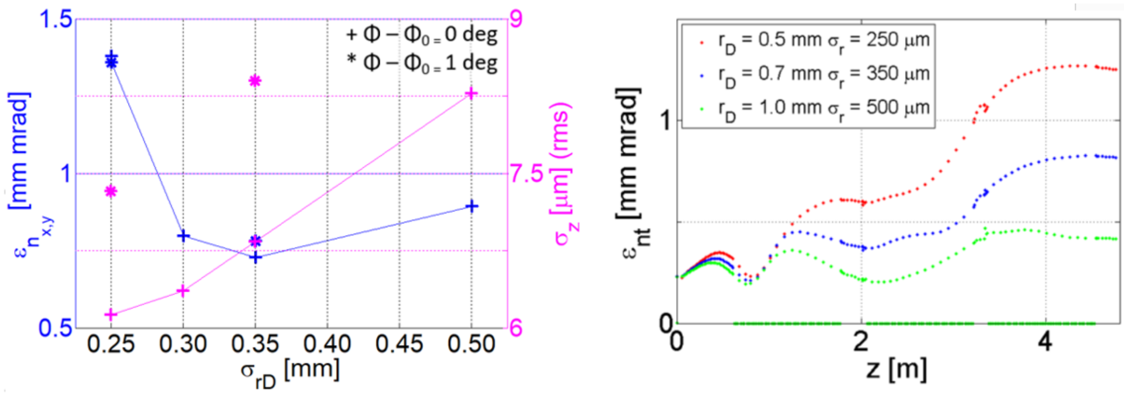

Figure 7.2: Left plot: RMS witness emittance and length as function of the driver spot size at the cathode (blue crosses are for nominal 2nd TW cavity RF phase, while magenta stars are for RF phase increased of 1 deg with respect to the nominal one). Right: transverse normalized emittance along the photo-injector for different driver spot radii.

Figure 7.2 reports the behavior of the witness emittance and length (left side) and the evolution of the transverse normalized emittance along the photo-injector (right side) as function of the driver spot size. In addition, it is worth to notice that by adopting a σ_D = 0.35 mm, the FWHM witness length does not suffer lengthening, as shown in Fig. 7.3, although the minimum RMS witness length is obtained for $\sigma_D = 0.25$ mm.

Besides of an appropriate shaping and relative spacing of the laser comb pulses at the cathode surface, a proper set of active and passive accelerator elements allows us obtaining the required comb beam at the photo-injector exit. The choice of the accelerator setup starts from the optimized witness working point illustrated in Section 6.1, with additional fine-tuning of accelerating cavity RF phases and solenoid magnetic fields.

The main operating parameters of the EuPRAXIA@SPARC_LAB photo-injector for the optimized comb beam in case of PWFA are summarized in Table 7.1.

Parameter	Unit	Value
Gun electric field amplitude	MV/m	120
Gun electric field operation phase	deg	30
Output gun beam energy	MeV	5.6
Amplitude of electric field in the three TW sections	MV/m	20.0/20.0/28.0
Magnetic field in the emittance compensating solenoid	kGauss	3
Magnetic field in the linac solenoid	kGauss	0.32/0.50
Total photo-injector length	m	12

Table 7.1: Main photo-injector parameters.

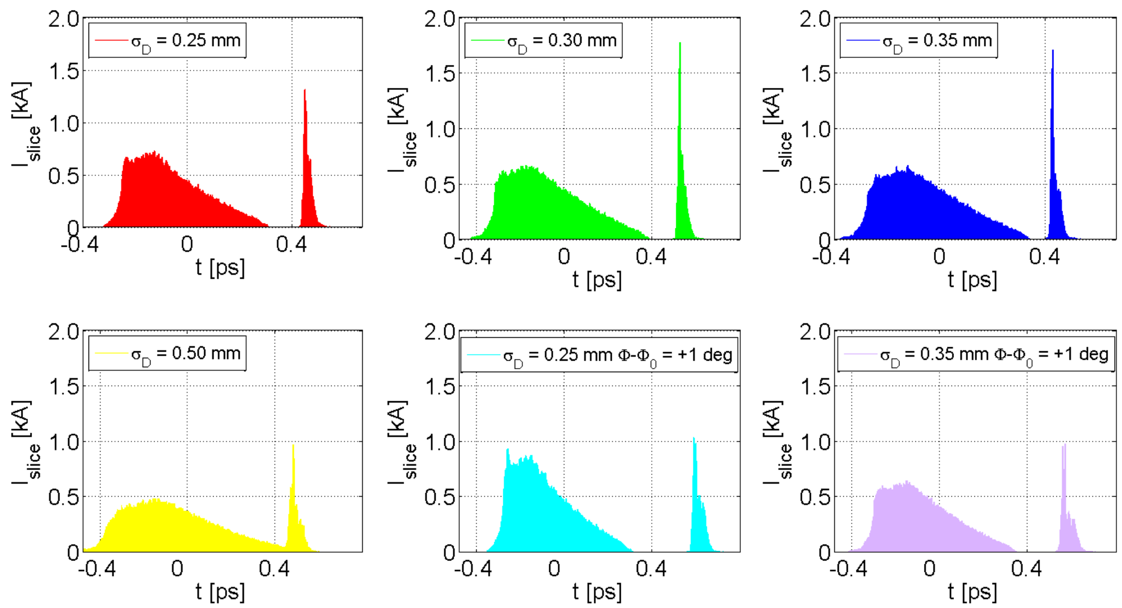

Figure 7.3: Longitudinal distribution of the comb beam at the photo-injector exit for several driver spot size and RF phases of the 2nd TW cavity. The beam is propagating from right to left with the driver arriving earlier than the witness.

The best compromise in terms of final spacing and witness profile has been obtained with a laser comb operation with two laser pulses spaced of $\Delta t = 4.8$ ps on the cathode. In this configuration, adopting the set-up described in Section 6.1, the beam crossing occurs in the second TW accelerating cavity and a fine-tuning of the RF phases suffices to provide 0.55 ps spaced beams, corresponding to $\lambda_p/2$, and the desired witness and driver longitudinal lengths, i.e. 3 μm FWHM and in the range 30 – 50 μm RMS, respectively.

Both witness and driver bunches have been simulated with 30k and 200k macro-particles, corresponding to 30 pC and 200 pC, respectively. In the described configuration the driver arrives 0.58 ps earlier than the witness at the X-band booster. The parameters of both witness and driver beams at the X-band linac entrance are listed in Table 7.2: it is worth to notice that the witness length is about 3 μm FWHM with a normalized transverse emittance of $\sim$0.7 mm mrad. Figure 7.4 reports longitudinal and transverse phase spaces at the photo-injector exit for both witness and driver beams as obtained with TStep.

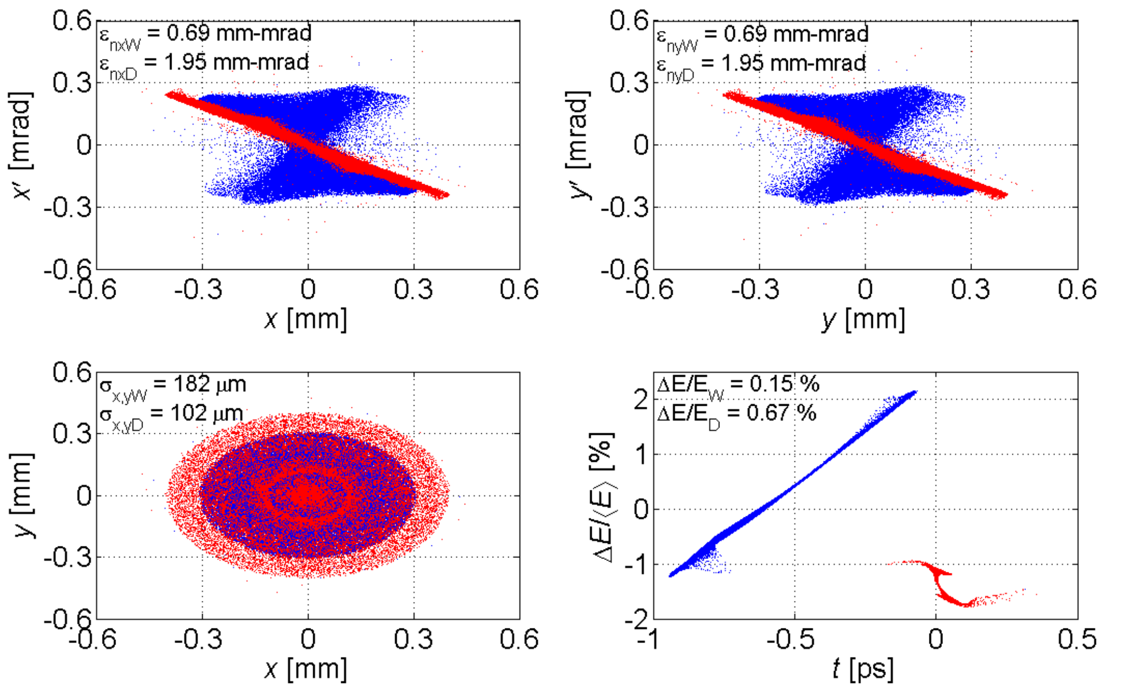

Figure 7.4: Upper plots: Transverse phase space (x and y). Lower plots: transverse distribution and longitudinal phase space for a comb-like beam at the photo-injector exit. The blue and red dots are related to the driver and witness, respectively.

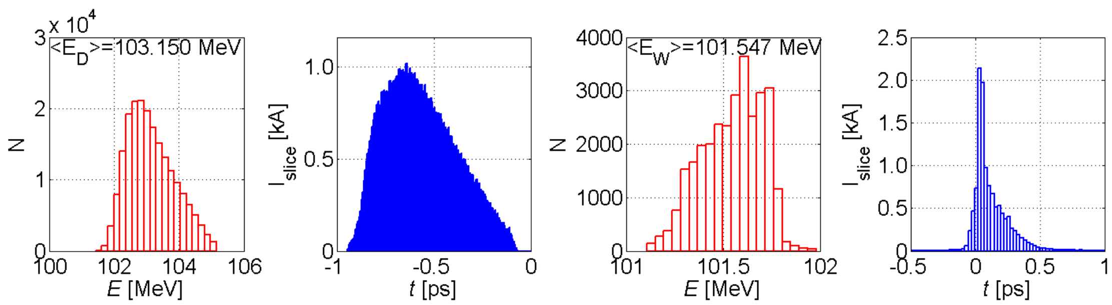

Figure 7.5: Driver (left plots) and witness (right plots) beams energy and current profiles (red and blue lines, respectively).

Figure 7.5 shows the energy and current profiles for both driver and witness bunches as naturally produced by the velocity bunching regime, i.e. a spike-like distribution with the charge gathered on the head of the bunch. Even though this particle longitudinal distribution is suitable for the witness beam in order to take profit of the beam loading, it is not the optimum for the driver beam. Indeed, to increase the transformer ratio the opposite charge distribution, i.e. low charge on the head and maximum charge on the tail, is mandatory. At this regard, further manipulation of the longitudinal phase space is required for the driver.

Parameter	Unit	Witness	Driver
Charge	pC	30	200
Energy	MeV	101.5	103.2
RMS energy spread	%	0.15	0.67
RMS bunch length	fs	12	20
Peak current (FWHM)	kA	6.0	0.37
RMS norm. emittance	mm mrad	0.69	1.95
Rep. rate	Hz	10	10

Table 7.2: Driver and witness beam parameters at the end of photo-injector.

7.2 Linac

The X-band RF linac has to provide an electron beam for injection in the plasma capillary with Q= 30 pC, I= 3 kA (FWHM), and 1–2 µm of transverse spot size; the comb-like electron beam undergoes deep over-compression in the photo-injector by means of the velocity bunching scheme. The same accelerating gradient of $E_{acc} \approx 20 - 36$ MV/m is applied in L1 and L2 linac section respectively, see Table 5.3, and the final electron beam energy is $E_{L2exit} \approx 580$ MeV, with an energy spread less than 0.1%, see Fig.7.6.

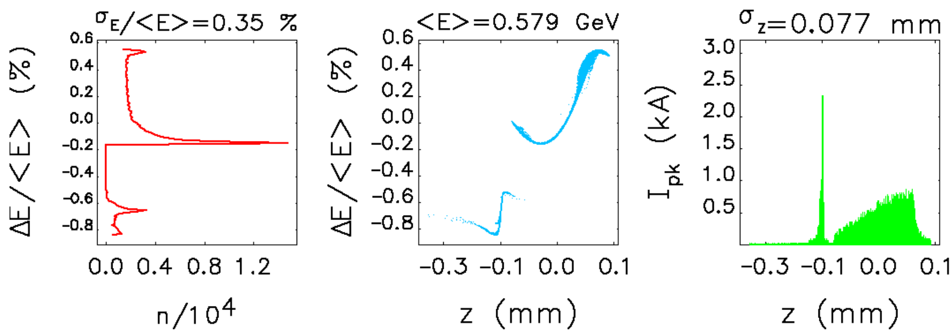

Figure 7.6: Longitudinal phase space of the PWFA accelerated electron beam at the L2 linac exit.

The driver and witness bunches are characterized by high charge/low current and low charge/high current, respectively. Moreover, the initial matching conditions for the injection in the X-band linac are quite different for the two bunches, as shown by their transverse phase space at the linac entrance (i.e. injector exit) and depicted in Fig.7.7. In this regard, an efficient sharing of the same lattice is achieved by means of a mild transverse focusing that aims to keep the RMS size of the comb beam compatible with the beam stay-clear-aperture through all the X-band accelerator, see Fig.7.8.

The same argument applies also to the focusing stage with the permanent quadrupoles at the entrance of the plasma capillary where a residual asymmetry between horizontal and vertical plane for the witness beams is present, see Fig. 7.9 and Fig. 7.10, unavoidable up to now if not at the expense of a much greater dilution of the transverse emittance of the driver bunch: optimization and improvement of the lattice are due in progress to minimize the issue.

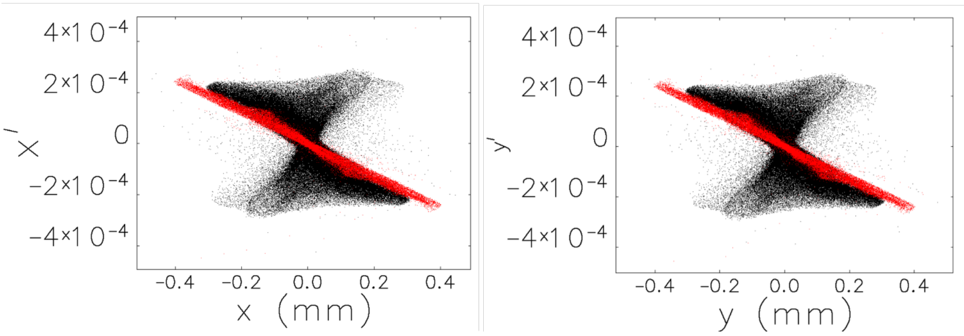

Figure 7.7: Horizontal and vertical phase space distribution of the PWFA driver (black dot) and witness (red dot) beams at the L1 linac entrance.

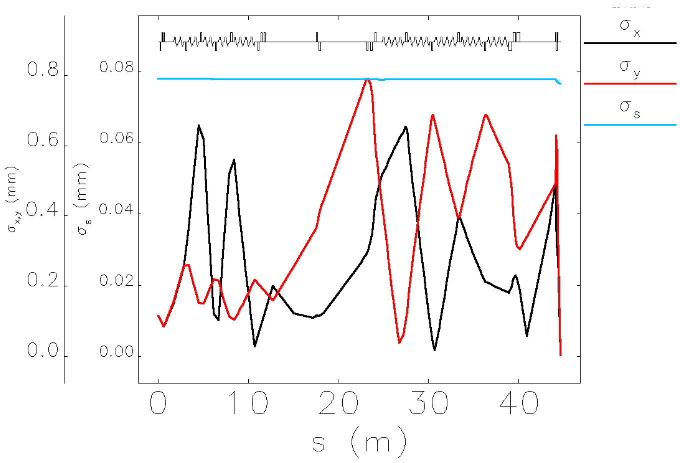

Figure 7.8: Transverse RMS size of the electron beam (driver plus witness) along the Linac.

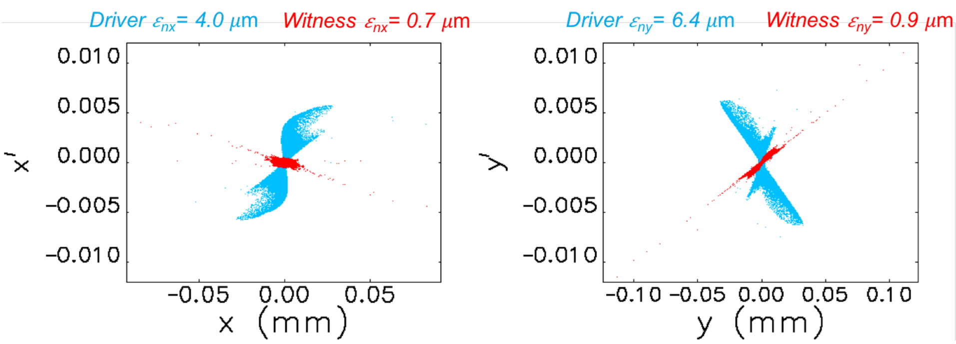

Figure 7.9: Horizontal and vertical phase space distribution of the PWFA driver (cyan dot) and witness (red dot) beams at the capillary entrance.

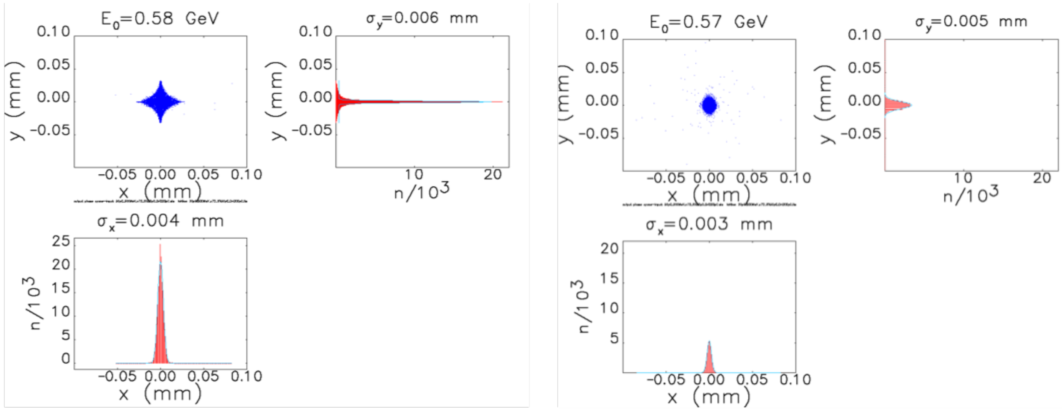

Figure 7.10: Transverse horizontal and vertical distribution of the PWFA driver (left) and witness (right) beams at the capillary entrance.

7.3 Plasma Accelerating Section

7.3.1 The Architect Code

Start-to-end simulations use, for the plasma section, the state-of-the-art code Architect [9, 10]. The use of Architect has been dictated by the necessity to run long simulations where a classical particle-in-cell approach would have been computationally too expensive. The Architect reduced model, which relies on a fluid background, has been tested and verified against a classical particle-in-cell code for the regimes of interest. In particular a comparison and a discussion is reported in [10]. Start-to-end simulations are performed by concatenating the use of codes without any phase space manipulation or remapping. The ELEGANT code is used to track particle up to the plasma entrance, the particle phase-space is then imported into the Architect code for the evolution in the plasma section. Simulations described in this section have been run with a longitudinal resolution of 1 µm and a transverse resolution of 0.4 µm a mesh that allows to resolve the fine structure with a reasonable computational cost. The advancing time step is of 1.1 fs. The number of particle used to discretize the driver is, on average, 30 particles per cell while the witness is discretized with an average of 100 particle per cell.

7.3.2 Parameters Choice

Driver and witness have been simulated from the photo-cathode, TStep is used to simulate the generation and photo-cathode transport for both bunches. Elegant, in cascade, is used to simulate the Linac part. Bunches are then imported into Architect for the plasma evolution. The final aim is to transport and accelerate the witness bunch at the end of the plasma section retaining the original quality as much as possible. To limit the energy spread growth, the witness has been designed with a (as much as possible) *triangular* shape. The triangular shape together with a specific value of peak charge represents the optimized longitudinal density profile that limits or neglect energy spread during propagation. The theoretical shape is not necessary trivial to be generated. In our case a pseudo-triangular shape is produced where the front profile is fairly peaked due to the necessity of a high current slice for FEL lasing necessity. On a FEL stand point, it is this high current slice that need to be transported with little phase space dilution.

Driver and witness have been designed to perform the best acceleration in terms of quality and in terms of energy transfer (*transformer ratio, R*) [11], that aims to maximize the energy transfer from the driver to the witness. In particular, the witness bunch has been designed with a shape as *triangular* [12, 13] as possible; the triangular shape is an optimized profile to limit the energy spread growth.

To maintain bunch quality and to ensure that both bunches, namely the driver and witness, evolve with as little as possible deterioration they have to be injected at matching conditions. The plasma transverse matching condition is given by,

$$\sigma_{x,\mathrm{matching}} = \sqrt[4]{\frac{2}{\gamma}}\sqrt{\frac{\varepsilon_x}{\kappa_p}} \tag{7.1}$$

where we recall, for sake of clarity, that ε_x is the normalised RMS emittance (in the transverse plane) in mm mrad while $\kappa_p = 2\pi/\lambda_p$ is the plasma wavenumber. Eq. (7.1) indicates a transverse micron size bunches. For our case, assuming $n_p = 10^{16}$ cm^{-3} as nominal density background, we calculate $\sigma_{x,D-\mathrm{matching}} = 4$ µm and $\sigma_{x,W-\mathrm{matching}} = 1.55$ µm. We have assumed a driver with a normalised emittance of 3 mm mrad and a witness with a normalised emittance of 1 mm mrad. This geometrical condition is closely related to the geometrical condition of symmetry, the bunch has to be as symmetric as possible, i.d. $\sigma_x \sim \sigma_y$. A driver length optimal condition also need to be considered [14], this condition is sometimes referred as the longitudinal matching condition. This condition reads $\kappa_p\,\sigma_{z,D} = \sqrt{2}$. The longitudinal matching condition is exploit to maximize the transformer ratio and partially to limit the quantity of driver charge recalled within the self wake (head-tail acceleration process). In numbers this condition reads $\sigma_{z,D} = 75$ µm.

The foreseen experiment is planned in the so-called *weakly-non-linear regime*, where the electric field induced by the driver bunch has neither a full sinusoidal behavior nor a full sawtooth shape. The parameter we used to measure the degree of nonlinearity is the *reduced charge parameter* [15, 16], $\mathcal{Q} = \frac{N_b}{n_0}\kappa_p^3$, with N_b the electron bunch number (bunch charge divided by the elementary charge). For the foreseen case $\mathcal{Q} \sim 0.8 - 0.9$ for a driver carrying a charge of 200 pC. For such a reason we need to leverage on both linear regime scaling laws together with nonlinear scaling laws to identify the best parameters to guide simulations. The injection phase φ_0, calculated with respect to the maximum accelerating field, in a linear regime can be calculated as $\varphi_0 \approx \frac{Q_{\mathrm{witness}}}{Q_{\mathrm{driver}}}$. The calculation is retrieved by assuming that a driver bunch produces a linear wake $E_{\mathrm{acc}} = G\cos(k_p\xi)$ while the witness produces a decelerating self-wake $E_{\mathrm{dec}} = -g\sin[k_p(\xi_0 + \sigma_z - \xi)]$, with G and g the accelerating and decelerating fields respectively, and ξ the longitudinal comoving coordinate. By requiring that the electric field felt by a particle located at the witness front $\xi = \xi_0 + \sigma_z$ experiences the same accelerating field of a particle in the bunch center $\xi = \xi_0$ we retrieve the given solution. Such a condition gives as a injection phase close to the half plasma wavelength with respect to the maximum decelerating driver field. Recalling that witness charge is fixed by upstream FEL applications, simulations identify that beam loading is compensated for a driver-witness distance 184 µm or $0.55 \times \lambda_p(n_0 = 10^{16})$.

Our setup, and specifically the driver, is characterised not only by a reduced charge factor that is just below one but also by a peak density that is about 10 times larger than the plasma background density, at plasma entrance the driver core is characterised by $n_b/n_p = 10 - 15$ with n_b the peak number bunch density. This condition, as discussed in [17], suggests that it is possible to achieve transformer ration larger than 2 also with a single bunch, eventually also symmetric. The transformer ratio, for our optimized distance, is estimated around 3, while the accelerating gradient is estimated around 1.1 GV/m field.

Since we operate in the so called weakly nonlinear regime we need to recall that the driver depletion is non-uniform along its length. We can, in fact, subdivide the driver into three sections. The driver front part plays a key role in generating the first lateral kick [18–20] to the background electrons that will lately be deflected to produce the bubble, but this part negligibly lose energy in favor of the wake. The drive core is the part that looses the energy to generate the wake, and so to transfer it to the witness. The driver tail, instead, already feels the accelerating field and is partially accelerated. In our foreseen experiment, but with general characteristics for the weakly nonlinear regimes, the central driver body that looses energy is about half of the entire charge, while the inert front part is about one third of the bunch.

At present simulations consider some density ramps of the order of 0.5 cm, that are experimentally reasonable and whose length is below the betatron wavelength assuring no bunch oscillations within the ramps to increase acceleration robustness.

Density choice and density manipulation

We recall that the accelerating field together with the plasma wavelength depend upon the plasma number density n_0, as $n_0^{1/2}$ and $n_0^{-1/2}$ respectively. The capability to control the density would permit some flexibility and adjustments in the bubble profile and accelerating fields, this to compensate – on site – whenever the distance between driver and witness would oscillate or change for experimental unforeseen reasons. The flat density profile, together with the required value is achieved with a capillary tube. The capillary tube, confining the ejected gas, permits a high degree of control to which we can rely on for experimental on site optimization.

7.3.3 Bunch acceleration in the Plasma section

Since driver and witness are transported along the same RF line, the bunches are delivered at their best at plasma entrance. The witness is delivered at plasma entrance with a shape that resemble the triangular required shape. Transversally the bunch is fairly symmetric in size and in emittance Table 7.3.

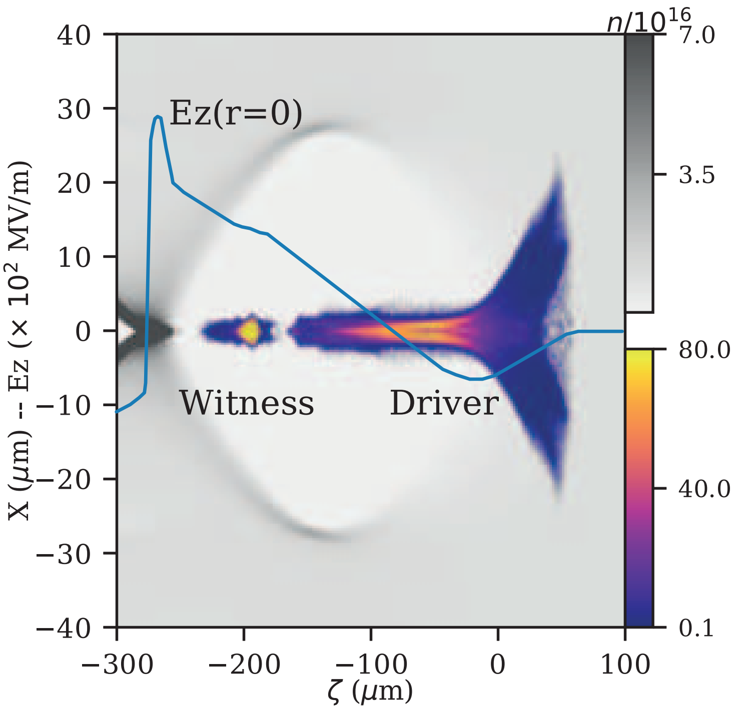

Figure 7.11: Bunch and background density colormaps after 5 mm within the plasma. The bunch density is plotted with a *plasma* colormap, while the background is plotted with a gray colormap. The longitudinal accelerating electric field, on axis, is over-imposed with a solid blue line. For scale purposes and for sake of clarity the Ez is plotted in hundreds of MV/m.

The witness brightness at plasma entrance is high. Lot of cure has been given to deliver the witness at the plasma according to plasma requirements. The driver exhibits, instead, a weaker degree of geometrical symmetry and it is delivered at plasma entrance larger than the matching condition. The higher witness quality compared to the driver quality can be explain as follow, the RF line has been set to deliver the witness at plasma entrance at specifications. The setting of the RF line in favor of the witness naturally bring the driver on a less optimised point that is delivered out of optimal conditions. Since the driver will be removed after the acceleration, the lower quality is acceptable. We also observe that the driver at entrance has the front part that is highly convergent, convergence that will cause a consequent expansion within the plasma channel producing a unique funnel shape as can been seen from Fig. 7.11. The front driver part, convergent, corresponds to 1/3 of the total beam charge. Nonetheless, the driver is capable to driver a weakly nonlinear wake with an effective maximum field that peaks around 2.5–3.0 GV/m, as can been retrieved from Fig. 7.11.

The maximum peak is achieved at the bubble closure where the room to allocate the witness will be limited and where the positioning of the witness would significantly change the bubble structure [12, 21, 22]. For the case of interest, a witness with a given current for FEL application, it requires a closer position to the driver to control at some level the energy spread. The non-bubble-rear witness positioning has some pro and some cons. The transformer ratio is limited, however the positioning within the bubble allows for a wider room where to place the witness avoiding that any part of the transverse distribution hits the bubble edge with a consequent quality deterioration. The central part of the driver that mostly contribute to generate the wake looses after 40 cm about 150 MeV, the witness gains about 460 MeV. This value indicates that the accelerating gradient is about 1.1 GV/m and that its transformer ratio is about 3.

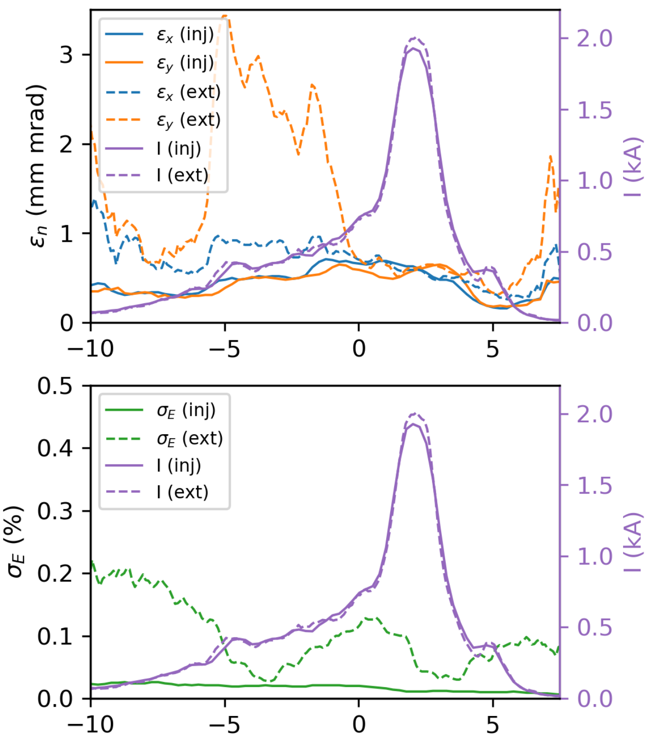

Figure 7.12: Rolling slice analysis for the witness bunch at plasma input, dashed line, and at plasma exits, solid line. The top panel report the emittance in both transverse plane and the current. The bottom panel plots the energy spread together with the current. The corresponding current axis is the left y axis.

The slice analysis, plotted in Fig. 7.12, and reported numerically in Table 7.3 suggests that the

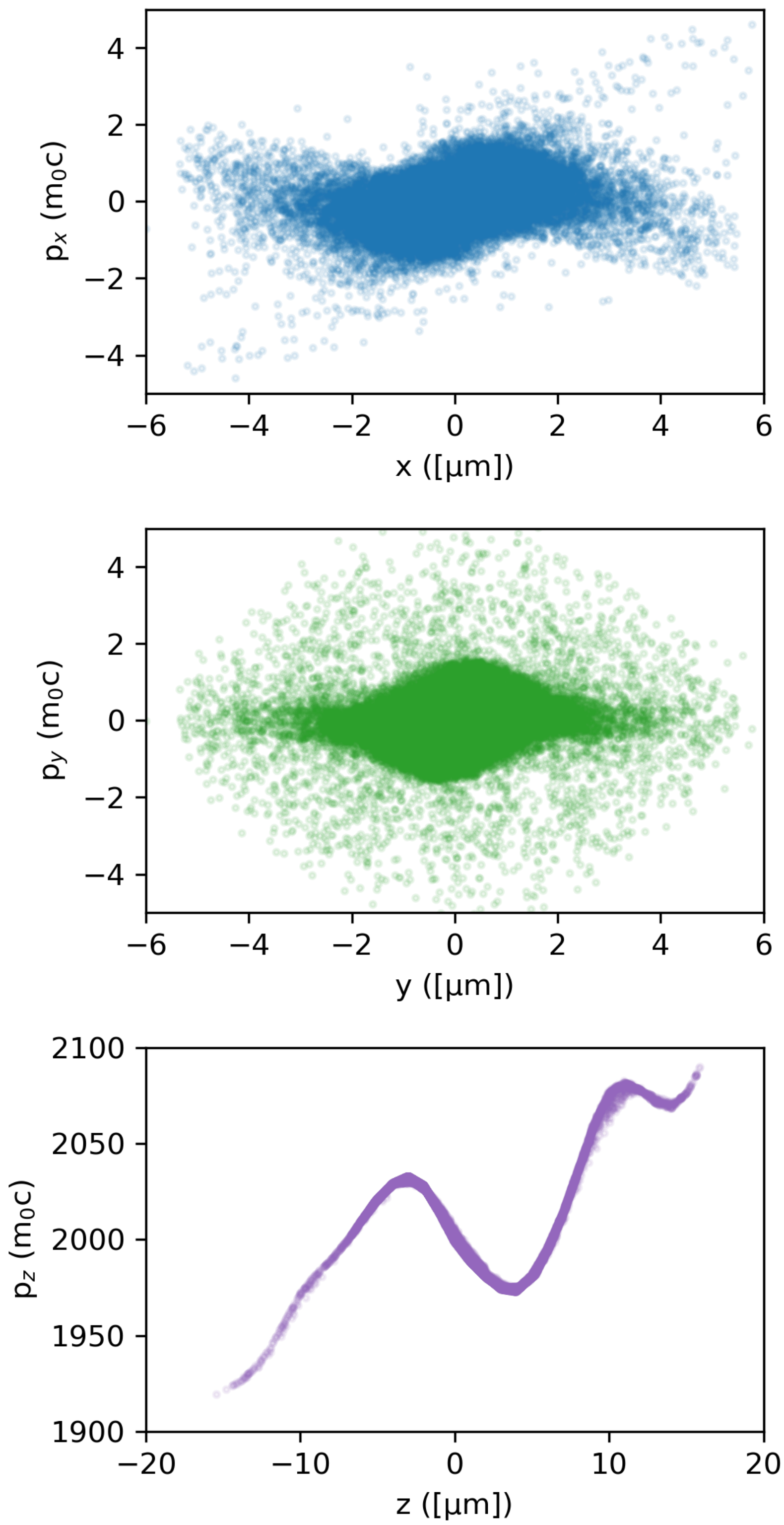

Figure 7.13: Witness phase space dotted-plots at the exit from the plasma accelerator section.

witness head and tail undergo a phase space dilution, while the central slice with very high current retain high quality. The witness, at plasma entrance, has the emittance in both planes as well as the energy spread almost uniform along the entire witness length. After the plasma acceleration section the bunch has lost this homogeneity, exhibiting a different slice quality along its length. The front part and the read part of the witness are characterised by large emittance and energy spread. While ideally we wish to preserve quality along all the trailing bunch, the head and tail are characterised by a lower current, condition that allow us some flexibility on these regions since their lasing within the FEL would be negligible. However, and most importantly, the region within the high current bell retains its quality. From Fig. 7.12, top panel, we notice that under the region of high current the emittance in both plane is almost conserved with little deterioration. The energy spread undergoes some general increase also in the region of maximum current. The slice value, in the region of maximum current, stays below 0.1%. The peak current value corresponds to the transition from a higher value to the lowest one. The best slice characterised by a 2 kA current, has an energy spread as low as 0.034% and an emittance of 0.57 mm mrad and 0.62 mm mrad in the x and y plane respectively.

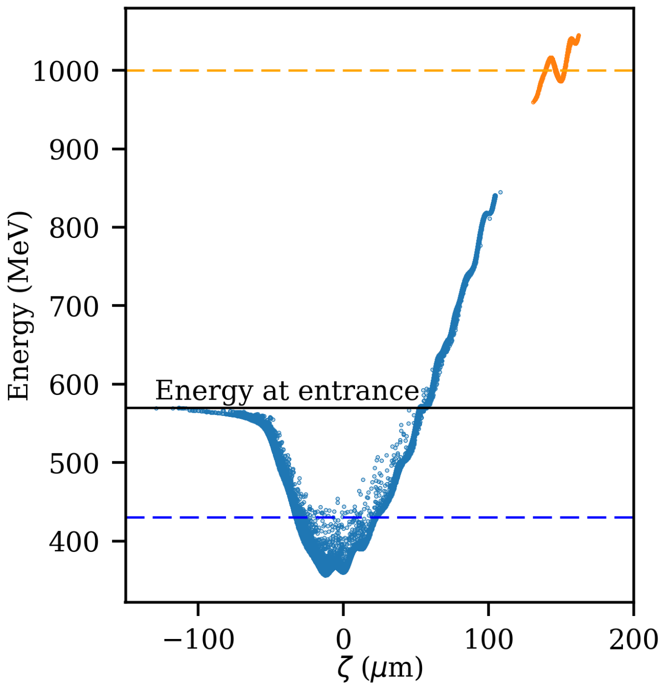

Figure 7.14: Longitudinal dotted-phase space at plasma exit, plotting both driver and witness.

Parameter of Acceleration

Table 7.3 summarizes the plasma-input and plasma-output parameters, for both driver and witness. The table reports the integrated parameters, for the whole bunch, while slice quantities can be retrieved from Fig. 7.12.

7.4 Transport

The transport line for matching the PWFA beam in undulator has been described in Section 6.4. In Figure 7.15 we report beam transverse properties (dimensions and emittances) along the transport line. Data have been analyzed as described in Section 6.3.2 and correspond to a $5\sigma_G$ cut. Longitudinal properties do not change significantly and are not reported.

Beam	units	Driver-IN	Driver-OUT	Witness-IN	Witness-OUT
Charge	pC	200	200	30	30
σ_x	μm	8	6.4	1.47	1.42
σ_y	μm	3.1	10	3.17	1.4
σ_z	μm	52	50	3.85	3.8
ε_x	mm mrad	2.56	4.1	0.6	0.96
ε_y	mm mrad	4.8	11.4	0.55	1.2
σ_E	%	0.2	20	0.07	1.1
E	MeV	567	420	575	1030
Best Slice					
current	kA			2	2.0
ε_x	mm mrad			0.59	0.57
ε_y	mm mrad			0.58	0.62
σ_E	%			0.011	0.034

Table 7.3: PWFA bunch parameters at plasma entrance and at plasma exit. The best slice value is also reported.

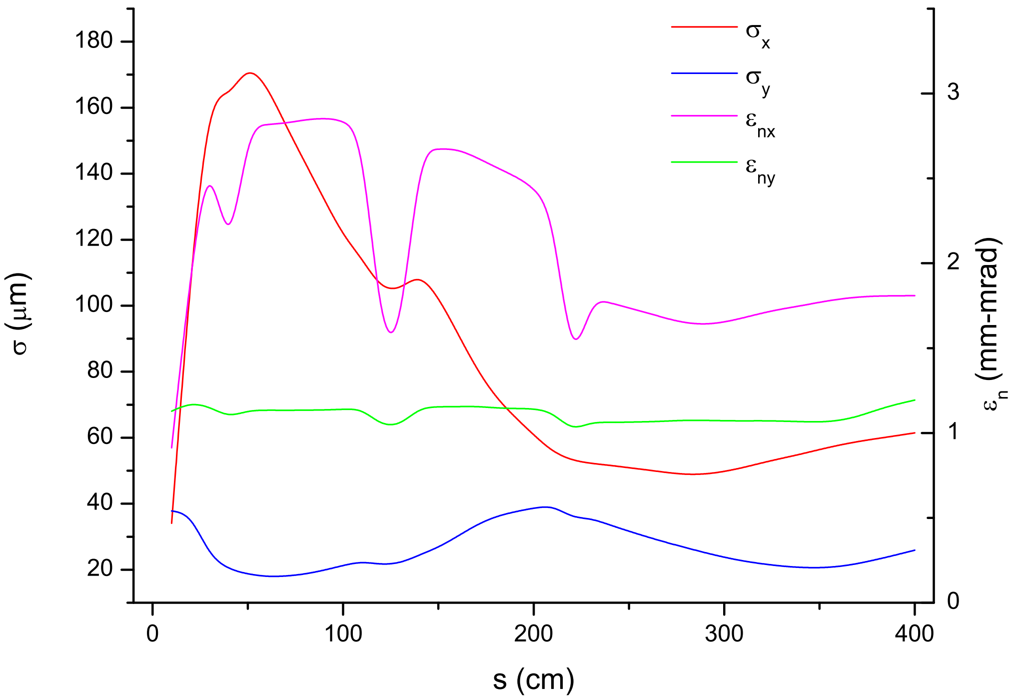

Figure 7.15: Bunch parameters along transport in the transfer line.

7.5 Transport of the PWFA beam inside the undulator

The electron beam accelerated by particle external injection (PWFA) has been described in Section 7.3. The optimized case (case (a)) is summarized in Table 7.4, third column, and shown in Fig. 7.16, where current I (kA), energy, emittance (in mm mrad) and energy spread are presented. The total charge is about 30 pC. Using $a_w = 0.8$, the resonant wavelength is $\lambda = 2.987$ nm. The matching to the undulator [23] leads to $\sigma_x = 40.6$ μm and $\sigma_y = 28.6$ μm with the quadrupoles 9 cm long and set at 18 T/m.

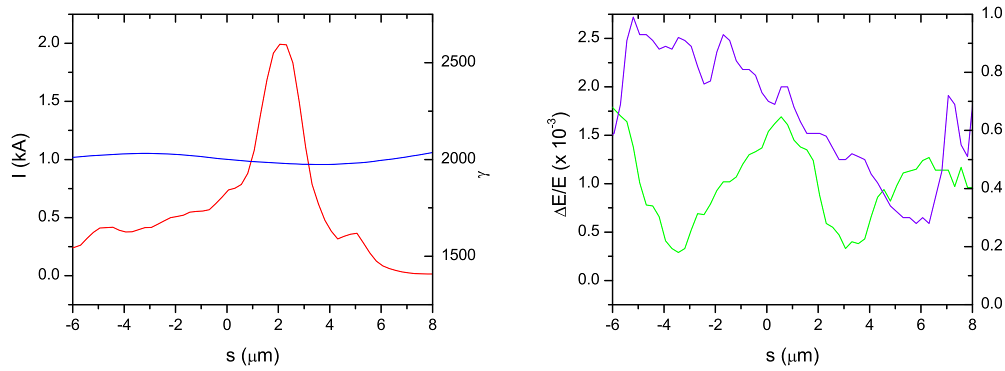

Figure 7.16: Cases (a1, a2): electron current (red line), Lorentz gamma factor (blue line), electron energy spread (green line), emittance (violet line).

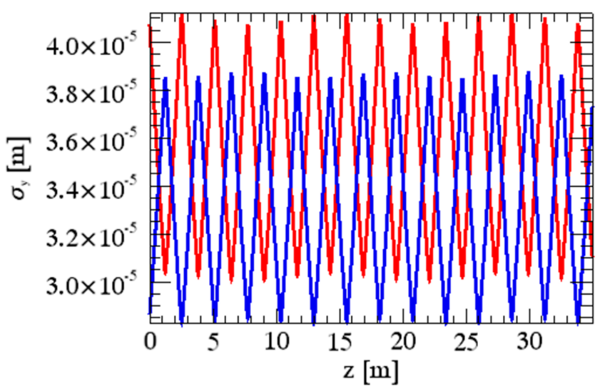

Figure 7.17: Transverse dimensionsσ_x (in red) and σ_y (in blue) of the PWFA electron beam along the undulator.

In Fig. 7.17 the evolution of the transverse dimensions σ_x and σ_y of the PWFA electron beam along the undulator is shown.

7.6 FEL performances

The FEL parameter evaluated with the slice values (see Table 7.4) [24, 25] is $\rho = 2.51 \times 10^{-3}$, its 3D value is $\rho_{3D} = 1.86 \times 10^{-3}$ for $L_{g,3d} = 0.37$ m. The growth of the radiation, as given by simulations with GENESIS 1.3 [26], is shown in Fig. 7.18. The saturation length is about 15–25 m with emitted energy 6.5 μJ at 30 m, for a photon flux of 9.76×10^{10} per shot. In Fig. 7.4 (b), the contour plot of the power for case a1 is represented in the plane (s, z), showing the single spike structure [27–29] during the exponential phase and superradiance after saturation. The minimum bandwidth value, achieved at 20 m is 0.3%, while at 30 m saturation effects have increased it to 0.9%.

The relevant power density and the spectrum at 30 m are shown in Fig. 7.18 (c) and (d). The structure of the radiation is of few spikes both in the time and in the spectral domain. Finally, the nominal case a1 has been worsened in current, emittance and energy spread by 5% and 10%. Table 7.4 shows the characteristics of the emitted pulse. Decrease in the emission respectively of 8% and 13% have been found.

Particle driven	Units	(a)
RMS Energy Spread	%	1.1
Peak current	kA	2.
Bunch charge	pC	30
Bunch length RMS	μm (fs)	3.82(12.7)
RMS norm. emittance	mm mrad	1.1
Slice Length	μm	1.2
Slice Charge	pC	8
Slice Energy Spread	%	0.034
Slice norm. emittance x,y	mm mrad	0.57-0.615
Undulator period	cm	1.5
Undulator strength K (a_w)		1.13(0.8)
Pierce parameter $\rho(1D/3D)$	$\times 10^{-3}$	2.5-1.8
Radiation wavelength	nm (keV)	2.98(0.45)
Undulator length	m	30
Energy at 30 m	μJ	6.5
Photons/pulse	$\times 10^{10}$	9.8
Bandwidth at 30 m	%	0.9
Divergence	μrad	50-51
Rad. size	μm	10
Brilliance per shot (30 m)	(s mm^2 mrad^2 bw(0.1%))$^{-1}$	8.1×10^{26}

Table 7.4: Electron beam, undulator and radiation characteristics for particle driven acceleration.

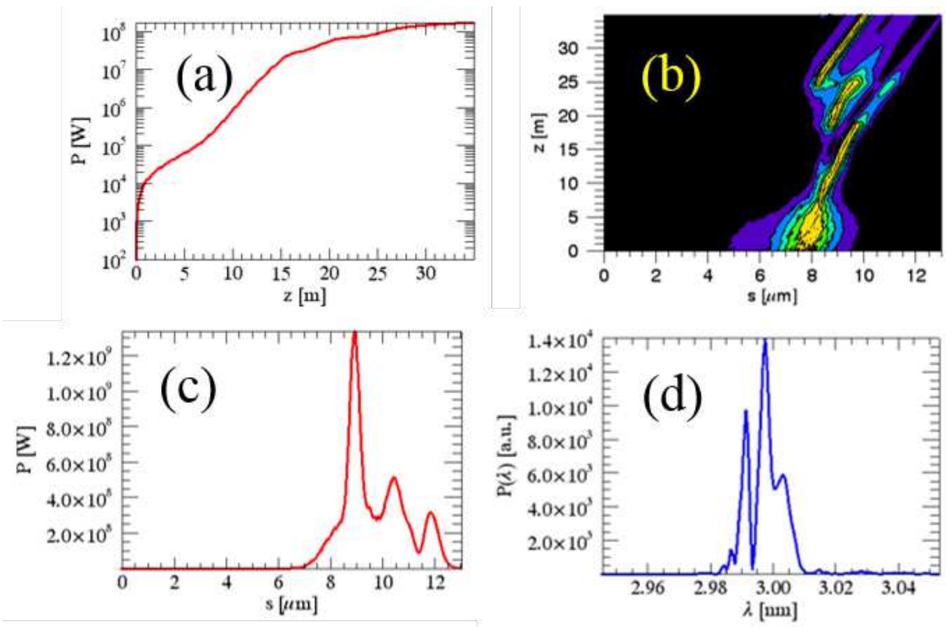

Figure 7.18: Particle driven acceleration: (a) Radiation growth along the undulator coordinate z(m). (b): Contour plot of the power P in the plane (s,z). (c) Power and (d) spectrum of the radiation at 30 m.

Bibliography

[1] E Chiadroni et al. "Beam manipulation for resonant plasma wakefield acceleration". In: *Nuclear Instruments and Methods in Physics Research Section A: Accelerators, Spectrometers, Detectors and Associated Equipment* 865 (2017), pp. 139–143.

[2] A. Giribono et al. "EuPRAXIA@SPARC_LAB: The high-brightness RF photo-injector layout proposal". In: *Nuclear Instruments and Methods in Physics Research Section A: Accelerators, Spectrometers, Detectors and Associated Equipment* (2018). ISSN: 0168-9002. DOI: https://doi.org/10.1016/j.nima.2018.03.009. URL: https://www.sciencedirect.com/science/article/pii/S0168900218303267.

[3] M Ferrario et al. "Laser comb with velocity bunching: Preliminary results at SPARC". In: *Nuclear Instruments and Methods in Physics Research Section A: Accelerators, Spectrometers, Detectors and Associated Equipment* 637.1 (2011), S43–S46.

[4] F Villa et al. "Laser pulse shaping for high gradient accelerators". In: *Nuclear Instruments and Methods in Physics Research Section A: Accelerators, Spectrometers, Detectors and Associated Equipment* 829 (2016), pp. 446–451.

[5] A Mostacci et al. "Advanced beam manipulation techniques at SPARC". In: *IPAC 2011-2nd International Particle Accelerator Conference*. 2011, pp. 2877–2881.

[6] Flavio Giorgianni et al. "Tailoring of highly intense THz radiation through high brightness electron beams longitudinal manipulation". In: *Applied Sciences* 6.2 (2016), p. 56.

[7] V Petrillo et al. "Observation of time-domain modulation of free-electron-laser pulses by multipeaked electron-energy spectrum". In: *Physical Review Letters* 111.11 (2013), p. 114802.

[8] A Petralia et al. "Two-Color Radiation Generated in a Seeded Free-Electron Laser with Two Electron Beams". In: *Physical review letters* 115.1 (2015), p. 014801.

[9] A Marocchino et al. "Efficient modeling of plasma wakefield acceleration in quasi-non-linear-regimes with the hybrid code Architect". In: *Nuclear Instruments and Methods in Physics Research Section A: Accelerators, Spectrometers, Detectors and Associated Equipment* 829 (2016), pp. 386–391.

[10] F Massimo, S Atzeni, and A Marocchino. "Comparisons of time explicit hybrid kinetic-fluid code Architect for Plasma Wakefield Acceleration with a full PIC code". In: *Journal Of Computational Physics* 327 (2016), pp. 841–850.

[11] F Massimo et al. "Transformer ratio studies for single bunch plasma wakefield acceleration". In: *Nuclear Inst. and Methods in Physics Research, A* 740.C (2014), pp. 242–245.

[12] M Tzoufras et al. "Beam loading by electrons in nonlinear plasma wakes". In: *Physics of Plasmas (1994-present)* 16.5 (2009).

[13] M Tzoufras et al. "Beam Loading in the Nonlinear Regime of Plasma-Based Acceleration". In: *Physical Review Letters* 101.14 (Sept. 2008), p. 145002.

[14] Thomas C Katsouleas et al. "Beam Loading in Plasma Accelerators". In: *Part.Accel.* 22 (1987), pp. 81–99.

[15] JB Rosenzweig et al. "Energy loss of a high charge bunched electron beam in plasma: Simulations, scaling, and accelerating wakefields". In: *Physical Review Special Topics-Accelerators and Beams* 7.6 (2004), p. 061302.

[16] P Londrillo, C Gatti, and M Ferrario. "Numerical investigation of beam-driven PWFA in quasi-nonlinear regime". In: *Nuclear Inst. and Methods in Physics Research, A* 740 (2014), pp. 236–241.

[17] A Martinez de la Ossa et al. “Wakefield-induced ionization injection in beam-driven plasma accelerators”. In: *Physics of Plasmas (1994-present)* 22.9 (Sept. 2015).

[18] W Lu et al. “Nonlinear Theory for Relativistic Plasma Wakefields in the Blowout Regime”. In: *Physical Review Letters* 96.16 (Apr. 2006), p. 165002.

[19] W Lu et al. “Limits of linear plasma wakefield theory for electron or positron beams”. In: *Physics of Plasmas* 12.6 (June 2005), p. 063101.

[20] W Lu et al. “A nonlinear theory for multidimensional relativistic plasma wave wakefields”. In: *Physics of Plasmas* 13.5 (2006), p. 056709.

[21] W Lu et al. “Nonlinear Theory for Relativistic Plasma Wakefields in the Blowout Regime”. In: *Physical Review Letters* 96.16 (Apr. 2006), p. 165002.

[22] W Lu et al. “A nonlinear theory for multidimensional relativistic plasma wave wakefields”. In: *Physics of Plasmas* 13.5 (2006), p. 056709.

[23] M Quattromini et al. “Focusing properties of linear undulators”. In: *Physical Review Special Topics-Accelerators and Beams* 15.8 (2012), p. 080704.

[24] Ming Xie. “Design optimization for an X-ray free electron laser driven by SLAC linac”. In: *Particle Accelerator Conference, 1995., Proceedings of the 1995*. Vol. 1. IEEE. 1995, pp. 183–185.

[25] G Dattoli, PL Ottaviani, and S Pagnutti. “Booklet for FEL design: a collection of practical formulae”. In: *Frascati: ENEA–Edizioni Scientifiche* (2007).

[26] Sven Reiche. “GENESIS 1.3: a fully 3D time-dependent FEL simulation code”. In: *Nuclear Instruments and Methods in Physics Research Section A: Accelerators, Spectrometers, Detectors and Associated Equipment* 429.1-3 (1999), pp. 243–248.

[27] R Bonifacio et al. “Spectrum, temporal structure, and fluctuations in a high-gain free-electron laser starting from noise”. In: *Physical review letters* 73.1 (1994), p. 70.

[28] JB Rosenzweig et al. “Generation of ultra-short, high brightness electron beams for single-spike SASE FEL operation”. In: *Nuclear Instruments and Methods in Physics Research Section A: Accelerators, Spectrometers, Detectors and Associated Equipment* 593.1-2 (2008), pp. 39–44.

[29] F Villa et al. “Generation and characterization of ultra-short electron beams for single spike infrared FEL radiation at SPARC_LAB”. In: *Nuclear Instruments and Methods in Physics Research Section A: Accelerators, Spectrometers, Detectors and Associated Equipment* 865 (2017), pp. 43–46.

III Machine Technology

8. S-band RF photo-injector

The RF photo-cathode gun and associated systems are meant to reliably produce, at the most critical point in the injector, the extremely high quality beam demanded by the EuPRAXIA@SPARC_LAB facility. For this reason, it has to be based on technology that is both proven and, at the same time, at the cutting edge. Similar considerations apply to the other critical component associated to the beam generation and emittance compensation process, i.e. the photo-cathode drive laser and the solenoid after the gun itself. The EuPRAXIA@SPARC_LAB electron bunches will be generated by the up to 170 MeV injector, which consists of a 1.6 cells RF Gun cavity, followed by three accelerating structures. The system will operate at the frequency of 2.856 GHz that is the same frequency of the SPARC photo-injector in operation at LNF since 2005. The RF Gun has a metallic photo-cathode, located in the high electric field region of the cavity and illuminated by short, ps scale, UV laser pulses at 50 Hz repetition rate.

8.1 RF Gun

The RF gun of the EuPRAXIA@SPARC_LAB facility will be a 1.6 cell gun of the BNL/SLAC/UCLA type [1, 2] with the modifications foreseen and implemented in the ELI-NP gun and integrated in the new gun recently developed for the SPARC photo-injector. With respect to the original design type [1, 2], this gun, whose parameters are given in Table 8.1, will implement several features described in the following.

The iris profile has been designed with an elliptical shape and a large aperture, to simultaneously reduce the peak surface electric field, increase the frequency separation between the two resonant modes (i.e. the working π-mode and the so-called 0-mode) and improve the pumping efficiency on the half-cell. Furthermore, a high frequency separation of the resonant modes strongly reduces the residual field of the 0-mode due to the transient regime, which is particularly important if the structure is fed with short pulses [3]. The coupling window between the rectangular waveguide and the full cell has been strongly rounded to reduce the peak surface magnetic field and, as a consequence, the pulsed heating [4]. Figures 8.1(b) and (c) show, respectively, the magnetic field in the coupler region at 120 MV/m cathode peak field and the longitudinal accelerating field profile. The input coupling coefficient (β) has been chosen equal to 3 to reduce the filling time allowing

Gun Parameter	Unit	Value
Resonant frequency	GHz	2.856
$E_{cath}/\sqrt{P_{diss}}$	MV/(m·MW$^{0.5}$)	37.5
RF input power	MW	14
Cathode peak field	MV/m	120
Rep. rate	Hz	50
Quality factor		14600
Coupling coefficient		3
RF pulse length	µs	1.0
Mode separation	MHz	41.3
E_{surf}/E_{cath}		0.9
Pulsed heating	deg C	<30
Average diss. power	W	400
Working temperature	deg	30

Table 8.1: RF gun main parameters.

operation with short RF pulses [5]. Finally, to compensate the dipole field component, induced by the presence of the coupling hole, a symmetric port (connected to a circular pipe below cut off) has been included in the gun [6–8] and is also used as pumping port. The residual quadrupole field component due to the presence of the two holes does not significantly affect the beam quality [9].

The e.m. design of the gun has been done using 2D and 3D e.m. codes (Superfish [10] and HFSS [11]). Figure 8.1(a) shows the HFSS geometry of the gun with its main dimensions.

A new fabrication technique for this type of structures has been recently developed at LNF [12] and successfully applied to the realization of two RF guns: the ELI-NP gun and the first prototype gun currently in operation at UCLA at low repetition rate (i.e. 5 Hz) and relatively low cathode peak field [13]. The new technology is based on the use of special RF-vacuum gaskets, which allow a brazing-free realization process, avoiding copper annealing from the brazing process itself, with the advantage of potentially reaching higher accelerating field with a lower breakdown rate [14].

The photo-cathode is centered on the flange that closes the half-cell. The requirement of short response time of the cathode to allow electron beam shaping through laser pulse manipulation limits in the case of EuPRAXIA@SPARC_LAB photo-injector the choice of the cathode materials to metals that usually present response time of the order of few tens of femtoseconds [15]. Based on the results so far obtained worldwide in different laboratories, the most promising candidates metals that can be used as sources for electron beam are copper (Cu) [16], magnesium (Mg) [17] and yttrium (Y) [18]. One of the parameters that is critical for the final choice and operation of the photo-cathode is represented by the Quantum Efficiency (QE) at the drive laser wavelength. The QE of these metals has been measured under similar condition under UV laser irradiation at 266 nm and resulting in values of about $4\cdot10^{-5}$ [19], $5\cdot10^{-4}$ [17] and $\sim 2\cdot10^{-4}$ [18] for Cu, Mg and Y, respectively.

In the first phase of EuPRAXIA@SPARC_LAB, a copper cathode will be adopted. Copper is a robust material with well proven photo-emissive behavior that guarantees uniformity of the emission distribution over the laser spot illuminated by the laser. Its drawback is the low emission efficiency (i.e. quantum efficiencies of the order of $5\cdot10^{-5}$), which entails large laser pulse energy. Different cathode materials, e.g. Mg, Yttrium, can be used in future phases, once their reliability

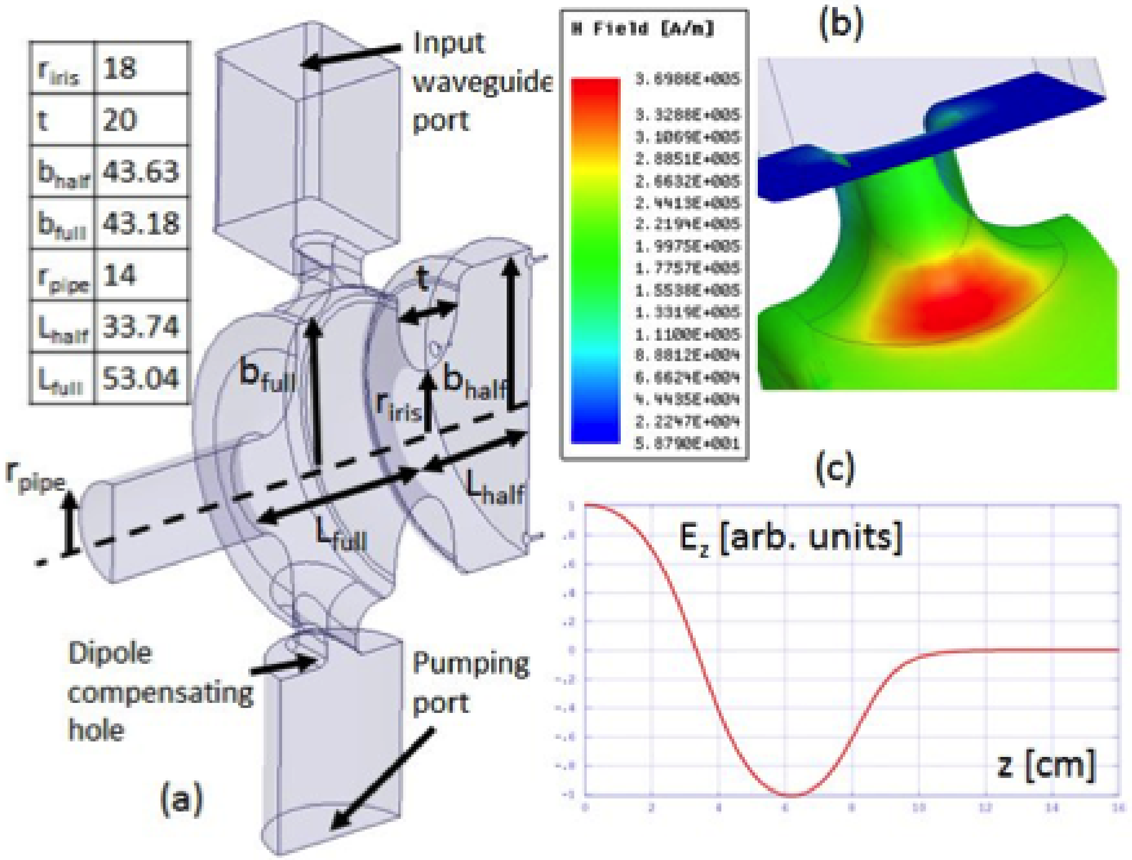

Figure 8.1: (a) HFSS geometry of the gun; (b) H field in the coupler region; (c) longitudinal accelerating field profile.

is demonstrated for operation in user facilities. In any case, all types of cathodes demand very good vacuum conditions, at the level of 10^{-9} mbar during high gradient operation, which typically implies that the vacuum without RF be one order of magnitude better in the absence of RF power. These demands are to be met by stringent control of the gun manufacturing and cleaning processes, and by implementing a pumping system with high pumping speed through direct pumping port on the accelerating cells waveguide and cathode flange.

8.2 RF Gun Solenoid

The design of the solenoid, immediately after the gun, together with the gun design itself, is crucial for the emittance compensation process [20] and final beam performances at the linac exit. The proposed design consists in four coils, embedded and separated by iron armatures, that can be powered independently. In this way it is possible to shape the magnetic field profile and move the field peak around the central position. This solenoid design, as tested at SPARC_LAB, allows to power the coils with alternate signs (e.g. + - + - or + + - -), giving a better compensation for alignment errors and multipolar components. The magnetic field lines of the solenoid, as computed by Poisson-Superfish FEM code [21], are shown in Fig. 8.2 while the main parameters are reported in Table 8.2.

The solenoid will be also mounted on a movable support to allow a beam based fine alignment of the magnetic center with precisions below 10 μm on the transverse planes.

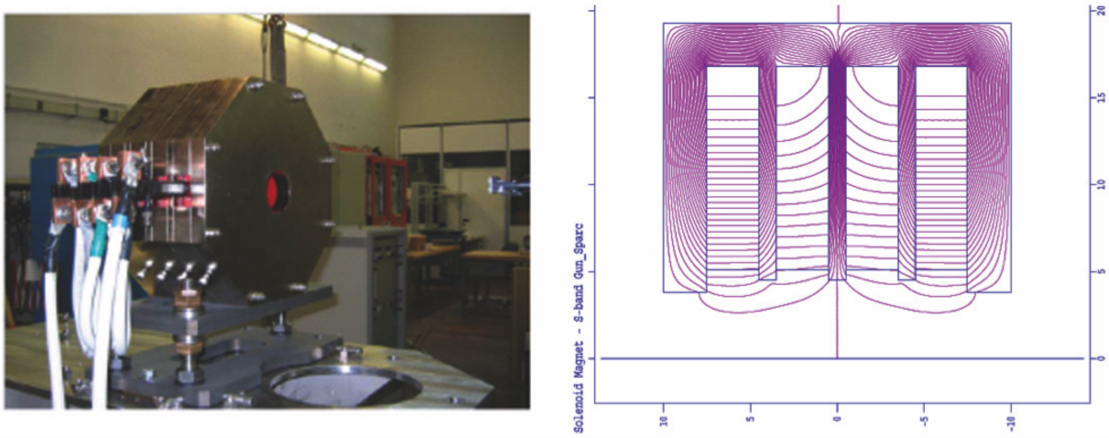

Figure 8.2: On left the SPARC Gun Solenoid, on right the field distribution, in SPARC configuration + + - -, as computed by Posson-Superfish code.

Parameter	Unit	Value	Conditions
Typical Operation Axial Field peak (+ + - -)	Gauss	2700 (-2700)	@ 14.3 cm (25.0 cm)
Residual Axial Field @ cathode	Gauss	<10	@ 2.7 kG field peak
Maximum Coils current (typical)	A	$\sim$280 (180)	
Cathode to Solenoid edge	cm	9.6	
Solenoid Bore	cm	7.6	

Table 8.2: Gun solenoid parameters.

8.3 Photo-cathode Drive Laser System

The EuPRAXIA@SPARC_LAB photo-injector is required to produce both single and comb-like electron bunches, with charge ranging from tens to few hundreds of pC, with high peak current and normalized transverse emittance < 1 mm mrad. Therefore the laser pulses have to be tailored to minimize the beam emittance and, at the same time, have enough power to produce relatively high current bunches.

Photo-cathode drive lasers for high brightness electron beam applications must have very specific capabilities driven by two major considerations: (1) the low photoemission efficiency for robust photo-cathodes requires high UV pulse energy given the needed charge; (2) the emittance compensation process is most successful with uniform temporal and spatial laser energy distribution. Additionally, low amplitude and time jitters from pulse-to-pulse, as well as pointing stability are needed to ensure repeatable SASE FEL performance. The laser pulses have to be synchronized with the master oscillator to extract electrons at the specified phase of the RF wave. Other laser systems will be used at EuPRAXIA@SPARC_LAB for laser-driven plasma acceleration, seeded FEL, electron and photon diagnostic and finally for a variety of possible pump and probe experiments. All these lasers are required to be synchronous within very tight tolerance. The timing and the synchronization of the lasers will be discussed in Chapter 12 (Timing and Synchronization). The allowed variations in parameters concerning the laser system and its relationship to the RF system have been specified with the aid of the simulation codes, as discussed in Section 6.1.

The laser system for EuPRAXIA@SPARC_LAB is required to deliver excess of 150 μJ energy per pulse at a wavelength of 266 nm to the photo-cathode at a repetition rate up to 50 Hz. This energy requirement comes out from the typical quantum efficiency of copper photo-cathode. Indeed, the drive laser supplies photons that are absorbed by electrons within the RF gun cathode, producing via the photo-electric effect emitted electrons if their kinetic energy exceeds the material's work function. The energy per laser pulse U (J), needed to produce a bunch of charge q (C) using photons of energy E_γ (eV) incident on a cathode surface with quantum efficiency QE, is given by $U = q\ E_\gamma/QE$. A cathode's quantum efficiency depends on many conditions, such as material, preparation, excess of photon energy over the work function, RF field and vacuum levels. Nevertheless, we may extrapolate the needed performance of the photo-cathode drive laser based on our experience at SPARC_LAB. Assuming a typical value $5 \cdot 10^{-5}$ for copper, 20 μJ are required to produce 400 pC; allowing for a energy overhead of one order of magnitude, this implies 200 μJ of laser energy. This required value at the photo-cathode must be considerably larger at the harmonic-generation crystal exit, as light will be absorbed by various optical elements needed for pulse shaping and transport to the photo-cathode. In addition, the emittance compensation scheme requires that the laser pulse must show uniform transverse and longitudinal profile in order to compensate the non-linear space charge field with an proper magnetic focusing. The temporal and spatial flat top laser energy distribution on cathode has been demonstrated to reduce the emittance [19,20]. We foresee to change the pulse length on a range between 100 fs to few ps (RMS) and the number of pulses from one to 5 to explore different machine working points, based on the different foreseen experiments. Further details on the photo-cathode drive laser system are reported in Chapter 11 (High power laser system).

8.4 S-band Linac

EuPRAXIA@SPARC_LAB photo-injector is finally completed with three S-band accelerating structures that allow to accelerate and manipulate the beam through the velocity bunching compression scheme. RF compression or velocity bunching technique [22] consists in compressing the beam by injecting it in the first RF structure ahead the crest with a phase near to the zero of the accelerating field: the beam slips back up to acceleration phases undergoing less than a quarter of synchrotron oscillation and is compressed. The emittance growth occurring during the compression can be taken under control by a proper shaping of an additional magnetic field around the accelerating structures. To this purpose, two solenoids, around the first two structures, are used for emittance compensation. Simulations show that compression factors larger than three require an accurate tuning of the coils composing the solenoids embedding the structures, as also experimentally demonstrated at SPARC_LAB [23].

The solenoid structure will be covered by de-mountable soft iron magnetic shields to shield the fringing field that, at a distance of 80 mm from the beam axis, is still not negligible (≈150 Gauss). Figure 8.3 shows the solenoid coils around the first linac sections with shielding opened.

The advantages of this configuration are

- a higher magnetic field, about 1900 Gauss, as opposed to the 1660 Gauss with the same number of Ampere-turns;
- a sharper magnetic fringe field tail;
- improved transverse alignment of the solenoid, as it will depend partially on machined iron, not simply on wound coils with dielectric coatings;
- no fringing field outside the structure, i.e. no constraints for materials, external apparata, and personnel safety;
- the iron shielding, realized by means of semi-annular rings, can be easily removed for checks, tests or other necessities;
- thermal confinement of the accelerating structure, that means less sensibility to ambient temperature variations.

The main parameters of each solenoid are summarized in the following Table 8.3.

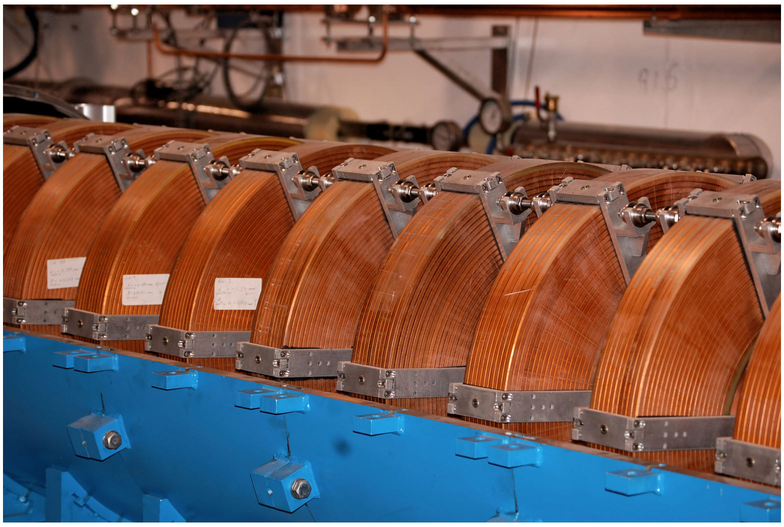

Figure 8.3: Solenoid coils embedding the first accelerating S-band structure; the upper iron shield is removed.

Parameter	Unit	Value
Number of coils		12
Inner diameter	mm	308
Outer diameter	mm	632
Coil cross section (insulated)	mm^2	162×82
Nom. Cu conductor size	mm^2	7.5×7.5
Nom. cooling hole diameter	mm	5
Turns per solenoid		200
Maximum excitation current	A	200
Current density	A/mm^2	5.05
Maximum voltage	V	30.15
Power per coil	W	5580
Hydraulic circuits per coil		5
Water velocity	m/s	0.9
Water flow per magnet	m^3/s	$9\cdot10^{-5}$
Water temperature rise	°C	15
Pressure drop per circuit	MPa	0.19

Table 8.3: Solenoid focusing magnet characteristics per linac section.

The accelerating structures of the EuPRAXIA@SPARC_LAB S-band linac are traveling wave (TW), constant gradient (CG), $2\pi/3$, 3 m long and operate at 2.856 GHz. These type of accelerating sections, known as the SLAC-type structures [24], are made of a series of 86 RF copper cells, joint with a brazing process performed in high temperature vacuum furnaces. The cells are coupled by means of on axis circular irises with decreasing diameter, from input-to-output, to achieve the constant-gradient field profile in case of uniform input power. The RF power is transferred to the accelerating section through a rectangular slot coupled to the first cell. The power not dissipated in the structure (about 1/3rd) is coupled-out from the last RF cell and dissipated on external load. To meet the severe emittance requirements for the injector, the single feed couplers (foresaw in the original SLAC-type structures) will be replaced by a dual-feed design [25] to minimize the multipole field effects generated by the asymmetric feeding, which induces transverse kicks along the bunch, causing beam emittance degradation.

The maximum achievable accelerating gradient is the most important parameters of such devices. To reach the maximum required nominal energy of about 180 MeV, the average accelerating field in the 3 SLAC-type sections S1, S2 and S3 needs to be 22, 25 and 28 MV/m respectively (see Table 5.1 for reference). The beam loading is negligible due to the very small average beam current (energy extracted by the beam is maximum 40 mJ per section, stored energy in each section is about 40 J).

Technical specifications of the S-band accelerating sections are reported in Table 8.4.

Parameter	Unit	Value
Structure type		Constant gradient, TW
Working frequency	GHz	2.856
Number of cells		86
Structure length	m	3
Working mode		TM_{01}-like
Phase advance between cells		$2\pi/3$
Max average accelerating gradient	MV/m	22 (S1)/ 25 (S2)/ 28 (S3)
Average RF input power (P_{IN})	MW	<40 (S1) /<50 (S2)/ <60 (S3)
Shunt Impedance per unit length	MΩ	53-60
Phase velocity		c
Norm. group velocity	v_g/c	0.0202–0.0065
Filling time (τ_F)	ns	$\sim$850
Structure attenuation constant	neper	0.57
Operating vacuum pressure (typical)	mbar	10^{-8}–10^{-9}
Rep. rate	Hz	50
Average dissipated power	kW	$\sim$1.3

Table 8.4: Technical specifications of the S-Band accelerating sections.

8.4.1 High Power System Components

The RF power stations needed to feed all the S-band active devices are 2. The first one will power the standing wave RF Gun cavity, requiring $\approx$1.5 μss long RF pulses of $\approx$15 MW. Because of the pulse length and of the moderate power request, this station will not be equipped with a pulse compressor. A total power of $\approx$25 MW is considered to provide a comfortable safety margin for operation and in case of future upgrade. A circulator will protect the klystron itself against the power reflected by the standing wave (SW) cavities. Due to the fact that this device employs ferrite materials, it usually operates in pressurized atmosphere of sulfur-hexafluoride (SF_6) to guarantee the required insulation. The waveguide vacuum system will be separated from the circulator SF_6 insulating system by means of RF ceramic windows. These type of windows will also be used to separate the accelerator and waveguide vacuum systems. A capillary distributed interlock/alarm system, managed by a complex of programmable logic controllers (PLC), will protect the linac and the RF stations in case of malfunction.

A second RF station will power the 3 accelerating sections S1, S2 and S3. The total power required is $\approx$150 MW in 0.85 μs long pulses, that can be obtained by compressing a $\approx$4 μs long, 60 MW pulse produced by a single klystron. Although the nominal accelerating fields are not extreme, they nevertheless require the use of selected materials, precise machining, high-quality brazing process, surface treatments and cleaning, ultra-pure water rinsing, careful vacuum and RF low power tests. In order to maintain the accelerating structures and the pulse compressor cavities precisely tuned, they are kept at very constant temperature, i.e. $\Delta T = \pm\ 0.1^\circ$, by means of regulated cooling water systems.

Parameter	Unit	Value
Frequency type	GHz	2.856
RF Pulse Duration	μs	4
Repetition Rate	pps	50
Cathode Voltage	kV	350-370
Beam Current	A	400-420
HV Pulse Duration	μs	6
RF peak power	MW	60

Table 8.5: S-band klystron main specifications.

Three manufacturers, Thales (F), CPI (US) and Toshiba (JP), produce 60 MW peak S-band klystrons, which meet the requirements of the second station of the EuPRAXIA@SPARC_LAB S-band linac. A set of klystron parameters is given in Table 8.5. Each klystron, equipped with beam focusing coils, will be supplied by a High Voltage (HV) Modulator.

As already mentioned the second klystron will be connected to a pulse compressor (SLED), which is used to increase the peak power, feeding the three accelerating structures in parallel. An important specification of the SLED system is the peak power gain, which usually ranges around 7.4 dB with maximum values of 7.8 dB. The power at the SLED output increases therefore, in average, by a factor 3 while the pulse length is reduced to 0.85 μs corresponding to one filling time of the S-Band TW structures.

A network of rectangular WR284 copper waveguides distributes the RF power from the klystrons to the gun, SLEDs and accelerating structures. The waveguides are pumped down to 10^{-8} mbar with a distributed pumping system and are connected to the accelerating structures through ceramic windows to protect the beam line vacuum.

Variable phase-shifters and splitters will be used to allow fully independent phase and amplitude regulation of the three TW accelerating structures. This option is critical in the optimization of the machine performance and, in particular, in providing all the capabilities needed for velocity bunching and chicane bunching working points. The phase-shifter and splitter/attenuators located in the waveguide arms are high power devices capable of operating in vacuum, and are commercially available. The variable power splitter/attenuators can be integrated in the waveguide network to route in each distribution arm the required power level. Figure 8.4 shows a scheme of the RF power distribution for the photo-injector.

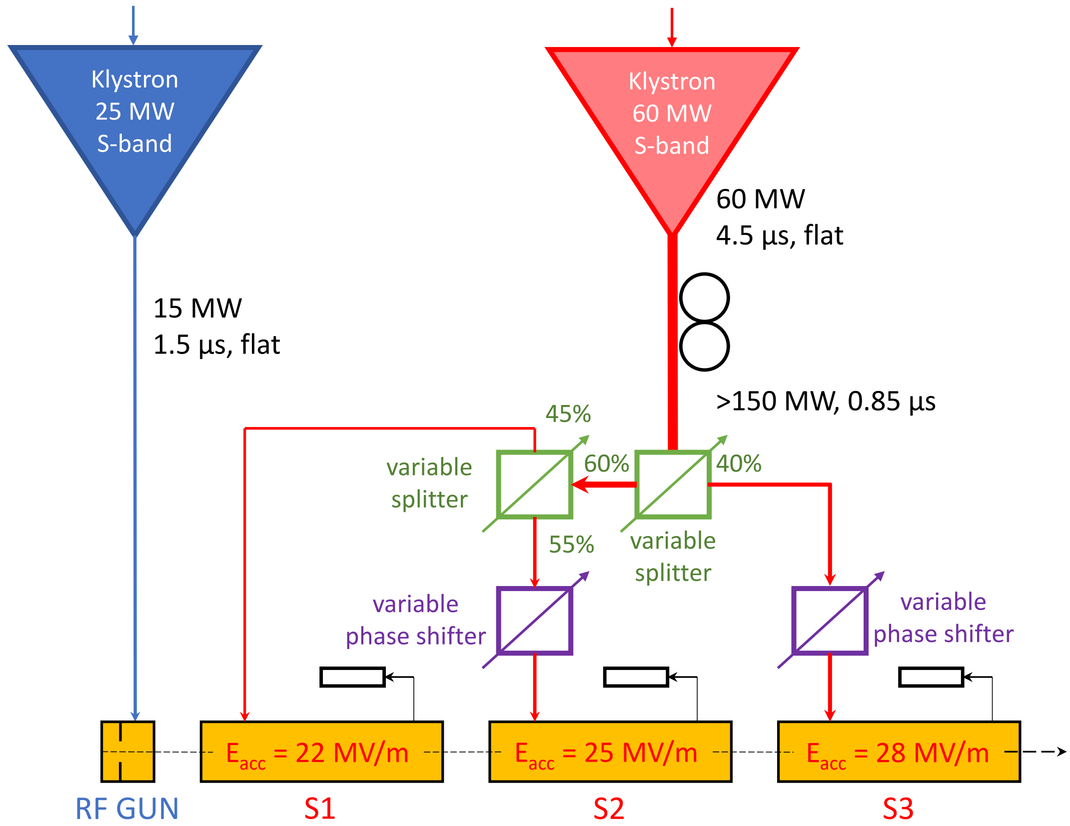

Figure 8.4: Layout of the EuPRAXIA@SPARC_LAB RF power station.

Bibliography

[1] Dennis Thomas Palmer et al. *The next generation photoinjector*. Tech. rep. Stanford Linear Accelerator Center (SLAC), 2005.

[2] DT Palmer et al. *Simulations of the BNL/SLAC/UCLA 1.6 cell emittance compensated photocathode rf gun low energy beam line*. Tech. rep. Stanford Linear Accelerator Center SLAC-PUB-95-6800, 1995.

[3] C Limborg-Deprey. *RF Design of the LCLS Gun*. Tech. rep. SLAC National Accelerator Laboratory (SLAC), 2010. URL: http://www-ssrl.slac.stanford.edu/lcls/technotes/lcls-tn-05-3.pdf.

[4] Valery A Dolgashev et al. "RF breakdown in normal conducting single-cell structures". In: *Particle Accelerator Conference, 2005. PAC 2005. Proceedings of the*. IEEE. 2005, pp. 595–599.

[5] O Adriani et al. "Technical design report EuroGammaS proposal for the ELI-NP gamma beam system". In: *arXiv preprint arXiv:1407.3669* (2014).

[6] DT Palmer et al. "Microwave measurements of the BNL/SLAC/UCLA 1.6 cell photocathode RF gun". In: *Particle Accelerator Conference, 1995., Proceedings of the 1995*. Vol. 2. IEEE. 1995, pp. 982–984.

[7] Xin Guan et al. "Study of RF-asymmetry in photo-injector". In: *Nuclear Instruments and Methods in Physics Research Section A: Accelerators, Spectrometers, Detectors and Associated Equipment* 574.1 (2007), pp. 17–21.

[8] MS Chae et al. “Emittance growth due to multipole transverse magnetic modes in an rf gun”. In: *Physical Review Special Topics-Accelerators and Beams* 14.10 (2011), p. 104203.

[9] *A. Bacci and A. Giribono, private communications*.

[10] URL: `http://laacg.lanl.gov/laacg/services/download_sf.phtml`.

[11] URL: `http://www.ansys.com`.

[12] D. Alesini et al. “Process for manufacturing a vacuum and radio-frequency metal gasket and structure incorporating it”. PCT/IB2016/051464. INFN. 2016.

[13] David Alesini et al. “New technology based on clamping for high gradient radio frequency photogun”. In: *Physical Review Special Topics-Accelerators and Beams* 18.9 (2015), p. 092001.

[14] R Kuroda et al. “Quasi-monochromatic hard X-ray source via laser Compton scattering and its application”. In: *Nuclear Instruments and Methods in Physics Research Section A: Accelerators, Spectrometers, Detectors and Associated Equipment* 637.1 (2011), S183–S186.

[15] SH Kong et al. “Photocathodes for free electron lasers”. In: *Nuclear Instruments and Methods in Physics Research Section A: Accelerators, Spectrometers, Detectors and Associated Equipment* 358.1-3 (1995), pp. 272–275.

[16] David H Dowell and John F Schmerge. “Quantum efficiency and thermal emittance of metal photocathodes”. In: *Physical Review Special Topics-Accelerators and Beams* 12.7 (2009), p. 074201.

[17] L Cultrera et al. “Mg based photocathodes for high brightness RF photoinjectors”. In: *Applied surface science* 253.15 (2007), pp. 6531–6534.

[18] A Lorusso et al. “Pulsed laser deposition of yttrium photocathode suitable for use in radio-frequency guns”. In: *Applied Physics A* 123.12 (2017), p. 779.

[19] F Zhou et al. “Recent photocathode R&D for the LCLS injector”. In: (2014).

[20] Bruce E Carlsten. “New photoelectric injector design for the Los Alamos National Laboratory XUV FEL accelerator”. In: *Nuclear Instruments and Methods in Physics Research Section A: Accelerators, Spectrometers, Detectors and Associated Equipment* 285.1-2 (1989), pp. 313–319.

[21] JH Billen and LM Young. *Poisson Superfish. Los Alamos Nat. Lab*. Tech. rep. LA-UR-96-1834, revised, 2006.

[22] L Serafini and M Ferrario. “Velocity bunching in photo-injectors”. In: *AIP conference proceedings*. Vol. 581. 1. AIP. 2001, pp. 87–106.

[23] M Ferrario et al. “Experimental demonstration of emittance compensation with velocity bunching”. In: *Physical review letters* 104.5 (2010), p. 054801.

[24] Richard B Neal. “THE STANFORD 2-MILE LINEAR ACCELERATOR”. In: *Phys. Today* 20.SLAC-PUB-0233 (1966), pp. 27–41.

[25] K Flottmann et al. In: *Particle Accelerator Conference, 2001, Proceedings of the 2001*. IEEE. 2001, p. 2236.

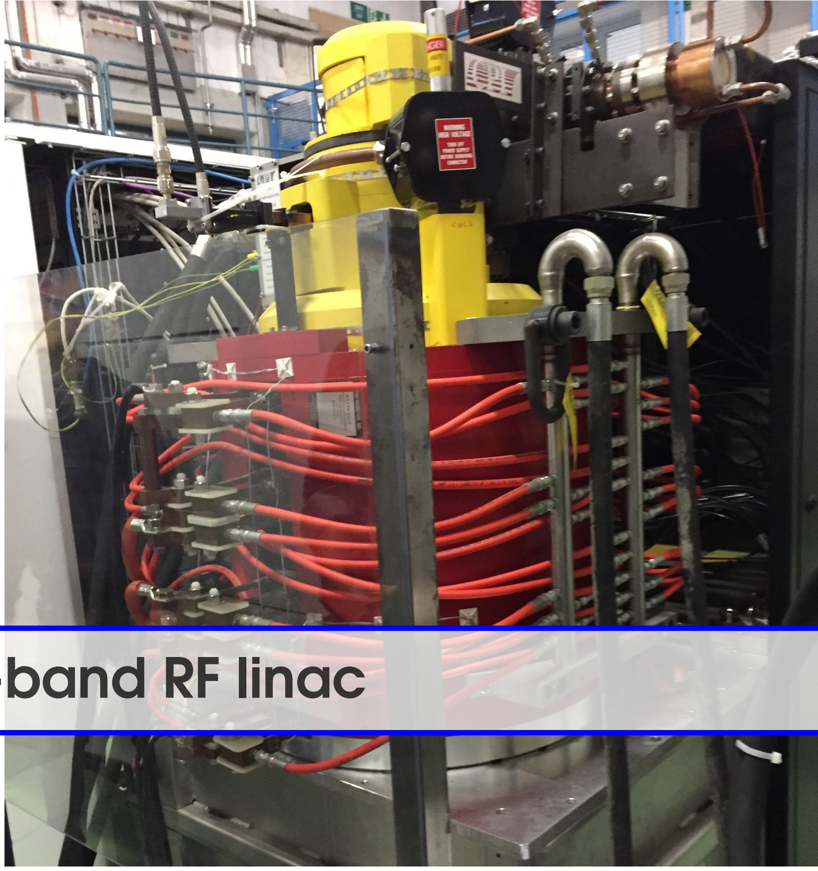

9. X-band RF linac

9.1 Introduction

The EuPRAXIA@SPARC_LAB linac is the core of the accelerator. It is designed to accept the beam coming from the injector and to accelerate it to the final energy with the proper characteristics to match the requirements of the various specific applications. In this respect, the linac needs to be flexible enough to cope with different scenarios: injection of a comb beam into a neutral plasma to both excite a plasma wave and exploit it to accelerate the last (or "witness") bunch of the train (PWFA case, Chapter 5), injection of a single bunch into a plasma wave excited by a laser pulse (LWFA case, Chapter 6), injection of a high brightness bunch directly into a magnetic undulator for FEL radiation production (Full X-band case, Chapter 7). The linac RF design is driven by the need of a high accelerating gradient, i.e. a gradient well above the operational values of the existing FEL sources. This is required by the limited space available in the new building and, more generally, to achieve facility compactness, which is one of the main goals of the EuPRAXIA project. Thus, the high gradient operation motivates the choice of the linac technology. In fact, the use of high RF frequencies is the most suitable and efficient solution for high gradients. C-band technology (f $\sim$ 6 GHz) is the chosen baseline of the most recent room-temperature FEL source facilities, such as SACLA at Spring 8 (Japan) and SWISSFEL at PSI (Switzerland), while X-band (f $\sim$ 12 GHz) is the proposed baseline for CLIC, the CERN multi-TeV linear collider project. In principle both technologies could fulfill EuPRAXIA@SPARC_LAB requirements. The guideline chosen for the EuPRAXIA@SPARC_LAB project is X-band for various reasons: it is more efficient, it has operated at higher gradients, its development is supported by a stronger international effort and experimental data are more abundant. Moreover, the possibility to establish a partnership with CERN represents an added value to the project. Nevertheless, it has to be mentioned that, at present, some X-band RF components are more expensive than C-band ones, although costs are decreasing as the technology is being adopted by different laboratories, and cavity fabrication and alignment tolerances are more stringent.

Beam Parameter	Unit	L1			L2		
		PWFA	LWFA	Full X-band	PWFA	LWFA	Full X-band
Initial energy	GeV	0.102	0.098	0.171	0.222	0.212	0.502
Final energy	GeV	0.222	0.212	0.502	0.582	0.550	1.052
Linac energy gain	GeV	0.120	0.114	0.331	0.360	0.338	0.550
Active Linac length	m		6.0			10.0	
Acc. Gradient	MV/m	20.0	20.0	57.0	36.0	36.0	57.0
RF phase (wrt crest)	deg	0	-20.0	-15.0	0	-19.5	+15.0
Initial energy spread	%	0.15	0.27	0.67	0.11	0.15	0.59
Final energy spread	%	0.11	0.15	0.59	0.07	0.07	0.14
Final Bunch length	mm	0.006	0.005	0.112	0.007	0.005	0.016
Bunch charge	pC	30.0	30.0	200.0	30.0	30.0	200.0

Table 9.1: L1 and L2 linac parameter list.

9.2 Beam parameters at linac entrance and exit

The characteristics of the beam at the linac entrance and exit for different applications are reported in Table 9.1.

As previously mentioned in the beam physics chapter, the beam energy required for injection in the plasma chamber is $\geq$ 550 MeV for both particle-driven and laser-driven plasma acceleration (PWFA case and LWFA case respectively). In these scenarios, the beam will be accelerated by the plasma wave to reach an energy $\geq$ 1 GeV at the entrance of the magnetic undulator. Then, the total contribution of the entire linac (L1 + L2) to the beam final energy will be limited to $\sim$ 450 – 480 MeV.

In the Full X-band scenario, which does not include plasma acceleration, the 1 GeV beam at the magnetic undulator has to be provided entirely by RF acceleration. Thus, the linac alone has to provide a beam energy increase of $\sim$ 900 MeV.

9.3 Linac technology and gradient choice

The total space allocated for the linac accelerating sections is $\sim$ 25 m, corresponding to an active length of $\sim$ 16 m, with the remaining space required to accommodate beam diagnostics, magnetic elements, vacuum equipment and flanges. The minimum gradient required to accomplish the most demanding scenario (1 GeV beam in the magnetic undulator without plasma contribution) is therefore $\sim$ 57 MV/m. However, the linac accelerating sections and the whole RF system need to be designed to ultimately reach a higher gradient, to guarantee a comfortable safety margin during operation. The need of generating such high accelerating gradients (i.e. in the range of $\geq$ 60 MV/m), has been indeed the strongest motivation addressing the RF technology choice.

In the last 25 years a huge effort has been made on the development and consolidation of the X-band as a fully reliable RF technology for the future linear colliders, initially at SLAC and KEK (NLC/JLC projects) and then at CERN (CLIC project) [1]. The work has led to a better understanding and control of high-gradient phenomena such as breakdown, as well as to the development and extensive experimental tests of all the RF components necessary to build a complete RF accelerating system. This includes RF power sources, pulse compressors, waveguide networks and vacuum components. In order to perform long term tests on various prototypes of the

CLIC accelerating structures, three test stand stations, the so-called “X-boxes”, have been put in operation at CERN. Many of the tested structures have exceeded the 100 MV/m threshold with a breakdown rate compliant with the CLIC specifications ($\leq 3 \times 10^{-7}$ in units of breakdowns per pulse per meter of active length).

The development work on the C-band technology, instead, has been more focused on the performances required by the FEL source facilities [2–4], so that less data are available on the ultimate achievable gradients with this approach compared to X-band.

Starting from these considerations, X-band RF technology has been evaluated to be the most appropriate choice for the EuPRAXIA@SPARC_LAB linac. In this regard, INFN has set up a collaboration agreement with CERN for a wide exchange of technical information, expertise and components. Short term goals of the collaboration are the refinement of the EuPRAXIA@SPARC_LAB linac RF design and the construction at LNF of an additional X-box to test accelerating structures prototypes.

9.4 Accelerating section design

The RF system for the EuPRAXIA@SPARC_LAB linac has been designed using the following procedure:

- define the optimal filling time of the structures, considering the necessity to use pulse compressors in the system;
- choose the iris aperture according to beam dynamics considerations. This allows to determine the dimensions of the single cell and the total length of the accelerating structure;
- define the layout of the complete RF system based on:
  - optimized TW section parameters;
  - RF power sources (klystrons) parameters;
  - the various operating scenarios that the linac must support.

The accelerating sections are of the Traveling Wave (TW) type, and will be powered by means of pulse compression systems. This choice maximizes the overall efficiency and decreases costs by reducing the number of power sources required to produce the necessary peak power [5]. Pulse compressors are widely used devices in the RF systems of room temperature linacs. By constructively interfering reflected power pulses of very high-Q cavities with properly phase modulated forward pulses it is possible to concentrate a large portion of a klystron RF pulse energy in a small fraction of the original pulse duration, as shown in figure 9.1.

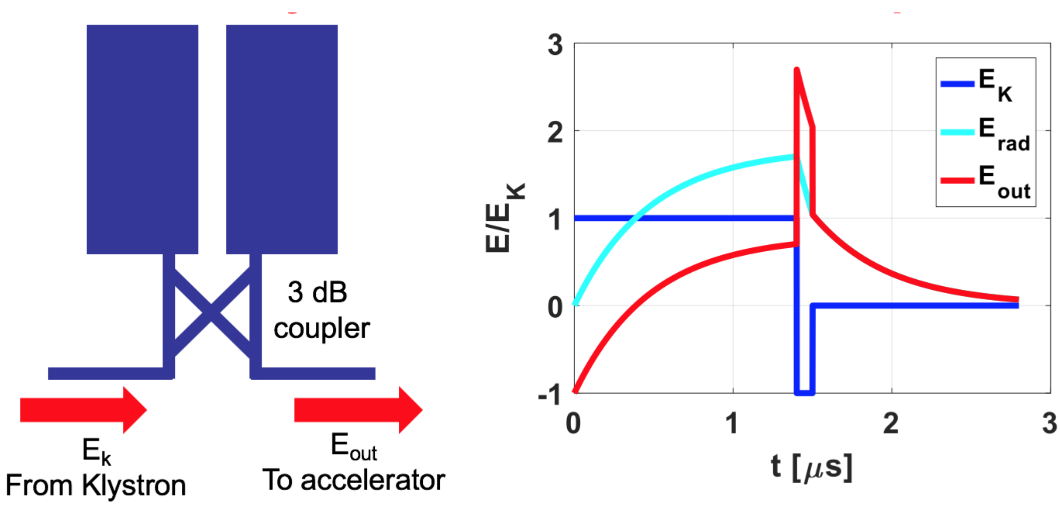

Figure 9.1: Pulse compression with a SLED-type system.

The peak power in the shortened RF pulse is considerably higher than the original one and the shorter the pulse, the larger the peak power. On the other hand the shorter is the RF pulse, the smaller is the fraction of its energy exploited for acceleration by the TW section. The optimal pulse length of the TW section powered by a compressed pulse can be calculated, and depends on the klystron pulse duration and on the Q factors of both the accelerating sections and the pulse compressor cavities. For typical values of an X-band system ($f_{RF} \sim 12$ GHz, $\tau_{kly} \sim 1.5$ µs, $Q_{TW} \sim 6500$, $Q_{SLED} \sim 180000$) the optimal duration of the compressed pulse can be derived from the plots shown in Figure 9.2.

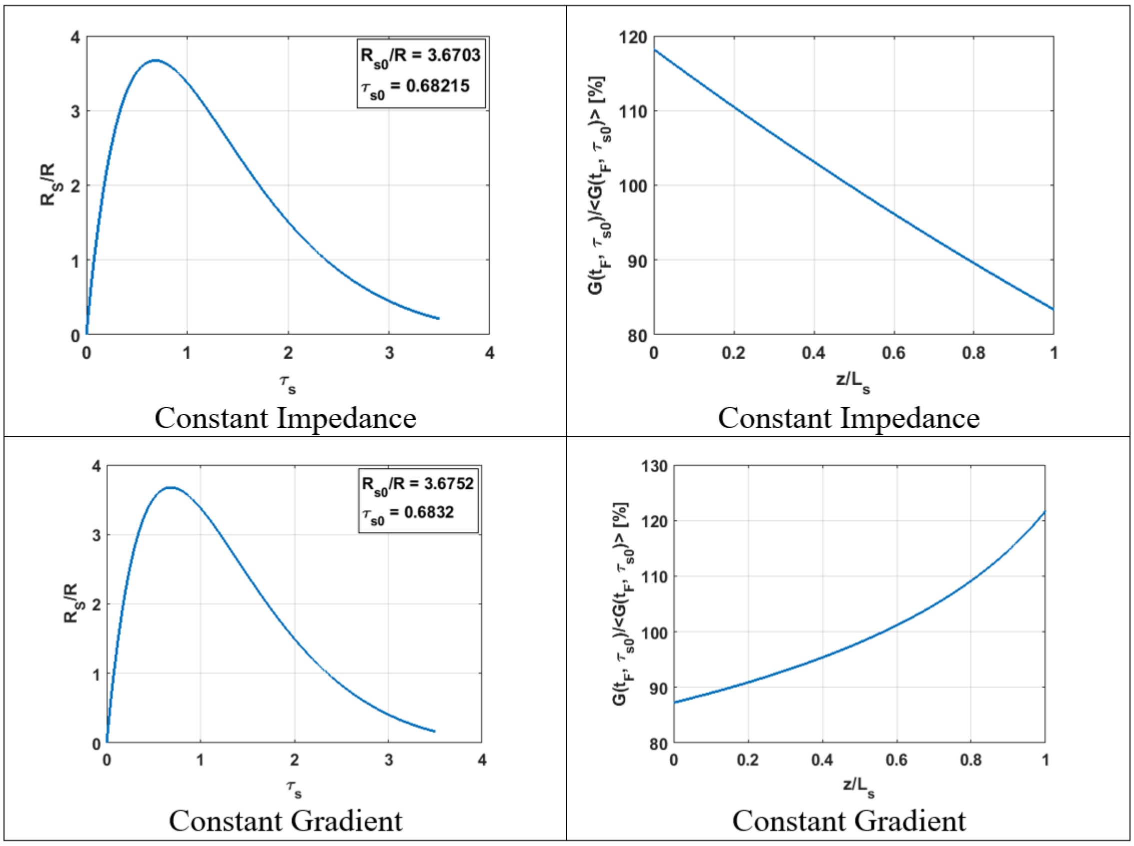

Figure 9.2: Effective shunt impedance as a function of the section attenuation and resulting accelerating field profile.

In the left column, the plots show the values of the "effective" shunt impedance per unit length R_s normalized to the ordinary shunt impedance per unit length R, as a function of the parameter $\tau_s = \alpha \cdot L_s = (\omega_{RF}/2Q) \cdot \tau_F$, being α the linear attenuation coefficient of the structure, L_s its length and τ_F the structure filling time. The definitions of R and R_s are the following:

$$R = \frac{E_{acc}^2}{|dP/dz|}; \qquad R_s = \frac{\langle E_{acc}^2 \rangle_{avg}}{P_{in}/L_s}$$

The maximum value of the R_s/R ratio is ~ 3.67, a number larger than 1 since it accounts for the peak power gain factor provided by the pulse compressor. It is reached when $\tau_{s0} \sim 0.68$ which corresponds to a filling time value $\tau_F \sim 120$ ns. The values obtained with constant impedance and constant gradient sections are similar, so this parameter does not determine the choice between the two options. The dimensions of the basic cell of the TW accelerating section have been parametrized and simulated with HFSS code to calculate all the characteristic parameters of the structure. The cell model for simulations is shown in figure 9.3.

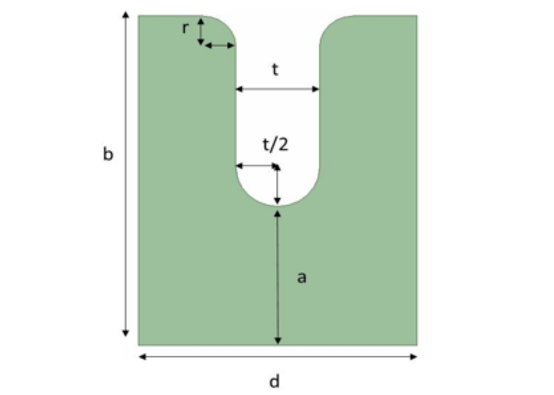

Geometrical parameters	
a[mm]	2 ÷ 5
b [mm]	9.828 ÷ 10.917
d [mm]	8,332 (2π/3 mode)
r [mm]	1
t [mm]	2.5

Figure 9.3: Basic EuPRAXIA@SPARC_LAB X-band accelerating cell.

The aim of the simulations was to scan the structure characteristics for iris radius values a varying in the $2-5$ mm range. For each value of a, the cell has been tuned to the nominal frequency (11.9942 GHz) by varying the cell radius b, while the other dimensions have been kept fixed. The chosen phase advance of the TW structure is $2\pi/3$, so that the length d of the cell is $1/3^{rd}$ of the RF wavelength.

The main characteristic parameters of the TW structure (such as attenuation constant, group velocity, shunt impedance per unit length, Q factor and modified Poynting's vector) have been calculated as function of the iris radius a and are reported in Figure 9.4 plots. The attenuation constant and group velocity depend critically on the iris aperture, while the shunt impedance per unit length shows an approximately linear dependence and the Q-factor excursion is very limited ($\sim 5\%$) in the explored range.

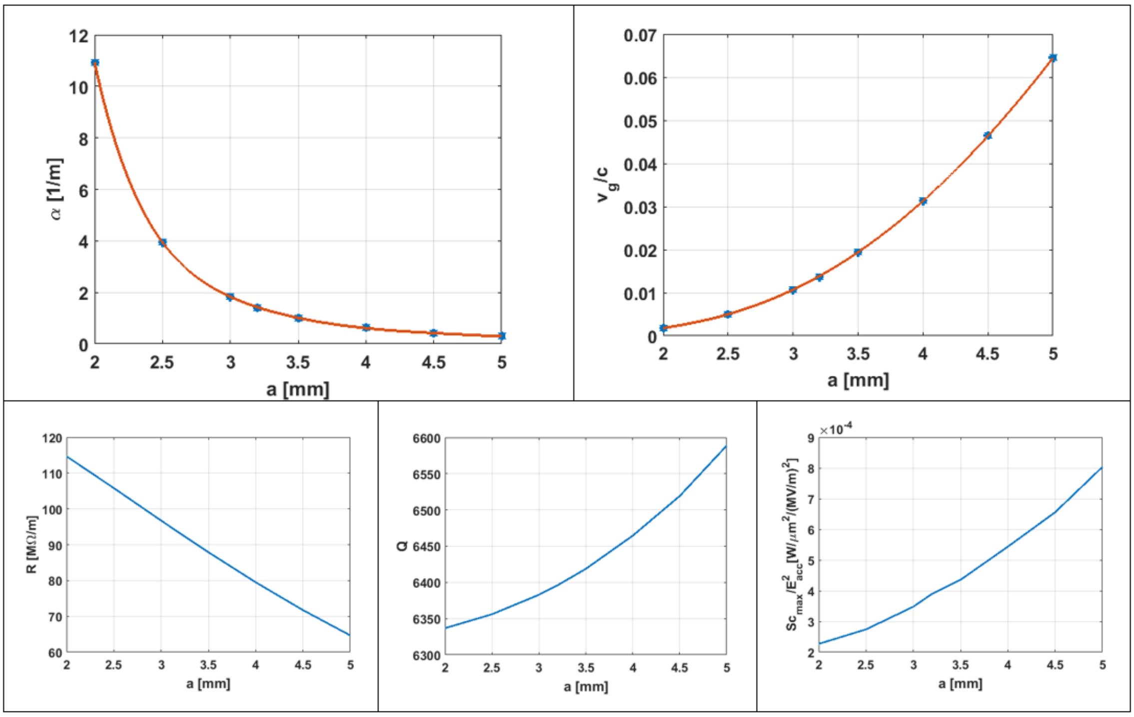

Figure 9.4: TW accelerating section characteristics as a function of iris radius.

The choice of the iris aperture design value is a trade-off between efficiency, that pushes towards small values of a, and different technical and beam dynamics related considerations (such as energy spread, emittance growth, beam stay clear margins, alignment tolerances and so on), pushing towards larger values of a. In particular, calculations on beam breakup (BBU) limits due to the transverse wakefield of the accelerating sections scaled to the EuPRAXIA@SPARC_LAB beam parameters have led to a minimum acceptable value of the iris aperture of a = 3.2 mm [6, 7]. This value, together with the optimal total attenuation and filling time reported in Figure 9.2, is sufficient to complete the TW section design. The main parameters characterizing a constant gradient TW X-band section for the EuPRAXIA@SPARC_LAB linac are summarized in Table 9.2 and thoroughly described in [8].

Accelerating section parameter	Symbol	Unit	Value
Average iris radius	$\langle a \rangle$	mm	3.2
Structure length	L_s	mm	500
Quality factor	Q		6400
Normalized group velocity	v_g/c	%	2.5 – 0.77
Filling time	τ_F	ns	121
Number of cells	N_c		60
Average shunt impedance per unit length	$\langle R \rangle$	MΩ/m	94
Effective shunt impedance per unit length	R_s	MΩ/m	345

Table 9.2: Characteristics of the EuPRAXIA@SPARC_LAB constant gradient accelerating section.

9.5 X-band linac layout

The TW X-band accelerating sections optimized for the EuPRAXIA@SPARC_LAB application are 0.5 m long and show an effective shunt impedance per unit length of $\sim$ 345 MΩ/m, value that accounts also for the peak power gain provided by the pulse compressor. The fraction of the klystron RF power required by each accelerating section to reach the $\sim$ 57 MV/m average gradient (i.e. the minimum needed to provide a $\sim$ 1.050 GeV beam to the magnetic undulator without plasma contribution) is then:

$$P_{in} = \frac{\langle E_{acc}^2 \rangle_{avg}}{R_s/L_s} = 4.7\,\mathrm{MW}$$

Commercially available X-band klystrons provide up to 50 MW peak power in $\sim$ 1.5 µs long pulses. RF losses in the waveguide distribution system are estimated to reduce the klystron available power to the accelerating sections by $\sim$ 20%, so that a single tube can actually deliver $\sim$ 40 MW. Thus, up to 8 TW structures can be fed in parallel at the required gradient by a single klystron. For this reason, the basic RF module of the EuPRAXIA@SPARC_LAB X-band linac can be conveniently composed by a group of 8 TW sections assembled on a single girder and powered by a single klystron connected to a pulse compressor system and a waveguide network splitting and transporting the RF power to the input couplers of the sections. Each RF module will provide an active length of 4 m, while its actual physical length will be $\sim$ 5 m to accommodate flanges, vacuum equipment, beam diagnostics stations and magnets. Linac 1 and Linac 2 will host 4 RF modules in total, corresponding to 32 accelerating sections. Since, at present, 12 out of 32 TW sections have been placed in L1 and 20 out of 32 have been placed in L2, one RF module needs to be split into 2 sub-modules of 4 sections each, to be placed on both sides of the magnetic chicane. This configuration (4 RF modules driven by 4 klystrons) is already sufficient to provide the minimum nominal beam energy for the different operational scenarios, however its optimization is still in progress.

The linac energy could be increased by doubling the RF power on one or more modules by simply adding a second klystron. Upgraded modules could run with an increased gradient up to ~ 80 MV/m. Thanks to the modularity of the RF system, the RF power upgrade of the modules can be planned in various steps according to the needs of the facility. This will provide a gradient overhead that could be exploited to increase the operation flexibility and, ultimately, to reach higher beam energies (up to ~ 1450 MeV). A sketch of one RF module powered in initial (left) and upgraded (right) configurations is shown in Figure 9.5, while the main parameters of the X-band linac RF system are reported in Table 9.3.

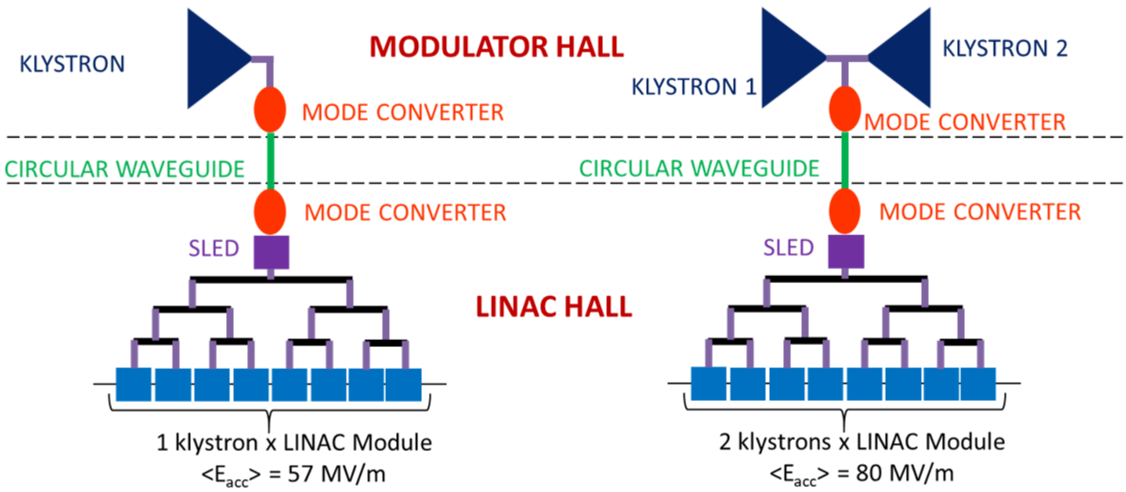

Figure 9.5: Schematics of a 8-sections RF module powered either by one (left) or two (right) klystrons.

	Parameter	Unit	Value		
N_s	Number of sections		32 (4 modules x 8 sections)		
P_k	RF power available/klystron	MW	50 (at klystron output couplers) 40 (at section input couplers)		
			PWFA – LWFA	Full X-band	Ultimate
$\langle E_{acc} \rangle$	Max. average gradient	MV/m	36	57	80
P_{RF}	Total RF power required	MW	46	158	310
N_k	Number of klystrons		4 (reduced power)	4 (full power)	8 (full power)

Table 9.3: Main parameters of the X-band linac RF system for different scenarios: injection in the plasma (LPWA – PWFA), injection in the undulator (Full X-band) and ultimate performance.

The RF system layout and the waveguide network distribution will remain unchanged downstream the 2-klystron power combiner. The standard WR-90 rectangular waveguide supporting the TE_{10} mode at 12 GHz shows a ~ 0.1 dB/m attenuation. Thus, the choice is not suitable for long distance connections, such as the one between the RF power station (klystron gallery) and the RF module (accelerator hall). For this reason, the majority of this length will be covered by a round overmoded WC-50 waveguide, showing a much lower attenuation of ~ 0.013 dB/m. Two mode converters need to be placed to interface the 2 waveguide standards. The pulse compressor (SLED) will be placed downstream the low attenuation connection, just in front of the power splitter network feeding the 8 TW structures.

Bibliography

[1] W. Wuensch. "Ultimate Field Gradient in Metallic Structures". In: *Proc. of International Particle Accelerator Conference (IPAC'17), Copenhagen, Denmark, 14-19 May, 2017*. 8. 2017, pp. 24–29.

[2] T. Shintake. "The SACLA X-Ray Free-Electron Laser Based on Normal-Conducting C-Band Technology". In: *Synchrotron Light Sources and Free-Electron Lasers: Accelerator Physics, Instrumentation and Science Applications*. Springer International Publishing, 2014, pp. 1–48.

[3] F. Löhl et al. "Status of the SwissFEL C-band Linac". In: *36th International Free Electron Laser Conference FEL 2014 (FEL 2014)*. Aug. 2014, pp. 322–326.

[4] D. Alesini et al. "The C-Band accelerating structures for SPARC photoinjector energy upgrade". In: *Journal of Instrumentation* 8.05 (2013), P05004.

[5] Z. D. Farkas et al. "SLED: A Method of Doubling SLAC's Energy". In: *Proceedings, 9th International Conference on the High-Energy Accelerators (HEACC 1974): Stanford, California, May 2-7, 1974*. 1974, p. 576.

[6] A. W. Chao. *Physics of collective beam instabilities in high-energy accelerators*. Wiley, New York, USA, 1993. ISBN: 9780471551843.

[7] K. L. F. Bane. *Short range dipole wakefields in accelerating structures for the NLC*. Tech. rep. 2003.

[8] M. Diomede et al. "Preliminary RF design of an X-band linac for the EuPRAXIA@SPARC_-LAB project". In: *In press, Nuclear Instruments and Methods in Physics Research Section A: Accelerators, Spectrometers, Detectors and Associated Equipment* (2018). ISSN: 0168-9002. DOI: https://doi.org/10.1016/j.nima.2018.01.032.

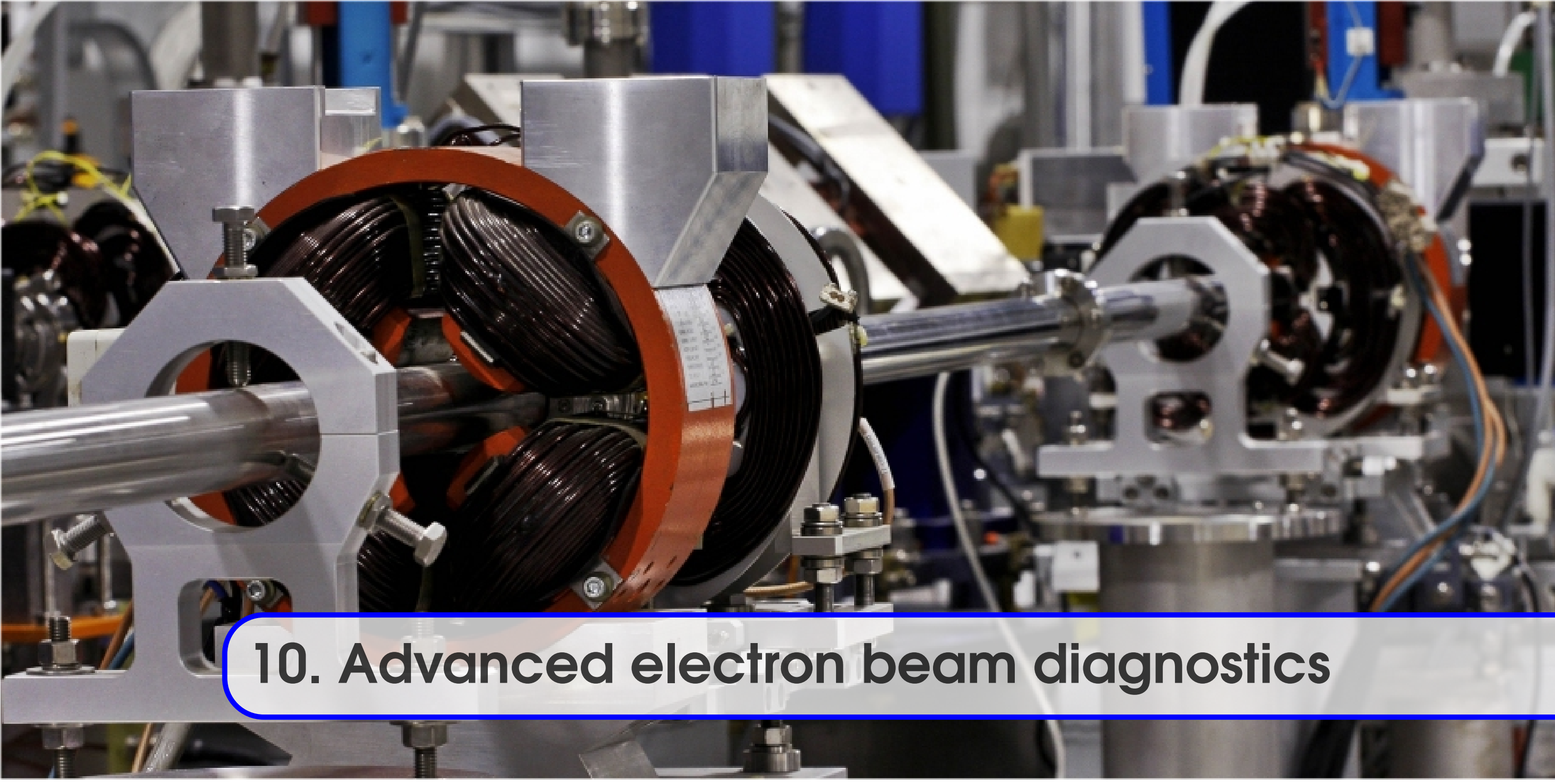

10. Advanced electron beam diagnostics

This machine will produce electron beams with high brightness, short temporal duration and small transverse emittance. Moreover, also plasma accelerated beams will be available in different schemes. To cover all the possible scenarios the beam diagnostics must be particularly advanced. For electron beam accelerated by the main linac, we can allow multi-shot measurements, mainly due to the inherent machine stability, while single shot measurements are preferable for the plasma accelerated beams. At the entrance of plasma booster the beam transverse dimension is in order of μm RMS, and its length is in the order of few fs. After the plasma acceleration, bunch length and emittance are quite preserved, but the inherent instability of the plasma acceleration demands also single shot measurements. We will divide our analysis in three different branches: transverse, longitudinal, charge and trajectory diagnostics. We will introduce first the suggested devices and later their exact positions inside the machine.

10.1 Diagnostics devices

For sake of simplicity we can divide the linac in four different areas: D1) gun; D2) injector up to the bunch compressor; D3) bunch compressor and linac; D4) plasma accelerator and undulator matching. For electron beam accelerated by the main linac, we can allow multi shot measurements, mainly due to the inherent machine stability, while for the plasma wake accelerated beams single shot measurements are mostly desirable. For the main linac a lot of state of art and conventional diagnostics are available. However, the resolution of such instrumentations must be pushed to the frontier of the available techniques. When we consider to build a compact machine also the diagnostics must be scaled in order to waste as less as possible space. This will translate in a completely rethinking of the actual devices used for instance in SPARC_LAB.

10.1.1 Transverse diagnostics

There are two main measurements for transverse diagnostics: emittance and envelope. The envelope is very important in order to properly match the beam along the machine comparing the measured dimension with the simulated ones. Usually scintillator screens, like YAG:Ce, or Optical Transition Radiation (OTR) monitors are in use for such a task. In particular, YAG screens are a must when the beam charge is below about few tens of pC, due to their better photon yield. In order to alleviate the problem of the depth of field and the crystal view angle [1], the conventional mounting considers to put the YAG normal to the beam line and a mirror placed at 45 degrees with respect to this direction to reflect the radiation at 90 degrees with respect to the beam line. This radiation is then extracted via a vacuum windows and imaged on a CCD. This scheme is already in use at SPARC_LAB.

Compact design is required in order to preserve the compactness of the whole machine. As an example in Fig. 10.1 is shown a new compact design that uses only 40 mm of longitudinal space to host this device.

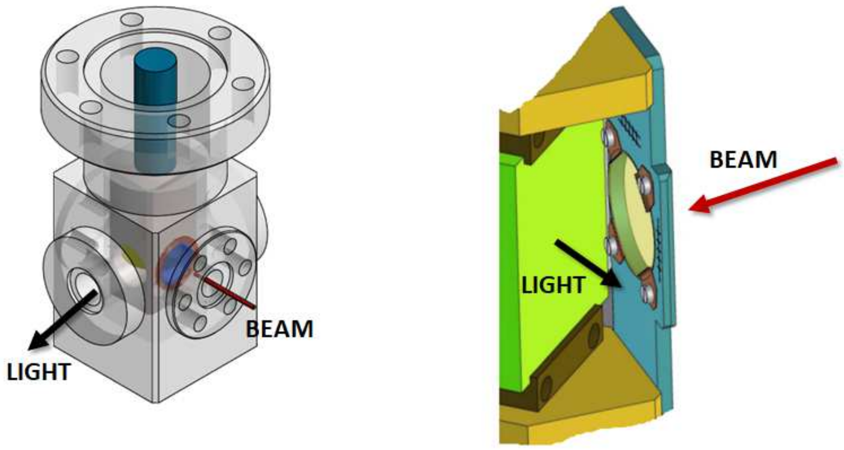

Figure 10.1: Example of a compact design for beam size measurements. The overall length is only 40 mm. Left: 3D CAD drawing of the whole vacuum chamber with the screen inside; Right: the geometry of the YAG:Ce and mirror holder.

Transverse emittance measurements will be performed with the well-known technique of quadrupole scan [2], where the beam size is recorded versus the current of a magnetic lens, in two different positions, one in D2 and the other in D4. However, this technique is inherently multi shot, so not suitable for plasma acceleration. However, for plasma accelerated beams the inherent shot by shot instabilities, with high beam divergence, and the needs to separate driver and witness, prevent the use of such a diagnostics just after the plasma channel. In particular the large energy spread (usually above % level) is a serious drawback. Its value must be also kept as low as possible because, following reference [3], even the 6D RMS normalized emittance is not preserved in a drift with energy spread, and so the measurement of the emittance is strongly dependent on the measurement position. This point is usually neglected but it deeply impacts on the beam quality. We recall that the total normalized emittance squared is:

$$\varepsilon_n^2 = \langle\gamma\rangle^2 \sigma_\varepsilon^2 \langle x^2\rangle \langle x'^2\rangle + \langle\beta\gamma\rangle^2 \left(\langle x^2\rangle \langle x'^2\rangle - \langle xx'\rangle^2\right) \tag{10.1}$$

where γ is the usual relativistic factor, β is the ratio of the speed of the particle to the speed of light, σ_ε is the percentage energy spread.

Due to the presence of a non negligible energy spread, and being the divergence term usually in the order of mrad, the first term will be the leading one after some drift. At this point the normalized emittance has grown significantly, spoiling the beam properties.

Recently it was introduced the concept of chromatic length [4], defined as the distance where the emittance grows of a factor $\sqrt{2}$ as

$$L_C = \frac{\sigma_x}{\sigma_x' \sigma_E} \tag{10.2}$$

where σ_x is the RMS beam size, σ_x' is the RMS beam divergence and σ_E is the relative RMS energy spread at plasma extraction. In a conventional accelerator L_C is usually longer than the whole machine, while in plasma accelerators, depending on the value of the energy spread, could be in a range between few centimeters and few meters. To overcome this problem the only solution is a fast capture of this beam and a mitigation of the energy spread, even at cost of some charge reduction.

For these reasons we consider the use of a different approach in order to measure the beam parameters. We plan to measure them inside the plasma channel, and only after the machine optics devoted to capture the beam, to separate the driver and witness and eventually to reduce the beam energy spread. So we do not foreseen any measurement just after the plasma channel.

The measurement inside the plasma can be performed by means of betatron radiation. The diagnostics based on betatron radiation [5] has been developed in recent years in several laboratories, relying on the measurement of the spectrum, (for instance among the other see [6]) or on the diffraction from a knife edge [7].

However, these systems were able to measure just the beam profile and divergence, neglecting the correlation term. Only recently we developed a new algorithm in order to retrieve the correlation term [8]. Using the simultaneous measurement of the electron and radiation energy spectrum together with the plasma density, it is possible to have a reconstruction of the whole phase space. This measurement relies on some approximation on the initial phase space of the particles, because it was performed on a beam produced by self-injection mechanics. If the beam is externally injected inside the plasma, the knowledge of the initial 6D phase space removes also this ambiguity.

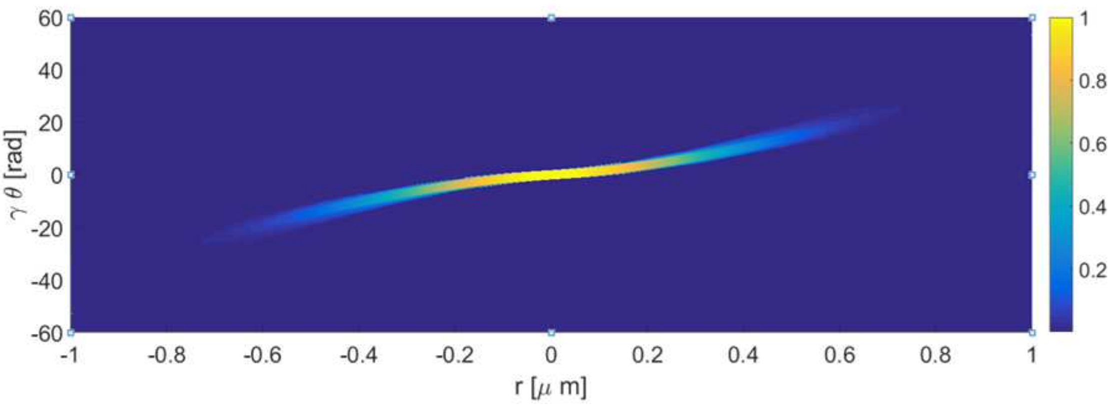

Figure 10.2: Reconstructed phase space with betatron radiation from self-injected electron beam.[8].

In Fig. 10.2 is reported a reconstructed phase space with this technique. Laser parameters: energy 1J, pulse duration 30 fs (FWHM), 10 μm diameter focus, $a_0 \approx 4.4$; plasma density $=(8 \pm 1) \times 10^{18}$ cm^{-3}.

This algorithm is based on the reconstruction of the beam 1D profile rather than just the beam size. Also the full 2D beam profile characterization has also been shown to be possible to be measured using the correlation between spectrum and angle [9]. In order to collect the betatron radiation, sooner or later we have to separate the radiation from the electron beam, with a dipole. Unfortunately the bending of the beam produces synchrotron radiation, and its spectrum can overlap with the betatron radiation.

We observe that usually the betatron radiation is much stronger with respect to synchrotron radiation, and there is the additional degree of freedom of the bending angle. The possibility to

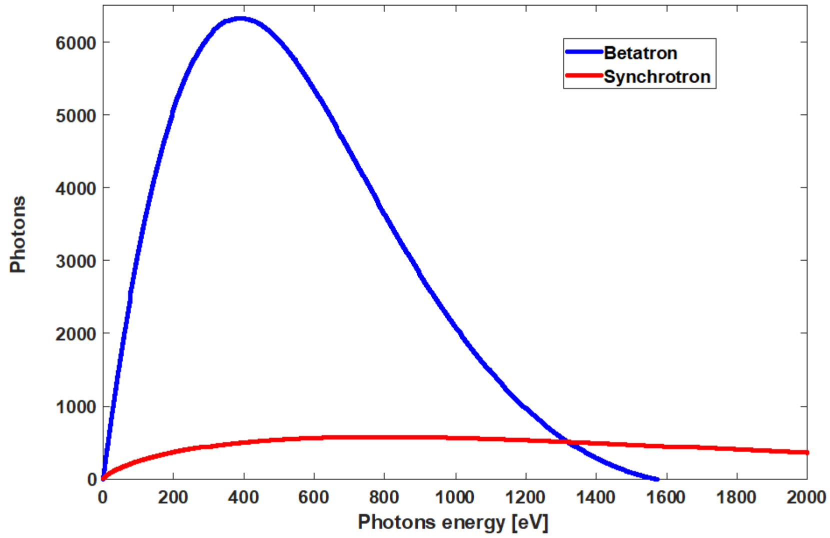

Figure 10.3: Comparison between Synchrotron radiation emitted by a bending magnet and Betatron radiation. Beam charge 30 pC, energy 1 GeV, plasma density 2 10^{16} cm^{-3}; magnet filed 1.5 T, radius of curvature 2.2 m

increase the magnetic field allows to move the peak of the synchrotron radiation at higher frequency, resulting in a better separation with betatron radiation.

In Fig. 10.3 we reported a comparison between the spectrum of the betatron radiation of 30 pC beam accelerated up to 1 GeV inside a plasma and the synchrotron radiation produced by a bending magnet. Details of the simulation are in the caption. However, an open problem is related to the separation between the betatron radiation coming from the witness and from the driver in the beam driven scheme. In this case the driver contains much more charge with respect to the witness and so only a clear energy separation of the two spectra can solve the problem. Obviously in the case of external injection this problem disappears.

In this case we are testing at SPARC_LAB a new diagnostics, called OSE (One Shoot Emittance) [10]. It is based on the analysis of the angular distribution of the OTR, sampled with a microlens array in order to retrieve also the correlation term. A R&D program is needed in order to fully develop this diagnostics.

We do not expect any contribution from coherent radiation, because our bunch length is quite longer than optical wavelength and the use of a moderate compression with velocity bunching should avoid the formation of microbunching inside the bunch. However our system is fully compatible with a possible upgrade to use the solution adopted at SACLA [11] to suppress the coherent radiation contribution.

10.1.2 Longitudinal diagnostics

Longitudinal diagnostics is mandatory to clearly set the correct compression phase in the velocity bunching and to recover the correlated energy spread induced in this way. We consider to use different methods, tailoring the instrumentations to the particular machine condition. The single shot longitudinal phase space measurement will be performed with an X-band RF deflector (RFD), i.e a RF cavity with a transverse deflecting mode, combined with a magnetic dipole. The need of an X-band cavity is mainly due to the fs scale resolution obtainable in such a way. While this device can reach such a resolution, particular attention must be put in its design. The reduced iris aperture and the possibility that the beam goes out of the center inside the device, due to the transverse field, must be considered with beam dynamics simulations. Only one X-band RFD is operating so far at SLAC [12]. It is designed for an energy one order of magnitude greater, so it could be used as a reference but it must be rescaled, at least in its length. Other studies are ongoing for instance in DESY for the SINBAD and EuPRAXIA project. We'll surely take profit from their development.

We consider to place this device in two positions, in D2 and D4 region. However, for one shot not intercepting bunch length measurement, useful for instance when the beam is sent in a plasma module to correlate input and output properties of the bunches, two other systems must be implemented. Diffraction radiation is emitted when a charged particle passes through a hole with transverse dimension smaller with respect to the radial extension of the electromagnetic field traveling with the charge. Coherent emission arises when the observed wavelength is longer with respect to the bunch length. For our case, where this time length can be in the range between few ps and few fs, it means to have several detectors each one sensitive to a range of wavelengths ranging from FIR to VIS light. This kind of measurement can be performed in multi shot mode using a Martin Pupplet or Michelson interferometer, or in a single shot (highly desirable) disperding the radiation and collecting it in a linear detector. The complete analysis of the spectrum leads to the reconstruction of the longitudinal bunch shape. There are so far only few prototypes of dispersive detector able to measure the radiation spectrum in one single shot, one based on a single KRS-5 (thallium bromoiodide) prism [13], and another on a series of diffracting grating [14]. So, an extensive R&D program must be started also for this device.

Also, in order to set the compression phase, sometimes only a relative measurement of the coherent radiation integrated on the whole bandwidth of the detector is enough. We foreseen to use this compression monitor in two positions, in D2 and D3, along the machine. This system can be also used to monitor the phase stability of the section used for compression and to eventually stabilize it with a feedback.

Another single shot device is based on EOS (Electro Optical Sampling). The electric field co-propagating with the bunch can rotate the polarization of a laser impinging on a non linear crystal such as GaP or ZnTe. Using a scheme called "spatial decoding" [15], realized with an angle of incidence between the probe laser and the crystal, it is possible to retrieve the longitudinal beam profile in one shot. The advantage of such a scheme with respect to coherent radiation is definitely that there is no reconstruction of the bunch shape starting with frequency analysis, with the problems related to the correct transport and propagation of all the wavelengths in the spectrum. But the disadvantage is the temporal resolution, limited or by the crystal bandwidth or by the length of the laser probe. Typical values are in the order of 40-50 fs. However, this diagnostics will be very important in our machine because while the X-band RFD offers a high resolution for the measurement of very short bunches, i.e. in the fs region, it will be not the best choice for ps bunch length. On the other end the EOS can cover easily this range of dimensions, being also not intercepting.

We should also consider to use a capillary in D4 as plasma deflector, a device recently proposed but not yet realized, with a resolution down to the as scale [16].

10.1.3 Charge and trajectory diagnostics

The control of the charge and the trajectory at a few pC and few μm is mandatory in this machine, especially in the D4 section. About the charge, Bergoz Turbo-ICT (integrated current transformer) can be the best choice, allowing the measurement of a charge as low as 50 fC. We consider to have 4 of them, one in D1, one in D3 and two in D4. Regarding the optics we are very sensitive to the beam trajectory at the entrance of every RF module, in particular the part of the machine in X-band, and inside the D4 section. Conventional stripline BPM (Beam position monitor), similar to those already in use at SPARC_LAB can be considered for such a task. They can offer good signal to noise ratio down to few pC charge and a resolution in the order of tens of μm . However, this kind of devices can be used only at the beginning of the accelerator, where the beam pipe is 40 mm. But starting from X-band structures, the pipe size will decrease. Also, one of the most important parameter is the length of the device. Due to the large number of such a system its length must be as short as possible.

There are several studies of very compact C or X-band cavity BPM [17], with a total length of about 10 cm, that can be useful consider for such a task. There is also another interesting possibility, successfully used at NLC [18] and under consideration at CALIFES at CERN: to use the dipole mode excited by an off-axis beam in the X-band accelerators modules. The resolution will decrease to about 10 µm, in any case absolutely sufficient for us, but at the same time there is no need to implement cavity BPMs, with a huge space economy. In reality, at least some cavity BPMs must be implemented to cross calibrated the dipole mode, but their number will substantially decrease.

10.2 Diagnostics layout

In this section we place the diagnostics devices on the machine layout. While the drawings are really a sketch, they are in scale, i.e. their relative dimensions are preserved.

10.2.1 D1: GUN

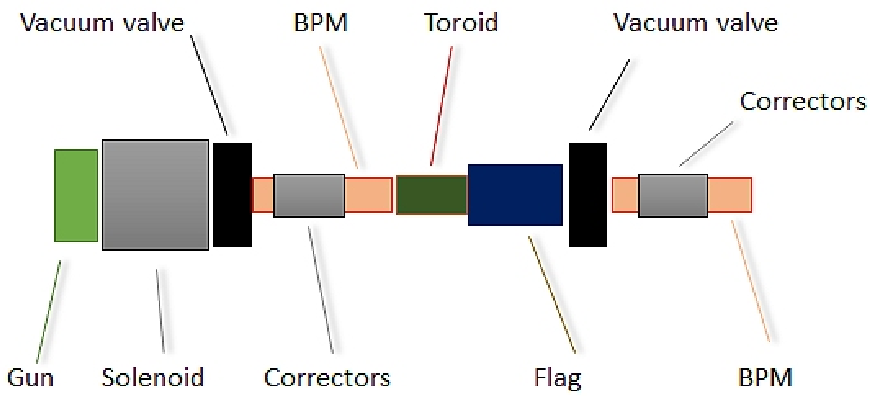

Figure 10.4: Sketch design of the gun section with the proposed diagnostics.

In the Gun area several measurements will be performed: energy, charge, trajectory, thermal emittance and cathode quantum efficiency map, check of the laser center on cathode, check of the spot size at the beginning of the first accelerating module. The energy will be measured by using the corrector just after the solenoid and recording the beam center of mass in the downstream flag versus the current. The toroid will record the charge, while the two striplines will monitor the beam trajectory just after the solenoid and before the injection in the first accelerating module. A couple of x-y correctors will be placed around the BPM to correct the position where it is measured. The Thermal Emittance will be measured using the so called Solenoid-scan technique [19], i.e. varying the current inside the solenoid will result in different focalization on the flag screen. This measurement, together with the control of the cathode quantum efficiency, will help also in the determination of the cathode performance. Also, the correct laser position on the center of the photo-cathode can be monitored imaging the beam on the flag and varying the injection phase. The envelope invariant emittance compensation scheme sets the beam spot at the entrance of the accelerating chain which can be measured on the flag.

10.2.2 D2: Injector up to the bunch compressor

In this sector the beam will be compressed by means of velocity bunching and later accelerated before entering in the bunch compressor. Between the S-band structure is very important to check the beam trajectory, to properly enter in the center of the structures, and the beam size, in order to reconstruct the envelope. We can figure to have a very compact diagnostics device, including a cross with a view screen, a stripline or cavity BPM embedded in a corrector. All of these devices will be hosted in a longitudinal space of about 300 mm, included a door for vacuum pumping. Of course, at least 2 different designs will be necessary, one for the S-band linac, the other for X-band in order to match the beam pipe size, and the beam different energy. We can refer to these devices as SNOB (ScreeN cOrrector and Bpm) system. We plan to place them every single S-band structure and every two X-band structures. In this region we consider to have a triplet of quadrupole to perform emittance measurement via quad scan. A dipole will allow the control of the energy and the energy spread after the first compression stage. The use of an X-band RFD will allow bunch length and longitudinal phase space measurements. We plan also to use one of the diagnostic station to allocate a non linear crystal to implement a longitudinal single shot not intercepting measurement via EOS.

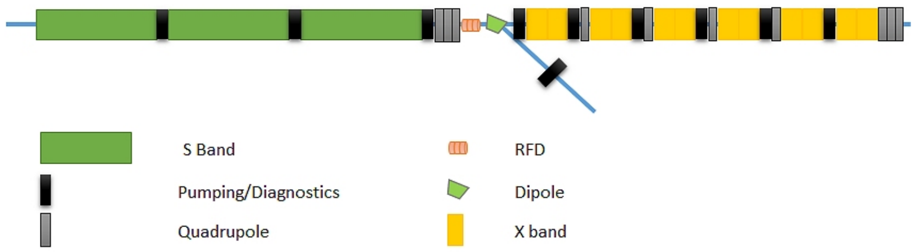

Figure 10.5: Sketch design of the injector and linac L1 section with the proposed diagnostics.

10.2.3 D3: Bunch compressor up to plasma module

In the bunch compressor we plan to install three SNOB devices in every arm, plus one in the straight line before the quadrupole duplet. The main goal is the control of the trajectory and the envelope.

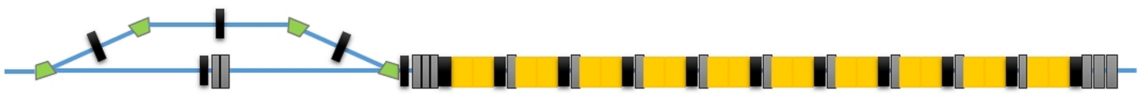

Figure 10.6: Sketch design of the BC and linac L2 section with the proposed diagnostics.

However, we can also consider to put a skew quad in the dispersive arm and to image the beam in a screen downstream in order to have also here a measurement of the bunch length. Also, the first screen after the last dipole can be equipped with a diffractor radiatior to host a single shot bunch length measurement based on coherent radiation.

10.2.4 D4: Plasma accelerator and undulator matching

This is the most crucial and challenging part for the diagnostics. Surely, we will measure the charge entering in the plasma accelerator and leaving from it. Inside the plasma accelerator will be view screens to image the beam before the plasma interaction and after. About these screens only OTR monitor allow a resolution below few µm needed in this case. Also in this sector we measure transverse emittance (via quad scan), and all the longitudinal parameters included the phase space, via the RFD. However, an OSE device will be placed to perform single shoot measurement, as well a X-ray detector to collect the betatron radiation emitted by the beam inside the plasma in order to measure the transverse parameter during the interaction [8].

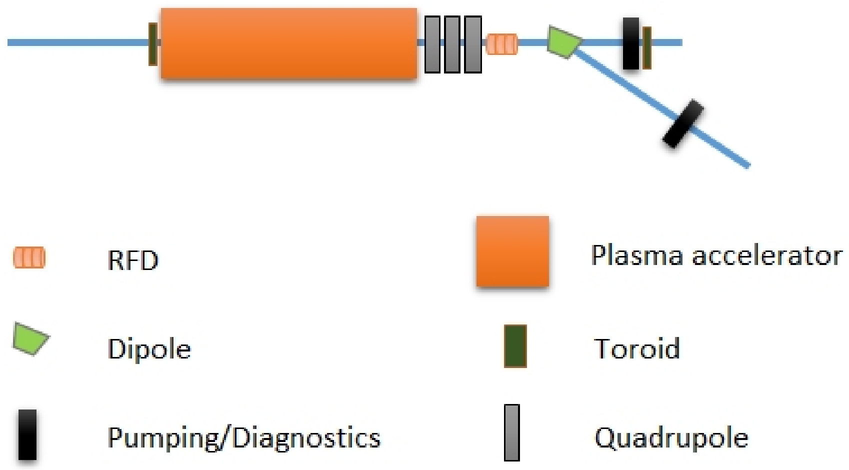

Figure 10.7: Sketch design of the plasma section with the proposed diagnostics.

Bibliography

[1] G Kube et al. "Inorganic scintillators for particle beam profile diagnostics of highly brilliant and highly energetic electron beams". In: *Proceedings of IPAC2012, New Orleans, Lousiana, USA* (2012).

[2] F Löhl et al. "Measurements of the transverse emittance at the FLASH injector at DESY". In: *Physical Review Special Topics-Accelerators and Beams* 9.9 (2006), p. 092802.

[3] M Migliorati et al. "Intrinsic normalized emittance growth in laser-driven electron accelerators". In: *Physical Review Special Topics-Accelerators and Beams* 16.1 (2013), p. 011302.

[4] M Rossetti Conti and al. "Electron beam transfer line design for plasma driven free electron lasers". In: *submitted toNuclear Instruments and Methods in Physics Research Section A: Accelerators, Spectrometers, Detectors and Associated Equipment* (2017).

[5] Antoine Rousse et al. "Production of a keV X-ray beam from synchrotron radiation in relativistic laser-plasma interaction". In: *Physical review letters* 93.13 (2004), p. 135005.

[6] GR Plateau et al. "Low-emittance electron bunches from a laser-plasma accelerator measured using single-shot x-ray spectroscopy". In: *Physical review letters* 109.6 (2012), p. 064802.

[7] S Kneip et al. "Characterization of transverse beam emittance of electrons from a laser-plasma wakefield accelerator in the bubble regime using betatron x-ray radiation". In: *Physical Review Special Topics-Accelerators and Beams* 15.2 (2012), p. 021302.

[8] A Curcio et al. "Trace-space reconstruction of low-emittance electron beams through betatron radiation in laser-plasma accelerators". In: *Physical Review Accelerators and Beams* 20.1 (2017), p. 012801.

[9] A Curcio et al. "Single-shot non-intercepting profile monitor of plasma-accelerated electron beams with nanometric resolution". In: *Applied Physics Letters* 111.13 (2017), p. 133105.

[10] A Cianchi et al. "Transverse emittance diagnostics for high brightness electron beams". In: *Nuclear Instruments and Methods in Physics Research Section A: Accelerators, Spectrometers, Detectors and Associated Equipment* 865 (2017), pp. 63–66.

[11] S Matsubara et al. "Improvement of screen monitor with suppression of coherent-OTR effect for SACLA". In: *Proc. of 1st Intl. Beam Instrumentation Conf., Tsukuba, Japan*. 2012, pp. 34–37.

[12] Valery A Dolgashev and Juwen Wang. "RF design of X-band RF deflector for femtosecond diagnostics of LCLS electron beam". In: *AIP Conference Proceedings*. Vol. 1507. 1. AIP. 2012, pp. 682–687.

[13] TJ Maxwell et al. "Coherent-radiation spectroscopy of few-femtosecond electron bunches using a middle-infrared prism spectrometer". In: *Physical review letters* 111.18 (2013), p. 184801.

[14] Stephan Wesch et al. "A multi-channel THz and infrared spectrometer for femtosecond electron bunch diagnostics by single-shot spectroscopy of coherent radiation". In: *Nuclear Instruments and Methods in Physics Research Section A: Accelerators, Spectrometers, Detectors and Associated Equipment* 665 (2011), pp. 40–47.

[15] R Pompili et al. "First single-shot and non-intercepting longitudinal bunch diagnostics for comb-like beam by means of Electro-Optic Sampling". In: *Nuclear Instruments and Methods in Physics Research Section A: Accelerators, Spectrometers, Detectors and Associated Equipment* 740 (2014), pp. 216–221.

[16] Irene Dornmair et al. "Plasma-driven ultrashort bunch diagnostics". In: *Physical Review Accelerators and Beams* 19.6 (2016), p. 062801.

[17] A Benot-Morell et al. *Status of the Stripline Beam Position Monitor developement for the CLIC Drive Beam*. Tech. rep. 2013.

[18] Chris Adolphsen et al. "Wakefield and beam centering measurements of a damped and detuned X-band accelerator structure". In: *Particle Accelerator Conference, 1999. Proceedings of the 1999*. Vol. 5. IEEE. 1999, pp. 3477–3479.

[19] Eduard Prat and Masamitsu Aiba. "Four-dimensional transverse beam matrix measurement using the multiple-quadrupole scan technique". In: *Physical Review Special Topics-Accelerators and Beams* 17.5 (2014), p. 052801.

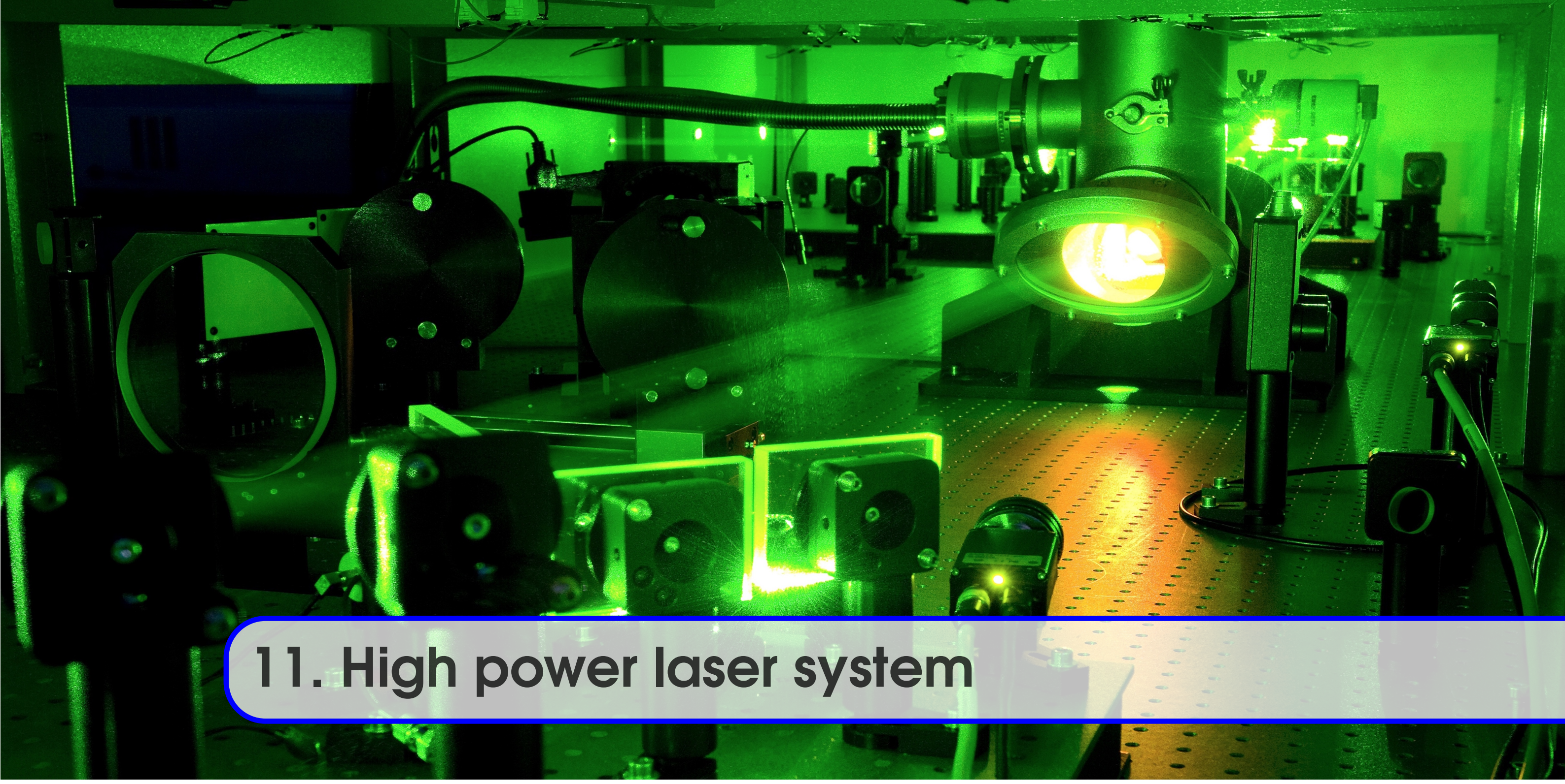

11. High power laser system

11.1 The high power laser FLAME: the existing infrastructure

FLAME is the acronym for Frascati Laser for Acceleration and Multi-disciplinary Experiments. The project that has seen FLAME installed was established in 2004 from a large collaboration between INFN in Frascati, CNR in Pisa, LOA in Palaiseau and CEA in Saclay. Since the beginning, the laser system has been used in a wide range of experiments ranging from self-injection of electrons, to light ion acceleration and Compton scattering. The laser is a standard CPA based 250 TW system, which is composed by the following subsystems:

- An ultra short (15 fs), large bandwidth oscillator at 85 MHz repetition rate;
- A booster to amplify the pulse and to enhance the temporal contrast ratio – this also reduces the repetition rate from 85 MHz to 10 Hz;
- A stretcher to pass from a short pulse to a long, chirped pulse;
- A regenerative amplifier to raise the pulse energy from the nJ level to the mJ level;
- A series of multipass amplifiers (three in the actual system) to increase the energy from the mJ up to 7 J;
- A compressor to compress the pulse duration back to the fs level (down to a minimum of 24 fs).
- Two different beam lines to transport the laser beam to the FLAME interaction chamber or to the accelerator bunker.

Table 11.1 summarizes the actual laser beam parameters.

A layout of the existing FLAME laboratory is shown in Fig. 11.1.

11.2 Laser systems for EUPRAXIA@SPARC_LAB

For the EUPRAXIA@SPARC_LAB project, the high power laser has a very important role, which is to drive the plasma wake in case of external injection operation. Moreover, as it is already in SPARC_LAB, the laser can be used also by itself in a large range of experimental configurations. The space allocated in EUPRAXIA@SPARC_LAB for the laser system is equivalent to what is needed for a 1 PW class laser (about 200 m^2 + a rack room). In particular, the laser room will be at

	Units	value
Central wavelenght	nm	800
Bandwidth	nm	60 – 80
Repetition rate	Hz	10
Max energy before compression	J	7
Max energy on target	J	4
Min pulse length	fs	25
Max power	TW	250
Contrast ratio		10^{10}

Table 11.1: Laser beam parameter for the actual FLAME laser.

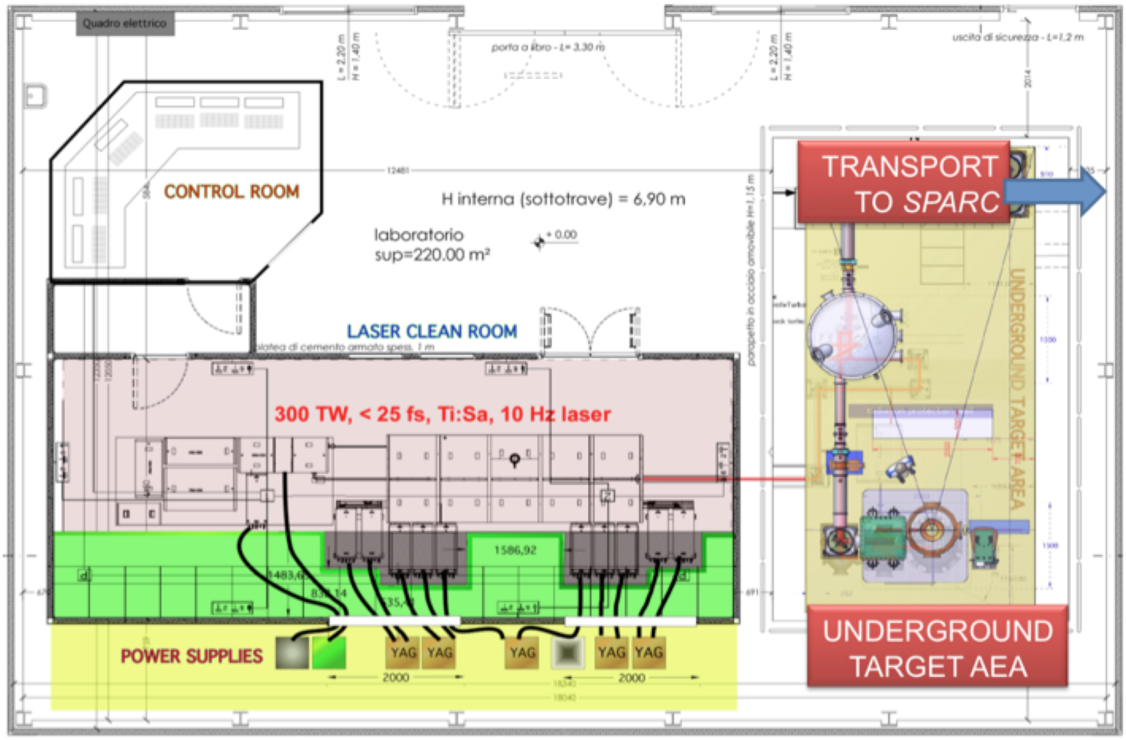

Figure 11.1: The FLAME laser laboratory layout.

the same level of the LINAC (see Fig. 11.2a), while the rack room will be placed on the upper floor, next to the control room (as shown in Fig. 11.2b).

As we can see from Figure 11.2a, next to the laser room (which is represented by the two rooms called «TW 500») used for the FLAME laser, there is a «laser sync» room. In the reality, all the space left - about 310 m^2 – will be filled with a clean room with internal walls that can be placed where needed. The clean room will be air-conditioned and stabilized to about $\pm$ 0.5 °C from the operating temperature (at the moment the FLAME laser works at 24$\pm$0.5 °C).

11.3 Upgrade of the FLAME laser system

Figure 11.2a shows the room allocated for the upgraded FLAME system: this space is divided in two parts, both called «TW 500». This space is that needed for a 1 PW class laser (a similar space,

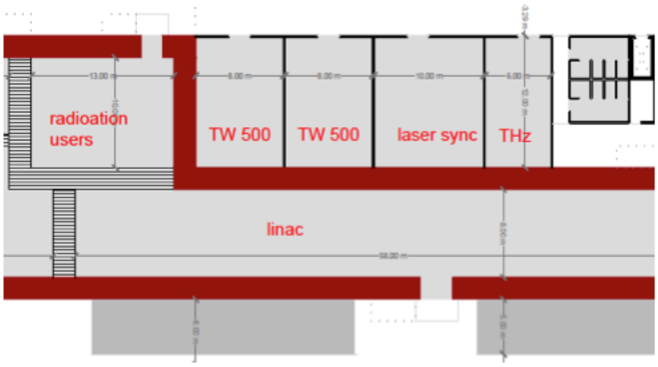

(a) Layout of the ground floor showing the room left for the high power laser and the photo-cathode/synch laser.

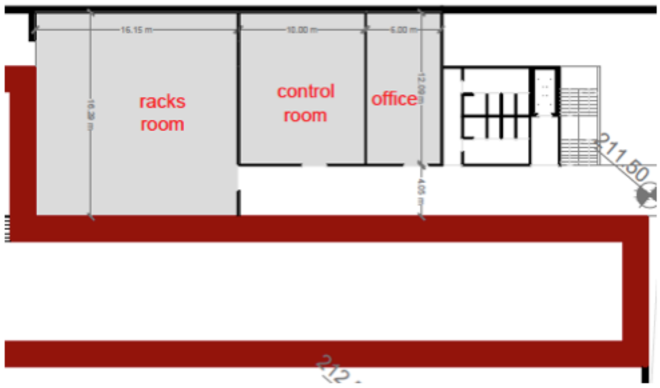

(b) Layout of the up floor showing the room left for the racks both for the high power laser and the photo-cathode/synch laser.

Figure 11.2: Layout of the laser rooms.

for example, is used by the VEGA 3 laser in Salamanca [1], which is the latest 1 PW laser built and which uses the some technology that we will use for the FLAME upgrade) or for two identical 500 TW lasers. At the beginning of the project, the laser will be upgraded at the 500 TW level (one room will be left empty) and only in a second stage the decision to duplicate it or to further upgrade will be made. The laser will use the some technology of the actual FLAME laser, which is a standard CPA and will be composed by the some subsystems but upgraded so to have higher performances:

- An ultra short (15 fs), large bandwidth oscillator at 85 MHz rep rate – which is the one of FLAME;
- A booster to amplify and to increase the contrast ratio – which will be upgraded to operate at the kHz level;
- A stretcher to pass from a short pulse to a long, chirped pulse – which is the one currently used in FLAME;
- A regenerative amplifier to raise the pulse energy to the mJ level – which will be upgraded to operate at the kHz level to increase the stability. The extraction rate will then be reduced to 10 Hz;
- A series of multipass amplifiers (three in the current system) to increase the pulse energy from the mJ level up to 20 J – which will be upgraded (a possible layout of the final amplifier is shown in Fig. 11.3). At the last amplifier the rep-rate will be reduced to 5 or 1 Hz(which is the maximum rep-rate available at the moment with such a high energy);
- A compressor to compress the pulse duration back to the fs level (down to a minimum of 24

fs) – which will be upgraded with bigger size optics.
- A transport line to reach the interaction point placed after the linac.

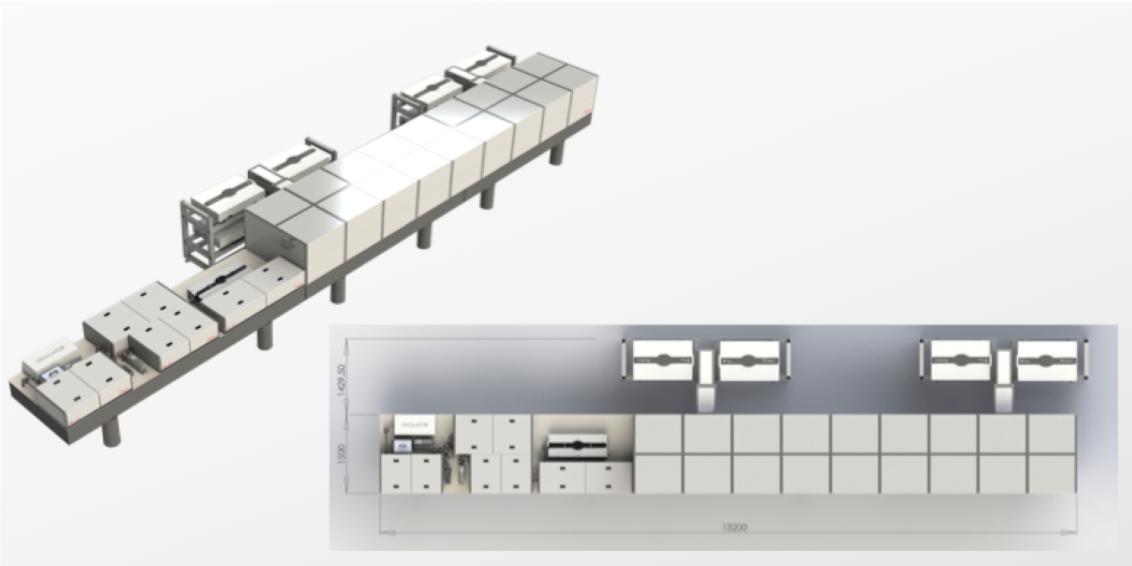

Figure 11.3: Possible layout of the 500 TW laser systems.

The rack room is placed on the upper floor but completely overlapped with the laser clean room. This choice is due to the fact that the maximum length for the cable can be only 8 m (mainly to avoid power dispersion). Therefore the rack room needs to be quite close to the laser room.

The 500 TW laser will have the parameters summarized in Table 11.2.

	Units	**value**
Central wavelength	nm	800
Bandwidth	nm	60 - 80
Repetition rate	Hz	1 - 5
Max energy before compression	J	20
Max energy on target	J	13
Min pulse length	fs	25
Max power	TW	500
Contrast ratio		10^{10}
Laser spot size at focus (optics dependent)	μm	2 - 50
Peak power density at focus (optics dependent)	W/cm^2	10^{22} - 10^{19}

Table 11.2: Laser beam parameter for the upgraded FLAME laser.

As we can see from Table 11.2, there are different peak power density that can be reached, from 10^{19} W/cm^2 to 10^{22} W/cm^2 which of course depends on the off-axis parabola focal length.

11.4 The photocathode laser

In order to guarantee easier daily operations of the laser systems, to have as much common parts as possible and to be self-synchronized, the front-end of the upgraded FLAME laser will be in common also with the photo-cathode laser. The common parts between the two lasers will be oscillator, booster, stretcher, regenerative and 2 multipass amplifiers (where the rep-rate is 10 Hz). At the second amplifier, a beam splitter will be inserted to split part of the main beam (up to 20 - 30 mJ) to be separately treated. The extracted beam will be amplified to the 500 mJ level (one multipass amplifier seeded by one Nd:YAG laser). The larger part of the beam energy (around 200 mJ) will be dedicated to the photo-cathode laser. This IR (800 nm) beam will be compressed, sent to a 3rd harmonic generator (to go from 800 nm to 266 nm) and then will pass through a UV stretcher in order to be able to switch easily from short pulse to long pulse depending on the linac operation requirements. The final maximum UV energy will be about 2 mJ but it will be possible to reduce it down to a few μJ using filters to have the possibility to explore a big range of energies.

11.5 The probe beamlines

Part of the extracted laser which will not be used for the photo-cathode laser, will be used for the diagnostic stations placed along the linac and for the FEL users. The rep-rate of the different probe beams will be 10 Hz. Each diagnostic beamline will be equipped with its own compressor so to guarantee the maximum flexibility in terms of laser beam duration (the minimum duration will be the same of the FLAME laser which is 25 fs). Delay lines will be used to synchronize the different beamlines with the electron beam.

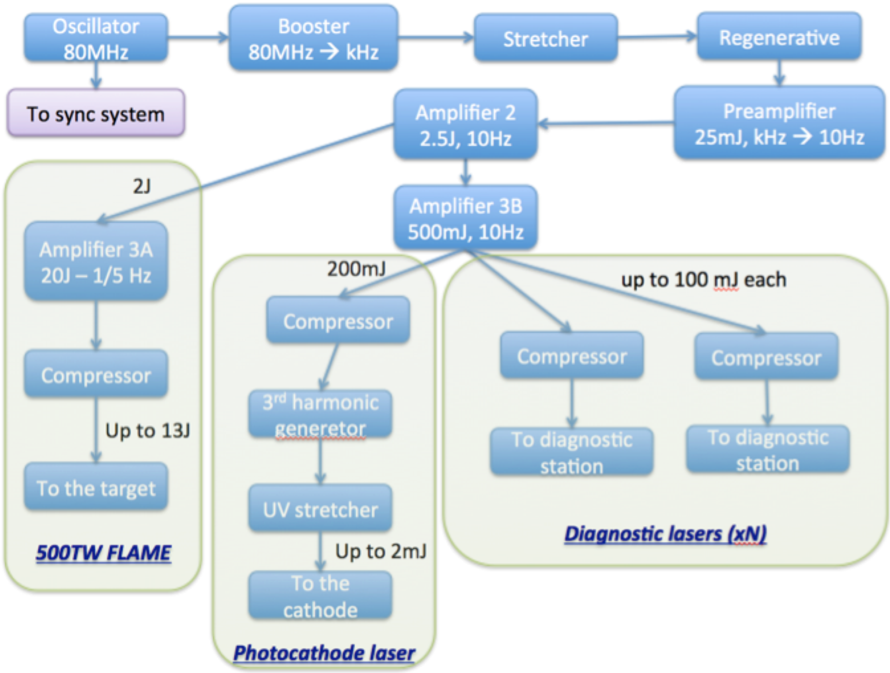

Figure 11.4: Scheme of the laser systems.

11.6 Final scheme of the laser systems

Figure 11.4 shows a simple scheme of how the laser systems will look like and how they will be integrated in order to have one single front-end. The scheme shows also that part of the oscillator beam is split and transported to the synchronization system, which allows to synchronize the electron bunches with the different laser beam-lines. More details about the synchronization system are summarized in Chapter 12 (Timing and Synchronization).

12. Timing and Synchronization

12.1 General considerations

The timing and synchronization system consists of three main parts:

- Timing generation and distribution. An ultra-stable reference signal generated in a central timing station will be distributed to the various clients through actively stabilized links. Due to the remarkable link lengths, an optical reference will be distributed to exploit the fiber-link low attenuation and the large sensitivity obtainable by optical based timing detection
- Client triggering (referred to as *timing*). Together with a continuous reference signal, low repetition rate trigger signals (100 Hz or less) must be provided to some clients, which contain essentially the information on the timing of the macro pulses needed to prepare all the systems to produce and monitor the bunches and the radiation pulses (laser amplification pumps, klystron HV video pulses, beam diagnostics, ...). The triggering system is a coarser timing line that can be distributed either optically (through fiber-links) or electrically (through coaxial cables)
- Client *synchronization*. Each individual client (laser systems, RF power stations, beam diagnostics hardware,...) has to be locked to the local reference provided by the timing distribution systems. The lock technique depends on the particular client (laser optical cavity PLL, RF pulse-to-pulse or intra-pulse phase feedbacks,...)

A block diagram describing the timing and synchronization system working principle is reported in Figure 12.1. Next paragraphs describe each component of the chains and the expected performance of the system. In the EuPRAXIA@SPARC_LAB project we can consider three experimental scenarios:

- injection and acceleration of a single bunch in a plasma wave excited by a laser pulse: in this case the relative jitter between laser pulse and electron bunch must be a fraction of the plasma wavelength (<20 fs RMS)
- injection of a beam comb in a neutral plasma to both excite the plasma wave and exploit it to accelerate the last (or "witness") bunch of the train: in this case the relative jitter between electron bunches and RF compression phase has to be kept below 50 fs RMS (estimated from

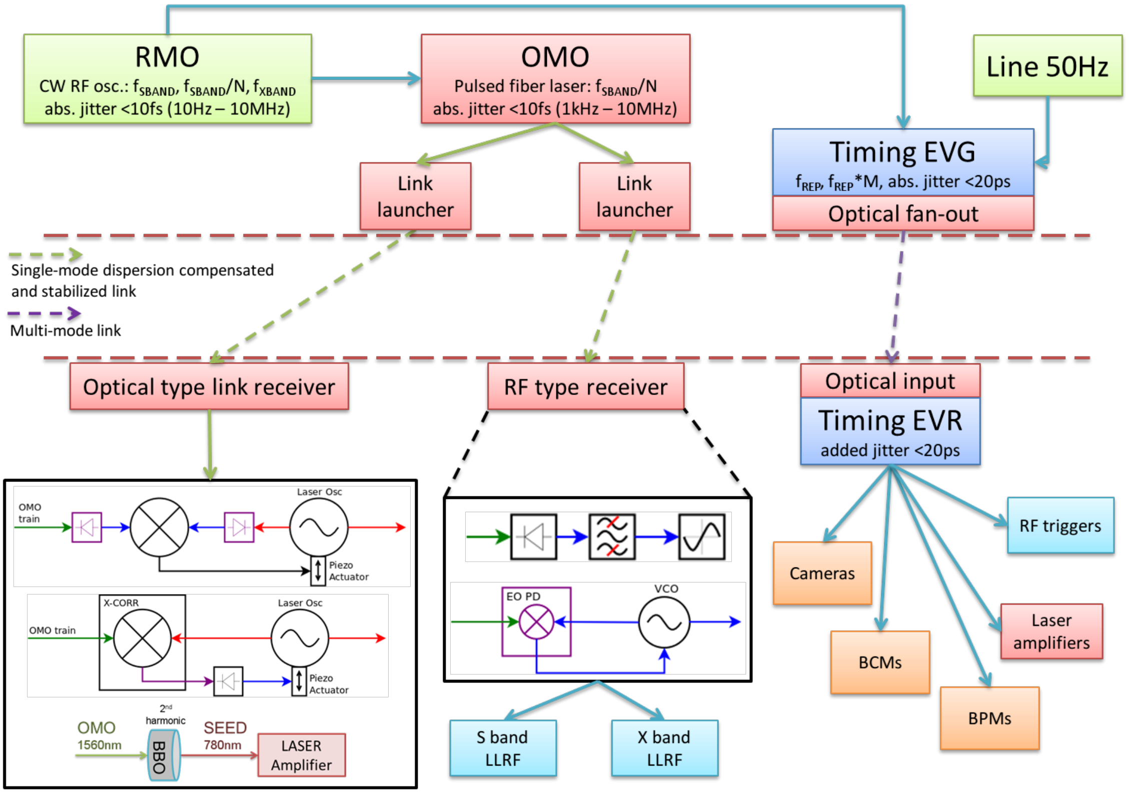

Figure 12.1: Timing and synchronization working principle diagram.

calculations made in [1])

- injection of a high brightness bunch directly in the magnetic undulator for FEL radiation production: in this case the requirements are relaxed and we can assume a jitter <100 fs RMS between the subsystems (mainly lasers and RF) to guarantee good beam quality

In any case the most stringent requirement for the first item of the list has to be met and the other experiments could benefit of the best synchronization performances.

12.2 Timing system

The aim of a timing system is to generate and distribute along a facility digital delayed signals that define the timing of events with a precision of 10 ns ÷ 10 ps depending on the hardware technology (RF pulse generation, lasers amplification temporal gate, BPM triggers, injection/extraction kickers, ...).

The EuPRAXIA@SPARC_LAB timing system will be based on industrial standard devices [2] already used in many accelerator infrastructures (LCLS, APS, Swiss Light Source, Diamond, ELI_NP GBS).

The system is based on an *event generator (EVG)* that provides a reference timing signal at the machine repetition rate. It is locked to the 50 Hz mains and to the facility RMO (Reference Master Oscillator) to minimize the timing fluctuations. This signal is then split, transduced and transmitted through fiber links by means of an integrated *optical fan-out*. Timing signals are delivered to the end stations through fiber links in order to reduce cable attenuation, e.m. interference coupling and grounding problems.

Each local *event receiver (EVR)* transduces the trigger signal back to electrical standard levels (TTL, NIM, LVPECL, ...) according to the requirements of the client devices (RF system, cameras, BPMs, ...). The local distribution of triggers (within 10 ÷ 20 m) is performed by standard coaxial

cables.
The event receiver also allows to delay or concatenate events with a time step that is the inverse of the internal event clock (typically <10 ns). The jitter of delayed signals is specified to be <20 ps RMS.
The timing information is sent using a specific protocol and, inter alia, a time stamp is assigned at each event to guarantee a correct offline measurement analysis and facility sub-system diagnostics. In EuPRAXIA@SPARC_LAB one event generator and 9 receivers are foreseen and their presumed locations are shown in Figure 12.2.

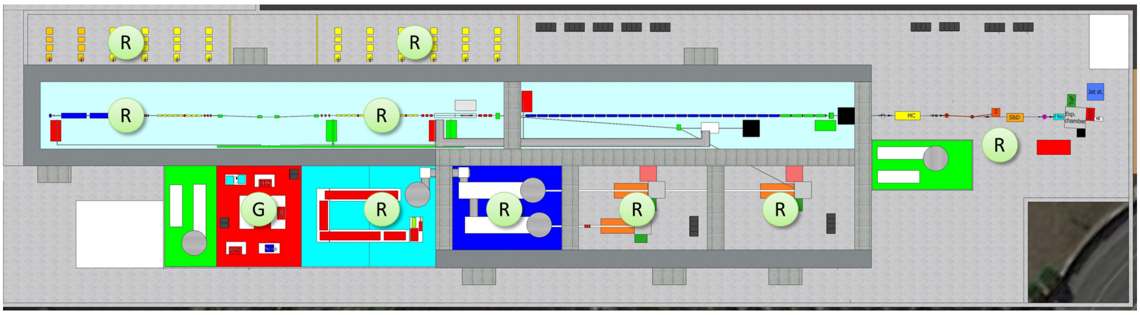

Figure 12.2: Layout of the timing system (green 'G' indicates the event generator location, green 'R' the event receivers).

12.3 Synchronization system

The aim of a synchronization system is to generate and distribute a reference signal to provide a fine temporal alignment among all the relevant sub-system oscillators that guarantees temporal coherence of their outputs with a precision of 10 ps ÷10 fs (coherence between RF accelerating fields, laser oscillators frequency, ADC/DAC clocks, . . .).
The EuPRAXIA@SPARC_LAB timing system will be based on industrial standard devices [3] already used in many accelerator infrastructures based on room-temperature RF (X-FEL, Flash, LCLS I & II, SwissFEL, ELI_NP GBS, . . .).

12.3.1 Reference signal generation

The reference signal is originated by a *Reference Master Oscillator (RMO)* which is a μ-wave crystal oscillator with ultra-low phase noise characteristics. The role of this device is to provide a reliable reference tone to an *Optical Master Oscillator (OMO)* which is a highly stable fiber-laser that encodes the reference timing information in the repetition rate of short optical pulse in the IR spectrum. The RMO guarantees the long term stability of the OMO, and, through the OMO locking system, imprints its low-frequency noise figure to the whole facility timing line. The state of the art low-noise μ-wave oscillators can provide pure sine tones with phase jitter of 10 ÷ 20 fs RMS over a spectral range from 10 Hz to 10 MHz. In addition to the OMO locking frequency (typically the S-band linac frequency) the RMO can provide also some service outputs at the S- and X-band linac frequencies and their sub-harmonics, if necessary.
The timing reference will be encoded in an optical signal before being distributed over the whole facility through a fiber network. The μ-wave to optical conversion is accomplished by locking a low noise fiber laser (the facility Optical Master Oscillator – OMO) to the RMO. The OMO to RMO synchronization is obtained by a locking system, which consists in a PLL scheme controlling the path length of the fiber laser cavity whether by using a piezoelectric fiber stretcher or an optical motorized delay line driven by the error signal proportional to the relative phase between the two oscillators. This is a standard technique to synchronize also in-air laser oscillators to external

references, with piezo actuators controlling the position of one or more mirrors. Due to the limited frequency response of piezo-controllers, the locking loop gain rolls off typically around 5 kHz. Above this cut–off frequency the OMO retains its typical noise spectral properties, while below the cut-off frequency the OMO phase follows the RMO one, and the phase power spectra of the two oscillators result to be very similar. However, the intrinsic phase noise spectrum of a good fiber laser oscillator above the locking cut-off frequency is comparable or even better respect to that of a μ-wave reference oscillator.
The overall phase noise of fiber laser OMO fairly locked to a high-class RMO can be as low as $\approx$ 10 fs in a wide spectral region spanning from 10 Hz to 10 MHz. The specifications of the OMO are reported in Table 12.1.

Parameter	**Symbol**	**Value**
Wavelength	λ	1560 nm
Pulse rep. rate	f_{rep}	$70 \div 110$ MHz
Pulse energy	E_{pulse}	>2 nJ ($\approx$ 180 mW)
Phase jitter	τ_{RMS}	<10 fs($SSB\,\Delta f > 1$ kHz)
Amplitude jitter	$(\Delta A/A)_{RMS}$	<0.05%
Locking bandwidth	f_{cutoff}	5 kHz
Phase jitter relative to reference	τ_{rel}	<10 fsRMS ($dc \div 1$ kHz)

Table 12.1: Optical Master Oscillator parameters.

12.3.2 Reference signal distribution

The optical reference signal generated by the OMO will be then amplified, split and distributed to the remote RF or optical subsystems that need to be synchronized with minimal residual noise. Precise transfer of timing signals through fiber links for timing information distribution has been recently demonstrated. Stabilized fiber links are now standard commercial products, capable to distribute the reference optical signal in a km scale complex with a *residual phase drift* down to <10 fs RMS. Figure 12.3 reports the operating principle of such a link. Relative fiber expansion by temperature change is typically on the order of 10^{-7}/K, which can be compensated by a fiber length control loop. The phase error information is extracted from a double balanced cross-correlator that use the non-linear interaction between the back reflected pulse from the fiber end with the forward pulse coming from the OMO output. The error signal is then sent to a fast actuator (typically a piezo-controller) that slightly changes the link length to compensate the elongation (due to thermal drifts or mechanical vibrations).
Since the link receivers (both optical and electro-optical) and the link stabilization process itself need a very short pulse (ideally transform limited), dispersion compensation is necessary to preserve the OMO pulse length. It is performed by adding a segment of dispersion compensating fiber (DCF) that has a dispersion coefficient opposite and larger with respect to standard 1550 nm telecom fibers.

12.3.3 Synchronization system in EuPRAXIA@SPARC_LAB

The synchronization system of EuPRAXIA@SPARC_LAB foresees one central station located on an optical table in the photo-cathode laser room, where the RMO and OMO are placed. Five stabilized links provide the reference signal to:

- S-band RF stations

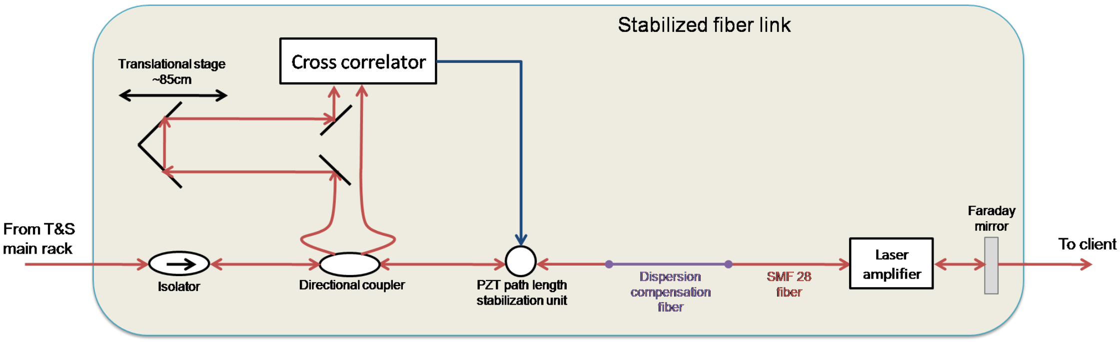

Figure 12.3: Working principle diagram of a fiber stabilized link.

- First X-band RF stations group (same hall of S-band)
- Second X-band RF stations group
- Diagnostics clients in the linac hall
- User experiments at the end of the tunnel

Other possible clients (THz, optional laser oscillators, . . .), located in the proximity of the link ends, could benefit of the locally distributed reference signal.
A sketch of the proposed layout of the synchronization system is reported in figure 12.4, where OMO and RMO and link end locations are highlighted.

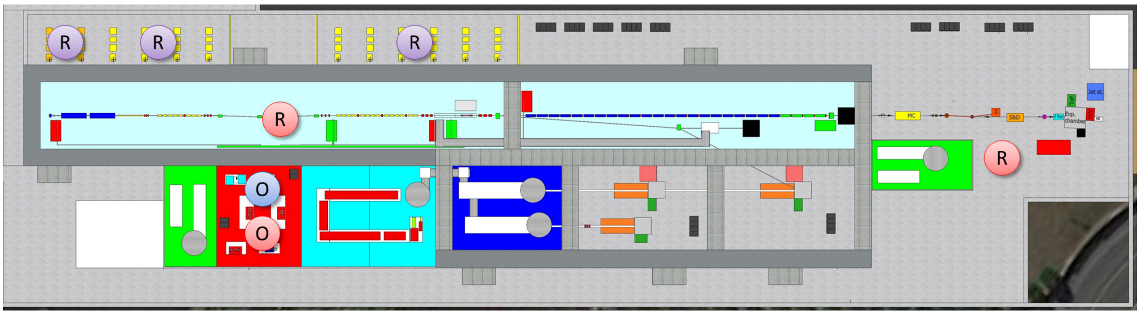

Figure 12.4: Layout of the synchronization system (blue and red 'O' indicate respectively the optical and electrical reference oscillators. Purple and red 'R' represent link ends respectively with RF extractor and with optical output).

12.3.4 European and American frequencies integration

In the EUPRAXIA@SPARC_LAB project, there is the possibility that two main different standard, the American S-band frequency 2856 MHz and the European X-band 11994 MHz , must coexist and be synchronous. In this case, the OMO repetition rate has to be a sub-harmonic of both the linac frequencies to allow beam acceleration. This can be achieved by using multiplier/divider stages for the frequency synthesis inside the RMO and also adding some external multiplier/divider, if needed, to generate the reference for the timing system, LLRF digitizers and other devices or sub-systems.
Table 12.2 shows two possible options (OMO1 and OMO2) for synchronous frequencies distribution in the facility.

	Frequency start [MHz]	**First Multiplier**	**Second Multiplier**	**Third Multiplier**	**Total Multiplier**	**Frequency end** [MHz]	
X-band	11994.2	1/7	1/3	5	5/21=0.238	2855.76	S-band
Comm1	571.152	7	3		21	11994.2	X-band
Comm1	571.152	5			5	2855.76	S-band
OMO1	95.192	7	6	3	126	11994.2	X-band
OMO1	95.192	6	5		30	2855.76	S-band
OMO1	95.192	6			6	571.152	Comm1
OMO1	95.192	3			3	285.576	Comm2
OMO1	95.192	2			2	190.384	Comm3
OMO2	71.394	8	7	3	168	11994.2	X-band
OMO2	71.394	8	5		40	2855.76	S-band
OMO2	71.394	8			8	571.152	Comm1
OMO2	71.394	4			4	285.576	Comm2
OMO2	71.394	2			2	142.788	Comm3

Table 12.2: RF frequencies in the facility. Two different options for OMO repetition rate.

Bibliography

[1] R Pompili et al. "Femtosecond timing-jitter between photo-cathode laser and ultra-short electron bunches by means of hybrid compression". In: *New Journal of Physics* 18.8 (2016), p. 083033. URL: http://stacks.iop.org/1367-2630/18/i=8/a=083033.

[2] *Micro Research Finland Oy*. URL: http://www.mrf.fi.

[3] *Menlo Systems Gmbh*. URL: http://www.menlosystems.com/products/timing-distribution-solutions.

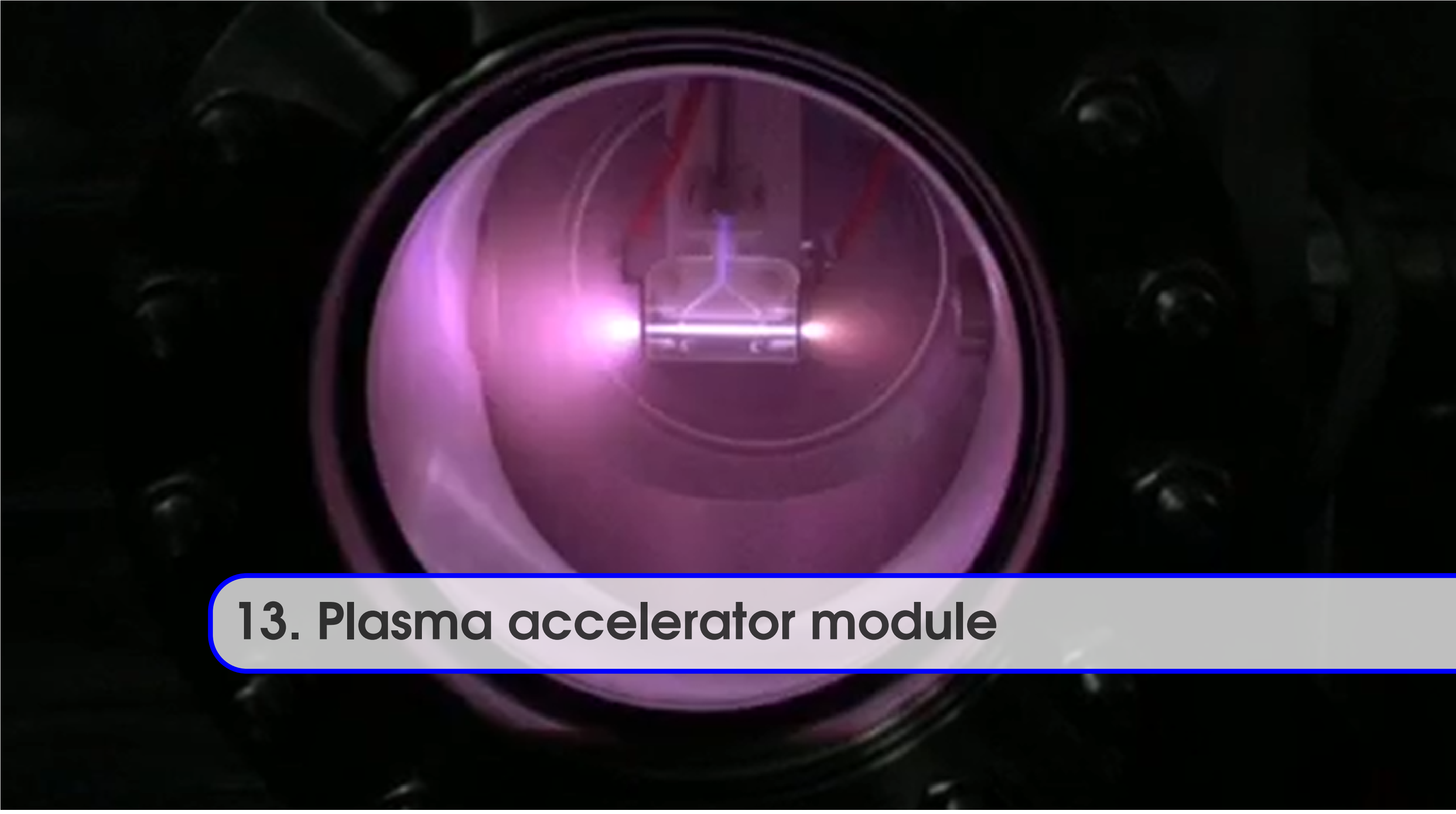

13. Plasma accelerator module

One of the main requirements to a prepared plasma structure is fine external tuning of the plasma parameters. These parameters are very important for injection and propagation of the laser/electron beams in the plasma channel and in the case of laser wake-field acceleration, matching of the accelerated electrons phase to the wake-field. These parameters include: radial and longitudinal plasma density distribution, plasma composition and degree of ionization, the plasma channel spatial dimensions and temporal dynamics, the plasma temperature. These parameters are very important for injection and propagation of the laser/electron beams in the plasma channel, in particular for matching the accelerated electrons phase to the wake-field along the entire acceleration path, which may require several centimeter of plasma. Multistage capillary discharge scheme has made possible easy online control of the most of these parameters, allowing to fit all the plasma characteristics to the different stages of the accelerator.

In external injection schemes, both laser or beam driven, a uniform, "low" ($10^{16} - 10^{17}$ cm^{-3}) plasma density for centimeter scale length is required, with sufficient transverse uniformity and relatively low temperature (< 10 eV). In order to control the plasma acceleration process and the particle bunch properties, very reliable plasma sources are mandatory.

In following section, the behavior of the ionized gas in the capillary plasma channel is reviewed and the solutions we propose to accomplish the requirements of this CDR will be described.

13.1 Capillary discharge

The plasma channel in the capillary is created by a high voltage electrical discharge. Original idea belongs to A. Zigler and Y. Ehrlich [1–3] that studied capillaries in which the initial plasma was produced by a capillary surface breakdown. This technique, referred as ablative capillary, has the drawback that the plasma is not a pure composition and it needs a laser to be triggered. Moreover, the quality of the so-generated plasma channel is ensured only for few hundreds of shots, since the ablation changes the radius of the capillary. Nevertheless, it takes some advantages given by the more precise trigger and by no needs of gas bottles [4, 5].

Later, the gas filled capillary was introduced [6, 7]. In these devices, a current pulse of several amperes passes through the capillary filled with neutral gas at pressure of few tens of millibar. The

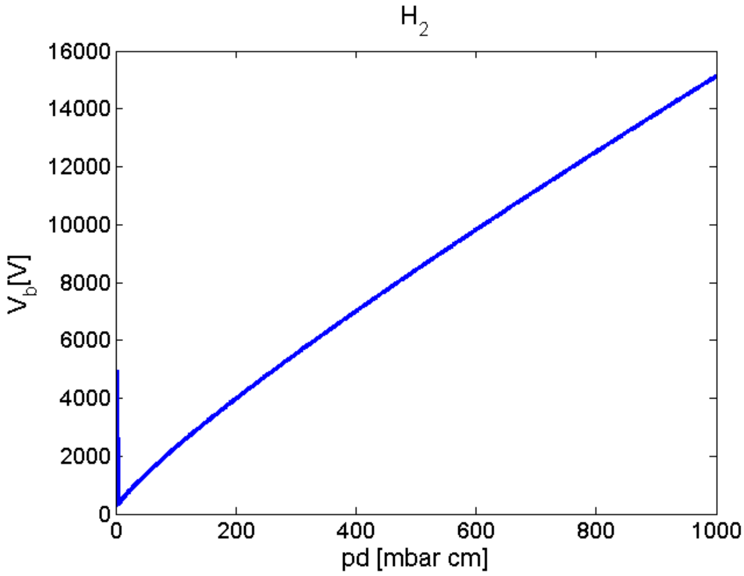

Figure 13.1: Paschen curve for molecular hydrogen.

current ionizes the gas, preforming the plasma channel before the interaction with the driver beam, avoiding ionization losses. Lifetime of these capillaries has been experimentally demonstrated to be longer than 10^5 shots even with high repetition rate discharge (of the order of the kHz) [8] with enough small ablation to not significantly affect the plasma density. Conventional "single stage" capillary (where a single discharge ionizes the entire gas volume contained into the capillary) could be operated at one particular voltage dictated by the length of capillary and gas density, but the initial plasma density cannot be easily controlled along the entire length of the capillary, especially when it requires several tens of plasma lengths.

We propose a new scheme based on the gas filled capillary discharge in which we preionize the gas with a preformed plasma prior to the main discharge. Similar mechanisms have been studied in the past for different purposes, such as cold cathode thyratron [9], trigatron [10] and segmented laser trigger ablative capillaries [11]. With this scheme, which may be referred as segmented or double capillary discharge, we aim to combine the advantages of the segmented discharge with the longer lifetime of the gas-filled capillaries to produce long plasma channel (tens of centimeters) for plasma-based acceleration schemes of the EuPRAXIA@SPARC_LAB project.

Going more in details, the gas which will be used in this project will have low atomic number and low ionization energy to reduce the influence of the impact ionization on the crossing beams [12] and to ensure high ionization degree of the plasma. Hydrogen well fits those requirements, since it has a low atomic number and ensures an high ionization degree even at lower plasma temperature (2 eV are enough to almost completely ionize the gas, as can be deduced by the Saha-Boltzmann equation and from simulations [7, 13, 14]).

The voltage required to ignite the discharge in a column of neutral gas is described by the Paschen law [14]. The Paschen law is an empirical relationship which relates the breakdown voltage V_b required to produce the electric discharge with the gas pressure p and the distance between the electrodes d, i.e. the capillary length.

$$V_b = \frac{B\,pd}{\ln(A\,pd) - \ln\left[\ln\left(1 + \frac{1}{\gamma_{se}}\right)\right]} \tag{13.1}$$

The breakdown voltage is the voltage (in V) necessary to start a discharge or electric arc between the electrodes. The constants A and B are determined experimentally and they are roughly constant over

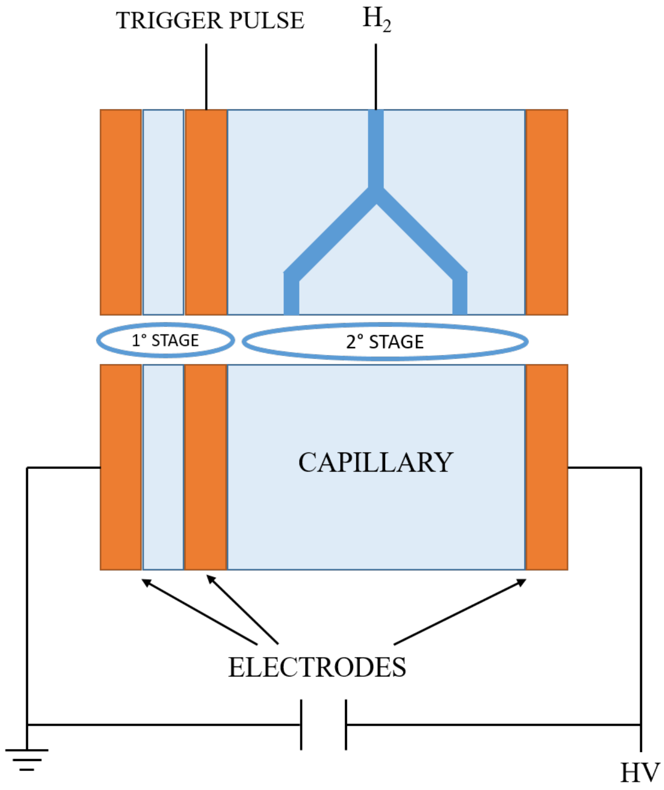

Figure 13.2: Double capillary schematic. In the first stage the trigger discharge starts the ionization of the entire gas confined into the capillary (second stage). This scheme can be reproduced for tens-of-centimeter capillaries. This single unit can be integrated simply by adding more units.

a restricted range of voltage over pressure for any given gas, while γ_{se} is the secondary-electron-emission coefficient and it fairly depends on the electrodes material. Given the gas pressure necessary for the required background plasma density, the longer the capillary, the higher is the voltage required to spark the discharge, as can be seen in Fig. 13.1. In fact, if we take into account a capillary length around 30 cm and a hydrogen pressure of about 20 mbar (required to obtain a plasma density of the order of 10^{17} cm^{-3}), $pd \approx 600$ mbar cm . In these conditions, assuming a 1 mm diameter capillary, the breakdown voltage is 10 kV but a full ionization of the gas constraints to use a breakdown voltage of 60 kV. This high voltage is not easy to handle and may also damage the capillary surface. Using a trigger discharge will reduce the breakdown threshold as well as the jittering time of the discharge.

In the double-capillary discharge proposed for this project will use a trigger discharge obtained with a pulsed high voltage signal to overcome the limits of the Paschen law. The schematic in Fig. 13.2 shows a possible implementation of this technique. A voltage of few kVs is imposed between the two external electrodes. The voltage, even high, is not enough to ignite the discharge because is still lower than the breakdown threshold obtained with the Paschen law. The initial plasma, instead, is formed in a short primary capillary (referred as first, or trigger stage). Part of this plasma and free electrons expand into the long capillary (the second or main stage) being accelerated by the potential of the last electrode. The electrons then gain in a short distance enough energy to ionize the neutral molecules, producing an avalanche-like effect in the neutral gas which lets the discharge to develop and ionize the entire gas column. The proposed technique let to produce ten-centimeters long plasma channel with reasonable applied voltage in controlled and homogeneous way. The plasma density can be controlled by the capacitor voltage and the initial gas density and could be changed between 10^{16} to 10^{20} electrons per cm^{-3}.

Due to the reduced requirement on the breakdown voltage, the basic structure of the double-capillary discharge can be repeated for many multistages without particular attention on the high voltage generator. The multistage capillary is just a connection of few assembled capillaries where only the some of them have a trigger stage as schematically represented in Fig. 13.3. A single double capillary unit can be integrated simply by adding more units obtaining up to tens of centimeter capillaries homogeneously ionized and controlled independently one to each other leading to the desired length of plasma (several tens of centimeters) with the proper density (10^{16} - 10^{17} cm^{-3}) required for this project. The possible interference between the electrodes are avoided by the use of the stripline in the discharge circuit, which allows to carry high voltage without crosstalk.

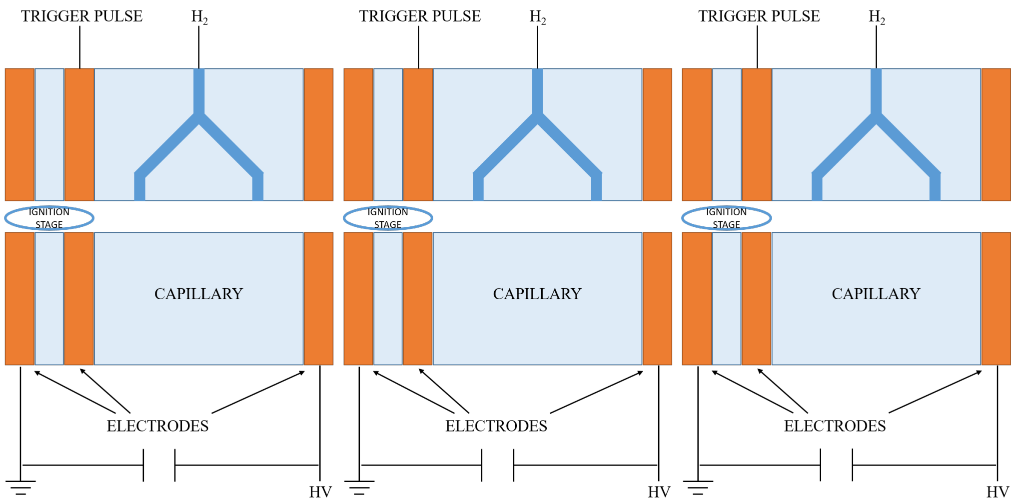

Figure 13.3: Multistage capillaries planned to reach tens-of-centimeter plasma channel.

13.2 Plasma channel formation

In order to guide the laser pulse during the LWFA, as well as to provide the flattest plasma density around the capillary axis for the PWFA, the formation of the plasma channel must be taken into account.

To allow the channel formation, the discharge in the main capillary should be slow enough so that its duration is much longer than any microscopic processes in the plasma. The relevant processes are: collisions between all kind of particles (atoms, ions and electrons), irradiation processes (recombination radiation, plasma emission by resonant lines of ions and atoms, bremsstrahlung) and ionization. The plasma density should be high enough that collisions dominate radiation processes. This means that at any moment of the plasma existence (excluding the short initial stage) we can consider the plasma as in local thermal equilibrium (LTE plasma).

In our experimental condition the capillary length is much longer then diameter, therefore all plasma parameters could be considered as functions of time and radius only, excluding the small regions near the open ends of the capillary. In this case we can introduce characteristic acoustic time $\tau_a = R/c_s$, were R is capillary radius and c_s plasma sound velocity. Sound velocity of the plasma has been measured experimentally and calculated [15], for some typical capillary discharge parameters τ_a varies around 100 nanoseconds. Therefore the discharge rise time τ_{dis} should be above a few hundreds nanoseconds. After few acoustic times the plasma pressure p along the radius of the capillary gets almost constant. Considering capillary plasma as a perfect gas, we can write its state equation at an almost constant pressure:

$$nT = p \approx \text{const} \tag{13.2}$$

The above condition is valid for any time period $\tau \gg \tau_a$.

When the current of the main discharge flows through the initial plasma, plasma temperature starts to rise due to Joule heat process. Both direct collisions of the hot electrons and ions with the capillary walls and absorption of radiation produced by the hot plasma transfer the energy to the gas in the vicinity and capillary walls. As a result of these processes, the plasma temperature becomes higher at the center of the capillary and lower at the peripheries [7] (as shown in Fig 13.4).

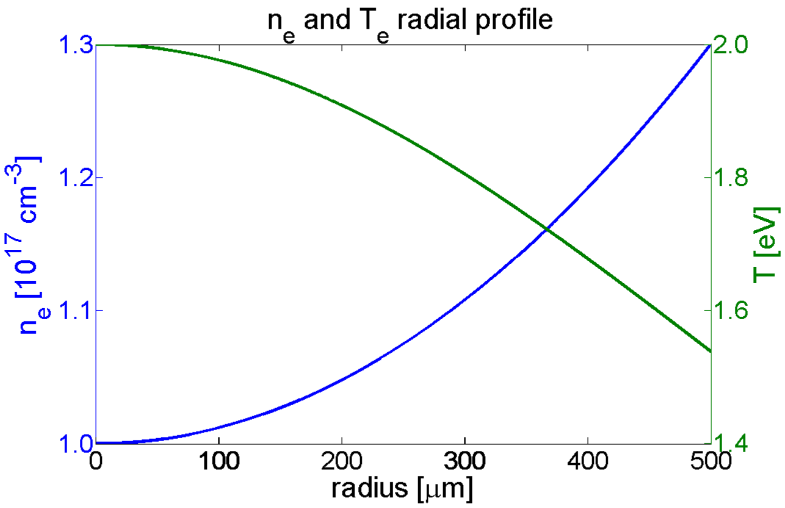

Figure 13.4: Plasma density and temperature distribution along 0.5 mm capillary radius at the equilibrium.

Considering the simplest two components plasma model, we can write an expression for plasma conductivity [16]:

$$\sigma \approx 3.44 \times 10^5 \, \frac{e^2 T_e^{3/2}}{m_e \ln \Lambda} \tag{13.3}$$

where e, m_e, T_e are electron charge, mass and temperature (in eV) respectively. The plasma conductivity is a very strong function of the plasma temperature, but is almost insensitive to the plasma density through a very slow-changing Coulomb logarithm $\ln \Lambda$. That means that the electrical current of the main discharge goes primary through the central part of the capillary plasma, since due to the Joule process, the plasma at the center of the capillary is heated more then at the peripheries. Finally, the plasma radial temperature distribution has a maximum at the center of the capillary. In order to satisfy condition (13.2), the density distribution has to be minimal at the center, the plasma channel is then created.

The created plasma channel has a short lifetime due to diffusion of the cold dense gas near the capillary walls to the center. The characteristic diffusion time τ_{diff}, that takes to smooth the plasma density over the capillary radius, could be estimated in terms of ambipolar diffusion coefficient D [16]:

$$\tau_{diff} = \frac{R^2}{D} \approx \frac{2T\,(\text{eV})}{m_e\, \nu_{ei}} \tag{13.4}$$

where ν_{ei} is electron–ion collisions frequency

$$\nu_{ei} \approx 3.62 \times 10^{-6}\, n_i T_e^{3/2} \ln \Lambda \tag{13.5}$$

and n_i is the density of ions in the plasma. For all interesting values of plasma density (10^{16} – 10^{19} cm^{-3}) diffusion time varies between 0.1 to few tens of microseconds. For LWFA the rise time of the main discharge current should satisfy the follow condition: $\tau_a \ll \tau_{dis} \ll \tau_{dif}$. That allows us to get the deepest plasma density profile at the maximum of the current.

In order to obtain the above conditions of collision limited discharge, we have to limit the value of the current driven through the capillary. Plasma pressure at the current maximum must be higher then the pressure of magnetic field generated by the main discharge current. Thus the Ampere force can be neglected and the capillary plasma is confined radially mainly due to the capillary walls. Otherwise conditions for a pinch effect will be developed, and plasma channel may become unstable. Considering all the current goes through the center of the capillary we can write this condition as:

$$nT = p > \frac{B^2}{8\pi} \approx 8 \times 10^{-4} \frac{I^2\,\mathrm{A}}{R^2\,\mathrm{cm}} \tag{13.6}$$

where I is the electrical current of the main discharge. For the most experimental configurations this condition limited the maximum current value to ten kA.

13.3 Technical description

We will now discuss some technical details of the proposed experimental system. The main parts of the proposed multistage capillary will be preformed by 3D printing process. The choice of the material for the capillary will be the lowest average molecular weight and highest ablation threshold creates fewer electrons from the laser ionization. The main capillary can be with 0.5-1 mm internal diameter. For the single main capillary, length can be varied from one to ten centimeters. Due to the reduced requirement on the breakdown voltage, the basic structure can be repeated for many multistages (we envision activation of 5-10 stages). For every single stage double capillary (one trigger and one main capillary) we will use three electrodes: one to connect to the ground, one to the trigger pulser and one to the main capillary high voltage. All electrodes are made out of copper and have 30 mm length and 1 mm thickness. The central hole is the same size as that at the main capillary.

The multistage capillary is just a connection of few assembled capillaries, were only the some of them have a trigger capillary. The external electrodes of the double capillary are connected to a high voltage capacitor (see Fig. 13.5). The voltage and the value of the capacitor determine the main discharge current amplitude and duration. The capacitor is charged to a high voltage through a load resistor. Discharge parameters are monitored using current monitor attached to a high voltage wire of the capacitor. These parameters will be used to estimate the plasma density and to synchronize the discharge to the laser pulse or the particle bunch. A high voltage pulser initiates the trigger discharge. The pulser creates short electric pulse that creates a discharge in the trigger capillary by using a high voltage solid switch as a fast switch, a pulse transformer and a stripline. This will allow reduction of the jitter and precise synchronization with the propagating high intensity pulse (laser or electron beam). For this purpose, will use light activated switches. Each stripline can be charged to a high voltage supply up to 6 kV. When the trigger voltage is sent to the switch, the electrical pulse is developing between two sides of the double stripeline and the voltage can be multiplied by the factor of N/2, where N is the number of the loops. The pulser output voltage can be up to 25 kV and can have nanoseconds rise time.

13.4 Local control of plasma density

The double capillary let to ionize most of the gas volume during the discharge. This allows to have homogeneous plasma profile even at low densities of the order of $\sim 10^{16}$ - 10^{17} cm^{-3} [17, 18] as typically requested by external injection experiments.

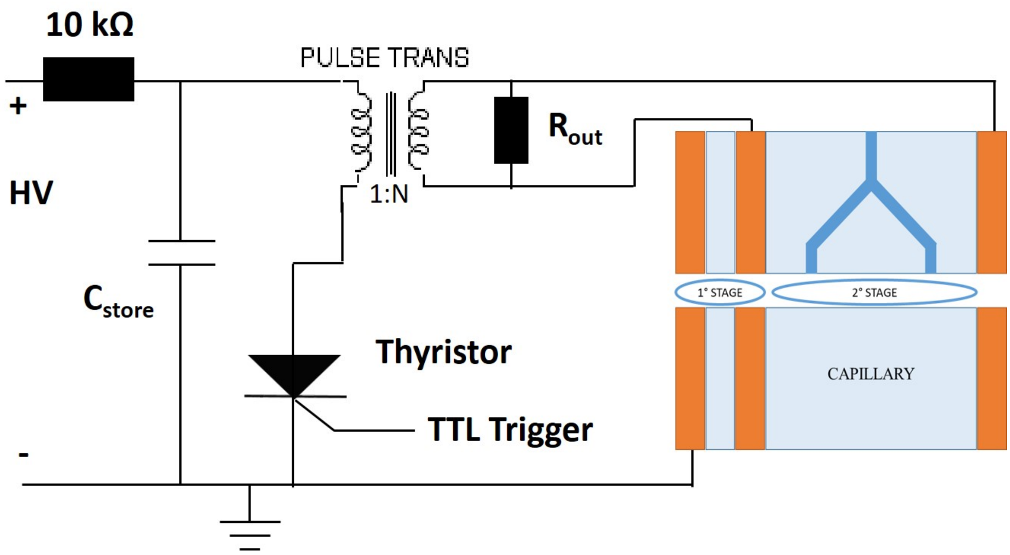

Figure 13.5: Schematic of the discharge circuit.

Local control of the plasma density is required to match the laser/electron beam into the plasma. Tapering the capillary diameter is the easiest way to change locally the density. By monotonically varying the radius of the capillary it is possible to change the density using the empirical formula [19]

$$n_e \left[\mathrm{cm}^{-3}\right] = 2.5 \times 10^{17} I_m^{1.2} \left[\mathrm{kA}\right] R_c^{-3.2} \left[\mathrm{mm}\right] \tag{13.7}$$

With this strategy it is possible to locally control the properties of the plasma channel by varying the capillary shape or by timing the discharge with the beams to wait for the desired plasma profile during the interaction.

Nevertheless, electron density creation inside these capillaries is sensitive to many parameters, such as the wall composition, the shape of the electrodes or the resistances of the discharge circuit, which require fine measurements and are not easy to control during the device manufacturing. The definitive characterization of the plasma target must be always performed experimentally.

Bibliography

[1] A Zigler et al. “Elongated high-temperature, dense plasma produced by a high-power-laser heating of a capillary discharge”. In: *Physical Review A* 35.10 (1987), p. 4446.

[2] B Brill et al. “Density measurement of dense capillary discharge plasma using soft X-ray backlighting”. In: *Journal of Physics D: Applied Physics* 23.8 (1990), p. 1064.

[3] Y Ehrlich et al. “Generation of large, high density, homogeneous plasma by capillary discharge”. In: *Applied physics letters* 64.26 (1994), pp. 3542–3544.

[4] Michael Levin. *Excitation of Plasma Wakefields and Electron Acceleration*. Hebrew University, 2009.

[5] Y Ehrlich et al. “Guiding of high intensity laser pulses in straight and curved plasma channel experiments”. In: *Physical review letters* 77.20 (1996), p. 4186.

[6] DJ Spence and Simon Mark Hooker. “Investigation of a hydrogen plasma waveguide”. In: *Physical Review E* 63.1 (2000), p. 015401.

[7] NA Bobrova et al. “Simulations of a hydrogen-filled capillary discharge waveguide”. In: *Physical Review E* 65.1 (2001), p. 016407.

[8] AJ Gonsalves et al. "Demonstration of a high repetition rate capillary discharge waveguide". In: *Journal of Applied Physics* 119.3 (2016), p. 033302.

[9] K Frank et al. "High-power pseudospark and BLT switches". In: *IEEE transactions on plasma science* 16.2 (1988), pp. 317–323.

[10] AM Sletten and TJ Lewis. "Characteristics of the trigatron spark-gap". In: *Proceedings of the IEE-Part C: Monographs* 104.5 (1957), pp. 54–61.

[11] D Kaganovich et al. "Velocity control and staging in laser wakefield accelerators using segmented capillary discharges". In: *Applied Physics Letters* 78.21 (2001), pp. 3175–3177.

[12] Efthymios Kallos. *Plasma wakefield accelerators using multiple electron bunches*. University of Southern California, 2008.

[13] MP Anania et al. "Plasma production for electron acceleration by resonant plasma wave". In: *Nuclear Instruments and Methods in Physics Research Section A: Accelerators, Spectrometers, Detectors and Associated Equipment* 829 (2016), pp. 254–259.

[14] Ian H Hutchinson. "Principles of plasma diagnostics". In: *Plasma Physics and Controlled Fusion* 44.12 (2002), p. 2603.

[15] HR Griem. "Plasma spectroscopy". In: *McGraw-Hill, New York* (1964).

[16] B Samuel Tanenbaum. *Plasma physics*. McGraw-Hill, 1967.

[17] Francesco Filippi et al. "Plasma Density Profile Characterization for Resonant Plasma Wakefield Acceleration Experiment at SPARC_LAB". In: (2016), pp. 2554–2556.

[18] F Filippi et al. "Spectroscopic measurements of plasma emission light for plasma-based acceleration experiments". In: *Journal of Instrumentation* 11.09 (2016), p. C09015.

[19] D Kaganovich et al. "Variable profile capillary discharge for improved phase matching in a laser wakefield accelerator". In: *Applied physics letters* 75.6 (1999), pp. 772–774.

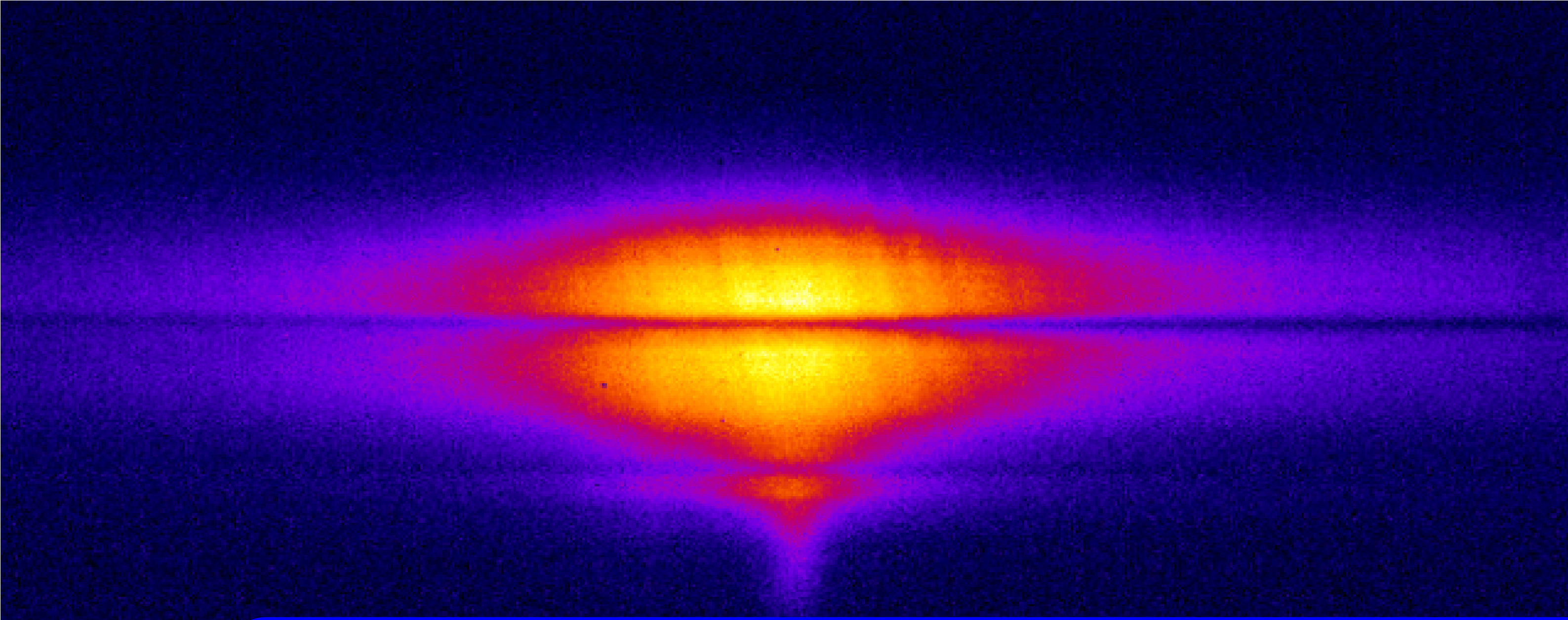

14. Plasma diagnostics

Any plasma source requires different diagnostic tools to determine the principal plasma characteristics needed for the acceleration. On-line and non-perturbing methods suitable for small ($\sim$1 mm thick or less) plasmas are mandatories. Due to the small dimension of the plasma, mechanical probing is unpractical since they interfere with the plasma changing its local conditions. On the opposite, spectroscopic techniques fit very well these requirements. Plasma density can be measured by the analysis of the broadening of self-emitted lines caused by the Stark effect [1–3]. Stark broadening is particularly affordable for hydrogen and can be used for pure hydrogen plasma or by doping a generic gas with hydrogen. An another non-perturbing diagnostic technique used to measure plasma density is the interferometry. This technique requires a low intensity laser beam which probes the plasma.

Both these methods allow for single shot and spatially resolved measurements, which are mandatories for the optimization of the beam quality during the acceleration.

14.1 Spectral analysis

Ionized plasma emits electro-magnetic radiation whose spectrum can be either continuous or discrete depending on the radiative mechanism [2]. In general, the properties of the emitted radiation depend on the plasma characteristics, and its analysis allows to reconstruct the plasma conditions in the vicinity of the emitters. This kind of analysis is developed in a specialized field of research often referred to as plasma spectroscopy. Plasma spectroscopy is a very interdisciplinary science [2–4]. Most of the theory used in this field has been developed for astrophysical observation where the plasma cannot be probed, nevertheless it is commonly used for experimental investigations in laboratory plasmas due to its high reliability. Because of the small dimensions of the plasma channel, Stark broadening is particularly suitable for cylindrical capillary where light or mechanical probing are unpractical.

Hydrogen plasma (and even hydrogen doped plasma) produces strong lines in the visible range, whose properties can be studied with good reliability with spectroscopic measurements and the light emitted do not suffer from capillary diffraction. The spectral analysis of these lines allows to reconstruct the electron density of the surrounding plasma due to the Stark effect. This technique can be used also in case of ablative capillaries, where multi-species of plasma are produced (including hydrogen), allowing the retrieval of plasma properties around the emitter [5].

In hydrogen and hydrogenic ions, indeed, the Stark broadening effect is linear for a plasma density higher than $\sim 10^{14}$ cm^{-3}. For denser plasmas instead ($\sim 10^{19}$ cm^{-3}), the self-absorption of the emitted radiation become important and its analysis may be unpractical [6, 7]. Actually, Stark profile simulations are accurate enough for electron densities between 10^{14} – 10^{19} cm^{-3} and temperatures well above the few eVs of the capillary discharge [2, 3, 8, 9]. The Stark broadening analysis allows to detect the spatial and temporal evolution of the plasma online in single shot analysis [10, 11].

A typical setup for the spectroscopic analysis (which lead to sub mm spatial resolution and 100 ns temporal resolution is shown in Fig. 14.1.

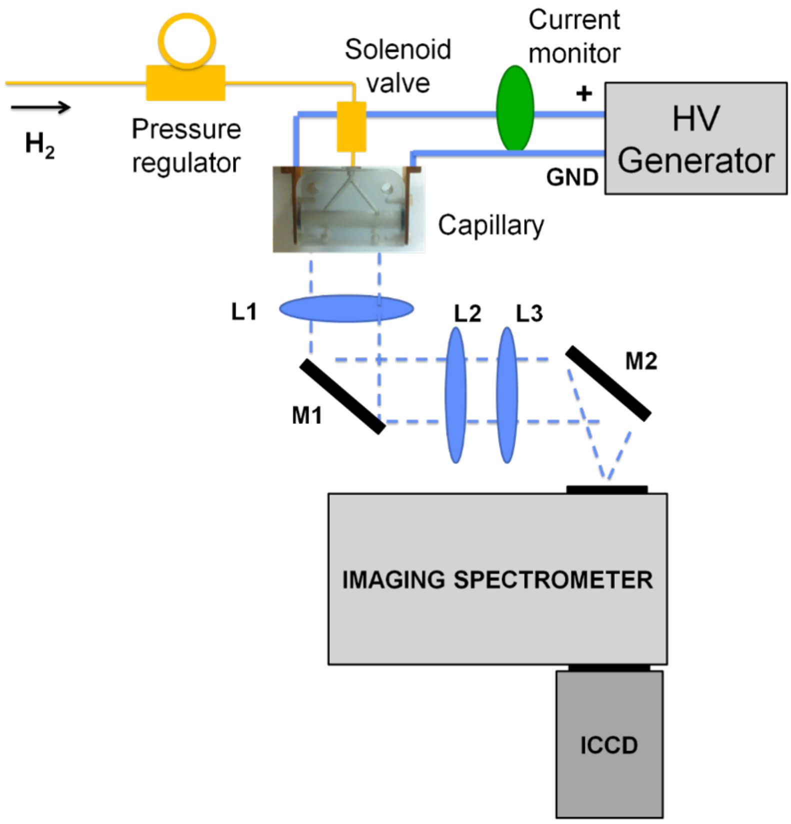

Figure 14.1: Schematic of the experimental setup proposed for the online plasma diagnostic.

Some authors have compared the results obtained with the Stark broadening analysis with the interferometric technique [12]. The density reached by Balmer beta analysis is close to the interferometric values within few tens of percentage point, confirming the quality of this method. In general, the reliability of the measurement obtained with the analysis of the Stark broadening is estimated to be of the order of 15% [3].

A typical results obtained with such technique for pure hydrogen single stage capillary discharge is shown in Fig. 14.2. Each delay from the discharge trigger has been measured with a single-shot acquisition. The knowledge of the temporal evolution of the plasma density allows also the fine tuning of the plasma density simply delaying the discharge of the capillary [13, 14].

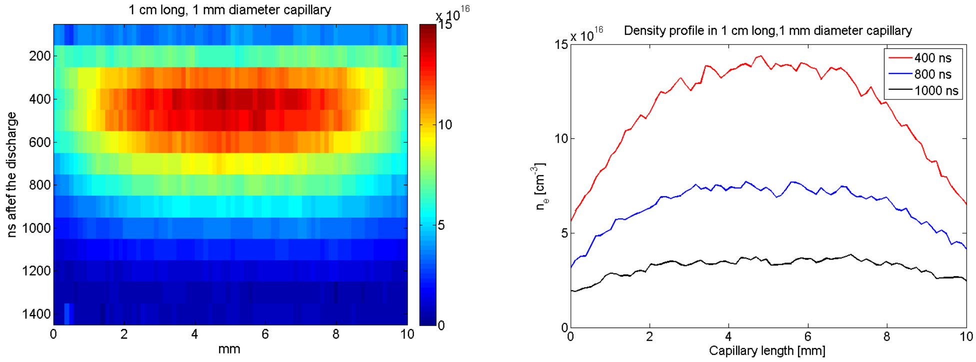

Figure 14.2: Temporal evolution of longitudinal density distribution along a 1 cm capillary with 20 kV of applied voltage measured with the Stark broadening analysis. On the left, the evolution of the plasma density along the entire capillary with 100 ns resolution time is plotted. The colorbar represents the density in cm^{-3}. On the right, the density profile for 400, 800 and 1000 ns delay are plotted.

14.2 Interferometry

Interferometric methods use the dependence of the refractive index on the density in a transparent medium. The refractive index variation can be detected by experimentally measuring the dephasing of a probe beam caused by the different phase velocity of the light propagating into the plasma. The phase velocity indeed is inversely related to the refractive index ($v_\phi = c/\eta$)) and by analyzing its variation it is possible to recover the plasma density crossed by the beam. To properly reconstruct the density the probe laser should not undergo to more complicated effects which are hard to discern by the signal [3, 4]. These effects can be the change of polarization produced by plasma anisotropy or refraction caused for example by the boundary walls of the plasma. Moreover, the signal should be intense enough to produce a significant shift of the fringes, then plasma density and plasma dimensions have to produce a measurable shift given by the formula

$$\Delta\phi \simeq \frac{2\pi}{\lambda} \int_0^L \frac{n(z)}{n_c} \partial z \tag{14.1}$$

where λ is the laser wavelength, L the plasma dimension, n_e the local plasma density (function of the position z) and n_c the critical plasma density, defined as $n_c = \left(m_e\, \omega_0^2\right) / \left(4\pi e^2\right)$. A typical setup used for the interferometric measurement based on the Mach-Zehnder interferometer is represented in Fig. 14.3

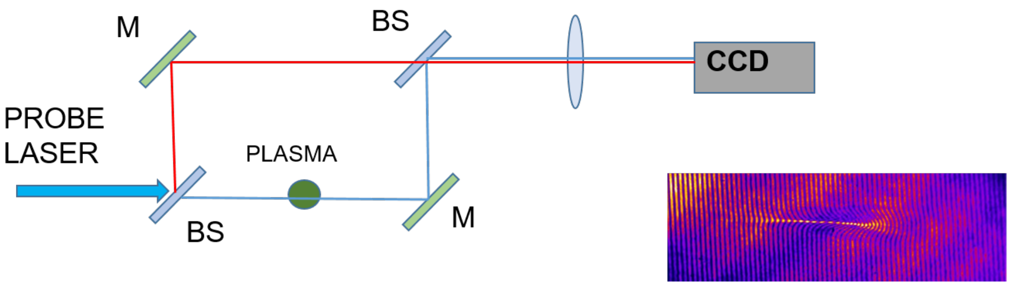

Figure 14.3: Schematic of Mach-Zehnder interferometer for interferometric measurements. Mach-Zehnder interferometer is composed by two beam splitters (BS) and two mirrors (M). On the right, an example of interferogram is plotted.

For that reasons, we propose to use interferometry for the characterization of the outer plasma flown from the capillary, whose effect is not negligible on the quality of the accelerated beam. The refraction caused by the walls does not let to use it for the characterization of the plasma into the capillary, unless a drastic change of the capillary geometry. For example, interferometric technique has been used to measure plasma density generated in a capillary discharge of square geometry [12] used to avoid laser beam diffraction. The density reached during these measurements was few times 10^{18} cm^{-3} in a 250-μm capillary width. In our setup, the density should be lower (up to 10^{17} cm^{-3}) but in a thicker capillary (1 mm diameter). The possibility to implement squared capillaries will be studied.

Interferometric technique can be considered as a complementary technique respect to the Stark broadening analysis, and both can be implemented for online single shot measurements on the same capillary. Moreover, it allows for higher temporal resolution (of the femtoseconds range, depending on the probe pulse length) and can be implemented for the control of the plasma density during the beam-plasma interaction.

Bibliography

[1] HR Griem. "Spectral line broadening by plasmas". In: *New York, Academic Press, Inc.(Pure and Applied Physics. Volume 39), 1974. 421 p.* (1974).

[2] Hans R Griem. *Principles of plasma spectroscopy*. Vol. 2. Cambridge University Press, 2005.

[3] Ian H Hutchinson. *Principles of plasma diagnostics*. Vol. 44. 12. IOP Publishing, 2002, p. 2603.

[4] AA Ovsyannikov and MF Zhukov. *Plasma diagnostics*. Cambridge Int Science Publishing, 2005.

[5] Michael Levin. *Excitation of Plasma Wakefields and Electron Acceleration*. Hebrew University, 2009.

[6] Marco A Gigosos and Valentín Cardeñoso. "New plasma diagnosis tables of hydrogen Stark broadening including ion dynamics". In: *Journal of Physics B: Atomic, Molecular and Optical Physics* 29.20 (1996), p. 4795.

[7] JM Palomares et al. "Hβ Stark broadening in cold plasmas with low electron densities calibrated with Thomson scattering". In: *Spectrochimica Acta Part B: Atomic Spectroscopy* 73 (2012), pp. 39–47.

[8] R Stamm et al. "Ion-dynamics effect on hydrogenic Stark profiles in hot and dense plasmas". In: *Physical review letters* 52.25 (1984), p. 2217.

[9] Hans R Griem, Jacek Halenka, and Wieslaw Olchawa. "Comparison of hydrogen Balmer-alpha Stark profiles measured at high electron densities with theoretical results". In: *Journal of Physics B: Atomic, Molecular and Optical Physics* 38.7 (2005), p. 975.

[10] Francesco Filippi et al. "Plasma Density Profile Characterization for Resonant Plasma Wakefield Acceleration Experiment at SPARC_LAB". In: (2016), pp. 2554–2556.

[11] F Filippi et al. "Spectroscopic measurements of plasma emission light for plasma-based acceleration experiments". In: *Journal of Instrumentation* 11.09 (2016), p. C09015.

[12] DG Jang et al. "Interferometric density measurement of the gas-filled capillary plasma and its comparison with the Hβ line measurement". In: *Journal of Instrumentation* 7.02 (2012), p. C02045.

[13] Francesco Filippi et al. "Gas-filled capillaries for plasma-based accelerators". In: *Journal of Physics: Conference Series*. Vol. 874. 1. IOP Publishing. 2017, p. 012036.

[14] F Filippi. *Plasma source characterization for plasma-based acceleration experiments*. University of Roma "La Sapienza", 2017.

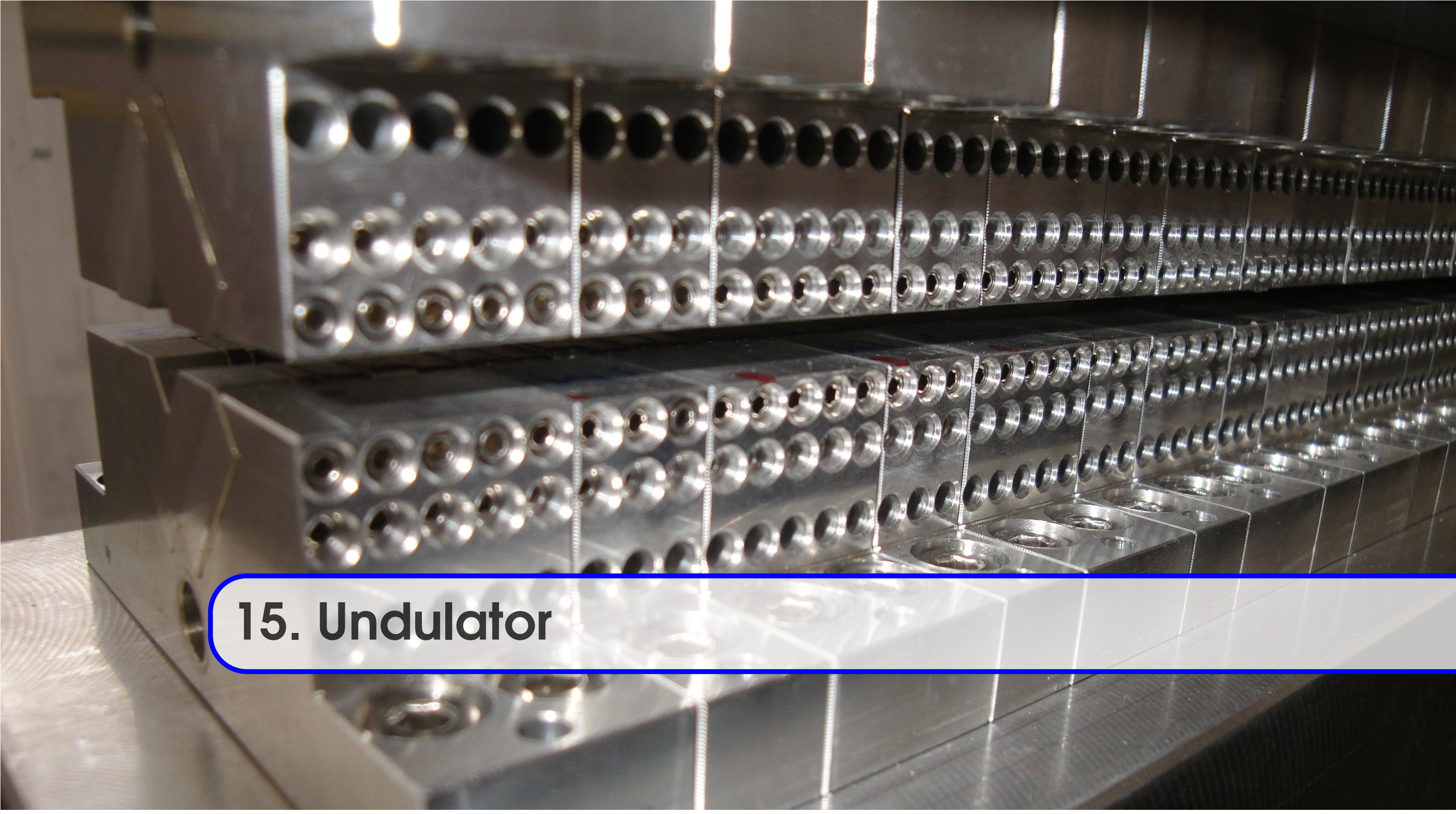

15. Undulator

The modeling of EuPRAXIA@SPARC_LAB Free Electron Laser has been accomplished by the use of scaling tools, capturing the laser performances in terms of semi-analytical formulae including beam and diffraction effects [1, 2] and on numerical simulations employing 1D and 3D FEL codes [3–5]. The result of these analyses has led to definition of the space of parameters that optimize the FEL operation in the water window region. The guiding assumption for the design at a wavelength of about 3 nm are listed below

1. minimize the overall size of the device to fit the bunker allocated spaces,
2. maximize the performance of the FEL in terms of versatility, power, coherence and stability to satisfy the users requests,
3. conceive a design allowing the transport of electron beams accelerated either with a linac or with a plasma through the same undulator,

The last item ensures the possibility of exploiting the same device to operate a conventional device and test a novel and advanced radiation source.

According to the previous prescription 1. we have excluded either seeding and cascaded operating modes (foreseeable for future upgrades) because of the requirement of linear dimensions exceeding those allowed by the space restrictions. We have accordingly chosen as primary option a conventional undulator and the operation in the SASE mode, with no harmonics up-conversion, with the possibility of exploiting the single spike regime possibly including the undulator tapering. The beam transport to and matching along the undulator is a delicate issue for manifold reasons, as e.g. minimization of inhomogeneous broadening effects and enhancement of the current intensity to increase the laser output brightness. Particular care has been therefore devoted to the design of the transport system and to the relevant optimization in terms of focusing lattice and strength, distributed and integrated along the magnetic device.

15.1 Definitions of the undulator type and main parameters

The FEL resonance wavelength is given, in terms of undulator period λ_u and strength K by

$$\lambda = \frac{\lambda_u}{2\gamma^2}\left(1+\frac{K^2}{2}\right) \tag{15.1}$$

where λ_u is the period of longitudinal variation of the on-axis magnetic filed for a planar undulator, $\gamma = E/(mc^2)$ is the Lorentz factor depending on the electron beam energy and K is the undulator parameter defined as:

$$K = \frac{eB\lambda_u}{2\pi mc} \tag{15.2}$$

being B the peak value of the on-axis magnetic field (assumed to be linearly polarized), e, m and c respectively the electron charge, the electron mass and the speed of light.

As reported above EuPRAXIA@SPARC_LAB is supposed to provide coherent radiation in the water-window region. The accelerating tools to bring the electron beam to the required energy to cover the desired wavelengths will be achieved by the use of an RF Linac with X-band accelerating structures or by the use of a plasma accelerating section. The foreseen maximum electron energy in the first stage is about 1 GeV. According to the previously quoted guidelines the undulator should be designed with short period and large strength parameter. The available space of parameters in terms of λ_u and K with the energy constraint of E = 1 GeV is given by the contour plots Fig.15.1.

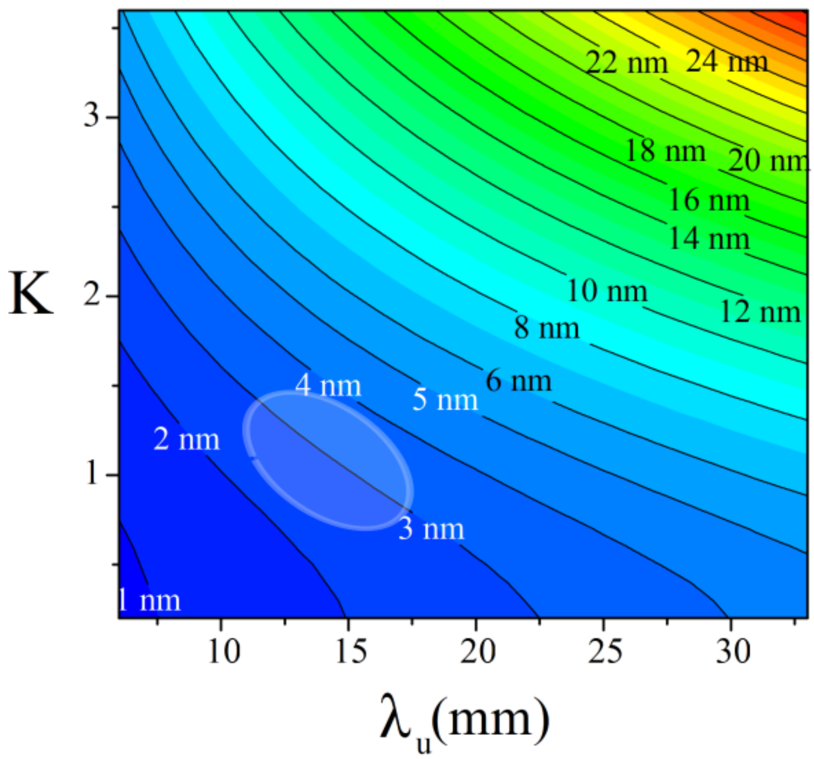

Figure 15.1: Resonance wavelength as a function of the undulator period λ_u and of the undulator strength contained in the K parameter. The region of interest for EuPRAXIA@SPARC_LAB is circled.

The undulator technology is a fairly mature field, therefore different options are available as summarized in Fig. 15.2, where we have displayed the field strength vs. gap performances for some of them listed below [6, 7]:

1. The conventional Halbach schemes (Pure Permanent Magnets PPM)
2. The Hybrid Permanent Magnets (HPM)
3. The Super Conducting Undulators (SCU)
4. The Electromagnetic Undulators (EM)

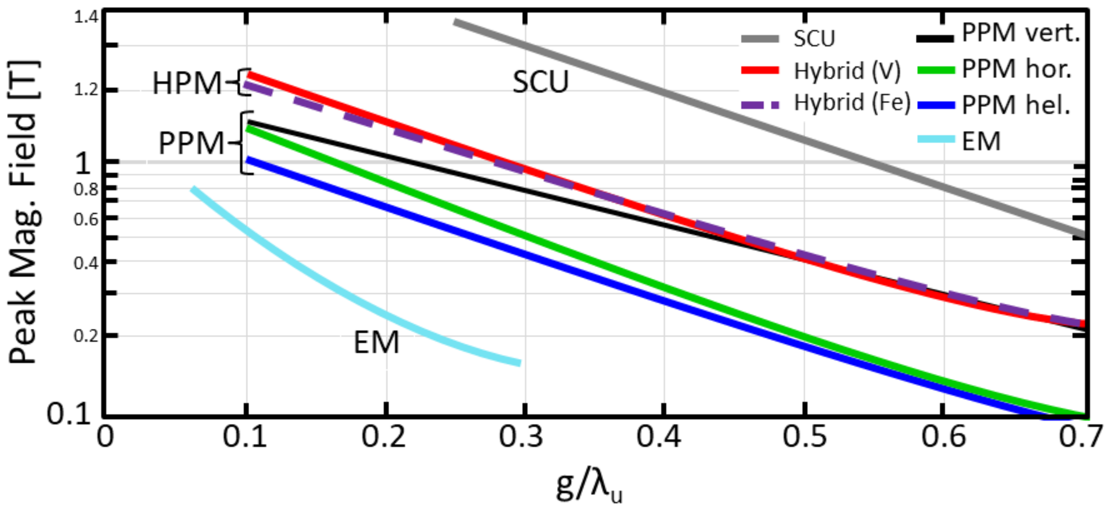

Figure 15.2: Comparison between different undulator technologies.

The EM solution is not viable due to the limited performances in terms of magnetic field vs. gap to period ratio $r = g/\lambda_u$.

The option of superconducting undulators could, in principle, meet the necessity of operating with large K and short undulators period. Significantly large values of K can be obtained for relatively small values of λ_u, thus yielding larger values of the corresponding Pierce parameter and thus a shorter saturation length. An example has been reported in Fig. 15.3. The on-axis magnetic field of these devices exhibits the following dependence on the r ratio

$$B = \alpha\, e^{\beta\, r + \gamma r^2 + \delta\, r^3} \tag{15.3}$$

with the coefficients specified in Tab. 15.1 [7].

	α[T]	β	γ	δ
Helical	11.9934	-3.7977	0.3364	0.0
Planar	22.0091	-9.0877	7.9639	-3.5986

Table 15.1: SC-Undulator fit coefficients.

The use of SCU would imply a cryogenic cooling system and so a more bulky and complicated structure and higher costs of construction and operation. In addition some complications arise in field measurement and field error tuning. For these reasons only some SCU devices have been used until now for special applications [8–10] but not for large scale use. In all these cases the value of the undulator period is around 1.5 cm , this means that we would still need a K value of 1 to lase at 3 nm . These parameters can be reached with the more simple setup of the Permanent Magnet Undulators (Pure or Hybrid).

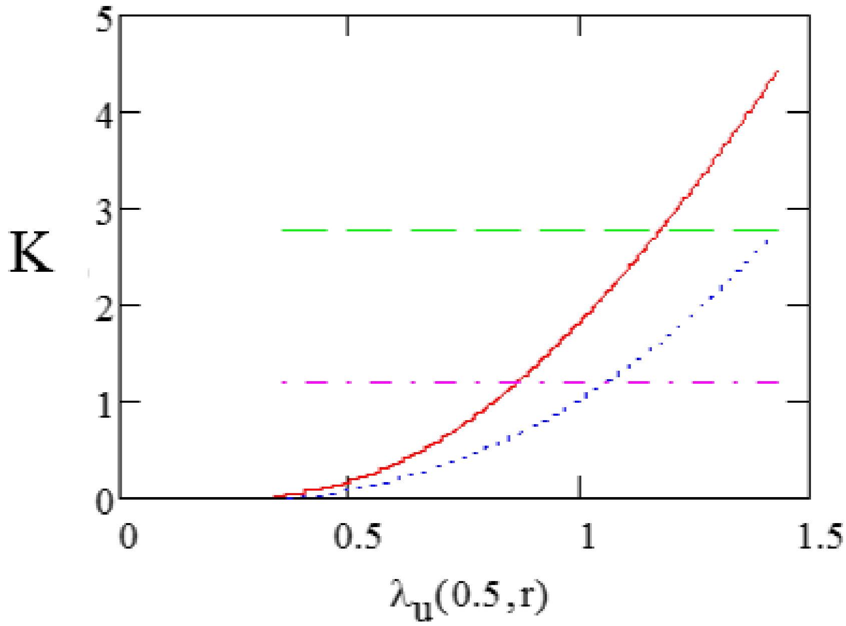

Figure 15.3: Behavior of the associated K parameter values vs. the undulator period for $g = 0.5$ cm , for Helical (continuous line) and Linear (dot) Undulator.

The PPM is the most commonly adopted technology for most of the worldwide FEL facilities. These magnetic devices operate without any additional cooling system in vacuum or in air. In this last case, a waveguide has to be installed between the two magnets bars to allow the electrons to move under vacuum. In order to have radiation at 3 nm with a 1 GeV electron beam, the optimum solution would be to minimize the undulator period λ_u and increasing K as much as possible. The values of K are related to λ_u, whose value determines the maximum available peak magnetic field. For a permanent magnet undulator with a K value of 1, the smallest period actually reached in an operating undulator is 1.4 cm , as demonstrated at SPARC_LAB Lab in the pilot experiment with the short period undulator developed by ENEA and realized by Kyma [11]. This value is close to that (1.5 cm) used by the SwissFEL undulators at PSI [12]. Prototypes at 8 mm and 4 mm are under study [13, 14] but not yet implemented on an operating FEL line. The K parameter is also related to the FEL gain and so it influences the saturation power and saturation length. A value of K less than 1 is considered not suitable for FELs.

According to the previous considerations, the undulator we propose for the EuPRAXIA @SPARC_LAB FEL is based on the ENEA experience with short period 1.4 cm , small gap, PM undulators [11]. The undulator has a quatrefoil structure, it focuses both in vertical and radial directions, with with $hx = 0.9$ and $hy = 2 - hx$, and has a high magnetic field homogeneity. A prototype of such a device has been developed by ENEA Frascati together with Kyma Trieste and built by Kyma. Its main characteristics are described in Fig. 15.4 and Fig. 15.5. The undulator has been tested on the FEL line at SPARC_LAB and is now used as afterburner for short wavelengths. The on-beam experimental calibration gives a measured value of $K = 1.145$ at totally closed bars ($g = 0$ measured between the parallel faces of the magnets).

For simulation in the present document, an undulator with the same geometry of the ENEA-Kyma, used at SPARC_LAB, with a period $\lambda_u = 1.5$ cm has been taken into account in order to be able to increase slightly the maximum magnetic field. The undulator parameters to lase in the

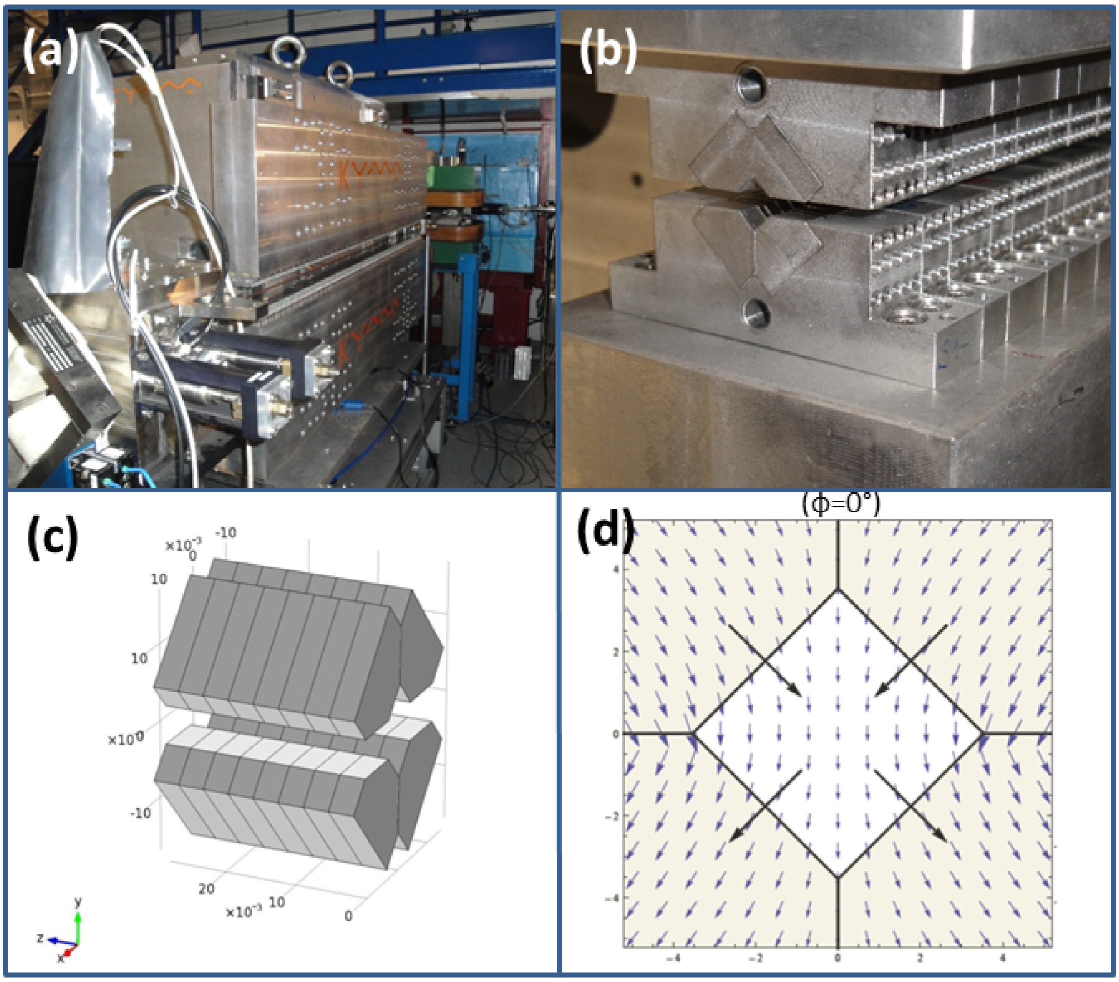

Figure 15.4: ENEA-Kyma short period quatrefoil undulator. The undulator (a) is now installed on the SPARC_LAB FEL line as afterburner for the short wavelengths. The quatrefoil structure is evident in picture (b) and in the 3D plot (c) and in (d) the magnetic field is shown in transverse plane at the initial phase ($\phi = 0°$at z=0).

water-window at $E = 1$ GeV are summarized in Tab. 15.2. A maximum K value can be reasonably assumed as $K = 1.2$ since it is close to the measured value for the ENEA-Kyma undulator and the same value of the SWISS-FEL Aramis undulator.

For a cold ideal beam the FEL performance is strongly influenced by the beam current and the transverse size of the electron beam. Saturation length and saturation power depend on the current density, as described in the previous paragraphs. To contain the saturation length, and therefore the undulator dimension, within the allocated experimental space, a maximum current value and a minimum beam size value are required. In the EuPRAXIA@SPARC_LAB bunker, the maximum available space for the undulators is about 40 m. All beam parameters have to be fixed therefore in order to lase within this length. The peak current can be controlled either by compressing the electron bunch or by increasing the total charge per bunch. Both solutions imply constraints that have been discussed in the machine physics part of this document. However, an increasing of the charge allows also to enhance the energy of the FEL light pulse and so the number of photons/pulse. Moreover, we have to consider that the three-dimensional and inhomogeneous effects due to beam emittance and energy spread affect the saturation length and power as well as the bandwidths, as described in Chapter 2 (FEL design principle).

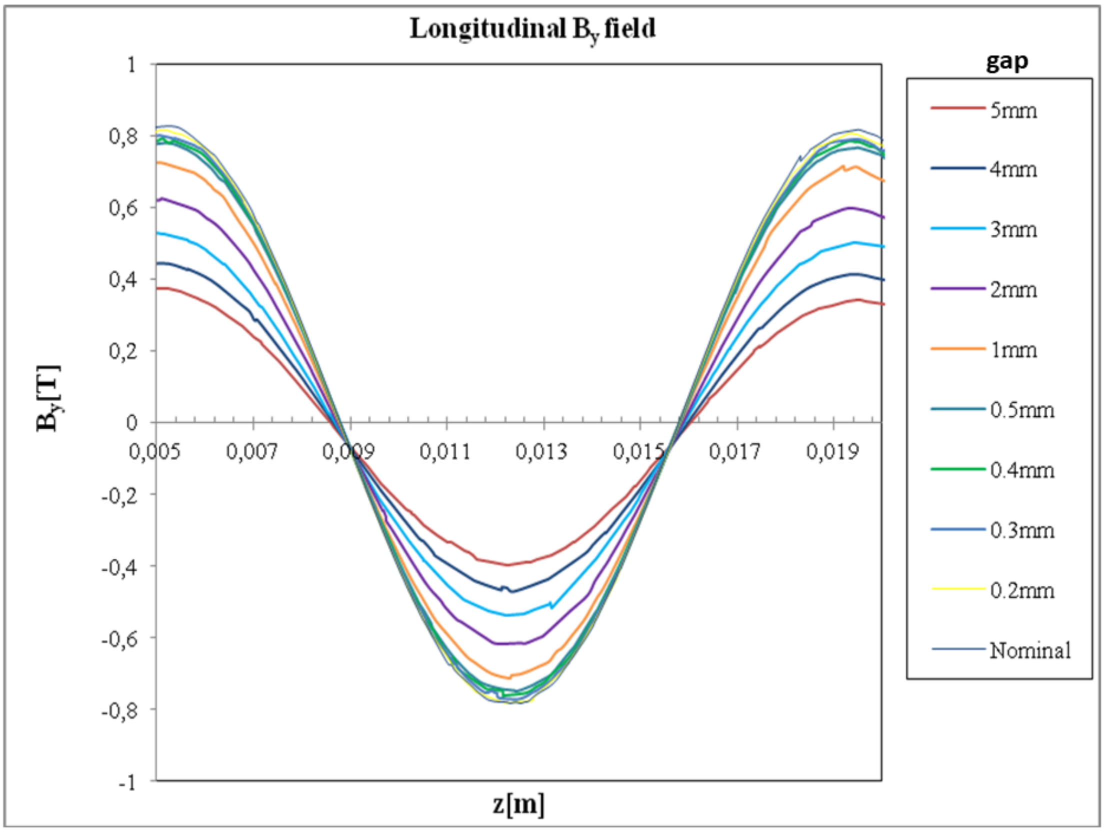

Figure 15.5: On-axis magnetic field for the ENEA-Kyma undulator. The longitudinal distribution over a period (phase $\phi = 2\pi$) for different values of the gap.

λ(nm)	2.94	3	2.25	3.37
λ_u(cm)	1.5	1.5	1.5	1.5
K	1	1.03	1.15	1.2

Table 15.2: Undulator K parameter for different resonance wavelength with $\lambda_u = 1.5$ cm at an electron beam energy $E = 1$ GeV.

15.2 Electron beam focusing and transport in the undulator

At an electron beam energy of 1 GeV, the natural focusing of the undulator is rather weak. The associated transport properties are therefore almost equivalent to those of a long drift section. If not constrained by other magnetic elements, the transported beam will undergo a significant increase of the transverse dimensions. For these reasons the undulator magnetic channel consists of several undulator modules with the total length covering the distance required to allow the FEL saturation. A magnetic channel for the transport of the electron beam is foreseen, it is provided by a Focusing-Drift-Defocusing-Drift (FODO) cell with alternate gradient quadrupoles. Focusing is indeed provided by placing electromagnetic quadrupoles in the breaks between the undulator modules. The distance between two consecutive undulator modules has to be minimized, in view of the insertion of suitably short diagnostics. The undulator modules have period $\lambda_u = 1.5$ cm , and the undulator parameter K ranges around 1. A sketched out picture of the undulator system is presented in Fig.15.6.

The undulator considered here is made by modules of $N = 77$ number of periods. With $\lambda_u = 1.5$

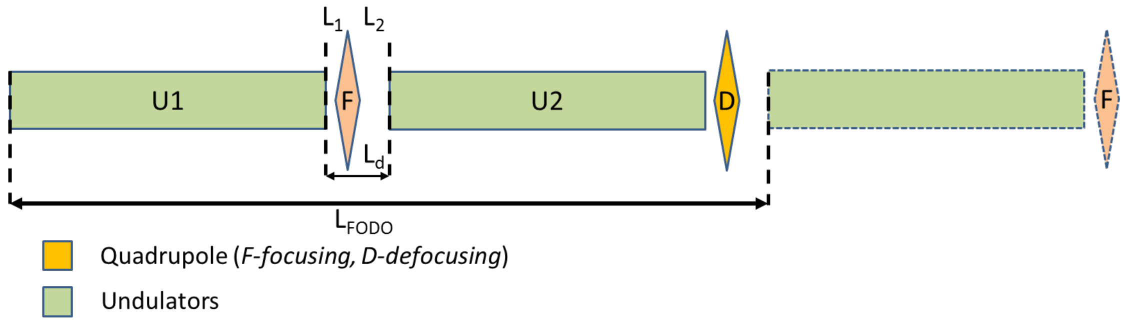

Figure 15.6: Layout of the undulator FODO lattice.

cm, the undulator module turns out to be $L_u = 115.5$ cm long, a gap $g = 22.5$ cm separate two undulator module. In this space a quadrupoles with a magnetic length of 9 cm long is placed between two drift section 3 cm and 10.5 cm respectively long. The second drift is long enough to allow the installation of a beam position monitor or some diagnostics for radiation. The quadrupole design has to be based on the idea of minimizing the longitudinal space occupation in the gap between undulators and steering correctors can be included in the quadrupoles design as additional coils. A list of the main parameters of the undulator line is summarized in Tab. 15.3.

Element length	cm	units λ_u
Undulator module L_u	115.5	77
Drift L_1	3	2
Quadrupole eff. lenth Q_l	9	6
Drift L_2	10.5	7
Gap between undulators L_d	22.5	15
FODO length L_{FODO}	276	184

Table 15.3: Length of the FODO elements. The undulator period λ_u has been fixed as 1.5 cm.

The length of the magnetic modules implies also effects on the focusing properties of the FODO and on the maximum focusing of the electron beam in the transverse plane. This affects the performance of the FEL since the smaller the electron beam transverse size, the higher the current density and, as a consequence, the FEL ρ parameter. On the other hand, a degradation on the FEL performance due to diffractive effects has to be considered. We define the average transverse Twiss parameters in the undulator as

$$\bar{\beta}_{x,y} = \frac{1}{L_{u1}} \int_0^{L_{u1}} \beta_{x,y}(z)dz + \frac{1}{L_{u1}} \int_{L_{u1}+L_d}^{L_{u1}+L_d+L_{u2}} \beta_{x,y}(z)dz \tag{15.4}$$

where L_{u1} and L_{u2} are the length (equal to $L_u = N\lambda_u$) of the two undulator module in the FODO elements. The matching condition is obtained by imposing the condition that the average value of the Twiss beta parameter in the two planes are equal for the two sections. Hence, we have to minimize the difference

$$\left|\overline{\beta}_x - \overline{\beta}_y\right| = min \tag{15.5}$$

A detailed discussion on transport optimization in undulators can be found in Ref. [15]. The beta function depends on the undulator strength K and the electron beam energy. In the

EuPRAXIA@SPARC_LAB case the undulator work at almost fixed gap (K slightly variating between 1 and 1.2) but the beam energy can vary in order to tune the wavelength of operation. According with the undulator parameters in Tab. 15.3, different sets of matching parameters have been considered and summarized in Tab. 15.4.

Case	E (GeV)	K	λ (nm)	$\overline{\beta}_x, \overline{\beta}_y$(m)	$\overline{\sigma}_x, \overline{\sigma}_y$ (μm)	Q_G (T/m)
A	0.5	1.2	13.47	4.34	46.09	22.19
B		1	11.75	4.3	47.38	22.53
C	0.8	1.2	5.26	4.45	37.68	36.57
D		1	4.59	4.47	37.77	36.78
E	1	1.2	3.37	4.47	33.80	46.02
F		1	2.94	4.48	33.84	46.19
G	1.2	1.2	2.34	4.48	30.90	55.43
H		1	2.04	4.49	30.93	55.57

Table 15.4: Twiss parameters and matching condition for transport in the undulator with $N = 77$, $\lambda u = 1.5$ cm, $\varepsilon = 0.5$ mm mrad . E is the electron beam energy, K the undulator strength, λ the FEL wavelength, $\beta_{x,y}$ the average beta Twiss parameter, $\sigma_{x,y}$ the average beam size, Q_G the quadrupole gradient.

The electron beam RMS size is defined as $\sigma_{x,y} = \sqrt{\beta_{x,y}\varepsilon/\gamma_0}$, where ε is the geometrical emittance and γ_0 the electron beam Lorentz factor. With this setup the average Twiss beta in the undulator is slightly larger than 4 m and this means that, for the nominal operation emittance $\varepsilon = 0.5$ mm mrad, the average beam size is around 30-40 μm both along the x and y axis. In Fig. 15.7, the Twiss beta parameter behavior in the undulator for the radial and vertical directions is shown in the FODO element. It has to be noted that the considered undulator type (Kyma-like) acts with a small focusing on both x and y. This slightly helps the quadrupoles in their focusing role and permits to have such small values of beta.

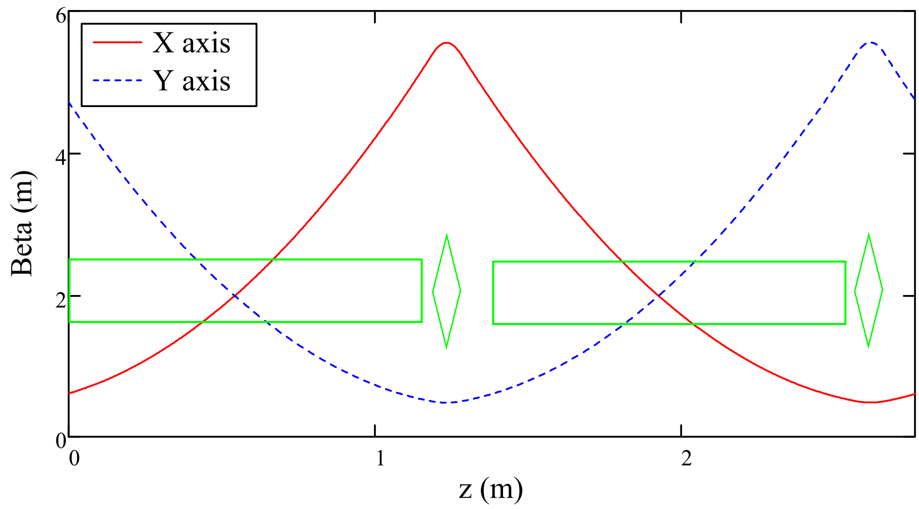

Figure 15.7: Twiss beta in the x and y plane for the FODO lattice with $N = 77$ undulator period, in case F of Tab. 15.4.

Bibliography

[1] G.Dattoli, P.L.Ottaviani, and S.Pagnutti. *Booklet for FEL Design*. http://www.fel.enea.it/booklet-presentation.html. Enea Edizioni Scientifiche, 2008.

[2] Ming Xie. "Design optimization for an X-ray free electron laser driven by SLAC linac". In: *Proceedings Particle Accelerator Conference*. Vol. 1. 1995, 183–185 vol.1. DOI: 10.1109/PAC.1995.504603.

[3] G Dattoli, PL Ottaviani, and S Pagnutti. "The PROMETEO Code: A flexible tool for Free Electron Laser study". In: *Nuovo Cimento. C* 32.2 (2009), pp. 283–287.

[4] L Giannessi. "Overview of Perseo, a system for simulating FEL dynamics in Mathcad". In: *Proceedings of the Free-Electron Laser Conference*. www.perseo.enea.it. 2006.

[5] Sven Reiche. "GENESIS 1.3: a fully 3D time-dependent FEL simulation code". In: *Nuclear Instruments and Methods in Physics Research Section A: Accelerators, Spectrometers, Detectors and Associated Equipment* 429.1-3 (1999), pp. 243–248.

[6] Klaus Halbach. "Physical and optical properties of rare earth cobalt magnets". In: *Nuclear Instruments and Methods in Physics Research* 187.1 (1981), pp. 109–117.

[7] Pascal Elleaume, J Chavanne, and Bart Faatz. "Design considerations for a 1 Å SASE undulator". In: *Nuclear Instruments and Methods in Physics Research Section A: Accelerators, Spectrometers, Detectors and Associated Equipment* 455.3 (2000), pp. 503–523.

[8] C Boffo et al. "Performance of SCU15: the new conduction-cooled superconducting undulator for ANKA". In: *IEEE Transactions on Applied Superconductivity* 26.4 (2016), pp. 1–4.

[9] Y Ivanyushenkov et al. "Development of a superconducting undulator for the APS". In: *Journal of Physics: Conference Series*. Vol. 425. 3. IOP Publishing. 2013, p. 032007.

[10] Nikolai Mezentsev et al. "Planar Superconducting Undulator With Neutral Poles". In: *25th Russian Particle Accelerator Conf.(RuPAC'16), St. Petersburg, Russia, November 21-25, 2016*. JACOW, Geneva, Switzerland. 2017, pp. 21–23.

[11] Franco Ciocci et al. "Segmented undulator operation at the SPARC-FEL test facility". In: *Advances in X-ray Free-Electron Lasers Instrumentation III*. Vol. 9512. International Society for Optics and Photonics. 2015, p. 951203.

[12] Romain Ganter. *SwissFEL-Conceptual design report*. Tech. rep. Paul Scherrer Institute (PSI), 2010.

[13] J Bahrdt and Y Ivanyushenkov. "Short period undulators for storage rings and free electron lasers". In: *Journal of Physics: Conference Series*. Vol. 425. 3. IOP Publishing. 2013, p. 032001.

[14] Shigeru Yamamoto. "Development of undulator magnets towards very short period lengths". In: *AIP Conference Proceedings*. Vol. 1741. 1. AIP Publishing. 2016, p. 020029.

[15] M Quattromini et al. "Focusing properties of linear undulators". In: *Physical Review Special Topics-Accelerators and Beams* 15.8 (2012), p. 080704.

16. Control system

16.1 General considerations

In the field of particle accelerators the term *Control System* refers to an ensemble of IT infrastructures and software services devoted to operate the accelerator plant. Besides the obvious task of controlling and monitoring devices, a modern Control System has to provide the staff involved in the plant management and the users utilizing its facilities with easy, powerful and robust services.

The EuPRAXIA@SPARC_LAB project is very complex in its technical implementation and ambitious in its openness to users and this emphasize even more the above statement.

The time horizon of the project can be defined as *medium term*, which suggests to stay open – to a certain extent – with respect to specific technical solutions, given the rapid evolution of technologies in the IT field.

Nevertheless, some important features that the EuPRAXIA@SPARC_LAB 's Control System (ECS) has to provide can be outlined.

16.1.1 Scalability

Even thought this is one of the most abused terms in the Control System field, it remains a dominant issue. The term scalability indicates the capability of a system to support replicas of its internal services that coordinate with each other and share the workload.

A *scalable* Control System architecture is able to grow in order to fulfill more demanding performances, reliability and dimension of the context it deals with.

16.1.2 Embedded data acquisition

In a scientific context, the possibility to analyze and correlate data coming from different systems is an all-important method for understanding the behavior of a machine such complex as a particle accelerator.

Analysis and correlations must be possible on data both dynamically acquired and stored over time. Of course, the fastest the data storage of the acquired physical quantities the better the time resolution users can count on when doing theirs calculations.

The practice of fast storage of large amount of data is generally addressed in DAQ applications though, modern software techniques allow natively integration of fast storage in a Control System framework, which guarantees a much better time-correlation among quantities.

16.1.3 Flexibility

A modern Control System must easily adapt to the always new needs coming from scientific issues and users demands. This means that it must be possible to smoothly insert new algorithms for realtime calculation of derived quantities, activate automatic feedbacks, process data, integrate external systems (e.g. user's apparatuses) and so on.

The ECS must allow for a *hot-insertion* of such processes, that is without interference with its run-time operation. It is also important that the development of these algorithms must be possible in many different languages, to widen the body of developers.

16.2 General description

16.2.1 Main features

The above considerations lead to the main features that the ECS has to provide:
- command execution
- data acquisition
- fast data storage
- stored data retrieval
- analysis on live data
- analysis on stored data
- automatic operations and feedbacks
- GUI (Graphic User Interface)
- alarms management
- interfacing to the machine timing system
- interfacing to the machine interlock system

16.2.2 System topology

EuPRAXIA@SPARC_LAB will be a complex made of many devices and subsystems distributed across an area larger than 5000 m^2 which leads to a distributed Control System architecture as described below.

Distributed Control Units

We define a Control Unit (CU) node as a process that executes commands and continuously monitors a set of devices, pushing the acquired data to the system *live* database and to the fast storage database. Considering the high performance and quantity of memory nowadays available on even small Single Board Computers (SBC), it is reasonable to assume to employ one CU for each machine device. In those cases where many identical devices are connected to each other through a dedicated bus (e.g. an array of sensors on CANBus), a single CU can handle the whole array.

A CU is an application that can be hosted by different processors, depending on the circumstances:
- CU on embedded processor on an acquisition bus (e.g. CompactPCI, PXI, etc...) for those devices or subsystems requiring a complex front-end (e.g. DAC, ADC, digital I/O, waveform generators, samplers, etc...);
- CU on SBC attached to the device (e.g. through serial port), when it is necessary to adapt the device custom protocol and communication channel to a standard protocol over a common network;

- CU running within the device itself: this is possible when the device provides the developers with processing resources and APIs to access its features (e.g. Libera BPM systems [1], high end oscilloscopes, etc...);
- CU on Virtual Machine running in a dedicated infrastructure in those cases where it is required a slow-control, and consequently the latencies due to the network are not an issue. This is a very convenient solution because the more centralized the hardware the easier its maintenance.

Distributed User Interfaces

We define a User Interface node (UI) as an integrated environment, dedicated to physicists and machine operators, for interacting with the machine. Even though the UIs will be concentrated in the machine control room for the most, the ECS must allow operations from remote, by using any physical device (tablets, smartphones, laptops, PCs).

A UI node must be able to handle configuration data, present live machine data both in text and graphic, perform searches in the stored machine data, show alarms and host applications developed by users for data processing.

The UI must provide users with many high level programming environment fitted with APIs to access the ECS resources (e.g. Root, Lua, MATLAB, etc...), besides conventional languages such as C, C++, JavaScript, Pyton and so on.

From a physical point of view, a UI consist in a console: at present, the thin-client technology has evolved so much that even *credit card* size SBC are powerful enough to drive multiple Hi-Res monitors and provide an excellent computing power.

Execution Units

Many of the features listed in par. 16.2.1 can be cunningly achieved by assuming the existence of generic computational nodes. We define an Execution Unit (EU) node as a process that gets data from one or more CUs, performs calculations and make the results available to the rest of the system. An EU can also receive and send commands from/to any other node of the system.

The implementation of EUs in the ECS will allow to insert feedback processes *on-the-fly* and realize proxies for the interfacing of external systems (interlocks, safety, users' experiments, etc...).

Framework core services

CUs, EUs and UIs, rely on the ECS framework core system for their operation. In this conceptual description, it is not useful to go into details of the framework software architecture but – in any case – it has to comply with the general considerations reported in section 16.1 and offer all the services listed in section 16.2.1.

The framework core will provide for all the system wide services, such as: configuration of all the machine devices, management of all the CUs and EUs (initialization, start, deinitialization, stop), notification to the UIs of devices data structures, commands dispatching from UIs to CUs and alarm notification, access to live data and stored data databases.

When looking for performances, databases are always an issue; in particular, relational databases are somehow slow for data insertion given that they have to apply a schema at write time. On the contrary, key-value databases allow for the insertion of data in a schema-less way. In this case, the inserted data – whichever their format is – are taken from the DB as an anonymous stream of bytes, associated to an identification key. Key-value databases are widely adopted in modern web applications and can be successfully used in the ECS framework for fast storage functionality.

16.2.3 Software

As said above, the framework core software to be adopted for the ECS must be thought as something which is provided as an already complete and working object.

Besides the framework core software, the specific implementation of the ECS will require to widen as much as possible the body of developers and reduce the development time of the the various CUs, EUs and UIs applications.

This can be accomplished by adopting languages and environments oriented towards the Rapid Application Development (RAD) approach (e.g. LabVIEW [2] for CUs EUs and UIs, Matlab [3] for EUs and UIs). The RAD basic idea is to lessen the planning phase and give more emphasis on an adaptive process, so that prototypes realized by personnel of the various services can be successfully used in addition to or sometimes even in place of design specifications.

16.3 Machine control

The EuPRAXIA@SPARC_LAB machine can be divided in three main parts: Linac, Laser and Radiation lines, each one having elements to be put under the management of the ECS.

16.3.1 Laser

The laser optimization – both at the cathode and the interaction point – requires a control over all the components of the apparatus from remote. The main operation is the alignment of the light beam with mirrors that can be done by moving mirrors with a motor while the laser light is acquired through a camera. Other parts can be controlled by means of standard interfaces such as Ethernet or serial interface.

16.3.2 RF

The RF section includes controls for the high power and low power sections. The modulator can be controlled with Ethernet or serial interface with an appropriate protocol.

Signal monitoring and synchronization can also be controlled via Ethernet or using a demodulation board and digitizers on PXI or CompactPCI bus. Data analysis and device control are performed by the processor board resident on the bus itself.

Other devices such as attenuators, phase shifters, amplifiers and so on will be controlled with serial or Ethernet interfaces.

16.3.3 Magnets

The accelerator employs different kind of magnets such as solenoids, correctors, dipoles and quadrupoles. The control of the magnets entails the control of their power supplies which – most likely – will come from different vendors. In order to keep as much uniform as possible the interfaces between the ECS and the Power Supplies it is very important to produce specifications requiring a standard communication channel (e.g. Ethernet) and a unique communication protocol (e.g. Modbus [4]).

16.3.4 Vacuum

The machine vacuum condition has to be constantly monitored and maintained through different apparatus.

Pumps

The most widely adopted pumping systems for ultra-high vacuum (UHV) is a combination of ion sputter pumps (briefly ion pumps) and titanium sublimation pumps (TSP). Control units for these pumps usually include a serial interface (RS-232 or RS-485) for remote control and a set of logical switches for alarm output. The brand and model of these controls should be the same for all the machine, to avoid differentiation of software versions and spare parts. For particular sections (those requiring gas differential pumping) turbomolecular pumps with scrolling fore pumps will be required whose control units are again equipped with serial ports and switches. Turbo and scroll pump combinations will be also required for first stage of evacuation of each section, but in this case a remote control should not be needed.

Vacuum gauges

Vacuum gauges allow an accurate measure of the vacuum in different point of the machine. The most widely used ion gauges controls are equipped with serial ports or a FieldBus equipped with analog and digital channels. Unfortunately, at the time of this writing, these gauges are designed for industrial applications, and the required pressure range needed for radiation beam lines applications (in the 10^{-9} Pa scale) is not achieved, so the serial approach would be chosen. Some sections will require low vacuum gauges, such as thermocouples or Pirani heads, also generally equipped with control units having serial interfaces.

Valves

All the valves should be electro-pneumatic gate type. The control units, generally custom-made, include a solid state switch for valve opening/closing and a couple of logical switches for valve status monitoring. All the valve control units will be logically (and in some case physically) connected to the vacuum gauge, ion pump and cooling system controls in order to avoid valve opening in unsafe vacuum/cooling conditions and to close them automatically in case of vacuum/cooling alarms. Valves belonging to the switching mirror chambers will be also connected to the chamber position encoders, so that valves may be only opened on safe beam path conditions. Also, the correct opening and closing sequence will be ensured in order to avoid radiation directly hitting the front-end valves without the beam stoppers inserted. All these conditions imply hardware controls for the safety-related situations and realtime software controls in the other cases.

One special valve, designed for protecting the accelerator and the undulator from sudden venting of the beam lines, is a fast valve, which has its own sensor and control unit.

16.3.5 Diagnostic

Some machine parameters (e.g. emittance, bunch length, energy) will be measured through imaging techniques so that the use of a versatile camera system is strategic in the realization of the specific diagnostic. The rapid evolution in image acquisition systems allows us to choose the camera and its own interface in a wide variety of products. The IEEE 1394 and GigE Vision protocols offer the possibility to interface different cameras with different specifications without changing the acquisition program. The cameras are acquired by different distributed CUs that make data available to the rest of the system. The network has to provide enough bandwidth to allow the integration of all the machine's cameras in the ECS.

Another important aspect in diagnostic is the control of motors (generally stepper motors) to move flags and slits for the acquisition of the beam spot.

The beam position and charge monitors acquisition system depend on the type of pickup used: in general – for this two kind of diagnostic – analog acquisition boards, with appropriate signal conditioning, are employed.

16.3.6 Motion and positioning

Most of the chambers holding optical elements, namely mirrors, gratings, target and slits, are coupled with suitable position encoders. Depending on the accuracy required for the placement, stepper motors or CC motors will be used, coupled with optical encoders or potentiometric transducers respectively. In both cases, motor embedded encoders will not be used, relying on the motor reproducibility and on the external encoders. Motor control units are currently available with the most common interfaces such as Ethernet, CANopen, Profibus-DP, serial ports and so on. The latter three are also generally available for potentiometric transducers. Each motor will be equipped with a couple of switches (end of travel) to be used for both motor stopping and alarm generation.

16.4 ECS infrastructures

16.4.1 Network

A star topology distribution shall provide Ethernet across all the machine area. The central node will be realized with a couple of switches in mutual fail-over. The connections of the central node to the host nodes will be realized with monomode fiber optic cable, to have a granted throughput of 10 Gbps on each uplink. Each host node physically consists of a switch that provides local end users and machine devices with connection.

16.4.2 Virtualization

As already said in sect. 16.2.2, vitrualization is a very convenient way to host processes and services for its intrinsic scalability and failover features.

Nowadays, the employment of virtual machines (VMs) in accelerators' Control Systems is quite common and the successful experience with the replacement of tens of processors of the DAFNE Control System with VMs shows that virtualization is a feasible solution in the *slow-control* area.

On the other hand, the growing on the market of low-cost mini-PCs, SBC and *barebone* controllers offers the opportunity to easily spread running process (the distributed CUs) over the accelerator area. The right choice between VMs and physical processors will come from the technical development of the various EuPRAXIA@SPARC_LAB systems and – most likely – the ECS will employ both.

16.4.3 Storage

An accelerator facility is a *factory* of data. Some data are necessary for the technical operation of the machine (e.g. devices' configuration parameters), some are are necessary to the machine Control System (addresses, host names, etc...), some are necessary for the machine operation (e.g. datasets that allow operators to save and recover working points) and some are produced by users running experiments.

As said above, the ECS will have to be able to handle all those data and put them in a storage system setup on purpose. To avoid a continuous increase of the stored data, the ECS will have to provide a proper data aging policy (e.g. decimation) and tools to dump old data to different supports.

16.5 Conclusions

Some standard solutions widely adopted by the scientific communities for the control of Particle Accelerators (e.g. EPICS [5], TANGO [6]) could – to a certain extent – be suitable for the EuPRAXIA@SPARC_LAB facility.

Nevertheless, other solutions are emerging, bringing new cutting edge software technologies in the panorama of Control Systems.

In particular, we strongly believe in !CHAOS [7]: a software framework developed at LNF to control scientific plants. Being extremely versatile and scalable, !CHAOS naturally fits all the general requirements discussed at the beginning of this document and stands out for its native fast storage capability.

!CHAOS (Control system based on Highly Abstracted and Open Structure) has been funded by MIUR as winning "progetto premiale" (in 2014 – 2015), has already been used on parts of the DAFNE accelerator at LNF, is being used in a project carried out in collaboration with industry and is integral part of the funded "progetto premiale" aiming at the upgrade of the SPARC_LAB accelerator at LNF.

!CHAOS has been presented in many international conferences and is in the main topics of the next PCaPAC 2018 conference [8], that will be hosted by NSRRC, in Hsinchu, Taiwan, October 2018.

Bibliography

[1] URL: http://www.i-tech.si.

[2] URL: http://www.ni.com.

[3] URL: https://www.mathworks.com.

[4] URL: http://www.modbus.org.

[5] URL: https://epics.anl.gov.

[6] URL: http://www.tango-controls.org.

[7] URL: http://chaos.infn.it/index.php/publications/publications.

[8] URL: https://indico.nsrrc.org.tw/event/1/.

IV Science with Free Electron Laser

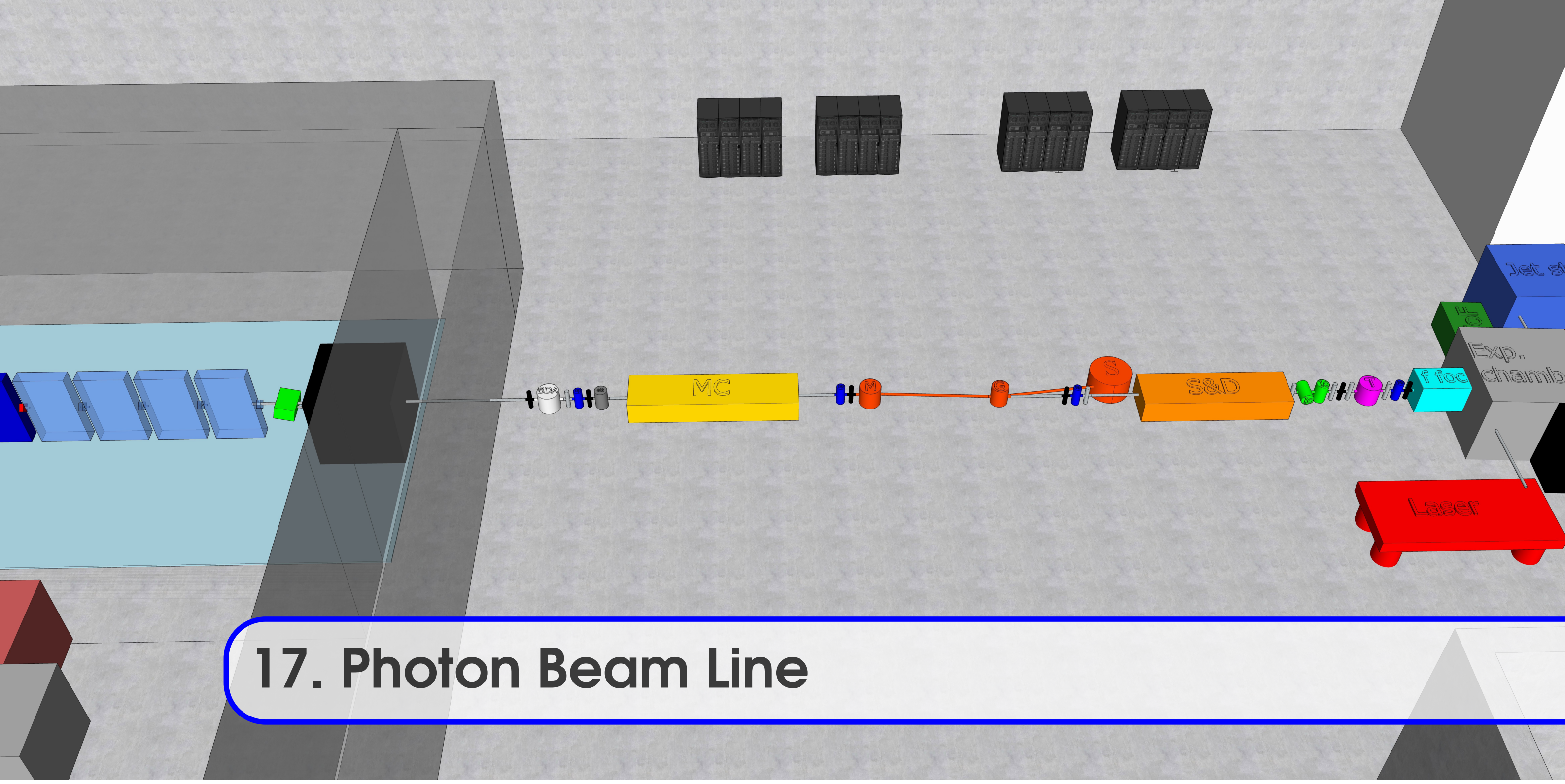

17. Photon Beam Line

Key elements of FEL radiation are the high peak brilliance, that can be higher than 10^{27} photons/s mm^2 mrad^2 0.1% bandwidth, and the short pulse duration, which is of the order of tens of fs. The EuPRAXIA@SPARC_LAB experimental activity will be focused on the realization of a plasma driven short wavelength FEL with one user beam line, according to the beam parameters reported in Table 17.1. The first foreseen FEL operational mode is based on the Self Amplification of Spontaneous Emission (SASE) mechanism [1]. Other schemes, like seeded and higher harmonic generation configurations, will be also investigated.

	Units	Full RF case	LWFA case	PWFA case
Radiation Wavelength	nm (keV)	2.87 (0.43)	2.8 (0.44)	2.98 (0.42)
Photon Energy	μJ	177	40	6.5
Photon per pulse	$\times 10^{10}$	255	43	10
Photon Bandwidth	%	0.46	0.4	0.9
Photon RMS Trans. Size	μm	200	145	10
Photon Brilliance per shot	(s mm^2 mrad^2 bw(0.1%))$^{-1}$	1.4×10^{27}	1.7×10^{27}	0.8×10^{27}

Table 17.1: FEL radiation parameters from start-to-end simulations for full RF and for plasma wakefield acceleration cases with electron (PWFA) or laser (LWFA) driver beam.

The SASE radiation presents strong shot-to-shot fluctuations in intensity, spectrum and position. The radiation diagnostics should therefore be single-shot and not-intercepting whenever possible. The beam will be characterized by measuring its dimensions, coherence and positions both in transverse (section 17.1) and longitudinal (section 17.2) directions, its spectrum and its intensity (section 17.3). The beamline will also be capable to optimize the beam for the running experiment (see chapter 18.2), to allow the fine tune of some characteristics. A scheme of the beamline is presented in Figure 17.1.

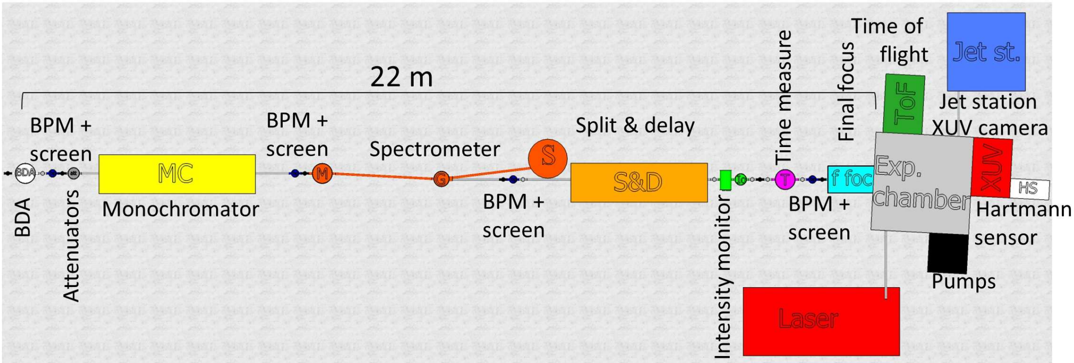

Figure 17.1: Scheme of the photon beamline. The distance of the experimental chamber from the undulators is about 33 m.

17.1 Transverse measure and control

17.1.1 Beam Defining Aperture

The first element on the beamline is the beam defining aperture (BDA). Mechanically, the BDA is formed by two trunks of pyramid (Figure 17.2), where the central aperture of each trunk will be 20×20 mm^2. They are independently movable to select the effective aperture up to complete closure. The aperture will be closed up to having its edges on the tails of the photon beam, so the beam will be almost unperturbed while the following optics and elements will be preserved by large fluctuations or accidental misalignment of the beam position or direction. Since the FEL radiation emitted from the undulators contains an intense coherent emission, with an angular divergence of few tens of µrads, surrounded by a broad spontaneous distribution with a larger angular divergence, this aperture will also act as a collimator.

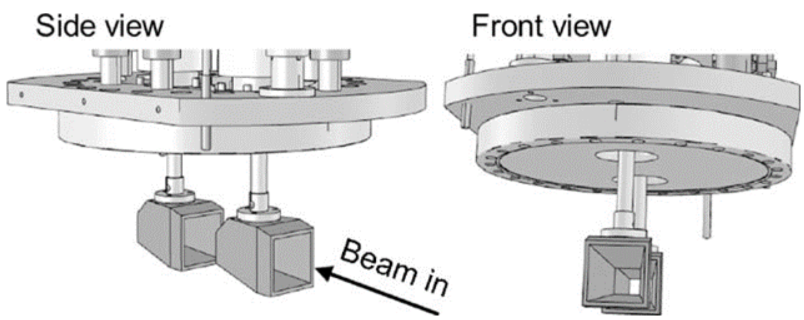

Figure 17.2: Scheme of the beam defining aperture chamber, from [2].

17.1.2 Beam Position Monitors

Several Beam Position Monitors (BPMs) will be installed along the line to monitor the trajectory of the photons. The BPMs will be based on the interception of the tails of the photon beam transversal intensity distribution by four metallic blades collecting a drain current. A polarized plate with a large hole compared to the beam can help to collect the stripped electrons and clean the current signal. The expected spatial resolution is determined by the accuracy in measuring currents generated on the blades and by the minimum mechanical step of the motors controlling the travel of the blades. In FERMI BPMs, for example, the current accuracy is about 10^{-6} A (AH401 picoammeter [2]) while on the step the accuracy is about 1 µm. To avoid ablation due to the high peak energy, the blades will be tilted by about 20°. Each blade may travel few cm, and a complete closure in both directions is possible. By reading simultaneously the four currents, it is possible to determine pulse-by-pulse the relative displacement of each pulse with a spatial resolution of about 2 μm RMS.

17.1.3 Transverse dimension measurement

We will measure the transverse dimension of the photon beam via a scintillating screen. The material commonly used as scintillator is YAG:Ce. It is cost-effective and it has a high yield of light (about 8 photons/keV [3]). However, the photon flux at high intensity may damage the crystal, and other materials with a higher damage threshold, such as pc–CVD diamond [3], can be envisaged. Behind the screen, a 45° mirror and a camera outside the screen vacuum chamber in a setup similar to those used for electron diagnostics will be available.

17.1.4 Mirrors and focusing

Few mirrors are required in the beamline: for steering the beam away from the undulator line, for a split and delay system, for the monochromator and for the final beam focusing. Each mirror will have two angular degrees of freedom and an insertion control. The mirror will be inclined to an angle of $90^\circ - \alpha$ (where α is the grazing angle of the mirror, in our case between 1 - 3°) in the horizontal plane with respect to the incoming beam direction. Their substrate will be made by fused silica, while the coating material is depending on the wavelength used [4]. We are studying different coatings that have a reflectivity > 70% at 3° grazing angle for almost all the spectral range 2–20 nm also when used in a single layer configuration to maximize durability and minimize the costs (Figure 17.3).

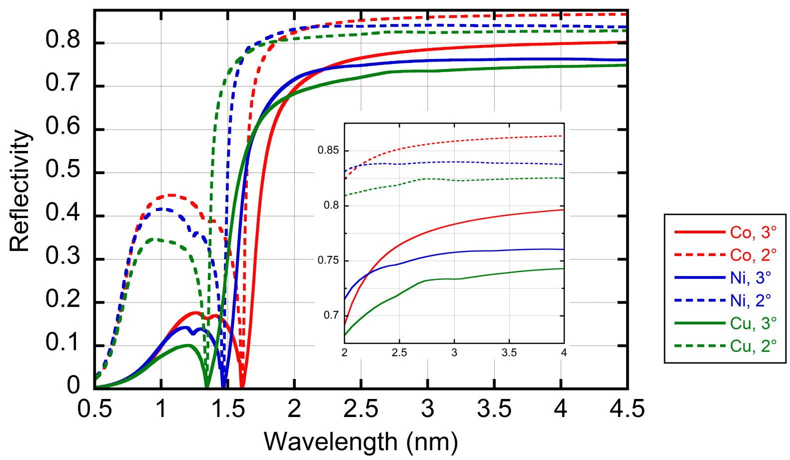

Figure 17.3: Reflectivity of thick layers of different metals (Cu, Ni, Co) at 2° and 3° grazing angle, extrapolated using data from [5]. The reflectivity remains almost constant at longer wavelengths.

For what concerns the focusing device, we plan to use two mirrors (spherical or plane elliptical) in a Kirkpatrick-Baez configuration. The curvature can be manufactured or implemented directly by slightly bending the mirrors [6]. The equivalent focal length can be in the range of few meters or less (as a reference, the bent mirror at FERMI can have a minimal focal length of ∼1.2 m and a minimum spot size of 2×3 μm^2 [7]). Depending on radiation parameters, distance from the undulators and mirror focus, the final spot size will be in the order of some microns RMS (Figure 17.4). Moreover, multi channel plates (MCPs) can be considered as they offer promising results for coherent X-ray imaging. The MCP parameters are very flexible thus becoming attractive to design novel X-ray optics [8, 9].

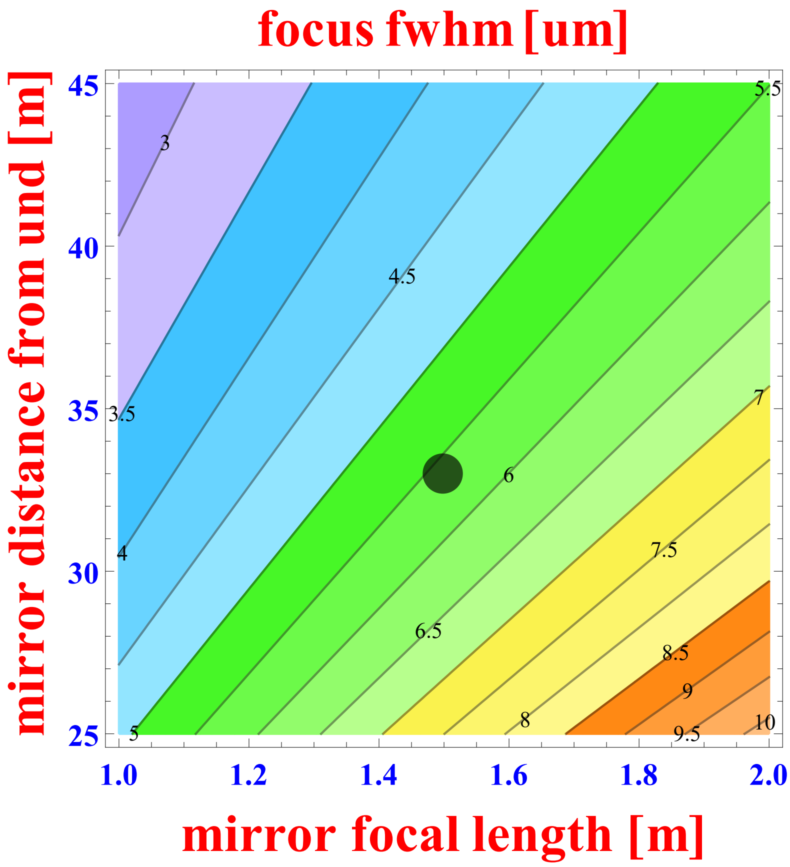

Figure 17.4: Preliminary focal spot dimensions, calculated with ideal Gaussian beam and aberration free focusing, as a function of mirror focal length and distance from the undulators for PWFA case. The black dot represents the actual working point, 33 m from the undulator and with 1.5 m focal length, of about 5.5 µm FWHM.

17.1.5 Transverse coherence measurement

Measurement of transverse coherence measurement will be possible, exploiting the visibility of an interference pattern from a double slit [10] or, as demonstrated also at SPARC_LAB, using the speckle pattern from small spheres [11, 12]. We will introduce the slits (or the spheres) in a dedicated chamber after the spectrometer, depicted in Section 17.3, and we will use a screen near to the experimental chamber to visualize the pattern.

17.2 Longitudinal measure and control

17.2.1 Longitudinal dimension measurement

Commercially available streak cameras have resolution in the order of few hundred fs . While the temporal length can be reconstructed by the electron longitudinal phase space after the undulators, as in [13], although with possible systematic errors, a dedicated diagnostic tailored to our photon characteristics could be investigated. Many technologies have been considered for the characterization of short X-ray pulses [14], based, for example, on interferometry [15, 16], transient reflectivity [17], cross-correlation [18] or THz streaking [19]. Interferometry requires a dedicated multishot measurement, so the SASE shot-to-shot fluctuation will be averaged and only averaged parameters will be accessible. Transient reflectivity and crosscorrelation can be single-shot measurements, but they intercept the beam. We plan to use THz streaking of gas ionization, that has the potential to be a single-shot non intercepting diagnostic, but is still under development.

The FEL wavefront will be measured by means of a Hartmann sensor, that is composed by a mask with several holes and a scintillating screen. The displacement between the image position of the holes respect to a reference plane wave will give information on the wavefront angle. Such instrument is routinely implemented at FEL facilities, such as FERMI [20] (Figure 17.5) and FLASH.

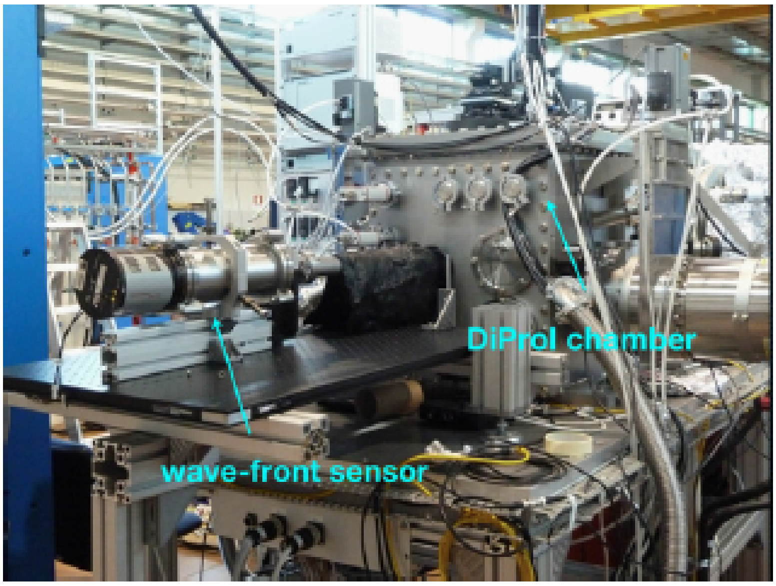

Figure 17.5: Wavefront sensor mounted one meter out of the focus, behind the FERMI DiProl experimental chamber, form [6].

Commercially available fast photodiodes have temporal resolution of few tens of ps, to increase the time resolution and to allow monitoring the time jitter and arrival time with tens fs resolution other techniques are required. We plan to develop the THz streaking measurement to obtain also the arrival time with high resolution [19], comparing the electron time of flight with the THz pulse. Alternative methods can be considered, which are based on spectral encoding [21] or transient reflectivity [17] using an external reference laser, but both are intercepting single-shot measurements.

17.2.2 Longitudinal manipulations

As some experiments require very short pulse (i.e. of the order of 10 fs), the pulse length exiting from the undulator should be preserved. The chromatic dispersion of the material is very low, as the beam goes through only thin attenuators and low pressure gases. The monochromator diffracting gratings, conversely, can induce a large pulse lengthening due to pulse front tilting. The path difference between tail and head of the pulse dispersed by one grating is equal to $N\,m\,\lambda$, where N is the number of grooves illuminated by the beam, m the diffraction order and λ the pulse central wavelength. For example, the pulse front tilt induced on the diffracted beam by a grating configuration similar to that considered for the spectrometer described in Section 17.3 is about 690 fs for a 1.5 mm full width beam. If short pulses with high spectral purity are required, it is possible to compensate the pulse front tilt of the monochromator via a pair of gratings working with opposite angles respect to the induced dispersion [22], but at the cost of higher losses due to the diffraction efficiency (that is in the order of few tens % even with high performance gratings [23]).

We also propose to include a split and delay system in the beamline for XUV pump-probe experiments. This system uses the edge of a mirror to split the beam in two components that are then reflected on a delay line and recombined on a final mirror, with a tunable delay typically ranging from 0 to few hundreds fs. Such devices are installed both at BL2 at FLASH [24] and at LCLS [25].

17.2.3 Longitudinal coherence measurement

We plan to measure the transverse coherence length of the beam using an interferometer in Michelson [26] or Fizeau configuration. The decay of the fringe visibility as a function of the arm length and the respective time delay will be used to determine the temporal coherence length. This is a multishot intercepting measurement and only the average behavior will be obtained. The interferometer can be set inside or just after the final experimental chamber.

17.3 Energy measure and control

17.3.1 Photon number measurements and control

We will measure the number of photons per pulse using gas-based intensity monitors (Figure 17.6) similar to those used for FLASH [27] and FERMI [2]. The working principle of the intensity monitor is the atomic photo-ionization of a rare gas at low particle density, in the range of 10^{11} cm^{-3} ($p \sim 10^{-5}$ mbar). The photon beam traveling through a rare gas-filled chamber generates ions and electrons, which are extracted and collected separately. This monitor is almost completely transparent due to the low pressure used for the rare gas in the vacuum chamber. It has a wide dynamical range and it does not suffer from saturation effects. Moreover, it is independent from the beam position fluctuations so it can be used continuously for on-line shot-to-shot intensity measurements. This monitor can be calibrated with different sources by using cross-calibrated photodiodes, with an expected precision of 3% in most of the range (slightly worse at lower energy). One of the limiting factors is the ability to read very low current, because the ionizing cross section of commonly used gas, nitrogen, decreases in the water window spectral region and the emitted photocurrent is typically low. Possible alternatives require the use of other gas (such as xenon [27] or oxygen [28]) or other methods of energy detection, e.g. using the spectrometer to obtain a relative intensity measurement.

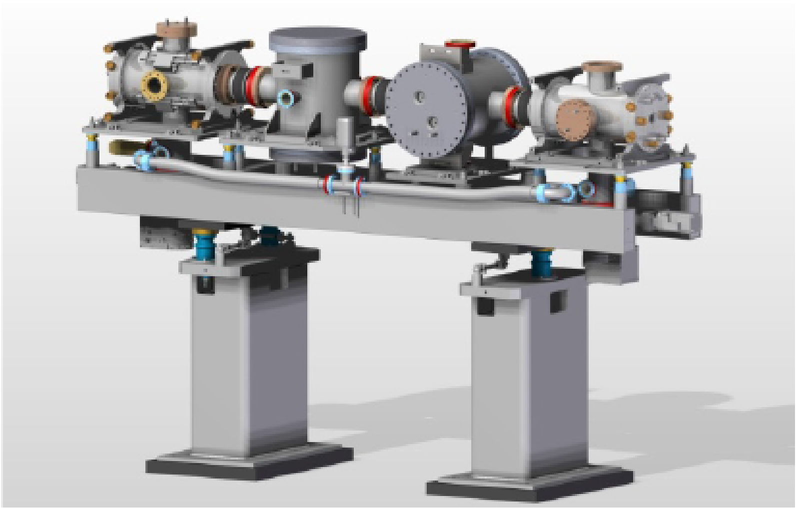

Figure 17.6: X-ray gas monitor, from [29].

In order to control the beam intensity, attenuators will be installed in the beamline. While gas attenuators have a continuous set of attenuation parameters and generally have a large spectral range, we have to manage photons in a relatively short bandwidth, so thin films can be used instead.

17.3.2 Spectrometer

We will measure the pulse spectrum with a spectrometer based on diffraction gratings [2, 30]. We plan to use a mirror at near grazing incidence (3°) to shift the beam from the undulator line. This will be useful to separate the desired radiation pulse from all the other radiations or particles that are propagating on axis. After the mirror a grating in 0^{th} order will reflect the beam toward the experimental chamber, whereas its first diffracted order will send a small portion of the FEL pulse toward a CCD camera for spectrum measurement. The grating will have a groove density between 1200-3600 grooves/mm. The separation space between the elements will be determined to avoid any eventual unwanted radiation to propagate through the pipe line, while a first estimation is in the order of few meters. After the grating chamber, the CCD camera will be about 2 - 3 m far from the grating, with an angle in the range of 2 - 7° relative to the reflected beam, depending on groove density and radiation wavelength. For a 2400 grooves/mm grating and 3 m of propagation, one camera pixel (about 13 μm for a back illuminated soft X-ray camera) will cover 2.4 10^{-4} nm (about 1/12 of the expected spectral width) at an angle of about 4.5° from the reflected beam. The high quantum efficiency (in the order of 30%) and the signal-to-noise ratio of the camera require only a small fraction of the photon beam to be diffracted. The grating will therefore be designed to have a low diffraction efficiency.

If high spectral purity or very narrow bandwidths are required, we should additionally filter the spectrum. For the considered materials and incidence angles, the mirror reflectivity drops sharply below 2 nm , with a smaller reflectivity peak at about 1 nm as reported in Figure 17.3. If a more precise or tunable spectrum should be used, we can consider the use of a monochromator [22] as discussed in Section 17.2.

17.4 Conclusions

We consider that the length of the beamline before the experimental apparatus required to host the above described diagnostics may range from 15 to 25 m, with a distance from the undulators not smaller than 10 – 15 m, mainly depending on photon intensity and optics damage thresholds. The expected total transmission of the beamline, when no intercepting devices are inserted in line, is ∼18%, eventually reduced to ∼6% when split and delay line is used. The monochromator will additionally reduce the transmission of about two orders of magnitude.

Bibliography

[1] R Bonifacio. "R. Bonifacio, C. Pellegrini, and LM Narducci, Opt. Commun. 50, 373 (1984)." In: *Opt. Commun.* 50 (1984), p. 373.

[2] M Zangrando et al. "The photon analysis, delivery, and reduction system at the FERMI@ Elettra free electron laser user facility". In: *Review of Scientific Instruments* 80.11 (2009), p. 113110.

[3] Natalia Gerasimova et al. "The Photon Beam Loss Monitors as a Part of Equipment Protection System at European XFEL". In: *36th International Free Electron Laser Conference*. PUBDB-2014-03602. European XFEL. 2014, MOP010.

[4] F Schäfers and R Cimino. "Soft X-ray reflectivity: from quasi-perfect mirrors to accelerator walls". In: *arXiv preprint arXiv:1308.1295* (2013).

[5] Burton L Henke, Eric M Gullikson, and John C Davis. "X-ray interactions: photoabsorption, scattering, transmission, and reflection at E= 50-30,000 eV, Z= 1-92". In: *Atomic data and nuclear data tables* 54.2 (1993), pp. 181–342.

[6] L Raimondi et al. “Microfocusing of the FERMI@ Elettra FEL beam with a K–B active optics system: Spot size predictions by application of the WISE code”. In: *Nuclear Instruments and Methods in Physics Research Section A: Accelerators, Spectrometers, Detectors and Associated Equipment* 710 (2013), pp. 131–138.

[7] Enrico Allaria et al. “The FERMI@ Elettra free-electron-laser source for coherent x-ray physics: photon properties, beam transport system and applications”. In: *New Journal of Physics* 12.7 (2010), p. 075002.

[8] Sultan B Dabagov et al. “Coherent and incoherent components of a synchrotron radiation spot produced by separate capillaries”. In: *Applied optics* 39.19 (2000), pp. 3338–3343.

[9] MI Mazuritskiy et al. “Excitation and propagation of X-ray fluorescence through thin devices with hollowed ordered structures: comparison of experimental and theoretical spectra”. In: *Journal of synchrotron radiation* 23.1 (2016), pp. 274–280.

[10] R Ischebeck et al. “Study of the transverse coherence at the TTF free electron laser”. In: *Nuclear Instruments and Methods in Physics Research Section A: Accelerators, Spectrometers, Detectors and Associated Equipment* 507.1-2 (2003), pp. 175–180.

[11] MD Alaimo et al. “Probing the transverse coherence of an undulator x-ray beam using brownian particles”. In: *Physical review letters* 103.19 (2009), p. 194805.

[12] Matteo D Alaimo et al. “Mapping the transverse coherence of the self amplified spontaneous emission of a free-electron laser with the heterodyne speckle method”. In: *Optics Express* 22.24 (2014), pp. 30013–30023.

[13] C Behrens et al. “Few-femtosecond time-resolved measurements of X-ray free-electron lasers”. In: *Nature communications* 5 (2014), p. 3762.

[14] Stefan Duesterer et al. “Development of experimental techniques for the characterization of ultrashort photon pulses of extreme ultraviolet free-electron lasers”. In: *Physical Review Special Topics-Accelerators and Beams* 17.12 (2014), p. 120702.

[15] Giovanni De Ninno et al. “Single-shot spectro-temporal characterization of XUV pulses from a seeded free-electron laser”. In: *Nature communications* 6 (2015), p. 8075.

[16] Yves Kayser et al. “X-ray grating interferometer for in situ and at-wavelength wavefront metrology”. In: *Journal of synchrotron radiation* 24.1 (2017), pp. 150–162.

[17] R Riedel et al. “Single-shot pulse duration monitor for extreme ultraviolet and X-ray free-electron lasers”. In: *Nature communications* 4 (2013), p. 1731.

[18] Paola Finetti et al. “Pulse duration of seeded free-electron lasers”. In: *Physical Review X* 7.2 (2017), p. 021043.

[19] Ivanka Grguraš et al. “Ultrafast X-ray pulse characterization at free-electron lasers”. In: *Nature Photonics* 6.12 (2012), p. 852.

[20] Cristian Svetina et al. “The Low Density Matter (LDM) beamline at FERMI: optical layout and first commissioning”. In: *Journal of synchrotron radiation* 22.3 (2015), pp. 538–543.

[21] Mina R Bionta et al. “Spectral encoding of x-ray/optical relative delay”. In: *Optics express* 19.22 (2011), pp. 21855–21865.

[22] F Frassetto et al. “Double-grating monochromator for ultrafast Free-Electron-Laser beamlines”. In: *FEL conference, Basilea (CH)*. 2014.

[23] Randall McEntaffer et al. “First results from a next-generation off-plane X-ray diffraction grating”. In: *Experimental Astronomy* 36.1-2 (2013), pp. 389–405.

[24] M Wöstmann et al. "The XUV split-and-delay unit at beamline BL2 at FLASH". In: *Journal of Physics B: Atomic, Molecular and Optical Physics* 46.16 (2013), p. 164005.

[25] JC Castagna et al. "X-ray split and delay system for soft x-rays at LCLS". In: *Journal of Physics: Conference Series*. Vol. 425. 15. IOP Publishing. 2013, p. 152021.

[26] V Hilbert et al. "Spatio-temporal coherence of free-electron laser radiation in the extreme ultraviolet determined by a Michelson interferometer". In: *Applied physics letters* 105.10 (2014), p. 101102.

[27] M Richter et al. "Measurement of gigawatt radiation pulses from a vacuum and extreme ultraviolet free-electron laser". In: *Applied physics letters* 83.14 (2003), pp. 2970–2972.

[28] JL Turner, RC Field, and SLAC NAL. "Oxygen Scintillation in the LCLS". In: *FEL conference, Basilea (CH)*. 2014.

[29] Jan Grünert et al. "Implementation Phase of the European XFEL Photon Diagnostics". In: *FEL14, Basel, Switzerland* (2014).

[30] L Poletto et al. "Compact spectrometer for single shot X-ray emission and photon diagnostics". In: *FEL conference, Basilea (CH)*. 2014.

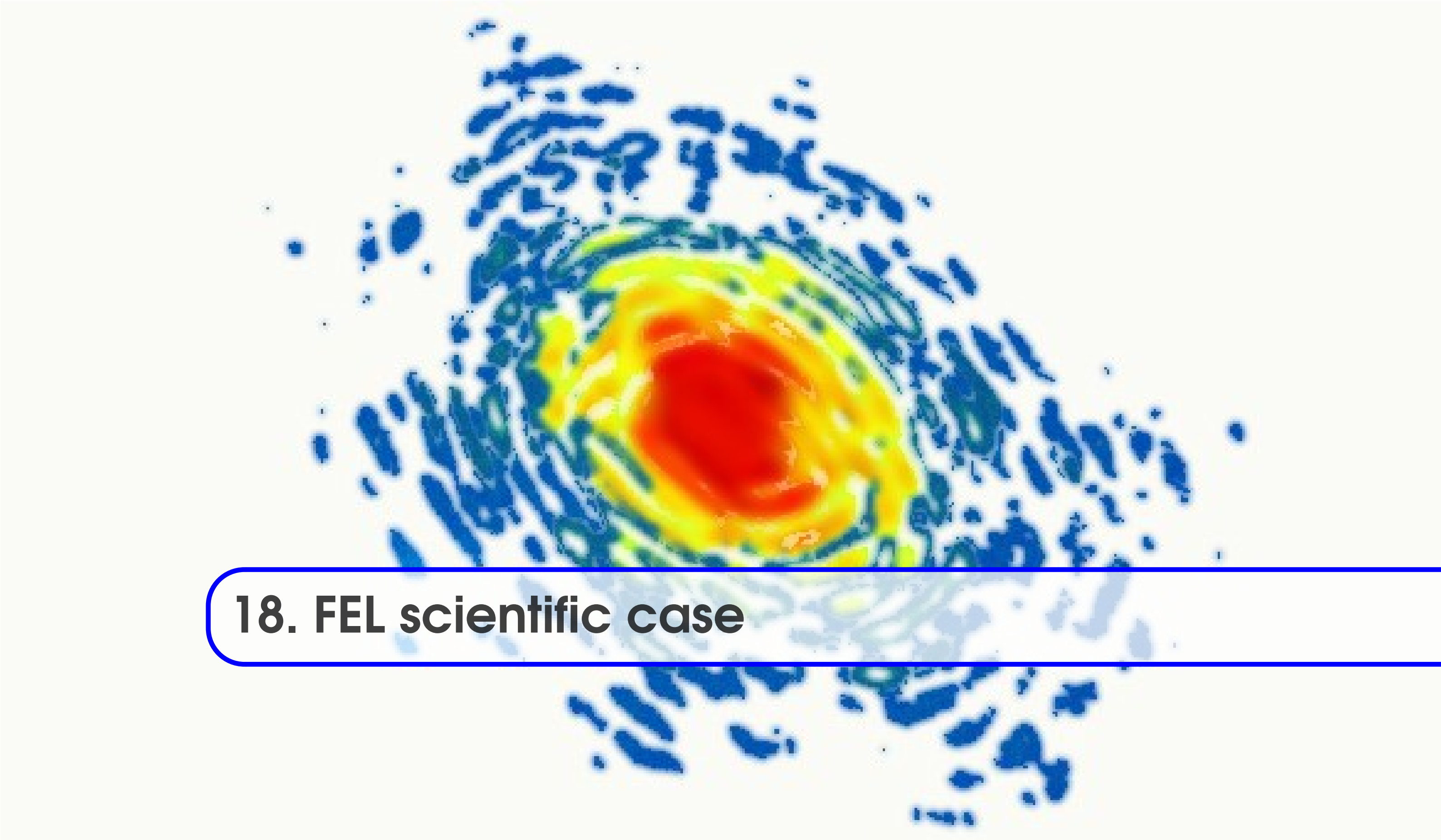

18. FEL scientific case

18.1 Introduction

The advent of Free Electron Lasers (FELs) opened up the way for an unprecedented, wide class of experiments exploiting the peculiar features of these radiation sources. Key elements are the high peak brilliance that can be higher than 10^{27} photons/s mm^2 mrad^2 0.1% bandwidth and the short pulse duration, which is of the order of tens of femtoseconds. FELs can therefore allow high time resolution measurements and may provide a high signal-to-noise ratio. By exploiting the high peak brilliance and the extremely short FEL pulses the so-called diffract-and-destroy regime, in which interpretable data are gathered before the sample is destroyed by the FEL pulse radiation [1] can be explored, overcoming one of the main limitations of synchrotron radiation based experiments that is the sample radiation damage. This principle has been proven in several experiments on various samples, both biological [1–6] and non-biological [7], at different wavelengths ranging from the UV to the hard X-rays region. Actually, this issue is particularly relevant since coherent diffraction imaging (CDI) of biological system using conventional methods is ultimately limited by radiation damage owing to the large amount of energy deposited in the sample by the photon beam [7, 8]. The unique FEL features (energy range, time resolution and brilliance) can be exploited in several branches of physics, chemistry, material science and biology. The EX-TRIM (EuPRAXIA@SPARC_LAB X-ray Time Resolved coherent IMaging) user end-station of EuPRAXIA@SPARC_LAB [9] FEL will be designed and built to allow performing a wide class of experiments using the schematic apparatus displayed in Figure 18.1. Details about the main research lines, requirements for FEL beam parameters and the EX-TRIM experimental end-station are given in the following pages.

18.2 Scientific case

18.2.1 Coherent Imaging of Biological samples in the water window

Exploiting the coherence of the EuPRAXIA@SPARC_LAB FEL beam, 2D images of biological samples can be obtained. In case of reproducible objects, it is also possible to combine many images to get a 3D reconstruction. This means that a wide class of biological objects, including

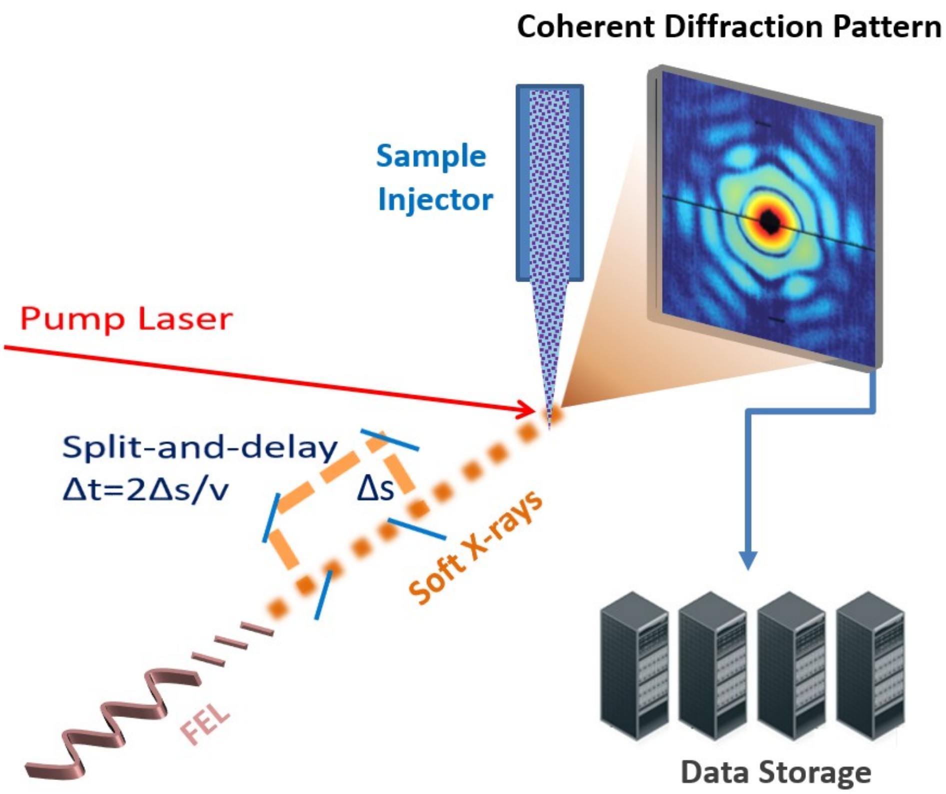

Figure 18.1: A simplified layout of a imaging experiment.

protein clusters, viruses and cells can be profitably studied at the EuPRAXIA@SPARC_LAB facility. The attainable resolution depends on the sample's scattering strength and it is limited by FEL wavelength and photon brilliance. When dealing with biological samples, which are mainly composed by light atoms and preferentially live in a water environment, there is a particular interest in performing measurement in the so-called water window, i.e., the energy range between carbon (282 eV) and oxygen (533 eV) K-edge, which will be one of the operational regions of this radiation source. In this range the absorption contrast between the carbon of organelles and the water of both cytoplasm and the liquid surrounding the cell is quite high. For this reason, cells can be imaged in their living, native state, without the need of cooling or staining them, as it is the case for other microscopy technique such as electron microscopy.

18.2.2 Clusters and nanoparticles

Considerable attention is continuously being addressed to the study of free clusters, since they are known to be a bridge between the gas and the condensed phases of matter. In particular, great interest arises in the correlations between the geometric structure and electronic properties of variable size clusters, underlying changes in optical, magnetic, chemical and thermodynamic properties. In the spectral range of 5–3 nm envisaged for the EuPRAXIA@SPARC_LAB FEL source, physical processes involving core levels are important. Clusters, as a form of matter intermediate among atoms and bulk solids, are ideal samples to study these processes. By varying their size, one can investigate the role of inner- and interatomic, i.e. collective, effects, thus contributing to our understanding of energy deposition, energy transfer, and radiation damage in matter. Due to the reduced target densities, the use of sources with a high brilliance such as FELs is essential. Additionally, unique insights into the electronic properties of free clusters will be attained by coupling multi-photon excitation schemes to CDI. For such experiments, in a second phase, it would also important to open the possibility of accessing the photon energy range associated to the higher harmonics of the FEL.

18.2.3 Laser ablation plasma

Laser ablation/desorption techniques are utilized extensively across a large range of disciplines, including production of new materials, and both extrinsic and in situ chemical analysis. Laser interactions may occur via direct absorption or through non-linear mechanisms such as multi-photon and avalanche excitation. In the case of ablation the use of ultra-fast laser pulses provides a powerful means of machining a wide variety of materials, including biological tissue. The absence of thermal relaxation of the energy allows unprecedented precision and essentially no associated damage, a fact that has stimulated considerable interest also for industrial processes and applications. Many important elementary processes, such as electron/hole recombination, excitation relaxation, etc., often occur on a very short time scale and only a time resolved spectroscopy is able to resolve the dynamics of charge and energy transfer processes. Ultra-short laser pulses limit the secondary ionization and photo-fragmentation, and exclude the laser/plume interaction. Therefore, only within such excitation regime, time- and space-resolved optical spectroscopy of the generated plasma provides a direct investigation of laser-target interaction and ultimately of particle emission. We propose to use EuPRAXIA@SPARC_LAB to study electronically induced surface reactions in semiconductors, metal/adsorbate systems and multiphase composite materials. Surface study of the irradiated area with chemical sensitivity of CDI diagnostics of the ablated species can elucidate the mechanism of the electronic melting, desorption, and multi-photon ablation. Time and space resolved spectroscopy of the plasma emission generated during the ablation will shed light on the formation and the dynamics of the species ejected from the target surface. As the use of ultrafast laser pulses minimizes the laser-plasma interaction, this can allow the nascent distribution emerging from the ablated target to be characterized with a negligible interference arising from secondary excitations. CDI studies of the processed region will allow also the characterization of the initial surface disorder, and elucidate the transition mechanism from the phase of defect nucleation of the surface layer to the onset of surface melting. Studies of the ablated species condensed on a substrate as a function of the laser pulses will be used for the analysis of the ablation products and for the optimization of the process with a view to thin films deposition applications.

18.2.4 Condensed Matter Science

A Free Electron Laser capable to deliver pulses in the 3 nm region is a great asset for Coherent Diffraction Imaging (CDI) experiments tackling many open questions in Condensed Matter physics. For instance, the quest for smaller and faster magnetic storage units is still a challenge of the magnetism. The possibility to study the evolution of magnetic domains with nanometer/femtosecond spatial/temporal resolution will shed light on the elementary magnetization dynamics such as spin-flip processes and their coupling to the electronic system. Moreover, the possibility to exploit different L-edges resonances would allow introducing the chemical selectivity necessary to account for the complex composition of technologically relevant magnetic media. CDI studies on nucleation dynamics are also of extreme interest in this wavelength range. Indeed, it is widely accepted that several phase transitions cannot be framed in the classical nucleation theory. Many systems go through intermediate states before reaching the stable phase. These multi-step nucleation processes require experimental efforts for the understanding of what determines the relative efficiencies of the various pathways leading to the final state. Nanometer resolution is necessary to distinguish the intermediate phases characterized by few nanometer nucleation domains. Photocorrelation Spectroscopy could also benefit from the use of photons in the water window energy region. This would allow, for example, studies of the structural relaxation in water in a wavevector region not accessible by other techniques. Shedding light on water dynamics is fundamental to discriminate among the different theoretical models that are invoked to describe the unique properties of water.

18.2.5 Pump and probe experiments

The possibility of inducing changes in a sample via a pump pulse such as the stimulation of a chemical reaction or the generation of coherent excitations would tremendously benefit from pulses in the soft X-ray region. Resonant experiments with short pulses tuned across electronic excitation will open up the way towards stimulated Raman or four wave mixing spectroscopies.

18.2.6 Perspectives

One of future possibilities could be the use of XUV FEL light carrying orbital angular momentum, also referred to as a light spring. This will make possible the study of new phenomena, such as induced dichroism, magnetic switching in organic molecules and violation of dipolar selection rules in atoms. FEL based second harmonic generation spectroscopy would also become an important technique for surface analysis in the VUV/Soft X-ray regimes. It offers the unique possibility to study the electronic structure of interfacial regions with a core-level spectroscopy, effectively allowing X-ray absorption spectroscopy of the first molecular layer on the surface of a bulk sample or of a buried interface using a photon-in/photon-out detection scheme. This approach would open the door to a new field of surface analysis relevant to the future studies of catalytic interfaces, electrode surfaces, photovoltaics, etc.

Harmonic generation in gas

The rapid development of ultrashort, powerful laser sources triggered the development of short wavelength sources based on the up-conversion of laser light in gas systems. The harmonic generation in gas is indeed one of the most promising methods to generate radiation at short wavelengths, in the VUV – EUV region of the spectrum.

The high order harmonics result from the strong non-linear polarization induced on the rare gases atoms, such as Ar, Xe, Ne and He, by the focused intense e.m. field E_{Laser} of a "pump" laser field at the level of 10^{14} W/cm^2. The most important characteristics of the process can be described by the three-step semi-classical model illustrated in figure 18.2 [10]. As the external electromagnetic field strength is comparable to the internal static field V_c of the atom, in the interaction region close to laser focus atoms ionize by tunneling of electrons. The ejected free electrons, far from the core, are then accelerated in the external laser field gaining the kinetic energy E_C. Those driven back close to the core can either be scattered or may recombine to the ground state emitting a burst of XUV photons every half-optical cycle. In summary, every half optical cycle, electrons that tunnel out of their parent atom, are accelerated in the intense electric field of the laser and then accelerated back to collide/scatter on the atom when the electric field reverses. In the spectral domain, the pulse structure typically includes the odd harmonics of the fundamental laser frequency, extending to the VUV-EUV range of the spectrum. The characteristic distribution of intensities is almost constant for the harmonic order in an extended "plateau" region, where, depending on the generating gas, the conversion efficiency varies in the range 10^{-4}-10^{-7}. This plateau is followed by a cut-off region where the conversion efficiency decreases rapidly. The transition from plateau to cutoff depends on the gas ionization energy V_p, and on the ponderomotive energy associated to the laser field U_p. The cut-off energy is given by $E_{cut-off} = V_p + 3.2U_p$ [11]. The ponderomotive potential scales with the laser field intensity I_L as $U_p = I_L/4\omega_L^2$. The condition of avoiding multiple ionization of the gas limits he value of U_p according also to the three-step model and the cut-off law. The lighter

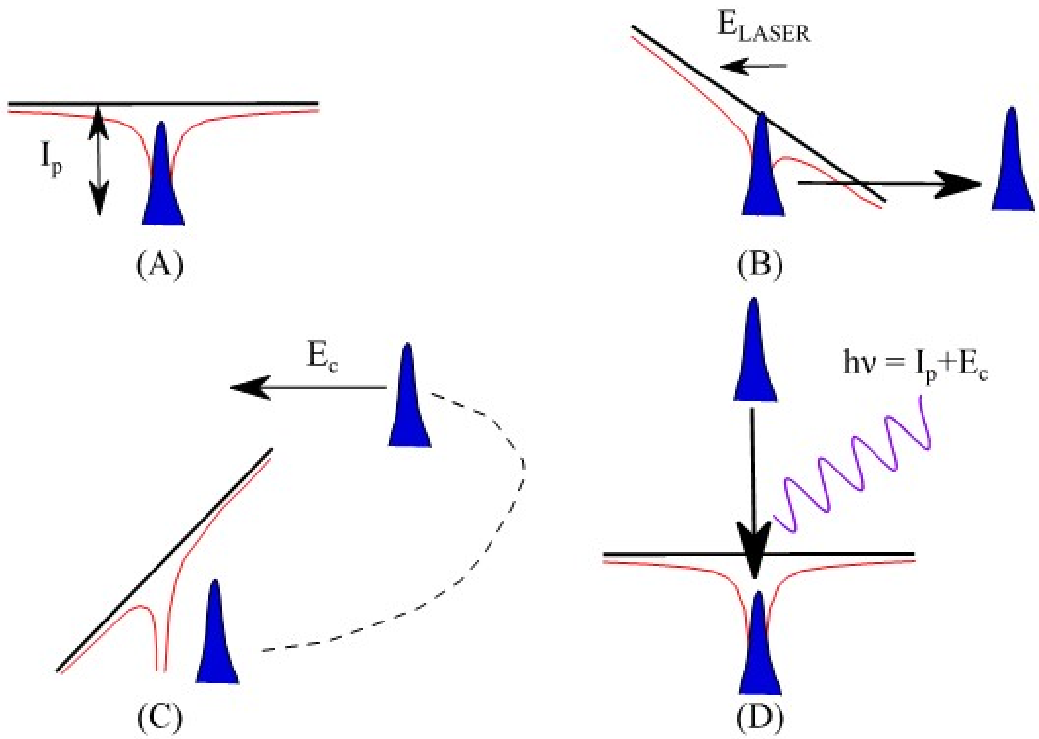

Figure 18.2: Three-step semi-classical model (A) initial state of the gas atom at zero field, V_C: Coulomb potential, I_p: ionization potential; (B) electron tunneling; (C) electron acceleration and gain of kinetic energy E_C; (D) radiative recombination and emission of XUV burst.

is the gas, i.e., the higher is the ionization energy and the laser intensity, which can be applied without ionizing the atom, the higher is the cut-off energy. The cut-off scaling law and the effective efficiency also depend on the phase matching conditions, determining the coherent superposition of the emission from different atoms. The geometry of emission, based on a gas jet, a cell or a capillary, as well as the focusing conditions of the laser, the position of the focus, pressure of the gas, etc. are all aspects to be accounted for, in the optimization of the conversion process. From this point of view, a sufficient laser pulse energy and a loose focusing geometry consisting in a mildly focused beam in a long homogeneous medium, may provide the best efficiency conditions and preserve the phase matching required to ensure the efficient conversion [12–15]. High order harmonics are typically linearly polarized sources between 100 and 3 nm (12–400 eV) of high temporal and spatial coherence. They emit very short pulses, depending on the drive laser pulse duration and typically less than 100 fs, with a relatively high repetition rate, up to several kHz. The radiation spectrum is completely tunable in the VUV-XUV region. The harmonic radiation is emitted on the axis of the laser propagation with a small divergence (1 to 10 mrad). Fraction of a micro-joule of energy can be obtained at wavelengths down to 25–30 nm. Elliptical polarization can be also produced, in a two colors field, $\omega + 2\omega$ setup [16–18]. In this condition both odd and even harmonic orders can be generated and the process may show an increased efficiency especially in the high-energy end of the spectrum. The main limitation of high harmonics from gas is their relatively moderate photon flux, but harmonics are naturally synchronized with the drive laser and the system and may be easily merged in the complex structure of a free electron laser facility, where the harmonics provide a low-cost multicolor-multiple pulses capability. The low flux would be perfectly acceptable when the source is used just as an experimental probe. A small fraction of the laser energy produced in a FLAME like framework [19] in a loose focusing geometry, would ensure a substantial amount of radiation energy on the experimental beamline, synchronized with the FEL beam.

18.3 The experimental hall and the experimental end-station

18.3.1 Overview

The EuPRAXIA@SPARC_LAB FEL will provide photon pulses with high intensity down to a wavelength between 4 and 2 nm (300 – 600 eV), in the so called "water window". From preliminary simulations we expect the radiation to have the characteristics summarized in Table 1.2.
Although, this represent only the design phase, it is interesting and useful to compare the design parameters of the flux available at the EuPRAXIA@SPARC_LAB FEL with those available at other FEL sources operational or in the advanced commissioning phase, when these data are available. At present, there are two soft X-rays dedicated, already operational, FEL radiation sources. The FERMI FEL at Trieste that can provide about $> 10^{11}$ photons/pulse in the water window region [20], while the FLASH FEL delivers about 10^{11-12} photons/pulse [21].

Also other photon sources, not specifically dedicated to soft X-rays, are (or will be soon) able to provide photons at wavelengths in the water window. LCLS at Stanford can deliver in this energy range a number of photons/pulse between 10^{12} [22] and 10^{13} [23], while according to the conceptual design report, since experimental figures are not yet published, the SwissFEL, that recently started its operation, will provide 5×10^{12} photons/pulse in the same energy region. A bit more photons are expected by the longest FEL: the SASE3 accelerator of the European XFEL that is expected to deliver $> 10^{13}$ photons/pulse [24].

The scenario is clearly not well established all over the world. However, it appears clearly from the above figures that the photon flux estimated for the EuPRAXIA@SPARC_LAB FEL is competitive with that of the already operational dedicated sources, namely FERMI and FLASH, and not far from those provided by FELs operational or going to open to the first users in the next months both in the soft and hard X-ray regions.

Apertures will be located right after the source to check and control the beam dimensions. Intensity and position monitors will be installed at multiple locations. These transmissive devices measure the position and the intensity of the FEL beam on a shot-by-shot basis. Filters will be used to attenuate the radiation intensity to the desired level. It is important that the most downstream of these monitors is installed close to the experimental station after the last slit system.

In order to perform the challenging experiments described in the previous section, it is essential to build a fully equipped experimental end-station, including a dedicated section with beam diagnostics and focusing devices and a highly flexible experimental chamber large enough to host different detectors and samples with their dedicated mountings. The whole system will have to operate in vacuum ($< 10^{-7}$ mbar), thus several pumps and valves located in appropriate positions to isolate the different components of the beamline are required. The experimental hall that will host the instruments and the vacuum systems will be about 900 m^2, large enough to host also the necessary ancillary equipment (gas lines, gas cylinders, computers, desks) and to allow the working space necessary to assemble and move other user instruments. A sketch of the experimental end-station is outlined in Figure 18.3. In the next sections a brief description of the main experimental components is given.

18.3.2 The experimental hall

A proposal for a complex experimental end-station to perform coherent imaging experiments not only require a fully equipped experimental end-station, but also a dedicated experimental hall with absolutely non-standard requirements. Indeed all the EuPRAXIA@SPARC_LAB project is a challenging project not only from the scientific and technological point of view, but also for what

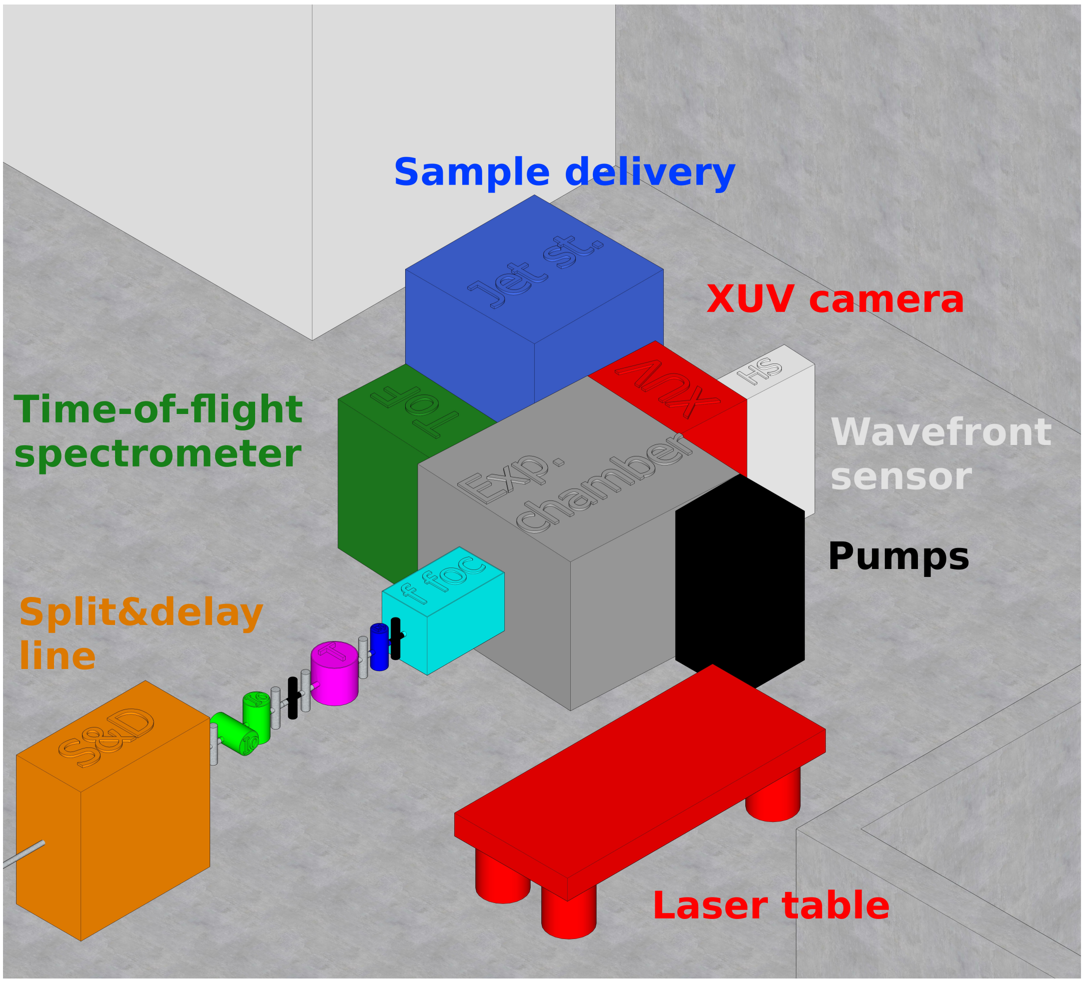

Figure 18.3: A schematic layout of the experimental end-station for CDI experiments.

concern the building that has to host the accelerator complex and the associated infrastructures, including the experimental hall. Actually, efficiency and safety, although very important, are not the only parameters relevant for the architecture project. The organization of the spaces has to be such to assist and support scientists in their daily work. Studies relating the needs of scientific activities with spaces and technologies required to perform these activities will be necessary. The collaboration with DADU – the Department of Architecture, Design and Urban studies of Sassari University - has been established in order to develop a really interdisciplinary project aimed at identify the accelerator machine and user needs to be integrated with all the architecture, implants and technology requirements. The dedicated building (see Figure 18.4 for a schematic view) will take into account the existing spaces and will have to become itself part of a new topography of the laboratory. The space dedicated to the scientific activities will be located in a close and protected environment, but still it will be in close contact with the environment allowing sunlight to enter the building and offering a view on the surrounding landscape. The experimental hall has been thought in order to allow the highest flexibility, with a large space and no pillars. Next to the experimental hall a large space for the support to the experimental activities, but also for rest breaks of people working on the experiments, will be available. From the technology point of view all up-to-date standards able to provide a good acoustic insulation and a comfortable and stable internal micro-climate, with a constant monitoring of temperature and humidity, will be adopted.

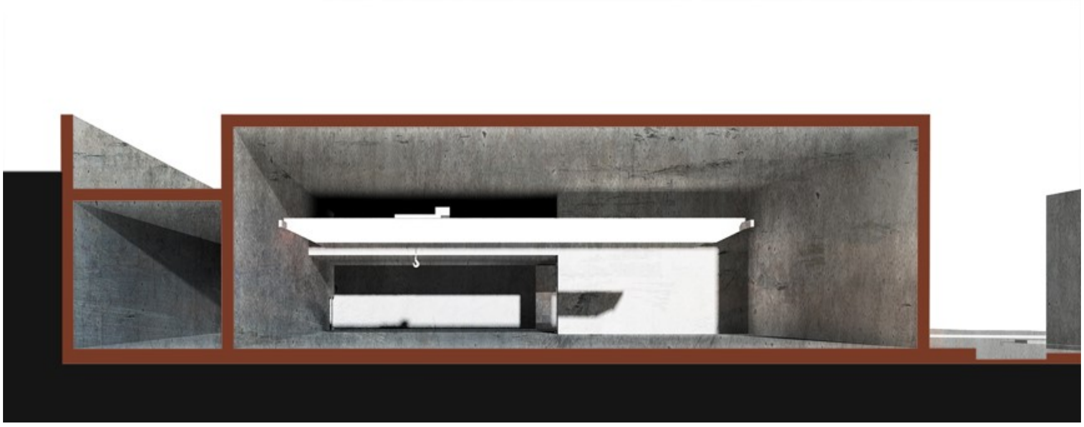

Figure 18.4: A possible layout of the experimental hall.

18.3.3 Instrumentation

The experimental chamber

A multi-purpose experimental chamber will be installed in order to allow performing the widest possible class of experiments, from coherent imaging, to diffraction and spectroscopy, emission, absorption, etc . The chamber will have the possibility to host solid samples on motorized stages and will have the possibility to be connected to a sample delivery apparatus to deliver also liquid and gaseous samples. One or more detectors, e.g. CCD cameras, will be located inside the chamber to allow performing the experiments. A reference example of a chamber with the above characteristics is the CAMP instrument successfully installed at FLASH and LCLS [25] whose dimensions are about $2.5 \times 1.5 \times 1.5$ m^3.

Sample delivery

Sample delivery is one of the key points to the success of a FEL based experiment. According to the kind of measurements and of the samples to be studied, a different sample delivery system will need to be used. For experiments on biological samples, aerosol and liquid jet injectors have the advantage of delivering the samples in their native, hydrated state and of continuously inserting new molecules under the FEL beam. An aerosol injector will be used to deliver hydrated samples in their native state. A sample delivery micro-jet based on the technology described in [26]. Systems of this kind have already been successfully used at existing FEL sources: FLASH, LCLS and SACLA. These sample delivery systems will require the installation of high pressure N_2 and He gas lines (up to 200 bar). The sample injection system is foreseen to be installed on an optical table with dimensions of the order of 2×2 m^2. For experiments on non-biological samples (or for biological samples not requiring to be in a hydrated state), a system in which samples are mounted on micrometer-precision stages will be built.

Time of flight spectrometer

A time of flight spectrometer connected to the experimental chamber will be used to analyze the molecules produced by the sample-beam interaction [27].

Laser

High power synchronized optical lasers should be made available to allow performing laser pump-FEL probe experiments. The maximum wavelengths flexibility will be secured to allow the broadest possible class of experiments. A laser tent, e.g., a removable structure covering an area of about 4×4 m^2 will be designed and installed. This structure is necessary to isolate the experimental area when performing experiments using class 3 and class 4 laser sources.

Split-and-delay line

We also propose to add a split and delay station in the beamline. This system uses the edge of a mirror to split the beam in two components that are then reflected on a delay line and recombined on a final mirror, where each part of the beam can have a tunable delay, typically ranging from 0 to few hundreds fs. This device will thus allow performing XUV-XUV pump-probe experiments. Devices of this kind are installed both at BL2 at FLASH [28] and at LCLS [29].

Support areas and laboratory for sample preparation

A supporting laboratory, in particular for biological/chemical preparations and manipulations, located in the building next to the beamline will allow last-minute sample preparations and characterizations. This laboratory with at least a 4 meters bench space for the sample preparation will include also a sink, a freezer, a fridge and a cabinet for storage of chemical substances. In terms of instrumentation, a fume hood, a vortex, an ultrasonic bath, a centrifuge and an optical microscope will be also available to users.

18.3.4 Data acquisition and treatment

A successful coherent imaging experiments does not exclusively rely on having a good quality photon beam with a sufficiently high brilliance, but also requires great care in beam characterization, diffraction pattern detection and data collection. For these reasons, dedicated servers and computers will be needed to control the beamline, the sample injection system, the sample position and possibly the pump-probe system.

Data acquisition system

An integrated data acquisition (DAQ) system, capable to store, for each recorded image, all the details of the FEL pulse, is needed. Given the fluctuations in the SASE-generated pulses, indeed, it is important to store on a shot-to-shot basis the number of photons, the energy and the beam position. Moreover, information about the sample, e.g., positions of the motors used to move it with respect to the beam, has to be recorded. In the case of pump-probe measurements, details about the pump pulse, like intensity, time-delay between pump and probe pulses, have also to be recorded. Finally, one (or more) large diffraction images will be registered for each pulse. An automatic data rejection protocol, able to record only images actually containing useful information, will be implemented.

Detectors

Two-dimensional, solid state detectors will be used to record the coherent diffraction patterns. Given the heterogeneous nature of samples to be studied at the EuPRAXIA@SPARC_LAB facility, the installed detector needs a wide dynamic range, a relatively small pixel size coupled to a large number of pixels, a low intrinsic noise and an image acquisition rate matching the FEL repetition rate. Moreover, in order to collect diffraction patterns for different scattering angles, detectors will be mounted on a movable slit to set them at a variable distance from the sample-FEL beam interaction region. Table 18.1 summarizes the main characteristic of the detector to be considered for imaging experiments.

Improvements of these parameters are certainly possible in the next years according to the technological trend and demands of similar sources in the existing international scenario.

Data storage and processing

Regarding data storage, CDI data are quite heavy. A 16-bit 2048×2048 pixel image corresponds indeed to 8 MB. Considering the maximum repetition rate of 10 Hz, a full 24 hours experimental session would require $\sim$ 10 TB of hard-disk space. For this reason, at least 10 PB of storage (part on hard-drive, part on tape) have to be considered and made available to users. It is also necessary

Parameters	Range
Photon energy range	(310–620) eV
Position sensing	2D
Quantum efficiency	> 0.9
Total angular coverage	> 200 degrees
Angular resolution	> 7 mrad
Number of pixels	$> 1000 \times 1000$
Acceptable tiling constraints	$> 1000 \times 1000$
Maximum local rate (i.e. on pixel)	10^5 photons/pixel/100 fs pulse
Maximum global rate (i.e. on detector)	$> 10^{13}$ photons/s
Timing	10 Hz
Noise (pixel channel)	< 1 photon/s
Operating environment	Laser in the HV experimental chamber
Vacuum compatibility	10^{-6} mbar

Table 18.1: Detector parameters and requirements.

to allow a fast access to the measured data for analysis during the experimental run. For this reason, data transfer and conversion into a user-readable format allowing a first data evaluation must be as fast as possible. Efficient on-line data reduction (or rejection) tools will be necessary to minimize the amount of stored data, allowing an almost real-time visualization of images.

Bibliography

[1] Henry N Chapman et al. “Femtosecond X-ray protein nanocrystallography”. In: *Nature* 470.7332 (2011), p. 73.

[2] Sébastien Boutet et al. “High-resolution protein structure determination by serial femtosecond crystallography”. In: *Science* (2012), p. 1217737.

[3] M Marvin Seibert et al. “Single mimivirus particles intercepted and imaged with an X-ray laser”. In: *Nature* 470.7332 (2011), p. 78.

[4] Max F Hantke et al. “High-throughput imaging of heterogeneous cell organelles with an X-ray laser”. In: *Nature Photonics* 8.12 (2014), p. 943.

[5] Gijs Van Der Schot et al. “Imaging single cells in a beam of live cyanobacteria with an X-ray laser”. In: *Nature communications* 6 (2015), p. 5704.

[6] Jiadong Fan et al. “Single-pulse enhanced coherent diffraction imaging of bacteria with an X-ray free-electron laser”. In: *Scientific reports* 6 (2016), p. 34008.

[7] Richard Henderson. “The potential and limitations of neutrons, electrons and X-rays for atomic resolution microscopy of unstained biological molecules”. In: *Quarterly reviews of biophysics* 28.2 (1995), pp. 171–193.

[8] C Gutt et al. “Single-pulse resonant magnetic scattering using a soft x-ray free-electron laser”. In: *Physical Review B* 81.10 (2010), p. 100401.

[9] Massimo Ferrario et al. “EuPRAXIA@SPARC_LAB”. In: *submitted to Nucl. Instrum. Meth. Phys. Res. A* (same volume) (2018).

[10] Maciej Lewenstein et al. “Theory of high-harmonic generation by low-frequency laser fields”. In: *Physical Review A* 49.3 (1994), p. 2117.

[11] Jeffrey L Krause, Kenneth J Schafer, and Kenneth C Kulander. “High-order harmonic generation from atoms and ions in the high intensity regime”. In: *Physical Review Letters* 68.24 (1992), p. 3535.

[12] E Constant et al. “Optimizing high harmonic generation in absorbing gases: Model and experiment”. In: *Physical Review Letters* 82.8 (1999), p. 1668.

[13] J-F Hergott et al. “Extreme-ultraviolet high-order harmonic pulses in the microjoule range”. In: *Physical Review A* 66.2 (2002), p. 021801.

[14] Eiji J Takahashi et al. “High-throughput, high-damage-threshold broadband beam splitter for high-order harmonics in the extreme-ultraviolet region”. In: *Optics letters* 29.5 (2004), pp. 507–509.

[15] W Boutu et al. “High-order-harmonic generation in gas with a flat-top laser beam”. In: *Physical Review A* 84.6 (2011), p. 063406.

[16] TT Liu et al. “Significant enhancement of high-order harmonics below 10 nm in a two-color laser field”. In: *Physical Review A* 73.6 (2006), p. 063823.

[17] I Jong Kim et al. “Generation of submicrojoule high harmonics using a long gas jet in a two-color laser field”. In: *Applied Physics Letters* 92.2 (2008), p. 021125.

[18] Guillaume Lambert et al. “An optimized kHz two-colour high harmonic source for seeding free-electron lasers and plasma-based soft x-ray lasers”. In: *New journal of physics* 11.8 (2009), p. 083033.

[19] Leonida Antonio Gizzi et al. “Laser-plasma acceleration with FLAME and ILIL ultraintense lasers”. In: *Applied Sciences* 3.3 (2013), pp. 559–580.

[20] URL: `http://www.elettra.eu/lightsources/fermi/fermi-machine/machineparameter.html`.

[21] URL: `https://flash.desy.de`.

[22] URL: `https://lcls.slac.stanford.edu/instruments/sxr/specifications`.

[23] URL: `https://lcls.slac.stanford.edu/instruments/amo/specifications`.

[24] URL: `http://xfel.desy.de/technical_information/photon_beam_parameter/`.

[25] Lothar Strüder et al. “Large-format, high-speed, X-ray pnCCDs combined with electron and ion imaging spectrometers in a multipurpose chamber for experiments at 4th generation light sources”. In: *Nuclear Instruments and Methods in Physics Research Section A: Accelerators, Spectrometers, Detectors and Associated Equipment* 614.3 (2010), pp. 483–496.

[26] DP DePonte et al. “Gas dynamic virtual nozzle for generation of microscopic droplet streams”. In: *Journal of Physics D: Applied Physics* 41.19 (2008), p. 195505.

[27] AA Sorokin et al. “Multi-photon ionization of molecular nitrogen by femtosecond soft x-ray FEL pulses”. In: *Journal of Physics B: Atomic, Molecular and Optical Physics* 39.14 (2006), p. L299.

[28] M Wöstmann et al. “The XUV split-and-delay unit at beamline BL2 at FLASH”. In: *Journal of Physics B: Atomic, Molecular and Optical Physics* 46.16 (2013), p. 164005.

[29] JC Castagna et al. “X-ray split and delay system for soft x-rays at LCLS”. In: 425.15 (2013), p. 152021.

V Machine Infrastructure

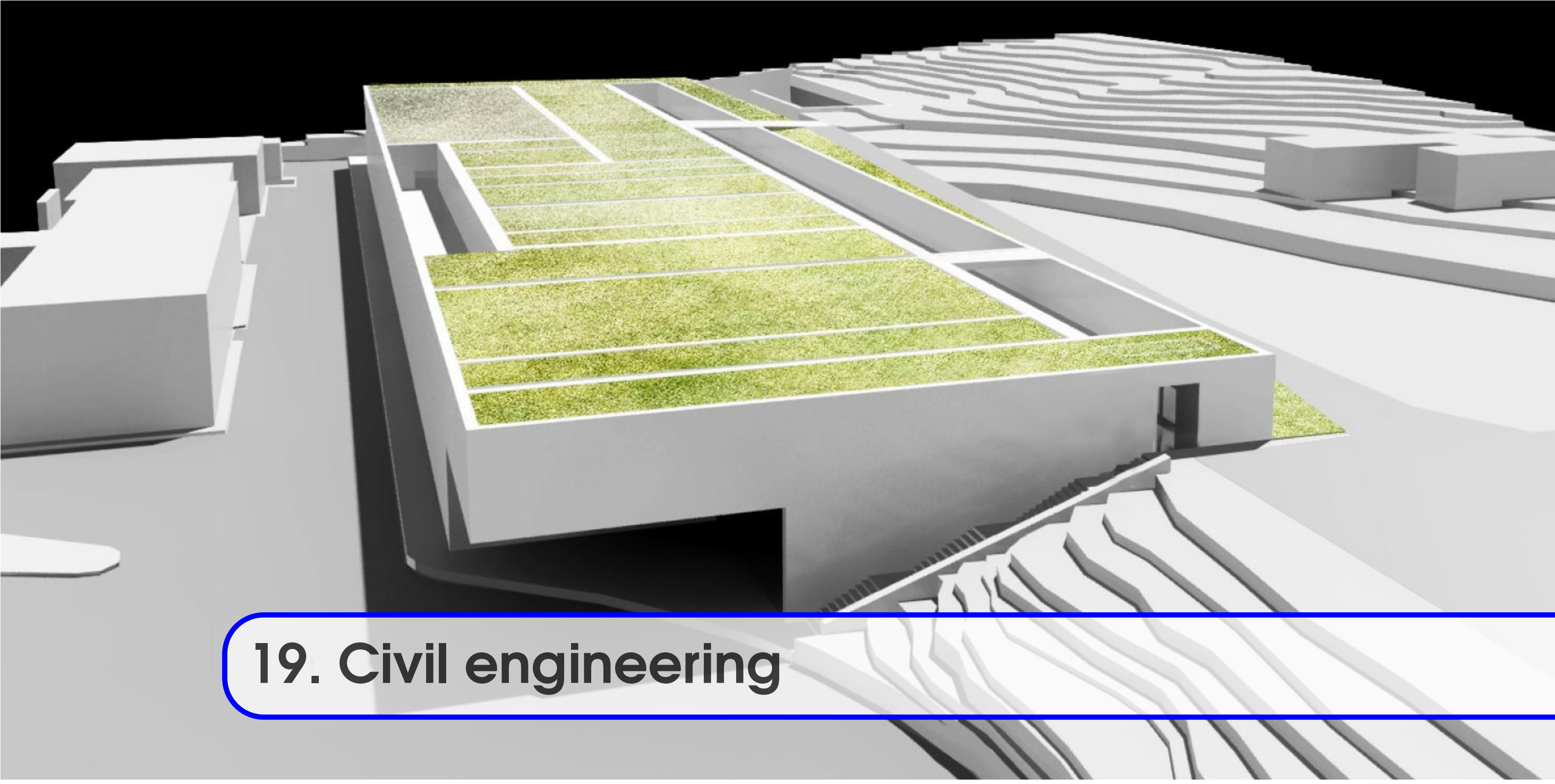

19. Civil engineering

19.1 Civil engineering

The EuPRAXIA@SPARC_LAB project requires the construction of new buildings to house the linac, the FEL, Experimental room and support laboratories. They will be supplied with conventional systems. The new infrastructures will be built inside the INFN LNF area (Fig. 19.1). The lab is situated about two kilometers North of Frascati (Rome) and about thirty kilometers from Rome. It is near ENEA and ESA.

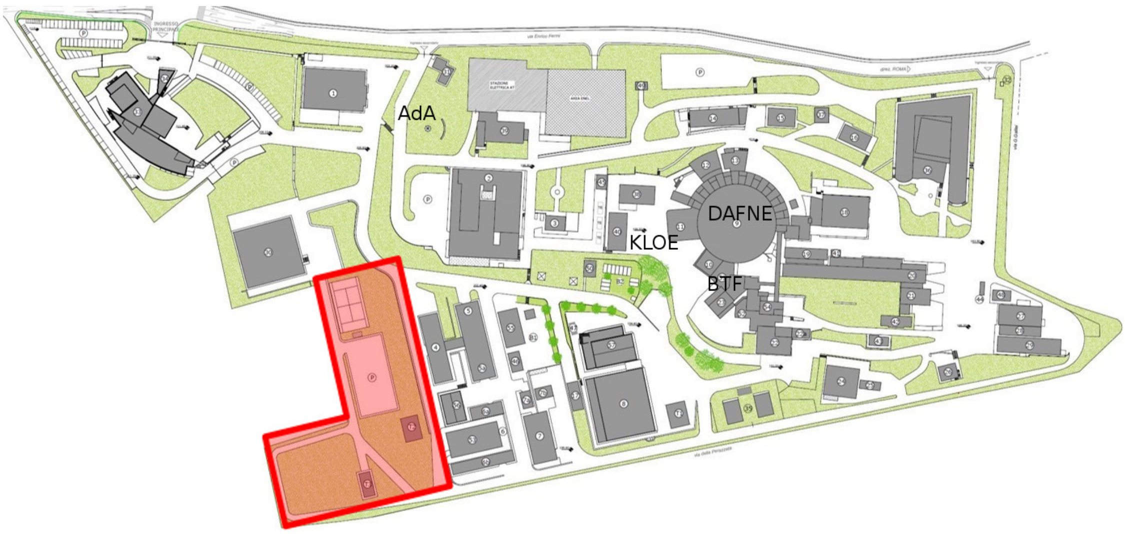

Figure 19.1: LNF – INFN lab area.

19.1.1 Site

The new facility will be built in the South-East part of LNF area. It covers approximately an area of 9000 square meters (Figure 19.2) and it is located at an elevation ranging from 205 to

218 m above sea level. At present the site is a green area housing a parking area (36 parking spaces), a football/tennis pitch and two temporary buildings.

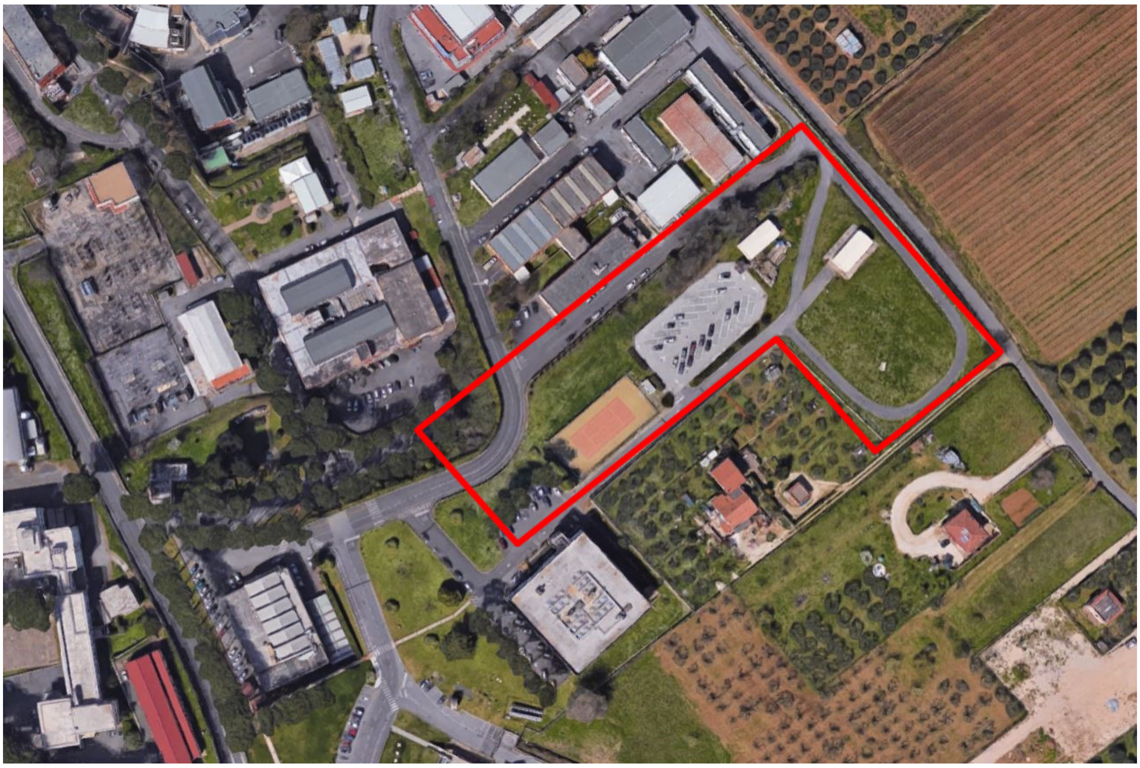

Figure 19.2: EuPRAXIA@SPARC_LAB area top view (from Google maps).

19.1.2 Geology and hydrogeology

Some geological and geognostic data of the site are known thanks to preliminary geological and exploratory drilling survey campaign performed inside the LNF area in 2009 and 2010 (during the SuperB project study), but geological investigation and site assessment must be reviewed in detail.

The morphology is typical of plan-altimetric sub-flat trends of the Colli Albani area. From a geological point of view, the site is related to the Lazio Volcano activity. The soil consist of volcanic products with different physical-mechanical characteristics and a fairly good degree of stability. Data are known up to a depth of about 40 – 50 m.

Starting from the ground surface, the soil includes the following main stratigraphic levels (see Figure 19.3):

- Layer of vegetable soil and fill material (about 1 m);
- Brown pyroclastic grounds (5 to 7 m layer);
- Lava rocks (1 to 5 m);
- Other layers of grey pyroclastic material, including pockets of scoria, lava tuff elements.

From this surveys' outcome the presence of underground water was not detected.

The site is able to support heavy loads and to damp vibrations coming from natural sources and cultural noise, as confirmed by vibration measurements carried out for SuperB project.

A thorough campaign of geological surveys will be organized to get the data needed for the advancement of the building design. The survey will be targeted to the precise definition of the geotechnical features and, in particular, to the aspects of deformation of the land affected by the experimental rooms.

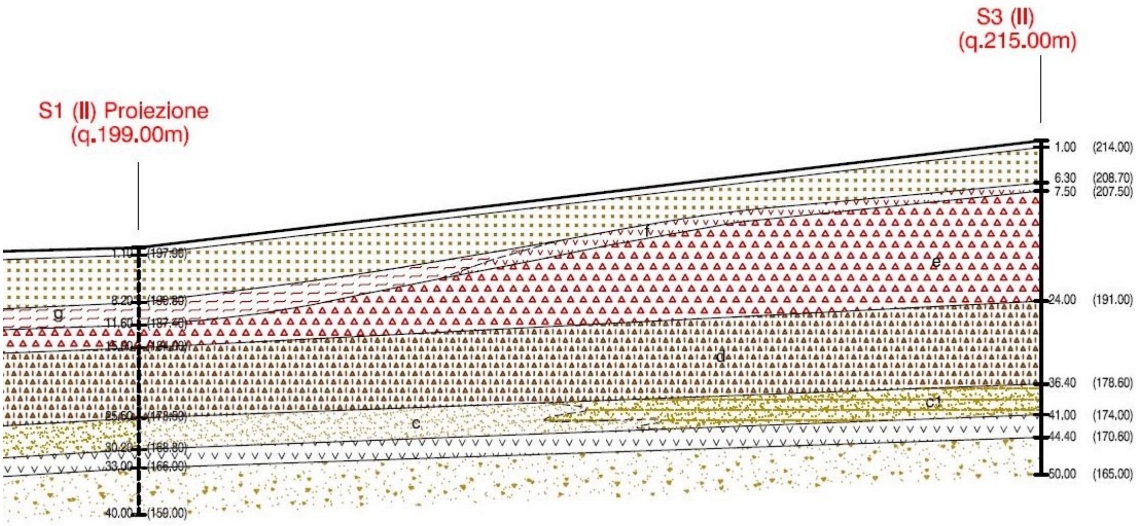

Figure 19.3: Geological stratigraphic section of the soil.

19.1.3 Civil Engineering

The main aim is to design a building with a simple architecture, but meeting efficiency and functionality, and also flexibility of internal spaces for future upgrades. The building design presented in this section, is subject to modification until it fulfills all necessary authorizations and machine requirements.

Before building construction, some preliminary activities are necessary, like explosive ordnance disposal, archaeological digging, and utilities connections to existing plants.

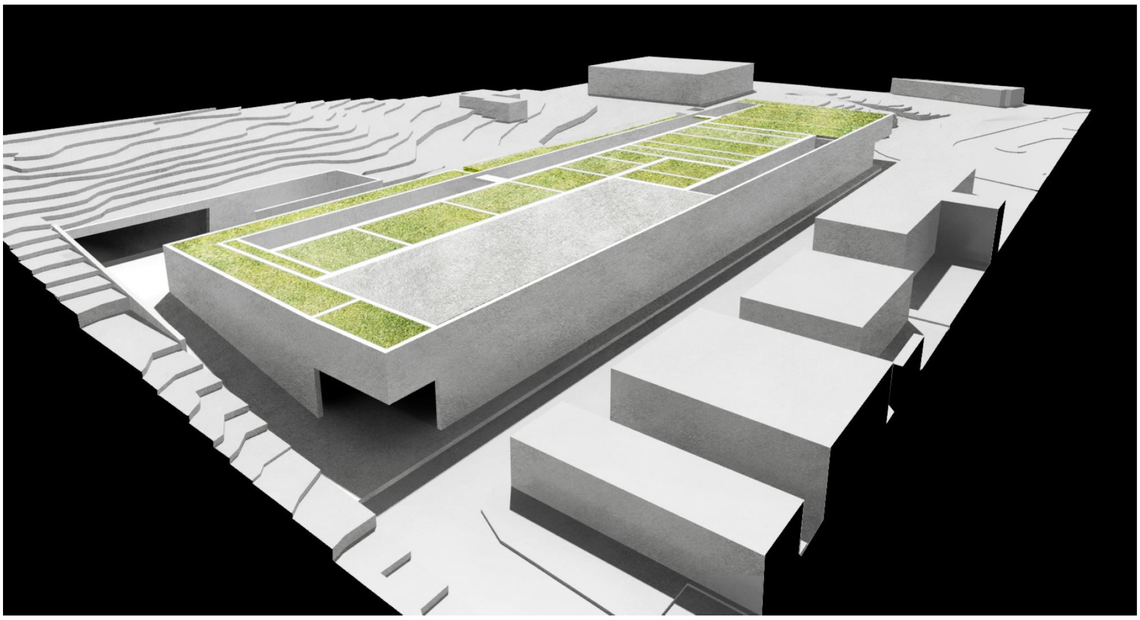

Figure 19.4: 3D view (East side) of the building.

Figures 19.4 and 19.5 show a 3D view of the new proposed building in its surroundings: the foreseen location takes advantage of the difference in height of the soil for a natural shielding from radiation.

The facility will have an L shape and present a total length of 130 m and a width ranging from

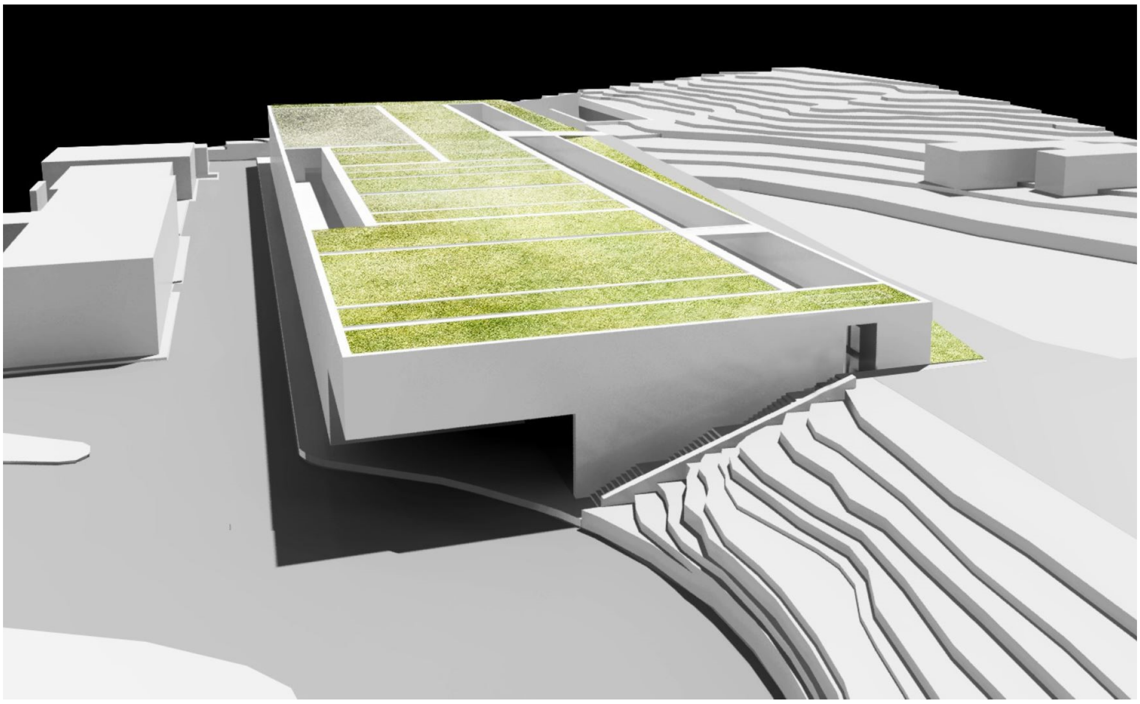

Figure 19.5: 3D view (West side) of the building.

35 to 86 m. It comprises a main building housing the accelerator machine and ancillary equipment, and another one under the natural ground level for plants and storage. Both will be built at the same depth, in cut and cover method.

The main building will be a parallelepiped 130 m long and 35 m wide, that will be developed in East/Sud–West direction. It will have a roof garden for radioprotection reason and to minimize the visual impact on the environment.

The building for auxiliary plants will house a new electrical substation, primary refrigerating plants (dry cooler and pumps) and primary cooling circuit distribution systems. It will also house a parking area and a storage area.

The current road network in this area will be restored but it will be adapted to allow the movement and the access of people, vehicles and equipment around and to the new buildings.

From a city planning point of view, the area is classified by Frascati general land-use plan as a zone with a special destination. A detailed urban plan specifies the available volumetric dimensions and the maximum height of new buildings inside the LNF area.

Frascati area is bounded by archaeological and environmental restriction, as defined by the *Piano Territoriale Paesistico Regionale* of Lazio region.

Furthermore, a study of environmental impact that takes into consideration geology, is foreseen to minimize the effects on the environment.

For the design of the buildings, three aspects are crucial: radioprotection shielding, slab stability against ground vibration and seismicity of the site.

For radiation safety reasons, the walls and roof of the linac tunnel will have a thickness of 2 m concrete and a ground cover will be on the roof, depending on detailed radioprotection calculations.

The slab stability is very important for accelerator reliable operation: the slab of accelerator rooms must be able to accommodate the machine mounting and movement and allow its repositioning without unsatisfactory deflection or settlement over time. The vibration limits are associated with the user-supplied research instruments. A campaign of detailed ground motion measurements in LNF is available (performed for the SuperB project).

For reference, Table 19.1 summarizes the acceptable tolerance defined for Soleil Synchrotron (France).

LONG TERM SETTLEMENT (vertical)	100 μm over 10 m per year
	10 μm over 10 m on a diurnal cycle
	1 μm over 10 m in short-term (about 1 hour)
PUNCTUAL STATIC LOAD OF 500 kg	Δz<6 μm under the load
	Δz<1 μm at 2 m
DYNAMIC LOAD OF 100 kg	Δz<1 μm (ptp) at 2 m
VIBRATIONS (0.1–70Hz) due to all effects induced by the facility	Δz<1 μm peak to peak
	Δz<4 μm peak to peak

Table 19.1: Long time settlement defined for Soleil Synchrotron (Extract from SuperB Committee report).

From a seismic point of view, the LNF site is an area classified as "2B category", in accordance with Lazio region classification, in force since 22nd May 2009 and adopted in March 2015. The structural calculations will be based on the current regulation (NTC 2008). Particular attention will be paid to building foundations, slabs, support structures and the placement of equipment to minimize vibration disturbance from cultural noise.

19.1.4 Buildings

The EuPRAXIA@SPARC_LAB facilities will be set in the South-East PART of LNF site, on the slope of a little hill. They will be built near the current facilities and offices of the Lab. The building will be covered by roof garden and the people and vehicles access is from *via Heisenberg*.

The layout of the building housing the accelerator machine is shown in Figures 19.6 and 19.7.

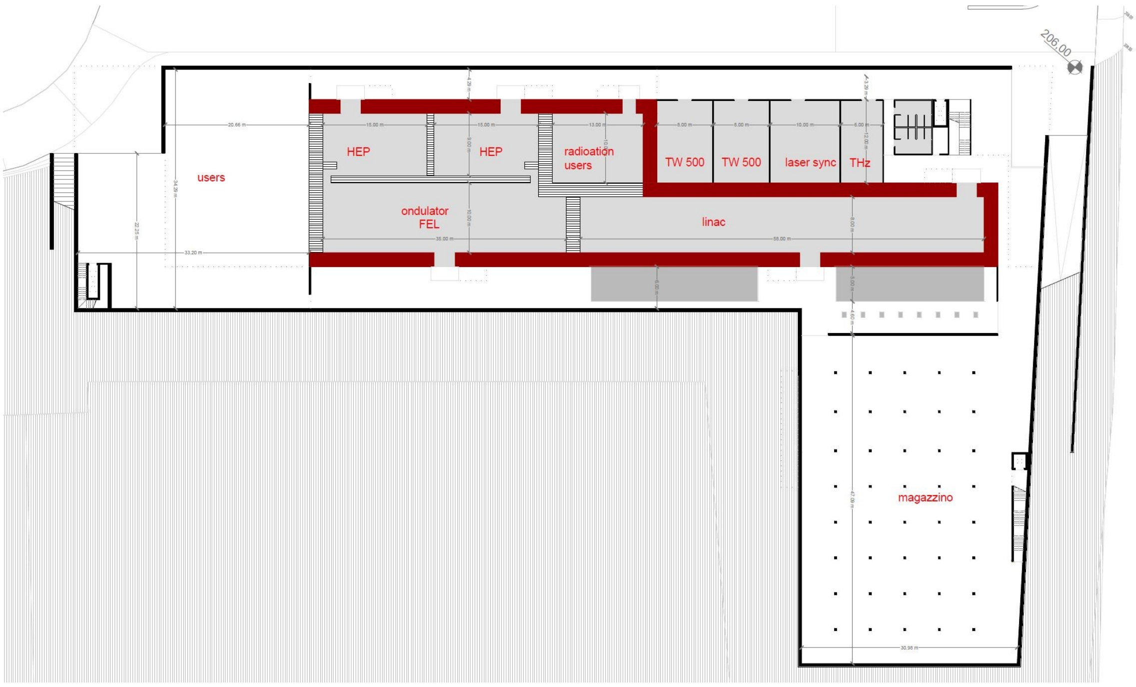

Figure 19.6: EuPRAXIA@SPARC_LAB building layout – level zero.

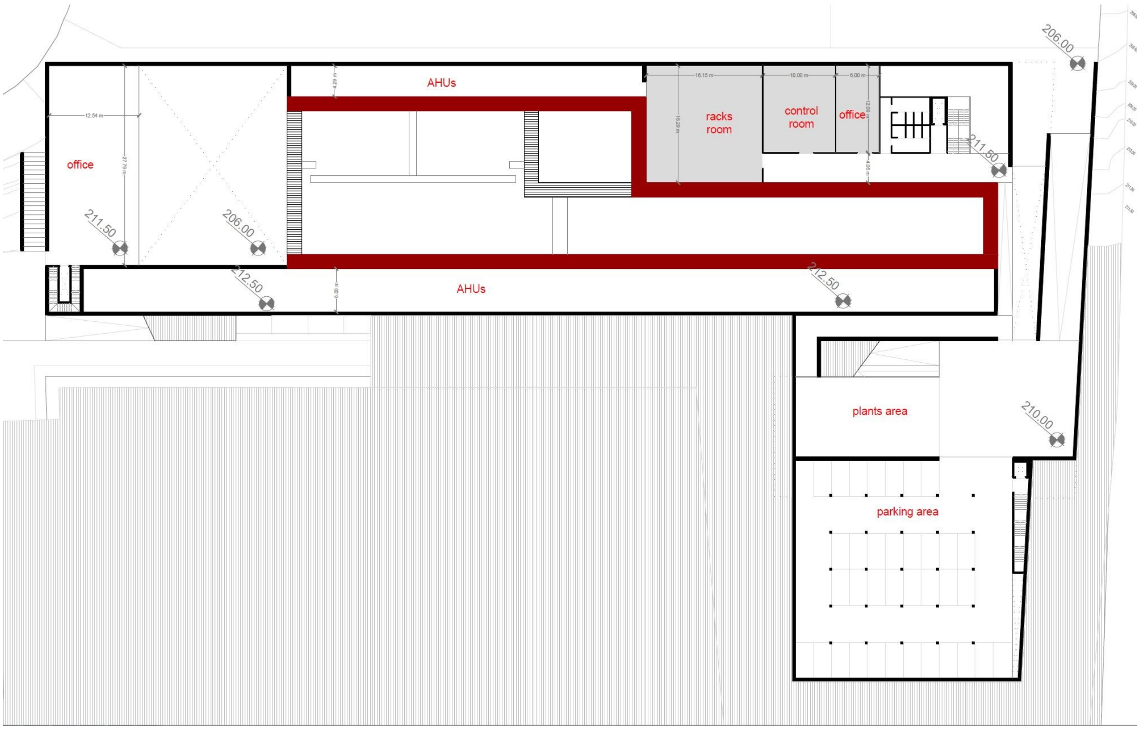

Figure 19.7: EuPRAXIA@SPARC_LAB building layout – level one.

The key of the architectural layout is dictated mainly by the requirements of the experiments. The building can be divided into three functional zones. The first includes:

- a Linac tunnel housing the injector, the main linear accelerator, plasma and matching. Its dimensions are approximately 58 by 8 m^2 with a height of 6 m. The tunnel will have the walls and a roof of concrete 2 m thick and two main access through shielding doors located on opposite sides.
- a modulators and klystrons gallery will be adjacent and parallel to the linac tunnel. 9 m wide and 6 m high, it will allow, with proper penetrations, the access of the waveguides feeding the linac sections. In this area a 5 Tons crane will be installed to facilitate the movement of klystrons. The gallery will be extended to the overall length of the building to allow access to experimental rooms and to house the main electrical and cooling distribution.
- some laboratories (THz , Laser Sync, 2x500 TW rooms), with different dimensions, will be distributed along the linac tunnel. A large corridor allows access into them.
- A radiation users room will be located adjacent the linac, in the opposite side of services gallery. Walls and roof will have the same thickness of linac tunnel (2 m concrete). The entrance will be through a shielding door.
- the part above the ancillary laboratories will be dedicated to the control room, the racks room, a meeting room and offices. The access to the first floor is through a lift and a staircase. The control room will be located approximately midway along the accelerator.

The second functional zone of the building consists of a large hall including the Undulator/FEL hall and 2 HEP rooms, both with a removable structure.

The Undulator/FEL hall is located downstream the linac tunnel and is at the same level. The dividing wall between the two areas will be a removable wall of 2 m concrete with adequate horizontal holes by means of which the electron beam vacuum chamber passes. The dimensions of this hall are approximately 35 by 10 m^2 with a height of 6 m. The roof will be 2 m concrete. The main access is in the services gallery by a shielding door. Adjacent to the undulator hall, two experimental rooms will be dedicated to HEP. 1 m thick wall separates the Undulator/FEL hall from HEP rooms, but two chicanes allow the access from side to side.

The third functional zone of the building is the Experimental room. It is a big open space of about 34 by 33 m^2, 8.5 m height. 2 m removable shielding wall separates it from Undulator/FEL hall. The Experimental room will have a little gallery housing a meeting room and some offices for the external users. The first level will be reached by a staircase from ground floor and through an external stairway from *via Heisenberg*.

The roof level will be devoted to a garden that must contribute to ionizing radiation shield and to minimize the impact on the environmental contest. At roof level the layout envisages some areas intended for AHUs hosting, but conveniently hidden, and appropriate paths for maintenance.

Another building, completely underground, will be built next to the MAIN building and connected to it. It will be approximately 50 by 35 m^2 and will have two levels. The first level will be at the same level of the Linac tunnel and will be a big storage area. The second one will be dedicated partly to conventional facilities for the experimental buildings and partly to a parking area. Here an electrical substation and cooling plants (dry coolers, chillers and pumping station) will be installed to feed and support the accelerator machine.

The building will have three main access for people and vehicles: one from *via Heisenberg* to the lower level, passes through the EuPRAXIA@SPARC_LAB building, near the linac tunnel; another one from *via Heisenberg* but through a sloping road accessing plants area and parking area. The third access will be from *piazzale Marconi* to the second level. In addition, an adequate number of emergency exits will be provided, conforming to the safety rules.

19.2 Electrical power distribution

The EuPRAXIA@SPARC_LAB project will be supplied by the 20 kV LNF grid, through two feeders, the main one from the 150/20 kV substation, the backup one from the closest cabin. A MV/LV substation equipped with 2 transformers will be located in a technical building central with respect to the electrical load.

Reactive power compensating system will be housed in the substation if necessary.

The technical areas for substations and the electrical installations as the cable try occupancy have to be integrated in the civil construction design.

The existing main substation backup power generator is available to supply up to 50 kW. In case of larger power demand, a dedicated gen–set has to be included in the project. Loads that have to be powered by gen-set are: vacuum and control devices, underground emergency lighting, some ventilation, auxiliary services and some UPS loads.

19.2.1 Redundancy criteria

Fault redundancy will be implemented for main components as the transformer bay and MV feeders. The unavailability of one component of a transformer bay, like MV or LV breaker, protection devices, auxiliary services, busbars, as well as the transformer will not compromise the operation.

Transformers will be sized in order to be fully loaded in case of unavailability of one per substation. Otherwise they will be loaded at 50%.

19.2.2 Low voltage power distribution

Power is distributed at level 400/230 V as TN-S distribution system.

LSOH Cables (fire retardant, Low Smoke - Zero Halogen) will be adopted for internal wiring.

Power cables will be drawn in metal ducting systems distinct and far from control and signal ducting system in order to minimize the electromagnetic coupling with electronic cables and devices.

Protection against indirect contact has to be achieved by overcurrent protective devices. Residual current devices will be adopted only on the load.

As a general consideration, important loads, over 125 A, will be feed by dedicated switch units from the low voltage main switchboard. Lower size devices will be supplied using 400 A busbars trunking systems that will serve all the power supply rooms. Busbar Tap-off units will be equipped with circuit breaker.

19.2.3 Electrical installation for the accelerator tunnel

Special care will be taken into account in order to minimize electrical devices radiation damage. Radiation tolerant materials and low maintenance systems will be selected for every component that has to be installed in the beam area. Electronic devices not strictly essential, like electronic ballasts and control devices, will be banned by the accelerator area.

With respect to lighting devices, polycarbonate and electronics suffer by radiations. Metal and glass luminaries with fluorescent bulbs with not electronic ballast will be adopted, and a central emergency lighting system will be preferred with respect to self-powered devices. Fire resistant cable FGT10OM1 will be adopted for the safety lighting power distribution.

Reduced maintenance devices and solutions will be adopted in the radiation safety restricted access area. Electrical switchboards will be placed out of the beam area of influence.

19.2.4 Grounding, bonding and low voltage distribution system

A dedicated buried earth electrode, integrated with the metal reinforcement of concrete and structural metalwork of all the building site will be integrated in the LNF grounding system.

A meshed common bonding network (CBN) will be distributed with 250 mm^2 of copper bar in all the beam and power supplies area, and will be used to bond all the devices in the beam line and the auxiliaries besides the proper protection earth.

The low voltage distribution system will be delivered as TN-S, whit separate neutral and protective earth (PE) wires. The PE will be distributed and bonded on the CBN wherever possible, in order to minimize conducted and radiated interference.

CBN will be the only reference potential inside the site.

19.2.5 Electromagnetic compliance

With respect to technical rules CEI–EN 50160, 61000–2–2 and 61000–2–12, electrical installations have to comply level 2 of CEI–EN 61000–2–4. Nevertheless, higher harmonic current distortion level has to be expected for power converter that will be powered by a "dirty" transformer bay.

19.2.6 Examples and references

- **EMC – Power Converters for Particle Accelerators** A. Charoy, `http://cas.web.cern.ch/cas/Warrington/PDF/Charoy.pdf`
- **Earthing of High-Energy Physics Detector Systems** F. Szoncsó CERN–TIS `http://szoncso.home.cern.ch/szoncso/EMC/Earth_new_Latin_020405.pdf`
- **EMC for Systems and Installations** T. Williams – K. Armstrong Ed. Newness (partially available in: `http://www.compliance-club.com/KeithArmstrongPortfolio.htm`)

19.3 Fluid plants

The EuPRAXIA@SPARC_LAB facilities will use water and air as main heat carriers. The fluid plants will be divided in:

- Water cooling plant (with set range from 15°C to 45°C)
- Refrigeration plant (with set range from 7°C to 10°C)

- HVAC plant
- Technical Gas plants (compressed air [e.g. vacuum valves operation] and SF_6 [RF wave–guides insulation])

In order to assure plants continuous operation, machine redundancy will be implemented and installation outside Controlled and Supervised areas will allow for maintenance activities also during machine operation.

19.3.1 Water heat carrier

Water of two different kinds will be used: tap and de-ionized (DI).

The electromagnets and RF systems require DI water in order to assure electrical insulation, to prevent erosion, activation, and pipes clogging.

DI water specifications will be:

- Conductivity < 0.3 μS/cm
- Dissolved Oxygen <20 ppb
- 6.8 < pH < 7.2

Conductivity and the other parameters will be maintained at the set point value by online polishing and controlled make up.

DI water usage require stainless steel, EPDM and copper as materials for supply network and users' construction material.

High performance Dry-Coolers will chill the DI water for most part of the year, while in the hottest months, Chillers will boost cooling power to maintain water temperature set-point.

The cooled tap water (7÷10°C) will be used to:

- supply the AHUs
- supply the Hi-Precision CRACs for the Data Centers

Thermal waste heat recovery will be implemented to warm up the civil infrastructure.

19.3.2 Air heat carrier

As heat carrier, air will assure:

- High performances for Clean Rooms;
- Radioprotection Control for Controlled and Supervised areas;
- Residual heat load removal, especially in high-density power rooms as the Data Center.

19.3.3 Auxiliary plants Control System

An industrial SCADA will supervise ancillary plants operation with respect to:

- interlocks and alarms
- faults
- parameters regulation
- remote supervision

in order to assure the highest possible up-time and to reduce MTTR helping in faults diagnosis.

20. Radiation safety and beam dumps

20.1 Introduction

High-energy electron accelerators are complex devices containing many components. All facilities contain the same basic systems:

- Accelerators structures
- RF power components
- Vacuum system
- Magnetic system associated with steering and focusing the beam
- Water-cooling
- Etc...

Prompt radiation and radioactivity induced by particle nuclear interaction in beam line elements and shielding structures represents the main radiation hazard of high energy accelerators.

The accelerator's design parameters are of crucial importance in the determination of the nature and magnitude of radiation source. The most important parameters are:

- Particle energy
- Beam power
- Target material
- Work load
- Beam losses

as well as the physical layout.

20.2 Operating parameter

The EuPRAXIA@SPARC_LAB project consists in an X-ray FEL facility in which an electron beam is accelerated at the energies of 1 GeV with average current up to 100 nC/s (0.1kW). It is foreseen to accelerate electrons up to 5 GeV by means of plasma acceleration with electron average currents significantly less than 100 nC/s.

20.3 Machine protection

20.3.1 Electron losses

Even if the maximum power of the beam is quite low, an active machine protection system in under study to limit beam losses.

20.3.2 Dose monitoring in the undulators section

The sensitivity of undulator magnets to radiation requires a dose monitoring in the undulator section. Active and passive systems are under evaluation.

20.4 Radiation Protection

20.4.1 Shielding outlines

The new machine general layout has been previously shown.

Using the previous operating parameters we have performed calculations of shielding. Because of a great number of the precautions introduced, the results should be a conservative approximation of the doses actually expected. During the commissioning phase, the reliability of the assumptions made will be verified and, if necessary, additional precautions will be made.

20.4.2 Shielding Design Criteria

The shielding design criteria have been based on the Italian legislation (D.Lgs. 230/95), according to European Directives as well as the recent ICRP recommendations (ICRP 103). According previous documents the individual limits are 20 mSv/y for radiation workers, and 1 mSv/y for the public.

Moreover the definitions of controlled and supervised areas are useful as guidelines. A controlled area is every area where 3/10 of the limits recommended for radiation worker may be exceeded. A supervised area is one area where the overcoming of 1/10 of the previous limit may occur.

Taking into account the dose levels normally found around accelerators, the thickness of the shielding was calculated maintaining the doses, within the areas outside the shield frequented by the staff, 1–2 mSv/y and 0.25 mSv/y within the areas outside the shield frequented by members of the "public".

A shifting from these values could at most change the radiation classification of some areas.

In normal working condition the dose rate outside shielding should not exceed a fraction of mSvy.

20.5 Radiation Source Terms

For shielding evaluation purposes, three components of radiation field which are produced when an electron beam, with an energy of hundreds of MeV – few GeV, hit either a vacuum chamber wall or a thick target have to be considered

20.5.1 Bremsstrahlung

Prompt photon fields produced by Bremsstrahlung constitute the most important radiation hazard from electron machines with thin shielding. Bremsstrahlung yield is very forward peaked, and increasingly so with increasing energy.

The following equation describes this behavior:

$$\theta_{1/2} = 100/E_0 \tag{20.1}$$

where $\theta_{1/2}$ is in the angle in degrees at which the intensity drops to one half of that at 0°, and E_0 is the energy of the initial electrons in MeV . In order to evaluate the shield thickness a "thick target", usually a target of sufficient thickness to maximize bremsstrahlung production, was considered. Photon yield from a thick target as a function of angle consists of two components: sharply varying forward component, described in Equation (20.1), and a mildly varying wide-angle component. Forward (or zero-degree) Bremsstrahlung contains the most energetic and penetrating photons, while Bremsstrahlung at wide angles is much softer.

The source term (per unit beam power) for Bremsstrahlung at 90° is independent of energy.

20.5.2 Neutrons

Photons have larger nuclear cross-sections than electrons, so neutrons and other particles resulting from inelastic nuclear reactions are produced by the Bremsstrahlung radiation. Neutrons from photonuclear reactions are outnumbered by orders of magnitude by electrons and photons that form the electromagnetic shower. However, some of these neutrons constitute the most penetrating component determining factor for radiation fields behind thick shielding.

Giant resonance production

The giant resonance production can be seen in two steps:

1. the excitation of the nucleus by photon absorption;
2. the subsequent de-excitation by neutron emission, where memory of the original photon direction has been lost.

The cross-section has large maximum around 20–23 MeV for light nuclei (mass number A$\leq$40) and 13–18 MeV for heavier nuclei.

The angular yield of giant resonance neutrons is nearly isotropic.

The giant resonance is the dominant process of photoneutron production at electron accelerators at any electron energy.

Pseudo-deuteron production

At photon energies beyond the giant resonance, the photon is more likely to interact with a neutron-proton pair rather than with all nucleons collectively. This mechanism is important in the energy interval of 30 to $\sim$300 MeV , contributing to the high-energy end of the giant resonance spectrum. Because the cross-section is an order of magnitude lower than giant resonance, with the added weighting of Bremsstrahlung spectra, this process never dominates.

Photo-pion production

Above the threshold of $\sim$140 MeV production of pions (and other particles) becomes energetically possible. These pions then generate secondary neutrons as byproduct of their interactions with nuclei. While substantially less numerous than giant resonance neutrons, the photo-pion neutrons are very penetrating and will be the component of the initial radiation field from a target (with the exception of muons at very high energies) that determines the radiation fields outside very thick shields.

Taking account all operating parameter as well as the foreseen beam losses (5%) and shielding design criteria, a lateral shielding wall and a roof of 2 m of ordinary concrete was chosen for machine tunnel (linac + undulators).

In following Figures 20.1 are reported the ambient dose equivalent rate at 4 m and 20 m (LNF Borders) from the source at 90° versus the thickness of concrete shield.

Calculations are in progress in order to define the thickness of the whole shield, following the final layout, the final definition of the beam parameters and the beam losses.

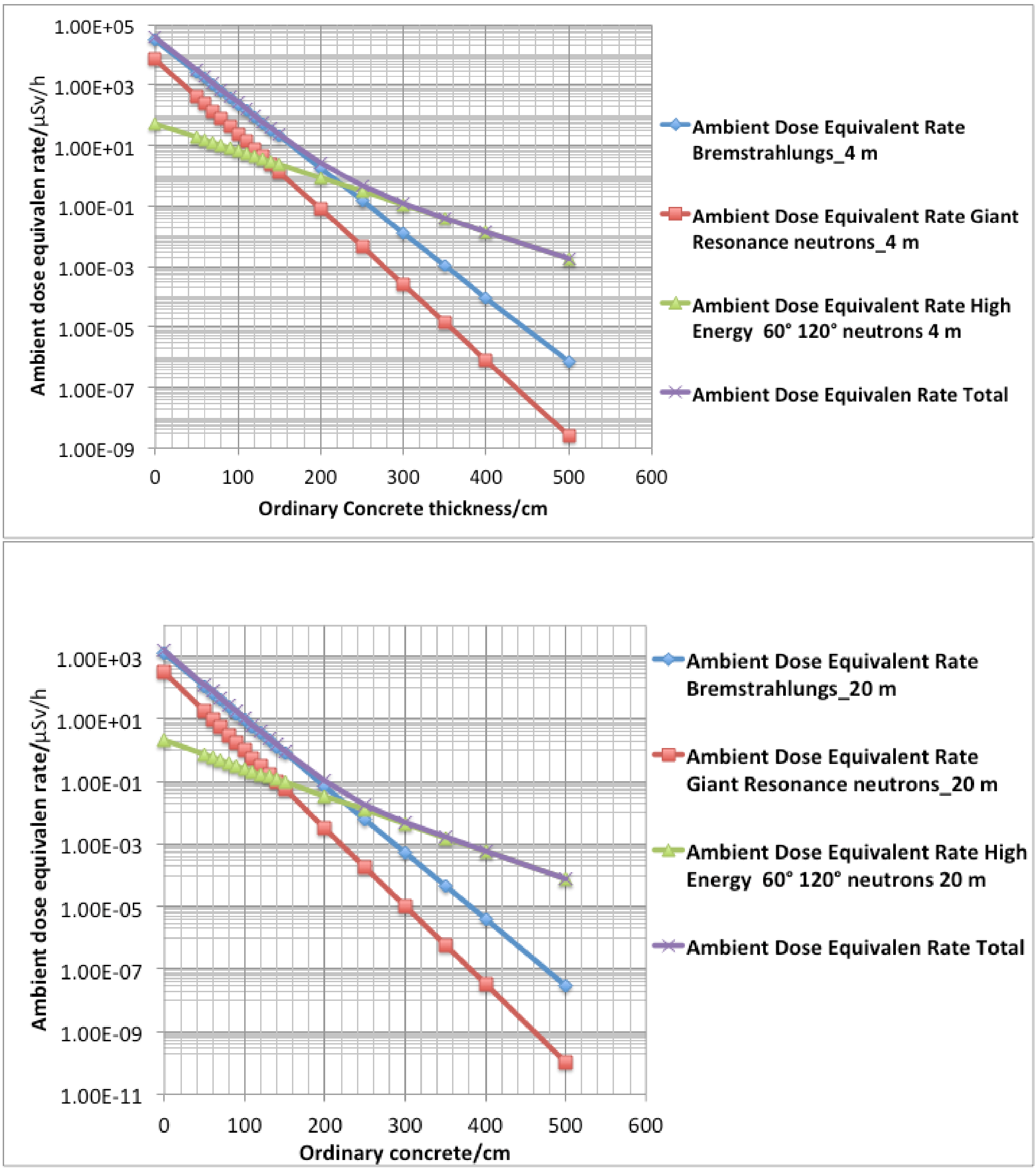

Figure 20.1: Ambient dose equivalent rate: top: 4 m 90°, bottom: 20 m 90°.

20.5.3 Muons

Muon production is analogous to e^+/e^- pair production by photons in the field of target nuclei when photon energy exceeds the threshold $2m_\mu c^2 \approx 211$ MeV.

Above a few GeV the muon yield per unit electron beam power is approximately proportional to electron energy E_0. Muon angular distribution is extremely forward-peaked, and this distribution narrows further with increasing energy. At energies of a few GeV adequate photon and neutron shielding will be also sufficient for muons. Calculation will be finalized when the final layout and characteristic will be frozen.

20.5.4 Gas Bremsstrahlung

The gas Bremsstrahlung is produced by the interaction of the electron beam with residual low-pressure gas molecules in the vacuum pipe. Bremsstrahlung on residual gas is one of the main cause of beam loss in a storage ring and may represent a radiation hazard at synchrotron radiation facilities. This type of radiation has been thoroughly investigated at circular storage rings, where the beam current is much more intense. It is mainly in the straight section that a radiation problem could arise. At EuPRAXIA@SPARC_LAB the straight length over which Bremsstrahlung is produced will be not less 85 m.

Calculation are in progress following the final layout, the final definition of the operating parameters.

20.5.5 Induced Activity

Personnel exposure from radioactive components in the beam line is of concern mainly around beam lines, collimators, slots, beam stopper or beam dump, where the entire beam or a large fraction of the beam is dissipated continuously, while unplanned beam losses result from beam mis-steering due to inaccurate orbit adjustment or devices failure.

Beam losses induce activation in machine component as well as in:

the beam pipe	(^{60}Co, ^{54}Mn, ^{51}Cr, ^{46}Sc, ^{22}Na, ^{11}C, ^{7}Be)
the cooling water	(^{3}H, ^{7}Be, ^{15}O, ^{13}N, ^{11}C)
the air	(^{15}O, ^{13}N, ^{38}Cl, ^{41}Ar)
the concrete walls	(^{152}Eu, ^{154}Eu, ^{134}Cs, ^{60}Co, ^{54}Mn, ^{22}Na)

The activation of soil as well as the groundwater by neutrons and other secondary particles can have an environmental impact but at electron accelerators the radioactivity levels are generally low and absolutely negligible with the previous beam parameters.

Calculations are in progress, following the final definition of the beam parameters and the beam losses and the characteristic of cooling water system, the air circulation system and the beam dump layout.

20.5.6 Beam line radiation shielding design

For each shielding situation (insertion device white beam, radiation transport, monochromator, hutches etc.) the synchrotron radiation, the gas bremsstralhung, the high-energy bremsstralhung, from beam halo interactions with the structures of the machine, will be calculate for a representative geometry.

20.6 Machine accesses

During machine operation the linac tunnel, the FEL tunnel, and all radiation areas will be excluded areas.

During no operation periods the linac tunnel will be a controlled area, due to the possible activation of the machine structure.

The technical areas behind the roof shield will be classified as controlled or supervised areas.

The experimental area will be a free access area except for the optics hutch and experimental hutches when the photon beam is on. Only areas close to the front ends or at the end of the beam line will be classified.

In order to protect workers in the experimental areas, the electron beam will be dumped below the floor after the FEL undulators. A deflection of 90° is effected by electromagnets.

For additional safety permanent magnets and active radiation detectors interlocked with the beam could be used.

20.6.1 The operational radiation safety program

The purpose of the operational safety system program is to avoid life-threatening exposure and/or to minimize inadvertent, but potentially significant, exposure to personnel. A personnel protection system can be considered as divided into two main parts: an access control system and a radiation alarm system.

The access control system is intended to prevent any unauthorized or accidental entry into radiation areas.

The access control system is composed by physical barriers (doors, shields, hutches), signs, closed circuit TV, flashing lights, audible warning devices, including associated interlock system, and a body of administrative procedures that define conditions where entry is safe. The radiation alarm system includes radiation monitors, which measure radiation field directly giving an interlock signal when the alarm level is reached.

The *access control system* (Figure 20.2) is conceived to allow the passage of only one person at a time both in entrance and in exit.

The worker is counted inside or outside if after the reading of the magnetic card the sequence is completed rotating the turn style and closing again the gates.

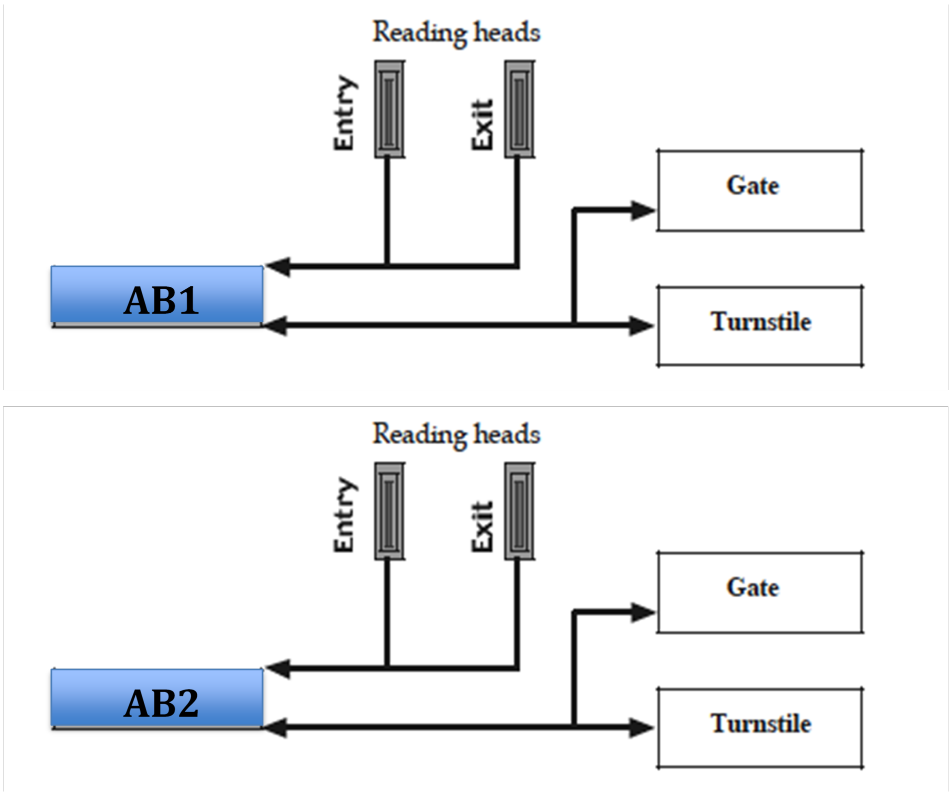

Figure 20.2: Interlocked accesses equipped with the Access Control System.

20.6.2 Radiation Alarm System

The EuPRAXIA@SPARC_LAB Radiation Alarm System consist of at least of

- 8 detectors for photon radiation
- 8 detectors for neutron radiation

- 1 detector for measurement of radioactive gases activity concentration in air
- 1 central data acquisition system
- 1 computer for control, data storage and elaboration, equipped with a 27" Display

For special assembly it is foreseen the possibility to separate the detectors from the associated electronic for a distance of at least 5 m.

Technical Specification for Photon Detectors

Detectors for Photon Radiation have been chosen preferably by high pressure ionization chambers. Each detector has to be compliant with the following characteristics:

1. Response in term of Ambient Dose Equivalent $\dot{H}^*(10)$ in the energy range from few dozens of keV up to 10 MeV.
2. Measurement range from 0.1 μSv/h up to 0.1 Sv/h.
3. Neutron insensitivity.
4. Generation of a pre-alarm signal when the radiation level exceeded a pre-settable alert level in the measurement range referred to in point 2.
5. Generation of an alarm signal when the radiation level exceeded a pre-settable alarm level in the measurement range referred to in point 2.
6. Alarm and alert signals must activate a buzzer and warning lights (red=alarm, yellow = alert, green = proper operation).
7. Possibility to introduce a delay, pre-settable in the range 10 s – 1 min, in the generation of the alarm signal in order to avoid any false signal or spike.
8. Automatic reset of pre-alarm and alarm signal when the radiation level come back under the relative threshold.
9. Indication of proper operation, available after the switch-on and every time it is required.
10. Generation of an interlock fail safe signal if the radiation level measured is greater than the pre-settable alarm level for the pre-settable length (of time), opening four independent contacts normally open of internal relays. The signal should be extracted through a connector to be agreed.
11. Relays referred to in point 10 must be compliant with SIL 3 safety integrity level of IEC (61508)* or better.
12. Each unit must be equipped with a backup battery.
13. Calibration certificate for each detector in term Ambient Dose Equivalent Rate $\dot{H}^*$ (10).

Technical Specification for Neutron Detectors

Detectors for neutron radiation have to be constituted by rem-meters.

Each detector has to be compliant with the following characteristics:

1. Response in term of Ambient Dose Equivalent $\dot{H}^*(10)$ in the energy range from thermal energy up to up to hundreds MeV.
2. Measurement range from 0.1 μSv/h up to 0.01 mSv/h.
3. Photon insensitivity to photon radiation up to 1 Sv/h.
4. Generation of a pre-alarm signal when the radiation level exceeded a pre-settable alert level in the measurement range referred to in point 2.
5. Generation of an alarm signal when the radiation level exceeded a pre-settable alarm level in the measurement range referred to in point 2.
6. Alarm and alert signals must activate a buzzer and warning lights (red=alarm, yellow = alert, green = proper operation).
7. Possibility to introduce a delay, pre-settable in the range 10 s – 1 min, in the generation of the alarm signal in order to avoid any false signal or spike.
8. Automatic reset of pre-alarm and alarm signal when the radiation level come back under the relative threshold.

9. Indication of proper operation, available after the switch-on and every time it is required.
10. Generation of an interlock fail safe signal if the radiation level measured is greater than the pre-settable alarm level for the pre-settable length (of time), opening four independent contacts normally open of internal relays. The signal should be extracted through a connector to be agreed.
11. Relays referred to in point 10must be compliant with SIL 3 safety level of IEC (61508)* or better.
12. Each unit must be equipped with a backup battery.
13. Calibration certificate for each detector in term Ambient Dose Equivalent Rate $\dot{H}^*(10)$.

Technical Specification for Radioactive Gas Detector

The detector has to be compliant with the following characteristics:

1. Measurement range from 0.1 Bq/g up to 10 Bq/g for a radioactive gas mixture mainly consisting of ^{11}C, ^{13}N, ^{15}O with spectrometric detection type.
2. Generation of a pre-alarm signal when the radiation level exceeded a pre-settable level in the measurement range referred to in point 1.
3. Generation of an alarm signal when the radiation level exceeded a pre-settable alarm level in the measurement range referred to in point 1.
4. Alarm and alert signals must activate a buzzer and warning lights (red=alarm, yellow = alert, green = proper operation).
5. Automatic reset of warning and alarm signal when the radiation level come back under the relative threshold.
6. Indication of proper operation, available after the switch-on and every time it is required.
7. Generation of an interlock fail safe signal if the radiation level measured is greater than the pre-settable alarm level for the pre-settable length (of time), opening 4 independent contacts, normally open of internal relays. The signal should be extracted through a connector to be agreed.
8. Relays referred to in point 7 must be compliant with SIL 3 safety level of IEC (61508)* or better.
9. Calibration certificate for gases referred to in point 1.
10. Predisposition of a possible installation of a calibration radioactive source.
11. Each unit must be equipped with a backup battery.
12. Calibration certificate for each detector in term Ambient Dose Equivalent Rate $\dot{H}^*(10)$.

Centralized system of data acquisition and management

The data acquisition and management software have to be installed on a work station, at least equipped with processor i7, 1 Tb of memory, RAM not less 8 Gb. The data acquisition system should be able to connect up to 50 detectors and must allow the following operation:

- Remote control of detectors.
- Storage of data, coming from each detector, every minute on files of 24 hours. File name GGMMAAAA (start acquisition at 00:00 stop acquisition at 24:00).
- Storage with time/date of maximum instant value of quantities measured, in case of exceeding the pre-settable alert or alarm level for the pre-settable length of time.
- Real time display of all detectors with automatic switch to a pre-alarming and alarming detector, using yellow color in case of a pre-alarm and red color in the case of an alarm.
- Storage of all signals of alert and alarm on files of 24 hour. File names are in the format "DetectorNameDDMMYYYY".
- Display for a single detector of the Ambient Dose Equivalent integrated on 24 hour or on any programmable time interval.
- Query archive independently from the data acquisition.

- Possibility to print stored data.
- Graphic display and print of stored data.
- Possibility to perform mathematical operations on selected portion of data.
- Quick scroll of entire archive.
- Possibility to display the graphical representation of all detectors or a selected number of detectors.
- Password access to various part of program.
- The system is equipped with a DC-UPS.

Interlock design and feature

The objective of a safety interlock is to prevent injury or damage from radiation. To achieve this goal the interlock must operate with a high degree of reliability. All components should be of high grade for dependability, long life and radiation resistant. All circuits and component must be fail safe (relay technology preferably).

To reduce the likelihood of accidental damage or deliberate tampering all cables must run in separate conduits and all logic equipment must be mounted in locked racks. Two independent chains of interlocks must be foreseen, each interlock consisting of two micro switches in series and each micro switches consisting of two contacts.

Emergency-off buttons must be clearly visible in the darkness and readily accessible. The reset of emergency-off buttons must be done locally. Emergency exit mechanisms must be provided at all doors. Warning lights must be flashing and audible warning must be given inside radiation areas before the accelerator is turned on.

Before starting the accelerator a radiation area search must be initiated by the activation of a "search start" button. "Search confirmation" buttons mounted along the search path must also be provided. A "Search complete" button at the exit point must also be set. Restarting of the accelerator must be avoided if the search is not performed in the right order or if time expires. The interlock system must prevent beams from being turned on until the audible and visual warning cycle has ended.

Any violation of the radiation areas must cause the interlocks system to render the area safe. Restarting must be impossible before a new search. Procedures to control and keep account of access to accelerator vaults or tunnels must be implemented. The routine entrance inside accelerators is allowed through a turnstile and a gate controlled by a magnetic card reader connected to a PC. The accelerator restarting in not possible if there isn't the parity between entries and exits. The entrance is allowed only for personnel equipped with a personal magnetic card.

20.7 Electron Beam Dump

The electron beam will be dumped below the floor at the end of the undulators in the linac tunnel. The beam deflection at least of 90° will be made using electromagnets. For additional safety permanent magnets and active radiation detectors interlocked with the beam could be used. The layout of beam dump as well as the size and type of shielding materials is under study.

20.8 Other Radiation Sources

The RF power sources for EuPRAXIA@SPARC_LAB are 410 kV klystrons. The klystrons will arrive already shielded from factory.

Additional shield will be installed in order eliminate and/or to reduce radiation escape. An interlocked fence around klystrons is foreseen in order to reduce as low as possible the radiation level behind the fence.

VI Appendixes

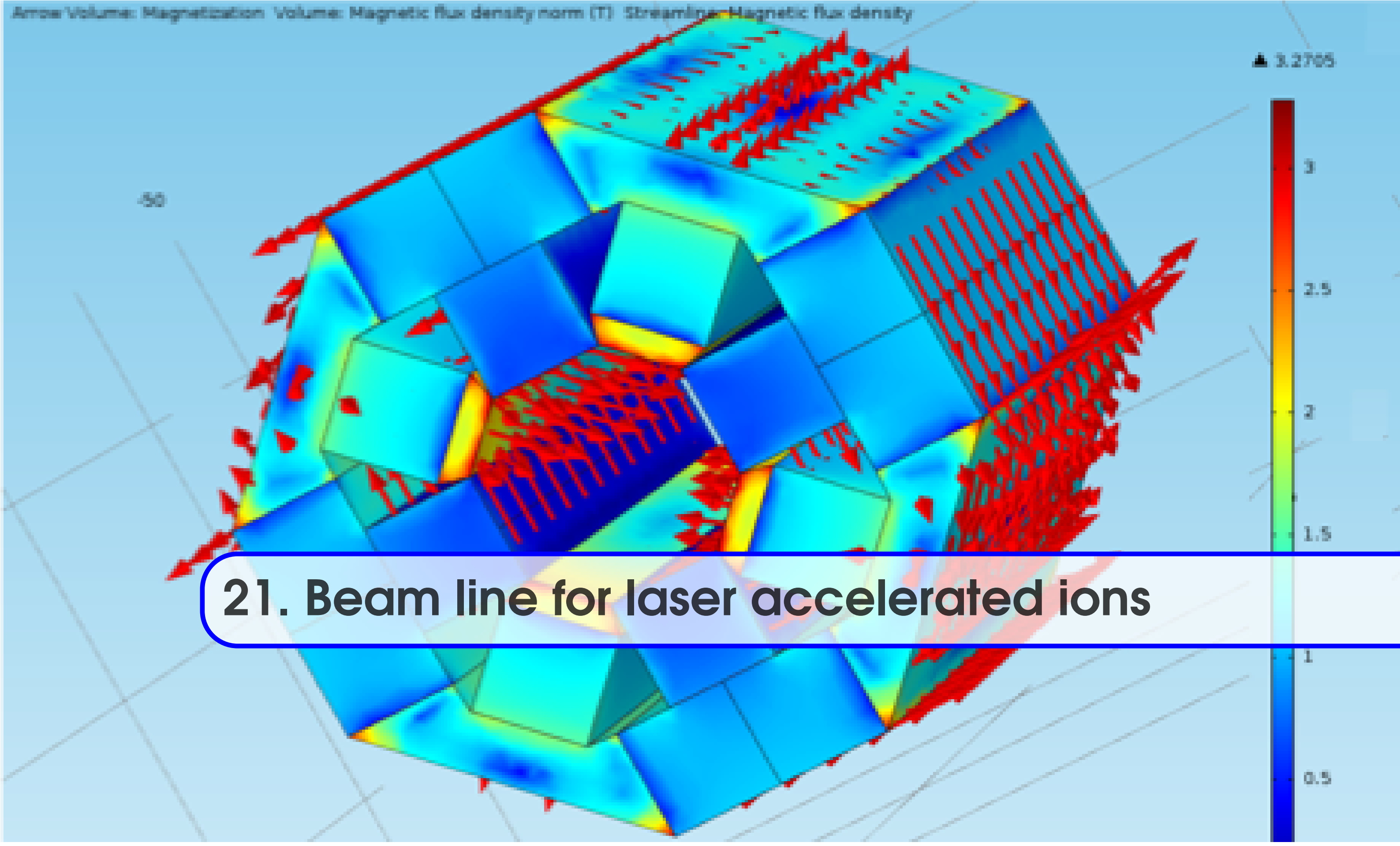

21. Beam line for laser accelerated ions

The INFN-LNS group will contribute in the realization of a compact transport beamline for 5 – 30 MeV laser accelerated proton/ion beams. The main goal will be the realization of beam transport elements capable to deliver energy selected and spatially controlled beam at the irradiation point. INFN-LNS will be also in charge to develop and realize new devices for the on-line proton/ion beam diagnostics (energy and flux measurements) and to perform relative and absolute dose measurements. The irradiation point will be in air as well as in vacuum. The beamline can be used as a multidisciplinary facility for proton and ion irradiation for all users interested in irradiation experiments with laser-generated beams.

21.1 Introduction

The charged particle beams produced by the new techniques of acceleration by using the high power lasers, have interesting features: they are characterized by a very high peak currents (10^{12} – 10^{13} particles per shot, I > 500 mA) and both the transverse and longitudinal emittance are rather small. In fact, the transverse emittance, although it is characterized by very large angular width (up to 30°) gets a very small radial dimension depending on the size of laser interaction point on the target (100 µm). The result is a geometric emittance of order of $< 0.1\ \pi$ mm mrad.

The energy spectrum of the produced particles varies from a minimum of energy of few keV to the maximum value derived from the electric fields which are reached during the process of plasma expansion for the first instants of the interaction laser-target. Also the spatial distribution of the emitted particles on the target depends on the energy.

These beams are particularly promising for interdisciplinary physics applications but they need to be characterized in energy and species and made with an emittance that they can be efficiently transferred to the apparatuses of measurement through the standard beamlines used for the transport of particle beams.

In order to achieve this goal, it is necessary to study focusing techniques to maximize the number of particles transported and to select the beam energy controlling and minimizing the corresponding energy spread.

21.2 Transport scheme

The general scheme that will be used to transport laser-accelerated beam is reported in Figure 21.1: it is composed by a first section, dedicated to focusing the beam generated in the interaction, followed by a second section dedicated to the beam energy selection. The beam selected in energy can be then transported with conventional elements down to the irradiation point.

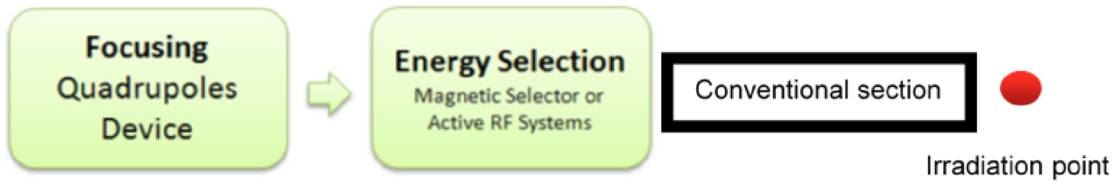

Figure 21.1: Laser-accelerated beam transport scheme.

21.2.1 Focusing

It will consist of four/five permanent magnet quadrupoles (PMQs) placed downstream the target to focus the beam on the transverse direction. Since the system must be able to focus beams with different energies and rather large transverse dimensions, it can be constituted by conventional electromagnetic or permanent based quadrupoles with wide acceptance. The configuration would ensure focusing particles in the two transverse space to a common point (waist). This would allow a subsequent focusing "point-to-point" of a possible conventional transport system. Also in this case a selection in energy by the above system is performed. The PMQ system will be made of Permanent Magnet Quadrupoles, based on hybrid Halbach design with a 20–30 mm net bore diameter. A prototype with similar characteristics has been already designed, realized and tested by the INFN-LNS [1]. The prototype consists of two PMQs 80 mm long with a gradient of 103 T/m and two PMQs 40 mm long with a gradient of 98 T/m. The magnetic features of the system have been thoroughly studied and described in [1]. The field quality, harmonic components and the related error study are reported in [2]. The PMQs can be provided with carriages, guides and step motors remotely controlled, in order to change the relative distances between magnets and tune the system for handling different energies. The system flexibility will allows, using different setups, to focus protons in a relative big energy range from a few MeV up to about 30 MeV. The optics of the PMQ prototype has been successfully studied with conventional accelerated proton beams delivered by the TANDEM at the INFN-LNS; the system has also been tested and used to focus low energy proton beams accelerated by the SAPHIR laser system at the LOA laboratory to maximize proton transmission and consequently increase the dose delivered per shot in cell irradiation campaigns [3–5].

21.2.2 Energy Selection

The beam after the focusing section will still present a rather broad energy spread. A magnetic system (consisting of permanent or resistive magnetic dipoles in alternating gradient) based on a classical chicane configuration can be used for a fine energy selection.

A prototype consisting of four permanent magnet dipoles, each with a magnetic field of about 0.8 T, has been designed, tested and calibrated with conventional accelerated proton beam at the INFN-LNS (see Figure 21.2) [6]. The second and the third magnetic fields are parallel with each other but oriented antiparallel to the first and the fourth ones. This configuration allows increasing the separation between the particle trajectories at different energy in correspondence of the central magnet doublets where, by means of a slit, the particles with a given energy are selected. The energy spread and the particle transmission through the slit depends on the size of the aperture. The lower the energy spread, the lower the number of particles will be transported through the energy selector due to the smaller slit aperture required and vice versa. The energy of the proton beam can be tuned by moving transversely the slit position between 30 mm and 8 mm from the target normal axis. A roller guide system where the central twin magnets are placed, allows displacing radially the two magnets in order to increase the transversal displacement and select the lowest energy particles.

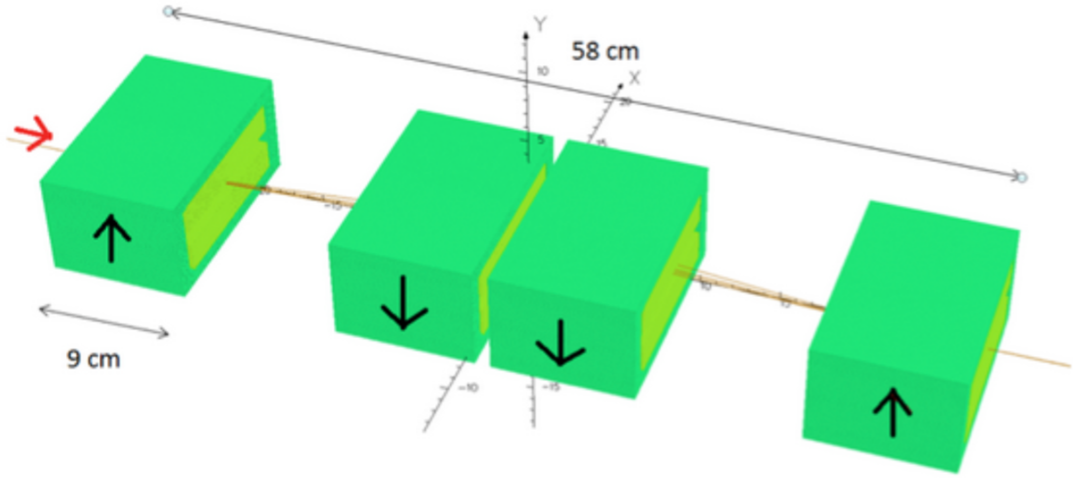

Figure 21.2: Scheme for beam energy selection.

In such a way, the energy can be varied within a wide range between 5 MeV and 50 MeV. The energy spread achievable by using 1 mm slit aperture ranges from 3 % for low energy up to 30 % for higher energy. The selection system prototype is about 700 mm long and can fit in a vacuum chamber together with the PMQ prototype system. Two collimators are placed upstream and downstream the selection system in order to reduce the possible spatial mixing effect and control the beam size.

The entire transport system will be simulated with the GEANT4 Monte Carlo toolkit in order to accurately predict the proton trajectories and the energy spectrum and bandwidth of the beam selected. Such information is crucial for preliminary calculations on proton fluence and dose delivered per pulse. Moreover, the simulation will give also a quantitative estimation of radioactive activation produced by protons inside the energy selector, for further radioprotection assessments.

21.3 Diagnostic and dosimetry

The pulse properties of optically accelerated ion beams differ significantly from those commonly provided by conventional accelerators in pulse duration, peak current and correspondingly pulse dose rate and energy spectrum. Thus, among obvious properties, such as operational stability, the development of innovative techniques for diagnostics and dosimetry represents a crucial step towards multidisciplinary applications of laser-driven beams with the required uncertainty. Typical laser-driven beam specifications report proton burst duration of the order of 0.1–1 ns, with intensity ranging from 10^{10} to 10^{12} p/burst. Therefore, the detectors developed for the on-line beam monitoring systems and for the relative dosimetry have to be dose-rate independent, in order to be able to measure very intense and short pulses without saturation effects and suitable to operate in presence of a strong electromagnetic pulse (EMP). Different alternative approaches will be followed in the development of detectors for on-line non-invasive beam current monitoring. In the last years, INFN-LNS gained a lot of experience in the development of for on-line and off-line diagnostics and dosimetry of laser-accelerator proton/ion beams. Different diagnostics detectors can be provided and set-up, in particular, after the focusing and the selection systems. A detector, based on the well-known pepper pot method, will be specifically designed and optimized for single shot emittance measurement of the laser-driven proton beam after the PMQs system. On the other hand, particle identification and fluence/current measurements can be performed using Silicon Carbide (SiC), CVD diamond detectors and secondary particle emission detectors (SEM), based on the secondary electron emission from a thin metallic foil hit by ion beams. These radiation-hard detectors, suitable to work in harsh radiation environments, can be used in Time Of Flight (TOF) mode for plasma ion intensity and energy distribution measurements in the energy range between few MeV/n up to 60 MeV/n [7–10]. They can be placed at different distances from the target along the beam transport, in particular, after the PMQs system and after the energy selection device. The high temporal resolution and the fast response of SiC and CVD detectors, together with the high signal-to-noise ratio characteristics, already tested in different experimental campaigns at PALS and at TARANIS laser laboratories and with a the VULCAN PW laser system at RAL facility [8], will allow determining the energy of the identified selected ions with resolution of about 20% for the maximum energy selected (i.e. 60 MeV/n).

So far, no protocol for absolute dosimetry for optically accelerated ion beams has been established. In order to fulfill this task, a reliable and accurate dosimetric characterization of laser-driven charged particle beams has to be performed. Therefore, devices and procedures to develop a calibration method for absolute dose evaluation have to be implemented.

In particular, for relative dosimetry different devices can be used such as a secondary electron monitor (SEM) and a multi-gap ionization chamber (IC); for absolute dosimetry, a Faraday cup (FC) prototype specifically designed to decrease uncertainties in the collected charge has been realized [11–13]. Moreover, a sample irradiation system (SIS) can be installed at the irradiation point downstream the transport elements and after the dosimetric systems, allowing the positioning of samples with a sub-millimetric precision.

The SEM is a thin metallic foil detector, whose working principle is based on the secondary electron emission (SEE).

The multi-gap IC is an innovative prototype designed to real-time measure the dose delivered per pulse, without affecting the beam transport downstream at the irradiation point. It is an in-transmission air-filled chamber and it will be cross-calibrated against the FC absolute dosimeter. The presence of a second gap close to the first one allows correcting for ion recombination effects caused by the very high dose rate per pulse. The working principle of this detector is based on the idea that the recombination effects can be corrected once the collection efficiency f in specific conditions is known. After a calibration procedure of the two gaps, the collection efficiencies of the gaps f_1 and f_2 as a function of the voltage can be obtained. Finally, a relation between f_1 and the ratio f_1/f_2 can be experimentally determined and the collected charge can be corrected for each pulse.

The FC has been designed including an additional electrode with a particular geometrical shape to further repel the secondary electrons and to increase the accuracy of the measured charge. Together with the collected charge, the effective beam area and the energy spectrum have to be retrieved for the measurement of the absolute dose with a FC. They can be both obtained using radiochromic films (RCF) that, in case of energy spectra measurements, have to be used in stack configuration. These dosimeters, although allow to obtain spatial dose distributions with high spatial resolution, are passive detectors, thus they need a post processing analysis. To have real-time information we foresee to use scintillating fibers for the beam spot measurement and stack of scintillators for the energy spectra.

Bibliography

[1] F Schillaci et al. "Design of the prototype of a beam transport line for handling and selection of low energy laser-driven beams". In: *Nuclear Instruments and Methods in Physics Research Section A: Accelerators, Spectrometers, Detectors and Associated Equipment* 837 (2016), pp. 80–87.

[2] F Schillaci et al. "Errors and optics study of a permanent magnet quadrupole system". In: *Journal of Instrumentation* 10.05 (2015), T05001.

[3] F Schillaci et al. "Characterization of the ELIMED Permanent Magnets Quadrupole system prototype with laser-driven proton beams". In: *Journal of Instrumentation* 11.07 (2016), T07005.

[4] L Pommarel et al. "Spectral and spatial shaping of a laser-produced ion beam for radiation-biology experiments". In: *Physical Review Accelerators and Beams* 20.3 (2017), p. 032801.

[5] AD Russo et al. "Characterization of the ELIMED prototype permanent magnet quadrupole system". In: *Journal of Instrumentation* 12.01 (2017), p. C01031.

[6] V Scuderi et al. "Development of an energy selector system for laser-driven proton beam applications". In: *Nuclear Instruments and Methods in Physics Research Section A: Accelerators, Spectrometers, Detectors and Associated Equipment* 740 (2014), pp. 87–93.

[7] D Margarone et al. "Full characterization of laser-accelerated ion beams using Faraday cup, silicon carbide, and single-crystal diamond detectors". In: *Journal of Applied Physics* 109.10 (2011), p. 103302.

[8] V Scuderi et al. "Time of Flight based diagnostics for high energy laser driven ion beams". In: *Journal of Instrumentation* 12.03 (2017), p. C03086.

[9] G Milluzzo et al. "Laser-accelerated ion beam diagnostics with TOF detectors for the ELIMED beam line". In: *Journal of Instrumentation* 12.02 (2017), p. C02025.

[10] G Milluzzo et al. "TOF technique for laser-driven proton beam diagnostics for the ELIMED beamline". In: *Journal of Instrumentation* 12.03 (2017), p. C03044.

[11] GA Cirrone et al. "Design and status of the ELIMED beam line for laser-driven ion beams". In: *Applied Sciences* 5.3 (2015), pp. 427–445.

[12] GAP Cirrone et al. "Transport and dosimetric solutions for the ELIMED laser-driven beam line". In: *Nuclear Instruments and Methods in Physics Research Section A: Accelerators, Spectrometers, Detectors and Associated Equipment* 796 (2015), pp. 99–103.

[13] F Romano et al. "The ELIMED transport and dosimetry beamline for laser-driven ion beams". In: *Nuclear Instruments and Methods in Physics Research Section A: Accelerators, Spectrometers, Detectors and Associated Equipment* 829 (2016), pp. 153–158.

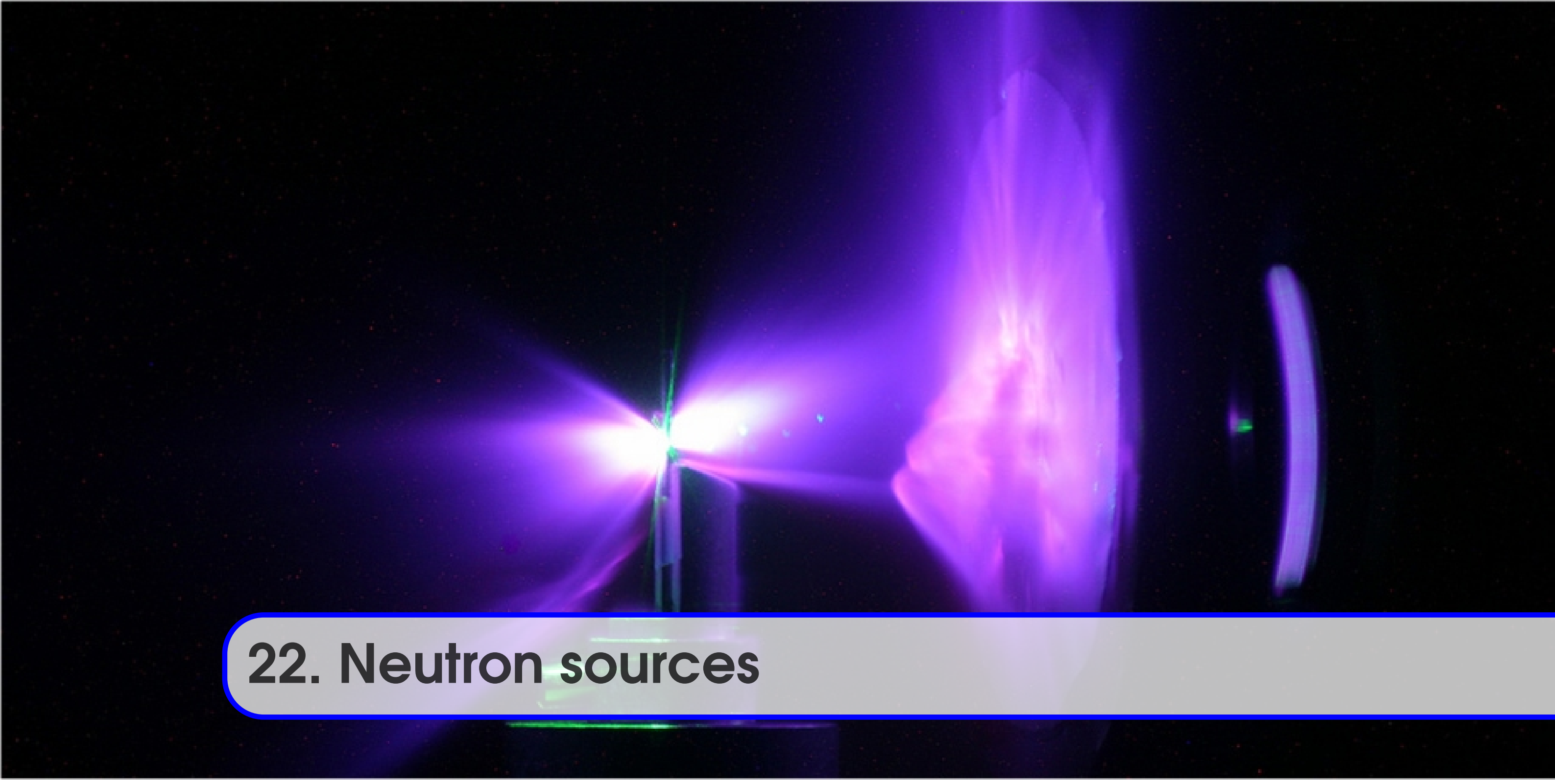

22. Neutron sources

22.1 Introduction

The need for accelerating gradient order of magnitudes larger than existing ones drives the research in particle accelerators to plasma-based accelerators [1–3]. These machines can sustain field greater than tens of GV/m paving the way to the realization of tabletop accelerators. Two main schemes are under consideration: Laser Wakefield Plasma Acceleration (LWPA) [4], without the need of any RF (Radio Frequency) conventional accelerator, or Plasma Wakefield Accelerators (PWFA) [5, 6] where both a high intensity laser and high brightness electron beam are foreseen. In both schemes, a PW class laser is used.

Likely, these lasers will not be considered uniquely to drive the main accelerator but they will also be devoted to other several activities. The interaction of such a laser with the matter produces a large number of electrons, ions, positrons, protons via several different mechanisms depending on the laser intensity and the target material compositions and dimensions [7]. While a lot of effort is dedicated nowadays to improve the quality of these charged or neutral beams of particles to use them, so far there is not yet a user facility using them. There are many studies concerning neutron production via laser-matter interaction (for instance among the others [8, 9]). The purpose of this appendix is to consider if the laser interested for these future accelerators, and for the EuPRAXIA@SPARC_LAB case, can be used to drive a user-oriented compact neutron source. With the words user-oriented, we mean a facility where neutron flux and spectrum are enough to be competitive with existing facilities [10], or in any case with neutron portable devices.

One of the main application that we can foresee for such kind of source is non destructive inspections for industry, research and cultural heritage. Usually many techniques are used to study the objects in this field, like THz, IR and X-ray radiation. All of these sources are foresee, sooner or later, in this project. Adding also, with the same instrumentation, a neutron source could be very interesting, giving the possibility of having on the same site all these techniques together, in views of an integrated suite of light and particle beams for materials and cultural heritage sciences. This would provide the complementary high penetration, isotope selectivity, and non destructive character of neutron based techniques within the suite of light and particle probes available within the proposed project. This neutron source could be fast (multi MeV) or, through the application of a dedicated compact moderator, thermal. The following analysis refers, as an exemplificative target, to the thermal neutron radiography. This application requires, in addition to a neutron source, a moderator. Further equipment as collimators and imaging systems are also required. In addition, a Prompt Gamma Activation Analysis (PGAA) system may be easily incorporated in the design, for expanded capability towards isotopic and elemental sensitivity.

22.2 Methodological analysis

A very compact neutron moderator is required to produce a small sized radiography facility. While a custom design for such kind of source should be consider, we use here the scheme HOTNES (Homogeneous Thermal NEutron Source) [11], implemented already in a thermal neutron irradiation facility with extended and very uniform irradiation area (HOTNES at ENEA-INFN, Frascati). Starting from a cm-sized fast neutron source (^{241}Am-B), this new type of moderator produces a highly thermalized and very uniform neutron field across a large irradiation area (30 cm in diameter). The moderating efficiency (thermal fluence per primary neutron) slightly depends on the fast neutron spectrum and is in the order of 2×10^{-4} cm^{-2}. For the purposes of the current project idea, fast neutrons from the laser compact source would be fed into the moderator, instead of the radionuclide neutron source.

22.3 Possible sources

Several possibilities can be explored, relying on primary electron, protons, or ions. These particles can be produced with the conventional RF linac or with a laser based machine.

22.3.1 RF linac based source

We consider the electron beam of 1 GeV energy, with bunch charge 100 pC, a repetition rate of 10 Hz and an average current of 1 nA. We use the production of neutron via bremsstrahlung, using a tungsten target of $5 \times 5 \times 9$ cm^3, being 9 cm the thickness corresponding to the maximum yield. We can obtain about 0.4 neutrons for primary electron. With the EuPRAXIA@SPARC_LAB design values it reflects in about 2.5×10^9 neutrons/s, which is similar to the yield of high-performance industrial neutron generators. A HOTNES-like moderator [11] would convert them into thermal neutrons with efficiency 2.3×10^{-4} cm^{-2}, producing a final non-collimated thermal fluence of about 6×10^5. Collimating devices would then reduce it of about one order of magnitude. In terms of overall efficiency, the non collimated thermal fluence per primary electron on the W target would be in the order of 9×10^{-5} cm^{-2}.

22.3.2 Protons/ions from laser acceleration

When a high intensity laser (10^{19} W/cm^2 or better) is focused on a solid target several effects can be triggered, like for instance Target Normal Sheath Acceleration (TNSA) [13], Radiation Pressure Acceleration (RPA) [14], collisionless shock acceleration [15] and Break Out Afterburner (BOA) [16], depending on target material, thickness and surface contaminations for instance. Let us focus on TNSA. Fast electrons are accelerated through the material by the laser. These electrons penetrate the target ionizing other particles and escaping from the other side. In this moment, they build up a very strong electric field, in the order of TV/m. This field extracts protons and ions from the rear surface, producing an intense beam of particles.

In Fig. 22.1 is shown a sketch describing the physics of the process [12]. While there are scaling laws of the process, being exhaustively reported in [17, 18], it is very difficult to define the energy spectrum, the flux intensity, and the particles geometrical distribution in a general case, being the emission strongly linked to target material, surface contamination, laser energy and intensity,

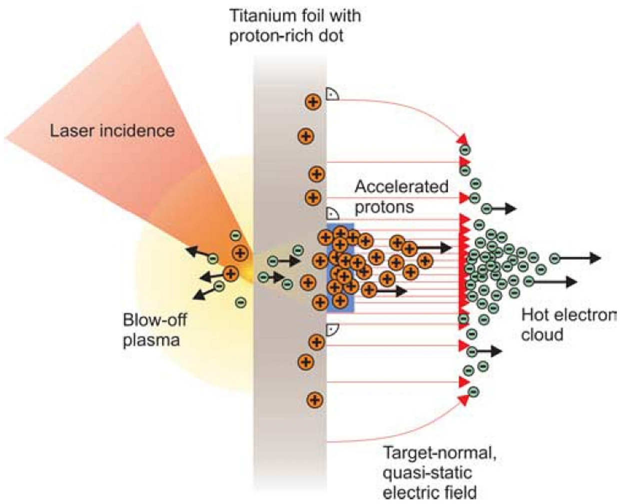

Figure 22.1: Sketch of TNSA effect, figure credits [12].

laser contrast. The main parameter is the conversion efficiency between laser and particles. If we consider for instance a 1% efficiency, we can have about 6×10^{11} proton at 10 MeV with a 10 J laser at a repetition rate of 10 Hz. The great varieties of results can be appreciate in Fig. 22.2.

We can see that the laser energies are quite different, while the intensities are much more similar. However, this dependence is not followed very strict, mainly due to some particular experimental arrangement of the target, in order to increase and to guide better the protons, as wells as the use of different kind of targets triggering mechanisms different from TNSA for instance.

What is important is the number of the proton in an energy range below 10 – 20 MeV, because even laser with energy around or below 40 J can already produce a protons number in the order of 10^{11} in such energy range.

Once that the primary beam is produced, the protons/ions hit a materials like for instance LiF or Be, in order to produce a neutron flux. This scheme is usually called pitcher-catcher scheme, as shown in Fig. 22.3.

We focus on a typical target of Lithium fluoride with the reaction ^{7}Li + p $\rightarrow$ ^{7}Be + n - 1.644 MeV. Different yields are found in literature for the same reaction. For this simulation and for the following, the neutron production yield was generated using a custom Labview^{TM} based software based on a continuous projectile slowing down in the target. The stopping power data were generated from PSTAR (NIST) [19] for protons and SRIM 2011 [20] for deuterons. Cross sections data were taken from ENDFB VII [21] and EXFOR [22] (protons) or TENDL2009 (deuterons) [23]. The differences in the yield in the range of the tens-few tens of MeV are only about a factor 2–4, much less than an order of magnitude, making appealing also proton of lower energy that can be produced by smaller laser with higher repetition rate. The thickness of the target was also optimized in order to maximize the neutron flux.

With 0.2 cm of LiF target the typical moderation yields in thermal neutron flux per primary fast neutron is 1.55×10^{-4} n/p per proton of 5 MeV.

We also considered the case of a Beryllium target with a deuteron beam because usually the targets are hydrogenated on the surface to increase the deuterons number. Considering 7 MeV deuteron we can have a moderation yields in thermal neutron flux per primary fast neutron of about 1.24×10^{-4} n/d. We are neglecting here the slightly different moderator efficiency of 7 MeV deuteron. Also in this case a custom and more refined designed should be implemented. However, we are considering just orders of magnitude to have a better understanding of the several

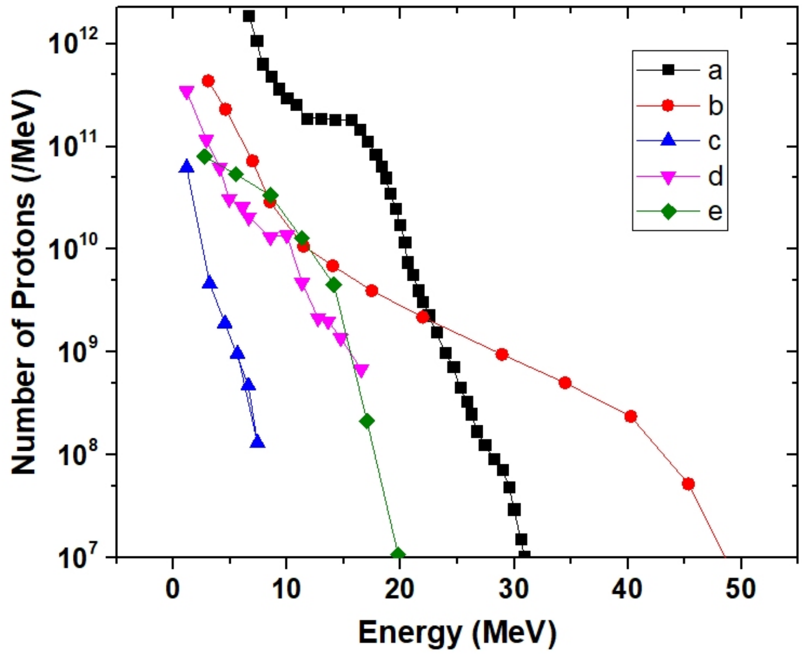

Figure 22.2: Comparison of proton spectrum emerging in different experiments. For the symbol caption see the Table 22.1.

Label	Intensity (W/cm^2)	Energy(J)	Reference
a)	2.0×10^{20}	200	[24]
b)	1.5×10^{20}	80	[25]
c)	1.0×10^{20}	3	[26]
d)	1.0×10^{20}	42	[27]
e)	1.0×10^{21}	10	[28]

Table 22.1: Symbol caption for spectrum in Fig. 22.2.

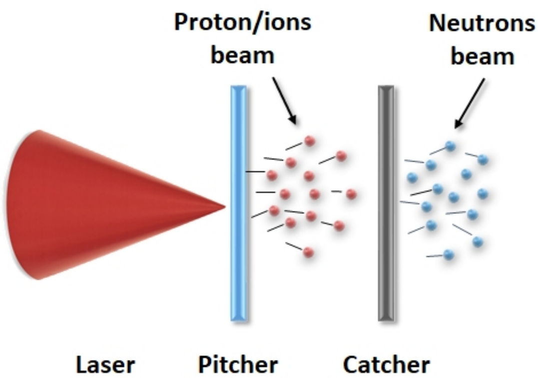

Figure 22.3: Sketch of the Pitcher-Catcher system.

possibilities offered by the actual technology.

22.3.3 Electrons from laser acceleration

There is another possibility, not yet fully explored, to produce neutron by a laser source: using electrons from self-injection [29]. A TW class laser is focused in a tight spot (few μm) on a supersonics gas jet. The laser ionizes the plasma and the ponderomotive force remove the plasma electron generating an intense electric field. Inside this bubble structure, the electrons are self-injected from the rear of the bubble experiencing a strong accelerating field.

If we consider having electron of about 250 MeV on tungsten, we can have about 0.08 neutron per primary particle, and about 0.4 at 1 GeV electron energy.

Regarding the charge there are scaling laws, as reported in [30], being the total number roughly proportional to the square of the laser power. With 1 PW laser about 1.2 nC of electrons can be produced. However, gas mixture can increase the number as recently proved in [31], where they obtained with a 200 TW laser about 0.5 nC at 250 MeV, with 20% energy spread, using several mixtures of helium and nitrogen.

Such kind of laser, similar to FLAME already existing in Frascati, can have a repetition rate of 10 Hz. Being it an experimental result we can use with baseline for our evaluation, obtaining about 2.5×10^9 n/s before the moderation. The increase of the energy is also a possibility. In [2] a beam of 4.2 GeV has been produced, even at low charge. The main difficulty in increasing the bunch energy is the dephasing between laser and electrons. It cannot be really addressed in a gas jet and more complex structures, like a capillary with modulated density profile, are needed.

Source	Primary	Energy (MeV)	Y(n/prim)	m (moder. efficiency)	Yxm	Neutrons /s/cm^2
RF	Electrons	1000	4.0×10^{-1}	2.3×10^{-4}	9.3×10^{-5}	5.8×10^5
Laser	Electrons	250	8.0×10^{-2}	2.0×10^{-4}	1.6×10^{-5}	5.0×10^5
Laser	Electrons	1000	4.0×10^{-1}	2.0×10^{-4}	8.0×10^{-5}	3.0×10^6
Laser	Protons	5	8.7×10^{-4}	2.2×10^{-4}	1.9×10^{-7}	2.0×10^5
Deuterons	Protons	7	7.6×10^{-4}	1.2×10^{-4}	9.4×10^{-8}	9.4×10^4

Table 22.2: Uncollimated thermal neutron fluence rate expected from different fast neutron sources. For Proton and Deuterons we assume 10^{11} particles per shot at 10 Hz, for laser electron 0.5 nC at 10 Hz for the 250 MeV case, while 1.2 nC at 5 Hz for 1 GeV case.

In Table 22.2 we collected the results of the simulations from different possible sources. For protons and deuterons, we estimated 10^{11} particles per shot and at 10 Hz, a result that today it is the borderline of what it is possible to obtain. For electron, we assumed the case of [31] being already obtained. Laser and RF source (with the EuPRAXIA@SPARC_LAB parameters) are giving roughly the same amount of neutrons. However, an improvement of the laser system to the PW scale or to the self-injection mechanics can really increase this number of a consistent factor. There are also two considerations about this number. First, the number from RF conventional source is the maximum achievable, today and likely in the future if the accelerating charge or the repetition rate will not increase, while the laser-based techniques are quite young and we expect to have an increase in these numbers in the following years. Second: even today, all of these solutions can drive easily a compact neutron source.

22.4 Conclusions

With modern neutron imaging systems, neutron radiography can be performed with a parallel beam of low energy neutrons with fluence rate 10^4 - 10^6 $cm^{-2}s^{-1}$. PGAA (Prompt Gamma Activation Analysis) are less demanding considering that even conventional portable sources are used for this end, giving flux on the sample in the order of 10^3 n/cm^2/s. These kind of numbers are in the same order of several CANS [10]. Investigations related to cultural heritage may represent a strong asset of the potential as a user-oriented facility. These can benefit from a large and easily accessible inventory of cultural heritage artefacts in the regional area where EuPRAXIA@SPARC_LAB will be implemented, fostering the access to such an infrastructure of users from museums, cultural heritage research centers, conservation and restoration centers. It is expected that these activities will in turn attract users from the industrial and research based community.

Both of these techniques are widely used in cultural heritage studies and can successfully implemented in EuPRAXIA@SPARC_LAB using the existing infrastructure. Laser based source have the great advantage to be very compact, to do not require the beam of the main machine, and in prospective they will allow to deliver brighter flux of neutrons.

However, electrons from self-injection are a great candidate to drive this research, requiring a modest laser energy, a simple setup, and they can produce enough neutrons for cultural heritage applications, that can benefit also from the presence of the radiation sources in the entire spectrum in the EuPRAXIA@SPARC_LAB facility.

Bibliography

[1] Jérôme Faure et al. “A laser–plasma accelerator producing monoenergetic electron beams”. In: *Nature* 431.7008 (2004), p. 541.

[2] WP Leemans et al. “Multi-GeV electron beams from capillary-discharge-guided subpetawatt laser pulses in the self-trapping regime”. In: *Physical review letters* 113.24 (2014), p. 245002.

[3] Patric Muggli and Mark J Hogan. “Review of high-energy plasma wakefield experiments”. In: *Comptes Rendus Physique* 10.2-3 (2009), pp. 116–129.

[4] Wim P Leemans et al. “GeV electron beams from a centimetre-scale accelerator”. In: *Nature physics* 2.10 (2006), p. 696.

[5] M Litos et al. “High-efficiency acceleration of an electron beam in a plasma wakefield accelerator”. In: *Nature* 515.7525 (2014), p. 92.

[6] Thomas C Katsouleas et al. “A plasma klystron for generating ultra-short electron bunches”. In: *IEEE transactions on plasma science* 24.2 (1996), pp. 443–447.

[7] KWD Ledingham and Wilfried Galster. “Laser-driven particle and photon beams and some applications”. In: *New Journal of Physics* 12.4 (2010), p. 045005.

[8] M Roth et al. “Bright laser-driven neutron source based on the relativistic transparency of solids”. In: *Physical review letters* 110.4 (2013), p. 044802.

[9] S Kar et al. “Beamed neutron emission driven by laser accelerated light ions”. In: *New Journal of Physics* 18.5 (2016), p. 053002.

[10] IS Anderson et al. “Research opportunities with compact accelerator-driven neutron sources”. In: *Physics Reports* 654 (2016), pp. 1–58.

[11] R Bedogni et al. “Experimental characterization of HOTNES: A new thermal neutron facility with large homogeneity area”. In: *Nuclear Instruments and Methods in Physics Research Section A: Accelerators, Spectrometers, Detectors and Associated Equipment* 843 (2017), pp. 18–21.

[12] H Schwoerer et al. “Laser-plasma acceleration of quasi-monoenergetic protons from microstructured targets”. In: *Nature* 439.7075 (2006), p. 445.

[13] Stephen P Hatchett et al. “Electron, photon, and ion beams from the relativistic interaction of Petawatt laser pulses with solid targets”. In: *Physics of Plasmas* 7.5 (2000), pp. 2076–2082.

[14] T Esirkepov et al. “Highly efficient relativistic-ion generation in the laser-piston regime”. In: *Physical review letters* 92.17 (2004), p. 175003.

[15] Dan Haberberger et al. “Collisionless shocks in laser-produced plasma generate monoenergetic high-energy proton beams”. In: *Nature Physics* 8.1 (2012), p. 95.

[16] Andreas Henig et al. “Enhanced laser-driven ion acceleration in the relativistic transparency regime”. In: *Physical review letters* 103.4 (2009), p. 045002.

[17] J Fuchs et al. “Laser-driven proton scaling laws and new paths towards energy increase”. In: *Nature physics* 2.1 (2006), p. 48.

[18] K Zeil et al. “The scaling of proton energies in ultrashort pulse laser plasma acceleration”. In: *New Journal of Physics* 12.4 (2010), p. 045015.

[19] NIST PSTAR. “URL http://physics. nist. gov/PhysRefData/Star/Text”. In: *PSTAR. html* ().

[20] J. F Ziegler and al. *SRIM code 2011*.

[21] MB Chadwick et al. “Nucl. Data Sheets 107, 2931 (2006)”. In: *V. NUCLEAR REACTION MECHANISMS* ().

[22] URL: `https://www-nds.iaea.org/exfor/exfor.htm`.

[23] AJ Koning and D Rochman. “TENDL-2009: consistent TALYS-based evaluated nuclear data library including covariance data”. In: *Nuclear Research and Consultancy Group, Petten* (2009).

[24] JM Yang et al. “Neutron production by fast protons from ultraintense laser-plasma interactions”. In: *Journal of applied physics* 96.11 (2004), pp. 6912–6918.

[25] SA Gaillard et al. “Increased laser-accelerated proton energies via direct laser-light-pressure acceleration of electrons in microcone targets a”. In: *Physics of Plasmas* 18.5 (2011), p. 056710.

[26] Satyabrata Kar et al. “Guided post-acceleration of laser-driven ions by a miniature modular structure”. In: *Nature communications* 7 (2016).

[27] Eugene Laurence Clark. “Measurements of energetic particles from ultraintense laser plasma interactions”. PhD thesis. University of London, 2002.

[28] JS Green et al. “High efficiency proton beam generation through target thickness control in femtosecond laser-plasma interactions”. In: *Applied Physics Letters* 104.21 (2014), p. 214101.

[29] Ishay Pomerantz et al. “Ultrashort pulsed neutron source”. In: *Physical review letters* 113.18 (2014), p. 184801.

[30] Wei Lu et al. “Generating multi-GeV electron bunches using single stage laser wakefield acceleration in a 3D nonlinear regime”. In: *Physical Review Special Topics-Accelerators and Beams* 10.6 (2007), p. 061301.

[31] Ulrich Schramm et al. “First results with the novel petawatt laser acceleration facility in Dresden”. In: 874.1 (2017), p. 012028.

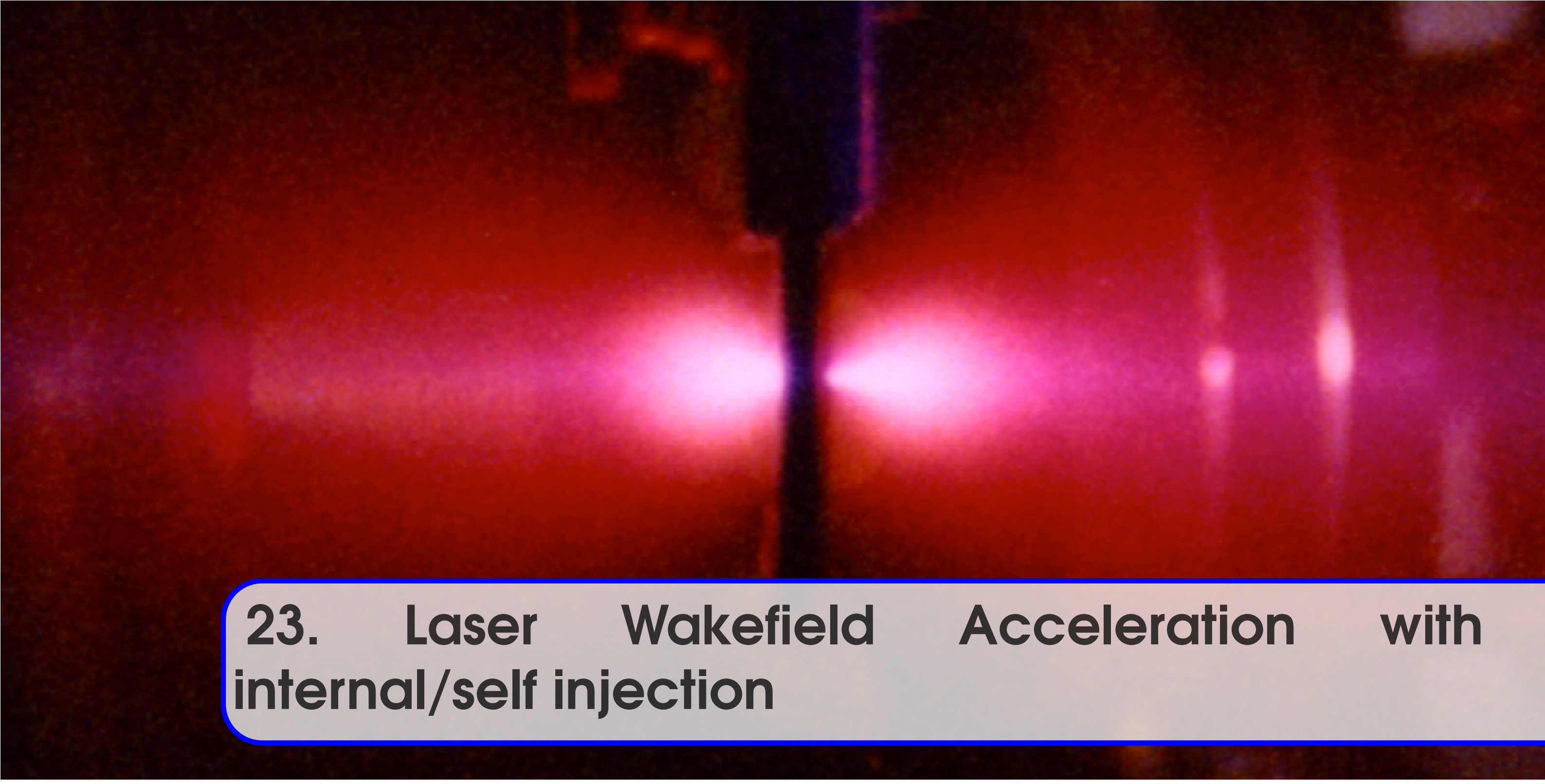

23. Laser Wakefield Acceleration with internal/self injection

23.1 High Quality LWFA development

EuPRAXIA@SPARC_LAB will be a leading facility in the field of plasma acceleration. In view of this, following the strategy of EuPRAXIA, we will also include developments based on the most advanced schemes of laser driven acceleration with internal injection currently available that promise to reach required specifications for novel source developments, including high brightness Thomson scattering and X-ray FEL operation. This will be done in collaboration with CNR-INO (Pisa) that has a long term collaboration with LNF on laser-driven plasma acceleration [1–5], has an established on-going program at the ILIL-PW Laser Facility on the development of new concepts for high quality acceleration based on internal injection. CNR-INO also has a leading role in the EuPRAXIA laser development aimed at the definition of a novel design of a high repetition rate PW scale laser and collaborates on the FLAME laser upgrade at EuPRAXIA@SPARC_LAB. CNR-INO in particular will take care of the full modeling of the acceleration scheme, the development of the required laser specifications and the experimental demonstration at the ILIL-PW facility in Pisa. Once established and demonstrated at the required performances, the set up will be implemented at EuPRAXIA@SPARC_LAB. This approach based on a collaborative effort of the ILIL-PW facility widens the R&D capabilities required to complete the facility and will enable parallel developments on laser based activities, effectively increasing dedicated laser beam time.

As discussed in details below, our strategy for the development of a laser-driven GeV scale accelerator relies on the most advanced concepts of LWFA with fine control of electron phase space properties, combining a set of concepts and tools that are now sufficiently established to allow a full system to be designed to reach the specifications required for the current EuPRAXIA objectives. These include the laser driver, the accelerator set up, namely the plasma target, the wakefield excitation mechanism, the injection scheme, and the overall control systems to enable and monitor the operation.

In the proposed scheme, laser wakefield acceleration is implemented separating the wakefield excitation from the electron injection to enhance and control the quality of the accelerated electron bunch. In this approach, a major role is played by the combination of required laser pulses set to optimize both wakefield excitation and injection. A range of techniques has already been explored and is undergoing experimental validation at ILIL-PW and is part of the present design. Of key importance is the modeling of the proposed scheme that has been developed during the past 18 months and is now established and provides a detailed list of parameters that match the EuPRAXIA requirements parameter table to a great extent. In the following a detailed description of the acceleration scheme is given.

23.2 A new low emittance self-injection scheme for LWFA

A new self-injection scheme *The Resonant Multi-Pulse Ionization injection (ReMPI)* for Laser Driven Wakefield Accelerators, aiming at generating bunches with tunable duration and normalized emittances as low as 80-100 nm, has been recently proposed [6–8]. Though the scheme has been initially developed as a bunch-injector, it can be successfully employed as the core of a a single injector-accelerator device generating >1 GeV ultrashort high-brilliant electron bunches with peak current in the kA scale [8].

The Resonant Multi-Pulse Ionization injection has the possibility to be operating with present-day *single* Ti:Sa laser systems. Simulations show that such a scheme is capable of generating ultra-low emittance GeV-scale bunches with easily tunable length and final energy.

In the ReMPI scheme (see Fig. 23.1) only one short-wavelength laser system (e.g. a Ti:Sa) is needed. The long wavelength driving pulse of the two-color scheme [9] is replaced by a short wavelength, resonant multi-pulse laser driver. Such a driver can be obtained via temporal shaping techniques from the *single*, linearly polarized, standard CPA laser pulse, while the minor fraction of the Ti:Sa CPA pulse is frequency doubled and used as an ionizing pulse.

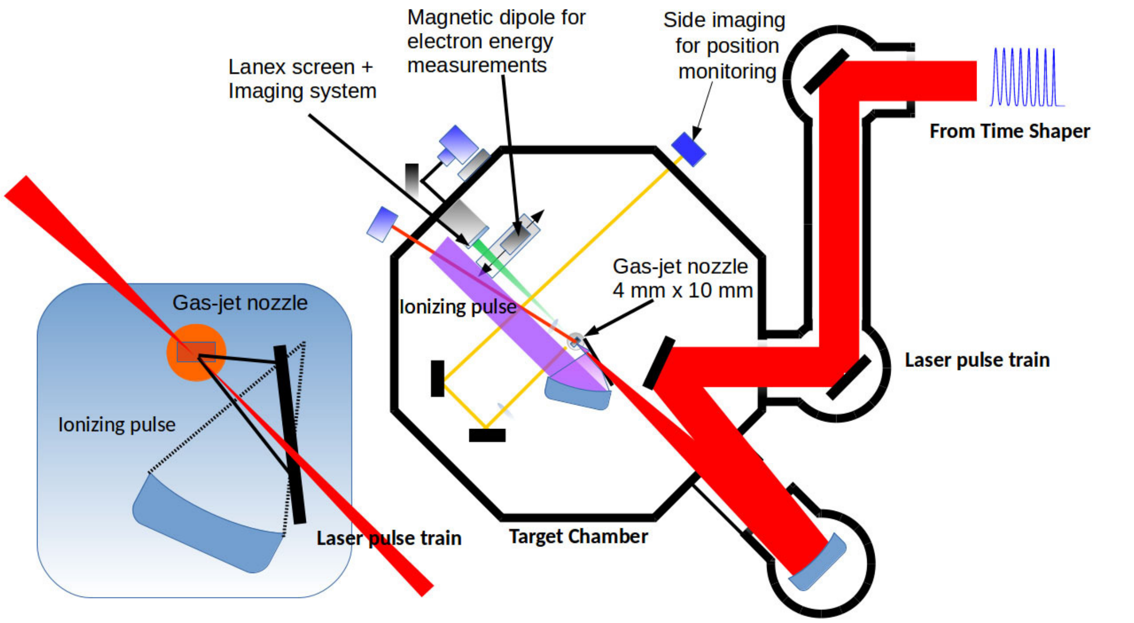

Figure 23.1: Multi-Pulse ionization injection scheme. A small fraction of a single Ti:Sa laser pulse is frequency doubled and, after focusing with a low F/# paraboloid, will constitute the ionizing pulse. The main portion of the pulse is temporally shaped as a train of resonant pulses that will drive a large amplitude plasma wave. Inset: the ionizing pulse focusing is achieved by using a mirror with a hole for the driving pulse passage.

Due to the resonant enhancement of the ponderomotive force, a properly tuned train of pulses is capable of driving amplitude waves larger than a single pulse with the same energy [10, 11]. Noticeably, since the peak intensity of the driver is reduced by a factor equal to the number of train pulses, it is also possible to match the conditions of *both* particle trapping and unsaturated ionization (i.e. with low ionization percentage) of the active atoms level. Recently [12] new experimental results on the generation of such a time shaped pulses demonstrate that a multi pulse scheme is obtainable with present day technology and that plasma waves can be excited with this scheme [13]. Using Argon ($Ar^{8+} \to Ar^{9+}$ with ionization potential $U_I = 422.5$ eV) as a dopant gives us the possibility to obtain bunches with tens of nm rad of normalized emittance. Multi-pulse ionization injection with Argon requires trains with more than four pulses since ionization level is saturated with amplitude above $a_0 = 0.8$ at $\lambda = 0.8$ μm (see Fig. 3 in [6]).

As an example of self-injection and GeV acceleration in a single stage we report on a long acceleration length (of about 4 cm) simulation performed in a 2D cylindrical geometry with QFluid [14] (see also the Appendix in [6]). The Ti:Sa laser system generates pulses that will pass through a beam splitter. The major portion of each pulse is time shaped as a train of resonant eight sub-pulses having FWHM duration of $T = 30$ fs each, with peak power of 200/8 TW. The driving train is subsequently focused down to a spot of $w_0 = 45$ μm waist onto a capillary filled with Argon, obtaining a sequence of pulses with peak intensity and normalized amplitude of $I = 7.9 \times 10^{17}$ W/cm^2 and $a_0 = 0.6$, respectively. The frequency doubled pulse from the minor portion of the Ti:Sa pulse delivers 13 mJ and is focused with a minimum waist of $w_{0,ion} = 3.6$ μm. On-axis plasma background density is set to $n_{axis} = 5 \times 10^{17}$ cm^{-3} and is obtained by assuming full ionization of Argon up to level eight (ionization potentials of Ar^{n+} are below 144 eV for $n \leq 8$ so Argon ionization up to Ar^{8+} is achieved within the first cycles of the pulse).

To obtain a so long acceleration length pulse guiding technique is necessary since low-density plasmas don't allow for pulse self-guiding at those pulse powers. The driver pulses are focused close to the entrance of the capillary (or gas-cell) and enter into the guide with a matched radius $w_m = w_0$ and radial density profile

$$n_e(r) = n_{axis}\left[1 + \eta \frac{1.1 \cdot 10^{20}}{n_{axis}\, w_0^2}\left(\frac{r}{w_0}\right)^2\right]. \tag{23.1}$$

The η factor accounts for weakly nonlinear corrections and in the case of short pulses ($T << 2\pi/\omega_p$) can be evaluated as [15]

$$\eta \cong 1 - \frac{1}{16}(a_0\, \omega_p\, T)^2 \cdot \left(1 + 4.6 \cdot 10^{-21} n_e\, w_0^2\right), \tag{23.2}$$

which is very close to unity in our simulations.

Simulation has been performed onto a moving cylinder of radius 160 μm, length 430 μm and a resolution in both radial and longitudinal directions of 150 nm. Due to the tight focusing of the ionization pulse that diffracts in a scale $Z_{r,ion} = \pi \times w_{0,ion}^2/\lambda_{ion} \simeq 100$ μm, the bunch population growths and saturates (bunch charging phase) in about 150 μm (see Fig. 23.2, green dots representing the longitudinal phase-space of the bunch in the charging phase) and the extracted bunch is trapped after ≈ 600 μm of propagation of the ionizing pulse (see red dots in Fig. 23.2) in a phase of the bucket intermediate between the weak-trapping and the strong-trapping conditions (see Eqq. 2 and 3 in Ref. [6]).

The driver pulses evolution through the 3.7 cm of plasma shows a twofold behavior. Though peak intensity is remarkably stable (see the black line in Fig. 23.3), and no visible self-steepening occurs (we are well below the threshold for the onset of self-steepening since $a_0\,(cT)\,k_p \approx 0.8$ and according to [16] the growth of self-steepening occurs if $a_0\,(cT)\,k_p > (32\log(2)/(\pi-1))^{1/2} \approx 3.2$) sub-pulses of the rear part of the train propagate in the wake generated by all the preceding pulses, thus being partially exposed to the defocusing effect of the wake. As a final effect, a radial breathing of the rear pulses occurs with possible off-axis maxima of the local intensity, as it is apparent in Fig. 23.4.

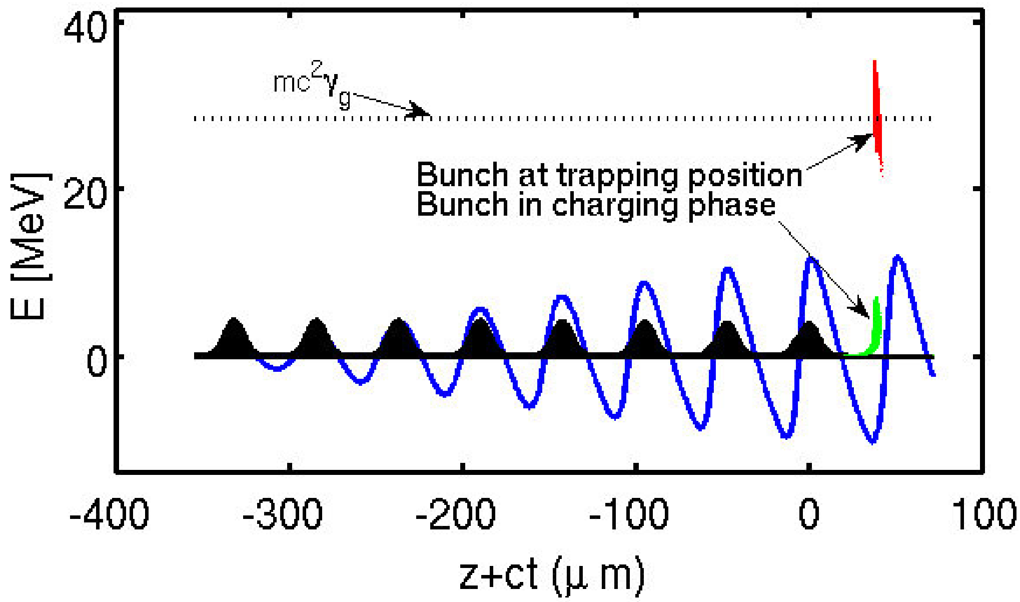

Figure 23.2: Line-out of the longitudinal electric field (blue line, a.u.) and pulse amplitude of the driver train at the early stage of bunch trapping. Green dots show the longitudinal phase space of the bunch after 100 µm of propagation. The horizontal dotted line shows the energy at the trapping point (γ_g is the Lorentz factor of the pulse train) and the red dots represent the longitudinal phase-space of the bunch at the trapping point (i.e. $<\gamma>=\gamma_g$)

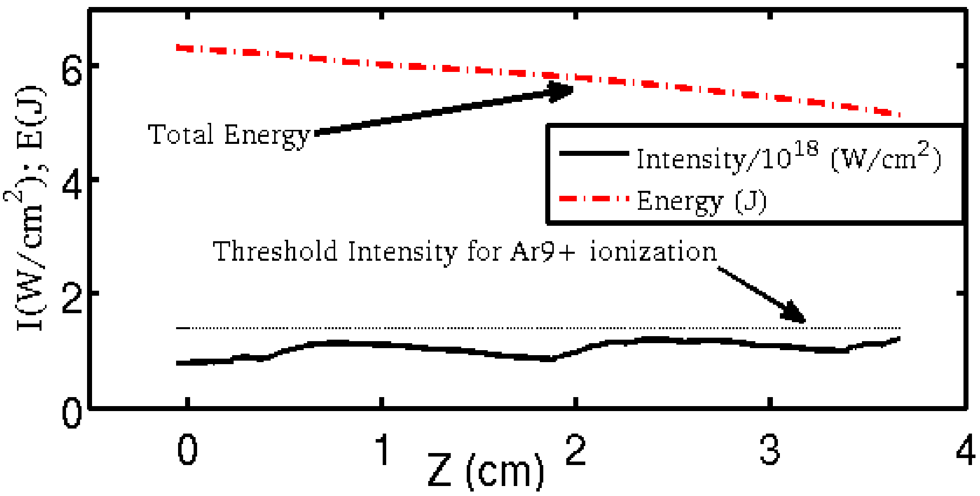

Figure 23.3: Evolution of the total energy (red line) an peak intensity (black line). The horizontal dotted line represents the intensity threshold for further ionization of the 9-th level of Argon.

The final electron bunch of charge 4.3 pC has energy 1.3 GeV, energy spread 0.49% RMS and normalized emittance of 0.08 mm mrad and 0.04 mm mrad in x (laser polarization) and y directions, respectively. After 3.7 cm of propagation the electron bunch is still far from dephasing (see Fig. 23.4) and almost 70 % of laser energy is still available for further energy boost. However, while normalized emittance looks stable in the last 3 cm (see Fig. 23.5) due to the matched-beam configuration, the relative energy spread finds its minimum at 3.7 cm and rapidly increases with further acceleration up to percent level. For high-quality oriented application, therefore, such a earlier truncation of particle acceleration limits the overall energy conversion efficiency of the scheme (at the present working point). We finally stress the remarkably low value of 0.2% for the slice energy spread (with slice thickness of 0.05 μm).

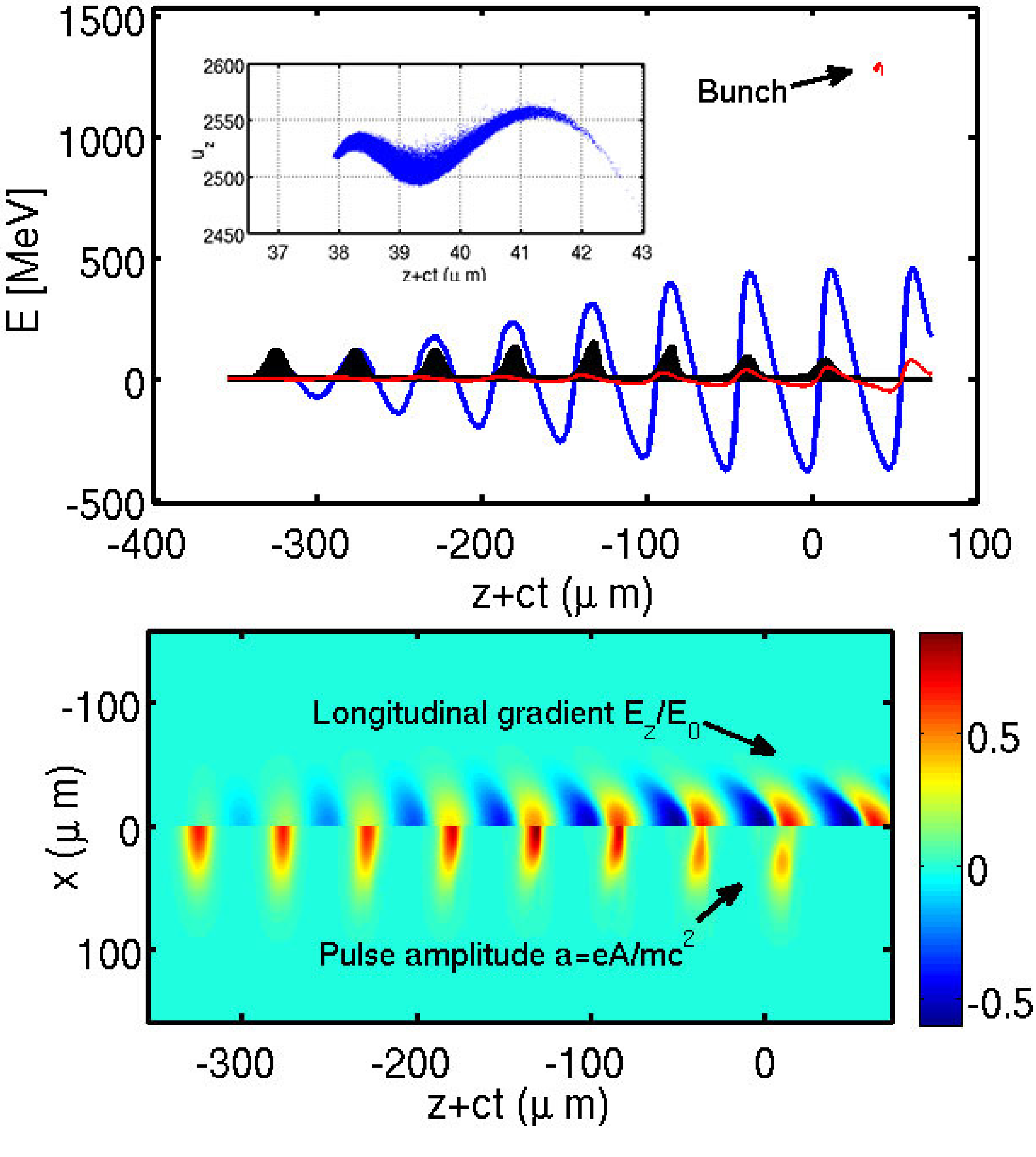

Figure 23.4: Top: longitudinal phase space of the electron bunch after 3.7 cm of propagation (red dots). The blue line shows the electric field on axis (a.u.), while the red line represents the transverse focusing force at a radius close to the beam radius (a.u.). Bottom 2D maps of the longitudinal normalized electric field E_z/E_0 and of the normalized laser amplitude.

The ReMPI scheme uses a single laser system so the driving train and the ionization pulse have no relative timing jitter. This opens the possibility of fine tuning the ionization-to-driver delay according to the requested bunch energy or length. The fine-tuning of the bunch duration is easily obtainable just by selecting the appropriate ionization-to-driver delay t_d. Numerical simulations (supported by theory in 1D) show that the minimum bunch length is obtained when the ionization

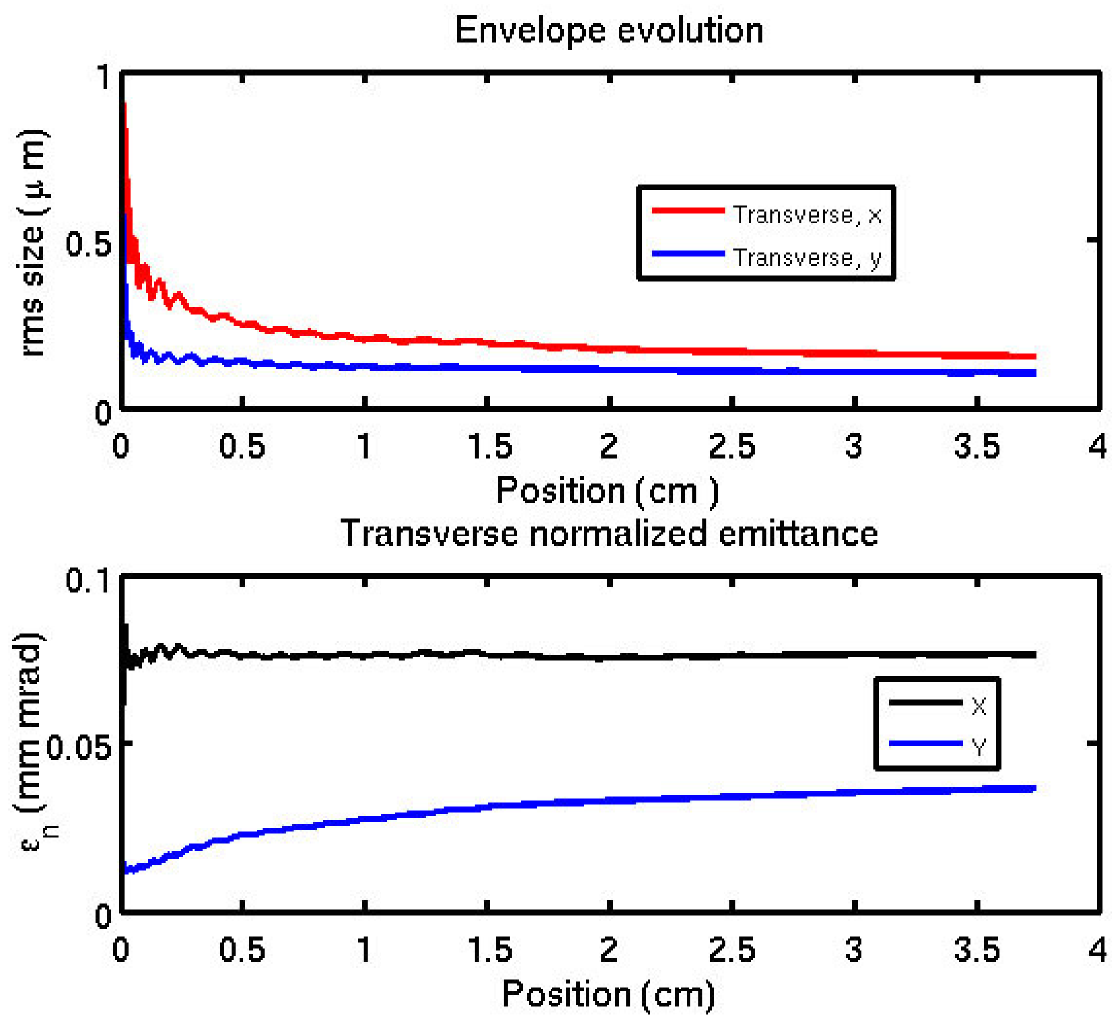

Figure 23.5: Transverse RMS size (top) and normalized emittance (bottom) in x (pulse polarization) and y directions.

pulse is placed at the position of maximum potential (zero longitudinal electric field) and the trapped bunch is placed at the position of maximum accelerating gradient (i.e. exactly at the strong-trapping point). Starting from that configuration and further delaying the ionization pulse, the final bunch length increases. The fulfillment of the weak-trapping condition for the whole set of bunch electrons makes an upper limit of the bunch duration. Both the minimum and maximum obtainable values depend on the working point. In the current setup bunch lengths that can be obtained by simply delaying the ionization pulse are in the range 360 as $< t_{RMS} <$ 2.2 fs. Optimization of the bunch length/energy tuning strategy is ongoing [17].

We employed the new ReMPI scheme to (numerically) generate a 1.3 GeV electron bunch with outstanding quality ($\sigma_E/E|_{\text{slice}} = 0.22\,\%$, $\varepsilon_n = 80$ nm and compactness by using a single Ti:Sa laser system and a preformed plasma channel of length 3.7 cm.

23.3 5GeV FEL-compliant quality electron beam for EuPRAXIA

A possible working point for an high-current 5GeV bunch satisfying EuPRAXIA requirement for FEL lasing ($\sigma_E/E|_{\text{slice}} = 0.1\%$, $\varepsilon_n < 1$ mm mrad , $I_{\text{peak}} \geq 2$ kA) uses a simplified experimental scheme with four pulses (instead of eight) and Nitrogen (instead of Argon). The final electron beam, therefore, will have good transverse phase-space quality though not as good as the ReMPI scheme could produce.

In the simulation a train of *four pulses*, each of duration T=45 fs, delivering 4.95 J of energy and waist $w_0 = 65$ μm, is focused on a capillary filled with Nitrogen. Due to the ASE and picosecond prepulses Nitrogen is expected to be pre-ionized up to level five, generating a plasma density of $n_0 = 2.5 \times 10^{17}$ cm^{-3}. Moreover, refractive guiding with plasma parabolic profile is assumed as in the 1 GeV simulation.

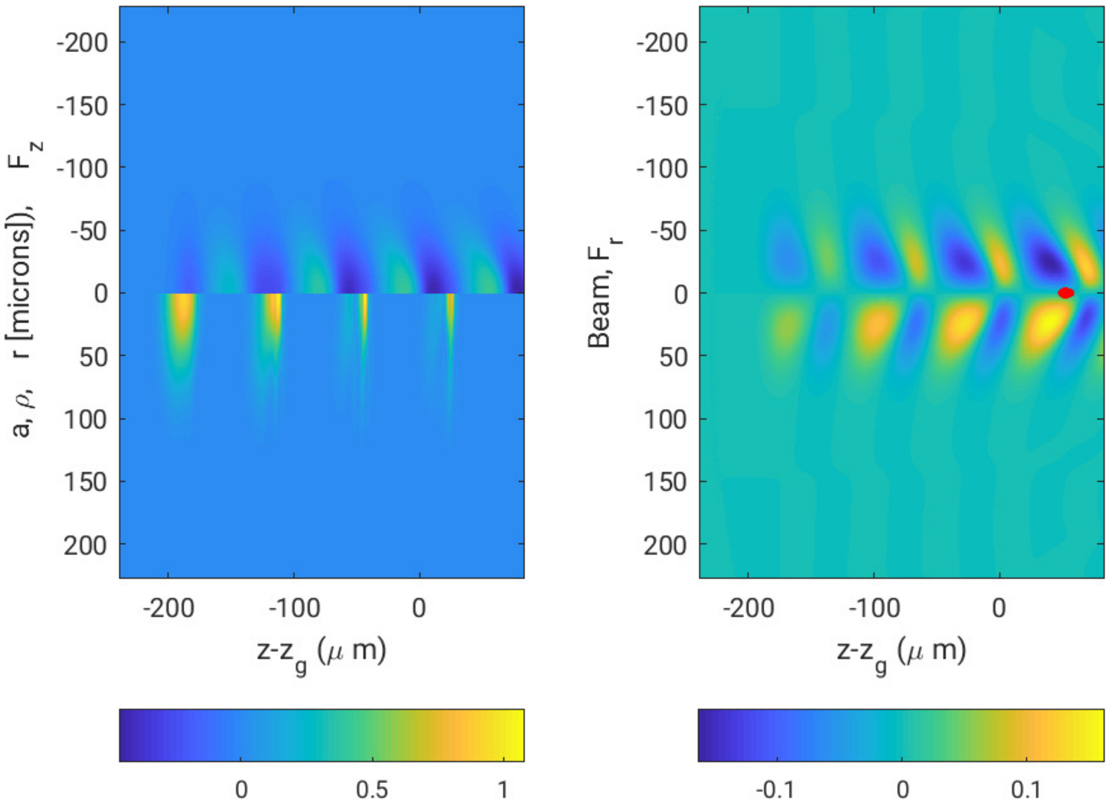

Figure 23.6: 2D maps just before plasma exit. Left: E_z/E_0 (upper) and amplitude (lower). Right: transverse force $(E_r + B_\phi)/E_0$. Red points represent bunch particles.

The simulation cylinder was 322 μm long with radius of 227 μm, with resolution of 0.38 μm in both directions, though *QFluid4.5 uses a mesh refinement in the cylinder slice occupied by the bunch* with a fine mesh of 0.04 μm and 0.2 μm in the longitudinal and transverse directions.

The injection-acceleration phases last about 16 cm, after which laser pulses deplete. In Fig. 23.7 the 2D maps of the longitudinal and transverse forces, as well as the pulses amplitudes just prior the plasma exit, are shown.

The final beam quality is mostly limited by beam loading effects. Tuning the parameters so as loaded longitudinal field is roughly flat on the bunch (see Fig. 23.8) causes an unwanted transverse gradient of the field which is, in turn, related to the minimum achievable slice energy spread.

Slice analysis (see Fig. 23.8) of the bunch just after plasma exit with a 600 μm ramp shows that the 3 kA bunch seems to comply with the EuPRAXIA requirements, being the slice energy spread (robust MAD analysis) of 0.15% at peak current and slice emittance 0.4 mm mrad, i.e. less than half the EuPRAXIA requirement.

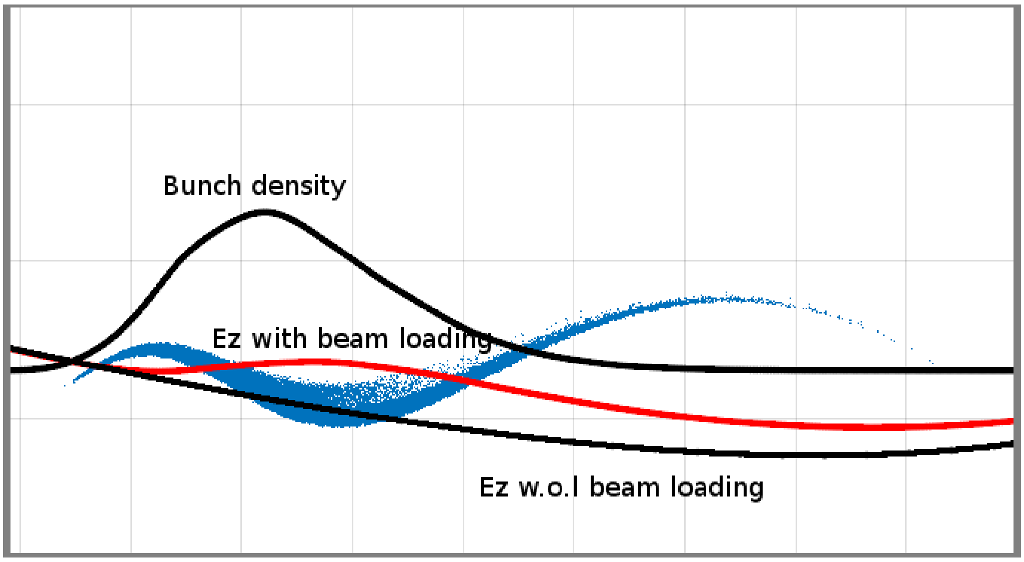

Figure 23.7: Bunch particles, loaded (red)/unloaded(black) accelerating fields on axis and bunch density on axis.

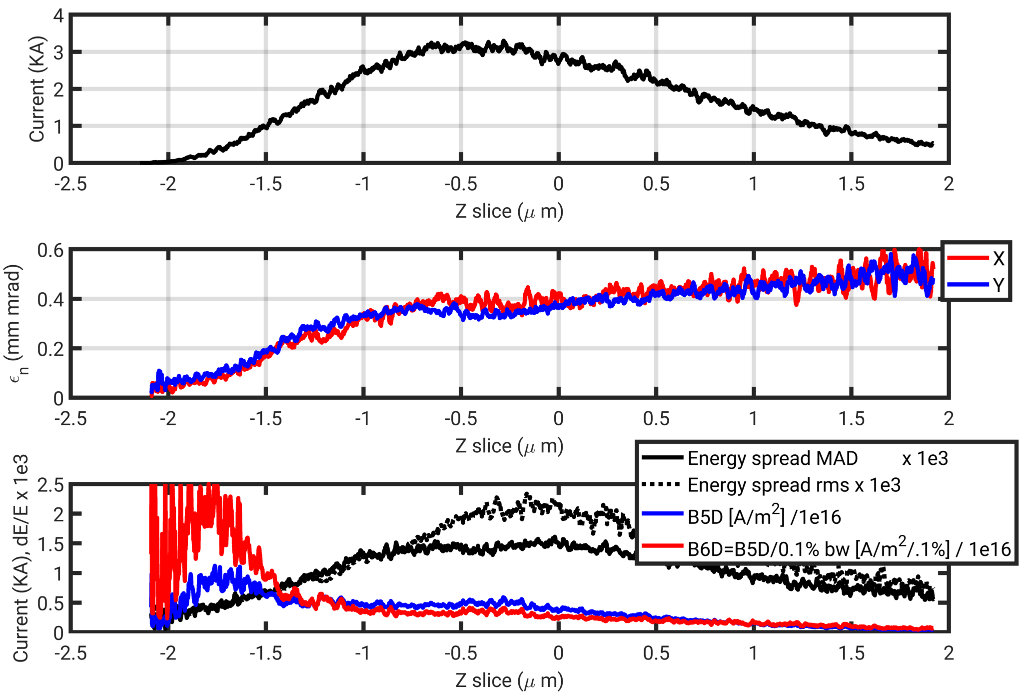

Figure 23.8: Slice analysis of the final beam with slice thickness of 20 nm. Upper: Current. Middle: Emittance. Lower: Robust (MAD) energy spread (black line), RMS energy spread (dotted), Brilliance 5D (blue) and Brilliance 6D (red)

23.4 ILIL-PW laser facility

The proposed scheme will be validated at the ILIL-PW Ti:Sa laser and interaction facility. The laser installation features a >200 TW laser system, a beam transport line and a multi-purpose interaction area with radiation shielding. An overview of the ILIL-PW facility is shown in Figure 23.9. In the 10 Hz front-end, the oscillator producing 15 fs pulses at approximately 6 nJ, is boosted to the 10 µJ and stretched to a chirped pulse of 600 ps duration to feed the regenerative amplifier.

The output mJ energy pulse is further amplified by a 5-pass amplifier followed by a 4-pass amplifier, finally delivering 600 mJ at 800 nm. In the final configuration the output pulses of the front-end are then transported to the final 4-pass amplifier, pumped by 4 Nd:YAG lasers (Titan6 by Amplitude Technologies) delivering a total of 24 J pulses at 532 nm at a maximum rep-rate of 5 Hz.

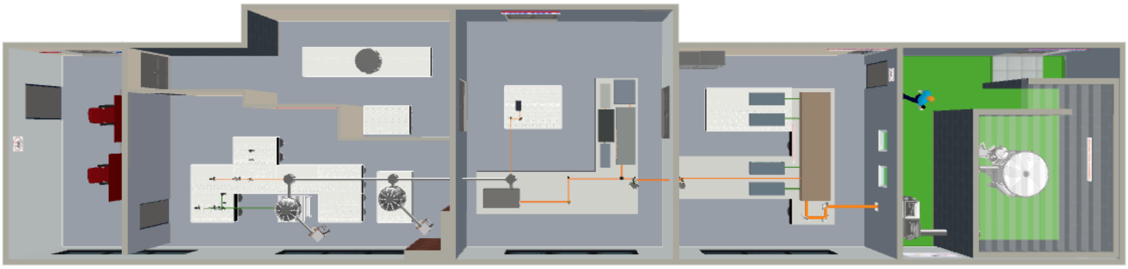

Figure 23.9: Schematic view of the ILIL-PW facility at CNR-INO, including (from left) the control room, the test experimental area, the laser front end room, the amplifier room and the shielded target area.

The 800 nm pulse is thus amplified up to >7 J and compressed down to <25 fs. Pulse duration control is achieved through standard techniques based on acousto-optical devices placed in the front end to achieve control of spectral gain, phase and amplitude. The pulse energy losses due to acousto-optics devices are compensated in the amplification stages. Pump fluence throughout the front-end system is kept below 1 J/cm^2 to operate well below the Ti:Sa crystal damage threshold, yielding a typical energy extraction efficiency of less than 30%. The compressed pulse is then transported under vacuum to the octagonal interaction chamber via two remotely controlled, beam steering chambers.

For the laser-plasma acceleration experiments the beam is focused on target by an F/15 off-axis parabolic mirror to an intensity in excess of 10^{20} W/cm^2. The interaction chamber is equipped with a remotely controlled motorized gas target mount with a sub-micrometer resolution capable of XYZ translation and azimuthal rotation around the vertical axis.

23.5 ReEMPI laser architecture

The ReMPI injection scheme uses currently available laser technology based on Ti:Sa, with only relatively easy beam manipulations. A single 100 TW-scale Ti:Sa laser pulse at 800 nm wavelength is modified by a time-shaping (e.g. multiplexing) device, based on known techniques that turn a single pulse into a train of pulses. In a recent study we also investigated the possibility of using a phase mask to generate pulse trains more efficiently and directly in the far field of the focusing optics to enable on line operation. It is worth mentioning that, in general, the relative timing between the different pulses and, in particular, between the ionization pulse and the driver train, is quite critical and should be controlled to the sub-10 fs level to inject electrons always in the same position of the wake field. In our scheme, the use of a single laser source ensures that no intrinsic jitter between the two pulses is present, thus limiting the fluctuations on the final bunch energy and duration.

Bibliography

[1] L A Gizzi et al. "Laser-plasma acceleration with self-injection: A test experiment for the sub-PW FLAME laser system at LNF-Frascati". In: *Il Nuovo cimento C* 32.3 (2009), p. 433.

[2] T Levato et al. "First electrons from the new 220 tw frascati laser for acceleration and multidisciplinary experiments (FLAME) at frascati national laboratories (LNF)". In: *Nuclear Instruments and Methods in Physics Research A* 720 (2013), pp. 95–99.

[3] L A Gizzi et al. "Acceleration with self-injection for an all-optical radiation source at LNF". In: *Nuclear Instruments and Methods in Physics Research B* 309 (2013), pp. 202–209.

[4] Leonida Antonio Gizzi et al. "Laser-plasma acceleration with FLAME and ILIL ultraintense lasers". In: *Applied Sciences* 3.3 (2013), pp. 559–580.

[5] G Grittani et al. "High energy electrons from interaction with a structured gas-jet at FLAME". In: *Nuclear Instruments and Methods in Physics Research A* 740 (2014), pp. 257–265.

[6] Paolo Tomassini et al. "The resonant multi-pulse ionization injection". In: *Physics of Plasmas* 24.10 (2017), p. 103120.

[7] Paolo Tomassini et al. "High-quality electron bunch production for high-brilliance Thomson Scattering sources". In: *Proceedings of the SPIE* 10240 (2017), 102400T.

[8] P Tomassini et al. "High-quality GeV-scale electron bunches with the Resonant Multi-Pulse Ionization Injection". In: *Nuclear Instruments and Methods in Physics Research A* (2018), in press.

[9] L-L Yu et al. "Two-color laser-ionization injection". In: *Phys. Rev. Lett.* 112.12 (2014), p. 125001.

[10] Donald Umstadter, Eric Esarey, and J Kim. "Nonlinear plasma waves resonantly driven by optimized laser pulse trains". In: *Phys. Rev. Lett.* 72.8 (1994), p. 1224.

[11] S M Hooker et al. "Multi-pulse laser wakefield acceleration: a new route to efficient, high-repetition-rate plasma accelerators and high flux radiation sources". In: *J. Phys. B* 47.23 (2014), p. 234003.

[12] R J Shalloo et al. "Generation of laser pulse trains for tests of multi-pulse laser wakefield acceleration". In: *Nuclear Instruments and Methods in Physics Research A* 829 (2016), pp. 383–385.

[13] James Cowley et al. "Excitation and control of plasma wakefields by multiple laser pulses". In: *Phys. Rev. Lett.* 119.4 (2017), p. 044802.

[14] P Tomassini and A R Rossi. "Matching strategies for a plasma booster". In: *Plasma Phys. and Control. Fusion* 58.3 (2015), p. 034001.

[15] W. Lu et al. "Generating multi-GeV electron bunches using single stage laser wakefield acceleration in a 3D nonlinear regime". In: *Phys. Rev. ST Accel. Beams* 10.6 (2007), p. 061301.

[16] J Vieira et al. "Onset of self-steepening of intense laser pulses in plasmas". In: *New Journal of Physics* 12.4 (2010), p. 045025.

[17] P. Tomassini et al. in preparation.

24. Support Letters

ORGANISATION EUROPÉENNE POUR LA RECHERCHE NUCLÉAIRE
CERN EUROPEAN ORGANIZATION FOR NUCLEAR RESEARCH

GENEVE, SUISSE
GENEVA, SWITZERLAND

Mail address: **CERN ATS-DO**
CLIC Project Office
CH-1211 GENEVE 23
Switzerland

Téléphone/Telephone :
Direct : +41 22 767 3706
Central/Exchange : +41 22 767 6111

E-mail : steinar.stapnes@cern.ch

Votre référence/Your reference:
Notre référence/Our reference:

Dr Pierluigi Campana
Director
INFN
Via Enrico Fermi 40
00044 Frascati RM
Italy

Geneva, 23 June 2017

Dear Dr Campana,

We wish to provide our very strong support for the EuSPARC project being proposed by INFN Frascati. We sincerely believe that this is an excellent choice for the future of the laboratory.
It is also very important for the CERN and the CLIC collaboration. We have discussed with INFN leaders and elaborated a mutually beneficial program of exchange of hardware and staff to advance both the EuSPARC and CLIC projects.

One of the key areas of the CLIC is the high-gradient, X-band radio frequency accelerator of the main linac. Significant resources have been invested to develop the necessary technology and considerable progress has been made and demonstrated by testing prototype systems in test stands at CERN. The EuSPARC proposal is an opportunity to now implement this accelerator technology on a much larger scale than is possible in our test facilities. EuSPARC will provide important benefits for high-gradient X-band technology including industrialization, larger-scale series production and long-term user operation.

For these reasons, we have identified an initial set of collaboration activities. At the core is the loan to Frascati of a 50 MW X-band klystron in order to jointly set up a local high-gradient testing facility. INFN would complete the test stand including the modulator and supporting infrastructure and then carry out high-gradient testing. Preparation for the test stand in Frascati would involve training INFN staff at CERN on the existing test stands. The experts would return to Frascati to build and operate the test stand there, experience which is directly applicable to EuSPARC linac. Overall this would be part of the strategy to introduce this innovative accelerator technology which will become a core component of the EuSPARC facility.

EuSPARC, with its high-gradient accelerator and very low emittance beam, will in the longer term provide a unique and important opportunity for the CLIC study for beam testing. This includes experiments and tests in a number of areas including beam dynamics, rf systems and beam instrumentation. Finally, the Frascati-based test stand and then the EuSPARC facility will provide important continuity for a long-standing and very productive collaboration which extends back to the early days of CTF3.

Sincerely,

Prof. Steinar Stapnes
CERN Linear Collider Study Leader

Dr Walter Wuensch
CLIC X-Band Activity Leader

Elettra Sincrotrone Trieste

LETTERA DI INTERESSE

Alla cortese attenzione di

Massimo Ferrario
Istituto Nazionale di Fisica Nucleare (INFN)
Laboratori Nazionali di Frascati
Via E. Fermi 40
00044 Frascati (RM)

Oggetto: Espressione di interesse all'iniziativa EuPRAXIA@SPARC_LAB

Il Free Electron Laser (FEL) FERMI è una macchina di luce di quarta generazione attualmente in *commissioning* con utenti esterni presso il laboratorio Elettra Sincrotrone Trieste (di seguito *"Elettra"*). FERMI è stato sviluppato per fornire impulsi di luce ultracorti (10-100 femtosecondi) e con una brillanza 10 miliardi di volte superiore a quella disponibile con macchine di luce di terza generazione.

FERMI ha raggiunto i valori di specifica, producendo fotoni con energie superiori a 300 electronVolt (eV). Tuttavia, esiste una forte motivazione scientifica ad estendere la massima energia dei fotoni prodotti fino ad almeno 600 eV, in modo da poter investigare con FERMI tutta la cosiddetta "*water window*".

Per raggiungere questo risultato, sono necessari sviluppi sia nel campo dell'accelerazione del fascio di elettroni che negli ondulatori che generano il FEL; di particolare interesse a tal fine risultano essere per Elettra le ricerche nel campo delle sorgenti FEL compatte.

Elettra - Sincrotrone Trieste S.C.p.A.
S.S. 14 Km 163,5 in Area Science Park
34149 Basovizza, Trieste, Italy
T. +39 040 37581
F. +39 040 938 0903

P.IVA e C.F. IT00697920320
Cap. Soc. € 47.632.663,00 i.v.
PEC: sincrotrone.trieste.elettra@legalmail.it
www.elettra.eu

Iscritta al Registro delle Imprese di Trieste
Società di interesse nazionale
ai sensi dell'art. 10, comma 4,
L. 19 ottobre 1999 n. 370

Elettra Sincrotrone Trieste

Inoltre, presso Elettra si sono sviluppate competenze specifiche su schemi FEL innovativi, inclusi nuovi concetti di ondulatori, come pure sulle linee di luce per il trasporto, la manipolazione e la diagnostica di impulsi FEL.
Infine, Elettra è il coordinatore del progetto europeo *CompactLight*, recentemente finanziato nell'ambito di Horizon 2020, di cui INFN è partner, e assieme a INFN risulta partner anche nella collaborazione europea *FELs of Europe*, che ha l'obiettivo di perseguire e sviluppare le sfide tecnico-scientifiche poste da questa tecnologia innovativa e in rapido sviluppo.

L'iniziativa EuPRAXIA@SPARC_LAB è valutata, quindi, di grande rilevanza scientifica per Elettra, che la considera sinergica con le proprie attività di ricerca.

Con la presente lettera Elettra intende esprimere, perciò, il proprio interesse a collaborare con INFN alla preparazione del TDR di EuPRAXIA@SPARC_LAB, con particolare attenzione allo sviluppo del linac in banda X, alla concezione di ondulatori compatti, allo studio degli schemi FEL più adatti allo scopo e alla progettazione delle relative linee di luce. Allo scopo di favorire la collaborazione con INFN in questi campi, Elettra potrà rendersi disponibile ad ospitare giovani ricercatori per brevi periodi di training.

Cordiali saluti

Il Presidente e Amministratore Delegato
Prof. Alfonso Franciosi

Trieste, 21/09/2017

Elettra - Sincrotrone Trieste S.C.p.A.
S.S. 14 Km 163,5 in Area Science Park
34149 Basovizza, Trieste, Italy
T. +39 040 37581
F. +39 040 938 0903

P.IVA e C.F. IT00697920320
Cap. Soc. € 47.632.663,00 i.v.
PEC: sincrotrone.trieste.elettra@legalmail.it
www.elettra.eu

Iscritta al Registro delle Imprese di Trieste
Società di interesse nazionale
ai sensi dell'art. 10, comma 4,
L. 19 ottobre 1999 n. 370

Funded by the European Union

Compact

EuSPARC (European Source for Plasma Accelerators and Radiation user Communities)

I am writing this letter on behalf of the CompactLight (XLS) Collaboration, in strong support of the EuSPARC initiative at INFN-LNF.

CompactLight is an International Collaboration, led by Elettra – Sincrotrone Trieste, that brings together 21 leading European Institutions, accelerator and light source laboratories, universities, and industries, together with 3 non-European Institutes, aimed to design an hard X-ray FEL Facility beyond today's state of the art, using the latest concepts for bright electron photo injectors, very high-gradient X-band structures operating at 12 GHz, and innovative compact short-period undulators. The objective is to facilitate the widespread development of X-ray FEL facilities across Europe and beyond, by making them more affordable to construct and operate through an optimum combination of emerging and innovative accelerator technologies.

INFN is currently investigating the possibility to design and build a new multi-disciplinary user-facility, EuSPARC, equipped with a soft X-ray Free Electron Laser (FEL) driven by a ~1 GeV high brightness electron linac based on X-band RF technology. The facility is conceived as an innovative and evolutionary tool for investigations in a wide field of scientific, technological and industrial applications. EuSPARC in its final stage will be a "particle beams factory", based on a combination of a new compact X-band high brightness electron linac and of a high power (~300 TW) laser, already available in Frascati. It will be able to produce high quality beams of electrons, photons (from THz to Compton backscattered ?-rays), protons and eventually positrons, neutrons and muons that will be available for a wide national and international scientific community interested to take profit of advanced particle and radiation sources.

EuSPARC will also address investigations on advanced accelerator techniques such as plasma accelerators, towards the realization of a plasma driven future Linear Collider (LC), with the integration of the new high gradient accelerating plasma modules in a short wavelength Free Electron Laser user facility (see for example the approved Design Study "European Plasma Research Accelerator with eXcellence In Applications" EuPRAXIA (INFRADEV-1-2014).

The capability of producing the required high quality beams and the operational reliability of the plasma accelerator modules will be certified when such an advanced FEL radiation source will be able to drive external user experiments. This fundamental goal will be integrated in the EuSPARC facility by using the proposed X-band linac to drive Plasma Oscillations in the so called Particle-driven Wake Field Acceleration (PWFA) scheme, in the EuPRAXIA@SPARC_LAB beam line.

The aims of EuSPARC are strongly aligned to those of CompactLight and so we are very supportive of this initiative.

Yours sincerely

Dr. Gerardo D'Auria

Chair of the XLS Collaboration Board